Vol. 161, July 1, 1984
Complete in one issue

ISSN 0003-2670

ANALYTICA CHIMICA ACTA

International journal devoted to all branches of analytical chemistry

ELSEVIER

ANALYTICA CHIMICA ACTA

International journal devoted to all branches of analytical chemistry
Revue internationale consacrée à tous les domaines de la chimie analytique
Internationale Zeitschrift für alle Gebiete der analytischen Chemie

PUBLICATION SCHEDULE FOR 1984

	J	F	M	A	M	J	J	A	S	O	N	D
Analytica Chimica Acta	156	157/1	157/2	158/1 158/2	159	160	161	162	163	164	165	166

Scope. *Analytica Chimica Acta* publishes original papers, short communications, and reviews dealing with eve aspect of modern chemical analysis, both fundamental and applied.

Submission of Papers. Manuscripts (three copies) should be submitted as designated below for rapid and efficie handling:

Papers from the Americas to: Professor Harry L. Pardue, Department of Chemistry, Purdue University, West Lafayett IN 47907, U.S.A.

Papers from all other countries to: Dr. A. M. G. Macdonald, Department of Chemistry, The University, P.O. Box 36 Birmingham B15 2TT, England. Papers dealing particularly with computer techniques to: Professor J. T. Cle Universität Bern, Pharmazeutisches Institut, Baltzerstrasse 5, CH-3012 Bern, Switzerland.

Submission of an article is understood to imply that the article is original and unpublished and is not being consider for publication elsewhere. Upon acceptance of an article by the journal, authors will be asked to transfer the copyrig of the article to the publisher. This transfer will ensure the widest possible dissemination of information.

Information for Authors. Papers in English, French and German are published. There are no page charge Manuscripts should conform in layout and style to the papers published in this Volume. Authors should cons Vol. 160 for detailed information. Reprints of this information are available from the Editors or from: Elsevier Editori Services Ltd., Mayfield House, 256 Banbury Road, Oxford OX2 7DH (Great Britain).

Reprints. Fifty reprints will be supplied free of charge. Additional reprints (minimum 100) can be ordered. An ord form containing price quotations will be sent to the authors together with the proofs of their article.

Advertisements. Advertisement rates are available from the publisher.

Subscriptions. Subscriptions should be sent to: Elsevier Science Publishers B.V., Journals Department, P.O. B 211, 1000 AE Amsterdam, The Netherlands. Tel: 5803 911, Telex: 18582.

Publication. *Analytica Chimica Acta* appears in 11 volumes in 1984. The subscription for 1984 (Vols. 156–166) Dfl. 2145.00 plus Dfl. 231.00 (p.p.h.) (total approx. U.S. $914.00). All earlier volumes (Vols. 1–155) except Vols. 2 and 28 are available at Dfl. 215.00 (U.S. $82.70), plus Dfl. 15.00 (U.S. $6.00) p.p.h., per volume.

Our p.p.h. (postage, packing and handling) charge includes surface delivery of all issues, except to subscribers Australia, Brazil, Canada, China, Hong Kong, India, Israel, Japan, Malaysia, New Zealand, Pakistan, Singapore, Sou Africa, South Korea, Taiwan and the U.S.A. who receive all issues by air delivery (S.A.L. — Surface Air Lifted) at extra cost. For the rest of the world, airmail and S.A.L. charges are available upon request.

Claims for issues not received should be made within three months of publication of the issues. If not they cannot honoured free of charge.

For further information, or a free sample copy of this or any other Elsevier Science Publishers journal, readers in t U.S.A. and Canada can contact the following address: Elsevier Science Publishing Co., Inc., Journal Informati Center, 52 Vanderbilt Avenue, New York, NY 10017, U.S.A., Tel: (212) 867-9040.

ANALYTICA CHIMICA ACTA
VOL. 161 (1984)

ANALYTICA CHIMICA ACTA

International journal devoted to all branches of analytical chemistry

ELSEVIER Amsterdam–Oxford–New York–Tokyo

0003-2670/84/$03.

Printed in The Netherlands

Analytica Chimica Acta, 161 (1984) 1—25
Elsevier Science Publishers B.V., Amsterdam — Printed in The Netherlands

INTEGRATED MICROCONDUITS FOR FLOW INJECTION ANALYSIS

JAROMIR RŮŽIČKA* and ELO H. HANSEN

Chemistry Department A, The Technical University of Denmark, Building 207, 2800 Lyngby (Denmark)

(Received 20th March 1984)

SUMMARY

A novel approach for constructing continuous flow systems for analysis is described and its versatility is demonstrated for a number of flow-injection systems with integrated potentiometric or optical detectors and with integrated gas-diffusion or ion-exchange units. Optimization of the miniaturized designs was achieved by means of scaling factors based on the theory of similarity.

The present work describes a departure from the traditional way of constructing flow-through systems for continuous flow analyses. Flow injection analysis (f.i.a.) [1] is used as an example to illustrate this novel approach and its versatility is demonstrated by means of several designs, which allow one to evaluate the new technology and its impact on the future construction of continuous flow systems. The idea, inspired by the concepts of integrated electronic circuitry, by discussions at the Gordon Conference in 1982, and by designs of gas chromatographs on silicone chips as originated at Stanford University [2], is based on miniaturization and integration of all components of a flow-through manifold into one unit, approximately of the size of a credit card. This means that instead of the individual manifold components (injection unit, mixing coils, dialysis or diffusion units and detectors) being joined by means of flexible tubing and connectors, the whole system of channels is fabricated into a planar surface of a plate, the plate being sufficiently thick to be mechanically stable and to accommodate optical flow cells, electrodes of electrochemical sensors, packed reactors, microcolumns, as well as inlets and outlets by means of which the integrated microconduits can be connected with external sources of liquids. The channels, imprinted or engraved in the planar surface, are sealed by another (thinner) plate, so that the cross-section of the channels is either semicircular or square. The thick and thin plates are bonded together and the resulting microconduits can even be stacked on top of each other to form a multilayered structure. Another attractive feature of this concept is that one or several detectors may be placed in the flow path exactly where desired, whereas in all previous constructions of flow-injection manifolds a compromise between the ideal and what was possible in practice was dictated by the physical size and geometry of the available flow-through detector.

0003-2670/84/$03.00

The development and construction of integrated microconduits was, however, a more complex task than might appear from the straightforward idea outlined above. Two groups of problems, conceptual and technological, were revealed as the work progressed, and although their solution is described separately below, it should be emphasized that it was the interplay of these two groups of problems which was the most difficult to solve, as material properties often imposed constraints on the intended design.

THEORY

Concepts of similarity

Any flow-injection system is built around a flow channel of certain dimensions and geometrical form (usually coiled tubing) and it would therefore seem to be an easy matter to miniaturize it by simply scaling down existing manifolds. The difficulty is that such an approach will not yield microchannels which would behave exactly like macrochannels, because a simple reduction of all dimensions does not produce channels which are physically similar. This may be better understood by briefly reviewing the concept of similarity as applied to fluid mechanics (e.g., [3]). The use of this concept for scaling and modelling of the behaviour of fluids is based on three types of similarities. The simplest, geometric similarity, is similarity of shape, and operates with a scaling factor which is the ratio of any length in one system to the corresponding length in the other system. Yet, when the channel for f.i.a. is miniaturized, perfect geometrical similarity will be impossible to obtain, because the roughness of the walls and other imperfections of the channels cannot be reduced proportionately when the overall dimensions are scaled down. Furthermore, an excessive reduction of the cross-sectional area of the channels is undesirable, because solid particles present in some sample materials (blood, fermentation liquids, etc.) could block a very narrow channel. Finally, since the idea was to imprint or to engrave a channel into a planar surface, rather than to wind a miniaturized coil, the concept of geometric similarity cannot be applied.

Kinematic similarity is similarity of motion and implies geometric similarity together with similar time intervals. Its scaling factors are velocities and accelerations. This would be a useful tool, if flow-injection systems of geometric similarity were available, because kinematic similarity would allow pumping rates to be adjusted. Dynamic similarity is a similarity of forces, which could also comprise a scaling factor; this type of similarity includes geometric and kinematic similarities, thus being a valuable tool for comparison of scaled models (e.g., for aircraft and ships). Outside the field of fluid mechanics, but still involving fluid properties, are thermal similarity which operates through differences in temperatures between model and prototype, and chemical similarity where the fixed ratios of reactants at corresponding points in the flowing streams serve as a scaling factor. Thus, in order for two systems to behave similarly, certain ratios of like magnitudes must be fixed.

Whatever quantities are chosen, the ratio of their magnitudes (i.e., the scaling factor) is dimensionless. Several scaling factors may be needed to describe a complex system like f.i.a., but once identified, they will allow a rational design and comparison of two flow-injection channels regardless of their geometric dissimilarity. To conclude, suitable scaling factors have to be identified and computed, as they will facilitate the design of miniaturized flow-injection systems which will behave similarly to the macrosystems (by yielding the same analytical readout) and yet will be more economical in terms of sample, reagents and space requirements.

Scaling factors

It is now widely recognized that flow injection analysis is based on the combination of three principles: sample injection of solution into an unsegmented carrier stream, controlled dispersion of the sample zone thus formed, and reproducible timing of the movement of the produced concentration gradient through the flow channel and detector.

A simple and practical method for designing a flow-injection system is based on the use of the dispersion coefficient $D = C^0/C$, where C^0 is the original sample concentration prior to injection and C is the concentration of the sample material in that element of fluid of the dispersed sample zone from which the analytical readout is to be obtained. As most f.i.a. methods are based on peak-height measurements, C is normally taken as the concentration of the dispersed sample solution in that element of fluid which corresponds to the peak maximum (C^{max}). The dispersion of sample solution is controllable by choice of sample volume and by geometry of flow and can be classified as limited dispersion (D = 1—3) if the system is to be used merely to transport samples reproducibly into the detector (e.g., for pH measurement); or as medium dispersion (D = 3—10), to provide a suitable mixing ratio between sample and reagent contained in the carrier stream (e.g., for spectrophotometry and chemiluminescence); or as large dispersion ($D > 10$), to be used when sample material has to be extensively diluted prior to measurement.

A response curve in f.i.a. is a result of two processes, the physical dispersion of the sample material in the carrier stream and the chemical reaction(s) forming the species to be measured, thus the dispersion coefficient D is a suitable scaling factor because it describes the ratio of reactants in that element of fluid which is chosen to yield the analytical readout. Because the physical dispersion and the chemical reaction are both kinetic in nature, and because they take place simultaneously, commencing at the same time (the moment of injection, S), they jointly yield a response curve, the time scale of which is the next scaling factor. As most methods in f.i.a. are based on peak-height measurements, the residence time, T, measured from the point of injection S to the peak maximum (Fig. 1), in conjunction with C^{max} allows (via D) the fixed ratios of reactants at corresponding times to be compared in geometrically dissimilar streams, thus yielding a basis for

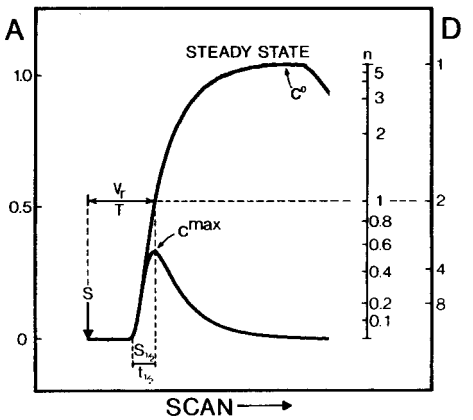

Fig. 1. The F curve and C curve obtained in a one-line flow-injection system (basic μ-conduit unit, cf. Fig. 3) by imposing a step and a pulse input, respectively, of a dye solution of concentration C^0 into an inert carrier stream, the signal being recorded as absorbance (A): S, point of injection; $S_{1/2}$ ($t_{1/2}$), sample volume (time) necessary to reach 50% of steady state; V_r, reactor volume; T, mean residence time; D, dispersion coefficient; n, sample volume expressed as number of $S_{1/2}$ values.

comparison of chemical similarity of otherwise dissimilar flow-injection systems. In other words, if a flow-injection procedure has been developed, optimized and tested in a macrochannel, it can be accommodated in a microchannel, provided that both systems yield similar D and T values. Going one step further, if D and T are identical for the micro- and macro-system, then both systems will yield identical readouts, which means that the same, say, spectrophotometric procedure will yield the same peak height (in terms of absorbance) provided that identical concentrations of sample and reagent materials are used in both systems, and that the flow cells have identical optical pathlengths and that the wavelength of the radiation to be absorbed is the same.

The last scaling factor to be identified must permit comparisons of economy of sample, reagent and time consumption in geometrically dissimilar flow-injection channels, as mere miniaturization of a system does not necessarily mean its optimization in terms of sampling frequency and consumption of liquid materials. In principle, one can use the D and T values for this purpose as well, for it has been shown [4] that

$$D = C^0/C^{max} = 2\pi^{3/2} r^2 D_f^{1/2} T^{1/2} S_v^{-1} \quad (1)$$

where r is the tube radius, and S_v is the injected sample volume. If D_f (the axial dispersion coefficient) can be isolated, its value can be computed for a macrochannel and compared with the value computed for a microchannel. The system with lower D_f value would be more economical, as lower axial dispersion means less zone spreading. Because it has not been much appreciated (see, e.g., [5]) that the D value is related to the sampling frequency via

D_f (Eqn. 1), it may be more practical to use a more explicit term describing system performance. Such a term should allow estimation of: (a) the duration of the measuring cycle t_{cyc} (as t_{cyc} allows computation of sampling frequency); (b) peak width at the baseline Δt_b (as suggested by Vanderslice et al. [6]); and (c) sample and reagent consumption per measuring cycle. Such a term could also be useful as a more easily understood scaling factor than the axial dispersion coefficient D_f. To find it, Eqn. 1 can be rewritten as

$$D = C^0/C^{max} = 2V_r(\pi\delta)^{1/2}S_v^{-1} \quad (2)$$

where V_r is the volume of the flow-injection channel from the point of injection to the point of detection. Equation 2 assumes a Gaussian form of the peak because D_f is replaced by the dispersion number $\delta = \sigma^2/2$, σ being half of the peak width at 0.61 peak height, and $C^{max} = (4\pi\delta)^{-1/2}$. It has been established [1] that

$$1/D = 1 - \exp(-kS_v) = 1 - \exp(-0.693n) = 1 - 2^{-n} \quad (3)$$

where $n = S_v/S_{1/2}$, $S_{1/2}$ being the injected sample volume necessary to reach 50% of steady state; thus for $D = 2$, Eqn. 2 can be rewritten as

$$S_{1/2}/V_r = (\pi\delta)^{1/2} \quad (4)$$

The dispersion factor, $S_{1/2}/V_r$ can be obtained by a simple dispersion experiment simultaneously with the other two scaling factors D and T (see Fig. 1 and below). Because this factor is proportional to D_f and δ, the lower is its value, the less will be the axial spreading of the sample zone. Thus a flow channel with lower dispersion factor will operate with higher frequency and better economy of reagent and time than a system with a higher $S_{1/2}/V_r$ value.

The length of the measuring cycle (t_{cyc}), the peak width at the baseline (Δt_b), the carrier stream consumption (r_{cyc}), and the sampling frequency (S_f) are all functions of $S_{1/2}$ and V_r. For $S_v \leqslant S_{1/2}$, the values are given by

$$t_{cyc} = (V_r + 4S_{1/2})/Q \quad (5)$$

$$\Delta t_b = 4\,S_{1/2}/Q \text{ (or more conservatively } 6S_{1/2}/Q) \quad (6)$$

$$r_{cyc} = V_r + 4S_{1/2} \quad (7)$$

while $S_f = 60/t_{cyc}$ samples per hour for pumping rate Q expressed in volume units per minute. The maximum attainable sample frequency, S_{max}, will thus be given by $S_{max} = 60/t_b = 15Q/S_{1/2}$ samples/h.

The dispersion factor also allows all the above values to be predicted for longer or shorter sections of a flow channel of certain geometry. Because $S_{1/2}$ (Eqn. 4) is proportional to $\delta^{1/2}$ which in turn is proportional to the square root of the variance σ^2, and because the overall peak variance σ^2_{tot} is the sum of the variances contributed by the individual sections 1, 2, 3 . . . i of the flow path, i.e.,

$$\sigma_{tot}^2 = \sigma_1^2 + \sigma_2^2 + \sigma_3^2 \ldots . \sigma_i^2 \quad (8)$$

and if the flow system is considered as a sum of N sections, each contributing the same $S_{1/2}^i$, then

$$S_{1/2} = N^{1/2} S_{1/2}^i \quad (9)$$

The dispersion factor is then obtained by dividing Eqn. 9 by the volume of the whole system, V_r

$$S_{1/2}/V_r = N^{1/2} S_{1/2}^i / V_r \quad (10)$$

If all sections are geometrically identical (i.e., each section contributes $S_{1/2}^i$), then $V_r = NV_r^i$, and

$$S_{1/2}/V_r = S_{1/2}^i / N^{1/2} V_r^i \quad (11)$$

Thus for a channel of uniform geometry, once $S_{1/2}$ has been established, it is possible to estimate the performance of a shorter or longer channel consisting of any number (N) of sections.

Straight channels or coiled tubing, or an imprinted channel of, say, sinusoidal form, or any channel of repeated geometry, may be viewed as consisting of a number of geometrically identical sections N. Because any deviation of geometry from a circular straight pipe will disturb the laminar pattern of the liquid flowing through the tube, the axial dispersion per reactor volume V_r will decrease from a straight pipe to a coiled pipe to a semicircular imprinted sinusoidal channel and will be smallest in a tube either packed with single beads (the SBSR reactor of Reijn et al. [7]) or three-dimensionally coiled (3-D coiled) [8] (cf. Table 1). The dispersion factor $S_{1/2}/V_r$ will decrease as the increased radial dispersion changes the character of the flow from mixed towards plug flow. Thus, once the scaling factors have been established for several types of channel, then the overall $S_{1/2}$ may be estimated for a system consisting of their combinations, by using Eqn. 10.

TABLE 1

Comparison of dispersion factors for five types of reactors of different geometry

Type of reactor	Cross-sectional reactor area (mm^2)	V_r (meas.) (μl)	$S_{1/2}$ (meas.) (μl)	Dispersion factor $S_{1/2}/V_r$
Microline[a]				
straight	0.2	172.9	70.6	0.41
coiled	0.2	193.7	66.4	0.34
3-D coiled	0.2	184.0	41.5	0.23
SBSR[b]	(0.6)	243.5	69.2	0.28
Basic μ-conduit unit	0.8	135.6	46.0	0.34

[a] 75 cm, 0.5 mm i.d. [b] Single bead string reactor (40 cm, 0.86 i.d.) filled with 0.5 mm glass beads; the effective cross-sectional area is different from the nominal one.

To summarize, the three scaling factors used here are the dispersion coefficient D, the residence time T and the dispersion factor $S_{1/2}/V_r$. The latter two can be obtained from a simple measurement, by injecting a large volume of a dye into a colourless stream and by recording the absorbance of the carrier stream with a flow-through colorimeter (Fig. 1). The step input, or F curve [1], thus obtained yields $V_r, S_{1/2}$ and C^0 (absorbance at steady state). Next, a sample volume of the size intended for use with the given flow-injection procedure is injected. This peak (C curve [1]) yields a D value, and a T value, and via Eqn. (3) reconfirms the $S_{1/2}$ value already obtained by the step input experiment. This in turn allows computation of t_{cyc}, r_{cyc}, etc. The D and T values are then compared with those of the macromethod and finally adjusted to match.

While the dispersion factor is determined mainly by the geometry of flow and to a lesser extent by the flow rate, D and T may be further manipulated by changing the injected sample volume (D), changing the flow rate (up to stopped flow) (T), and choosing the point of readout within the concentration gradient (D and T).

It is unnecessary here to reiterate the previously described gradient techniques [9], yet it is useful to illustrate how the D and T values can further be manipulated by a proper choice of the point of readout. So far, only the D and T values connected to the peak maximum have been discussed because most methods of f.i.a. are based on peak-height measurements at peak maximum. One may, however, choose any other element of the dispersed sample zone as a point of readout, if a finer adjustment of the D and T values is required. Thus two geometrically dissimilar flow-injection systems A and B may yield identical D and T values, as shown in Fig. 2. By injecting identical concentrations C^0 of a dye into these two channels, two response curves can be recorded from the same starting point (S). The peak-height measurement for

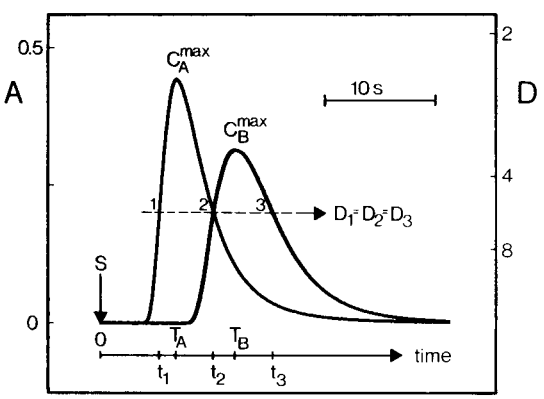

Fig. 2. Signal output for two dissimilar flow-injection systems where identical sample concentrations of a dye were injected, the responses being recorded from the same starting point (S). The two peak maxima, C_A^{max} and C_B^{max}, are related to the two residence times T_A and T_B, while times t_1, t_2 and t_3 correspond to fluid elements (1, 2, 3) with identical dispersion coefficients situated along the gradients of the dispersed sample zones.

channel A in this example has $D_A = C^0/C_A^{max} = 2.4$ and $T_A = 7.0$ s, whereas channel B has $D_B = C^0/C_B^{max} = 3.4$ and $T_B = 12.3$ s. These are the minimum D values obtainable in the given channel geometries, for the given sample volume injected. Higher D values can be obtained by fixing the readout at times other than those corresponding to the peak maximum. For illustration, points 1, 2 and 3 all have identical values ($D_1 = D_2 = D_3 = 5.2$), i.e., the same mixing ratio between sample and reagent (contained in the carrier stream). Point 2 also represents identical reaction times ($t_2 = 10.3$ s) for the two systems A and B, thus the readouts obtained at point 2 will be identical for both the A and B channels, regardless of how much these channels may differ geometrically. This observation has been exploited for evaluation of the selectivity of flow-injection methods [10] and will also be useful when the chemical scaling factor has to be adjusted for merging zones and instrumental pumping methods in macro- or micro-channels.

EXPERIMENTAL

Apparatus

All experiments were done with a Bifok-Tecator FIA-5020 Flow Injection Analyzer equipped with an injection valve of variable volume (Bifok, model L-100-1). For delivery and aspiration of liquids, both peristaltic pumps of the analyzer were used. The automated sequential operation of the pumps, and the timing of the valve functions, were controlled by the microprocessor of the FIA-5020. Optical measurements were made by means of a Bausch and Lomb Mini-20 spectrophotometer from which the light source (the tungsten lamp) was removed. The light from an external light source (20 W), powered by a variable power supply (4—8 V), was piped by an acrylic optical fibre (1.6 mm o.d.; Optronics, Cambridge, England) into the microconduit with integrated flow cell (see Figs. 6, 8 and 10) and from there by means of a second piece of optical fibre, the other end of which was placed where the tungsten lamp had originally been situated in the photometer. Both fibres were protected from ambient illumination by black PVC sleeving, and the cell compartment of the spectrophotometer was made light-tight. The transmittance signal from the spectrophotometer was fed to a logarithmic converter and then to the recorder (Radiometer Servograph REC-61, furnished with a REA-112 high-sensitivity interface), and from there to the FIA-5020. Results were displayed digitally on the FIA-5020 and also recorded on an attached printer (Alphacom, Sprinter 40). For potentiometric measurements, a digital pH meter (Radiometer PHM 64 Research pH meter) was used, the recorder being equipped with a REA-100 pH-meter interface (Radiometer).

Microconduits

All the microconduits for f.i.a. (Figs. 3, 4, 6, 8, 10, 12 and 13) were made from 70 × 45 × 10 mm transparent PVC blocks into which appropriate channel patterns were impressed or engraved. When closed by a transparent

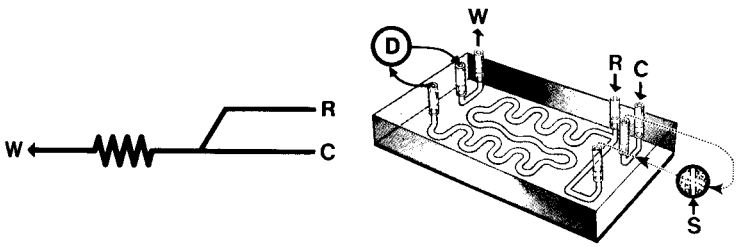

Fig. 3. Basic microconduit unit for f.i.a., designed to accommodate a carrier stream (C) to which a side stream (R) can be added in confluence, and to be attached to an externally placed injection valve (S) and detector (D). For the dispersion experiments shown in Fig. 1, the side stream R was not used. The channel length from the confluence point with R to the detector D is 15.6 cm.

plate with the aid of pressure-sensitive polymeric glue, the channels formed conduits of semicircular cross-section, typically with an area of 0.8 mm^2. Introduction of liquids into the channels and their withdrawal were effected through small perpendicular holes drilled at appropriate positions and furnished at the top with sleeving in order to facilitate connection to exterior tubing. Electrodes were implanted into the flow channels and milled flat so as not to protrude from the walls of the channel. In those microconduits where an optical flow cell was integrated, a 10-mm circular section of the transparent PVC block was replaced by a plug of black PVC of identical dimensions into which a hole serving as the flow cell (1.6 mm i.d., 10 mm optical path) was drilled perpendicularly to the conduit pattern. Covered on both sides with transparent plates, this construction ensured that only the light passing through the flow cell was transmitted to the acceptor light fibre (see Figs. 6, 8 and 10).

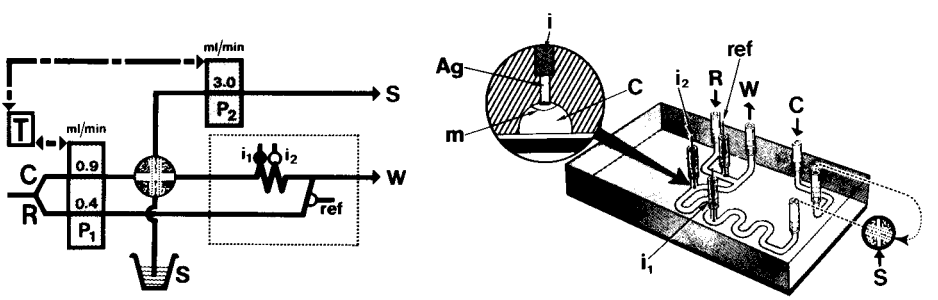

Fig. 4. Manifold and microconduit unit for potentiometric determination of pH, the components within the boxed area of the manifold being those contained in the microconduit. Pumps P_1 and P_2 are operated sequentially, controlled by timer T, so that sample (S_V = 30 μl) is first aspirated by P_2 into the injection valve (during which period P_1 is stopped) and subsequently propelled forward by carrier stream C (diluted buffer, c.f. Fig. 5) towards indicator electrode i_1 (or i_2), the construction details of which are shown in the inset (m is the pH-sensitive membrane). The reference electrode (ref) is placed in a side channel fed by stream R, and the combined streams are ultimately led to waste, W.

Electrodes

Silver wire (0.7 mm diameter) was implanted into the PVC block, and its surface, milled flush with the channel wall, was plated with silver chloride; this served as a reference electrode (cf. Fig. 4). The pH electrode was prepared as follows. First, a reference layer of $NaH_2PO_4/Na_2HPO_4/KCl$ was applied to the Ag/AgCl surface and then a pH-sensitive PVC-based membrane containing tri-n-dodecylamine [11] was cast over its surface. The casting procedure was repeated three times, and the membrane was then allowed to dry overnight. After the channel had been closed, the structure obtained was as shown in the inset of Fig. 4.

Reagents

All reagents were of analytical-reagent grade. Distilled and degassed water was used throughout.

For the dispersion experiments, the carrier stream used was 1×10^{-2} M sodium tetraborate to which was added 0.05% Brij. The bromothymol blue dye stock solution used for preparation of samples was made as described earlier [12]; a 1:200 dilution of this solution had an absorbance of 1.044 at 600 nm in a cell of 10-mm path length.

The carrier solution for the pH measurements consisted of 10^{-2} M sodium dihydrogenphosphate adjusted to pH 7.6 or 8.0, to which sodium chloride was added to give a final concentration of 0.10 M. This solution also served as reference solution for the Ag/AgCl reference electrode. Buffer standards in the pH range 2—12 were prepared as described in Tables 10.25, 10.37, 10.43, 10.45 and 10.5 in the monograph by Perrin and Dempsey [13].

The reagent carrier stream for the spectrophotometric determination of calcium was identical to that described previously [12], except that the alkaline solutions of diethylamine and *o*-cresolphthalein complexone, which in the earlier version were pumped separately into the flow-injection manifold, were here premixed in a container before being pumped. Calcium standards in the range 2.5—15 mg l^{-1} were prepared by dilutions of a 100 mg l^{-1} calcium stock solution [12].

RESULTS

Comparison of channels of different geometry, and design of basic microconduit unit

In order to verify the concept of the dispersion factor and use it for optimizing the geometry of the imprinted microconduit channels, $S_{1/2}/V_r$ values of various channel geometries were measured and compared by dispersion experiments. A step pulse of bromothymol blue in a colourless carrier stream of sodium tetraborate with ensuing colorimetric detection (*F* curve, Fig. 1) was used for this purpose. According to Eqn. 8, $\sigma^2_{tot} = \sigma^2_{inj} + \sigma^2_{reactor} + \sigma^2_{det}$, where $\sigma^2_{reactor} = \sigma^2_1 + \sigma^2_2 + \sigma^2_3 + \ldots$. Obviously, the dispersion factor will reflect the contributions from all these variables. Therefore,

the same injection and detector units were used in all experiments so that the contributions of these two components to the overall variance were kept constant. Furthermore, by keeping their volume minimal, σ^2_{inj} and σ^2_{det} were minimized. It should be realized, however, that because the total volume of the system, V_{tot}, is given by $V_{tot} = V_{inj} + V_{reactor} + V_{det}$, these non-reactor contributions, although constant, will become dominant when the reactor volume is very small. (Further, it should be noted that when the F curves are measured, i.e., the leading edge dispersion is recorded, σ^2_{inj} is independent of the injected volume, S_v, but reflects the volume, V_{inj}, of the connector between the valve rotor and the start of the investigated channel). Except for the SBSR reactor (which had an internal diameter of 0.86 mm and was packed with glass beads of 0.5 mm diameter) and the microconduits (imprinted into flat plates), all reactors were made of Microline tubing (70 cm, 0.5 mm i.d.) which was straight, coiled (coil diameter 10 mm) or 3-D coiled (by tying tight knots irregularly [8]). For coiled and 3-D coiled reactors, F curves were recorded as a function of reactor lengths L, starting with 100-cm long reactors, from which 25-cm sections were cut after each dispersion experiment (this was preferred to connecting shorter pieces of tubing, which could introduce changes in the flow pattern at the connecting points). The results of these experiments, summarized in Tables 1 and 2, show that the 3-D coiled reactor has the lowest dispersion factor (i.e., the lowest axial dispersion) and that this reactor (and the SBSR reactor) conform with Eqns. 8—11, because the radial dispersion promoted by secondary flow is sufficient, even in the shortest reactor length, to convert the flow-injection peak (C curve) to a near-Gaussian shape. In the coiled reactor, however, the secondary flow requires a longer length of line (L) to develop, and as σ^2_{inj} and σ^2_{det} become significant compared to $\sigma^2_{reactor}$ for 25 cm $< L <$ 100 cm, the development of the Gaussian shape of the C curves requires line lengths exceeding about 75 cm [1].

TABLE 2

Comparison of dispersion factors for Microline reactors (0.5 mm i.d.) coiled or three-dimensionally coiled, as a function of reactor lengths

Reactor type	Length (cm)	V_r (meas.) (μl)	$S_{1/2}$ (meas.) (μl)	Dispersion factor $S_{1/2}/V_r$	$(S_{1/2}/V_r)/(S_{1/2}/V_r)_{100}$	
					Measured	Theor.[a]
Coiled	25.5	85.7	31.8	0.37	1.08	1.98
	50	138.3	47.0	0.34	1.00	1.41
	74	192.0	66.2	0.34	1.00	1.16
	100	238.5	81.6	0.34	1.00	1.00
3-D coiled	25	85.7	27.7	0.32	1.79	2.00
	48	130.0	34.6	0.27	1.47	1.44
	71	179.0	38.7	0.22	1.20	1.19
	100	229.9	41.5	0.18	1.00	1.00

[a]According to Eqn. 11.

The microconduit (of 135-μl volume) has a dispersion factor of 0.34 which is similar to that of a 70-cm coiled tube (0.5-mm i.d.; 140-μl volume). Taking into account that the cross-sectional area of the coiled tubing is 0.2 mm^2 and that the microconduit channel is 0.8 mm^2, the geometry of the imprinted channel yields a lower axial dispersion than that of the coiled tube (cf. Eqn. 1). The basic microconduit unit (Fig. 3, where the basic unit is shown furnished with a second inlet, allowing addition of a side-stream R) is thus identical with a 70-cm coil of 0.5-mm i.d. tubing, in terms of sample, reagent consumption and time, provided that the same pumping rate Q is used. Conventional flow-injection systems are made of such coils (longer or shorter, as required), thus the basic unit may serve as a building block for those applications of f.i.a., which were designed originally for conventional systems with coiled tubing, because an appropriate choice of S_v and Q will yield identical or similar D and T values in microconduits and coils. For limited dispersion applications (such as pH measurements), a shorter channel has to be imprinted; for medium dispersion (e.g., methods for spectrophotometry or luminescence), one or two basic blocks are used, whereas for flow-injection titrations, the basic channel must be supplemented by a gradient tube.

Microconduit for pH measurement

As pH measurements require a system with low D value (1—3) and no chemical reaction is needed in the flow channel (thus allowing a short residence time T), a single line system with the lowest possible dispersion factor offers optimum economy of sample and carrier stream consumption per measuring cycle. Accordingly, the channel volume (between the point of injection and the indicator electrode i_1 in Fig. 4) was reduced to 20 μl, corresponding to $S_{1/2} \simeq 7$ μl, thus requiring $S_v = 30$ μl to reach $D = 1.05$. With $Q = 0.9$ ml min^{-1}, this yields theoretically $S_f = 60/t_{cyc} \approx 60\ Q/(V_r + 10\ S_{1/2})$ or a sample throughput of 600 h^{-1} (provided that the speed of response of the electrode is not the limiting factor).

The microconduit (Fig. 4) comprised the indicator electrode, i (two such electrodes, i_1 and i_2, are shown in Fig. 4 to indicate multisensor capability) and the Ag/AgCl wire reference electrode situated in a side channel and connected to the main channel downstream from the indicator electrodes. The manifold construction is such that the reference solution and thus the liquid junction are renewed during each sampling cycle when carrier stream is pumped (by pump P_1) through both channels. The construction of the pH electrode is described under Experimental. A typical pH readout, obtained by injecting buffers in the pH range 2.0—12.0 into a carrier stream consisting of phosphate buffer at pH 7.6 is shown in Fig. 5A; a recording obtained for the narrow pH range 7.0—7.8 (Fig. 5B, pH 8.0), corresponding to clinical applications, confirms the high reproducibility of this type of measurement (RSD 0.003 pH).

Because of the anion-exchange properties of the electroactive material

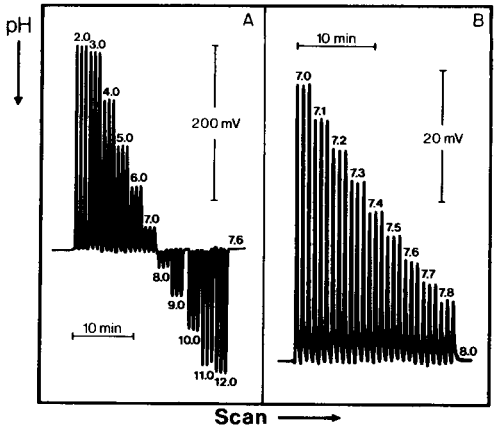

Fig. 5. pH-Response curves obtained with the microconduit system of Fig. 4. (A) A series of pH standards in the range 2.0—12.0; the carrier solution was a 0.01 M phosphate buffer containing 0.1 M NaCl, at pH 7.6. (B) Performance of the system in the physiologically important pH range; the carrier solution was at pH 8.0.

which is, like many other tertiary amines, capable of extracting anions into an organic phase (see, e.g., [14]), the electrode does not respond to pH changes below pH 3 in the presence of 0.1 M NaCl. The extraction of anions by tri-n-dodecylamine increases in the order $SO_4^{2-} < PO_4^{3-} < Cl^- < Br^- < I^- < ClO_4^-$, and it can be expected that the electrode selectivity will follow the same pattern, so that pH measurements would be unreliable even in neutral solutions in the presence of high concentrations of perchlorate. Above pH 10, interference is caused by alkali metal cations. In its present configuration, the sensitivity of the sensor towards chloride and alkali metal ions may give rise to a fine trough atop the peak if the dispersion is low and the pH is <3 or >9 in buffers without chloride, because the transition from the chloride-containing carrier stream to the chloride-free centre of the sample-buffer zone will affect the loading of the exchange sites on the electrode surface. Therefore, for more precise measurements, buffers should be used, containing chloride (and sodium ion) activities similar to those of the carrier stream. Despite these shortcomings, the electrode is very well suited to applications in f.i.a., as it has a fast response and low impedance, even when miniaturized. It is a useful device not only for direct pH measurement but also for indirect applications like pCO_2, ammonia and enzymatic measurements where the pH, generated on the other side of a gas-permeable membrane, reflects the concentration of analyte in the carrier stream (cf. Fig. 12). Its usefulness for blood gas measurements has already been confirmed [17].

In addition to the pH electrode, potassium-, calcium- and nitrate-selective PVC-based membranes have been applied in microconduits with success. Platinum and silver electrodes have also been tested for voltammetric and potentiometric applications.

Microconduit for spectrophotometry

Spectrophotometric measurements require medium dispersion of the sample zone within the carrier stream containing a colour-forming reagent. The basic unit, which has a volume of 135 μl and a dispersion factor of 0.34, yielded $D \approx 7$ with a sample volume of 10 μl. The determination of calcium, based on formation of the red-violet complex with *o*-cresolphthalein complexone, was used to test the performance of the microconduit with an integrated optical flow cell (Fig. 6). The reagents and sample concentrations were the same as described previously [12] and the manifold used was also similar (Fig. 6), except that the alkaline reagents of diethylamine and *o*-cresolphthalein complexone were premixed before use to avoid refractive effects (caused by the relatively high viscosity of the diethylamine reagent). To ensure sufficient supply of the reagents along the whole dispersed zone, a two-line system with a confluence point was used. The pumping rate Q was decreased to 0.75 ml min^{-1} in each line in order to achieve a residence time T of 6.5 s. Also, the sample volume was decreased to 10 μl in order to obtain a D value similar to the one used in the conventional flow-injection system for spectrophotometry of calcium. The resulting calibration curve (Fig. 7) is similar to that obtained with the macrosystem, but the sample

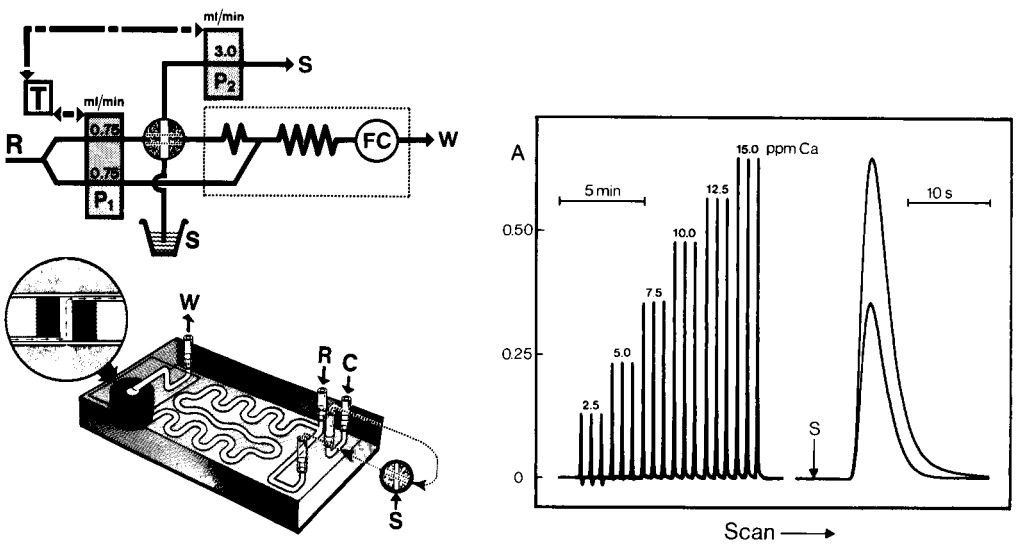

Fig. 6. Manifold and microconduit with integrated optical flow cell (FC), details of which are shown in the inset. Light is piped via optical fibres (see Fig. 10). The pumping rates indicated are for the determination of calcium (cf. Fig. 7) with this manifold.

Fig. 7. Response curves for the determination of calcium obtained with the microconduit system shown in Fig. 6 (S_v = 10 μl), where the reagent stream of alkaline *o*-cresolphthalein complexone was pumped to both inlets C and R, the stream being monitored at 580 nm. To the left is shown a series of standards in the range 2.5—15.0 mg l^{-1} Ca; to the right, standards containing 7.5 and 15.0 mg l^{-1} Ca are recorded at high chart speed.

and reagent consumption were reduced by about 50%. The dispersion factor for this flow channel is 0.34, thus the computed sampling frequency is S_f = 250 h^{-1}. The actual sampling frequency was lower because in automated operation additional time (in this case 11 s per cycle) is needed to fill the sample loop prior to injection, and this time interval must be added to each cycle. As there was no pressing need to operate at very high sampling rates, the cycle length was electronically selected in the Bifok/Tecator system to be 35 s, yielding a sampling rate of 103 h^{-1} (Fig. 7). As seen from the peaks recorded at high chart speed (Fig. 7), the sampling frequency could readily have been increased to the computed one (S_f) without carry-over. The flow cell functioned very well, though its windows became cloudy with use if any polymeric glue was left on the inside surfaces when the transparent plates were mounted. Thus, either both plates were replaced every two weeks, or the glue was carefully removed from the plates at the window areas before mounting. For u.v. measurements, thin quartz plates can be used instead of the thin plastic to cover the windows; the optical fibres connecting the light source to the flow cell and from the cell to the spectrophotometer must then also be made of quartz.

The experiments with the integrated optical flow cell have implications for fluorescence and chemiluminescence applications of f.i.a. The integration of potentiometric (pH) detectors and optical detectors on the same flow path will find many interesting applications.

Microconduit for high-speed titrations

Flow-injection titrations [4, 15] require medium to high dispersion, because it is not the peak height but the peak width which is the basis for the analytical readout. The theory of these titrations has been discussed [4, 15]. Essentially, the concentration C^0 of an analyte to be titrated is a function of the time span Δt between the two equivalence points situated on the rising and falling edges of the peak

$$\Delta t = (V_m/Q) \ln 10 \log [(S_v C^0)/(V_m C_{titr} n)]$$

where V_m is the volume of the mixing chamber, Q is the pumping rate, C_{titr} is the concentration of titrant pumped and n is the equivalent ratio of reacting species. Thus if phosphoric acid is injected into a carrier stream of sodium hydroxide, two equivalence points will be obtained (for n = 1 at pH 4.7, and for n = 2 at pH 9.6). It was shown previously [15] that a chamber with a mechanical stirrer can be replaced by a gradient tube (G) and the present design of the microconduit for fast flow-injection titrations reflects this feature (Fig. 8). For detection of the two equivalence points, by means of a spectrophotometer, a flow cell was integrated into the micro-conduit, and a mixture of the acid-base indicators, bromocresol green and thymol blue, which are both blue in the alkaline form and yellow in the acidic form, were added to the carrier stream of sodium hydroxide. Bromo-cresol green has its colour change in the pH range 3.8—5.4 and thymol blue

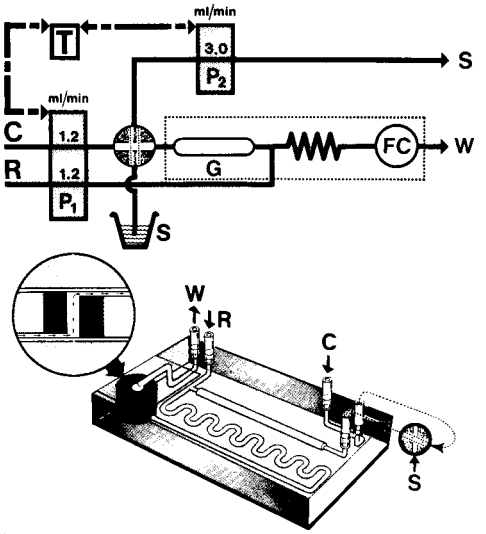

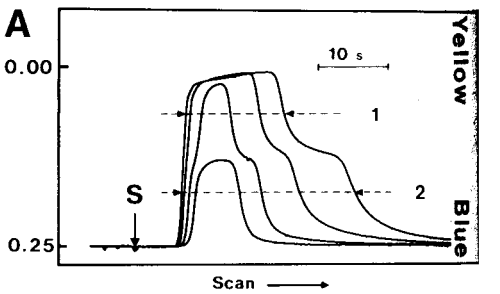

Fig. 8. Manifold and microconduit titration unit with integrated optical flow cell. After injection into carrier stream C (water) the sample is passed into the gradient chamber G and subsequently merged with the reagent stream R (NaOH + indicators), the combined streams being mixed in the coil before the flow cell.

Fig. 9. Titration of phosphoric acid with sodium hydroxide (1×10^{-3} M), using the microconduit system (and the pumping rates) described in Fig. 8 and an injected sample volume of 42 μl. See text for details. The titration curves are for $C^0_{H_3PO_4} = 2 \times 10^{-3}$, 4×10^{-3}, 1×10^{-2} and 2×10^{-2} M, respectively. The equivalence points are indicated by 1 and 2.

in the pH range 8.0—9.4, thus an abrupt change in the intensity of the blue indicators takes place when phosphoric acid is converted to $H_2PO_4^-$ and another change occurs on conversion to HPO_4^{2-}. The colour changes are detected by monitoring the absorbance of the carrier stream at 600 nm. The titration curves (Fig. 9) show the two equivalence points and the plateaux of least indicator change and maximum buffering capacities are visible on the leading and falling edges of the peaks, in analogy with classical titrations done batchwise.

Because the peak widths provide the analytical data for these titrations, the flow channel has to be designed to yield a large dispersion of the injected sample zone. This was achieved in the present design by incorporating a gradient chamber (G), 40 mm long, 2.1 mm wide and 1.8 mm deep (volume 138 μl); the D values at the two equivalence points 1 and 2 (Fig. 9) were then 7 and 21, respectively. Ideally, the volume of the gradient chamber should dominate the system because the concentration gradient would be purely exponential if the chamber were well stirred. But, for slower chemical reactions, sufficient reaction time would not then be allowed between the confluence point and the detector. This is why an additional length of channel was imprinted between the confluence point and flow cell; because

of radial dispersion within that section of the manifold, the exponential concentration gradient formed in G was partly transformed to a Gaussian shape. Consequently, Δt versus log C^0 did not yield a straight line over a very wide concentration range. A solution to this problem, together with results of flow-injection titrations based on redox, precipitation and complexiметric reactions, monitored by optical and electrochemical detectors, will be described separately [16].

Integrated microconduits

In all the above examples, the sample zone was injected into the microconduit channel from an external sampling valve, yet ultimately this function should also be integrated into the microconduit. Miniaturization of a rotary valve is one possibility, while another is the use of the hydrodynamic injection principle [9], which involves a combination of hydrodynamic and hydrostatic forces to aspirate, meter and inject the sample solution in the form of a well defined plug into the carrier stream.

To test this approach for sample injection and to demonstrate its flexibility, a manifold operated by two peristaltic pumps, controlled by timer T (Fig. 10), was constructed; two microconduits were used, the basic unit furnished with a flow cell, and the injection unit with an imprinted volumetric channel and two sample cups S_1 and S_2. The volumetric channel (17 μl) is shown in the manifold as the coil situated between points a and b, and is served by pump P_2. This channel forms part of two circuits; an open circuit starting in S_1 and leading through P_2 to S, and a closed circuit in which the inlets (R and C) and the outlet (to W) are hydrodynamically balanced so that the combined volumetric delivery of liquids to R and C equals the outflow to W. Thus when pump P_1 operates and P_2 does not, there is no movement of liquid between b and S_1 in either direction. The sampling cycle starts with P_1 in the stop position while P_2 is operating, as indicated by the solid lines in the upper corner of Fig. 11. During that delay period (DE1) the sample loop is washed and filled by sample solution from cup S_1. Next, pump P_2 is stopped and P_1 is activated, thus injecting the sample zone, located between a and b,

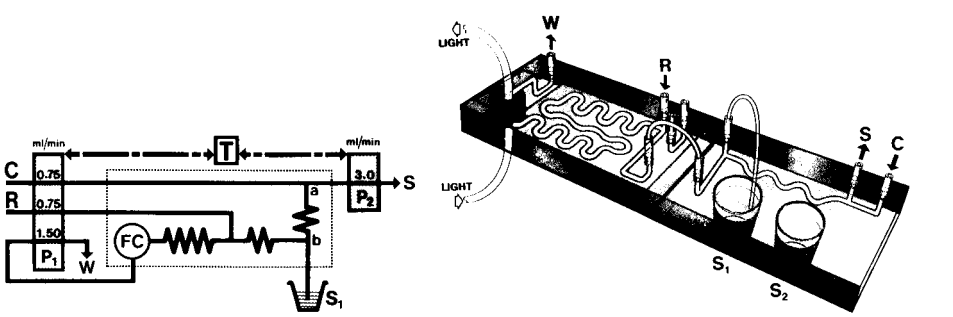

Fig. 10. Manifold and microconduit incorporating hydrodynamic injection and integrated optical flow cell. For details, see text.

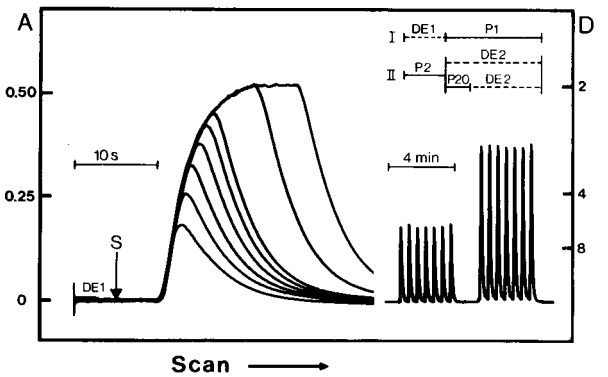

Fig. 11. Hydrodynamic injection of increasing sample volumes of a dye solution (bromothymol blue) into a carrier stream (1×10^{-2} M sodium tetraborate), using the manifold depicted in Fig. 10, monitoring the colour at 600 nm. To the left is shown a series of curves with increasing overlap times (P20) of the two pumps (0, 1, 2, 3, 4, 5, 10 and 15 s). Thus the smallest peak corresponds to an injected volume equal to the volume of conduit a—b in Fig. 10 (17 μl); for increasing overlap times, and so increasing S_v values, progressively higher peaks are recorded until the steady-state plateau is reached. To the right is shown the reproducibility of measurement for signals corresponding to P20 values of 0 and 3 s.

into the coil and through the analytical channel. By using a colourless carrier stream (1×10^{-2} M sodium tetraborate) and bromothymol blue as "sample" solution, the smallest peak shown in Fig. 11 was recorded. (The reproducibility of injection is demonstrated on the right-hand side of the figure, which shows the traces from repeated (7) injections of the same concentration of dye). In this mode of operation, the injected sample volume S_v corresponds exactly to the physical volume of the imprinted channel between a and b and therefore this approach may be termed as hydrostatic injection.

If the timing cycles of pumps P_1 and P_2 are allowed to overlap, the injected volume of sample can be increased at will. This can be understood by referring to Fig. 10 (left) and Fig. 11 (top right). In this mode, the cycle starts with a period during which P_1 is stopped (DE1) and P_2 is activated, filling the sample loop, but instead of the stop/go pattern being reversed after the DE1 period, both pumps are operated simultaneously for an overlap period (marked P20), during which pure sample solution is directed at point b towards the detector at a volumetric rate corresponding to that of the carrier stream C, while stream C itself is directed at point a towards S (along with an amount of sample corresponding to the volumetric pumping rate of pump 2 minus that corresponding to C). When pump 2 is stopped, carrier stream C is redirected through the sample loop and carries its content of sample towards the detector. Thus the amount of sample introduced is that aspirated directly during the overlap period, P20, plus the volume of the sample loop a to b; by increasing the overlap time, increasingly larger sample volumes can be injected, until the steady-state plateau is reached (Fig. 11). This is a true hydrodynamic injection as the sample zone is formed

by a combination of hydrostatic and hydrodynamic forces exerted on the columns of liquids by the two peristaltic pumps.

The reproducibility of the hydrodynamic injection (for an overlap time P20 of 3 s, corresponding to a total injected volume of 55 μl) is as good as that of the hydrostatic injection, as demonstrated by the second series of seven injections on the right-hand side of Fig. 11. In this connection, it is of interest that with the aid of hydrodynamic injection it is easy to measure all the experimental parameters discussed in connection with Fig. 1. Also, the curves recorded in Fig. 11 conform exactly with Eqn. 3, the only difference being that the steady state shown in Fig. 11 is now at $D = 2$. This is, of course, a natural consequence of adding a colourless stream R via the merging point to the injected sample zone in an exact proportion of 1:1 (0.75 ml min^{-1} + 0.75 ml min^{-1}); the original concentration of sample solution C^0 is halved and $D = 2$ is the minimum dispersion achievable.

It should be noted that the hydrostatically injected volume (S_v = 17 μl) and the sequentially increasing hydrodynamically injected volumes would not have conformed with Eqn. 3, if points a and b of the volumetric channel had been connected in the opposite manner, i.e., point a to the sample cup and point b to S, because sample material would then have been diluted by the carrier stream during the overlap interval P20 within the conduit a—b. This observation may serve as a warning as well as a hint to how various concentration gradients may be formed by means of the hydrodynamic injection principle. Finally, a drawback of both the hydrostatic and hydrodynamic injection methods should be mentioned: if the incoming and outgoing streams of the closed circuits are not perfectly balanced, then the sample solution in the cups S_1 will either be continuously aspirated (resulting in an increased and irregular baseline), or diluted by the carrier stream (thus yielding irreproducible result in repetitive sampling from the same cup S_1). Satisfactory balancing of the streams can be achieved by adjusting individually the tension of the pump tubes in the peristaltic pumps, because narrower, i.e., more elongated pump tubes, deliver liquids at lower rates.

Microconduit with diffusion unit

It is possible to laminate several layers of materials on top of each other and thus form channels which can be separated from each other within a selected section by a semipermeable membrane. Detail of such a structure is shown in the inset of Fig. 12: the flat channel for carrier stream C is separated by a gas diffusion membrane (d) from the acceptor channel (A) which is monitored by the above-described pH-sensitive electrode (i) with the treated PVC membrane (m), the Ag/AgCl reference electrode (r) being placed slightly downstream. Thus changes of pH caused by gas diffusing from the donor stream are easily monitored. The diffusion membrane has a very small area, usually 10 mm^2, and the diffusion time is very short because the dispersed sample zone passes through the diffusion unit in a matter of seconds. Thus the pH change in the acceptor stream would be too small if the acceptor

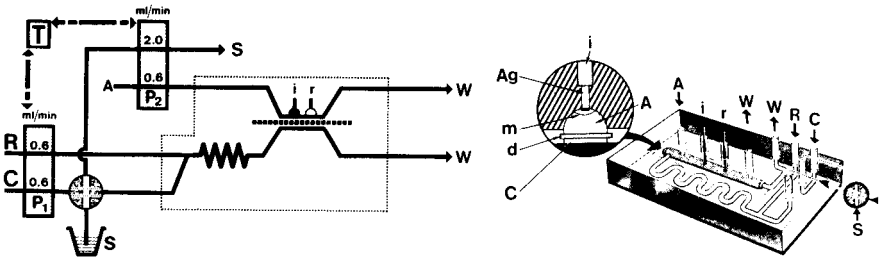

Fig. 12. Manifold and microconduit with integrated gas diffusion unit and potentiometric detection. The membrane (dashed line) separates two channels, containing the donor and acceptor streams, respectively. Any change in the composition of the acceptor stream is monitored by the electrode couple. The pumps are operated sequentially, controlled by timer T, and thus the acceptor solution is renewed after each measuring cycle. For details, see text.

solution were to move continuously during the measuring cycle. For this reason, carrier stream C and acceptor stream A are propelled by two different pumps (Fig. 12) so that when the carrier stream is in motion (P1), the acceptor stream stands still (P2). Thus, the diffusing gas material is concentrated in the vicinity of the electrodes, while the sample zone passes along the membrane. When the signal resulting from the pH change has been recorded, pump 2 is activated so that new sample solution is aspirated from the sample cup into the valve and fresh acceptor stream replaces the old solution around the electrodes.

This approach has been used successfully for measurements of CO_2 in blood [17] and, by analogy with conventional flow-injection systems [1], should be applicable to any diffusible species (e.g., CO_2, SO_2, NH_3). The use of an optical detector rather than electrodes may, however, require a more sophisticated flow cell of a smaller volume than the optical cell described above, should only a low concentration of a diffusible material be available. The reason is that a small volume behind a diffusion membrane of small area results in sufficiently high concentrations to be sensed by an electrode, but optical detection requires a certain optical path length, which can be obtained only by having a larger volume of a liquid than that surrounding the electrodes in the present construction.

Microconduit with an ion-exchange column

Previous work on preseparation of traces of heavy metals from sea water prior to atomic absorption spectrometry [18] demonstrated that a microcolumn filled with Chelex 100 (50—100 mesh) can be used to preconcentrate lead, cadmium and copper 20 times within a sampling cycle lasting 60—100 s. In this flow-injection system (Fig. 13), the column is first loaded by injecting 2 ml of sample by means of the valve and pump P1, and in the next cycle the metals are eluted with strong acid (E) by means of pump P2 which propels a zone of acid through the column and into the detector. Balancing of the

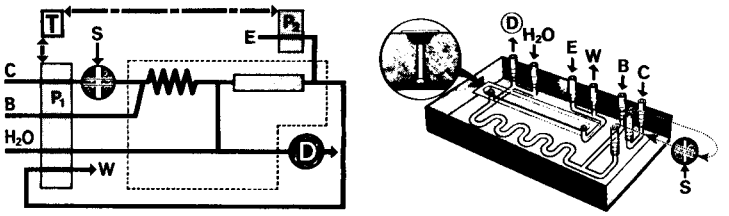

Fig. 13. Manifold and microconduit incorporating an ion-exchange column as used for preconcentration of metal ions [18]. The sample, injected into the carrier stream C, is mixed with buffer B to adjust the pH before entering the column. Metal ions are retained on the column and are eluted countercurrently by a small zone of eluent (E, acid) pumped by P_2. As the two pumps are operated sequentially, the eluted sample is carried to detector D (atomic absorption spectrometer).

streams and timing of the pumping cycles are in principle similar to those explained above for hydrodynamic injection; the nebulizer is supplied with wash solution (water) during the preconcentration cycle and the column is converted from the H^+-form to the NH_4^+-form after each elution sequence by means of buffer (B) which was also used to maintain and adjust the pH of the injected sample zone during the preconcentration cycle. Details of the procedure have been given [18]. The purpose of describing this approach here is to indicate the versatility of the microconduit concept, which allows incorporation of ion exchanging material into the flow channel. The groove filled with the ion exchanger (Fig. 13, inset), situated on the thicker plate on the opposite side of the channel system, allows renewal of the exchanger independently from the rest of the channel system.

Not only ion-exchanger columns of this type, but also columns filled with glass beads with enzyme attached to the surface are now being incorporated into microconduits. It is clear that many different combinations of detectors, diffusion units and enzyme reactors can be integrated into a unit of the size of a credit card. Such miniaturized flow systems can be manufactured reproducibly and, because of their small holdup volume, will serve well in economical serial analyses of discrete samples, or will become central components of continuous flow monitors for clinical and biotechnical applications.

DISCUSSION AND CONCLUSIONS

From a strict theoretical viewpoint, it might be objected that the assumption made in the derivation of Eqn. 11 is not justified because typical responses in f.i.a. are skewed and not Gaussian curves. This is why $S_{1/2}$ was assumed to be proportional (not equal) to σ, because increasing skewness of peaks obtained for short channels will cause increasing difference between σ and $S_{1/2}$. This can be seen from the results presented in the last two columns of Table 2 where nearly Gaussian peak shapes are obtained for the 3-D coiled reactors, whereas increasing skewness for decreasing coiled tube lengths causes increasing discrepancy between the measured and theoretical

values. A more detailed treatment of the limitations of Eqn. 1 has been presented [4]. However, the scaling factors suggested above are based on experimental values, accessible to direct measurements (V_r, $S_{1/2}$, Q, T, C^0, C), and can therefore be used for rapid and reliable estimation of characteristic properties and for mutual comparison of any flow-injection systems (S_{max}, t_{cyc}, S_v, N, n and D) without any reservations. Thus, existing methods of f.i.a. may be accommodated in channels of different dimensions and geometrical form by comparing the scaling factors, D, T and $S_{1/2}/V_r$, and by adjusting S_v and Q (and possibly the point of readout for gradient techniques) accordingly.

The dispersion factor, used here to optimize microconduit design, also allows macrochannels of different geometries to be compared, as illustrated by the results summarized in Table 1. Since Tijssen [19] suggested the use of tightly coiled tubes of narrow diameter (down to 10 μm), van den Berg et al. [20] proposed reactors packed with small particles and Reijn et al. [7] recommended the single bead string reactor (SBSR), it has become realized that each of these ingenious suggestions represents a compromise between what is ultimately desirable and what is practical, because high flow resistance, entrapment of air bubbles and danger of clogging the channels must be avoided. Given these practical limitations, and given the surprisingly low dispersion factor of the tightly knitted 3-D coiled flow channel suggested by Neue [8], the latter seems to be the best choice and therefore its features will be reflected in future designs of macro- as well as micro-conduits for f.i.a.

The concept of similarity has led to identification of scaling factors, which serve as practical guidelines for designing flow-injection systems. Similarly to D and T, $S_{1/2}/V_r$ describes all components of the particular system under investigation (i.e., the injection system, the flow channel, including sidestreams merging into it, and the detector). This is the strength, and weakness, of the present approach: it describes exactly the concentration ratios, residence times, sampling frequency and reagent consumption, but it is not precisely related to the variables strictly defined by the theory of flowing liquids (i.e., dispersion number δ, variance σ^2, and axial dispersion coefficient D_f). Several significant papers on flow theory have recently been published which use more rigorous approaches to the description of flow-injection systems. Thus the work of Reijn et al. [21] on optimization offers a valuable viewpoint, as does the work of van der Linden [22] on the theory of gas diffusion. The work of Pardue and Fields [23] also clarifies the interdependence of peak height and peak width relevant to the understanding of the dispersion process. A treatment of transport phenomena in f.i.a. without chemical reactions has been presented by Reijn et al. [24]. Recently, an instructive computer simulation, based upon the random walk model, was developed by Betteridge [25], describing the interplay of the dispersion process and the chemical reactions as they simultaneously occur in a f.i.a. system.

There is more than one way to describe the dispersion phenomena which occur during the movement of the sample zone towards the detector. They are all valuable, yet the choice of a general model describing the system satisfactorily is difficult because of the large variety of analytical problems to which f.i.a. is being applied. The theory describing a simple one-line system with a straight tubular channel designed for measurement of diffusion coefficients is straightforward, more complex flow-injection systems intended to handle sequential chemical reactions and separations have to be designed and optimized largely on empirical basis. The present approach, based on the use of D, T and $S_{1/2}/V_r$, is useful as a guideline for an initial design of a flow-injection system, and further optimization may be achieved by the conventional univariate optimization procedure or by computer-assisted modified simplex methods [26].

The examples of microconduit designs described above [27] amply illustrate the versatility of this new approach, which allows a wide range of combinations of basic components to be integrated into a compact unit. It is obvious that individual components, such as electrodes, optical flow cells, microcolumns with ion exchangers or immobilized enzymes, or gas-diffusion and dialysis units, may be combined and connected by channels of chosen geometry and length. These components can be placed exactly where required and not in a less favourable geometry as in conventional systems where the physical size and length of the connectors of the individual units dictate their minimum possible distance. By integration of all units, any connectors in the flow path through which the sample zones move are eliminated and so is the possibility of leaks and misconnections. Though certain skills and know-how are needed, it is relatively easy to make uniform microconduits. In the present version, a pressure-sensitive polymeric glue is used to bond the plates and to make laminated structures of layered channels, comprising all the required components including membranes. With this bonding technique, it is easy to reopen channels, remove individual layers, replace them, renew membranes, ion exchangers or immobilized enzymes, clean or renew electrode surfaces, replace optical windows in flow cells (should they have become translucent) or even to reroute those channels which have been cut within the sandwich of the bonded baseplates. This can be done quite quickly, if necessary under a microscope, with only a few tools; it is a matter of minutes to remove old layers and to replace them with new ones furnished with a fresh layer of glue. The price paid for this versatility is the low resistance of the materials used towards certain organic solvents, and swelling of the polymeric glue which causes blocking of channels if more concentrated acids (above 2 M) or alkalies are handled. So far, a wide variety of aqueous reagent solutions with additions of methanol, ethanol or diethylamine, has been used routinely for prolonged periods without any leak or blockage of the channels. Generally, it has been our experience that the microconduits are compatible with any solutions that PVC pump tubing can handle. The more aggressive solvents, such as chloro-

form, carbon tetrachloride, cyclohexanone, concentrated acids and alkalies, as well as higher temperatures (above 60° C), or pressures above the normal range for f.i.a. (>1 atm.), will require use of other materials and technology of bonding, such as photosensitive etching and bonding of glasses.

Further miniaturization of the microchannels by reducing the channel cross-section area (e.g., 4—10 times from the present area of 0.8 mm^2) would be easy even with the present technology and materials. However, the peripheral devices (pumps, injection valves, sample changers) are still relatively large so that there is not much point in making the integrated microconduits and their internal volumes smaller. The only commercially available instrument suitable for incorporation of microconduits (Bifok/ Tecator FIA 5020) is about the size of an office typewriter, a size which, if further reduced, would motivate further reduction of the flow channels. Recent work on f.i.a. in the nanolitre range [28], with a flow channel built around a quartz capillary of 0.3 mm i.d., shows that further miniaturization is possible, provided that the channel geometry used allows operation at low pressure and reliable handling of liquids with particulate matter (such as blood). Future miniaturized flow-injection systems may operate with total volumes in the range of 10—100 μl per measuring cycle and sample volumes in the nanolitre range. The degree of scaling down will always be a matter of compromise between economy of sample and reagent and what is mechanically possible. If sample material is scarce and reagents are expensive (or toxic), or if multisensor units are required, the advantages of the miniaturized systems are obvious.

The authors express their appreciation to Jiri Janata, University of Utah, Salt Lake City, who, as an early participant in the construction of microconduits, has played a vital role in this project.

REFERENCES

1 J. Růžička and E. H. Hansen, Flow Injection Analysis, Wiley-Interscience, New York, 1981.
2 J. B. Angell, S. C. Terry and P. W. Barth, Sci. Am., 248 (1983) 36.
3 B. S. Massey, Mechanics of Fluids, 3rd edn., Van Nostrand Reinhold, New York, 1975.
4 A. U. Ramsing, J. Růžička and E. H. Hansen, Anal. Chim. Acta, 129 (1981) 1.
5 C. C. Painton and H. A. Mottola, Anal. Chim. Acta, 154 (1983) 1.
6 J. T. Vanderslice, K. K. Stewart, A. G. Rosenfeld and D. J. Higgs, Talanta, 28 (1981) 11.
7 J. M. Reijn, W. E. van der Linden and H. Poppe, Anal. Chim. Acta, 123 (1981) 229.
8 U. Neue, Chromatographia, 15 (1982) 403.
9 J. Růžička and E. H. Hansen, Anal. Chim. Acta, 145 (1983) 1.
10 E. H. Hansen, J. Růžička, F. J. Krug and E. A. G. Zagatto, Anal. Chim. Acta, 148 (1983) 111.
11 P. Schulthess, Y. Shijo, H. V. Pham, E. Pretsch, D. Amman and W. Simon, Anal. Chim. Acta, 131 (1981) 111.
12 J. Růžička, E. H. Hansen and A. U. Ramsing, Anal. Chim. Acta, 134 (1982) 55.
13 D. D. Perrin and B. Dempsey, Buffers for pH and Metal Ion Control, Chapman and Hall, London, 1974.

14 Y. Marcus and A. S. Kertes, Ion Exchange and Solvent Extraction of Metal Complexes, Wiley-Interscience, New York, 1969, Ch. 10.
15 J. Růžička, E. H. Hansen and H. Mosbæk, Anal. Chim. Acta, 92 (1977) 235.
16 T. G. Petersen, J. Růžička and E. H. Hansen, unpublished work.
17 L. Andisheh, N. J. Ho, J. Kratochvil, J. E. Moore, J. Růžička, L. Spritzer and B. Thompson, Int. Symp. Ion Select. Elect. Physiol. Med., Burg Rabenstein, Germany, Sept. 1983.
18 S. Olsen, L. C. R. Pessenda, J. Růžička and E. H. Hansen, Analyst (London), 108 (1983) 905.
19 R. Tijssen, Anal. Chim. Acta, 114 (1980) 71.
20 J. H. M. van den Berg, R. S. Deelder and H. G. M. Egberink, Anal. Chim. Acta, 114 (1980) 91.
21 J. M. Reijn, H. Poppe and W. E. van der Linden, Anal. Chim. Acta, 145 (1983) 59.
22 W. E. van der Linden, Anal. Chim. Acta, 155 (1983) 273.
23 H. L. Pardue and B. Fields, Anal. Chim. Acta, 124 (1981) 39, 65.
24 J. M. Reijn, W. E. van der Linden and H. Poppe, Anal. Chim. Acta, 126 (1981) 1.
25 D. Betteridge, private communication.
26 D. Betteridge, T. J. Sly, A. P. Wade and J. E. W. Tillman, Anal. Chem., 55 (1983) 1292.
27 J. Růžička, E. H. Hansen and J. Janata, Danish Patent Appl. No. 4296/82; U.S. Patent Appl. No. 478,227.
28 G. G. Vurek, 9th Int. Symp. Microchem. Tech., Amsterdam, The Netherlands, 1983 (Abstract No. VIII-21).

Analytica Chimica Acta, 161 (1984) 27–35
Elsevier Science Publishers B.V., Amsterdam — Printed in The Netherlands

THE APPLICATION OF STRONGLY REDUCING AGENTS IN FLOW INJECTION ANALYSIS
Part 3. Vanadium(II)

R. C. SCHOTHORST*, J. J. F. VAN VEEN and G. DEN BOEF

Laboratory for Analytical Chemistry, University of Amsterdam, Nieuwe Achtergracht 166, 1018 WV Amsterdam (The Netherlands)

(Received 31st January 1984)

SUMMARY

The application of vanadium(II) as a powerful reducing reagent in flow injection analysis is described. Results are presented for the determination of various organic and inorganic substances. With spectrophotometric detection, based on the absorption by vanadium(II)-EDTA at 350 nm, limits of determination were about 5×10^{-5} mol l^{-1}. Nitrate, nitrite and hydroxylamine were measured with amperometric detection. The limit of determination was about the same as with spectrophotometric detection. In a slightly acidic medium, hydrazine could be determined with the amperometric detector, with a limit of determination of about 10^{-4} mol l^{-1}. By coupling an ammonia detection device to the reduction system, the percentage conversions of nitrate, nitrite and hydroxylamine to ammonia were shown to be 26%, 54% and 47%, respectively.

In previous papers [1, 2], the application of chromium(II)-EDTA as a powerful reducing agent in flow injection analysis (f.i.a.) was described. Apart from the spectrophotometric detection, polarographic detection was studied in order to achieve lower limits of determination. In the present paper, a similar study is described for vanadium(II)-EDTA. The same inorganic and organic reducible substances as for chromium(II)-EDTA as reducing agent were tested. Spectrophotometric detection was used at 350 nm, where vanadium(II)-EDTA absorbs. Again to achieve lower limits of determination, polarographic detection was also examined.

The normal redox potentials in acidic solution for some half-reactions involving vanadium are

$$VO_2^+ + 2H^+ + e^- \rightleftharpoons VO^{2+} + H_2O \qquad E^0 = +1.00 \text{ V}$$

$$VO^{2+} + 2H^+ + e^- \rightleftharpoons V^{3+} + H_2O \qquad E^0 = +0.36 \text{ V}$$

$$V^{3+} + e^- \rightleftharpoons V^{2+} \qquad E^0 = -0.26 \text{ V}$$

The regular increase of these potentials with increasing oxidation state accounts for the fact that both vanadium(IV) and vanadium(III) are stable against disproportionation. Thus, if vanadium(II) is oxidized by a reducible

0003-2670/84/$03.00

species, the end product of the oxidation can be any of the vanadium oxidation states, depending on the reducing power of the reducible species and on the reaction time.

The polarographic behaviour of the various oxidation states of vanadium in the presence of excess of EDTA was investigated by Pecsok and Juvet [3]. The halfwave potential of the reaction V(III)-EDTA + $e^- \rightleftharpoons$ V(II)-EDTA, which appears to be reversible at a dropping mercury electrode (DME), is independent of pH in the pH range 4.5—8.5 and is about the same as for the reaction Cr(III)-EDTA + $e^- \rightleftharpoons$ Cr(II)-EDTA (—1.27 V vs. SCE).

The pH at which reductions are possible with vanadium(II)-EDTA is less critical than for chromium(II)-EDTA. An attempt to use vanadium(II) EDTA in slightly acidic medium is described here. The last part of this paper deals with the reduction of nitrate, nitrite, hydrazine and hydroxylamine with vanadium(II)-EDTA and the extent to which these substances are reduced to ammonia.

EXPERIMENTAL

The experimental design for both the spectrophotometric and the polarographic part of the work was described earlier [1, 2].

To minimize pump pulsations, a small glass vessel filled with air (about 15 cm^3) was used. This device gave a slightly better result than the packed column used for the determinations with chromium(II)-EDTA [2]. In the flow system (Fig.1) the position of this device is indicated by K. The sample solution was introduced by means of an injection valve (Rheodyne) with a loop volume of 25 μl.

In the case of the spectrophotometric detection, the concentration of vanadium(IV) sulphate entering the Jones reductor (zinc with a 1% degree of amalgamation) was 10^{-3} mol l^{-1} in sulphuric acid solution (6×10^{-2} mol l^{-1}). The buffer solution contained 3×10^{-1} mol l^{-1} Tris and 3.3×10^{-2} mol

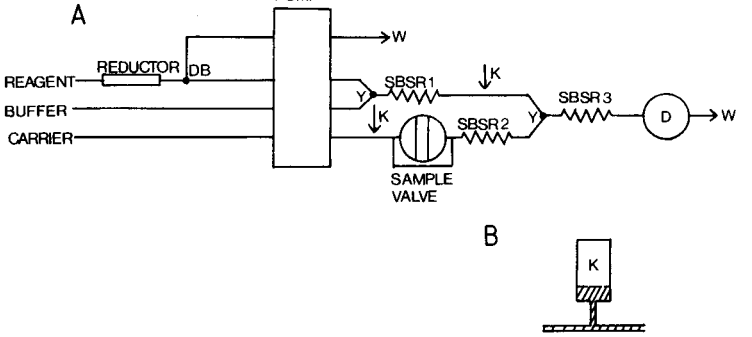

Fig. 1. (A) Flow diagram. Length of single bead string reactors (SBSR): (1) 0.2 m; (2) 0.2 m; (3) 0.4 m. DB, debubbler. K, damping device; D, detector; W, waste. All connecting and SBSR tubing is 1 mm i.d. nylon. SBSR's are packed with 0.6 mm glass beads. (B) Damping device (15 cm^3).

l^{-1} EDTA (disodium salt); the pH was adjusted to 8.6 with sulphuric acid. The vanadium(IV) sulphate concentration in the case of polarographic detection was 2×10^{-3} mol l^{-1} in 10^{-2} mol l^{-1} hydrochloric acid. The buffer solution contained 3.5×10^{-2} mol l^{-1} ammonium chloride, 10^{-1} mol l^{-1} KCl and 10^{-2} mol l^{-1} EDTA (disodium salt); the pH was adjusted to 9.3 with concentrated ammonia.

For the determinations in acidic medium, the buffer solution contained 7×10^{-2} mol l^{-1} ammonium chloride, 10^{-1} mol l^{-1} KCl and 10^{-2} mol l^{-1} EDTA (disodium salt); the pH was adjusted to 8.1 with concentrated ammonia. The degree of amalgamation of the Jones reductor with either 1 or 5%; both worked equally well.

For both detection methods, the carrier stream was distilled water. All solutions and samples were carefully deaerated with nitrogen.

RESULTS AND DISCUSSION

Spectrophotometric detection

To compare the practical performance of vanadium(II)-EDTA and chromium(II)-EDTA, the test substances were the same as before [2]. The results of these experiments are presented in Table 1. The results are very similar to those observed for chromium(II)-EDTA. Again there is a linear response of the absorbance vs. the concentration of the analyte over about one decade. The limit of determination, which corresponds to the analyte concentration for which the absorbance change is ten times the peak-to-peak noise, is lower for vanadium(II)-EDTA, which can be ascribed to the higher molar absorptivity of vanadium(II)-EDTA ($\epsilon \approx 600$ l mol^{-1} cm^{-1} at 350 nm) in comparison with chromium(III)-EDTA ($\epsilon \approx 140$ l mol^{-1} cm^{-1} at 600 nm). For this

TABLE 1

Calibration graphs for the flow injection system with spectrophotometric detection (reagent, 10^{-3} mol l^{-1} vanadium(IV)sulphate)

Sample	Sample concentration range (mol l^{-1})	Regression line[a]	Regression coefficient r	Limit of determination (mol l^{-1})
$VOSO_4$	10^{-4}—10^{-3}	$A = (113 \pm 0.5)C$	0.9999	1.8×10^{-4}
NH_4VO_3	10^{-4}—7.5×10^{-4}	$A = (265 \pm 10)C$	0.9986	7.5×10^{-5}
$UO_2(Ac)_2$	10^{-4}—7.5×10^{-4}	$A = (256 \pm 4)C$	0.9997	7.8×10^{-5}
$K_3Fe(CN)_6$	10^{-4}—10^{-3}	$A = (121 \pm 3)C$	0.9987	1.7×10^{-4}
KIO_3	1.66×10^{-5}—1.66×10^{-4}	$A = (851 \pm 29)C$	0.9988	2.4×10^{-5}
Methyl red	5×10^{-5}—2.5×10^{-4}	$A = (406 \pm 16)C$	0.9985	4.9×10^{-5}
o-Nitrophenol	8.3×10^{-5}—1.66×10^{-4}	$A = (408 \pm 7)C$	0.9998	4.9×10^{-5}
Maleic acid	10^{-3}—10^{-2}	no signal	—	—
Formaldehyde	10^{-3}—10^{-2}	no signal	—	—

[a] A = absorbance; C = concentration of analyte.

reason, the reagent concentration of vanadium(IV) entering the Jones reductor is 10^{-3} mol l^{-1}, instead of 10^{-2} mol l^{-1} in the case of chromium(III)-chloride.

Amperometric detection in alkaline medium

Apart from the working potential of the amperometric flow-through detector, the experimental set-up was identical with that in the paper on chromium(II) [2].

The selection of a suitable working potential is a problem in the case of vanadium(II) because four valency states of vanadium, viz. vanadium(II), vanadium(III), vanadium(IV) and vanadium(V), may occur in the reaction mixture entering the detector. The occurrence of these valency states can depend on the analyte. The following procedure was applied to select the best working potential. Four polarograms were recorded in the flow system (see also Fig. 1). First, a polarogram (A) of the reagent solution (vanadium(II) with buffer and EDTA) and a polarogram (B) for which 10^{-2} mol l^{-1} hydrochloric acid entered the Jones reductor, instead of the vanadium(IV) solution (background current) were recorded. These two polarograms also give information about the reduction efficiency in the Jones reductor and about the decomposition of vanadium(II)-EDTA during its transport in the flow system. Then a polarogram (C) was recorded, for which the water in the carrier stream was replaced by a solution of the analyte under investigation; this polarogram should give a picture of the reaction products for that particular analyte, particularly those of vanadium. Finally, a polarogram (D) was measured, for which 10^{-2} mol l^{-1} hydrochloric acid entered the Jones reductor and the analyte under investigation replaced water in the carrier stream; this polarogram gives a picture of the polarographic behaviour of the analyte itself.

In Fig. 2, these four polarograms are presented for sodium nitrite as the analyte. In polarograms C and D the concentration of the analyte in the carrier stream was 10^{-2} mol l^{-1}. From polarograms A and B in the figure it can be seen that no reducible substances of vanadium are present. The oxidation wave starting at about −1.4 V probably corresponds to the reaction V(II)-EDTA $\rightleftharpoons$ V(III)-EDTA + e^-. This is in accord with the results obtained by Pecsok and Juvet in a quiescent solution [3]. The decomposition of the reagent must therefore be negligible and the reduction efficiency in the Jones reductor must be very close to 100%. The reduction efficiency of the Jones reductor was also tested by a batch titration procedure, in which the vanadium solution (10^{-2} mol l^{-1}), which had passed through the Jones reductor, was collected in excess of potassium iodate; the excess was determined iodimetrically. The reduction efficiency was again very close to 100% for flows from 0.2 to 1.4 ml min^{-1} through the Jones reductor.

Polarogram D shows that sodium nitrite itself is not electroactive. Polarogram C gives information about the end products of the reaction of vanadium(II)-EDTA with sodium nitrite. The vanadium(II)-EDTA oxidation

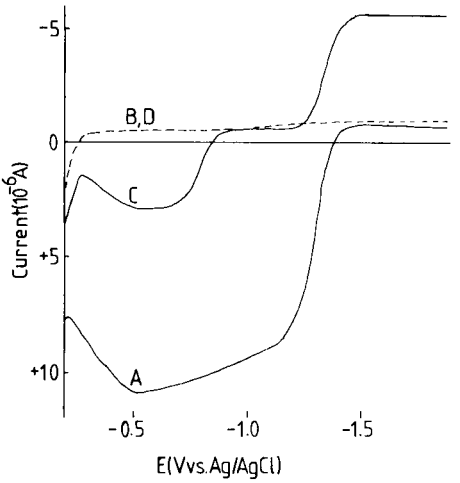

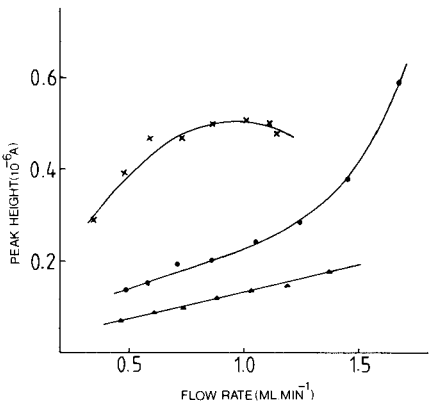

Fig. 2. Polarograms in flow for nitrite. For explanation of A, B, C and D, see text.

Fig. 3. Peak height as a function of the flow rate for the amperometric measurement of: (•) 10^{-4} mol l^{-1} sodium nitrite; (▲) 10^{-4} mol l^{-1} hydroxylamine; (×) 10^{-3} mol l^{-1} sodium nitrate (with a 1-m SBSR 3).

wave has disappeared. The reduction wave at about —1.3 V must be ascribed to the reaction V(III)-EDTA + $e^- \rightleftharpoons$ V(II)-EDTA, again in agreement with the results obtained by Pecsok and Juvet. Therefore, in the case of sodium nitrite, all the vanadium(II)-EDTA is converted to vanadium(III)-EDTA and no higher oxidation states occur. The oxidation wave in polarogram C, which starts at about —0.7 V, also appears if nitrate is the analyte but not for hydrazine and hydroxylamine. When the medium was slightly acidic (pH 5.7 in the detector), a reduction wave occurred at the same potential but only when nitrite was the analyte. So far no satisfactory explanation for these waves has been found. As these waves do not interfere at the working potential, no further work was done to explain the waves. The conclusion from these experiments is that a working potential of —1.5 V is very suitable for sodium nitrite. At this potential the noise in the baseline is minimal.

The same procedure was followed for all the species determined in the polarographic part of the work. For nitrate the oxidation of vanadium(II)-EDTA was not complete, polarogram C still having an anodic wave corresponding to vanadium(II)-EDTA. Nitrate itself was also not electroactive. Therefore, the same working potential as in the case of nitrite was suitable.

Hydrazine showed no reaction at all with vanadium(II)-EDTA and was itself not electroactive under the conditions used. For hydroxylamine, the oxidation of vanadium(II)-EDTA again appeared to be complete in experiment C; hydroxylamine itself appeared to be electroactive. The polarogram of hydroxylamine in the flow system (as for polarogram D) showed a reduc-

tion wave starting at about −1.4 V. The only possible working potential in this case was −1.43 V, at which the reduction of vanadium(III)-EDTA was very near its limiting current and the contribution of hydroxylamine to the current was very small. The working potentials for the amperometric flow-through detector, established in this way, are summarized in Table 2.

Dependence of the signal on the flow rate

The peak height is dependent on the flow rate in an unpredictable way [2]. Therefore, the dependence of the signal on the flow rate must be determined experimentally for every analyte. For nitrite and hydroxylamine, peak heights resulting from the injection of a 10^{-4} mol l^{-1} sample solution were recorded at different flow rates; the peak height increased with increasing flow rate in both cases. For these species, the highest flow rate (about 1.4 ml min^{-1}) that can be achieved with the pump and pump tubes used is the optimum flow rate.

Peak heights resulting from the injection of 10^{-4} mol l^{-1} sodium nitrate were very low and irregular. Increasing the residence time by lengthening the SBSR 3 in the flow system to 1 m still resulted in low peak heights, but the shape of the peaks became more regular. All further determinations of nitrate were therefore done with a 1-m SBSR 3. Because of the small peaks recorded for the 10^{-4} mol l^{-1} nitrate samples, the influence of the flow rate on the peak height was investigated for 10^{-3} mol l^{-1} sodium nitrate. The graph of peak height vs. flow rate then showed a maximum at a flow rate of 1 ml min^{-1}, which is the optimal flow rate for nitrate. Injections of 10^{-3} mol l^{-1} hydrazine samples showed no peak, even when SBSR 3 was lengthened to 1 m.

The resulting peak heights as a function of the flow rate for nitrate, nitrite and hydroxylamine are presented in Fig. 3.

Results of amperometric detection in alkaline medium

Results of the determinations of hydroxylamine, nitrate and nitrite are summarized in Table 3. The correlations for the current (I) and the concentration of the analyte in the sample solution (C) show a good linearity. The maximum sampling rate [4] for nitrite and hydroxylamine is $S_{max} = 3600/4\ \sigma_t = 190\ h^{-1}$ for $\sigma_t = 4.7$ s (σ_t is the standard deviation in seconds). For nitrate, S_{max} is 135 h^{-1} ($\sigma_t = 6.7$ s).

TABLE 2

Working potentials of the amperometric flow-through detector

Sample	Working potential (V)	Sample	Working potential (V)
$NaNO_3$[a]	−1.50	NH_2NH_2[b]	−1.43
$NaNO_2$	−1.50	NH_2OH	−1.43

[a]With SBSR 3 = 1 m. [b]In acidic medium.

TABLE 3

Calibration graphs for the flow injection system with amperometric detection (reagent, 2×10^{-3} mol l^{-1} vanadium(IV) sulphate)

Sample	Sample concentration range (mol l^{-1})	Regression line	Regression coefficient r	Limit of determination (mol l^{-1})
$NaNO_3$[a]	10^{-4}—10^{-3}	$I = (5.83 \pm 0.10)\ 10^{-4}\ C$	0.9996	1.53×10^{-4}
$NaNO_2$	10^{-5}—10^{-4}	$I = (2.90 \pm 0.07)\ 10^{-3}\ C$	0.9991	1.44×10^{-5}
NH_2NH_2[b]	10^{-4}—10^{-3}	$I = (5.26 \pm 0.11)\ 10^{-5}\ C$	0.9994	9.50×10^{-5}
NH_2OH	5×10^{-5}—1.5×10^{-4}	$I = (1.54 \pm 0.07)\ 10^{-3}\ C$	0.9965	3.25×10^{-5}

[a]With SBSR 3 = 1 m. [b]In acidic medium.

The limits of determination with this amperometric detection and with the spectrophotometric detection [1] are about the same.

Amperometric detection in acidic medium

Because the pH at which reductions are possible for vanadium(II)-EDTA is less critical than for chromium(II)-EDTA, an attempt was made to use vanadium(II)-EDTA in slightly acidic medium. Care must be taken at pH values below 3, because EDTA then starts to precipitate [5]. Also at pH values below 4, vanadium(II) is no longer completely complexed by EDTA. The "buffer" solution used has such a small buffer capacity that, after mixing with the acid vanadium(II) solution, the pH drops to 5.7. Some acidic buffer solutions were tried, but all these caused the disappearance of the vanadium(III)-EDTA wave into the hydrogen wave.

The same procedure as for the determinations in alkaline solutions was applied to find the best working potential for the amperometric flow-through detector. Polarograms A and B were much the same as those in alkaline solution. The hydrogen wave started at about —1.6 V. The other polarograms, C and D, showed that nitrate and nitrite reacted equally well in acidic as in alkaline medium, that hydroxylamine did not react at all, and that hydrazine reacted with vanadium(II)-EDTA under acidic conditions.

Because the hydrogen wave is very close to the vanadium(III)-EDTA wave at pH 5.7, it was not worthwhile to examine the determinations of nitrate and nitrite in acidic solutions. However, as hydrazine did not react in alkaline solutions, its determination in acidic medium was studied briefly. The best working potential for the amperometric detector was —1.43 V and the best flow rate was 1.4 ml min^{-1}. The results for hydrazine are also given in Table 3.

Ammonia detection

Recently, a new method for the determination of ammonia in a flow injection system was described [6]; in the flow stream, diffusion of ammonia

through a gas-permeable membrane caused an absorbance change of an acid-base indicator solution. This system was modified to enable the extent of conversion of nitrate, nitrite, hydrazine and hydroxylamine to ammonia to be determined. The reaction products of the reduction of the nitrogenous substance by vanadium(II)-EDTA were led into the device.

The flow diagram is shown in Fig. 4. The concentration of vanadium(IV) sulphate entering the Jones reductor was 10^{-2} mol l^{-1} in 6×10^{-2} mol l^{-1} sulphuric acid. The buffer solution contained 10^{-1} mol l^{-1} disodium tetraborate and 3.3×10^{-2} mol l^{-1} EDTA (disodium salt). The pH was adjusted to 10 with 1 mol l^{-1} sodium hydroxide. The indicator was aqueous 10^{-4} mol l^{-1} bromothymol blue, the pH of which was adjusted to 6.5 with 10^{-2} mol l^{-1} sodium hydroxide. The detector was set at 620 nm, the wavelength of maximum absorption for the alkaline form of the indicator. The system was calibrated by injection of samples of ammonium chloride in the concentration range 10^{-4}—10^{-3} mol l^{-1}.

The conversion of the analyte in the sample solution to ammonia was measured by injection of a 10^{-3} mol l^{-1} sample solution into the system. The conversions thus found were 26% for nitrate, 54% for nitrite and 47% for hydroxylamine. Hydrazine caused no absorbance change.

Conclusions

When chromium(II) and vanadium(II) are compared as strongly reducing reagents, it can be concluded that, in the case of spectrophotometric detection, vanadium(II) provides lower limits of determination. With regard to the substances that can be determined with amperometric detection, nitrate is better determined with chromium(II) because the limit of determination is then lower by a factor of about 5. For nitrite, both reducing reagents gave about the same results. Hydroxylamine can be determined only with vanadium(II), and hydrazine can be determined by using vanadium(II) in slightly acidic medium.

The chromium(II) system [2] and the vanadium(II) system are easily interchangeable simply by changing the reagent solution. In this way, fast

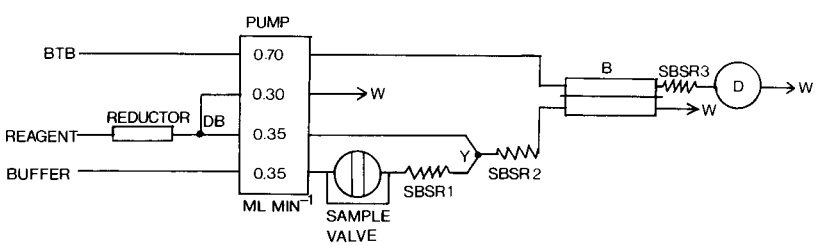

Fig. 4. Flow diagram for the ammonia detection. Length of SBSRs: (1) 0.2 m; (2) 40 cm; (3) 0.05 m. DB, debubbler; D, detector; B, cell with a gas-permeable membrane; W, waste. All connecting and SBSR tubing is 1 mm i.d. nylon. SBSRs are packed with 0.6 mm glass beads. Sample size 32 μl.

and convenient application of these reducing reagents is feasible in flow systems.

The authors thank Mr. W. Ozinga for experimental aid with the spectrophotometric part of the work.

REFERENCES

1 R. C. Schothorst, J. M. Reijn, H. Poppe and G. den Boef, Anal. Chim. Acta, 145 (1983) 197.
2 R. C. Schothorst and G. den Boef, Anal. Chim. Acta, 153 (1983) 133.
3 R. L. Pecsok and R. S. Juvet, J. Am. Chem. Soc., 75 (1953) 1202.
4 J. Růžička and E. H. Hansen, Flow Injection Analysis, Wiley-Interscience, New York, 1981.
5 J. Kragten and L. G. Decnop-Weever, Talanta, 30 (1983) 623.
6 M. van Son, R. C. Schothorst and G. den Boef, Anal. Chim. Acta, 153 (1983) 271.

Analytica Chimica Acta, 161 (1984) 37—51
Elsevier Science Publishers B.V., Amsterdam — Printed in The Netherlands

LASER MICROPROBE MASS ANALYSIS OF *o*-PHENYLENEDIAMINE ON ASBESTOS FIBRES

J. K. DE WAELE, E. F. VANSANT and F. C. ADAMS*
Department of Chemistry, University of Antwerp (U.I.A.), B-2610 Wilrijk (Belgium)
(Received 23rd January 1984)

SUMMARY

The adsorption behaviour of *o*-phenylenediamine and its catalytically formed oxidation products such as 2,3-diaminophenazine and higher-molecular-weight compounds on different varieties of asbestos is studied by using laser desorption mass spectrometry. The results prove that amosite adsorbs the product more easily than do crocidolite and anthophyllite, whereas U.I.C.C. chrysotile A does not give rise to detectable adsorption, and the adsorption observed for U.I.C.C. chrysotile B is only fair. The method shows potential for the investigation of the surface reactivity of pure and industrially transformed asbestos and other fibrous materials.

Asbestos is a generic term covering several fibrous silicate minerals, classified into two groups: the serpentines with chrysotile asbestos and the amphiboles encompassing amosite, crocidolite, anthophyllite, actinolite and tremolite. The industrial usefulness of asbestos stems particularly from its natural properties: non-flammability, flexibility, tensile strength, low density, resistance to acids and alkalies, and high electrical resistivity [1—3].

The factors relevant to the assessment of public health risks caused by exposure to asbestos fibres are now well documented [3, 4]. Asbestos inhalation may cause not only asbestosis, a fibrous induration of the lungs, but also pleural calcification, pleural plaques, lung cancer and mesotheliomas originating from pleura or peritoneum. Malignancies arise primarily after long-term occupational exposure extending over 20 or more years [1, 3—10]. It has been reported that there is a synergic toxic effect of a number of organic pollutants when they are associated with asbestos as a pollution source [7, 8, 11—13]. Because of the hypothesis that the toxicity of the asbestos fibres is correlated with the adsorptive power of the asbestos for carcinogenic organic pollutants or precursors of carcinogenic compounds [14, 15], research in this laboratory has been directed towards characterization of the fibre surface [16—24].

The oxidative properties of different asbestos varieties have been studied previously with *N,N*-dimethylaniline, which adsorbs and then reacts at the fibre surface, yielding strongly coloured oxidation products [17, 20, 25]. Moreover, in strong oxidizing conditions, the formation of methyl violet has

0003-2670/84/$03.00

been observed with amosite and chrysotile asbestos [17, 20]. The oxidation products of *N,N*-dimethylaniline formed are known to depend on the structural characteristics of the mineral [25]. Both surface properties and the presence of active sites are important in this context.

This paper is concerned with the results of a similar investigation on the catalytic oxidizing effects of asbestos fibre surfaces. It deals with the adsorptive behaviour of *o*-phenylenediamine and its oxidation products [26, 27] on different varieties of asbestos by laser microprobe mass analysis.

EXPERIMENTAL

Apparatus

The commercially available laser microprobe mass analyzer (LAMMA-500, Leybold-Heraeus, Cologne, Germany) has been described in detail [28—31]. The most important claims made for the technique are its speed of operation, its microbeam capability (spatial resolution ≈ 1 μm), its high sensitivity (down to 10^{-20} g) and its applicability to both inorganic and organic (including biological) samples [30, 31]. Asbestos fibres can be held in a Formvar film fixed to a standard copper electron microscope grid. Organic impurities adsorbed onto the surface of individual asbestos fibres can be detected at low laser irradiance, in the laser desorption mode [16—21, 32—37]. Details on sample preparation have been given by De Waele et al. [17].

Materials and reagents

The U.I.C.C. (Union Internationale Contre le Cancer) standard asbestos samples used were South African crocidolite and amosite, Zimbabwean (type A) chrysotile, Canadian (type B) chrysotile and Finnish anthophyllite were used [38—40]. The U.I.C.C. has sponsored the preparation and distribution of standard reference samples of each class of asbestos, and these samples have been employed in standardization of conventional fibre counting, ingestion, inhalation, inoculation and in in vitro experiments [41].

The chemicals used were *o*-phenylenediamine (zur Synthese, 99%; Merck), 0.1 M hydrochloric acid (Titrisol; Merck) and hydrogen peroxide (30% (w/w) in twice-distilled water, A.C.S. Reagent; Janssen Chimica, Belgium).

Preparation of asbestos samples

Procedure 1. A portion (25 ml) of 0.1 M *o*-phenylenediamine in twice-distilled water was added to 40 mg of U.I.C.C. amosite asbestos at room temperature. The mixture was stirred and warmed to 80°C under reflux for 17 h. The fibres were then filtered on a Schleicher & Schüll filter (no. 589[1] Schwarzband, 110 mm diameter) and washed five times with twice-distilled water. The fibres were dried at 65° C in a drying oven.

Procedure 2. Aqueous solutions containing 25 ml of *o*-phenylenediamine (0.04 or 0.1 M), in the absence or presence of 15 ml of 0.1 M HCl, and 15 ml

of hydrogen peroxide (3, 6 or 12%) were added to 40-mg portions of standard amosite. The heterogeneous mixtures were stirred for 17 h at room temperature and filtered, and the fibres were washed and recovered for spectrometry.

Procedure 3. Portions (40 mg) of the five U.I.C.C. samples were treated with 0.1 M *o*-phenylenediamine, 0.1 M HCl and 6% hydrogen peroxide as in procedure 2 but for 22 h.

RESULTS AND DISCUSSION

Catalytic oxidation of o-phenylenediamine

The most characteristic property of *o*-diamines is the ease with which they form heterocyclic oxidation products [26, 27]. When a colourless aqueous solution of *o*-phenylenediamine (OPDA) is warmed with iron(III) chloride in the presence of hydrogen chloride, long deep red needles of 2,3-diaminophenazine crystallize. The *o*-quinone diimine is formed first and subsequently condenses with more diamine. The reaction scheme can be presented as follows [26]

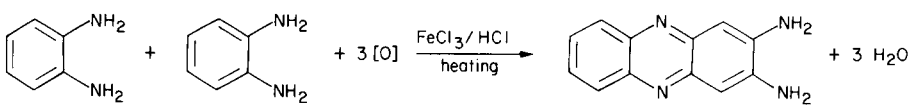

The behaviour of a heated aqueous 0.1 M o-phenylenediamine solution on amosite

In order to check whether the oxidation reaction of OPDA observed in solution in the presence of iron(III) chloride and hydrogen chloride also occurs in the presence of asbestos fibres, the adsorptive behaviour of a hot aqueous 0.1 M OPDA solution onto amosite asbestos fibres was studied using procedure 1. The treated brown amosite fibres were recovered for laser microprobe mass analysis.

The recorded positive mass spectra show considerable amounts of information on reaction products of OPDA. A very intense protonated molecular ion peak ($(M_A + H)^+$, $m/z = 211$) of the principal OPDA oxidation product, M_A is observed in the positive laser desorption mass spectra of the treated amosite fibres (Fig. 1), showing clearly the presence of 2,3-diaminophenazine at the amosite fibre surface. In addition to the protonated molecular ion peak of residual unreacted OPDA at $m/z = 109$, a systematic feature is also that at m/z values below 211, there is a characteristic fragmentation pattern, which can be identified with the fragment ions indicated in Fig. 1; they are due to the loss of —CN and —NH_2 from the M_A parent molecules [42, 43]. Other characteristic peaks around $m/z = 298$ and 400 are observed which can be ascribed to fragment ions of further catalytic oxidation products, M_B and M_C, respectively, as explained in Fig. 1. The general conclusion is that, in addition to the main principal oxidation product of OPDA, 2,3-diamino-

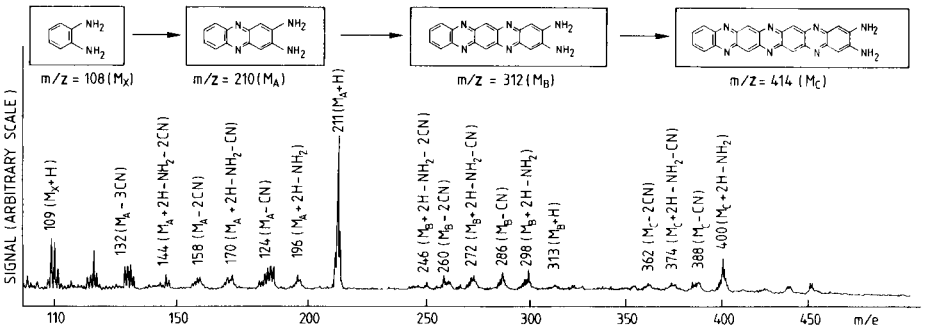

Fig. 1. Positive laser desorption mass spectrum of an amosite asbestos fibre treated with a hot aqueous 0.1 M OPDA solution and subjected to a laser shot of 0.18 μJ.

phenazine (M_A), detected previously in the presence of iron(III) chloride and hydrogen chloride as a catalyst [26, 27], other catalytic oxidation products, assigned as M_B and M_C, can also be detected on the surface of hot OPDA-treated amosite fibres.

Figure 2(A—F) gives typical examples of positive mass spectra, when six consecutive shots of comparable and low laser energy ($\approx$0.04 μJ) were directed at the same location of one 0.1 M OPDA-treated amosite fibre. At the first laser shot, the protonated molecular ion peak $(M_A + H)^+$ at m/z = 211 is the only detectable feature of the mass spectrum (Fig. 2A). Its intensity reaches a maximum at the second and third shot (Figure 2B—C) and, beside the characteristic fragmentation pattern of the oxidation product M_A, other fragment ions of the above-mentioned oxidation products M_B and M_C also become detectable around m/z = 298 and 400. After three consecutive shots (Fig. 2D, F), their intensities start levelling off gradually but still remain detectable, and the inorganic elemental and cluster ions of the amosite fibre substrate become the dominant peaks in the mass spectrum. These and other observations indicate that laser microprobe mass analysis can be used as a fast depth-probing device [17—20].

It appears that the major catalytic oxidation products of OPDA (M_A, M_B and M_C) are clearly detectable on individual amosite fibres. When OPDA is adsorbed at a similar concentration (0.1 M) on amosite standard fibres, without heating, none of the oxidation products can be detected. This is in accordance with previous experience [26, 27] which proves that an oxygen donor is needed for completion of the oxidation reaction scheme.

The influence of hydrogen peroxide on the oxidation of OPDA on amosite at room temperature

Treatment of the amosite standard with a hot 0.1 M OPDA solution is a rather drastic treatment. Previous experiments with *N,N*-dimethylaniline in the presence of hydrogen peroxide as a strong oxidant showed that the method offers potential for investigations of the reactivity of asbestos fibre

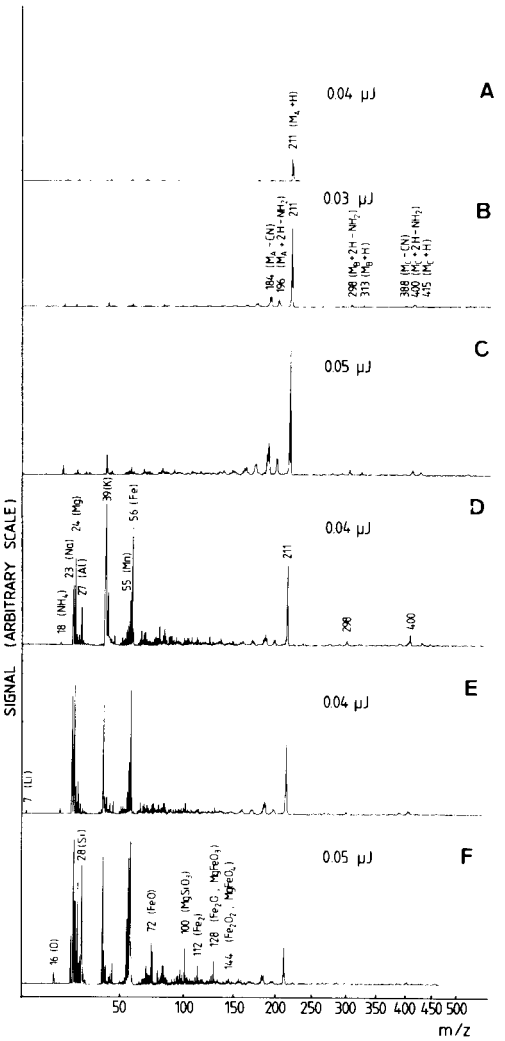

Fig. 2. Positive laser desorption mass spectra of an amosite fibre doped with a hot 0.1 M OPDA solution, which was subjected to 6 consecutive laser shots of comparable energy (A—F), from top to bottom.

surfaces [20]. Therefore, similar adsorption experiments (procedure 2) were repeated for amosite fibres in the absence of hydrogen peroxide or with 3 or 6% hydrogen peroxide in the aqueous solution in order to check the reaction behaviour at room temperature. In the presence of the highest peroxide concentrations, the OPDA/amosite mixtures became orange or dark brown even after only a few minutes, indicating fast formation of the main oxidation product(s) of OPDA at the fibre surface.

o-Phenylenediamine/hydrogen peroxide adsorbed on the amosite standard

fibres, as in procedure 2, showed the following behaviour in the recorded positive mass spectra. Figure 3(B, C) gives some characteristic examples of positive spectra taken at ca. 0.2 μJ compared with that obtained for a pure standard amosite fibre with similar laser energy conditions (Fig. 3A). The spectrum in Fig. 3B which is characteristic for amosite treated directly with 0.1 M OPDA at room temperature, does not show any detectable protonated molecular ions or related fragmentation peaks of the oxidation products. After treatment with 6% H_2O_2/0.1 M OPDA (Fig. 3C), a significant

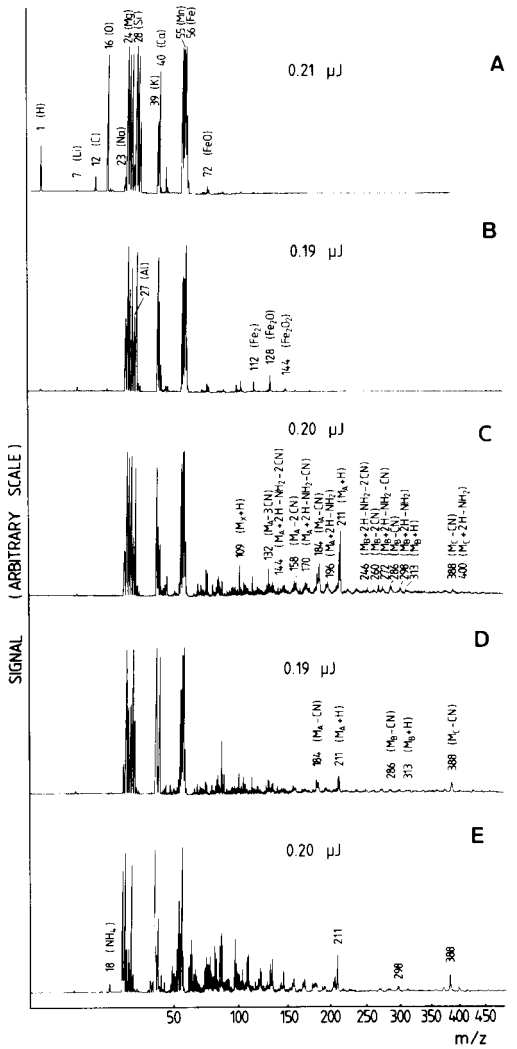

Fig. 3. Positive laser desorption mass spectra of a pure standard amosite fibre (A) and of amosite asbestos fibres treated at room temperature with: (B) 0.1 M OPDA; (C) 0.1 M OPDA/6% H_2O_2; (D) 0.1 M OPDA/0.1 M HCl/6% H_2O_2; (E) 0.1 M OPDA/0.1 M HCl/ 12% H_2O_2.

$(M_A + H)^+$ peak and typical M_A fragment ions are observed on the amosite fibre surface, because of the formation of the main principal oxidation product, M_A. The presence of peroxide therefore appears to be important as, in similar reaction conditions without the oxidant, the organic impurities are systematically undetectable.

Table 1 summarizes the quantitative results for at least 10 individual measurements, for three laser energy (E_1) ranges after three distinct peroxide/OPDA treatments, and compares the results with those obtained for the untreated standard amosite. These values show that below 3% hydrogen peroxide, there is no detectable surface adsorption and oxidation. Only with $\geqslant$6% hydrogen peroxide solution can an intensive $(M_A + H)^+$ peak of the first oxidation product (M_A) be observed. At these peroxide concentrations in the lowest laser energy range ($E_1 < 0.1$ μJ), the contribution of elemental ions is minimal, whereas the intensity of the characteristic fragment ions and protonated molecular ion of the catalytic oxidation product passes through a maximum. The results obtained at higher laser energy ranges show a rapidly increasing contribution of the inorganic amosite substrate. In general, it can also be noted that the reproducibility of the mass spectra of individual amosite fibres doped with the different OPDA/peroxide solutions, as shown in Table 1, is excellent (10—30% r.s.d.).

These measurements indicate that the positive mass spectra allow the ready detection of 2,3-diaminophenazine and its related fragmentation pattern on the surface of single fibres of amosite treated with OPDA and hydrogen peroxide. Previous experience [26, 27] showed the formation of 2,3-diaminophenazine in the presence of hydrogen chloride. A study was therefore made of the effect of hydrochloric acid in the solution on the oxidation behaviour and consequent laser desorption spectra.

The influence of hydrochloric acid on the oxidation of OPDA on amosite in the presence of hydrogen peroxide

o-Phenylenediamine/hydrogen peroxide adsorbed on the amosite fibres in the presence of 0.1 M HCl (procedure 2) showed systematic trends in the recorded positive mass spectra. The spectrum in Fig. 3D, which is typical for amosite treated with 0.1 M OPDA/0.1 M HCl/6% H_2O_2, shows not only the presence of 2,3-diaminophenazine (M_A) with its related fragmentation pattern but also the fragment ions of the oxidation products M_B and M_C. These OPDA oxidation products become more easily detectable when the concentration of hydrogen peroxide is increased to 12%, as shown in Fig. 3E. Hence, the oxidation reactions with peroxide appear to proceed more fully in hydrochloric acid medium at room temperature, and the catalytic oxidation products, which had previously been identified on hot 0.1 M OPDA-treated amosite, were easily detectable on single amosite fibres. With 0.04 M OPDA in the presence of 6% H_2O_2/0.1 M HCl, no detectable surface adsorption and oxidation seemed to occur. Only with 0.1 M or more concentrated OPDA solutions was it possible to observe intense fragment and exceptionally

TABLE 1

Intensities of elemental and molecular ion peaks for U.I.C.C. amosite standard treated with OPDA/peroxide at room temperature, compared with untreated standard fibres, taken at 3 different laser energy E_1 (μJ) ranges

m/z	Peak intensities (relative unit) for different treaments											
	Untreated			0.1 M OPDA treated			0.1 M OPDA/3% H_2O_2 treated			0.1 M OPDA/6% H_2O_2 treated		
	$E_1 < 0.06$	$0.06 \leqslant E_1 \leqslant 0.16$	$E_1 > 0.16$	$E_1 < 0.06$	$0.06 \leqslant E_1 \leqslant 0.16$	$E_1 > 0.16$	$E_1 < 0.06$	$0.06 \leqslant E_1 \leqslant 0.16$	$E_1 > 0.16$	$E_1 < 0.06$	$0.06 \leqslant E_1 \leqslant 0.16$	$E_1 > 0.16$
23	65 ± 25	100 ± 50	140 ± 80	61 ± 15	300 ± 30	220 ± 40	80 ± 20	290 ± 50	150 ± 60	36 ± 14	250 ± 80	560 ± 40
24	150 ± 40	280 ± 40	1140 ± 20	157 ± 15	370 ± 8	1050 ± 130	330 ± 19	550 ± 60	800 ± 110	12 ± 8	460 ± 170	700 ± 50
27	50 ± 40	130 ± 100	210 ± 70	26 ± 13	120 ± 50	140 ± 55	40 ± 20	120 ± 50	220 ± 70	34 ± 9	220 ± 60	540 ± 50
28	n.d.	1.0 ± 1.0	1210 ± 40	1.0 ± 0.6	23 ± 5	650 ± 230	6.8 ± 1.4	30 ± 7	600 ± 220	13 ± 3	160 ± 140	250 ± 160
39	290 ± 110	450 ± 40	270 ± 100	200 ± 19	640 ± 30	450 ± 75	140 ± 60	320 ± 80	340 ± 90	82 ± 8	430 ± 130	830 ± 70
40	27 ± 9	19 ± 6	320 ± 40	9.7 ± 1.3	80 ± 25	310 ± 80	30 ± 4	130 ± 14	250 ± 50	8 ± 4	120 ± 70	190 ± 20
55	32 ± 11	80 ± 30	670 ± 60	52 ± 9	230 ± 40	670 ± 130	120 ± 13	330 ± 40	480 ± 60	19 ± 3	300 ± 150	460 ± 20
56	260 ± 40	420 ± 40	1220 ± 40	203 ± 18	480 ± 30	1190 ± 110	460 ± 60	700 ± 60	980 ± 160	11 ± 4	610 ± 160	800 ± 60
109	n.d.[a]	n.d.	n.d.	n.d.	n.d.	n.d.	10.0 ± 1.7	13.7 ± 2.0	n.d.	8.7 ± 0.9	48 ± 6	32 ± 6
158	n.d.	n.d.	n.d.	n.d.	n.d.	n.d.	1.3 ± 0.3	8 ± 3	n.d.	7.0 ± 1.2	56 ± 6	28 ± 7
184	n.d.	n.d.	n.d.	n.d.	n.d.	n.d.	2.3 ± 0.3	25 ± 9	n.d.	7.3 ± 0.8	155 ± 25	60 ± 13
211	n.d.	n.d.	n.d.	n.d.	n.d.	n.d.	7.3 ± 2.0	36 ± 10	n.d.	13.7 ± 2.9	180 ± 16	95 ± 8
286	n.d.	n.d.	n.d.	n.d.	n.d.	n.d.	n.d.	2.0 ± 0.6	n.d.	1.0 ± 1.0	33 ± 5	7.0 ± 1.5
298	n.d.	n.d.	n.d.	n.d.	n.d.	n.d.	n.d.	5.0 ± 1.5	n.d.	0.3 ± 0.3	35 ± 4	15 ± 5
388	n.d.	n.d.	n.d.	n.d.	n.d.	n.d.	n.d.	n.d.	n.d.	n.d.	25 ± 5	4.8 ± 1.4

[a]Not detected.

protonated molecular ions of the three formed oxidation products (M_A, M_B and M_C). The reproducibility of the mass spectra of individual amosite fibres doped with OPDA/HCl/H_2O_2 under different reaction conditions was in general excellent. This is shown in Table 2 which, for three different laser energy ranges, summarizes the average absolute intensities of some characteristic spectral components and the standard deviations (at least 10 individual measurements). With 0.1 M OPDA/0.1 M HCl, the intensity of these characteristic organic ions increases only slightly with the H_2O_2 concentration (between 3 and 12%). It should be noted that the results in this table were obtained under closely similar laser energies and working parameters as the results shown in Table 1.

The results in Tables 1 and 2 indicate that the positive mass spectra of all the treated amosite fibres do not correspond to those obtained for the pure standard amosite fibers, obtained at similar laser energy conditions. The magnesium and iron ion peaks are considerably decreased in intensity after treatment, especially for the low laser energy range ($E_1 < 0.1$ μJ) in laser desorption conditions. In these conditions, the ion intensities of the catalytic oxidation fragments are maximal, whereas the intensities of the Mg^+, Fe^+ and other related elemental ions on the fibre surface become low. The reduction of apparent magnesium and iron intensity on the surface of the treated amosite fibres is in agreement with the results for amosite treatment of procedure 1 as shown in Fig. 2 (A—F). A similar behaviour was also observed in previous experiments with benzo[a]pyrene, benzidine, aliphatic alkylammonium chlorides and *N,N*-dimethylaniline oxidation products (e.g., methyl violet) adsorbed on asbestos fibres [17—20]. Attempts are now being made to establish if this decrease in intensity of the elemental constituents is the result of a real surface depletion [44—48] or rather originates from phenomena connected with the laser interaction process itself [35, 49, 50]. Secondary ion mass spectrometry (s.i.m.s.) is being used to obtain real depth-profile information, which will enable the two possibilities to be distinguished. Preliminary results show that the effect is real [22]; hence laser desorption mass spectrometry (l.d./m.s.) can provide a powerful tool for probing small changes in inorganic surface composition [17—20]. The results obtained with s.i.m.s. will be reported elsewhere [24].

Comparative oxidation behaviour of 0.1 M OPDA/0.1 M HCl/6% H_2O_2 on U.I.C.C. asbestos standards

In order to check whether the oxidation sequence derived above for amosite is also valid for the other asbestos minerals, the adsorption of 0.1 M OPDA in the presence of 0.1 M HCl/6% hydrogen peroxide onto the U.I.C.C. asbestos standards was studied by using procedure 3. The positive mass spectra of the amphiboles, crocidolite and anthophyllite (Fig. 4B and C) are qualitatively identical to the mass spectra of amosite (Fig. 4A and Fig. 3D), with the main oxidation products detectable. For the serpentines (chrysotile), the picture is less clear; the (Canadian) chrysotile B sample gives results similar to the amphiboles whereas the (Zimbabwean) chrysotile A shows no

TABLE 2

Intensities of elemental and molecular ion peaks for OPDA/H_2O_2/HCl-treated amosite fibres, taken at 3 different laser energy E_1 (μJ) ranges

m/z	Peak intensities (relative unit) for different treatments								
	0.1 M OPDA/3% H_2O_2/0.1 M HCl			0.1 M OPDA/6% H_2O_2/0.1 M HCl			0.1 M OPDA/12% H_2O_2/0.1 M HCl		
	$E_1 < 0.06$	$0.06 \leqslant E_1 \leqslant 0.16$	$E_1 > 0.16$	$E_1 < 0.06$	$0.06 \leqslant E_1 \leqslant 0.16$	$E_1 > 0.16$	$E_1 < 0.06$	$0.06 \leqslant E_1 \leqslant 0.16$	$E_1 > 0.16$
23	90 ± 30	380 ± 40	390 ± 40	140 ± 20	200 ± 50	600 ± 140	210 ± 100	240 ± 60	490 ± 110
24	15 ± 5	340 ± 50	780 ± 70	70 ± 20	590 ± 30	800 ± 110	70 ± 30	530 ± 30	970 ± 60
27	35 ± 17	180 ± 60	410 ± 80	28 ± 9	490 ± 110	230 ± 60	4.0 ± 1.5	85 ± 19	260 ± 50
28	8 ± 3	21 ± 5	210 ± 80	7.1 ± 0.9	70 ± 30	450 ± 240	2.5 ± 1.2	31 ± 8	750 ± 90
39	270 ± 60	780 ± 140	910 ± 160	410 ± 70	770 ± 150	790 ± 110	340 ± 120	380 ± 80	890 ± 230
40	2.0 ± 1.1	60 ± 30	85 ± 19	1.7 ± 1.1	117 ± 19	320 ± 100	0.5 ± 0.5	110 ± 30	380 ± 40
55	14 ± 4	160 ± 40	280 ± 30	22 ± 5	380 ± 50	240 ± 40	19 ± 8	260 ± 60	630 ± 70
56	40 ± 13	440 ± 70	790 ± 80	100 ± 20	737 ± 25	770 ± 60	50 ± 30	590 ± 80	1070 ± 80
109	11.0 ± 1.3	24 ± 7	12.3 ± 1.3	11.3 ± 1.8	16.7 ± 2.1	10.3 ± 1.7	7.3 ± 0.9	16.3 ± 2.0	16 ± 4
158	5.1 ± 1.0	22.0 ± 2.7	12.4 ± 1.8	7.0 ± 0.7	34 ± 4	11.3 ± 2.6	8.0 ± 1.6	29 ± 5	17 ± 4
184	8.6 ± 1.6	28 ± 3	17.6 ± 2.5	16 ± 4	54 ± 4	24 ± 6	18 ± 5	75 ± 12	33 ± 8
211	19.0 ± 2.3	75 ± 16	36 ± 4	22 ± 3	77 ± 8	44 ± 4	28.3 ± 1.8	140 ± 20	57 ± 6
286	3.0 ± 0.7	9.2 ± 2.8	4.3 ± 1.2	4.3 ± 1.5	9.3 ± 1.5	3.6 ± 1.2	2.4 ± 0.5	10.2 ± 2.2	6.5 ± 2.7
298	4.0 ± 0.9	13 ± 3	7.7 ± 1.5	5.5 ± 1.8	13 ± 4	6.0 ± 2.1	4.4 ± 0.8	16 ± 4	9.0 ± 1.5
388	21.3 ± 2.2	47 ± 19	27 ± 5	24 ± 4	58 ± 7	26.6 ± 2.3	27.6 ± 1.6	66 ± 11	30 ± 5

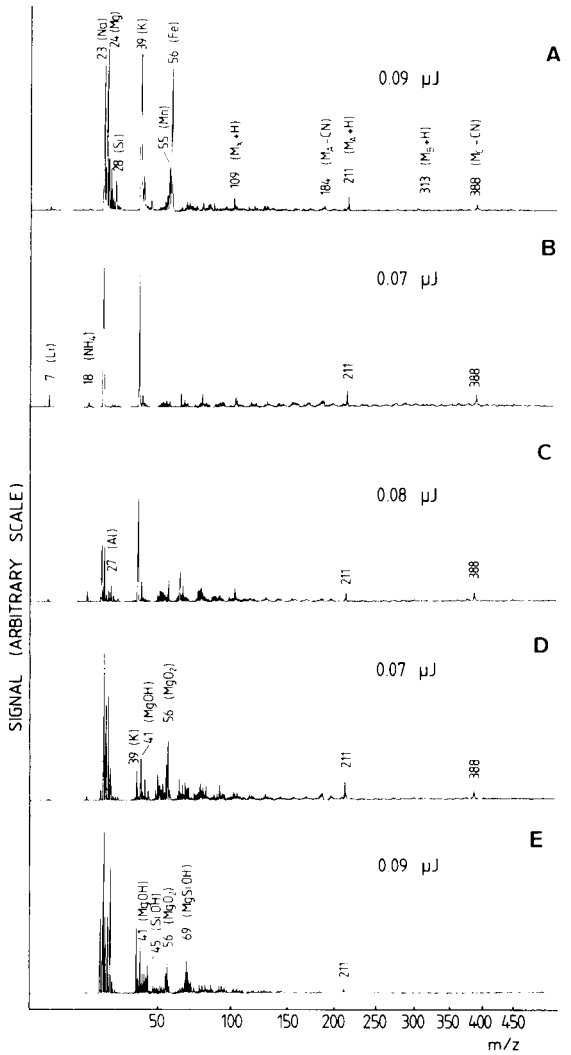

Fig. 4. Positive laser desorption mass spectra of U.I.C.C. asbestos standards doped with 0.1 M OPDA/0.1 M HCl/6% H_2O_2: (A) amosite; (B) crocidolite; (C) anthophyllite; (D) Canadian chrysotile B; (E) Zimbabwean chrysotile A.

significant organic mass spectral features with only the m/z = 211 barely appearing above background noise.

The reason for the difference in behaviour between the chrysotiles is unclear at present but may be connected with the differences in incorporation of magnetite impurities in the two standards [51]. Luys et al. [51] have shown from Mössbauer spectra of the two materials that magnetite is present as a separate phase in chrysotile B whereas it is incorporated in the chrysotile structure in chrysotile A. Current work is devoted to using s.i.m.s. to establish

the surface predominance and depth distribution of iron in these chrysotiles in order to obtain more information on this behaviour.

Table 3 summarizes the quantitative differences of the positive organic ions for 4 different varieties of asbestos after identical treatment (procedure 3) and obtained with similar mass spectrometric conditions at a laser energy around 0.08 μJ. The results are the average absolute intensities and the standard deviations for ca. 20 individual measurements. Results for Zimbabwean chrysotile A are not listed as the material systematically yielded nearly undetectable mass peaks. The mass spectra of Canadian chrysotile B and anthophyllite are quite similar, which stresses their similarity in adsorption and reaction behaviour. The two important amphiboles, amosite and crocidolite, give rise to different mass-spectral intensities, which proves the lesser reactivity of the latter variety; this is in accordance with previous experimental data using *N,N*-dimethylaniline as a probe for studying adsorption and oxidation [17, 20]. Compared with the latter compound, it appears that anthophyllite more readily adsorbs OPDA and its condensation products, whereas it does not adsorb or give significant reactions with *N,N*-dimethylaniline [20].

Negative spectra of all those OPDA/HCl/H_2O_2-treated asbestos varieties, taken in similar laser conditions and working parameters, do not provide ready detection of the adsorbent and the catalytic oxidation products. The spectra correspond closely to those obtained for untreated asbestos fibres. With dimethylaniline, the negative mass spectra allow the detection of the organic material through a number of $N_xCl_y^-$ fragment ions which prove the presence of chlorine-containing oxidation products in hydrochloric acid medium. When these fragments are not detectable, as in the present case, chlorine is not incorporated in the adsorbed entities. The adsorption for the two organic probes (OPDA and dimethylaniline) may thus proceed by different processes. This could account for the significantly different behaviour in surface reactivity for the U.I.C.C. standards between the two organic probes.

TABLE 3

Intensities of molecular ion peaks for U.I.C.C. asbestos standards treated with 0.1 M OPDA/0.1 M HCl/6% H_2O_2

m/z	Peak intensities (relative units)			
	Amosite	Crocidolite	Anthophyllite	Chrysotile B
109	12.3 ± 1.3	12.6 ± 1.9	11.8 ± 2.1	8.5 ± 1.4
158	20 ± 4	6.0 ± 1.7	5.7 ± 0.7	10.6 ± 1.5
184	37 ± 6	10.1 ± 2.5	13.8 ± 2.4	30.9 ± 2.3
211	54 ± 5	23.2 ± 2.7	33 ± 3	32 ± 3
286	6.2 ± 1.2	3.9 ± 1.4	3.6 ± 0.8	6 ± 3
298	8.3 ± 1.5	3.0 ± 0.8	5.0 ± 0.9	2.3 ± 0.4
388	38 ± 4	21 ± 4	28 ± 3	30.6 ± 2.6

Carbon and nitrogen determinations suggested that after treatment by procedure 3, the concentration of organic products present on the asbestos surface was 30—40%.

Conclusion

This work confirms the evidence available from previous studies namely that laser microprobe mass analysis is able to detect the presence of organic compounds at the surface of small (10^{-13} g) fibrous samples. The adsorption of selected organic compounds at the surface of asbestos fibres provides information on the surface adsorption capacity and, through the measurement of reaction products, on the surface reactivity. This would allow evaluation of the hazard of industrially produced fibrous dusts, e.g., transformed asbestos or substitution products. Differences in the behaviour of the OPDA used as the organic probe in this work, with earlier studies involving *N,N*-dimethylaniline suggest that results have to be interpreted carefully. The results clearly are connected with the processes responsible for the adsorption process.

One of us (J.K.D.W.) is indebted to the Instituut tot Aanmoediging van het Wetenschappelijk Onderzoek in Nijverheid en Landbouw for financial support. This research was funded by the E.E.C. through research grant no. ENV-620-B (RS) and by the Interministerial Commission for Science Policy, Belgium, through research grant 80-85/10. We acknowledge the assistance of Dr. R. Amsler, NOVO Industri A/S, Bagsvaerd, Denmark, for the elemental organic analysis.

REFERENCES

1 A. S. Hammons and J. E. Huff, Int. J. Environ. Stud., 6 (1974) 247.
2 A. A. Hodgson, Philos. Trans. R. Soc. London, Ser. A, 286 (1977) 611.
3 L. Michaels and S. S. Chissick, Asbestos — Properties, Applications and Hazards, Vol. 1, Interscience-Wiley, New York, 1981.
4 International Agency for Research on Cancer, Asbestos, IARC Monographs on the Evaluation of Carcinogenic Risk of Chemicals to Man, Vol. 14, 1977.
5 J. Bignon, P. Sebastien and A. Gaudichet, Proc. Workshop on Asbestos: Definitions and Measurement Methods, Gaithersburg, MD, July 1977, National Bureau of Standards Spec. Publ. 506, 1977, p. 95.
6 J. A. Moore, Proc. of the Workshop on Asbestos: Definitions and Measurement Methods, Gaithersburg, MD, July 1977, National Bureau of Standards Spec. Publ. 506, 1977, p. 153.
7 D. L. Coffin and L. D. Palekar, Proc. of the Workshop on Asbestos: Definitions and Measurement Methods, Gaithersburg, MD, July 1977, National Bureau of Standards Spec. Publ. 506, 1977, p. 163.
8 P. C. Elmes, R. Soc. Health J., 96 (1976) 248.
9 D. Gloag, Br. Med. J., 281 (1981) 623.
10 D. Gloag, Br. Med. J., 282 (1981) 551.
11 J. Bignon, M. Bientz, P. Sebastien and G. Bonnaud, Pollut. Atmos., 26 (1976) 2353.
12 J. S. Harrington, A. C. Allison and D. U. Badami, Adv. Pharmacol. Chemother., 12 (1975) 291.

13 I. J. Selikoff, E. C. Hammond and J. Churg, J. Am. Med. Assoc., 204 (1968) 104.
14 J. P. Contour, I. Guérin and G. Mouvier, Atmos. Pollut. 1 (1978), Proc. 13th Int. Colloquium, Paris, April 1978, in M. M. Benarie (Ed.), Studies in Environmental Science, Elsevier, Amsterdam, 1978.
15 J. P. Contour, J. Guérin and G. Mouvier, Environ. Pollut., Ser. B, 1 (1980) 243.
16 J. K. De Waele, P. Van Espen, E. F. Vansant and F. C. Adams, Proc. 17th Annual Conf. Microbeam Analysis, Washington DC, August 1982, in K. F. J. Heinrich (Ed.), San Francisco Press, CA, 1982, p. 371.
17 J. K. De Waele, E. F. Vansant, P. Van Espen and F. C. Adams, Anal. Chem., 55 (1983) 671.
18 J. K. De Waele, I. Verhaert, E. F. Vansant and F. C. Adams, Surf. Interface Anal., 5 (1983) 186.
19 J. K. De Waele, J. J. Gÿbels, E. F. Vansant and F. C. Adams, Anal. Chem., 55 (1983) 2255.
20 J. K. De Waele, E. F. Vansant and F. C. Adams, Mikrochim. Acta, III (1983) 367.
21 J. K. De Waele and F. C. Adams, Presented at 9th Course NATO Int. School Quantum Electron. Anal. Laser Spectrosc., Erice, Italy, September, 1982.
22 P. Van Espen, J. K. De Waele, E. F. Vansant and F. C. Adams, Int. J. Mass Spectrom. Ion Phys., 46 (1983) 515.
23 P. Surkÿn, J. K. De Waele and F. C. Adams, Int. J. Environ. Anal. Chem., 13 (1983) 257.
24 J. A. Verlinden, J. K. De Waele, I. M. Swenters and F. C. Adams, Surface and Interface Analysis.
25 E. F. Vansant and S. Yarif, J. Chem. Soc., Faraday Trans. 1, 73 (1977) 1815.
26 N. Sidgwick, The Organic Chemistry of Nitrogen, 3rd edn., Millar and Springall, Oxford University Press, Oxford, 1966, p. 182.
27 I. L. Finar, Organic Chemistry, Vol. 1, 6th edn., Longman, London, 1973, p. 665.
28 H. Vogt, H. J. Heinen, S. Meier and R. Wechsung, Z. Anal. Chem., 38 (1981) 195.
29 R. Kaufmann, H. Hillenkamp and R. Wechsung, Med. Prog. Technol., 6 (1979) 109.
30 E. Denoyer, R. Van Grieken, F. C. Adams and D. F. Natusch, Anal. Chem., 54 (1982) 26 A.
31 D. M. Hercules, R. J. Day, K. Balasanmugam, T. A. Dang and C. P. Li, Anal. Chem., 54 (1982) 280 A.
32 M. J. Heinen, S. Meier, H. Vogt and R. Wechsung, Z. Anal. Chem., 308 (1981) 290.
33 K. L. Busch, S. E. Unger, A. Vincze, R. G. Cooks and T. Keough, J. Am. Chem. Soc., 104 (1982) 1507.
34 K. Balasanmugam, R. J. Fuan Anh Dong and D. M. Hercules, Anal. Chem., 53 (1981) 2296.
35 G. J. Van Der Peyl, Ph.D. Thesis, University of Amsterdam, 1984.
36 R. J. Day, A. L. Forbes and D. M. Hercules, Spectrosc. Lett., 14 (1981) 703.
37 R. J. Cotter and J.-C. Tabet, Int. J. Mass Spectrom. Ion Phys., 53 (1983) 151.
38 V. Timbrell and R. Rendall, Powder Technol., 5 (1971/1972) 279.
39 V. Timbrell, in H. A. Shapiro (Ed.), Proc. Int. Conf. Pneumoconiosis, Johannesburg, 1969, Oxford University Press, London, 1970, p. 28.
40 V. Timbrell, J. Gibson and I. Webster, Int. J. Cancer, 3 (1968) 406.
41 V. Timbrell, in J. Wagner (ed.), Biological Effects of Mineral Fibers, IARC Scientific Publications no. 30, Lyon, 1980, p. 127.
42 J. H. Beynon, R. A. Saunders and A. E. Williams, The Mass Spectra of Organic Molecules, Elsevier, Amsterdam, 1968, p. 264.
43 F. W. McLafferty, Interpretation of Mass Spectra, 3rd edn., University Science Books, Mill Valley, CA, 1980, p. 221.
44 J. H. Thomassin, J. Goni, P. Baillif, J. C. Touray and M. C. Jaurand, Phys. Chem. Minerals, 1 (1977) 385.
45 P. Baillif and J. C. Touray, J. Electron Spectrosc. Relat. Phenom., 32 (1983) 223.

46 M. C. Jaurand, J. Bignon, P. Sebastien and J. Goni, Environ. Res., 14 (1977) 255.
47 S. Chowdhury, J. Appl. Chem. Biotechnol., 25 (1975) 347.
48 J. Goni, J. H. Thomassin, in L. H. Ahrens (Ed.), M. C. Jaurand and J. C. Touray, Origin and Distribution of the Elements, Pergamon Press, Oxford, 1979, p. 807.
49 F. P. Novak, K. Balasanmugam, K. Viswanathan, C. D. Parker, Z. A. Wilk, D. Mattern and D. M. Hercules, Int. J. Mass Spectrom. Ion Phys., 53 (1983) 135.
50 R. B. Van Breemen, M. Snow and R. J. Cotter, Int. J. Mass Spectrom. Ion Phys., 49 (1983) 35.
51 M.-J. Luys, G. De Roy, E. F. Vansant and F. C. Adams, J. Chem. Soc., Faraday Trans. 1, 78 (1982) 3561.

Analytica Chimica Acta, 161 (1984) 53—64
Elsevier Science Publishers B.V., Amsterdam — Printed in The Netherlands

DEPTH PROFILE MEASUREMENT BY SECONDARY ION MASS SPECTROMETRY

M. MOENS, M. VAN CRAEN and F. C. ADAMS*
Department of Chemistry, University of Antwerp (U.I.A.) B-2610 Wilrijk (Belgium)
(Received 3rd February 1984)

SUMMARY

The possibilities of measuring depth profiles by secondary ion mass spectrometry are evaluated. The influence of different instrumental and experimental parameters on depth resolution in the profiles are studied: the effects of primary ion beam characteristics, reactive gas adsorption and mechanical aperturing in secondary ion extraction are discussed. Beam effects are studied from the point of view of surface damage. The effects of secondary processes, such as crater edge effects, element mixing, preferential sputtering, background signals, (residual) gas contamination and ion-induced topographical and compositional changes are studied for thin metal films and binary materials.

In chemical and microchemical characterization of materials and surfaces, instrumental analytical methods are far more widely used than more classical wet-chemical methods. Amongst the possible techniques are Auger electron spectroscopy, electron probe microanalysis, electron spectroscopy for chemical analysis, ion-induced x-ray spectrometry, ion-scattering spectrometry, Rutherford backscattering spectroscopy, laser microprobe mass analysis, and secondary ion mass spectroscopy (s.i.m.s.). Each of these methods has its specific advantages and shortcomings in different fields of application. Amongst the surface-sensitive methods, s.i.m.s. lends itself very well to evaluation of depth profiles, owing to its combined possibilities of detection of all elements including isotopes, its low information depth (≈ 0.5 nm), its low overall detection limits in the ng g^{-1} to μg g^{-1} range and its intrinsic profiling characteristics arising from the sputtering process.

In s.i.m.s., an energetic ion beam is used to sputter away the sample on a layer-by-layer basis. Simultaneously, the secondary ion current of one or more elements is monitored as a function of time. At a constant erosion rate, time is, to a first approximation, proportional to the sputtered depth. This depth profiling capacity is one of the most valuable characteristics of s.i.m.s. It has thus proven to be a powerful technique for surface and depth profile measurements in many diverse fields: thin film studies, semiconductor technology, implantation and diffusion studies, metallurgy, geochemistry, microelectronics and also in more fundamental disciplines, such as studies of adsorption and oxidation phenomena and catalysis. However, more recently,

0003-2670/84/$03.00

several authors, e.g. [1—9], have proved that instrumental as well as ion bombardment-induced artifacts can lead to errors when depth profiles are measured. Consequently, the correct interpretation often becomes difficult, and in some cases impossible. Some practical and methodological phenomena, which are primary causes of these problems, are investigated and illustrated in this paper in some detail on the basis of examples of practical interest.

EXPERIMENTAL

All measurements were made with a CAMECA IMS-300 ion microscope/ion analyzer [10]. The normal working pressure, obtained by three oil-diffusion pumps is 10^{-2} Pa in the ion gun, $\approx 2 \times 10^{-5}$ Pa in the central part of the spectrometer and in the sample chamber, and about 10^{-4} Pa in the image convertor compartment. Ion currents ranging between 0.1 and 1 μm are monitored by using a Faraday cup detector. The ion beam is rastered with a line and frame deflection of 3000 and 300 Hz, respectively. The ion analyzer used was connected to a microcomputer to allow a more versatile and accurate control of the mass spectrometer and to better the spectral data acquisition and processing [11, 12].

Thin film samples of chromium, copper, cadmium sulphide and copper(I) sulphide were prepared by evaporation of the high-purity materials on a Corning 7059 glass substrate. Silicon nitride films were prepared by the chemical vapor deposition at atmospheric pressure. Tantalum pentoxide layers were anodically formed on tantalum. The thickness of the films was determined by energy-dispersive x-ray fluorescence spectrometry or by ellipsometry.

RESULTS AND DISCUSSION

The accuracy with which the original atomic depth profile is reflected in the raw depth profile data is a function of various parameters, particularly the sputtering yield and the primary ion density. Often, reliable determinations of the eroded depth can be obtained by mechanical or interferometric measurements of the crater depths or by sputtering through standard samples of known and uniform thickness. The quality of a depth profile is best defined from the location of the interface between two layers with different composition. In Fig. 1, the idealized profile is compared to a measured one. The interface width Δt (in time) or Δz (in depth) is commonly defined as the interval between 84 and 16% of the maximum (steady-state) intensity and is equivalent to twice the standard deviation on the error curve which characterizes the measured profile [13].

Table 1 presents a scheme of the most important phenomena that degrade depth resolution and influence experimental depth resolution. They depend on the sample properties and ion beam characteristics and on the intrinsic characteristics of the sputtering process itself.

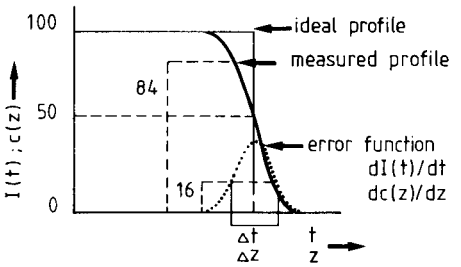

Fig. 1. Definition of the parameters defining the depth resolution (absolute Δt ($\approx \Delta z$); relative $\Delta t/t$ ($\approx \Delta z/z$)).

Crater edge effects

The crater for depth profile measurements is ideally shaped when it is flat-bottomed with perfectly vertical edges. However, the interaction between a stationary ion beam and the sample usually results in a crater shape which reflects the Gaussian intensity distribution of the beam. Therefore, the primary beam is normally rastered over the sample in both x - and y-directions. In addition, ion optical and/or mechanical apertures are often used to select the central part of the crater for measurements, thus discriminating against the ions originating from the edges.

The effects of the immersion lens diaphragm width (F_l), which delineates the area viewed by the detector, and of the magnetic field diaphragm width (F_d), which governs the dispersion of the secondary ion beam at the entrance of the magnetic sector of the ion microscope, were carefully determined in this work, using a 200-nm thick film of copper(I) sulphide bombarded with 6-keV Ar^+ ions at a current density of ca. 60 μA cm^{-2}. The energy window of the analyzer and the collector window of the electron multiplier were opened for maximum intensity of Cu^+ ions. The results are summarized in Table 2. As expected, small F_l and F_d widths provide optimal resolution. However, the reduction of the analyzed surface area reduces the transmission of the spectrometer. Hence, a compromise is needed between depth

TABLE 1

Factors which influence and degrade the resolution in depth profiling

Constant with time and depth	Information depth, crater edge effects, original surface roughness
Time-dependent	Ion-induced surface roughening by differential erosion, knock-on effects, cascade mixing, ion bombardment enhanced diffusion, implantation, preferential sputtering
Rate-dependent	Impurity or residual gas contamination by adsorption, surface diffusion
Depth-dependent	Non-uniformity of the beam, sputter-induced topography

TABLE 2

Influence of limiting the analyzed area extracted from the bombarded surface, by the immersion lens diaphragm (F_1) and the dispersion diaphragm (F_d), on the relative depth resolution (target: Cu_2S, 6 keV Ar^+, $p_{O_2} = 4.5 \times 10^{-4}$ Pa)

F_1 (μm)	30	30	60	60	200	200
F_d (mm)	2	6	0.75	6	0.75	6
$\Delta t/t$ (%)	4.7	10.6	3.7	18.8	14.0	17.4

resolution and secondary ion intensity. The resolution is also a function of the rastered ion beam diameter (Fig. 2). It approaches a limiting value at high beam diameters, for which the resolution is not much influenced by crater edge effects but becomes dependent on other phenomena caused by atomic mixing.

Atomic mixing effects

Recoil implantation. Here the direct transfer of momentum from bombarding ions to the lattice atoms results in their forward movement. The profiles are broadened by this forward scattering of atoms at the interface. The effect is a function of the masses of the primary and secondary species, and the interface broadening caused by this knock-on effect depends on the primary ion energy. For example, when a sample of Cu_2S-coated cadmium sulphide was bombarded with 6- and 4.5-keV Ar^+ ions in vacuum conditions, the interface widths were 673 and 611 nm, respectively.

Cascade mixing. Ion bombardment of the solid surface results in displacement of the lattice atoms, either by direct energy transfer or by the energy cascade originating from the collisions between excited atoms and lattice atoms at rest. The overall effect is a homogenization and mixing of all atoms. Obviously, the depth resolution is limited by the depth to which the cascade-induced atomic mixing extends. The width of the mixing layer was deter-

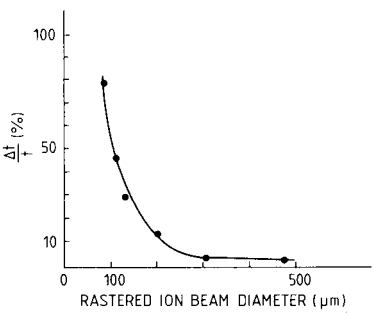

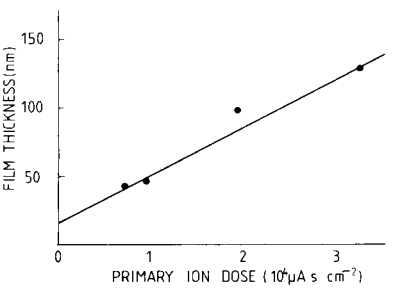

Fig. 2. Relative depth resolution as a function of the rastered ion beam diameter for a copper target, bombarded with 6-keV Ar^+ ($p_{O_2} = 3 \times 10^{-4}$ Pa, $F_1 = 55$ μm, $F_d = 0.75$ mm).

Fig. 3. Primary ion dose required to reach the interface modified by cascade mixing, as a function of the sputtered film thickness.

mined by measurement of the broadening at the interface of a silicon nitride layer on silicon. The primary ion dose needed to reach the altered interface is plotted versus the film thickness in Fig. 3. The ordinate intercept indicates the full width of the mixing layer, 15.5 nm for 15-keV Ar^+ ions. For 6- and 2-keV bombarding energies at an angle of incidence relative to the normal surface of 64° and 45°, the width is 6 and $\leqslant$4.5 nm, respectively. The data at 15 keV can be compared to the penetration depths of argon in silicon nitride and silicon, which are 11.3 and 18.8 nm, respectively. In a similar approach, Tsong et al. [14] found 8.7 nm for the width of the mixing layer of SiO_2/Si at 7-keV Ar^+; the penetration depths of argon atoms in silica and silicon are 8.7 and 10.0 nm, respectively, under these conditions. However, Degrève and Ged [15] indicated that in the case of SiO_2/Si interfaces, the values reported by Tsong et al. are not necessarily due to cascade mixing alone, but may also involve sputtering yield or variations of ionization probability at the interface region.

Ion bombardment-induced diffusion and evaporation. Displacement of atoms in the sample is also caused by ion bombardment-induced diffusion, possibly followed by surface segregation, which also results in degradation of depth resolution. However, surface transport induced by the ion bombardment can lead to better interface resolution, because microroughness can be partly diminished, at least in some conditions. A recent example from this laboratory involves the bombardment of silver bromide crystals [16], which led to large distortions of the original cubic shape of the microcrystals; moreover, an effective depletion of bromine was caused by ion bombardment-enhanced diffusion because of the creation of point defects by the projectile ions [17]. The production of these defects is constant in time and ultimately a steady state will be reached, depending on the rates of vacating the lattice, interstitial annihilation and migration to the surface or to grain boundaries or the other large defects which are abundantly present in these close-packed microcrystals. At the surface, the bromide species are then preferentially sputtered off. However, the bromide migration does not reach equilibrium with the surface removal by preferential sputtering, because of the evaporation of surface bromine, which is continuously pumped away by the vacuum system of the s.i.m.s. instrument. Similar effects were observed by Nitz et al. [18] for $Cd_xHg_{1-x}Te$ samples, where mercury was depleted by evaporation from the surface.

Time-dependent changes in erosion rate

A prerequisite for obtaining a linear relationship between sputtered depth and erosion time is a constant primary ion beam density. A constant ion current is obtained by stabilization of the duoplasmation ion gun and by the use of a constant primary gas pressure in the ionization chamber. But variation of the current density is necessary for several experiments, because it is a basic parameter for controlling the erosion rate and secondary ion intensity:

$v_{er} = 3.6 \times 10^{-4}\, S\, M\, j_p\, \rho^{-1}$ and $I_s = \eta\, S\, \alpha\, C\, j_p\, A_b$

Here, v_{er} is the erosion rate (μm h^{-1}), S is the sputtering yield (atoms per ion), M is the target mass (a.m.u.), ρ is the target density (g cm^{-3}), η is the mass spectrometer transmission, α is the ionization ratio of the element and C its atomic concentration; I_s is the measured secondary ion current and A_b is the bombarded area (cm^2); j_p is the primary ion current density (μA cm^{-2}).

Figure 4 shows the relationship between the erosion rate and the current density for a 48-nm film of chromium. A constant erosion rate was obtained only when the sputtering yield also remained constant during the experiment. Strictly speaking, this is valid only for monatomic targets and homogeneous alloys, in which the composing elements have about the same yield, and for matrices with very low concentrations of impurities and negligible primary ion implantation. However, implantation of oxygen atoms in the target lattice by oxygen gas flooding is often used in s.i.m.s. to increase the sensitivity of detection by increasing the efficiency of atomic ionization. This process obviously affects the sputtering yield, as is illustrated in Fig. 5 which gives the yield for copper as a function of the partial oxygen pressure in the sample chamber. The yield decreases when the flux density of the penetrating oxygen atoms becomes equal to the flux of the sputtered atoms, because of dilution. At high partial pressures, the surface of the copper target is composed of copper oxides and the sputtered flux will be enriched in oxygen atoms as a result of preferential sputtering phenomena.

Preferential sputtering: changes in surface composition by ion bombardment

When a multicomponent target is exposed to energetic ion bombardment, the component with the highest sputtering yield will be removed preferentially. This results in enrichment of the low sputtering species in the near-surface region. Amongst others, Coburn [19] studied extensively the preferential sputtering of some binary metal alloys. Kelly [20] related the

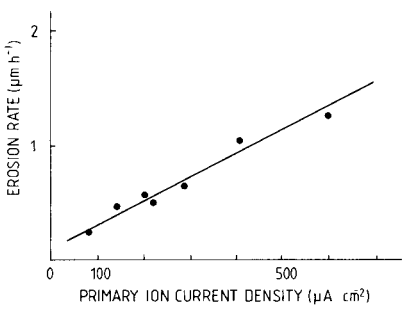

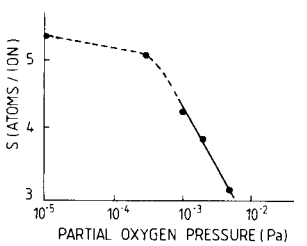

Fig. 4. Relationship between the primary ion current density for a chromium target at 6-keV Ar^+ bombardment.

Fig. 5. Sputtering yield of copper as a function of the partial oxygen pressure in the sample chamber (6-keV Ar^+). The decrease in yield is correlated with the implantation of adsorbed oxygen and subsequent dilution of the target atoms.

observed effects to differences in mass between the components. However, in some cases, Kelly and others found that sputtering is influenced by other factors, such as differences in surface-binding energies [21], segregation effects [17], and direct energy transfer (knock-off effect) [22]. Here, the sputtering behaviour of three binary materials, i.e., silicon nitride, cadmium sulphide and tantalum oxide were studied by s.i.m.s.

Silicon nitride. A typical s.i.m.s. depth profile of N^+/Si^{2+} for a Si_3N_4 film on silicon is shown in Fig. 6. Preferential sputtering of silicon is due to differences in direct energy transfer between Ar^+ primary ions and the sample atoms [22]. The transfer energy factors, defined by $\gamma = 4M_1M_2/(M_1 + M_2)^2$, are 0.97 and 0.77 for Si and N, respectively; here M_1 and M_2 refer to the masses of the primary and secondary ions.

After some time, a steady situation is reached at the plateau in Fig. 6, when the diffusive transport of silicon atoms from the near-surface region and bulk is in equilibrium with the preferential removal of silicon from the surface. As is apparent from Fig. 7, more preferential sputtering occurs at low ion energies, where stoichiometry changes at the surface are governed by direct knock-off effects in the binary collisions. At higher energies, the Ar^+ ions penetrate farther into the silicon nitride lattice, resulting in a damaged zone well beneath the surface. In that case, sputtering is controlled by collisional cascade processes and the contribution of direct knock-off becomes smaller. Also the sputtered depth to obtain a steady-state situation, which is ca. 12 nm for 6-keV Ar^+, decreases to about 1 nm when oxygen is passed continuously over the sample surface. This is due to the increase of defects in the silicon nitride lattice, caused by oxygen implantation beneath the surface, by which the diffusive transport of silicon species to the surface becomes enhanced.

Cadmium sulphide. As would be expected from the γ values ($\gamma_{Cd} = 0.68$, $\gamma_S = 1.00$) for O_2^+ bombardment, sulphur is preferentially sputtered from cadmium sulphide. When the S^+/Cd^+ intensity ratio is taken as a measure of

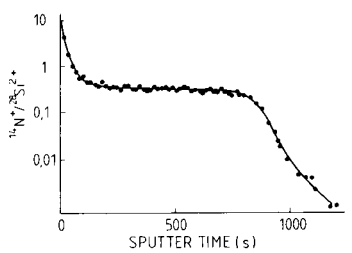

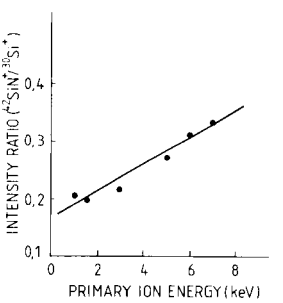

Fig. 6. Relative intensity profile of a silicon nitride film on silicon, indicating the surface region, which is distorted by preferential sputtering, the steady-state region and the interface.

Fig. 7. Preferential sputtering of silicon in silicon nitride as a function of the primary ion energy.

the preferential sputtering effect (Fig. 8), it is again found that more direct knock-off sputtering occurs at low energies. For Ar^+ bombardment, Griffis and Linton [23] found a reduction of the cadmium sulphide species, using auger electron and x-ray photon spectroscopy. In the present experiments, however, this reduction was minimized by the reoxidation of cadmium with oxygen bombardment.

Tantalum pentoxide. Holloway and Nelson [24] have shown that oxygen is preferentially removed from the tantalum pentoxide surface by Ar^+ ions. In this work, the position of the maximum of the parabola (G^+) for the yields of the TaO_x^+ fragments versus the fragment valence [25] of the metal atom in the clusters of TaO_x^+ was taken as a measure of the oxidation state of tantalum. In Fig. 9, the surface G^+ values are plotted against the ion energy. It appears that more reduction takes place at low projectile energies, whereas more oxygen is available at the surface at high energies. Under steady-state conditions, where oxygen diffusion is in equilibrium with its preferential removal by sputtering, the lattice valence is independent of the ion energy [26].

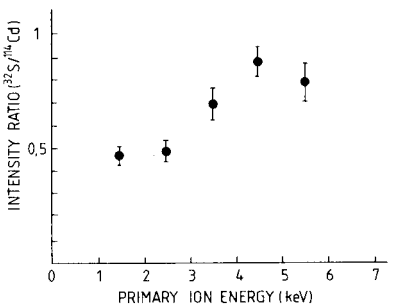

Fig. 8. Preferential removal of sulphur in CdS for O_2^+ bombardment.

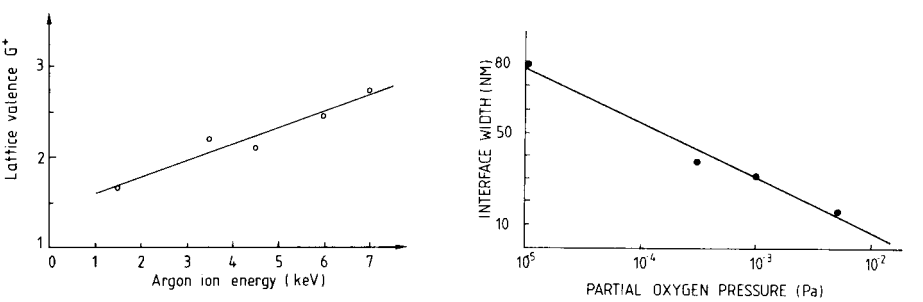

Fig. 9. Lattice valence (G^+) of TaO_x ion clusters as a function of the ion energy.

Fig. 10. Interface width as a function of the oxygen pressure in the sample chamber. At high partial pressures, the influence of surface microtopography decreases because of the formation of an amorphous oxide layer at the surface.

Surface microtopography

It is well known that solid surfaces can develop microroughness under ion bombardment. This effect influences the depth resolution in different ways. The depth resolution decreases according to the degree of roughness, while erosion rates also change. The formation of typically conical and pyramidal structures at the surface is due to differential erosion from different crystal orientations. The influence of impurities with relative low sputtering yields is also important for the initiation and development of these structures. Auciello and Kelly [27] showed that secondary and ternary particles are of importance in the process. The literature contains electron microscopic images of surface roughness induced by ion bombardment [27, 28]. The effect of tunnelling [29], resulting in different yields from different crystal grains, can be minimized by using reactive primary ions or reactive background gases (oxygen, nitrogen) to form oxide or nitride layers, which induce an amorphous structure. Figure 10 illustrates the effect of oxygen flooding on depth resolution for a polycrystalline copper target. Further, in multicomponent systems, preferential sputtering phenomena can contribute to the initiation of surface roughness. An illustrative example of a pyramidal structure developed under Ar^+ bombardment is given in Fig. 11. In other cases, selective erosion of crystal phases leads to a "cracked-glass" structure, as can be seen in Fig. 12 for tantalum pentoxide on tantalum.

Implantation of inert gases

During the sputtering process, primary ions are implanted in the target lattice. A steady-state situation is reached when equilibrium exists between implantation and particle emission at a depth 2 to 3 times the implantation

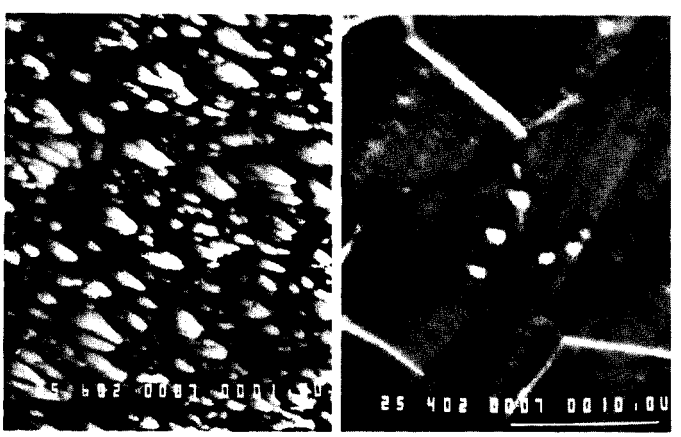

Fig. 11. Formation of cones and ridges by differential erosion of a gold matrix containing gold cyanide precipitates (SEM, 6000X, secondary electron image).

Fig. 12. Formation of a broken-plane structure under selective erosion through a Ta_2O_5 layer on Ta (SEM, 4000X, topography image).

depth of the primary ions. Figure 13 shows part of a depth profile of a copper film on coated glass. The sputtered depth to reach equilibrium is 11 nm, whereas the calculated implantation depth for 6-keV Ar^+ ions in copper is 3.6 nm.

Instrumental background

Spectral interferences can easily be eliminated by applying either high mass resolution or energy selection of the secondary ions. Contamination of any pure surface by residual gases in the sample chamber of the spectrometer can be neglected if the primary ion density is large compared to the adsorption rate. Hofmann [30] gives an upper limit for the residual gas pressure (p) for obtaining a constant erosion rate, defined in the empirical relation: $j_p\,(\mathrm{A\ cm^{-2}}) \gg p\ (\mathrm{Pa})$.

Impurities in the primary ion beam can be removed adequately by mass selection of the primary beam by a magnetic sector. The use of highly pure gases for the production of the primary ions is a prerequisite. Typically, oxygen and argon of $\geqslant 99.998\%$ and $\geqslant 99.9995\%$ purity are used.

Redeposition and memory effects also have repercussions on depth profile information. Background material, originating from the crater edges and from the surroundings of the crater, can be redeposited into the crater, leading to ill-defined crater shapes. The halo effect, caused by sputtering of particles by uncharged, unfocussed fractions of the primary beam can also lead to poor depth resolution. Redeposition and resputtering of sample material originating from the immersion lens system can be minimized by increasing the distance between the sample and the secondary ion extraction lens, but this results in a decrease of the transmission of the spectrometer.

The effect of correction for background signals on the profile is shown in Fig. 14 for a copper(I) sulphide layer (165 nm) sputtered by 5.5-keV O_2^+ ions. The signal-to-background ratio is increased from 23 to ca. 10 000 by

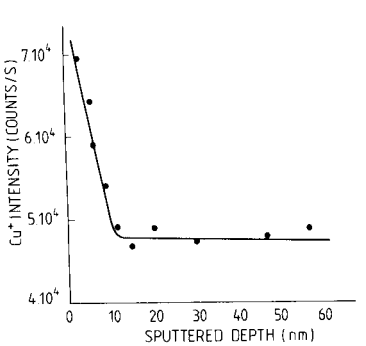

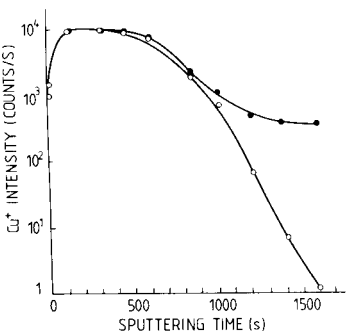

Fig. 13. The $^{63}Cu^+$ ion intensity as a function of the sputtered depth; steady state is reached at a depth of 11 nm.

Fig. 14. The effect of background correction on the depth profile of a Cu_2S layer deposited on a glass substrate: (•) original profile with a signal/background (S/B) ratio of 23; (○) after background subtraction (S/B = 10 000).

elimination of redeposition effects and through a slight defocusing of the ion beam.

CONCLUSIONS

The s.i.m.s. technique is powerful for surface and depth profile analysis of solid samples. The advantages over other surface-sensitive methods are its elemental detection range and limits, its speed of spectrum recording and its inherent profiling capacities. Its major shortcomings are connected with quantification and speciation problems. It is clear that a lot of care and considerable experience are needed for interpreting depth profiles obtained by using s.i.m.s. (and other techniques using ion beam etching). Hofmann [31] has presented a survey of the precautions that must be taken to obtain optimum sputtering depth profiles, because numerous effects, either connected to the physical sputtering process itself or related to the sample and instrument specifically, can obscure the original profile distribution. Some of these disturbing effects can readily be overcome or at least minimized.

The basic requirements for obtaining valid profiles can be deduced from the experimental results presented above. They are related to the ambient gas, the sample and the ion beam. The residual gas pressure of reactive gases in inert gas sputtering should be very low. The sample surface should be smooth and flat (i.e., polished) and should preferably be amorphous. Further, it should be composed of components with similar sputtering yields and it should have adequate electrical conductivity (or be rendered conductive by, e.g., metal diaphragms or gold films). The primary ion beam should have constant density, while beam rastering and raster gating should be applied in order to avoid edge effects. Reactive ion sputtering can reduce the effects of crystalline structures and impurity-dependent effects. This also favours quantification in s.i.m.s. Many disturbing phenomena are energy-dependent, so that bombardment at low energies, if possible, and at glancing incidence is favourable.

The authors thank Prof. Dr. M. Grasserbauer (Technical University of Vienna), Dr. R. Vanden Berghe (Bell Telephone Manufacturing Co., Gent) for interesting discussions and Dr. Ir. M. Burgelman (University of Gent) for preparing most of the evaporated metal films. This work was made possible through financial support from the Instituut ter aanmoediging van het Wetenschappelijk Onderzoek in Nijverheid en Landbouw and from the Interministerial Commission for Science Policy, Belgium, through research grant 80-85/10.

REFERENCES

1 P. H. Holloway, Surf. Sci., 66 (1977) 479.
2 R. Kelly and J. B. Saunders, Nucl. Instrum. Methods, 132 (1976) 335.
3 J. W. Coburn and E. Kay, Crit. Rev. Solid State Sci., 4 (1974) 561.

4 G. J. Coyle, T. Tsang, I. Adler and L. Yin, J. Electron Spectrosc. Relat. Phenom., 20 (1980) 169; Surf. Sci., 112 (1981) 197.
5 P. Williams, Appl. Phys. Lett., 36 (1980) 758.
6 R. A. Kubiak, E. H. C. Parker, R. M. King and K. Wittmaack, J. Vac. Sci. Technol., A1 (1983) 34.
7 W. Vandervorst, H. E. Maes and R. De Keersmaecker, Surf. Interface Anal., 4 (1982) 245.
8 D. K. Skinner, J. G. Swanson and C. V. Haynes, Surf. Interface Anal., 5 (1983) 38.
9 L. E. Rehn and H. Wiedersich, Thin Solid Films, 73 (1980) 139.
10 G. H. Morrison and G. Slodzian, Anal. Chem., 47 (1975) 932A.
11 P. Van Espen, M. Van Craen and R. Saelens, J. Microsc. Spectrosc. Electron, 6 (1981) 195.
12 M. Van Craen, P. Van Espen and F. Adams, Rev. Sci. Instrum., 53 (1982) 1007.
13 C. W. Magee and R. E. Honig, Surf. Interface Anal., 4 (1982) 35.
14 I. S. T. Tsong, J. R. Monkowski and D. W. Hoffman, Nucl. Instrum. Meth., 182/3 (1981) 237.
15 F. Degrève and Ph. Ged, Surf. Interface Anal., 5 (1983) 83.
16 J. Van Puymbroeck, R. Gijbels and L. Ketellapper, Photogr. Sci. Eng., (1984) in press.
17 D. G. Swarzfager, S. B. Ziemicki and M. J. Kelley, J. Vac. Sci. Technol., 19 (1981) 185.
18 H. M. Nitz, O. Ganshow, U. Kaiser, L. Wiedmann and A. Benninghoven, Surf. Sci., 104 (1981) 365.
19 J. W. Coburn, Thin Solid Films, 64 (1979) 371.
20 R. Kelly, Surf. Sci., 100 (1980) 85.
21 R. Kelly, Nucl. Instrum. Meth., 149 (1978) 553.
22 R. Bhattacharya and P. Holloway, Appl. Phys. Lett., 38 (1981) 545.
23 D. P. Griffis and R. W. Linton, Surf. Interface Anal., 4 (1982) 197.
24 P. Holloway and G. Nelson, J. Vac. Sci. Technol., 16 (1979) 793.
25 C. Plog, L. Wiedmann and A. Benninghoven, Surf. Sci., 67 (1977) 565.
26 M. Van Craen and F. Adams, Surf. Interface Anal., 5 (1983) 239.
27 O. Auciello and R. Kelly, Nucl. Instrum. Meth., 182/3 (1981) 267.
28 V. Naundorf and M. P. Macht, Nucl. Instrum. Meth., 168 (1980) 405.
29 O. Auciello and C. J. Alsteller, Radiat. Eff., 51 (1980) 241.
30 S. Hofmann, Appl. Phys., 9 (1976) 59.
31 S. Hofmann, Surf. Interface Anal., 2 (1980) 148.

Analytica Chimica Acta, 161 (1984) 65—74
Elsevier Science Publishers B.V., Amsterdam — Printed in The Netherlands

ASPECTS OF BIOMARKER ANALYSIS BY GAS CHROMATOGRAPHY/MASS SPECTROMETRY WITH SELECTIVE METASTABLE ION MONITORING
Part 1. Experimental Techniques

TRYGVE MEYER and OLAV H. J. CHRISTIE*

Rogaland Research Institute, P.O. Box 2503, Ullandhaug, N-4001 Stavanger (Norway)

PAUL W. BROOKS

Institute of Sedimentary and Petroleum Geology, Geological Survey of Canada, 3033-33 St. NW, Calgary, Alberta (Canada)

(Received 21st November 1983)

SUMMARY

Biological markers such as steranes and triterpanes in source rocks and oils are important because they reveal the origin, alteration and maturation history of geological organic matter. Metastable multiple ion detection combined with high-resolution capillary-column gas chromatography provides a better solution to some of the interference problems involved than more conventional methods. The method is sensitive and allows separation by carbon number of homologous series; minor amounts of diagnostic biomarker components of crude oils and rock extracts can be estimated with no, or very little, sample clean-up. The limitations of the method are also discussed.

The distribution of the polycyclic hydrocarbons, steranes and triterpanes, is used widely for correlation of unaltered crude oils and source rocks. Such compound distributions are used, in the main, for oil/oil and oil/source rock correlations. Indeed, the usefulness of the distributions of steranes and triterpanes in petroleum exploration for correlation and for estimation of maturity and, possibly, migration, is well established [1—12].

The distribution of steranes and triterpanes is normally determined by a combination of high-resolution gas chromatography and a mass spectrometer operated in a low-resolution multiple ion detection mode. This g.c./m.s. methodology calls for extensive sample fractionation. Because of the low abundance of steranes and triterpanes in oils and source rocks relative to other hydrocarbons in the matrix, reliable quantitative results are difficult to obtain even after extensive sample purification. The use of high-resolution multiple ion detection has shown great promise in obtaining reliable and meaningful data [13]. Because of the increased selectivity of detection, high-resolution mass spectrometry has also led to an increase in sensitivity. Therefore, this technique requires little or no sample fractionation prior to g.c./m.s.

0003-2670/84/$03.00

Multiple ion detection methods for biomarker analysis rely on the specific detection of fragment ions, notably m/z 177 and 191 for pentacyclic triterpanes, m/z 217 and 218 for normal and 14β(H) steranes, and 259 for rearranged steranes. These ions have major contributions, and are in most cases the base peak of the electron-impact spectra of C_{27}—C_{35} triterpanes and C_{27}—C_{30} steranes. However, the resulting multiple ion detection traces are very complex, especially for the steranes, and chromatographic interferences are common because isomers and carbon number homologues can co-elute during the gas chromatographic separation even when high-resolution capillary columns are used.

The use of metastable transitions in organic geochemistry was first demonstrated by Gallegos [14] for a mixture of biological markers. Recently, Warburton and Zumberge [15] reported further use of this selective metastable monitoring technique to obtain clearly defined chromatographic profiles for C_{27}, C_{28}, and C_{29} steranes from fractionated crude oils, claiming an increase in selectivity. In their work, the spontaneous fragmentation of three sterane parent ions was monitored in the first field-free region of a double focusing mass spectrometer. Similar results on molecular distributions of biological markers in organic geochemical samples can be obtained by use of the linked scan technique with B^2/E scans. This method was reported by Moldowan et al. [16] for identification of a series of tricyclic terpanes up to C_{45}.

In the present study, the use of the selective metastable ion monitoring technique described by Gallegos [14] and Warburton and Zumberge [15] is extended to include the monitoring of four different sterane parent ions for the C_{27}—C_{30} steranes, two parent ions for the C_{21} and C_{22} steranes, nine parent ions for the C_{27}—C_{35} pentacyclic triterpanes, as well as twelve parent ions of the C_{19}—C_{30} tricyclic terpanes. Furthermore, the whole oil is subjected to gas chromatography to allow an assessment of the sensitivity and selectivity of the method.

EXPERIMENTAL

The integrated VG-7050 GC-MS-DS system used included a double-focusing mass spectrometer, and was operated at 70 eV in the electron-impact mode. Low resolution (ca. 500) was used for the metastable work and high resolution (ca. 2.500) was used for normal multiple ion detection.

Metastable transitions were monitored under data system control as follows: after the accelerating voltage (V) had been decoupled from the electrostatic voltage (E), the magnet current (B) and the accelerating voltage reference were supplied by the programmable digital scanner driven by the data system. For the steranes, the daughter ion at m/z 217 was focused at an accelerating voltage at 2 kV. With B and E kept constant, an increase in the accelerating voltage (V) allowed the transitions to the fragment ion m/z 217 of the molecular ions at the m/z values 372, 386, 400, and 414, respectively, to be located at the collector (see Table 1 for the kV values).

TABLE 1

Sterane molecule ion mass and accelerating voltages employed for metastable ion monitoring

Carbon no.	Molecular ion	kV value	Carbon no.	Molecular ion	kV value
19	260.2496	2.396	27	372.3756	3.429
20	274.2652	2.526	28	386.3913	3.558
21	288.2808	2.655	29	400.4069	3.687
22	302.2964	2.784	30	414.4225	3.816

For a separate g.c./m.s. analysis for the pentacyclic triterpanes (mainly hopanes), the common daughter ion at *m/z* 191 was focussed at 1.5 kV and the accelerating voltage was increased to allow the transition to the fragment ion *m/z* 191 of the molecular ions at the *m/z* values 370, 384, 398, 412, 426, 440, 454, 468, and 482, respectively, to be located at the detector (Table 2). In this way the C_{21}—C_{22} steranes and the C_{19}—C_{30} tricyclic terpanes could also be monitored (Tables 1 and 3, respectively). The series of tricyclic terpanes was analysed in two separate runs because of small limitations in the available data system of the mass spectrometer.

For gas chromatography, a Hewlett-Packard HP-5710A gas chromatograph

TABLE 2

Pentacyclic triterpane metastable transitions and related accelerating voltages

Carbon no.	Molecular ion	kV value	Carbon no.	Molecular ion	kV value
27	370.3588	2.906	32	440.4369	3.456
28	384.3744	3.016	33	454.4526	3.566
29	398.3900	3.126	34	468.4683	3.676
30	412.4056	3.236	35	482.4840	3.786
31	426.4212	3.346			

TABLE 3

Tricyclic terpane metastable transitions and accelerating voltages

Carbon no.	Molecular ion	kV value	Carbon no.	Molecular ion	kV value
19	262.2652	2.058	25	346.3588	2.717
20	276.2808	2.167	26	360.3744	2.827
21	290.2964	2.277	27	374.3900	2.937
22	304.3120	2.387	28	388.4056	3.047
23	318.3276	2.497	29	402.4212	3.157
24	332.3432	2.607	30	416.4368	3.267

was used with a standard (HP) type of split/splitless injector and a standard narrow-bore fused silica column coated with CP-Sil-5 (Chrompack). The column temperature was programmed at 6° min^{-1} from 60 to 310°C. The helium flow rate was ca. 2 ml min^{-1} with the column taken directly into the ion source of the mass spectrometer.

RESULTS

Steranes

Figure 1 shows the metastable ion sterane distributions for one whole oil sample: Fig. 1(a) represents the *m/z* 372 to 217 transition for C_{27}

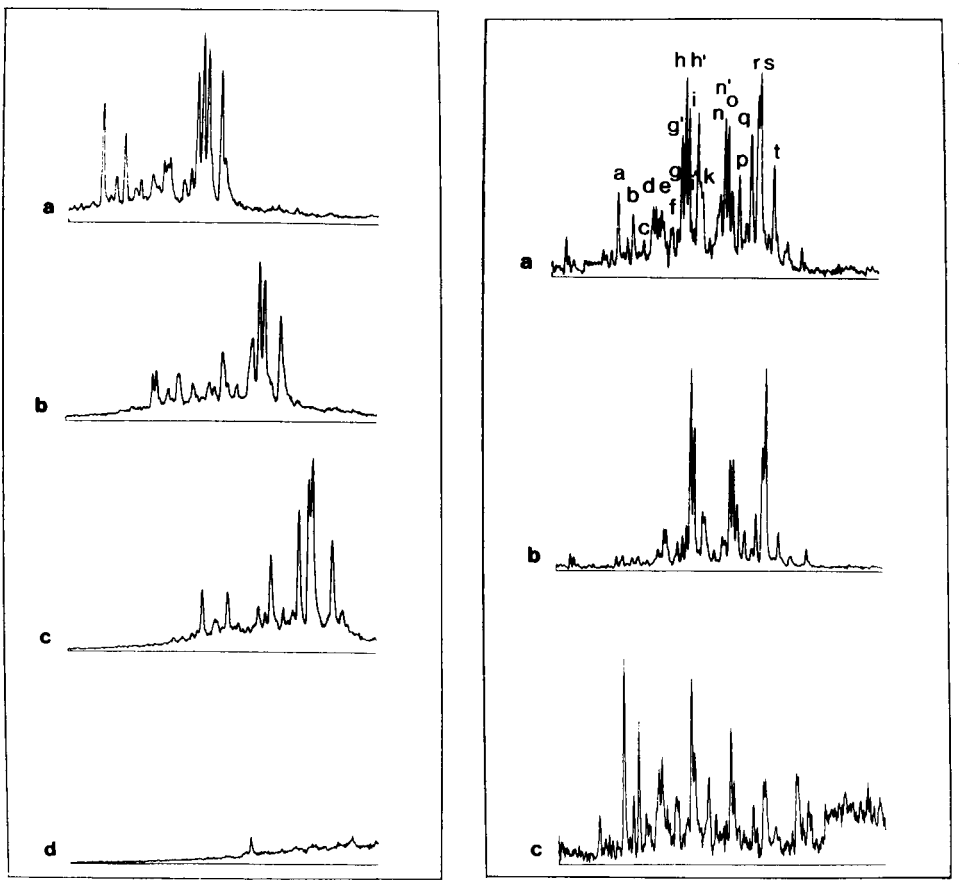

Fig. 1. Metastable multiple ion detection for C_{27}—C_{30} steranes: (a) *m/z* 372.3756; (b) *m/z* 386.3913; (c) *m/z* 400.4069; (d) 414.4225.

Fig. 2. High-resolution multiple ion detection trace for C_{27}—C_{30} steranes: (a) *m/z* 217.1955; (b) *m/z* 218.203; (c) *m/z* 259.242. See Table 4 for peak notation.

steranes, and Fig. 1(b), (c) and (d) represent the C_{28}, C_{29} and C_{30} steranes, respectively. Figure 2(a) shows the same whole oil sample examined by high-resolution (ca. 2.500) multiple ion detection monitoring *m/z* 217.1955, the exact mass of the fragment ion characteristic of C_{27}—C_{30} steroidal alkanes. Figure 2(b) and (c) show the *m/z* 218.203 and *m/z* 259.242 of 14β(H) steranes and rearranged steranes, respectively.

Two observations in favour of selective metastable ion monitoring are immediately apparent from Figs. 1 and 2. First, the signal/noise ratio is excellent, even though the sample analysed was a whole crude oil. Secondly, the sensitivity, and thus the detection capability, is even greater for the selective metastable multiple ion monitoring than for conventional high-resolution multiple ion detection. Furthermore, as noted by Warburton and Zumberge [15], the *m/z* 217.1955 chromatogram shows an extremely complex distribution of components not completely separated even by high-resolution capillary columns. Consequently, the selective metastable monitoring technique offers an improved method for identification of the peaks of the chromatograms. A revised identification of the sterane chromatogram peaks is given in Table 4.

Evidently, the *m/z* 217.1955 sterane chromatogram contains a large

TABLE 4

Identification of steroidal alkanes based on retention time and mass spectral characteristics

Peak notation	Identity	No. of carbons
a	13β,17α-Diacholestane (20S)	27
b	13β,17α-Diacholestane (20R)	27
c	13α,17β-Diacholestane (20S)	27
d	13α,17β-Diacholestane (20R)	27
e	24-Methyl-13β,17α-diacholestane (20S)	28
f	24-Methyl-13β,17α-diacholestane (20R)	28
g	14α,17α-Cholestane (20S)	27
g_1	24-Methyl-13β,17β-diacholestane (20S)	28
h	24-Ethyl-13β,17β-diacholestane (20S)	29
h_1	14β,17β-Cholestane (20R)	27
i	14β,17β-Cholestane (20S)	27
i_1	24-Methyl-13α,17β-diacholestane (20R)	28
k	24-Ethyl-13α,17β-diacholestane (20R)	29
m	24-Methyl-14α,17α-cholestane (20S)	28
n	24-Methyl-14β,17β-cholestane (20R)	28
n_1	24-Ethyl-13α,17β-diacholestane (20R)	29
o	24-Methyl-14β,17β-cholestane (20S)	28
p	24-Methyl-14α,17α-cholestane (20R)	28
q	24-Ethyl-14α,17α-cholestane (20S)	29
r	24-Ethyl-14β,17β-cholestane (20R)	29
s	24-Ethyl-14β,17β-cholestane (20S)	29
t	24-Ethyl-14α,17α-cholestane (20R)	29

number of overlapping components leading to qualitative and quantitative problems. Thus, the frequently measured 24-ethyl-14α,17α-cholestane (20S) peak (marked (q) on Fig. 2) used for maturation studies is hampered by interference from a relatively strong C_{30} sterane peak, probably a C_3-substituted 13α,17β-diacholestane (20R). Furthermore, the component marked (h) on Fig. 2 is a mixture of 24-ethyl-13β,17α-diacholestane and 14β,17β-cholestane (C_{27}). Even for correlation work, the *m/z* 217.1955 sterane chromatogram seems to be of limited value (see also [17]). In the selective metastable ion monitoring chromatograms, these compounds are observed as discrete peaks (Fig. 1). Thus, it has proved possible to obtain relative abundance data on all the major C_{27}—C_{30} individual steranes for all the whole oil samples investigated so far. The correlation between oil samples in terms of their metastable multiple ion monitoring peaks was studied by multivariate analysis, as described in the following paper [17].

Figure 3(a—c) shows the high-resolution *m/z* 217.1955, *m/z* 218.203, and *m/z* 259.242 multiple ion detection chromatograms for the low-molecular-weight sterane region. Figure 4(a, b) shows the corresponding region examined

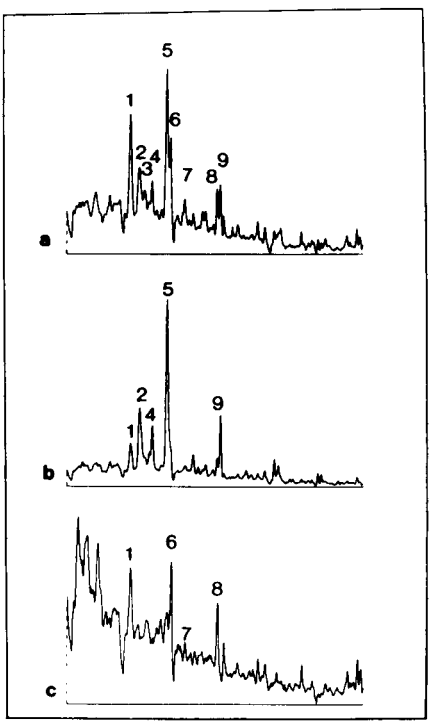

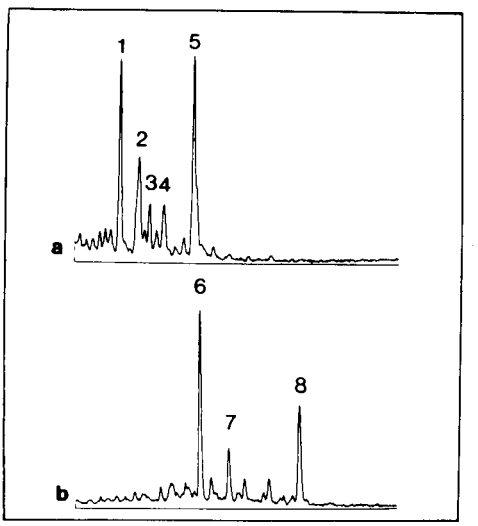

Fig. 3. High-resolution multiple ion detection traces for C_{21}—C_{22} steranes: (a) *m/z* 217.1955; (b) *m/z* 218.203; (c) *m/z* 259.242.

Fig. 4. Metastable multiple ion detection traces for C_{21}—C_{22} steranes: (a) *m/z* 288.2808; (b) *m/z* 302.2964.

by metastable multiple ion detection for the parent ions of C_{21} and C_{22} steranes. Clearly, the selective metastable ion monitoring chromatograms of Fig. 4 show enhanced signal-to-noise compared with the high-resolution chromatogram of Fig. 3.

It seems obvious that the high-resolution chromatogram would be inadequate for quantitative work whereas quantitation could be done with confidence from the selective metastable ion monitoring chromatogram. This statement will be more closely supported in the following paper [17].

Terpanes

Figure 5(a—i) shows the metastable ion monitoring chromatograms for C_{27}—C_{35} pentacyclic triterpanes. Figure 6 shows the high-resolution ion chromatogram for *m/z* 191.1792 (the base peak common to all 17α(H)-hopanes). As for the steranes, the high-resolution multiple ion detection chromatogram has a complex distribution of components, dominated by the C_{27}—C_{35} 17α-hopane homologues with the minor triterpanes being difficult to distinguish because of either a large background signal or overlapping peaks. However, Figs.5 and 6 show again the major improvement

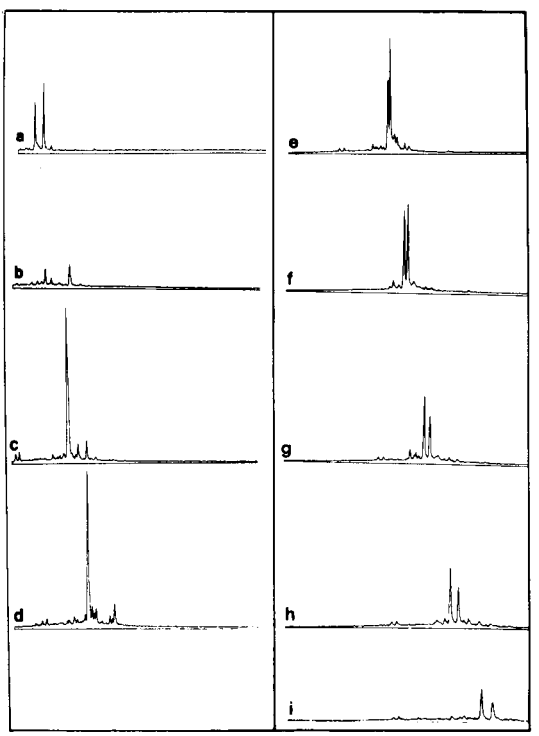

Fig. 5. Metastable multiple ion detection traces for C_{27}—C_{35} pentacyclic triterpanes: (a) *m/z* 370.3588; (b) *m/z* 384.3744; (c) *m/z* 398.3900; (d) *m/z* 412.4056; (e) *m/z* 426.4212; (f) *m/z* 440.4369; (g) *m/z* 454.4526; (h) *m/z* 468.4683; (i) *m/z* 482.4840.

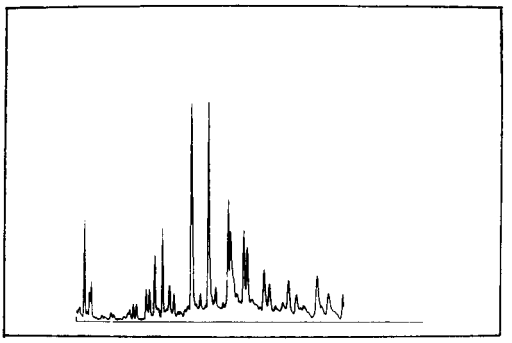

Fig. 6. High-resolution multiple ion detection traces for C_{27}—C_{35} pentacyclic triterpanes (*m/z* 191.1792).

for characterization of the samples by their pentacyclic triterpane concentration ratios. The dominant discrete 17α-hopane components of each chromatogram are easily discernible together with the C_{28} 17α(H)-28,30-bisnorhopane shown in the *m/z* 384—191 metastable transition chromatogram. Minor amounts of the moretane series used for maturation studies [18] are also present in each chromatogram.

Many chemically unidentified triterpane compounds, particularly the early eluting compounds of each chromatogram, can be studied with greater accuracy and precision by means of selective metastable ion monitoring. There are indications that trisnorhopane (C_{27}) peak ratios can be used for migration and maturation studies [7]. The present technique offers the possibility of more detailed studies along these lines.

The improvement of the metastable multiple ion detection technique (Fig. 7, a—l) over high-resolution multiple ion detection (Fig. 8) is evident. The complex chromatogram of Fig. 8 with many interfering peaks is resolved into the clean chromatograms of Fig. 7. The signal-to-noise ratio of the metastable multiple ion detection chromatograms is excellent and makes it possible to use them for detailed characterization and correlation purposes.

DISCUSSION

Biological markers such as steranes and triterpanes have been determined in source rocks and oils because they reveal the origin, alteration and maturation history of geological organic matter. Correlation studies based on the relative abundance of numerous steranes and triterpanes is now widely used. However, the chromatograms obtained from conventional low-resolution multiple ion detection g.c./m.s. are very complex and their use is hampered by many interferences, which makes their reliable quantitative evaluation for diagnostic components sometimes questionable. The use of high-resolution multiple ion detection has increased the selectivity of these analyses and hence the confidence in peak assignment, but the problems of gas chroma-

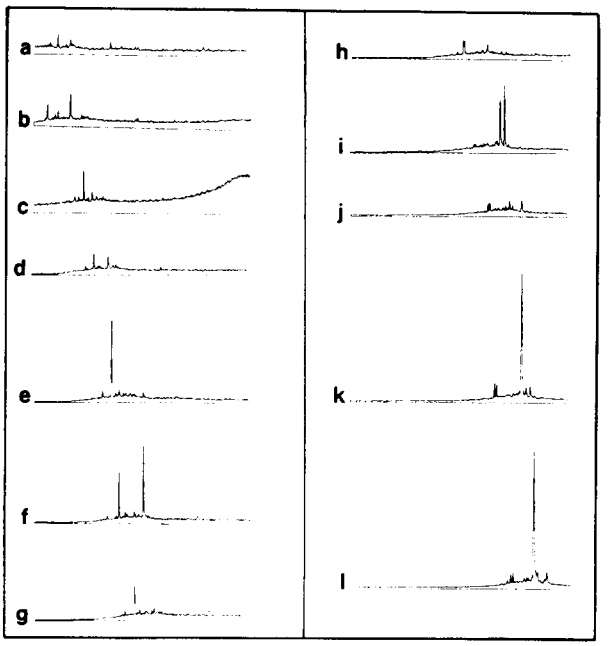

Fig. 7. Metastable multiple ion detection for C_{19}—C_{30} tricyclic terpanes: (a) *m/z* 262.2682; (b) *m/z* 276.2808; (c) *m/z* 290.2964; (d) *m/z* 304.3120; (e) *m/z* 318.3276; (f) *m/z* 332.3432; (g) *m/z* 346.3588; (h) *m/z* 360.3744; (i) *m/z* 374.3900; (j) *m/z* 388.4056; (k) *m/z* 402.4212; (l) *m/z* 416.4368.

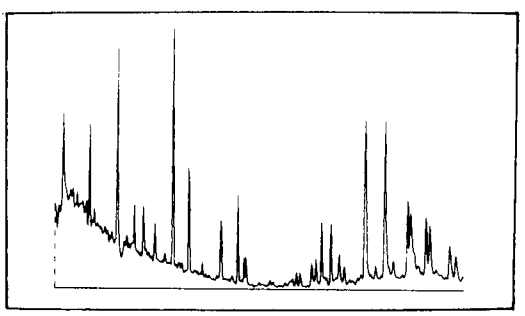

Fig. 8. High-resolution multiple ion detection traces for C_{19}—C_{30} tricyclic terpanes (*m/z* 191.1792).

tographic co-elution of isomers and homologues cannot be fully overcome by this method even though the improvement over conventional methods is substantial.

Metastable multiple ion detection can only be done in double-focusing mass spectrometers. Combined with high-resolution capillary column gas chromatography, it provides a better solution to some of the chromatographic

interference problems of biomarker analysis than conventional methods. It offers a very sensitive method for quantitative evaluation and it allows separation by carbon number of homologous series. This makes it possible to quantify diagnostic biomarker components of crude oils and rock extracts present in minor amounts without, or for components present in very low concentrations, with very little or simple, sample clean-up procedures.

The advantage of the proposed method lies in its potential ability to separate members of a homologous series giving the same prominent fragment ion. The evident limitation of the method lies in the nature of metastable peaks, which are much broader than stable peaks of a mass spectrum. Therefore, peak overlapping of transitions from molecular ions of small molecular mass differences to the same fragment ion cannot be avoided. This overlapping has nothing to do with the performance of the mass spectrometer, and cannot be improved by updating the instrumental resolution parameters. This is exemplified by pentacyclic and tricyclic terpanes. The two groups of components have a common fragment ion, and the accelerating voltages related to the metastable transitions of a given carbon number differ only in the second decimal (Tables 2 and 3). This implies a mass spectrometric interference of compounds of the two groups of terpanes as shown in Figs. 5 and 7. This is a general limitation which is not restricted to terpanes.

REFERENCES

1 F. R. Aquino Neto, J. M. Trendel, A. Restle, J. Connan and P. A. Albrecht, in M. Bjorøy (Ed.), Advances in Organic Geochemistry 1981, Wiley-Heyden, Chichester, 1983, p. 659.
2 A. van Dorsselaer, P. Albrecht and J. Connan, in R. Campos and J. Goni (Eds.), Advances in Organic Geochemistry 1975, Enadimsa, Madrid, 1977, p. 53.
3 D. M. McKirdy, A. K. Aldridge and P. J. M. Ypma, in M. Bjorøy (Ed.), Advances in Organic Geochemistry 1981, Wiley-Heyden, Chichester, 1983, p. 99.
4 M. Schoell, M. Tecshner and H. Wehner, in M. Bjorøy (Ed.), Advances in Organic Geochemistry 1981, Wiley-Heyden, Chichester, 1983, p. 156.
5 W. K. Seifert, Geochim. Cosmochim. Acta, 42 (1978) 473.
6 W. K. Seifert and J. M. Moldowan, Geochim, Cosmochim. Acta, 42 (1978) 77.
7 W. K. Seifert and J. M. Moldowan, Geochim. Cosmochim. Acta, 43 (1979) 111.
8 W. K. Seifert and J. M. Moldowan, in A. G. Douglas and J. R. Maxwell (Eds.), Advances in Organic Geochemistry 1979, Pergamon, Oxford, 1980, p. 229.
9 W. K. Seifert and J. M. Moldowan, Geochim. Cosmochim. Acta, 45 (1981) 783.
10 W. K. Seifert, J. M. Moldowan and R. W. Jones, Proc. 10th World Petroleum Congr., Bucharest, September 1979, Paper SP8, Wiley-Heyden, Chichester, 1980, p. 425.
11 J. Y. Shi, A. S. Mackenzie, R. Alexander, G. Eglinton, A. P. Gowar, G. A. Wolff and J. R. Maxwell, Chem. Geol. 35 (1982) 1.
12 R. P. Philp, Geochim. Cosmochim. Acta, 47 (1983) 267.
13 M. Bjorøy, P. W. Brooks and K. Hall, in M. Bjorøy (Ed.), Advances in Organic Geochemistry 1981, Wiley-Heyden, Chichester, 1983, p. 87.
14 E. J. Gallegos, Anal. Chem., 48 (1976) 1348.
15 G. A. Warburton and J. E. Zumberge, Anal. Chem., 55 (1983) 123.
16 J. M. Moldowan, W. K. Seifert and E. J. Gallegos, Geochim. Cosmochim. Acta, 47 (1983) 1531.
17 O. H. J. Christie, T. Meyer and P. W. Brooks, Anal. Chim. Acta, 160 (1984) 75.
18 A. S. Mackenzie, R. L. Patience, J. R. Maxwell, M. Vandenbroucke and B. Durand, Geochim. Cosmochim. Acta, 44 (1980) 1709.

Analytica Chimica Acta, 161 (1984) 75—82
Elsevier Science Publishers B.V., Amsterdam — Printed in The Netherlands

ASPECTS OF BIOMARKER ANALYSIS BY GAS CHROMATOGRAPHY/MASS SPECTROMETRY WITH SELECTIVE METASTABLE ION MONITORING
Part 2. Information Content of Biomarkers in Some Light Oils

OLAV H. J. CHRISTIE* and TRYGVE MEYER

Rogaland Research Institute, P.O. Box 2503, Ullandhaug, N-4001 Stavanger (Norway)

PAUL W. BROOKS

Institute of Sedimentary and Petroleum Geology, Geological Survey of Canada, 3303-33 St. NW, Calgary, Alberta (Canada)

(Received 21st November 1983)

SUMMARY

The information content of steranes and pentacyclic triterpanes is extracted by means of eigenvector (factor) analysis. Steranes carry information different from that of hopanes even though they both provide information about the maturity of the source rock. Moretanes and 20R hopanes provide similar information which differs from that of 20S hopanes. The steranes carry somewhat different information, which is opposite to that carried by a series of unidentified triterpanes. The diacholestanes and cholestanes yield different types of information.

Biomarker molecules, such as steranes and triterpanes, are of considerable interest in petroleum chemistry and organic geochemistry because they can be used to solve specific problems in connection with maturity of natural hydrocarbon source rocks and, partly, migration of natural hydrocarbons from source rocks to petroleum reservoirs (see, e.g. [1—4]). Such compounds are identified and quantified by gas chromatography/mass spectrometry (g.c./m.s.), which until recently has been hampered by considerable interference problems limiting quantitative measurements of sterane and pentacyclic triterpane chromatograms to a few peak ratios. With the introduction of metastable ion monitoring g.c./m.s. it became possible to record carbon number-specific chromatograms of steranes and triterpanes [5—7]. This helped to solve the interference problem and opened the way for more selective surveys of the significance of biomarkers.

In view of the increased selectivity provided by the new measurements, some criticisms may now be raised against current methods for data analysis of biomarker constituents in natural hydrocarbon mixtures. A major objection concerns the use of ratios. It is well known that information is lost when data are transformed to ratios, e.g., percentages. Decrease in the percentage of men in a population does not indicate whether some men have

0003-2670/84/$03.00

died, more men than women have died, some girls have been born, or more girls than boys have been born, all of which information could have been understood directly from the original data. This exemplifies how pertinent information may be lost by transformation of raw data to ratios.

A more serious problem, however, is that present techniques allow measurement of more than sixty molecule-selective sterane and triterpane concentrations. This means that the samples can be described in terms of a variable space with more than sixty dimensions. The location of sample plots in this multidimensional space is vastly more informative than a few ratios. Thus, by using ratios rather than plots in a multidimensional biomarker space, the organic geochemist virtually discards a large proportion of the information inherent in the data. Therefore, new techniques of data analysis, e.g., disjoint principal components analysis and eigenvector projections, are likely to be used to a larger extent in future organic geochemistry (see e.g., [8]).

In order to learn more about the multidimensional variable space constructed from the biomarker variable axes, measurements from a small set of oil samples from the North Sea were investigated by means of eigenvector analysis, one of the many methods of pattern recognition. The goal of the present study is to clarify the correlations between the biomarker molecules. As the behaviour of steranes and triterpanes represents one of the best clarified fields in organic geochemistry, these compounds were selected for an introductory survey of how useful eigenvector analysis would be for the study of variable interrelations.

DATA AND METHODS

A set of seven light oil and condensate samples was analysed by metastable ion monitoring g.c./m.s. The present data for 63 ion specific peaks of pentacyclic triterpanes and steranes in the carbon number range 27—34 were obtained by the method described by Brooks et al. [5]. The peak identification is given in Tables 1 and 2.

The information carried by the different molecules was studied by means of multivariate correlation in terms of eigenvector loadings. Excellent descriptions of eigenvectors and factor analytical approaches have been given elsewhere [9, 10] and will not be reiterated here. This method was particularly chosen because it treats the data in a multivariate manner (i.e., simultaneously) in contrast to the pairwise sequential treatment of conventional cluster analytical algorithms.

The basic idea of the approach is that the chemical difference between samples can be read from the sample plots in a variable space diagram consisting of as many axes as there are variables measured. In the present study, the variable space is 63-dimensional, because 63 variables were measured. According to the fundamentals of pattern recognition (e.g., [8, 11]), large point scatter in the variable space is consistent with high density of informa-

TABLE 1

Peak identification of triterpanes

Peak no.	No. of carbons	Identification	Peak no.	No. of carbons	Identification
1	27	18α(H)-trisnorneohopane	19	31	unident.
2	27	17α(H)-trisnorneohopane	20	31	unident.
3	28	unident.	21	31	unident.
4	28	unident.	22	31	17α(H)-homohopane (22S)
5	28	unident. (Bisnorneohopane?)	23	31	17α(H)-homohopane (22R)
6	28	unident. (Bisnorneomoretane?)	24	31	Homomoretane
7	29	unident.	25	31	unident.
8	29	unident.	26	31	unident.
9	29	unident.	27	32	unident.
10	29	Norhopane	28	32	17α(H)-bishomohopane (22S)
11	29	Normoretane	29	32	17α(H)-bishomohopane (22R)
12	29	unident.	30	32	Bishomomoretane
13	30	unident.	31	33	17α(H)-trishomohopane (20S)
14	30	unident.	32	33	17α(H)-trishomohopane (20R)
15	30	unident.	33	34	17α(H)-tetrakishomohopane (20S)
16	30	unident.	34	34	17α(H)-tetrakishomohopane (20R)
17	30	17α(H)-hopane			
18	30	Moretane			

tion. The direction of largest point scatter corresponds to the direction of the first eigenvector, and the direction of highest point scatter at right angles to the first eigenvector is consistent with the direction of the second eigenvector. Consequently, the first-to-second eigenvector plane corresponds to the direction of largest point scatter and thus contains more information than any other two-dimensional plane of projection. The third eigenvector is perpendicular to this plane.

The multivariate correlation becomes evident from the direction of the eigenvectors in the variable space. The eigenvector direction is described in terms of a linear combination of all the variables, and the weighting of each variable defines the direction. This weighting is called the eigenvector (or factor) loading, and the correlation between the loadings of each eigenvector carries pertinent information about the data structure.

The loadings were computed with the aid of the SIMCA program [12].

RESULTS AND DISCUSSION

All the recorded biomarkers

The first-to-second eigenvector loading plot of all the recorded biomarker peaks is given in Fig. 1, with the known categories of molecules indicated. The most obvious feature of Fig. 1 is that the main groups of biomarker molecules form clusters: cholestanes to the right, moretanes and the 20R epimers of the hopanes at the top, and the hopane 20S epimers at the bottom. Further, most of the unidentified C_{28}—C_{31} triterpanes form a cluster to the left.

TABLE 2

Peak identification of steranes

Peak no.	No. of carbons	Identification	Peak no.	No. of carbons	Identification
35	27	13β,17α-diacholestane (20S)	49	28	24-Me-13α,17β-diacholestane (20
36	27	13β,17α-diacholestane (20R)	50	28	24-Me-13α,17β-diacholestane (20
37	27	unident.	51	28	unident.
38	27	13α,17β-diacholestane (20S)	52	28	unident.
39	27	13α,17β-diacholestane (20R)	53	28	24-Me-14α,17α-cholestane (20S)
40	27	unident.	54	28	24-Me-14β,17β-cholestane (20R)
41	27	unident.	55	28	24-Me-14β,17β-cholestane (20S)
42	27	unident.	56	28	24-Me-14α,17α-cholestane (20R)
43	27	14α,17α-cholestane (20S)	57	29	24-E-13β,17α-diacholestane (20S)
44	27	14β,17β-cholestane (20R)	58	29	24-E-13β,17α-diacholestane (20R
45	27	14β,17β-cholestane (20S)	59	29	24-E-13α,17β-diacholestane (20S)
46	27	14α,17α-cholestane (20R)	60	29	24-E-13α,17β-diacholestane (20R
47	28	24-Me-13β,17α-diacholestane (20S)	61	29	24-E-14α,17α-cholestane (20S)
48	28	24-Me-13β,17α-diacholestane (20R)	62	29	24-E-14β,17β-cholestane (20R&S)
			63	29	24-E-14α,17α-cholestane (20R)

[a]Poorly resolved.

For the samples studied, the most important data structure is consistent with the direction of the first eigenvector (β_1). This gives information on the segregation into two groups: cholestanes, and the triterpanes including the hopanes. There are a few exceptions to this general observation which will be discussed below. The second important feature of Fig. 1 is the segregation of the hopanes along the direction of the second eigenvector (β_2). The location of the 20R and 20S clusters is in harmony with the well-known inverse proportionality of these hopane epimers which has been used for evaluation of

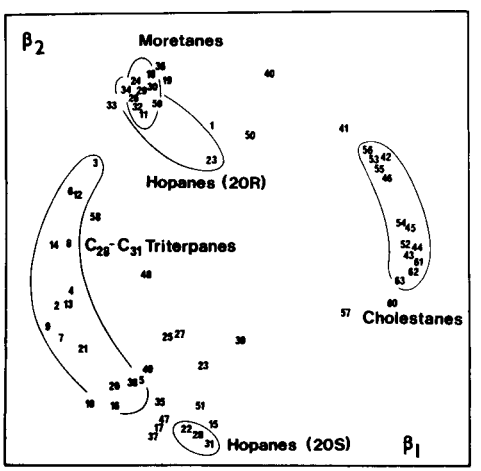

Fig. 1. First (β_1) to second (β_2) eigenvector plot of the variables of the light oil and condensate oil samples studied. Clusters of steranes and triterpanes indicated. Variables not included in clusters are mostly diasteranes.

maturity [1, 3, 13]. Further, the moretane and the hopane (20R) clusters overlap in Fig. 1. This indicates that these two groups of biomarker molecules yield similar information in the set of samples studied. That is in harmony with the observation that 20R hopanes and moretanes both disappear with increasing maturity of the source rock [14].

In order to avoid interferences from other groups, a closer analysis of each of the main groups of the studied biomarkers is given below. The point locations in the following diagrams cannot be directly compared to those of Fig. 1 because the directions of the eigenvectors are different from those for the whole set of data.

Hopanes and moretanes

The complete separation of moretanes and the hopane epimers is seen from the eigenvector diagram of Fig. 2(a). The diagram reflects the present theories on the geochemistry of these triterpanes: the moretanes and the 20R hopane epimers cluster close together on the right of the diagram. This demonstrates that they carry similar geochemical information, and the inverse proportionality of the 20S and 20R hopanes is illustrated by the 20S cluster being located at the edge opposite to the 20R cluster.

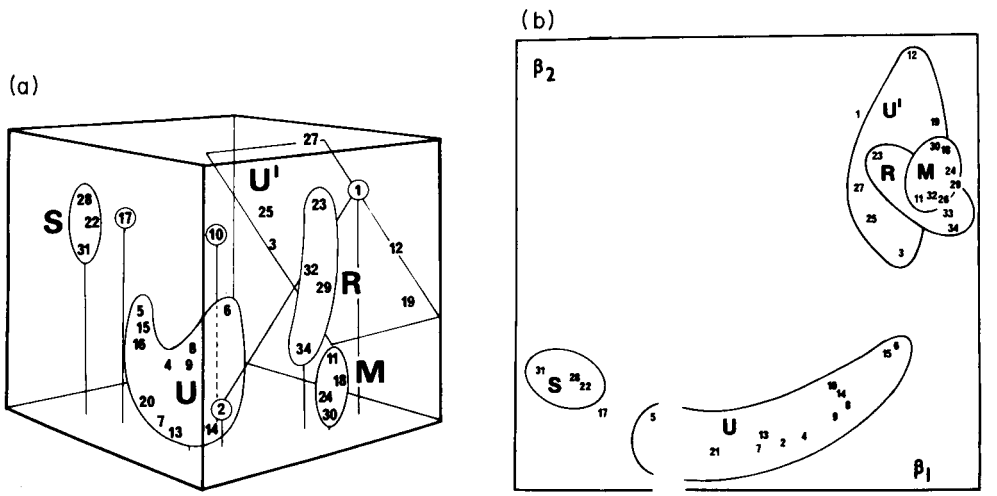

Fig. 2. (a) First to second to third eigenvector plot of triterpanes. Third eigenvector along the vertical direction. S and R are the hopane epimer clusters, and M the moretanes; U denotes the two groups of unidentified triterpanes, one forming a flat U-shaped cluster at the bottom of the diagram, and the other a straight plane in the upper right half. Variables 1 and 2 are the 18α(H) and 17α(H) isomers of trisnorneohopane; variables 10 and 17 are norhopane and 17β(H)-hopane, respectively. The no. 21 lies between 7 and 20 and has been omitted for clarity; 26 lies on the straight U plane behind the R cluster, and 33 was probably erratic and was omitted.

(b) First to second eigenvector plot of triterpanes, demonstrating the main density points of information. U and U' indicate the two groups of unidentified triterpanes.

The 18α/17α inversion of trinorneohopane upon increasing maturity is also clearly seen from the inverse proportionality shown in Fig. 2(a) (points 1 and 2), the 18α-isomer (point 1) being consistent with relative immaturity. The inverse proportionality of point 17 (C_{30} hopane) and points 11 and 18 (C_{29} and C_{30} moretanes) is in harmony with the findings of Seifert and Moldowan [14] who introduced the ratio of C_{30} hopane to the sum of C_{29} and C_{30} moretanes as a specific indicator of maturation; their work was later supported experimentally [15]. Norhopane (point 10) falls intermediately between the 20R and the 20S epimers of the heavier hopanes. There seems to be inverse proportionality between norhopane and normoretane (points 10 and 11).

Among the unidentified triterpane peaks, a certain information structure may be observed in the set of samples studied. There seem to be two groups of unidentified isomers in the C_{28}—C_{30} range: one consists of points 4—9 and 13—16 and carries information similar to that of 17α-trisnorneohopane (point 2), whereas the second group (points 3, 11, 12, and 18) can provide information similar to that of the C_{31} hopane 20R epimers and 18α-norneohopane (point 1). Further clarification of the geochemical information of these compounds must await clarification of their chemical identity.

The major feature of Fig. 2(a) is that there seem to be three main density points of information. This is more clearly seen from the first-to-second eigenvector plot of Fig. 2(b), even though the information about the cluster separation along the third eigenvector is omitted from this diagram. One type of information is carried by the C_{31+} hopane 20S epimers, another type of information seems to be carried by the majority of unidentified triterpanes making up the cluster U, and a third type of information is carried by the 20R epimers, the moretanes and the smaller group of unidentified triterpanes U′.

Steranes

The eigenvector loading plots of the steranes and diasteranes are given in Fig. 3. As can be seen, the information content of the steranes is different from that of the diasteranes. The steranes are characterised by forming dense clusters in the diagram, whereas the diasterane clusters are much less dense. This may indicate that the steranes inform about only a simple process and the diasteranes about a variety of independent factors.

The sterane isomers of carbon numbers 27 and 28 fall in clusters that are elongated along the second eigenvector. The 14α,17α 20R and 20S epimers are inversely proportional (points 43 and 46, and 53 and 56, respectively). This is consistent with the well known epimerisation of the steranes on increasing maturity [3, 4, 13, 15] and, from the clustering in Fig. 3, this direction in the data matrix studied can be assigned to maturity.

The 20R epimer of C_{27}—C_{29} sterols seems to be a sensitive indicator of the origin of sedimentary organic matter in terms of land plant versus marine organism [16], and the corresponding steranes have been used as source

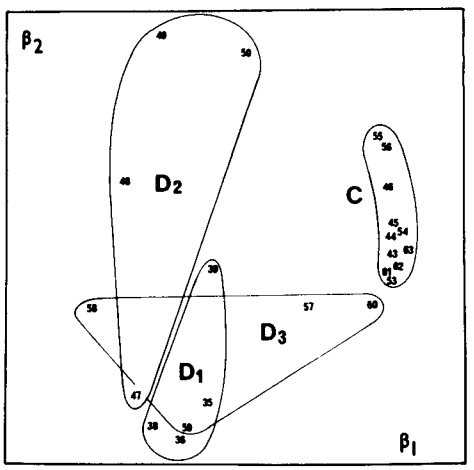

Fig. 3. First to second eigenvector plot of the identified C_{27}—C_{29} steranes. The cholestanes form a well defined cluster to the right of the diagram (C), whereas the diasteranes are spread around (D_1, D_2 and D_3). This indicates that the information supplied by the steranes is uniform and different from that of the diasteranes.

indicators because they seem to be but little influenced by thermal stress [2, 4, 13]. These compounds are not segregated in the direction of the second eigenvector in Fig. 3 (points 44, 46, 54, 56, 62, and 63), and, consequently, this direction is not consistent with source differences in the samples studied (cf. [17]).

The C_{29} sterane epimer and isomer relations were used for an estimate of combined maturation and migration [4] with the use of the ratio of the 20S and 20R epimers of the 14α,17α-isomer versus the ratio of the 20R epimers of the 14β, 17β to 14α,17α isomers (points 61 to 63 versus 62 (poorly resolved) to 63 in Fig. 3). These compounds lie close to another in this diagram, and it is a notable fact that the C_{27} and C_{28} analogs are preferable because of their larger chromatographic peak separation as well as their larger separation in the present diagrams, and, consequently, their higher load of information. For the C_{27} steranes, the corresponding variable ratio 43 to 46 versus 44 to 46 would result in a line of nearly the same angular coefficient as the line of first-order kinetic conversion in Fig. 10 of the paper by Seifert and Moldowan [4]. This is true for the C_{28} steranes also (points 53 to 56 versus 54 to 56). If the statement by Seifert and Moldowan [4] about the influence of maturation on these peak ratios and the selective influence of migration upon the 20R 14β, 17β- and 14α,17α-isomers is correct, this gives further support to the statement that migration cannot be assigned to the variation along the first eigenvector of Fig. 3. However, it remains a fact that the data structure of the steranes of the samples studied is dominated by segregation of the diasteranes from the normal steranes. This point calls for further studies in order to be clarified.

Conclusion

The geochemical information carried by biomarker molecules analysed by metastable ion monitoring can be illustrated by means of eigenvector analysis. This method indicates that in the set of samples studied, the information carried by the steranes is different from that carried by the hopanes, although they carry information about maturity common to both groups of biomarkers. Evidently, diasteranes carry information very different from that carried by the steranes.

The well-known segregation of the 20R and 20S hopanes, and the similarity of 20R hopanes and moretanes is also seen from the eigenvector diagrams.

Even information about unidentified triterpanes can be read from eigenvector diagrams based on measurements of peak heights in metastable monitoring chromatograms. The information appears to fall into two quite different groups, one being somehow related to the 20R hopanes, and the other carrying unidentified information.

REFERENCES

1 W. K. Seifert, Geochim. Cosmochim. Acta, 42 (1978) 473.
2 W. K. Seifert, in A. Prashnowsky (Ed.), Int. Alfred Treibs Symp., Munich. Bayr Julius-Maximil.-Univ. Würtzburg, 1980, p. 13.
3 A. S. Mackenzie, R. L. Patience, J. R. Maxwell, M. Vandenbroucke and B. Durand, Geochim. Cosmochim. Acta, 44 (1980) 1709.
4 W. K. Seifert and J. M. Moldowan, Geochim. Cosmochim. Acta, 45 (1981) 783.
5 T. Meyer, O. H. J. Christie and P. W. Brooks, Anal. Chim. Acta, 160 (1984) 65.
6 P. W. Brooks, T. Meyer and O. H. J. Christie, in P. A. Schenck (Ed.), Advances in Organic Geochemistry 1983, Elsevier, 1984.
7 G. A. Warburton and J. E. Zumberge, Anal. Chem., 55 (1983) 123.
8 O. H. J. Christie, K. Esbensen, T. Meyer and S. Wold, in P. A. Schenck (Ed.), Advances in Organic Geochemistry 1983, Elsevier, Amsterdam, 1984.
9 J. C. Davis, Statistics and Data Analysis in Geology, Wiley, New York, 1973.
10 K. G. Jöreskog, J. E. Klovan and R. A. Reyment, Geological Factor Analysis, Elsevier, Amsterdam, 1976.
11 K. Varmuza, Pattern Recognition in Chemistry, Springer Verlag, Heidelberg, 1980.
12 S. Wold, Pattern Recog., 8 (1976) 127.
13 W. K. Seifert and J. M. Moldowan, Geochim. Cosmochim. Acta, 42 (1978) 77.
14 W. K. Seifert and J. M. Moldowan, in A. G. Douglas and J. R. Maxwell (Eds.), Advances in Organic Geochemistry 1979, Pergamon, Oxford, 1980, p. 229.
15 M. Schoell, M. Teschner, H. Wehner, B. Durand and J. L. Oudin, in M. Bjorøy (Ed.), Advances in Organic Geochemistry 1981, Wiley, Chichester, 1983, p. 156.
16 C. Lee, J. W. Farrington and R. B. Gagosian, Geochim. Cosmochim. Acta, 43 (1979) 35.
17 P. F. V. Williams and A. G. Douglas, in M. Bjorøy (Ed.), Advances in Organic Geochemistry 1981, Wiley, Chichester, 1983, p. 568.

Analytica Chimica Acta, 161 (1984) 83—90
Elsevier Science Publishers B.V., Amsterdam — Printed in The Netherlands

THE POLAROGRAPHIC DETERMINATION OF STABILITY CONSTANTS OF UREA/CROWN ETHER COMPLEXES IN METHANOL

D. PH. ZOLLINGER, M. BOS, A. M. W. VAN VEEN-BLAAUW and W. E. VAN DER LINDEN*

Department of Chemical Technology, Twente University of Technology, Enschede (The Netherlands)

(Received 13th February 1984)

SUMMARY

A general method for determination of the stability constants of complexes of crown ethers and related compounds with small organic molecules in polar solvents is described, based on an indirect polarographic procedure. Computerized evaluation of the data forms an essential part of the procedure.

Since the publication of the pioneering paper of Pedersen in 1967 [1], interest in the chemistry of crown ethers and related compounds has steadily increased, not only from a purely scientific point of view, but also with regard to possible applications of crown ethers in (organic) synthesis, analytical chemistry and in the field of physiological processes and pharmacology [2, 3].

Apart from the abundance of data on complexes of various crown ethers with metal ions and other cations that can be found in the literature, complexes with neutral molecules are also mentioned [4]. Complexation of (uncharged) molecules plays an essential role in many biological processes such as enzyme-substrate and pharmacon-receptor interactions. In this respect, the study of the interactions between crown ethers and neutral molecules could eventually lead to the design of specific host molecules for compounds of biological significance like neurotransmitters, drugs and toxic compounds.

For a number of complexes of crown ethers with neutral molecules, the crystal structure has been elucidated (Table 1), but crystalline complexes for which the crystalline structure has not yet been resolved have been reported for many other compounds [4]. In this Department, interest in these neutral compound complexes was aroused during consideration of the possibility of using crown ethers in the selective removal of urea from dialysis fluid, one of the major problems in the current practice of kidney dialysis.

In order to obtain guidelines for the synthesis of possible urea-selective crown-type ligands, it was necessary to have information concerning the

0003-2670/84/$03.00

TABLE 1

Crystalline complexes of crown ethers with neutral compounds

Host	Guest	Stoichiometry	Ref.
18C6	Dimethylacetylenedicarboxylate	1:1	[5]
18C6	Benzenesulfonamide	1:2	[6]
18C6	Malononitrile	1:2	[7]
18C6	Urea	1:5[a]	[8]
18C6	bis-Dimethylsulfone	1:2	[9]
18C6	Guanidiniumnitrate	1:2	[10]
18C6	*S*-t-Butylthiouronium perchlorate	1:2	[11]
18C6	Uronium nitrate	1:1	[12]
B27C9	Uronium perchlorate	1:1	[12]
B27C9	Guanidinium perchlorate	1:1	[13]
18C6	Nitromethane	1:2	[14]
DB18C6	t-Butylammonium perchlorate/DDQ	1:1:1	[15]
DB27C9	Guanidinium perchlorate	1:1	[16]
DB30C10	Guanidinium perchlorate	1:1	[16]

[a]Only two urea molecules are hydrogen-bonded to both sides of the 18-crown-6 molecule; the remaining molecules form hydrogen-bonded layers.

degree of binding of urea by these ligands; in other words, to determine the stoichiometry and the corresponding stability constants of the complexes between these compounds. The aim was to develop suitable methods for this purpose, and the study was limited to polar solvents in view of the use of the compounds to be synthesized in biomedical applications where aqueous systems are involved.

A large number of techniques and methods is available for the determination of stability constants and many of these have been used in studies of the complexation of metal ions by crown ethers; for example, potentiometry, conductometry, polarography/voltammetry, calorimetry, n.m.r. spectroscopy, liquid-liquid extraction methods and osmometry have been applied [17]. Among the factors that determine the choice of technique and method appropriate for a certain problem are the physicochemical properties of the compounds of interest, the solvent to be used and the availability of instrumentation.

In the problem given, two classes of compounds must be considered: crown ethers and related compounds on one side and small organic molecules like urea, acetonitrile, malonitrile and nitromethane on the other side. The physicochemical properties of urea and similar compounds and of crown ethers that carry no chromophoric substituents do not allow the application of u.v.-visible spectrophotometry; also potentiometry, another technique often used in complexation studies, is not applicable as such. The use of aqueous systems and the need for a high degree of automation eliminate some other techniques, such as osmometry. Therefore, attention was focussed on the development of an electrochemical method, particularly polarography.

THEORY

As the system of particular interest (urea/crown ether complexes) does not contain any compounds that can be reduced and/or oxidized at the DME under normal conditions, it is necessary to add an auxiliary compound that forms complexes with one or both of the components present and that can be determined polarographically. (This approach was originally described by Schwarzenbach and Ackermann [18] and by Ringbom and Eriksson [19] for stable 1:1 complexes and stepwise complex formation, respectively).

In view of the characteristic properties of crown ethers and related compounds, the use of an alkali metal ion for this purpose seemed to be an obvious choice. The equilibria in solution, assuming 1:1 complexation and neglecting solvation are

$$\mathrm{M} + \mathrm{CE} \rightleftarrows (\mathrm{MCE}); \quad \mathrm{Urea} + \mathrm{CE} \rightleftarrows (\mathrm{urea{-}CE}) \tag{1}$$

where M denotes the metal ion and CE is the crown compound.

The polarographic determination of stability constants is nowadays generally based on the method of DeFord et al. [20, 21] or a modification of it. For the reversible reduction of a metal ion in the presence of an excess of the ligand, the cathodic displacement of the half-wave potential and the change in limiting current value as a function of the (free) ligand concentration are used to determine the consecutive stability constants $K_1 \ldots K_n$

$$\mathrm{M} + \mathrm{L} \rightleftarrows \mathrm{ML}; \mathrm{ML} + \mathrm{L} \rightleftharpoons \mathrm{ML}_2; \ldots; \mathrm{ML}_{n-1} + \mathrm{L} \rightleftharpoons \mathrm{ML}_n \tag{2}$$

with $K_n = [\mathrm{ML}_n]/[\mathrm{ML}_{n-1}][\mathrm{L}]$ and $\beta_n = [\mathrm{ML}_n]/[\mathrm{M}][\mathrm{L}]^n$ (L is the ligand, K_i the stability constant for the ith complex and β_i the overall stability constant for the ith complex).

In a medium of constant ionic strength, a formation function F_0 can be defined as

$$F_0 = C_\mathrm{M}/[\mathrm{M}] = \beta_0 + \beta_1[\mathrm{L}] + \ldots\ldots + \beta_n[\mathrm{L}]^n, \tag{3}$$

C_M and [M] representing the analytical and free metal concentrations, respectively. F_0 can also be expressed as a function of experimental parameters:

$$F_0 = \exp[(nF/RT)(E_\mathrm{s}^{1/2} - E_\mathrm{c}^{1/2}) + \ln(I_\mathrm{s}^\mathrm{d}/I_\mathrm{c}^\mathrm{d})] \tag{4}$$

The subscripts c and s denote the cases for complexation and no complexation, respectively, and the other symbols have their usual meaning. Further functions F_i can be derived from the preceding formation functions F_{i-1} and the corresponding value of the stability constants β_{i-1}:

$$F_i = (F_{i-1} - \beta_{i-1})/[\mathrm{L}], \tag{5}$$

where [L] is the free ligand concentration of the solution.

From these formation functions F_i, the number of complexes present and their stability constants β_i can be found by means of graphical analysis as well as by (computerized) mathematical processing of the data. The latter

approach certainly is to be preferred, especially because powerful and cheap (micro)computers are available in many laboratories. (Nevertheless, Gaizer [22] as well as Rossotti et al. [23] in their reviews on computerized evaluation of complex equilibria, stress the importance of using graphical analysis alongside the computer method and point out the danger of relying exclusively on the outcome of the calculations).

COMPUTER PROGRAM

The automation of the polarographic determination of stability constants is almost a necessity in order to obtain reliable and precise results [24, 25]. Besides, (computerized) statistical evaluation of the data provides a means of calculating the errors of the parameters sought.

The DeFord—Hume method has been computerized by several authors [26—30]; all these programs are based on a form of least-squares analysis. The Legget method (POLAG [30]) is the most general in approach and uses well-known procedures, as it is based on earlier programs for the calculation of stability constants (SQUAD) [31] and SCOGS [32]).

The least-squares approach is aimed at minimizing U, the sum of the residuals

$$U = \sum_{1}^{N} w_i (F_{obs} - F_{calc})^2, \tag{6}$$

where N denotes the number of data points and w_i is the weighting factor (which is set to one in the POLAG program); F_{obs} is obtained from the experimentally found parameters using Eqn. 4 and F_{calc} is calculated from Eqn. 3.

As a first step in the automation of the procedure for the system described, the POLAG program was edited for the 2 metals +1 ligand model used. The MAIN part of the program was adapted in order to be able to use the program for experiments with variable metal concentrations, an option not available in the original program. Further, the data input was modified so that it could be checked before the actual start of the refinement procedures.

EXPERIMENTAL

Chemicals and apparatus

Tetramethylammonium chloride (Merck, zur Synthese) and tetraethylammonium chloride (Fluka, purum) were recrystallized from water or from water and ethanol, depending on the solvent used.

Benzo-15-crown-5 and dibenzo-24-crown-8 (Merck) were used without further purification. Benzo-27-crown-9 was synthesized in the Department of Organic Chemistry of this University and was used as received.

18-Crown-6 (Merck) was purified from the acetonitrile complex as described by Gold and Rice [33].

Double-distilled water was used throughout the experiments and all other chemicals were at least of analytical-reagent grade.

A Metrohm Polarecord E506 in conjunction with the E505 polarographic stand was used, operating in the 3-electrode mode. The auxiliary electrode was a platinum wire and a laboratory-made silver/silver chloride electrode served as reference electrode. Glass capillaries (Metrohm) were used as obtained.

Polarographic procedure and data evaluation

Purified nitrogen was led over heated copper (350°C) and pre-saturated with the solvent used before it was led through the solutions to remove oxygen. The polarographic cell was kept at 25.0 ± 0.1°C.

Concentrated solutions of crown ethers and urea were added stepwise to solutions containing the alkali metal salts by means of a burette. After each addition, nitrogen was bubbled through for another 3 min and the polarogram was recorded.

The polarograph was operated in the d.c.-Tast mode with the drop time set to 0.8 s; the scan speed was 2.5 or 5 mV s^{-1}.

From a series of current-potential data pairs, the limiting current values and halfwave potentials were calculated from the d.c. polarograms by means of a 3-parameter curve-fitting procedure based on least-squares [34]. The results of these calculations were used as the input values for the modified POLAG program from which the stability constants and their standard deviations were obtained.

RESULTS AND DISCUSSION

In order to test the procedure described and the modification of the computer program, an experiment was done in which potassium ion competed with thallium(I) ion for 18-crown-6 in aqueous solution. Complexation of Tl^+ by 18-crown-6 was reflected by a small cathodic shift of the halfwave potential and by a decrease in the limiting current value for the reduction wave of the thallium ion. Upon addition of the potassium ion, a reversed effect was observed, indicating a replacement of Tl^+ by K^+ in the cavity of the crown ether. The results, summarized in Table 2, show that the method can be used for the indirect determination of stability constants of crown ether complexes.

In the search for an appropriate indicator system, the first point studied was the influence of the composition of the solvent with regard to the water content on the stability constant of the potassium/18-crown-6 complex (Table 3). As expected, an increase in water content lowers the stability of the complex, which can be regarded as the effect of an increase in dielectric constant of the solvent.

TABLE 2

Competition between Tl^+ and K^+ for 18-crown-6 in 0.1 M tetramethylammonium hydroxide in water, at 25.0°C

		log K	s.d.[a]	Lit. value	Ref.
Direct	Tl^+	2.3	0.1	2.27	[35]
Indirect	K^+	2.1	0.1	2.06	[36]

[a]The standard deviation of the stability constant was calculated from the data set of a single experiment.

TABLE 3

Influence of water content on the stability constant of the potassium/18-crown-6 complex (electrolyte, 0.1 M tetramethylammonium hydroxide; temperature 20.0°C; solvent, isopropanol(IPA)/methanol(MeOH)/water)

IPA-MeOH (3:1)	Water	log K[a]	IPA-MeOH (3:1)	Water	log K[a]
10	0	7.3 ± 0.36	6	4	3.48 ± 0.06
9	1	5.23 ± 0.06	5	5	3.04 ± 0.04
8	2	4.38 ± 0.05	3	7	2.79 ± 0.02
7	3	4.02 ± 0.06	0	10	2.32 ± 0.15

[a]With standard deviation.

When potassium was used as the indicator ion in water/methanol mixtures (water content 30—70%), it was not possible to determine the stability constant of the urea/18-crown-6 complex in these solutions: no shift in halfwave potential and/or limiting current could be observed upon addition of urea. Apparently, the interaction between urea and 18-crown-6 under the conditions used is too weak to be studied in this way.

As the reduction of the potassium complex of 18-crown-6 in these solvents gave rise to rather unfavorably defined polarographic waves, potassium was replaced by rubidium which is reduced at a slightly more positive potential and has comparable properties towards crown ethers. Methanol was used as solvent in the first studies of 18-crown-6 complexes. In this case, addition of urea to a solution of the metal/crown complex produced a change in the reduction wave characteristics, but the effects observed were very small. The stability constants found for the urea-complex varied from 0.2 to 0.7 with a standard deviation for the individual determinations of 0.15 to 0.20.

From x-ray crystal structure data, it can be seen [9] that the ring of the 18-crown-6 molecule is too small to envelop the urea molecule and that larger rings are necessary for this purpose [11—13]. Therefore, three other crown ethers were used to study the influence of the ring size upon complexation of urea in competition with the rubidium ion (Table 4).

For benzo-15-crown-5, no convergence of the computer calculations was

TABLE 4

Stability constants of rubidium complexes in methanol and of urea complexes with rubidium as the indicator ion (temperature 25.0°C; electrolyte, 0.1 M tetraethylammonium iodide)

Crown	Rb complex		Urea complex	
	log K	s.d.	log K	s.d.
Benzo-15-crown-5	3.11	0.05	—[a]	
18-crown-6	5.47	0.04	—[b]	
Dibenzo-24-crown-8	3.76	0.03	1.1	0.1
Benzo-27-crown-9	3.78	0.03	1.2	0.1

[a]No convergence. [b]No reproducible value: log K varied from 0.2 to 0.7 with s.d. 0.15 to 0.20.

obtained at all, indicating no complexation of urea. For the two benzo-substituted crown ethers with larger rings (dibenzo-24-crown-8 and benzo-27-crown-9), the values of the stability constants were small. This demonstrates that the cavity size of these crown ethers is better suited for the urea molecule than the smaller cavity of 18-crown-6.

The approach described is considered to provide a suitable method for obtaining information about the complexation of small organic molecules such as urea in polar solvents. However, improvement of the precision of the data obtained is necessary in order to gain more insight into the physicochemical parameters that determine the stability of the complexes involved. This can be achieved by further automation of the procedure described, which will be the subject of a forthcoming paper.

The authors thank Dr. D. J. Leggett (Dow Chemical USA, Freeport, TX) for providing them with a listing of the computer program POLAG, J. Geevers (Department of Organic Chemistry, Twente University of Technology) for the synthesis and purification of benzo-27-crown-9 and Mrs. B. Verbeeten-van Hettema for preparing the manuscript. These investigations were supported (in part) by the Netherlands Foundation for Technical Research (STW), future Technical Science Branch/Division of the Netherlands Organization for the Advancement of Pure Research (ZWO).

REFERENCES

1 C. J. Pedersen, J. Am. Chem. Soc., 89 (1967) 7017.
2 F. de Jong and D. N. Reinhoudt, Adv. Phys. Org. Chem., 17 (1980) 279.
3 E. Weber and F. Vögtle, Top. Curr. Chem., 98 (1981) 1.
4 F. Vögtle, H. Sieger and W. H. Müller, Top. Curr. Chem., 98 (1981) 107.
5 I. Goldberg, Acta Crystallogr., 31B (1975) 754.
6 A. Knöchel, J. Kopf, J. Oehler and G. Rudolph, J. Chem. Soc., Chem. Commun., (1978) 595.

7 R. Kaufman, A. Knöchel, J. Kopf, J. Oehler and G. Rudolph, Chem. Ber., 110 (1977) 2249.
8 S. Harkema, G. J. van Hummel, K. Daasvatn and D. N. Reinhoudt, J. Chem. Soc., Chem. Commun., (1981) 368.
9 J. A. Bandy, M. R. Truter and F. Vögtle, Acta Crystallogr., 37B (1981) 1568.
10 J. A. Bandy, M. R. Truter and J. N. Wingfield, J. Chem. Soc., Perkin Trans. 2, (1981) 1025.
11 J. W. H. M. Uiterwijk, S. Harkema, G. J. van Hummel, J. Geevers and D. N. Reinhoudt, Acta Crystallogr., 38B (1982) 1862.
12 J. W. H. M. Uiterwijk, S. Harkema, D. N. Reinhoudt, K. Daasvatn, H. J. den Hertog Jr. and J. Geevers, Angew. Chem. Suppl., (1982) 1100.
13 J. W. H. M. Uiterwijk, S. Harkema, J. Geevers and D. N. Reinhoudt, J. Chem. Soc., Chem. Commun., (1982) 200.
14 J. A. A. de Boer, D. N. Reinhoudt, S. Harkema, G. J. van Hummel and F. de Jong, J. Am. Chem. Soc., 104 (1982) 4073.
15 J. A. A. de Boer, D. N. Reinhoudt, J. W. H. M. Uiterwijk and S. Harkema, J. Chem. Soc., Chem. Commun., (1982) 194.
16 J. A. A. de Boer, J. W. H. M. Uiterwijk, J. Geevers, S. Harkema and D. N. Reinhoudt, J. Org. Chem., 48 (1983) 4821.
17 F. Vögtle and E. Weber, in S. Patai (Ed.), The Chemistry of functional groups, Suppl. E, Wiley and Sons, Chichester, 1980, p. 59.
18 H. Ackermann and G. Schwarzenbach, Helv. Chim. Acta, 35 (1952) 485.
19 A. Ringbom and L. Eriksson, Acta Chem. Scand., 7 (1953) 1105.
20 D. D. DeFord and D. N. Hume, J. Am. Chem. Soc., 73 (1951) 5321.
21 D. N. Hume, D. D. DeFord and G. B. C. Cave, J. Am. Chem. Soc., 73 (1951) 5323.
22 F. Gaizer, Coord. Chem. Rev., 27 (1979) 195.
23 F. J. C. Rossotti, H. S. Rossotti and R. J. Whewell, J. Inorg. Nucl. Chem., 33 (1971) 2051.
24 M. Tkalcec, B. S. Grabaric, I. Filipovic and I. Piljac, Anal. Chim. Acta, 143 (1982) 255.
25 M. Tkalcec, B. S. Grabaric and I. Filipovic, Anal. Chim. Acta, 122 (1980) 395.
26 D. L. McMasters and W. B. Schaap, Proc. Indiana Acad. Sci., 67 (1957) 111.
27 K. Momoki, H. Sato and H. Ogawa, Anal. Chem., 39 (1967) 1072.
28 I. Piljac, B. S. Grabaric and I. Filipovic, J. Electroanal. Chem. Interfacial Electrochem., 42 (1973) 433.
29 L. Meites, Talanta, 22 (1975) 733.
30 D. J. Leggett, Talanta, 27 (1980) 787.
31 D. J. Leggett and W. A. E. McBryde, Anal. Chem., 26 (1975) 1065.
32 I. G. Sayce, Talanta, 15 (1968) 1397.
33 H. S. Gold and M. R. Rice, Talanta, 29 (1980) 637.
34 M. Bos, Anal. Chim. Acta, 81 (1976) 21.
35 R. M. Izatt, R. E. Terry, B. L. Haymore, L. D. Hansen, N. K. Dalley, A. G. Avoudet and J. J. Christensen, J. Am. Chem. Soc., 98 (1976) 7620.
36 H. K. Frensdorff, J. Am. Chem. Soc., 93 (1971) 600.

Analytica Chimica Acta, 161 (1984) 91—99
Elsevier Science Publishers B.V., Amsterdam — Printed in The Netherlands

KINETIC DETERMINATION OF SUBSTRATES AND ENZYMES BY INTEGRATION OF RESPONSE CURVES WHICH SHOW MAXIMA, MINIMA OR INFLECTIONS

GAROLD E. RADKE and LAWRENCE C. THOMAS*
Department of Chemistry, Oregon State University, Corvallis, OR 97331 (U.S.A.)
(Received 26th September 1983)

SUMMARY

This paper describes quantitative kinetic procedures based on the integration of response vs. time curves. In these procedures, concentrations or activities are evaluated from the difference between integrals of signal vs. time before the reaction has been initiated and during a significant fraction of the reaction. The procedures have the advantage that they are applicable to response curves with maxima, minima, or inflections. Results are presented for computed response curves and for experimental measurements on selected enzyme-catalyzed reactions used for quantifying glucose, ethanol and creatine kinase. For situations in which calibration plots pass through maxima or minima, supplementary information such as the times at which maxima or minima occur in response curves are used to differentiate between low and high values of concentration that could yield the same differences between integrals. Relative standard deviations of triplicate runs are generally quite good, ranging from 0.5% to 1%.

Of the many kinetic approaches that have been described [1, 2], only a few have involved integration procedures [3—6]. In the integration methods described to date, a time-dependent signal is integrated over two different time intervals and the difference between those integrals is related to the concentration or activity of the rate-limiting species of interest.

This paper describes a method in which data are integrated over a single time interval. In this method, transducer signals are integrated over a selected period of time. The difference between an integral of the signal before the reaction is initiated and an integral of the time-dependent response after the reaction has been initiated is related to concentration or activity. The method offers several advantages relative to conventional rate methods [6]. For example, these integration methods are not restricted to reactions that follow zero- or first-order kinetics. In addition, knowledge about the kinetics of the reactions is not necessary. Also, improved precision may be gained by integrating noisy signals.

When maxima or minima in transducer responses are spanned or signal-time curves show inflections, single integrations may yield ambiguous results. In such cases, supplementary first- or second-derivative data can be used to identify the region of a calibration curve to which an ambiguous result belongs.

0003-2670/84/$03.00

Three reactions were studied to evaluate the efficacy of the methods. For one system involving reduced nicotinamide adenine dinucleotide (NADH), the reaction produced a fluorescence response curve with a maximum at elevated concentrations of NADH caused by attenuation of the signal. For a second system, amperometric detection of the time-dependent concentration of oxygen consumed in a glucose oxidase reaction resulted in a minimum in the response curve which was attributed to diffusion of oxygen into the reaction solution from the surrounding environment. A third system involved a three-reaction sequence to produce reduced nicotinamide adenine dinucleotide phosphate (NADPH) in the final step. Absorbance varied in a sigmoidal manner with time.

EXPERIMENTAL

Reagents

Alcohol dehydrogenase (ADH, 325 IU mg^{-1}), nicotinamide adenine dinucleotide (NAD), glucose oxidase (130 IU mg^{-1}), adenosine diphosphate (ADP), creatine kinase (CK, 130 IU mg^{-1}), creatine phosphate (CP), adenosine monophosphate (AMP), cysteine hydrochloride, hexokinase (85 IU mg^{-1}), glucose-6-phosphate dehydrogenase (G6PD, 220 IU mg^{-1}), glucose-6-phosphate (G6P) and nicotinamide adenine dinucleotide phosphate (NADP) were obtained from Sigma Chemical Company. All other chemicals were reagent grade and deionized water was used in the preparation of all solutions.

Apparatus

Amperometry. The amperometric cell used for the glucose reaction was constructed from a 30-ml beaker and a Beckman oxygen sensor. A 6-mm diameter hole was bored into the side of the beaker about 2 cm from the bottom. The sensor tip was introduced through this hole far enough to permit the membrane to be flush with the interior wall of the beaker. The sensor tip was sealed in place with Tore Seal (Varian Assoc., Palo Alto, CA) and a 1.5-cm thick epoxy base was cast around the bottom half of the beaker for structural support. The sensor was easily inserted and removed from the mounted tip to permit the membrane and electrolyte solution to be changed.

A platinum working electrode and a Ag/AgCl reference electrode were connected to a Princeton Applied Research (PAR) model 174A potentiostat and the working electrode was maintained at −0.55 V vs. Ag/AgCl. The electrolysis current was monitored as voltage via the y-axis output of the potentiostat.

The assembly was mounted on a ring stand and positioned about 7 cm above a stirring motor to provide thermal insulation from the motor. A teflon-covered circular stirring bar was placed inside the beaker and the stirring rate was held constant for each group of assays.

Fluorimetry. Ethanol was quantified by catalysis with alcohol de-

hydrogenase using NADH as the indicator species. The fluorescence of NADH was measured with a Varian SF-330 spectrofluorimeter at excitation and emission wavelengths of 340 and 474 nm, respectively. The cell compartment of the fluorimeter was modified slightly to accommodate a stirring motor.

Absorbance. Creatine kinase was assayed by coupling the creatine kinase reaction to hexokinase and glucose-6-phosphate dehydrogenase systems and measuring the absorbance of NADPH at 340 nm [7] with a Cary 118 spectrophotometer.

Data handling. The transducer output from each instrument was monitored through an active filter and variable gain amplifier. The amplifier was constructed from a TL-081 operational amplifier configured as a noninverting amplifier with an 8.2 kohm feedback resistor and a 0—2 kohm variable input trimming resistor. The trimming potentiometer was adjusted to make the maximum transducer response yield a 10-V output. The amplifier output was connected to a 12-bit analog-to-digital converter (ADC).

An Apple II computer was interfaced to the ADC through parallel ports on a 6522 versatile interface adapter (John Bell Engineering, San Carlos, CA). The adapter includes addressable timers which were programmed to set interrupts every 10 ms. The data-acquisition rate was programmed to be a multiple of the 10-ms interrupt rate and was controlled by selection of the desired rate at the start of the program.

The high-resolution-graphics mode of the computer was used to display data on the monitor screen. Data files were created and stored on 5.25-in. Verbatim floppy disks.

Time-dependent indicator responses, I_t, were calculated by extrapolating rate data over time increments, Δt. These were stored as an array in computer memory. At the completion of a run, I_t values were numerically integrated over a fixed time interval using Simpson's rule, and integrals were transferred to disk storage. Difference integrals were calculated from the integral of the difference between I_t and the initial value, I_0. Derivatives were estimated using a time-averaging least-squares procedure. Maxima, minima, and inflections were located by noting the time when appropriate derivatives were zero. At the completion of a specified number of runs, differences between integrals were plotted as functions of substrate concentration or enzyme activity and transferred to disk storage.

Procedures

Calculated response curves. Response curves which exhibit maxima, minima or inflection points were generated from kinetic data [8—11] using computer programs. Families of curves were generated by selecting initial substrate concentrations and varying the initial enzyme activity, C_E°, or by holding C_E° constant and changing the initial substrate concentration, C_S°.

Changes in the concentration of the indicator substance, ΔC_I, were

approximated from the rate equation at increments of Δt. Time-dependent values of ΔC_I were summed to obtain the concentrations of indicator species, $C_I^t = C_I^0 + \Sigma\Delta C_I$, and the indicator response was calculated from C_I^t.

For glucose oxidase, the reaction rate was evaluated using the expression [8]

$$-d(C_{O_2}/dt)_E = C_E^t(1/k_1C_G + 1/k_2 + 1/k_3C_{O_2} + 1/k_4)^{-1} \quad (1)$$

where the k values are kinetic constants, C_G is glucose concentration, C_{O_2} is oxygen concentration, and C_E^t is the concentration of glucose oxidase at time t. The overall rate of change of oxygen concentration is given by $dC_{O_2}/dt = (dC_{O_2}/dt)_D - (dC_{O_2}/dt)_E$, where E indicates a rate of depletion of oxygen by the enzymatic reaction and the subscript D indicates a rate of diffusion of oxygen into the solution from the surrounding environment [9]. The rate of diffusion is given by $(dC_{O_2}/dt)_D = k[(C_{O_2}^{eq} - C_{O_2}^t)/C_{O_2}^{eq}]$, where k is an empirically determined constant [9] and $C_{O_2}^{eq}$ is the oxygen concentration when the solution is equilibrated with air.

Response vs. time curves were generated for lactate dehydrogenase from published kinetic data [10]. A computer program calculated reaction rates from published kinetic constants, maximum forward and reverse reaction velocities, and assumed initial concentrations of lactate dehydrogenase, lactate, NAD, pyruvate, and NADH [6, 10].

The fluorescence signal was calculated from the relation

$$(E_f)_t = k'(10^{-\epsilon b_1 C_Q^t})(1 - 10^{-\epsilon\Delta b C_Q^t})(10^{-\epsilon' b C_Q^t/2}) \quad (2)$$

where ϵ' is the molar absorptivity at the emission wavelength, ϵ is the molar absorptivity at the excitation wavelength, the b values are cell pathlength parameters, and k' is a collection of variables independent of analyte concentration.

The program calculated the time-dependent concentration of each species at each iteration by approximating ΔC_{NADH} and adding ΔC_{NADH} to $C_{pyruvate}^t$ and C_{NADH}^t, and subtracting ΔC_{NADH} from $C_{lactate}^t$ and C_{NAD}^t.

Theoretical response curves modeling creatine kinase assays were generated from published kinetic data [8, 11, 12] using three equations in a consecutive coupled reaction. A computer program computed the rate for the first step of the reaction (ADP + creatine phosphate $\overleftrightarrow{CK}$ creatine + ATP) [11] and the rate of the second step (ATP + glucose $\overleftrightarrow{HK}$ G6P + ADP) [12]. The rate of the final step of the reaction (G6P + NADP $\overleftrightarrow{G6PD}$ 6-phosphocluconate + NADPH), was approximated using assumed initial concentrations of glucose-6-phosphate, NADP, 6-phosphogluconate and NADPH. Kinetic parameters for lactate dehydrogenase were used to approximate catalysis by glucose-6-phosphate dehydrogenase because the reactions are similar [13].

The program calculated time-dependent concentrations of each species, including the indicator species, NADPH, by approximating changes in concentrations during incremental time intervals, Δt, and summing the changes over the iterations.

Ethanol, glucose and creatine kinase. Ethanol, glucose and creatine kinase were quantified by using differences between integrals. The difference integral for glucose was calculated by subtracting the integral of the time-dependent current from oxygen, $i^t_{O_2}$, from the integral for the initial oxygen current, $i^0_{O_2}$, found before the reaction was initiated. For ethanol and creatine kinase, the difference integral was equal to the integral of the response curve, because C^0_{NADH} or C^0_{NADPH} was negligible in all cases.

A 10^{-1} M solution of glucose was diluted sequentially in the range of 10^{-4} to 10^{-2} M with 0.1 M phosphate buffer and the pH was adjusted to 5.5. Solutions were allowed to stand overnight to achieve mutarotation. A solution of 5.4 mg ml^{-1} glucose oxidase was prepared in 0.1 M phosphate buffer (pH 7.3). Aliquots of glucose solution, 10.0 ml each, were placed in the 30-ml beaker and allowed to equilibrate with oxygen from the air. After equilibration, 100 μl of glucose oxidase solution was added and data acquisition was initiated. The sensor response was sampled every 250 ms for 1.5 min.

To quantify ethanol, a 10 g l^{-1} solution was prepared in 0.032 M pyrophosphate buffer and diluted sequentially in the concentration range 0.006—6 g l^{-1} and the pH was adjusted to 8.8. A NAD/alcohol dehydrogenase solution was prepared by dissolving 20 mg of alcohol dehydrogenase and 250 mg NAD in 10.0 ml of 0.1 M phosphate buffer and the pH was adjusted to 7.5. Aliquots of ethanol, 2.5 ml, were placed into a 1-cm^2 cell inside the spectrofluorimeter. The NAD/alcohol dehydrogenase solution, 100 μl, was added and the solution was stirred for 4 s prior to acquisition of fluorescence data. The fluorescence response was sampled every 500 ms for 3 min.

A creatine kinase solution was prepared by dissolving 9.4 mg of creatine kinase in 5.0 ml 0.05 M Tris buffer. The pH was adjusted to 7.3 and serial dilutions were made over three orders of magnitude. Creatine phosphate and reagents for auxiliary reactions were prepared by previously published procedures [7]. Creatine phosphate solution, 2.5 ml, and 100 μl of creatine kinase solution were mixed by gently swirling in a 10-ml beaker. After mixing, the content of the beaker was poured into the sample cell of the spectrophotometer. Data acquisition was initiated 15 s after addition of creatine kinase and was continued for 7 min at 500-ms intervals.

RESULTS AND DISCUSSION

Activity of lactate dehydrogenase

Figure 1 illustrates calculated fluorescence signal vs. time curves computed for different lactate dehydrogenase concentrations and constant initial concentrations of lactate and NAD. Maxima are observed for NADH concentrations greater than 2×10^{-4} M [14]. For lactate dehydrogenase (LDH) concentrations less than 2.2×10^{-8} M, there is no maximum within the 60-s integration period. Three characteristics are demonstrated by the curves. At higher concentrations of LDH, the maximum occurs earlier in the reaction;

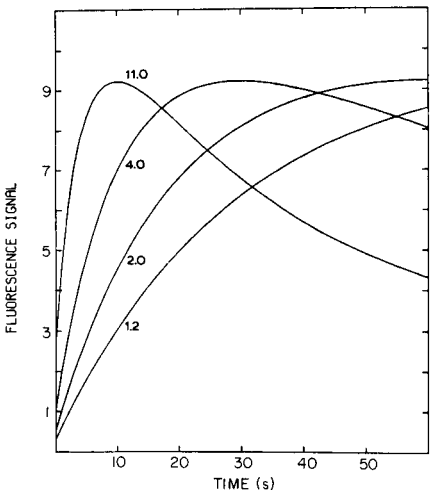

Fig. 1. Computer-generated fluorescence response curves at lactate dehydrogenase concentrations of 1.2, 2.0, 4.0 and 11.0 × 10^{-8} M and fixed NAD and lactate concentration.

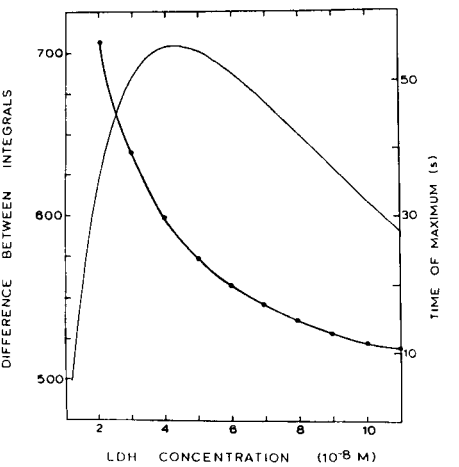

Fig. 2. Differences between integrals (—) and time at which maximum occurs (•) vs. LDH concentration for computer-generated response curves.

the heights of all the maxima are the same, and the positive and negative slopes increase with increasing LDH concentration. Thus, the difference between integrals may decrease with increasing LDH concentration and the time at which the maximum occurs can be used to determine if the data are for low or high LDH activities.

Figure 2 shows differences between integrals for calculated response curves for LDH concentrations ranging from 1.2 × 10^{-8} M to 1.1 × 10^{-7} M as well as the times at which maxima occur for different LDH concentrations. The plot of the difference integrals vs. LDH concentration passes through a maximum near 4.2 × 10^{-8} M LDH. The fluorescence response curve for this concentration of LDH exhibits a maximum at 29 s. Although two different concentrations may yield the same value for the difference between integrals, it is possible to use the time at which the maximum in the response curve occurs to determine whether the LDH concentration is below or above 4.2 × 10^{-8} M, and then to use the calibration curve (Fig. 2) to obtain the concentration.

Determination of ethanol

Figure 3 shows difference integrals as a function of ethanol concentration for the reaction described above. The maximum at 56 s in Fig. 3 corresponds to an ethanol concentration of 60 mg ml^{-1}. As was illustrated above for LDH, the times at which maxima occur in response curves can be used to differentiate between low and high values of alcohol concentrations that

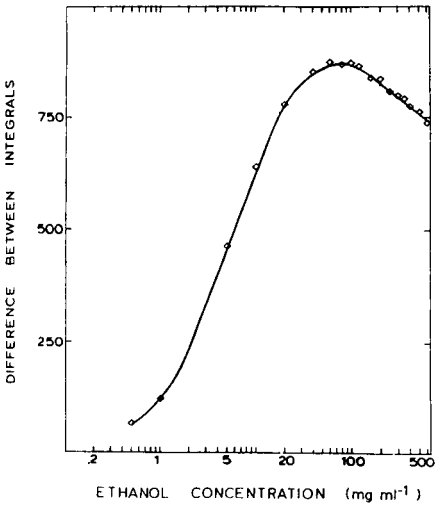

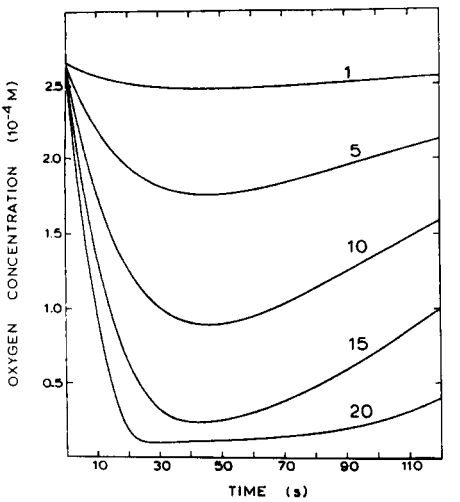

Fig. 3. Semilog plot of differences between integrals of fluorescence response vs. ethanol concentration.

Fig. 4. Computer-generated oxygen vs. time curves at glucose concentrations of 1, 5, 10, 15 and 20 × 10^{-4} M and fixed glucose oxidase activity.

have the same values for differences between integrals. Relative standard deviations for triplicate runs at different ethanol concentrations from 5 to 150 mg ml^{-1} were in the range of 0.5%.

Determination of glucose

Figure 4 shows calculated response curves for different glucose concentrations and fixed glucose oxidase activity. A minimum occurs at the point at which the rate of diffusion of oxygen into the system equals the rate of depletion of oxygen by the reaction [9]. The decrease in the reaction rate with time is due to a reduction in glucose concentration and inhibition of glucose oxidase by peroxide formed in the reaction [6].

Figures 5 and 6 show difference integrals as functions of glucose concentration. Figure 5 represents the difference integrals from calculated response curves and Fig. 6 shows experimental results. Although the differences between integrals are not very useful for glucose concentrations above 2 × 10^{-3} M, the times at which minima occur (Fig. 5) can be used to estimate glucose concentration for carefully controlled conditions. Relative standard deviations for triplicate runs for different glucose concentrations between 5 and 25 × 10^{-4} M were in the range of 1%.

Determination of creatine kinase

Figure 7 shows C_{NADPH} vs. time curves computed from kinetic data [9—11] with different concentrations of creatine kinase (CK) and fixed initial concentrations of all other components. At higher concentrations of

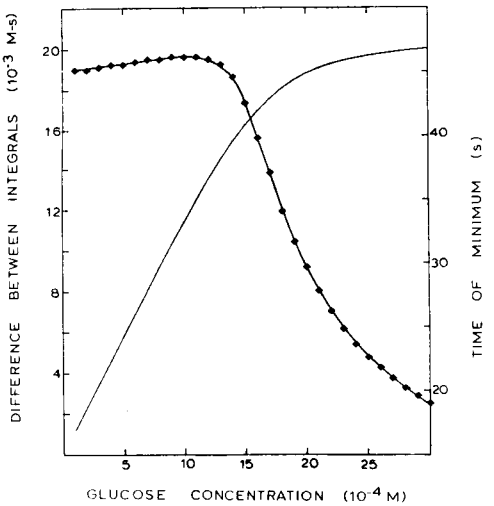

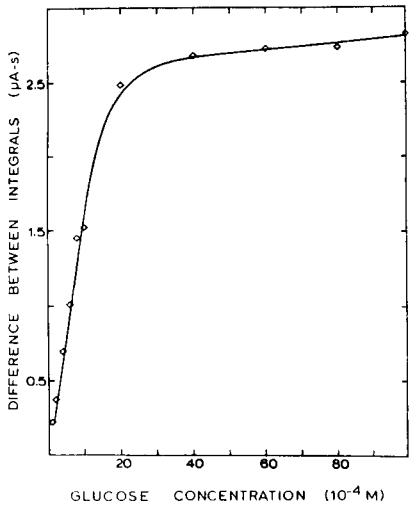

Fig. 5. Differences between integrals (—) and time of minimum (•) vs. glucose concentration for computer-generated curves.

Fig. 6. Experimentally determined difference integrals as functions of glucose concentration.

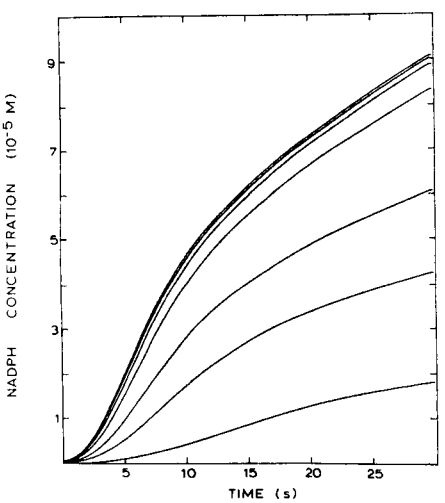

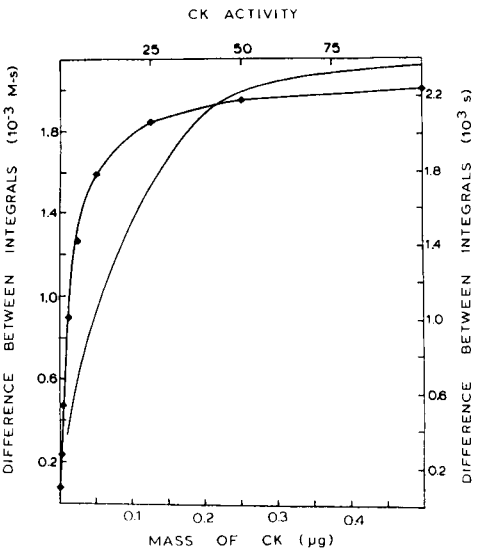

Fig. 7. Computer-generated plots of NADPH as functions of time. Starting from the lower curve, the amounts of creatine kinase are 0.01, 0.05, 0.1, 0.2, 0.3, 0.4 and 0.5 μg.

Fig. 8. Differences between integrals for computer-generated (—) and experimental (•) response curves. Computer-generated curves (—) are based on mass of enzyme, and experimental (•) curves are based on activity (IU ml^{-1}).

the kinase, intermediates are produced at increased rates, thus decreasing the lag phase and increasing the rate at which NADPH is formed. Also, the inflection points are more distinct and occur at shorter times for higher activities of creative kinase. Figure 8 shows difference integrals as functions of concentration of creatine kinase from calculated and experimental response curves. For the useful range of the calibration curves (0.01—0.2 μg CK), the relative standard deviations for triplicate runs are in the range of 2%.

Results presented here indicate that the proposed method is applicable to a variety of nonideal kinetic responses and that supplementary data can be used to help resolve situations in which two different concentrations may yield the same difference between integrals.

This work was funded in part by the American Chemical Society Petroleum Research Foundation Grant No. 13933G3, and in part by NIH Biomedical Research Grant No. PR07079.

REFERENCES

1 H. L. Pardue, Clin. Chem., 23 (1977) 2189.
2 H. A. Mottola and H. B. Mark, Jr., Anal. Chem., 52 (1980) 31R.
3 J. D. Ingle, Jr. and S. R. Crouch, Anal. Chem., 42 (1970) 1055.
4 G. P. Hicks, A. A. Eggert and E. C. Toren, Jr., Anal. Chem., 42 (1970) 729.
5 E. M. Cordos, S. R. Crouch and H. V. Malmstadt, Anal. Chem., 40 (1968) 1812.
6 L. C. Thomas and G. D. Christian, Anal. Chim. Acta, 77 (1975) 153.
7 N. W. Tietz, (Ed.), Fundamentals of Clinical Chemistry, W. B. Saunderson Company, Philadelphia, PA, 1970, p. 468.
8 F. R. Duke, M. Weber, D. S. Page and J. Luthy, J. Am. Chem. Soc., 91 (1969) 3904.
9 L. C. Thomas and G. D. Christian, Anal. Chim. Acta, 89 (1977) 83.
10 V. Bloomfield, L. Peller and R. A. Alberty, J. Am. Chem. Soc., 84 (1962) 4367.
11 J. F. Morrison and E. James, Biochem. J., 97 (1965) 37; J. Chem. Soc., 84 (1962) 4367, 4375.
12 G. G. Hammes and D. Kochavi, J. Am. Chem. Soc., 84 (1962) 2069.
13 C. Walter, Steady State Applications in Enzyme Kinetics, Ronald Press, New York, 1965.
14 H. R. Willard, L. L. Merritt, Jr., J. A. Dean and F. R. Settle, Jr., Instrumental Methods of Analysis, 6th edn., D. Van Nostrand, New York, 1981, p. 110.

Analytica Chimica Acta, 161 (1984) 101—108
Elsevier Science Publishers B.V., Amsterdam — Printed in The Netherlands

THERMOGRAVIMETRY OF METAL CHELATES OF 1,1,1-TRIFLUOROPENTANE-2,4-DIONE IN A FLOW OF HELIUM AND HELIUM CONTAINING LIGAND VAPOR

NORIO MATSUBARA and TOORU KUWAMOTO*
Department of Chemistry, Faculty of Science, Kyoto University, Kyoto 606 (Japan)
(Received 4th January 1984)

SUMMARY

Thermogravimetry of 22 metal chelates of 1,1,1-trifluoropentane-2,4-dione, H(tfa) in a flow of helium and helium containing H(tfa) vapor is described. Samples were placed in an inserted tube in the inlet port of a gas chromatograph and heated stepwise. The presence of H(tfa) vapor in the helium flow was very effective in suppressing thermal dissociation of hydrated tfa chelates, which decomposed in a helium flow but could be completely vaporized, after dehydration, in a flow of helium containing H(tfa) vapor. The relationship between the volatility and the structure of the tfa chelates is discussed. Results obtained by the proposed method and with a conventional thermobalance are compared.

The gas chromatography of volatile metal chelates has been examined extensively [1], as have the thermal properties of such chelates. Particular attention has been given to β-diketonates which exhibit high vapor pressure, but the problem of thermal dissociation of the chelates is usually troublesome. Other types of chelate, such as monothio-β-diketonates, tetradentate ketoaminates and dithiocarbamates, have also been investigated but problems then arise in practical analysis because the thio ligands and chelates are unstable in solution, and monothio-β-diketones and ketoaminates do not form stable chelates with tervalent or quadrivalent metals. Fujinaga et al. [2—5] proposed the use of a carrier gas containing ligand vapor in gas chromatography and achieved quantitative elution of some β-diketonates without thermal decomposition. It was also shown [6, 7] that thermograms of metal chelates could be obtained by using the injection chamber of a gas chromatograph instead of a thermobalance. This method is simple and practicable for obtaining thermograms in a flow of helium containing ligand vapor.

The present paper deals with the thermal characteristics of 22 metal chelates of 1,1,1-trifluoropentane-2,4-dione, H(tfa), in a flow of helium and helium containing H(tfa) vapor. An improved device for obtaining thermograms with a gas chromatograph is described.

EXPERIMENTAL

Reagents and preparation of chelates

Commercial 1,1,1-trifluoropentane-2,4-dione was purified by refluxing in the presence of disodium hydrogenphosphate, which was added to remove highly acidic impurities, and distilled at 107°C. Other chemicals were extra pure or guaranteed reagents and were used without further purification.

Preparation of tfa chelates. The following chelates were prepared: $Be(tfa)_2$, $Al(tfa)_3$, $Sc(tfa)_3$, $Fe(tfa)_3$, $Ni(tfa)_2 \cdot 2H_2O$, $Cu(tfa)_2$, $Ga(tfa)_3$, $Y(tfa)_3 \cdot 2H_2O$, $In(tfa)_3$, $Gd(tfa)_3 \cdot 2H_2O$, $Tb(tfa)_3 \cdot 2H_2O$, $Dy(tfa)_3 \cdot 2H_2O$, $Ho(tfa)_3 \cdot 2H_2O$, $Er(tfa)_3 \cdot 2H_2O$, $Tm(tfa)_3 \cdot 2H_2O$, $Yb(tfa)_3 \cdot 2H_2O$ and $Lu(tfa)_3 \cdot 2H_2O$. About 1 g of metal, oxide or salt was dissolved in water or acid, the acid used depending on the sample characteristics. For example, gallium metal and indium oxides were dissolved in hot concentrated nitric acid, scandium, yttrium and rare earth oxides in hot concentrated hydrochloric acid, and copper sulfate, beryllium nitrate, nickel nitrate, aluminium chloride and iron chloride in water. These solutions were neutralized with aqueous 1 M ammonia or, for nickel and copper solutions, with 1 M sodium hydroxide. The precipitated metal hydroxides were centrifuged and washed twice with distilled water. A small excess over the calculated amount of H(tfa) was added to the precipitate and the mixture was warmed to about 80° C. The supernatant liquid was removed by decantation, and the chelate was filtered off on a glass filter crucible and washed successively with water and hexane. The copper and nickel chelates were dissolved in diethyl ether, yttrium and heavy rare-earth chelates in diisopropyl ether, and the other chelates in benzene. The insoluble materials, if any, were removed by filtration and the chelates were recovered by evaporation of the organic solvent in a clean air stream. The other chelates studied were prepared by previously reported procedures [8—11]. The results of elemental analysis of these chelates (carbon-hydrogen, fluorine and metal) agreed well with the calculated values.

Apparatus and procedures

A Shimadzu Model GC-4B gas chromatograph with a glass insert in the injection port and equipped with a ligand vapor generator was used for measurements of the temperature dependency of the vaporization of the tfa chelates. The concentration of ligand vapor in the carrier gas was about 1.0% (v/v) and was kept constant by controlling the temperature in the thermostat. The pyrex sample tube (glass insert) was 3.5 mm i.d., 77.5 mm long and 0.5 mm in wall thickness.

For thermal measurements with the modified device, a definite amount (10.0 mg) of chelate was placed in the sample tube, and held in position with wads of quartz wool (Fig. 1). The precisely weighed sample tube was inserted into the injection port (5 mm bore) which was preheated at a fixed temperature, and the entrance of the injection port was tightly closed with a silicone rubber stopper. The carrier gas (helium or helium containing H(tfa) vapor)

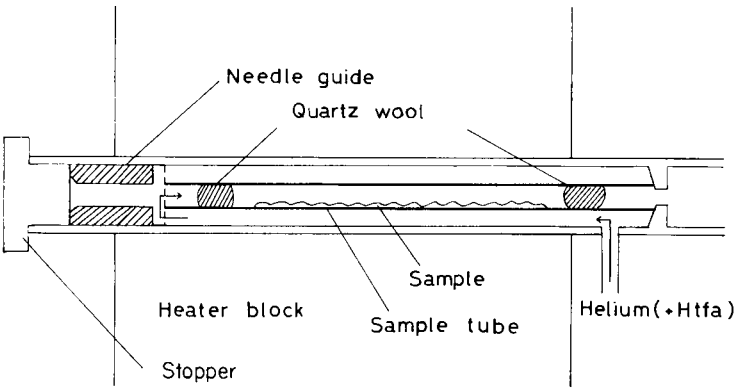

Fig. 1. Sample chamber.

was passed through the tube at a flow rate of 30 ml min^{-1}. The tube was kept at the chosen temperature for 10 min, removed from the injection chamber, cooled in a desiccator, and then weighed again. The temperature of the injection chamber was raised stepwise in 20°C increments, and the sample was reheated and weighed as before.

For thermogravimetry and differential thermal analysis, the instrument used was a Rigaku Model 8075. The temperature was calibrated by using the melting point of tin (231.9°C) as reference. The ligand vapor generator was used as necessary. Exactly 10.0 mg of sample was taken in an aluminium crucible and set in position in the thermobalance. After the carrier gas had been passed through at 80—150 ml min^{-1} in order to purge any air from the sample chamber, the flow rate was set at 20 ml min^{-1}, and the temperature was raised at a rate of 2.5°C min^{-1}.

RESULTS AND DISCUSSION

Classification of tfa chelates

As shown in Fig. 2, the tfa chelates can be classified into two categories according to the difference in their vaporization behaviors in helium and in helium containing H(tfa) vapor. In the first group are the chelates which are completely vaporized in both atmospheres: $Be(tfa)_2$, $Al(tfa)_3$, $Sc(tfa)_3$, $V(tfa)_3$, $VO(tfa)_2$, $Cr(tfa)_3$, $Fe(tfa)_3$, $Co(tfa)_3$, $Cu(tfa)_2$, $Ga(tfa)_3$, $In(tfa)_3$. For these chelates, the thermogravimetric curves in helium and helium containing H(tfa) vapor overlap. All these chelates are anhydrous and their coordination sites are saturated with tfa ligand.

The second group comprises those chelates which are decomposed in helium but are completely vaporized in helium containing H(tfa) vapor: $Co(tfa)_2 \cdot 2H_2O$, $Ni(tfa)_2 \cdot 2H_2O$, $Y(tfa)_3 \cdot 2H_2O$, $Dy(tfa)_3 \cdot 2H_2O$, $Ho(tfa)_3 \cdot 2H_2O$, $Er(tfa)_3 \cdot 2H_2O$, $Tm(tfa)_3 \cdot 2H_2O$, $Yb(tfa)_3 \cdot 2H_2O$, $Lu(tfa)_3 \cdot 2H_2O$. All these chelates have water of coordination.

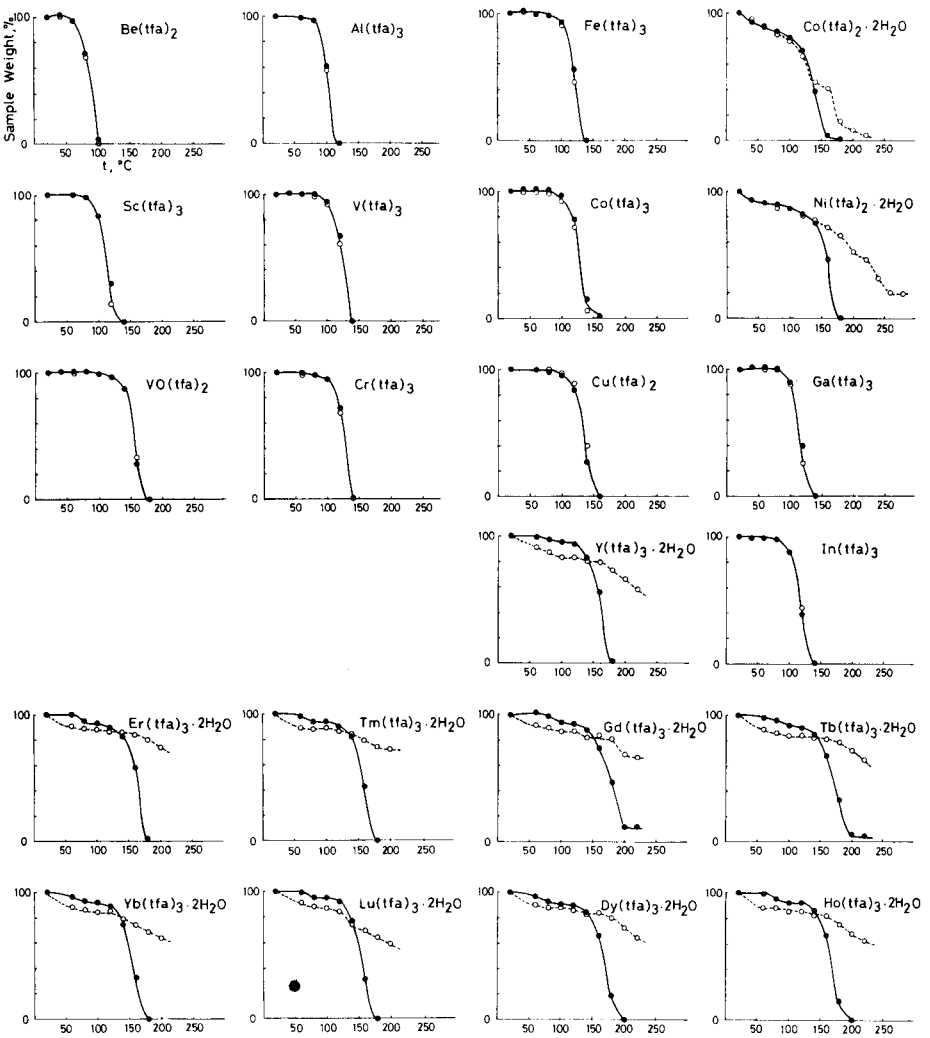

Fig. 2. Thermogravimetric curves of 1,1,1-trifluoropentane-2,4-dionates with the tube device in the injection port of the chromatograph: (○) in helium; (●) in helium containing H(tfa) vapor.

Volatility of tfa chelates

The order of volatility of tfa chelates of the first category is decided by the temperature of complete vaporization: $Be(tfa)_2$ (100°C) > $Al(tfa)_3$ (120°C) > $Sc(tfa)_3$, $V(tfa)_3$, $Cr(tfa)_3$, $Fe(tfa)_3$, $Ga(tfa)_3$, $In(tfa)_3$ (140°C) > $Co(tfa)_3$, $Cu(tfa)_2$ (160°C) > $VO(tfa)_2$ (180°C). In previous reports [12], the volatility of tfa chelates has generally been discussed according to the difference in the characteristics of the ligands, but it is better to consider the differences in the structure of the chelates. Berg and Truemper [13] investi-

gated the relationship between the structure of β-diketonates and their vapor pressure or heat of sublimation, but it was impossible to find a clear correlation for a series of β-diketonates. It was later pointed out [14, 15] that this result was caused by the decomposition of the chelates which occurred during the actual measurement. As is well known, $Be(tfa)_2$ is tetrahedral, $Cu(tfa)_2$ is square planar, $VO(tfa)_2$ is tetragonal pyramidal, and the other tfa chelates in the first category are octahedral. The most decisive factor of volatility is the structure of the chelates. The order of volatility is as follows: tetrahedral > octahedral > square planar > tetragonal pyramidal. The more sphere-like chelates, such as tetrahedral and octahedral chelates, are more volatile than the other chelates. The nine octahedral chelates have similar volatility. Square planar $Cu(tfa)_2$ which has a more closely-packed structure and $VO(tfa)_2$ which has a polar V=O bond are less volatile. These facts indicate that the molecular interaction in the solid state establishes the volatility of the chelate. Similar results were observed [16] in a study of platinum group metal tfa chelates; $Pd(tfa)_2$ and $Pt(tfa)_2$ are less volatile than $Ru(tfa)_3$, $Rh(tfa)_3$ and $Ir(tfa)_3$.

The volatility of hydrated tfa chelates cannot be evaluated in a helium atmosphere because thermal decomposition accompanies the vaporization process, but in helium containing H(tfa) vapor, thermal decomposition was either not observed or much depressed, and the volatility of the chelates became distinct. The volatility of heavy rare earth chelates increased with a decrease in the ionic radius of the central ion. The $Y(tfa)_3 \cdot 2H_2O$ chelate, which has an ionic radius equivalent to the heavy rare earth chelates, showed the same volatility as $Er(tfa)_3 \cdot 2H_2O$. In contrast, $Sc(tfa)_3$, which has no coordinated water, was much more volatile than heavy rare earth chelates and was completely vaporized even in helium carrier gas. All of the hydrated chelates used were less volatile than the anhydrous chelates, except for $Co(tfa)_2 \cdot 2H_2O$ which was more volatile than $VO(tfa)_2$. This seems to be because hydrated tfa chelates are easily polymerized on heating [17, 18].

Dehydration of the coordinated water in tfa chelates

Figure 2 shows that anhydrous tfa chelates were vaporized in one step with increasing temperature, whereas heating of the hydrated tfa chelates produced two steps corresponding to dehydration and vaporization of anhydrous chelate. As shown in Table 1, the percentage weight loss at the first stage was usually close to the value calculated from elemental analysis when the chelates were heated in helium containing H(tfa) vapor. However, the initial weight losses for the heavy rare earth Ln(tfa) chelates were larger than the expected values as a result of partial dissociation of the chelates when they were heated in helium [19, 20]

$$Ln(tfa)_3 \cdot 2H_2O \rightarrow Ln(tfa)_2(OH) \cdot H_2O + H(tfa)$$

TABLE 1

The percentage weight loss at the first stage and its temperature range (cf. Fig. 2)[a]

Chelate	In helium		In helium with H(tfa) vapor		Calcd. Wt. loss (%)
	Wt. loss (%)	Temp. (°C)	Wt. loss (%)	Temp. (°C)	
$Co(tfa)_2 \cdot 2H_2O$	10	60	11	60	9.0
$Ni(tfa)_2 \cdot 2H_2O$	13—14	80—100	9—10	60—80	9.0
$Y(tfa)_3 \cdot 2H_2O$	17	100—120	5	100	6.2
$Gd(tfa)_3 \cdot 2H_2O$	13	100—120	6—7	100—120	5.5
$Tb(tfa)_3 \cdot 2H_2O$	16—18	100—160	8—10	100—120	5.5
$Dy(tfa)_3 \cdot 2H_2O$	12—14	80—120	9—10	100—120	5.5
$Ho(tfa)_3 \cdot 2H_2O$	13—15	80—120	7—8	100—120	5.5
$Er(tfa)_3 \cdot 2H_2O$	12	100	7	100	5.4
$Tm(tfa)_3 \cdot 2H_2O$	11—12	60—100	6	80—100	5.4
$Yb(tfa)_3 \cdot 2H_2O$	14—16	80—120	7—8	80—100	5.4
$Lu(tfa)_3 \cdot 2H_2O$	12—13	80—100	5	80—100	5.4

[a]Results obtained with the tube insert device.

Comparison of the results obtained with the tube insert device and a conventional thermobalance

The order of the volatility of the anhydrous tfa chelates agreed with that of a conventional thermobalance (Table 2). However, the temperature of complete vaporization as measured by the thermobalance was higher than that measured when the tube insert device was used even when the flow rate in the thermobalance was raised to 80 ml min^{-1}. It is considered that the deficiency of the vaporization of chelates depends on the size and shape of the aluminum cup used.

Thermogravimetric curves of hydrated tfa chelates have been reported previously for divalent metals of the first transition series [21] and rare

TABLE 2

The temperatures of complete vaporization of tfa chelates obtained with the tube insert device and a thermobalance

Chelate	Temp. of total vaporization (°C)		Chelate	Temp. of total vaporization (°C)	
	Device	Thermobalance		Device	Thermobalance
$Be(tfa)_2$	100	132	$Fe(tfa)_3$	140	172
$Al(tfa)_3$	120	156—159	$Co(tfa)_3$	160	175—179
$Sc(tfa)_3$	140	170	$Cu(tfa)_2$	160	182
$V(tfa)_3$	140	172	$Ga(tfa)_3$	140	167
$VO(tfa)_2$	180	198	$In(tfa)_3$	140	167—169
$Cr(tfa)_3$	140	172			

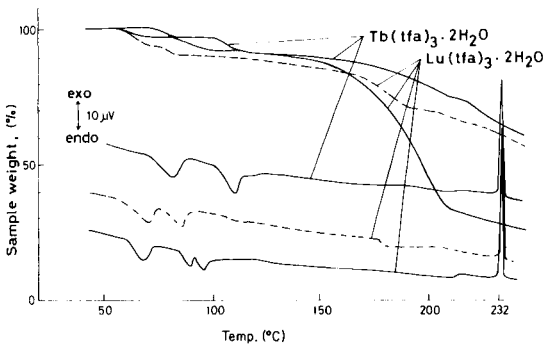

Fig. 3. Thermogravimetric curves and differential thermal analysis curves of $Tb(tfa)_3 \cdot 2H_2O$ and $Lu(tfa)_3 \cdot 2H_2O$ obtained with a thermobalance: (---) in helium; (—) in helium containing H(tfa) vapor.

earth chelates in air [22] and in nitrogen [23]. However, the thermal behavior of tfa chelates is difficult to interpret because of dehydration, polymerization and decomposition reactions. In helium containing H(tfa) vapor, the thermograms obtained with the proposed insert device were remarkably improved because of the suppression of thermal dissociation, but the addition of H(tfa) vapor for the usual thermobalance had little effect because the chelates were not entirely in contact with the ligand vapor atmosphere in the small crucible (Fig. 3).

The authors thank Mr. Masamichi Furukawa of the Government Industrial Research Institute, Nagoya, for his cooperation in the measurements with the thermobalance.

REFERENCES

1 P. C. Uden and D. E. Henderson, Analyst (London), 102 (1977) 889.
2 T. Fujinaga, T. Kuwamoto and S. Murai, Talanta, 18 (1971) 429.
3 T. Fujinaga, T. Kuwamoto and S. Murai, Anal. Chim. Acta, 71 (1974) 141.
4 T. Fujinaga, T. Kuwamoto and T. Kimoto, Talanta, 23 (1976) 753.
5 T. Fujinaga, T. Kuwamoto, K. Sugiura and N. Matsubara, Anal. Chim. Acta, 136 (1982) 175.
6 T. Fujinaga, T. Kuwamoto, K. Sugiura, S. Ichiki and N. Matsubara, Bunseki Kagaku, 29 (1980) 796.
7 T. Fujinaga, T. Kuwamoto, K. Sugiura and S. Ichiki, Talanta, 28 (1981) 295.
8 W. C. Fernelius and J. E. Blanch, Inorg. Synth., 5 (1957) 130.
9 B. E. Bryant and W. C. Fernelius, Inorg. Synth., 5 (1957) 188.
10 J. B. Ellern and R. O. Ragsdale, Inorg. Synth., 11 (1968) 82.
11 S. Dilli and E. Patsalides, Aust. J. Chem., 29 (1976) 2369, 2389.
12 R. C. Mehrotra, R. Bohra and D. P. Gaur, Metal β-Diketonates and Allied Derivatives, Academic Press, London, 1978, p. 58.
13 E. W. Berg and J. T. Truemper, J. Phys. Chem., 64 (1960) 487; Anal. Chim. Acta, 32 (1965) 245.

14 W. R. Wolf, R. E. Sievers and G. H. Brown, Inorg. Chem., 11 (1972) 1995.
15 I. K. Igumenov, Yu. V. Chumachenko and Z. V. Zemskov, Sov. J. Coord. Chem., 5 (1979) 25.
16 K. Sugiura, Bunseki Kagaku, 31 (1982) 197.
17 G. J. Bullen, R. Mason and P. Pauling, Inorg. Chem., 4 (1965) 456.
18 F. A. Cotton and R. C. Elder, Inorg. Chem., 4 (1965) 1145.
19 R. G. Charles and A. Perotto, J. Inorg. Nucl. Chem., 26 (1964) 373.
20 J. K. Przystal, W. G. Bos and I. B. Liss, J. Inorg. Nucl. Chem., 33 (1971) 679.
21 M. Z. Gurevich, T. M. Sas, V. V. Zelentsov, B. D. Stepin and N. E. Mazepova, Russ. J. Inorg. Chem., 20 (1975) 250.
22 M. Z. Gurevich, T. M. Sas, B. D. Stepin and N. E. Levedeva, Russ. J. Inorg. Chem., 16 (1971) 1119.
23 J. W. Mitchell and C. V. Banks, Anal. Chim. Acta, 57 (1971) 415.

Analytica Chimica Acta, 161 (1984) 109—114
Elsevier Science Publishers B.V., Amsterdam — Printed in The Netherlands

IMMOBILIZED *anti*-α-FETOPROTEIN DISCS PREPARED BY RADIATION POLYMERIZATION FOR ENZYME IMMUNOASSAY

MINORU KUMAKURA* and ISAO KAETSU

Takasaki Radiation Chemistry Research Establishment, Japan Atomic Energy Research Institute, Takasaki, Gunma (Japan)

MIEKO SUZUKI and SHOICHI ADACHI

Japan Immunoresearch Laboratories Co. Ltd., Takasaki, Gunma (Japan)

KENICHI IMAGAWAWA

Otsuka Pharmaceutical Co., Ltd., Otsuka Assay Laboratories, Kawauchi-cho, Tokushima (Japan)

(Received 20th December 1983)

SUMMARY

Immobilized *anti*-α-fetoprotein discs for enzyme immunoassay of α-fetoprotein were prepared by radiation polymerization of hydroxyethylmethacrylate at −78°C. The activity (determined by absorbance at 492 nm) of the discs varied with monomer concentration and disc thickness, the optimum values being 200—400 g l^{-1} and 10—30 μm, respectively. The discs have a porous polymer matrix, are flexible, and can be dried and stored for long periods. The correlation coefficient for α-fetoprotein concentration determined in sera by radioimmunoassay and by enzyme immunoassay with the discs was high (0.97). The recovery of α-fetoprotein added to serum was 99.0—105%.

Diagnostic tests requiring high sensitivity often involve immunochemical methods such as radioimmunoassay or enzyme immunoassay [1—4]. Recently, various assay kits containing immunoreagents have been developed. In general, diagnostic kit assays are done with immunoreagents in which antibodies or antigens are coated or immobilized on the surface of various carriers. The carrier may be beads, tubes or plates. In most coating methods only a crude mixture of antigens is used [4]. For these, the only practical way of determining the correct amount needed for coating is to carry out "checker-board" titrations against positive and negative sera. The antigen dilution that gives the best discrimination between the positive and negative sera is used in subsequent tests. Where pure antigens are available, absolute measurements of the optimum coating can be determined and used for later batches of antigen. Similarly, for antibody coating of plates, if a specific antibody is used, an absolute, measured quantity can be used each time. However, antibodies or antigens coated physically on plates frequently leak from the plate during assay. Immunoreagents in which antigens or antibodies

0003-2670/84/$03.00

are covalently bound have been used to prevent leakage. Glutaraldehyde and silane derivatives, for example, have been used as chemical binding reagents, but they require long binding times and an excess of antigens or antibodies in order to bind sufficient antigens or antibodies to the carrier.

Immobilization methods have been developed for biological substances such as enzymes [5] and microbial cells [6] by using radiation polymerization at low temperatures. In this paper, immobilized antibody discs are prepared as thin films by this method and their performance studied. *Anti*-α-fetoprotein was used as the antibody. Enzyme immunoassays and radioimmunoassays for α-fetoprotein (AFP) have been studied by many workers [7—11]. However, immunoreagents such as those used in this study have not previously been used for AFP determinations.

EXPERIMENTAL

Reagents and apparatus

Anti-sera to α-fetoprotein (*anti*-AFP) were produced in rabbits by injecting an emulsion of human AFP with an equal volume of complete Freund's adjuvant. Human AFP, obtained from the plasma of a patient with primary hepatoma, was purified by affinity chromatography on an *anti*-AFP Sepharose 4B column (Pharmacia Japan, Tokyo), followed by gel-filtration on a Sephacryl S-300 column (Pharmacia Japan, Tokyo). To prepare peroxidase-labeled *anti*-AFP, *anti*-AFP serum was purified by ammonium sulfate fractionation, followed by ion-exchange chromatography on diethylaminoethylcellulose. The purified immunoglobulin fraction was coupled with peroxidase by the method of Wilson and Nakane [12]. Standard human AFP was obtained from Dinabott Radioisotope Laboratories, Tokyo. The buffer solution was phosphate-buffered saline, 1×10^{-3} mol l^{-1}, pH 7.2. Hydroxyethylmethacrylate (Mitsubishi Gas Chemical Co., Tokyo) was used as the monomer in the immobilization process.

Irradiation with γ-rays from cobalt-60 was done at the Japan Atomic Energy Research Institute. A cryostat (Model FE-FCS; Bright Institute Co., England) was used when the immobilized *anti*-AFP was sliced. The absorbance of the sample in the enzyme immunoassay was measured with a double-beam spectrophotometer (Model UV-140; Shimadzu Scientific Instruments, Tokyo).

Procedures

Immobilization of anti-*AFP*. *Anti*-AFP dissolved in the buffer solution was mixed with the monomer, poured into a glass tube (20 × 0.8 cm diameter), and quickly shaken. Without delay, the contents of the tube were frozen at −78°C and irradiated (1 MR) with γ-rays for 1 h. After irradiation, the *anti*-AFP immobilized in the polymer formed was removed from the tube and sliced into thin discs (20 μm thick, 0.8 cm diameter) at low temperature in the cryostat. The discs were immersed in the buffer solution at 4°C

for 10 min, and dried with a lyophilizer (Kyowa Vacuum Engineering Co., Tokyo).

Enzyme immunoassay. One immobilized *anti*-AFP disc was placed in a test tube containing 100 μl of serum sample or standard AFP solution, and incubated at room temperature for 1 h. After incubation, the solution was removed, the *anti*-AFP disc was washed thrice with the buffer solution, and 50 μl of peroxidase-labeled *anti*-AFP and 100 μl of the buffer solution was added to the tube, which was incubated at 37°C for 1 h. The *anti*-AFP disc was again washed thrice with the buffer solution to remove the unreacted peroxidase-labeled *anti*-AFP. The enzyme reaction was done with 200 μl of a solution of hydrogen peroxide (0.3 g l^{-1}) and *o*-phenylenediamine (3 g l^{-1}) at room temperature for 30 min and terminated by adding 200 μl of 1 M hydrochloric acid. The absorbance of the solution was measured at 492 nm, to measure the peroxidase activity.

Radioimmunoassay. For comparison, AFP in patients' sera was also determined with a commercial radioimmunoassay kit (Otsuka Pharmaceutical Co., Kawauchi-cho, Tokushima) involving the use of iodine-125.

Pore diameter. The average diameter of the pores in the polymeric disc was measured with a scanning electron microscope (Model JSM-03, Japan Electron Optics Laboratory Co., Tokyo).

RESULTS AND DISCUSSION

Effect of monomer concentration and disc thickness on activity

Because the properties of the immobilized *anti*-AFP disc obtained by radiation polymerization might vary with the immobilization conditions, the relation between immobilization conditions and activity (absorbance at 492 nm) was studied. The effect of monomer concentration on absorbance and average pore diameter is shown in Fig. 1. As the monomer concentration increased, the absorbance increased to a maximum, and then decreased. The optimum monomer concentration for immobilization was 200—400 g l^{-1}.

At lower monomer concentrations, some antibody leaked from the porous polymer matrix. The matrix had a soft, sponge-like, porous structure in which *anti*-AFP was trapped on the surface (Fig. 2). The formation of the porous structure occurred because, before irradiation, most of the water in the solution containing the antibody and monomer had frozen, and a eutectic mixture, consisting mainly of monomer with a small amount of water, had been supercooled. The monomer phase, a suspension of ice in supercooled monomer, acts as the dispersion medium. Thus, by irradiating this cooled system, the monomer and ice phases are converted to polymer and pore, respectively.

The porous structure of the polymer matrix was affected by monomer concentration. The average pore diameter decreased with increasing monomer concentration, as shown in Fig. 1. The pore diameter at low monomer concentrations ($<$100 g l^{-1}) was about 3 μm. At high monomer concentra-

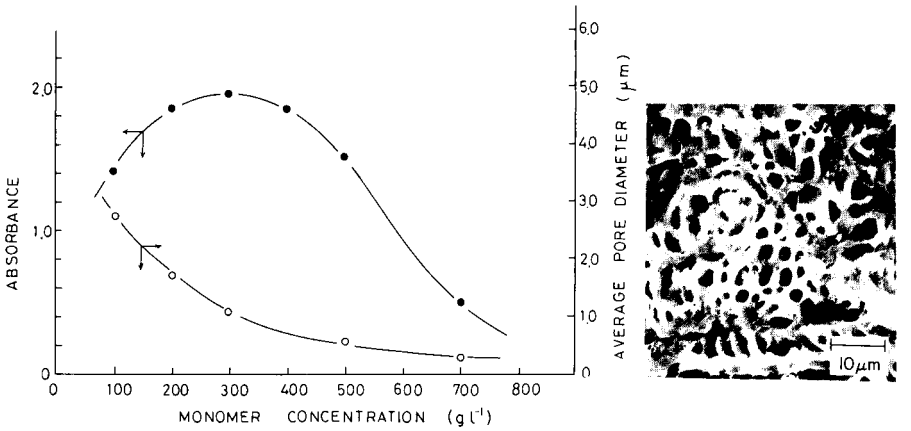

Fig. 1. Effect of monomer concentration on (○) pore size; (●) absorbance at 492 nm (20-μm thick disc, 50 ng ml^{-1} AFP).

Fig. 2. Scanning electron micrograph of the surface of an immobilized *anti*-AFP disc (300 g l^{-1} monomer, 20-μm thick disc).

tions, >700 g l^{-1}, the pore diameter was <1.0 μm and the pore structure became discontinuous because of the lower ice content of the system. In such a matrix, the amount of *anti*-AFP trapped in the matrix, and thus less available for AFP binding, increased. Therefore, the activity at high monomer concentrations was decreased.

The relation between absorbance and the thickness of the immobilized *anti*-AFP disc is shown in Fig. 3. The absorbance increased with increasing thickness to a maximum at 10—30 μm and then decreased. The discs were flexible, owing to the swelling of the polymer matrix in the buffer solution, and were not destroyed by repeated operations of washing and reaction in the assay.

Analytical performance

A typical calibration graph for enzyme immunoassay with immobilized *anti*-AFP discs is shown in Fig. 4. The slope is large, e.g., the absorbance at 10 ng ml^{-1} AFP is 0.4. Because the boundary value of AFP in sera from normal (healthy) and abnormal (primary liver cancer) is 10—20 ng ml^{-1}, immobilized *anti*-AFP discs can be used for the enzyme immunoassay of AFP.

When discs prepared at the optimum monomer concentration and disc thickness were used, the minimum sample volume was 20 μl, and the minimum detectable concentration of AFP in serum was 1.0 ng ml^{-1}. To assess the within-assay precision of the procedure three standard samples (18, 32 and 180 ng ml^{-1}) were assayed 10 times each. The relative standard deviations (r.s.d.) were 6.5, 5.2 and 4.5%, respectively. Assay of the same samples

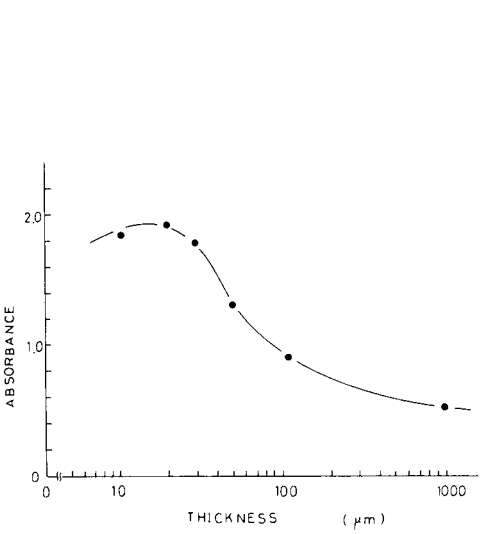

Fig. 3. Effect of disc thickness on absorbance (300 g l^{-1} monomer, 50 ng ml^{-1} AFP).

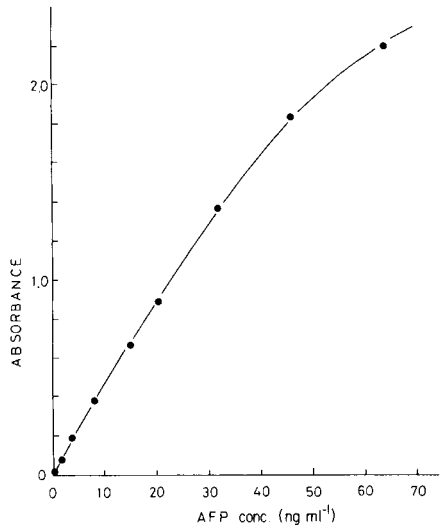

Fig. 4. Calibration graph for enzyme immunoassay of AFP with immobilized *anti*-AFP (disc as in Fig. 2).

on each of seven different days gave between-assay r.s.d.'s of 7.0, 5.6 and 4.5%, respectively. Known amounts of AFP were added to each of three patients' sera, for which the respective AFP concentrations had been determined by radioimmunoassay to be 35, 58 and 82 ng ml^{-1}. Average recoveries of added AFP of 10, 30 and 50 ng were 99.5, 105 and 99.0%, respectively.

The AFP concentrations in sera from 104 patients were determined by the present procedure (x) and by radioimmunoassay (y). The results were related by the regression line $y = 1.06x + 10.1$. The correlation coefficient was 0.97, indicating good agreement between the values for AFP determined by the two methods.

Antibody binding

The preparation of immobilized *anti*-AFP discs by radiation polymerization at low temperatures is based on physical trapping, together with covalent binding caused by radiation cross-linking. Therefore, large amounts of antibodies or antigens can be immobilized in the porous discs. The average pore diameter (1 μm) at the concentration at which the absorbance was a maximum and at which the *anti*-AFP did not leak, was relatively large in comparison with the size of the *anti*-AFP molecule. This suggests that *anti*-AFP is trapped by the small rather than the large pores, as observed with the scanning electron microscope.

The porous structure resulted in a large surface area. Therefore, the minimum detectable concentration of AFP (1.0 ng ml^{-1}) obtained by the present

method is lower than that (5 ng ml^{-1}) obtained with other enzyme immunoassay kits prepared by chemical covalent binding methods [9, 10]. Furthermore, the immobilized *anti*-AFP discs were flexible, and therefore less fragile. As little as 20 μl of serum was required for analysis.

The preparation of the discs is simple and many discs can be sliced from each piece of immobilized material prepared. Thus, in <2 h, 1000 discs can be obtained from 0.05 ml of *anti*-AFP serum and 0.3 ml of monomer. Immobilization by silanization onto glass beads [13] requires at least 27 h and a more complex procedure. Generally, commercial immobilized *anti*-AFP reagents, obtained by chemical binding, have to be immersed in the buffer solution to retain their activity. The immobilized *anti*-AFP discs can be dried safely, and stored for long times, whilst retaining a high sensitivity. Their handling and transport is therefore simple.

REFERENCES

1 G. B. Wisdow, Clin. Chem., 22 (1976) 1243.
2 S. L. Scharpe, W. M. Cooreman and W. J. Blomme, Clin. Chem., 25 (1979) 733.
3 J. Woo and D. C. Cannon, Am. J. Pathol., 66 (1976) 854.
4 A. Voller, D. E. Bidwell and A. Bartlett, Bull. WHO, 53 (1976) 55.
5 M. Yoshida, M. Kumakura and I. Kaetsu, Polymer, 20 (1979) 3.
6 M. Kumakura, M. Yoshida and I. Kaetsu, Appl. Environ. Microbiol., 37 (1979) 310.
7 L. Belanger, D. Hamel, D. Dufour and M. Pouliot, Clin. Chem., 22 (1976) 198.
8 B. Maiolini, B. Ferrua and R. Masseyeff, J. Immunol. Methods, 6 (1975) 355.
9 R. Maiolini and R. Masseyeff, J. Immunol. Methods, 8 (1975) 223.
10 L. Belanger, C. Sylvestre and D. Dufour, Clin. Chim. Acta, 48 (1973) 15.
11 H. Hirai, S. Nishi and H. Watabe, Tanpakushitsu Kakusan Koso (Japan), 18 (1973) 998.
12 M. B. Wilson and P. K. Nakane, in W. Knapp (Ed.), Immunofluorescence and Related Staining Techniques, Elsevier/North Holland, Biomedical Press, Amsterdam, 1978, p. 215.
13 H. H. Weetall, Immobilized Enzymes, Antibodies and Peptides, M. Dekker, New York, 1975, p. 158.

Analytica Chimica Acta, 161 (1984) 115—123
Elsevier Scientific Publishing Company, Amsterdam — Printed in The Netherlands

THE IMPROVEMENT OF SIMCA CLASSIFICATION BY USING KERNEL DENSITY ESTIMATION

Part 1. A New Probabilistic Classification Technique and How to Evaluate Such a Technique

HILKO VAN DER VOET* and DURK A. DOORNBOS

Research Group Optimization, Laboratory for Pharmaceutical and Analytical Chemistry, State University of Groningen, A. Deusinghlaan 2, 9713 AW Groningen (The Netherlands)

(Received 5th December 1983)

SUMMARY

One of the disadvantages of SIMCA pattern recognition is its inability to produce probabilistic classifications. Attempts to correct this involve distributional assumptions. It appears that SIMCA can handle the residual error terms efficiently, but that inside the class model subspace a crude truncation is used for determining a "normal range", inside which all points are treated as equal. An improvement is made by applying kernel density estimation to the scores inside the class model subspace in combination with a normal error distribution in the remaining dimensions (CLASSY method). The evaluation of these probabilistic classification methods is discussed theoretically.

Pattern recognition is used here in the sense of discrimination between groups, although other authors include also other techniques such as cluster analysis and regression [1, 2]. In the extensive literature on pattern recognition, many techniques have been proposed; several reviews have been published [3—5]. A detailed discussion of all these techniques is not the object of this paper. Each technique has its own advantages and disadvantages and the best choice to make will often depend on many factors, including the type of data under examination.

A pattern recognition technique that presently receives much appraisal is SIMCA; this method uses principal component analysis to construct a class analogy model for each training class separately. Although the underlying philosophy and the main ideas of SIMCA are very appealing, the method has a weak point, which causes it to behave very crudely sometimes. This paper describes an attempt to repair this deficiency by incorporating kernel density estimation in SIMCA, a method borrowed from another pattern recognition program, ALLOC.

CLASSIFICATION METHODS

The two methods that can be called the parents of the method proposed here are SIMCA and ALLOC.

0003-2670/84/$03.00

The SIMCA (Soft Independent Modeling of Class Analogy) method constructs class models with the use of principal components [6]. Each class is modelled by a small number of principal components. This class analogy model can be considered as a displacement of the axes in the original multidimensional space. The first step is to shift the origin to the centre of gravity (middle point) of the class. Then principal components are computed one by one, which can be considered as choosing a new axis in a direction such that it accounts for as much of the intra-class variation present as possible. The optimal number of components for each class can be determined by a cross-validation technique [7]. In fact, the optimal dimensionality is almost always very small. Wold [6] reports that, in his experience, most matrices examined contain only a few components, usually 1 or 2.

The idea behind the SIMCA classification is to look at the residuals, i.e., to project the data points from the original p-dimensional space onto the A-dimensional class model. This is illustrated best in a simple example with some objects, for which only two variables are measured ($p = 2$) and which can be fitted reasonably by a line for each class ($A = 1$); the distance from each point to such a line is an indication of how well this object fits into the class under examination. When there are two or more classes, each fitted with a principal component model, the object is assigned to a class by using the minimum distance as criterion (see Fig. 1a). There is one additional rule: when the projection of a test object onto one of the principal component (PC) axes falls outside the "normal range" of the projections of

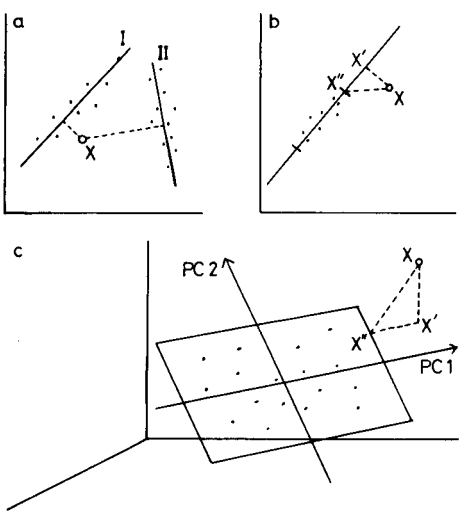

Fig. 1. Distance from a point X to SIMCA class models. (a) The distance from X to class I is smaller than the distance to class II ($p = 2$, $A_I = A_{II} = 1$). (b) The augmented distance XX'' is the geometrical sum of the OMS distance XX' and the IMS distance X'X'' ($p = 2$, $A = 1$). (c) X' is outside the normal range on the PC 1 axis but not on the PC 2 axis ($p = 3$, $A = 2$).

the training objects, the orthogonal distance is not used, but instead the distance to the nearest end of this normal range (see Fig. 1b). In this manner, the class model is truncated: for $A = 1$, the model is a line segment instead of a line; for $A = 2$, the model is a rectangle instead of a plane, etc. (Fig. 1b, c). The general term for an A-dimensional model is a hyperbox. The "normal range" for each PC axis is established on the basis of the training set for this class. The projections of the training set objects on the PC axis are the factor scores θ. For component A, the normal range is given by $(\theta_{\min} - \frac{1}{2}s_\theta, \theta_{\max} + \frac{1}{2}s_\theta)$, where s_θ is simply the standard deviation of all factor scores on component A. An unwanted consequence of the dependence on $\theta_{\min}$ and $\theta_{\max}$ is that the sample size of the training set influences the size of the hyperbox.

A completely different approach to the pattern recognition problem is used in ALLOC (an abbreviation of allocation). As in SIMCA, each class is fitted with its own model, but this model is built up by a technique called kernel density estimation [8, 9]. Basically, this means that around each data point (kernel) in the p-dimensional space, a p-dimensional Gaussian density is assumed. An important step is the determination of the width (standard deviation) of these kernel densities (the so-called smoothness parameter $\hat{o}$). The procedure has been described in detail [9]. When all these densities belonging to kernels of one training class are averaged, the resulting class density is obtained for each point of the data space. Again, as with SIMCA, test objects can be classified when there are two or more classes: one simply calculates the densities for each class at the coordinates of the test point and then assigns this object to the class with the highest class density. Moreover, by using Bayes' formula, it is possible to deal with a priori information and different costs for misallocation.

In this way, the ALLOC classification becomes probabilistic, which means that it is possible to formulate statements like: "object i belongs to class 1 with 75% probability and to class 2 with 25% probability". Probabilistic classification is very important in many situations, e.g., in medical diagnosis. There will always be objects (patients), which are on the borderline between two classes (diseases), and it does make a large difference for a physician to know whether a patient can be assigned to a specific disease class with 51 or with 100% probability. In general, when an individual is more important than the class as a whole, probabilistic classification seems essential. For this reason, probabilistic methods are emphasized below.

The simplest form of Bayes' formula, with all prior probabilities and all costs for misassignment equal, is

$$P(C_q|\mathbf{X}) = P(\mathbf{X}|C_q) / \sum_{j=1}^{k} P(\mathbf{X}|C_j)$$

in which $\mathbf{X}$ is the vector of outcomes for one specific object and C_q is class q (which is one of k classes under consideration). $P(\mathbf{X}|C_q)$ is the probability that an object from class q will yield outcomes $\mathbf{X}$, which corresponds to the

probability density for class q evaluated at the position $\mathbf{X}$ $P(C_q|\mathbf{X})$ is the probability that the object will belong to class q. This is called the posterior probability; from Bayes' formula it is seen to be just a normalized version of the corresponding probability density, such that the sum of all posterior probabilities is one (as it should be, of course).

Thus the problem of classification is reduced to the simpler problem of estimating the probability density for each training class, as outlined above for ALLOC. However, the SIMCA-3B programs [10] do not give probabilistic output, and this concept was only partially applicable for the SIMCA method. To clarify this point, two types of data space can be distinguished. Of the original p dimensions, there are A dimensions which make up the so-called inside-model-space (IMS), while the remaining $p - A$ dimensions constitute the outside-model-space (OMS). The IMS is spanned by the first A principal components of a class model, and the OMS by the remaining $p - A$ principal components. The distinction between IMS and OMS is thus linked to any specific class. It seems reasonable then to postulate a $(p - A)$-dimensional normal distribution for the OMS, because, when A is made sufficiently large, there will be only error terms outside the class model. In fact, this is implicitly done by the authors of SIMCA, when they propose computation of an (approximate) F-statistic to establish if some object is an outlier [10].

In the IMS, the situation is different: no assumption whatsoever is made about the distribution of the scores and therefore it is not possible to calculate a probability density for the IMS. However, because probabilistic classification was essential for the present purpose, an attempt was made to translate the SIMCA rules to densities anyway.

The only distance inside the IMS that matters in SIMCA, is the distance from points outside the hyperbox to this hyperbox. These distances are added geometrically to the distance in the OMS (see Fig. 1b, c). Here, the SIMCA densities are computed simply as OMS densities using these "augmented" distances instead of the pure OMS distances.

The method proposed in this paper and which is named provisionally CLASSY (CLassification by Alloc and Simca SYnergy) has the following characteristics. First, class modelling with principal components is taken from SIMCA. After the optimal number of components A has been established for each class model, the original p-dimensional data space is subdivided into an A-dimensional IMS and a $(p - A)$-dimensional OMS. Secondly, when sufficient components have been taken, the OMS will contain only noise. This noise is assumed to be normally distributed with mean zero and an equal variance in all $p - A$ dimensions. This residual variance is estimated from the data. When there are more class models, it is assumed that all training objects are subject to the same noise in all the measured variables, and so the values of the residual variance for all class models are pooled to one overall residual variance.

Thirdly, in the IMS, a kernel density is computed based on the scores on

the first A principal components to estimate the true probability density. For this purpose, the scheme of Hermans and Habbema [9] is used and the smoothness parameter is calculated with a leave-one-out modification of the maximum likelihood estimation procedure. Fourthly, because the IMS as well as the OMS is built up from principal components, which are uncorrelated by definition, it is easy to compute a total probability density for each point in the data space. The OMS and IMS densities at the desired location are simply multiplied. Finally, with the aid of Bayes' formula, the probability densities are converted to posterior probabilities for class membership.

These are the three pattern recognition methods considered here. As an example of how they differ, a very simple data set with only two measured variables and one class, fitted by the first principal component (Fig. 2), may be considered. For this example ($p = 2$, $A = 1$), it is possible to visualize the probability densities for SIMCA, ALLOC and CLASSY (see Fig. 3). The SIMCA density surface looks simple: no account is made of the data structure inside the hyperbox (here a line segment). The ALLOC density surface, however, is a complicated landscape with many peaks. The CLASSY surface is intermediate, as would be expected.

EVALUATION METHODS

The evaluation of pattern recognition methods is not easy. One can never be sure that a particular method is superior in every situation, because the evaluation is done with a specific data set. Only for data sets with a similar structure (whatever this rather vague description may mean) is it possible to

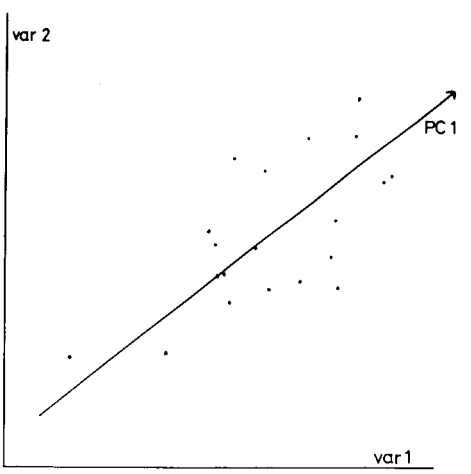

Fig. 2. Simple example ($p = 2$, $A = 1$) of a PC class model. The SIMCA, ALLOC and CLASSY densities for this example are shown in Fig. 3.

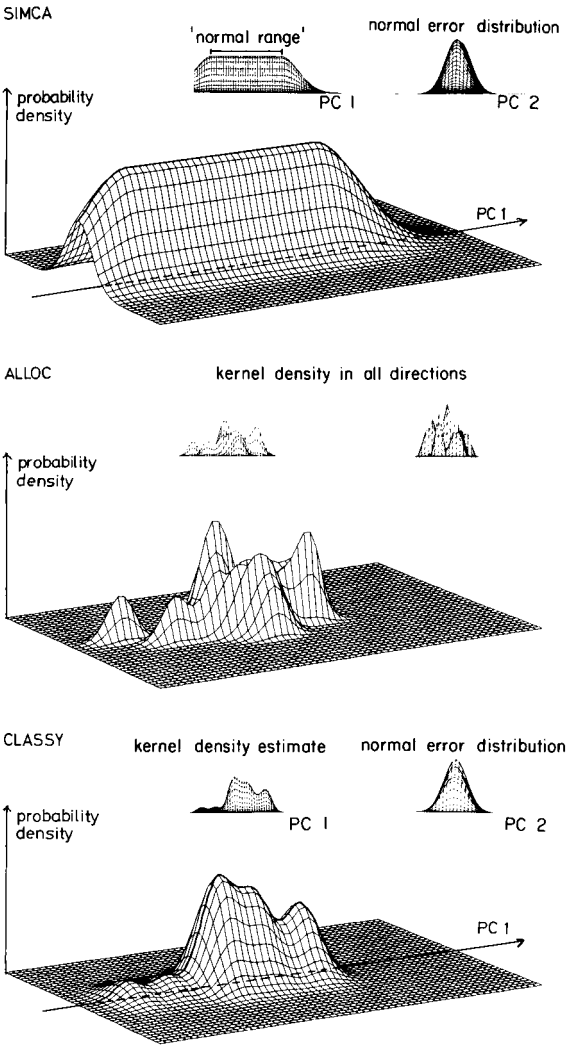

Fig. 3. Probability density surface for the example in Fig. 2 obtained by SIMCA, ALLOC and CLASSY.

expect similar treatment by the classification procedure. When a real evaluation is not possible or when the aim is to construct a quite general method suited for all kinds of data, the method must be evaluated on several very different data sets.

Another problem is to decide which objects of the data set under examination should be used for evaluation. In many of the older publications on this subject, the same objects were used for the construction of the classification rule (the training phase) and for the evaluation of this rule. This reclassi-

fication may lead to serious bias, yielding far too optimistic results [9]. A much better procedure is to divide the data set randomly in two parts: one part (the training set) is used for the training phase and the other part (the test or evaluation set) for the evaluation. In practice, however, the results may vary wildly depending on which objects are in the training and test sets, when the total number of objects is small or moderate. Moreover, by deleting half of the objects from the training set, the ratio of number of objects to number of variables may decrease so much that catastrophe ensues for some pattern recognition methods (a notorious example is the linear learning machine).

For small data sets (i.e., a small number of objects) the leave-one-out method can be used: the n objects are split into a training set with $n - 1$ objects and a test set with only one object. The whole procedure of training and evaluation is then repeated n times, each object being deleted once from the training set and used once for evaluation. This method is clearly time-consuming and it is sometimes reasonable to make a compromise with the previous method. The data set is then split into c more or less equally sized groups, and then each group is deleted once from the training phase and used for evaluation. This may be called the leave-1/c-out method. In the evaluation study described in the next paper [11], the leave-one-out method was used for two small data sets ($n = 40$) and the leave-half-out method for a larger data set (with $n = 100$).

Another important aspect of evaluation is of course the criterion to use. In discussing classification methods, the most straightforward approach is to check if the test objects are classified properly. The number of correct classifications divided by the total number of test objects is called the non-error-rate (NER). This fraction or its complement, the error rate (ER), is the criterion most commonly used.

For probabilistic pattern recognition techniques, however, it is possible to make a more sophisticated evaluation, which uses not only the correctness of the classifications, but also their strength. These methods have been discussed extensively in a series of papers by Hilden, Habbema and Bjerregaard [12—16]. Here, only the measures for discriminatory ability and for reliability, applied in this study, are considered.

The information available consists of all probabilities P_{ij} given by the pattern recognition method; P_{ij} is the posterior probability, that object i belongs to class j. However, the true class of each evaluation object i is known and this true class is denoted by $d(i)$. Thus $P_{id(i)}$ is the probability that is assigned by the program to the actual class of object i.

The ideal situation for good discrimination is clearly when $P_{id(i)} = 1$ and $P_{ij} = 0$ $(j \neq d(i))$ for each object. It seems reasonable to measure the distance from this ideal behaviour as $(1 - P_{id(i)})^2 + \Sigma_{j \neq d(i)} P_{ij}^2$ for object i. By averaging this score over all n evaluation objects, the quadratic score or Brier score is obtained

$$Q_{30} = \frac{1}{n} \sum_{i=1}^{n} [(1 - P_{id(i)})^2 + \sum_{j \neq d(i)} P_{ij}^2]$$

It is easily seen that ideal behaviour leads to $Q_{30} = 0$, while the worst possible behaviour, $P_{id(i)} = 0$ and $P_{ij} = 1$ for some $j \neq d(i)$, leads to $Q_{30} = 2$. It is customary to scale Q_{30} by computing $Q_{31} = 1 - 0.5 Q_{30}$, so that Q_{31} is always in the range [0, 1] with 1 representing ideal behaviour (like the simple NER). In the following paragraphs this Q_{31} value is what is meant by the quadratic or Brier score. Some rearrangements give the formula by which Q_{31} is computed easily

$$Q_{31} = \frac{1}{n} \sum_{i=1}^{n} [P_{id(i)} - 0.5 \sum_{j=1}^{k} P_{ij}^2 + 0.5]$$

When the number of training classes k is only two, this simplifies further to

$$Q_{31} = \frac{1}{n} \sum_{i=1}^{n} [(2 - P_{id(i)}) P_{id(i)}]$$

The quadratic score is a strictly proper scoring rule (SPSR), which means that no method can score higher on Q_{31} than a hypothetical method that knows and outputs the true probabilities π_{ij}, which we try to estimate with P_{ij} [14]. This implies that Q_{31} can be safely used as the criterion in attempts to optimize the discriminatory ability of a classification method by heuristic modifications.

There is another aspect to the performance of probabilistic methods than the discriminatory (or predictive) ability. The concept of sharpness should be considered. A sharp classification is simply a classification where for each object one of the probabilities is close to 1 (and the rest close to 0). The sharpness is computed by $Q_2 = 1/n \; \Sigma_{i=1}^{n} \Sigma_{j=1}^{k} P_{ij}^2$. The point is that the real classes need not be known to decide if a classification is sharp. A method that always assigns 100% probability to a randomly chosen class, will be 100% sharp. However, such a method is obviously not reliable in the sense that the probabilities obtained can be trusted. Reliability here means that the sharpness of the classifications should be in accordance with the predictive power.

When a method is very sharp in its predictions, it may be considered as having a high esteem of its own predictive ability, i.e., it is self-confident. But if it also makes many errors, it is over-confident rather than reliable. In contrast, a method that makes no errors but outputs only probabilities near 0.5 is an example of diffident behaviour.

These kinds of behaviour, which clearly involve a different aspect of the classification performance than the predictive ability, can be quantified in a reliability score which is computed by

$$Q_5 = \sum_{i=1}^{n} (P_{id(i)} - \sum_{j=1}^{k} P_{ij}^2) \Big/ \left\{ \sum_{i=1}^{n} \sum_{j=1}^{k} \left[P_{ij} \left(P_{ij} - \sum_{h=1}^{k} P_{ih}^2 \right)^2 \right] \right\}^{1/2}$$

The derivation of this formula and a more fundamental explanation have been described [13, 14]. The indices of the symbols Q_2, Q_5, Q_{30} and Q_{31} have no implicit meaning, but are the same as used by Hilden et al. For the present purpose (evaluation of the reliability) it is sufficient to know that Q_5 is a reliability measure and that under the null hypothesis of a perfectly reliable system, Q_5 follows approximately a standard normal distribution, i.e., the values +1.96 and −1.96 can be used for a two-sided test of reliability (α = 0.05). Over-confident behaviour of a classification method will make Q_5 negative and diffident behaviour will lead to positive values.

In summary, two quite different aspects of the classification performance of probabilistic methods can be studied. If one is only interested in the correctness of the classifications, it is sufficient to consider a measure for the discriminative ability such as Q_{31}. If one also wants the given probabilities to be trustworthy, it is necessary to check the reliability measure Q_5. In Part 2 of this series, both functions are used for the evaluation of the SIMCA, ALLOC and CLASSY methods on three different data sets.

REFERENCES

1 C. Albano, W. Dunn III, U. Edlund, E. Johansson, B. Norden, M. Sjöström and S. Wold, Anal. Chim. Acta, 103 (1978) 429.
2 B. R. Kowalski and C. F. Bender, J. Am. Chem. Soc., 94 (1972) 5632.
3 L. Kryger, Talanta, 28 (1981) 871.
4 M. P. Derde and D. L. Massart, Fresenius Z. Anal. Chem., 313 (1982) 484.
5 I. E. Frank and B. R. Kowalski, Anal. Chem., 54 (1982) 232R.
6 S. Wold, Pattern Recognition, 8 (1976) 127.
7 S. Wold, Technometrics, 20 (1978) 397.
8 D. Coomans, D. L. Massart, I. Broeckaert and A. Tassin, Anal. Chim. Acta, 133 (1981) 215.
9 J. Hermans and J. D. F. Habbema, Manual for the ALLOC Discriminant Analysis Programs, CRI University Leiden, 1976.
10 C. Albano, G. Blomqvist, D. Coomans, W. J. Dunn III, U. Edlund, B. Eliasson, S. Hellberg, E. Johansson, D. Joknels, B. Norden, M. Sjöström, B. Söderström, H. Wold and S. Wold, in A. Höskuldsson and K. Esbensen (Eds.), Proc. Symp. on Appl. Stats., NEUCC, RECAU, RECKU and Danish Society of Theoretical Statistics, Copenhagen, 1981.
11 H. van der Voet and D. A. Doornbos, Anal. Chim. Acta, 161 (1984) 125.
12 J. D. F. Habbema, J. Hilden and B. Bjerregaard, Methods Inform. Med., 17 (1978) 217.
13 J. Hilden, J. D. F. Habbema and B. Bjerregaard, Methods Inform. Med., 17 (1978) 227.
14 J. Hilden, J. D. F. Habbema and B. Bjerregaard, Methods Inform. Med., 17 (1978) 238.
15 J. D. F. Habbema and J. Hilden, Methods Inform. Med., 20 (1981) 80.
16 J. D. F. Habbema, J. Hilden and B. Bjerregaard, Methods Inform. Med., 20 (1981) 97.

Analytica Chimica Acta, 161 (1984) 125—134
Elsevier Science Publishers B.V., Amsterdam — Printed in The Netherlands

THE IMPROVEMENT OF SIMCA CLASSIFICATION BY USING KERNEL DENSITY ESTIMATION
Part 2. Practical Evaluation of SIMCA, ALLOC and CLASSY on Three Data Sets

HILKO VAN DER VOET* and DURK A. DOORNBOS

Research Group Optimization, Laboratory for Pharmaceutical and Analytical Chemistry, State University of Groningen, A. Deusinghlaan 2, 9713 AW Groningen (The Netherlands)

(Received 5th December 1983)

SUMMARY

The performance of the new probabilistic classification method CLASSY is evaluated on three different data sets, together with its predecessors SIMCA and ALLOC. The improvement made over ALLOC is only marginal, whereas CLASSY shows better predictive ability and greater reliability than SIMCA in most cases.

The evaluation of pattern recognition techniques was considered theoretically in Part 1 of this series [1]. The present paper is concerned with what information is provided by the selected measures for predictive ability [the number of errors, NE, and the quadratic score (Q_{31}), sharpness (Q_2)] and reliability (Q_5) about the SIMCA method (made probabilistic as described in Part 1) and the ALLOC and CLASSY methods. Because the optimal dimensionality for the principal component (PC) class models in SIMCA and CLASSY was unknown, and because the same optimum was not expected for both methods, all possible values of class dimensionality A were examined systematically.

DATA AND COMPUTER PROGRAMS

The pattern recognition methods SIMCA, ALLOC and CLASSY were evaluated on three data sets.

Data sets

Iris data. The well known iris data from Fisher have been analysed by several authors [2—4]. The data set consists of measurements made on flowers from three species of iris: *Iris setosa*, *Iris versicolor* and *Iris virginica*. *Iris setosa* was very easily distinguished from the other two by all methods, so only the latter two species were used here. There are four variables: sepal length, sepal width, petal length and petal width. Each class contains 50 individuals, which were divided randomly in two groups, a training and a test

0003-2670/84/$03.00

group of 25 objects each. The data and the division in groups were taken from the paper by Wold [2]. After the training and test groups had been exchanged and evaluated again, the results were averaged, so that the present conclusions are based on an evaluation set of 100 objects, analysed by the leave-half-out method.

Three kinds of data scaling were applied on the iris data: autoscaling, class scaling and no scaling. In autoscaling, which is the most popular kind of scaling in multivariate analysis all variables are scaled over the entire training set to mean 0 and variance 1. In class scaling, for which an improvement of the classification results with SIMCA is claimed [5, 6], the difference from classical autoscaling is that each training class is scaled separately; this method prevents a large variance caused by between-class differences from being "scaled away". No scaling at all is a possible option for this data set, because the four variables are measured in the same units and have similar variances.

Wine data. In the wine data set, twenty chemical and physical variables were measured on 40 samples from French wines, 21 from the Bordeaux and 19 from the Bourgogne region. This data set has been analysed by several pattern recognition techniques [7] and in general a good discrimination was obtained. Evaluation was done with the leave-one-out method. This data set has an entirely different structure from the previous one. The object-to-variable ratio is only 2 (instead of 25 for the iris data) and the variables are not measured in the same units, but are very different from each other (physical properties such as absorbance and concentrations of constituents such as organic acids and ions). This means that data scaling is essential and class scaling was applied here.

Wine data with head-space analysis. The same 40 wine samples were additionally analysed by head-space gas chromatography (h.s./g.l.c.). Eleven peak heights were measured in the chromatogram and used as variables for discrimination. Again the data were class-scaled and the leave-one-out method was used for evaluation.

Programs

The computer programs used for the SIMCA and ALLOC methods were SIMCA-3B, written in BASIC [5], and ALLOC, written in FORTRAN-IV [8]. For the CLASSY method some of the SIMCA-3B programs were modified and a further BASIC program for kernel density estimation was attached.

The results were evaluated by PASCAL and BASIC programs especially written for this purpose. All computations were performed on the CDC CYBER 170/760 computer of Groningen State University.

RESULTS AND DISCUSSION

Iris data

The SIMCA and CLASSY programs were evaluated with three kinds of scaling and for $A = 1$, 2 and 3 (A is the number of components used in both

class models). For CLASSY, $A = 4$ was also investigated. The ALLOC method is invariant under scaling. In addition to a full analysis with all four variables, ALLOC was also evaluated for 1, 2 or 3 variables. The selection order was obtained by the inbuilt procedure in the ALLOC package, which is based on non-error rates. In previous work [7], it was found that this was a good variable selection procedure in combination with ALLOC classification.

The results are shown in Fig. 1. It can be seen that the (non)error rate is very uninformative. Almost all methods misclassify between 2 and 8 objects out of 100; SIMCA ($A = 3$) is worse with 14—21 misclassifications. For each object, there are only 2 possible results (right or wrong classification), thus the results can be considered as a sample from a binomial distribution. For a sample size of 100, the 95% confidence interval for the error rate is then 0.01—0.06 when 2 misclassifications are found, and 0.04—0.15, when 8 misclassifications occur. Therefore, only very large differences in the sample (non)error rates (e.g., that between SIMCA ($A = 3$) and the other methods) can be considered significant. In fact, it is easily shown that a difference of 5 or less in the number of misclassified objects is never significant at the 95% confidence level, regardless of the size of the evaluation set [9]. A difference of 6, 7 or 8 is significant only when all misclassifications of the best method are also made by the worst method. The conclusion must be that the (non)-error rate fails to distinguish clearly between the methods investigated in the evaluation of this and, in fact, most other data sets.

The quadratic score, Q_{31}, permits a more sensitive evaluation of the discriminatory ability. As can be seen from Fig. 1(b), both SIMCA and CLASSY show an optimum when the number of components in the class models is varied. These results confirm the conclusion of Wold [2] that the optimum dimensionality for SIMCA is maximally 2. This is, however, not the result of any supposed underlying simplicity in the data matrix, for in that case it would be reasonable to expect the same A_{opt} for CLASSY. But the maximum score for CLASSY is reached for $A = 3$, and it is difficult to believe that the inclusion of merely errors in the class models would lead to better performance. It can be seen that CLASSY always scores better than SIMCA, and this gap tends to widen as A increases. This may be interpreted as an inability of SIMCA to "look" inside the A-dimensional hyperboxes; the method seems to make incomplete use of the information that is available in the data.

The significance of the differences found in Q_{31} can be tested by pairing techniques [10]. As explained before, the quadratic score is just the average of the individual quadratic scores for each object evaluated. Two classification methods A and B can be compared by computing the difference $dQ_{31} = Q_{31}(B) - Q_{31}(A)$ for each object evaluated. The null hypothesis: $\Delta Q_{31} = 0$ (no real difference between A and B) can then be tested with a t-test. The results of these pairing comparisons show that the better score for CLASSY compared to SIMCA is significant (at the 95% level), when 2 or more components are used in both methods.

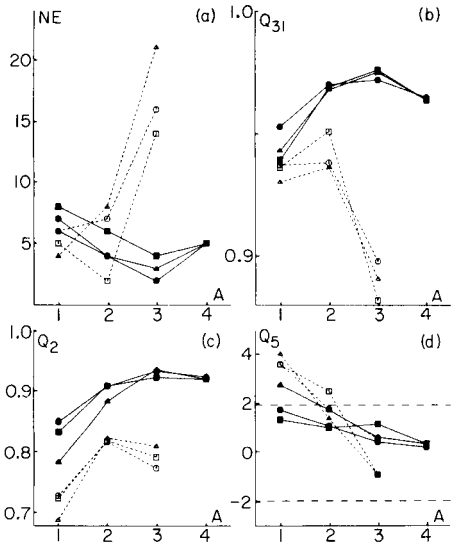

Fig. 1. Evaluation of the Iris data for a varying number of components (A). Solid lines and symbols: CLASSY. Dashed lines and open symbols: SIMCA. (■, □) no scaling; (●, ○) class scaling; (▲, △) autoscaling. (a) Number of errors (out of 100); (b) quadratic score; (c) sharpness; (d) reliability score.

In the paired comparisons (see Table 1) between the best SIMCA method (with $A = 2$), the best CLASSY method (with $A = 3$) and ALLOC, CLASSY had a significantly higher score than SIMCA for all three types of scaling. The higher score for ALLOC compared to SIMCA is significant only in the case of autoscaling. The improvement that CLASSY makes over ALLOC, finally, is only marginal (not significant).

One might object that ALLOC was somewhat handicapped because SIMCA and CLASSY were optimized with respect to the number of principal components to use, which was of course impossible for ALLOC. To give

TABLE 1

Paired comparisons between the best SIMCA, CLASSY and ALLOC models in the evaluation of the Iris data set

Method A	Method B	Mean dQ_{31} = $Q_{31}(B) - Q_{31}(A)$	Difference between A and B
SIMCA ($A = 2$) no scaling	CLASSY ($A = 3$) no scaling	0.025	significant ($p < 0.001$)
SIMCA ($A = 2$) no scaling	ALLOC (4 variables)	0.013	not signif. ($p = 0.32$)
ALLOC (4 variables)	CLASSY ($A = 3$) no scaling	0.012	not signif. ($p = 0.10$)

ALLOC an equal chance, it was also evaluated when the number of variables was reduced by variable selection. The best result was, however, obtained by using all four variables, so that the optimal ALLOC dimensionality can be regarded as 4.

The reliability analysis of the results is discussed only briefly for this data set. In most cases, reliable predictions were obtained (Fig. 1d). Only SIMCA (A = 1) with all three kinds of scaling, SIMCA (A = 2) without scaling and CLASSY (A = 1) with autoscaling were diffident. It may be noted that this includes the best SIMCA method in terms of predictive ability.

Wine data

The structure of the Wine data is quite different from that of the Iris data. In fact, the number of variables (20) is even greater than the number of objects in the Bourgogne class (which is 19 and, with the leave-one-out method used, often only 18). Therefore, the number of principal components which could be extracted from this class is theoretically 18, but, for programming reasons, is only 17 in practice.

The results obtained after SIMCA and CLASSY analysis using 1—17-component models for both classes, are shown in Fig. 2. Again the number of errors (Fig. 2a) gives indications, but almost no proof, about the superiority of one method over the other; a difference of at least 6 between the numbers of misclassified objects is the minimum requirement for detecting statistical significance.

The quadratic scores (Fig. 2b) confirm the first impression given by the

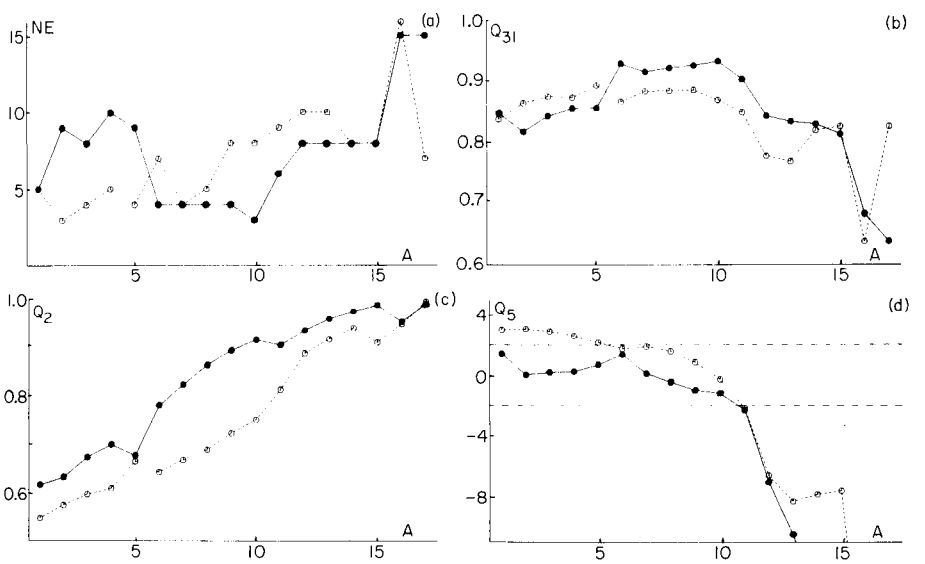

Fig. 2. Evaluation of the Wine data for a varying number of components (A). Solid lines and symbols: CLASSY. Dashed lines and open symbols: SIMCA. (a) Number of errors (out of 40); (b) quadratic score; (c) sharpness; (d) reliability score.

error rates, but more definite conclusions can be drawn. Roughly there are three regions in the graph. In the first region (A = 2 to 5), SIMCA scores better than CLASSY. SIMCA reaches its overall maximum score 0.893 at A = 5. However, the difference found between the two methods is never significant. In the second region (A = 6 to 10), the SIMCA scores remain at about the same level, but the CLASSY scores increase rapidly, reaching the nearly maximum score 0.928 at A = 6 and the overall maximum score 0.932 at A = 10. For A = 6, 8 and 10, CLASSY outperforms SIMCA significantly (α = 0.05). In the third region (A = 11 to 17), the discriminative ability deteriorates for both methods. As the number of components approaches the number of objects in each class, the scores become very unstable, which can lead to wild variations when one other component is added. Surprisingly, the SIMCA result for A = 17 is significantly better than the CLASSY score.

The optimal class dimensionality A_{opt} is not as clearly seen as for the Iris data. The Q_{31} graphs are rather flat and a prudent conclusion might be that A_{opt} for SIMCA is somewhere in the region 2—10, while for CLASSY it lies in the region 6—11. But the general form of the graphs confirms the conclusion already drawn from the Iris data, i.e., with the same data set CLASSY can handle more principal components than can SIMCA, and thereby attains a better discriminative performance.

A paired comparison between the best SIMCA (A = 5) and the best CLASSY (A = 10) method was attempted, but the distribution of the differences dQ_{31} was so skew that a valid t-test was impossible. A non-parametric alternative, the sign test, was also not useful, because this is a test for the median rather than for the mean score, and Q_{31} is meaningful as a measure of discrimination only when it is averaged over a number of objects [10]. The results of some comparisons between best and near-best methods that were possible with a t-test are shown in Table 2.

The above-mentioned skewness arises in any comparison between methods with very different dimensionalities for their IMS (inside model space). This may be understood by looking at the sharpness of the predictions. Figure 2(c) shows how the sharpness increases almost linearly with A. For A = 17, almost all probabilities are 1.00 or 0.00. There is no obvious explanation for this relationship, but it is clear that this increasing self-confidence of a method is justified only as long as it is accompanied by an increase in dis-

TABLE 2

Paired comparisons between the best and near-best SIMCA and CLASSY models in the evaluation of the Wine data

Method A	Method B	Mean dQ_{31} = $Q_{31}(B) - Q_{31}(A)$	Difference between A and B
SIMCA (A = 5)	CLASSY (A = 6)	0.035	significant (p = 0.042)
SIMCA (A = 9)	CLASSY (A = 10)	0.047	significant (p = 0.006)

criminative ability. The reliability score Q_5 was introduced as a measure for the trustworthiness of the probability values (see above). The numerator of Q_5 is $Q_{31} - 0.5Q_2 - 0.5$; it measures if discriminative ability (Q_{31}) and sharpness (Q_2) are in concordance with each other.

In Fig. 2(d), Q_5 is plotted for the SIMCA and CLASSY evaluations of the Wine data. The most remarkable feature is the enormous over-confidence of both methods when A gets too large (e.g., >10). In this region, the predictions are very sharp, but this is not matched by a corresponding low error rate. In contrast, SIMCA shows slightly, but significantly, diffident behaviour for small values of A. If the output of the selected method is to be trusted as being real probabilities, then the choice is between CLASSY in the range $A = 1$—10 and SIMCA in the range $A = 6$—10. Again, the SIMCA method with best discrimination ($A = 5$) is not reliable.

The results obtained with ALLOC were surprising. It was thought likely that the ALLOC results would suffer from the large number of variables, as has been reported [11]. However, the results with ALLOC, using all twenty variables, were nearly as good as those with the optimal CLASSY method (with $A = 10$); there were only 3 erroneous classifications and the quadratic score was 0.930 (vs. 3 errors and $Q_{31} = 0.932$ for CLASSY). The only point of criticism was its slightly over-confident behaviour ($Q_5 = -2.32$).

The authors of ALLOC claim that a leave-one-out method is automatically provided in their program by the nature of the kernel density estimation procedure used [8]. This is, however, only partly true because the smoothness parameter (kernel function width) is computed on the basis of all objects in the class, including the one under classification. There is still some over-optimistic bias left in the results produced by ALLOC. The above results were obtained with a real leave-one-out method, which simply means that the program was run 40 times. For comparison, the partial leave-one-out method yielded $Q_{31} = 0.950$.

Wine data with head-space gas chromatography

These data are discussed to give a complete picture, for the pattern is much less clear than for the iris and wine data and there are several effects for which there is no immediate explanation.

The wine data set with h.s./g.l.c. data added have 11 variables, so that the evaluation comprised runs with A varied between 1 and 10 for SIMCA (programme restriction) and between 1 and 11 for CLASSY. ALLOC was evaluated with all 11 variables. The results are shown in Fig. 3. The error rate is again uninformative (Fig. 3a): only SIMCA with $A = 9$ or 10 can be disqualified for bad discrimination.

The SIMCA method exhibits the normal pattern for the quadratic scores (Fig. 3b); the scores rise to a maximum (0.943) in the early phase ($A = 2$—4) and then decrease when too many components are used. For CLASSY, however, there is no such pattern: the scores form a quite irregular graph with (sub)maxima at $A = 1$, 5 and 10, and (sub)minima at $A = 3$ and 8. The

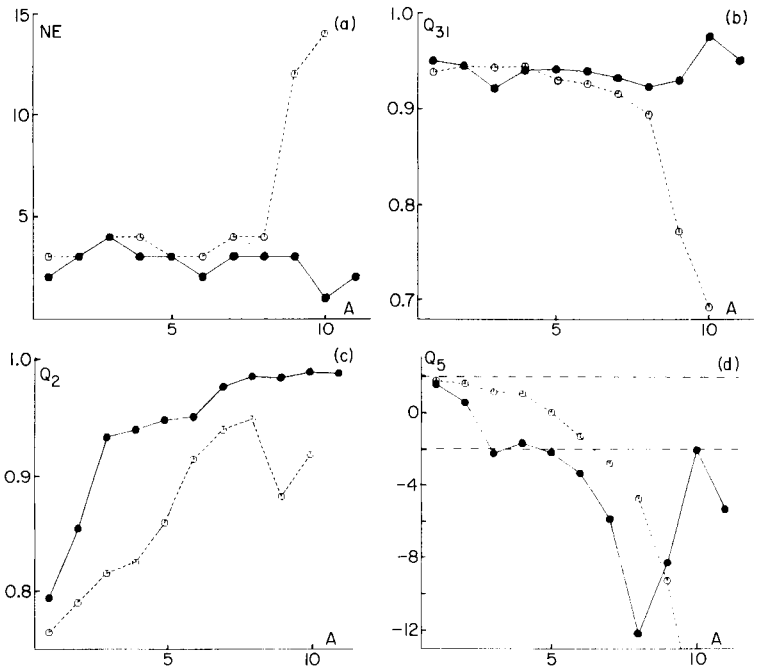

Fig. 3. Evaluation of the wine data with h.s./g.l.c. for a varying number of components (A). Solid lines and symbols: CLASSY. Dashed lines and open symbols: SIMCA. (a) Number of errors (out of 40); (b) quadratic score; (c) sharpness; (d) reliability score.

general maximum Q_{31} is 0.975 at $A = 10$. Even the difference between the highest and the lowest CLASSY score is not significant; it seems that the discriminative ability of CLASSY is not much influenced by the class dimensionality.

In contrast, the reliability of the CLASSY output is greatly affected by the choice of A (Fig. 3d). The only reliable methods are SIMCA with A = 1—6 and CLASSY with $A = 1$, 2 or 4 (also with $A = 3$, 5 or 10 if slight over-confidence is allowed).

The results from ALLOC are comparable with those of CLASSY with $A = 11$ (as might be expected, for the only difference is a rotation of the axes); there were 2 errors, the quadratic score was 0.949 and the reliability measure was —4.24 (over-confident).

The general conclusion for this data set is that there are no really important differences between SIMCA, ALLOC and CLASSY.

Some restrictions

Before general conclusions can be made, the restrictions of this study and of this kind of research in general must be considered. This paper has been concerned with three pattern recognition methods which have been eval-

uated by using different data sets, i.e., the approach is method-orientated, not data-orientated. The problem of how to convert real-life problems into a manageable form for the application of pattern recognition has not been discussed although this is certainly an important step, perhaps the most important, in the overall classification process.

There are of course also practical limitations with such evaluations. Here, the effect of varying A, the class dimensionality, was studied but A was not varied for each class separately, though this is readily possible in principle with both SIMCA and CLASSY. The above results are not intended to suggest that such evaluations should be used to determine the optimal class dimensionality A_{opt}. That would involve too much work for any practical application. The choice of varying A systematically resulted from the lack of a simple reliable method for finding A_{opt}, and this remains a big problem. Many methods have been advocated for this purpose [12—14], including a cross-validatory method which is included in the SIMCA package, but our experience with most of these methods is not very encouraging. Indeed, it was shown above that A_{opt} may be quite different depending on which classification method is used. Thus the dimensionality of a data matrix (in a practical rather than mathematical sense) may be rather an elusive concept, in the same way as the "optimal" variable selection.

Conclusions

The two distinct aspects of classification, predictive ability and reliability, must be considered. With respect to predictive ability, both theoretical studies [1] and practical evaluation have shown that the performance of SIMCA can be improved by applying kernel density estimation in the IMS. More information can then be extracted from the data. It appears that the optimal class dimensionality is in general higher for CLASSY than for SIMCA. The third method investigated, ALLOC, also performed very well. Although in all cases it was possible to construct a CLASSY method with higher predictive ability and better reliability, much more research is needed to assess the possible superiority for one or the other method.

A general result concerning the reliability of the methods is the increasing sharpness as the class dimensionalities increase. This increasing sharpness is, however, only partly justified by better agreement between prediction and outcome, so that the reliability score of SIMCA and CLASSY generally decreases as A increases. This is acceptable if the method was initially diffident, but the choice of A should not be so high that over-confident predictions are obtained. The CLASSY method is almost always more self-confident than the corresponding SIMCA method. For the Iris and Wine data, this produces better reliability at the class dimensionality which gives the best discrimination.

We thank Jan Hemel for many helpful discussions on the subject.

REFERENCES

1 H. van der Voet and D. A. Doornbos, Anal. Chim. Acta, 161 (1984) 115.
2 S. Wold, Pattern Recognition, 8 (1976) 127.
3 M. Sjöström and B. R. Kowalski, Anal. Chim. Acta, 112 (1979) 11.
4 D. Coomans, D. L. Massart, I. Broeckaert and A. Tassin, Anal. Chim. Acta, 133 (1981) 215.
5 C. Albano, G. Blomqvist, D. Coomans, W. J. Dunn III, U. Edlund, B. Eliasson, S. Hellberg, E. Johansson, D. Joknels, B. Norden, M. Sjöström, B. Söderström, H. Wold and S. Wold, in A. Höskuldsson and K. Esbensen (Eds.), Proc. Symp. Applied Statistics, NEUCC, RECAU and RECKU in cooperation with the Danish Society of Theoretical Statistics, Copenhagen, 1981.
6 M. P. Derde, D. Coomans and D. L. Massart, Anal. Chim. Acta, 141 (1982) 187.
7 H. van der Voet, D. A. Doornbos, M. Meems and G. van de Haar, Anal. Chim. Acta, 160 (1984) 159.
8 J. Hermans and J. D. F. Habbema, Manual for the ALLOC Discriminant Analysis Programs, CRI Univ. Leiden, 1976.
9 Wissenschaftliche Tabellen, 7th edn., Geigy, Basel, 1968, p. 85.
10 J. Hilden and J. D. F. Habbema, in A. Alpérovitch, F. T. De Dombal and F. Grémy (Eds.), Evaluation of Efficacy of Medical Action, North-Holland, Amsterdam, 1979, p. 123.
11 D. Coomans, M. Derde and D. L. Massart, Anal. Chim. Acta, 133 (1981) 241.
12 S. Wold, Technometrics, 20 (1978) 397.
13 E. R. Malinowski and D. G. Howery, Factor Analysis, Wiley, New York, 1980.
14 H. T. Eastment and W. J. Krzanowski, Technometrics, 24 (1982) 73.

Analytica Chimica Acta, 161 (1984) 135—148
Elsevier Science Publishers B.V., Amsterdam — Printed in The Netherlands

COMPUTER-ASSISTED MULTICOMPONENT SPECTRAL ANALYSIS WITH FUZZY DATA SETS

T. BLAFFERT

Philips GmbH Forschungslaboratorium Hamburg, Vogt-Kölln-Straße 30, D-2000 Hamburg 54 (West Germany)

(Received 20th December 1983)

SUMMARY

A new approach to the interpretation of spectra with "fuzzy sets" is described. A computer program CIF (Compound Identification with Fuzzy sets) is applied. This program is capable of finding components in a mixture by comparing the sample spectrum with reference spectra in a library. The applications discussed involve the interpretation of infrared spectra. The problems of spectral library search are discussed, an elementary introduction to fuzzy set theory is given, and applications to spectral library search are demonstrated.

The identification of compounds and the determination of their concentration in a multicomponent unknown sample is a basic problem in analytical chemistry. Various wet chemical or spectroscopic identification methods can be applied to obtain an answer from one experiment or from the combination of various measurements. Experience and expertise are necessary to correlate the data with a chemical structure. Such work is now frequently supported by a computer, which can calculate mathematical models or search reference libraries much more quickly than a human being.

Spectroscopic methods are well adapted to being supported by a computer because the output of the instrument is readily digitized and stored in computer memory. Many data points have to be reduced to position, height, width and shape of a few spectral lines, a typical problem of data processing. After this step, the reduced data are evaluated according to a mathematical model (as with n.m.r.) or, if this is unsatisfactory, compared with reference lines in a reference library (e.g., infrared, x-ray diffraction). In this article, a new approach to the latter method will be given, the identification procedure being treated as a pattern recognition problem.

Compound identification as a pattern recognition problem

The above-mentioned steps in computerized compound identification can be formulated as a common pattern recognition scheme [1]

spectral input data → feature extraction → feature vector or set → classification → decision

In feature extraction, the lines of a spectrum (peaks) with their position, height and width are measured from the input data. In classification, the procedure is to search in a reference library, compare references and unknown sample spectra with respect to the features selected, and to reach a decision on the compound(s) present.

As an example, an infrared spectrum of a mixture of benzyl alcohol, butan-2-one, carbon tetrachloride and hexane is shown in Fig. 1, where an automated peak-search program found the positions of the measured peaks. The spectra of all the components are plotted in Fig. 2. The position scale is instrument-dependent (wavenumbers for infrared spectra, 2θ for x-ray diffractometry, time for gas or liquid chromatography) but arbitrary for the present purpose. In Fig. 1, the peaks found are marked by lines. The positions and heights of these lines are compared with the lines in reference spectra in the classification step to establish the sample components.

Because line positions are most relevant, the introduction to fuzzy sets is described in terms of this feature, but it is also applicable to intensities and other features.

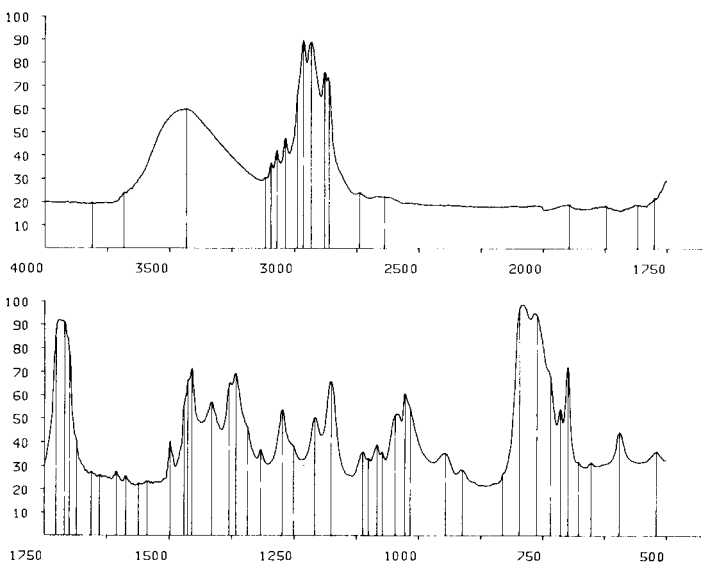

Fig. 1. Infrared spectrum of a mixture of benzyl alcohol, butan-2-one, carbon tetrachloride and hexane, plotted in wavenumbers vs. % absorption. The peaks are located by an automated peak search program and marked by lines in the diagram.

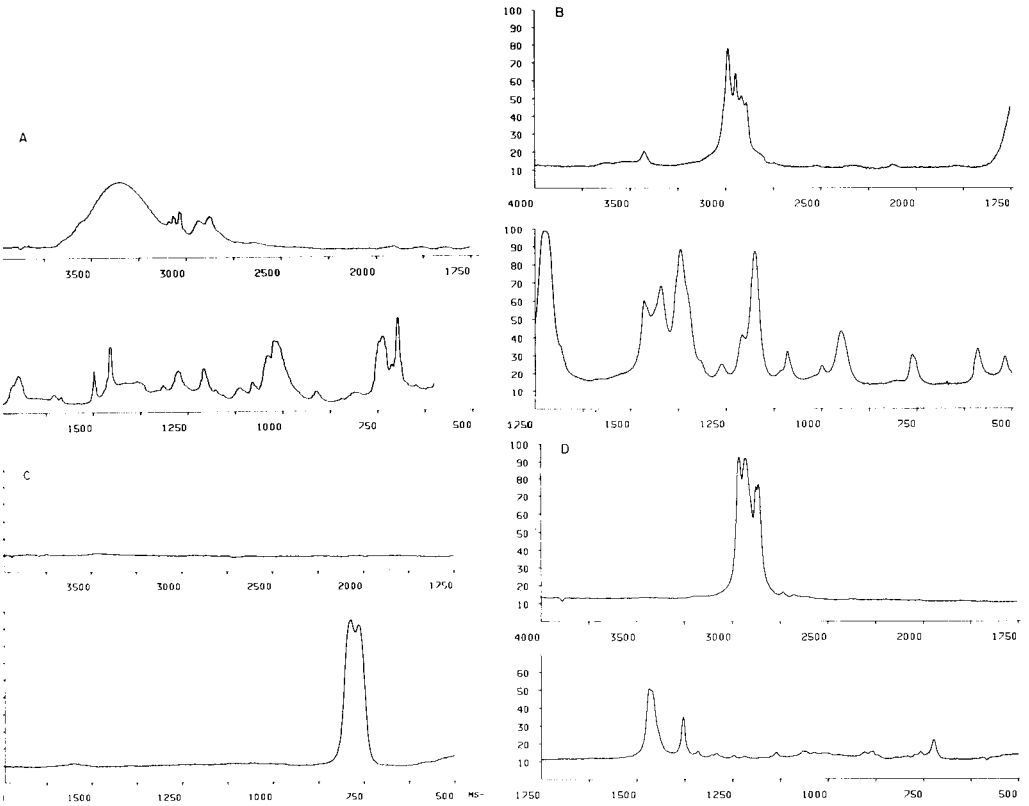

Fig. 2. Infrared spectra of the components in the sample used for Fig. 1: (A) benzyl alcohol; (B) butan-2-one; (C) carbon tetrachloride; (D) hexane.

FUZZY SET APPROACH

Comparison of spectra formulated in conventional set theory and fuzzy set theory

After all measured peaks have been located by a peak search, the spectrum is characterized by a collection of features like position (2θ, wavenumber, time, etc.), height and width. It is important to treat these features as a set of features rather than a feature vector because there is no relation between a spectral line and a certain dimension. In Fig. 3A, the members of the set are illustrated by single lines. The reference spectrum is also a set of reference lines (Fig. 3B). The goodness of fit of the sets even in a multicomponent sample must be considered, i.e., the number of lines of the reference spectrum that are present in the measured set. In conventional set theory, the answer to this basic problem is given by counting the number of members of the sets in the intersection of the two sets; this is the conventional set power of the intersection. The advantage of the intersection operation

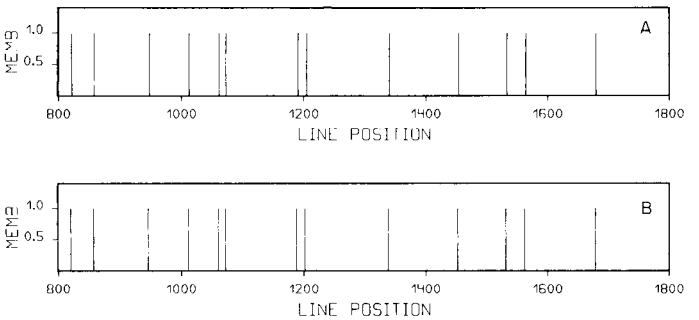

Fig. 3. Fuzzy set connections. Comparison of measured set of lines (A) and reference set of lines (B) using conventional intersection. There are no lines in the intersect set. Membership of the set is indicated by MEMB.

will be fully understood if the comparison of a reference with a multicomponent sample is considered. A multicomponent set of lines is the union of the constituent sets and the intersection operation extracts the lines belonging to the reference (see below). Unfortunately, the result of a conventional set operation on the lines in Fig.3 is unsatisfactory because the true line positions are distorted by small random variations and therefore the intersect set (not shown) shows no lines at all.

These random variations are taken into account in the present search method by introducing the theory of fuzzy sets. In fuzzy set theory, it is not only valid to say that a spectrum line does or does not belong to a set but also to say that a spectrum line belongs to a set to a certain degree. A reference line which has a slightly different position from a measured line does not abruptly disappear in the intersection; it is still present, but with a lower degree of membership. This point is illustrated in Fig. 4, and the exact mathematical formulations are presented in the next sections.

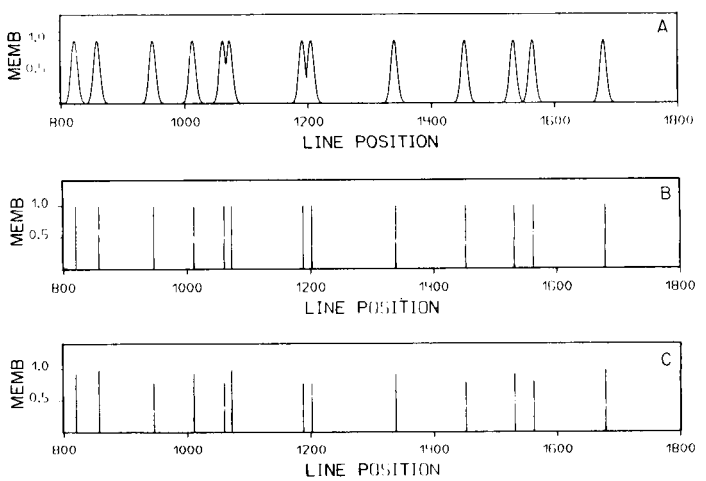

Fig. 4. Fuzzy set connections. Comparison of a fuzzed set of measured lines (A) and a reference set of lines (B) using the fuzzy intersection. The intersect set (C) reflects all lines, but some of them have a degree of membership smaller than 1. The peaks in A represent position distribution, not intensity distribution.

Elementary fuzzy set theory

A big advantage of the fuzzy set theory, which was introduced by Zadeh [2], arises from the continued use of conventional concepts and nomenclature of set theory. Overviews of fuzzy set theory have been given by Zadeh [3] and Kandel and Byatt [4]; here, only the concepts relevant to a spectral library search are considered. The fuzzy set operations are illustrated in Fig. 5.

The range of all spectral values possibly measured by the specific instrument is denoted by X. A fuzzy set A of $X = \{x\}$ is characterized by a membership function f_A: $X \rightarrow [0, 1]$. The value $f_A(x)$ represents the grade of membership for each point x in the fuzzy set A. The membership function f_A can be defined objectively by probability distributions, but it can also be used to incorporate personal subjective experience. If f_A assumes only two values 0 and 1, it reduces to the characteristic function of conventional set theory, which is $f_A(x) = 1$ for $x \in A$ and $f_A(x) = 0$ when x is not a member of set A.

Set A is contained in set B if $A \subset B \langle = \rangle f_A(x) \leqslant f_B(x)$, for all $x \in X$ (Fig. 5A). An intersection of two fuzzy sets A and B in X is defined as the membership function of $A \cap B$ given by

$$F_{A \cap B}(x) = \min[f_A(x), f_B(x)] \tag{1}$$

as shown in Fig. 5(B). Similarly, the union $A \cup B$ is defined by

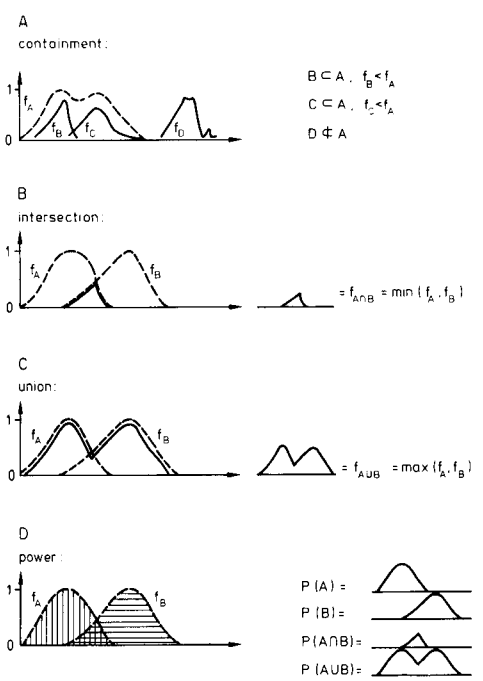

Fig. 5. Fuzzy set connections: illustration of fuzzy set operations.

$$f_{A\cup B}(x) = \max[f_A(x), f_B(x)] \tag{2}$$

as shown in Fig. 5(C). The power of a fuzzy set A, for a finite population X, is

$$N_A = \sum_{x\in X} f_A(x) \tag{3}$$

(see Fig. 5D). The last four definitions are consistent with conventional set theory if f is limited to the dual set $\{0;1\}$.

An important relationship exists between the containment and the intersection: if a (reference) set A is contained in a (measured unknown) set B, then the equation $A\cap B = A$ holds, and the fuzzy set power of the intersection set is equal to the power of A. Thus the fuzzy set power of an intersection is a measure of containment of a (reference) set A within the (measured) set B. The containment measure can be normalized by $C_{AB} = N_{A\cap B}/N_A$.

Fuzzing of the spectrum

The peak-search step enables the x values (line positions) which are contained in the measurement to be identified. This usually produces a list of n peaks, and the spectrum can be described as a union S of single lines S_j by

$$S = \bigcup_{j=1}^{n} S^j \tag{4}$$

with $f_{S^j}(x) = 1$ if x is the location of the jth peak but $f_{S^j}(x) = 0$ otherwise.

So far, S is a conventional set (Fig. 3A). Of course, a measured spectrum is not exact because random errors introduce uncertainty about which features are really related to the measured values; not only a spectral line with the exact measured value, but also lines in its neighbourhood may in fact be the same. One solution is to define a "hard window"; this is an interval of m points around a measured line. All lines in this interval may then belong to the spectrum. This can be expressed by $\bar{S} = \cup_{j=1}^{n}\bar{S}^j$, with $f_{\bar{S}^j}(x) = 1$ if $x\in[x - m, x + m]$ and x is the location of the jth peak, but $f_{\bar{S}^j}(x) = 0$ otherwise. Figure 6 demonstrates the hard window approach.

Various search programs use this hard window. The disadvantage in this concept is that a small variation around $x - m$ or $x + m$ can make a large difference to belonging or not belonging to a set. This disadvantage can be avoided by using a continuous grade of membership between 0 and 1. A reference line with exactly the same x as the measured line has a membership value of 1. The membership value diminishes with increasing distance from the measured line, and if the distance is very large, the membership value becomes zero. The shape of the membership function might be Gaussian or Lorentzian, but it is not necessary to choose statistical functions. The degree of membership expresses at least a subjective estimate of uncertainty, which is established by the experience of the operator. Nevertheless,

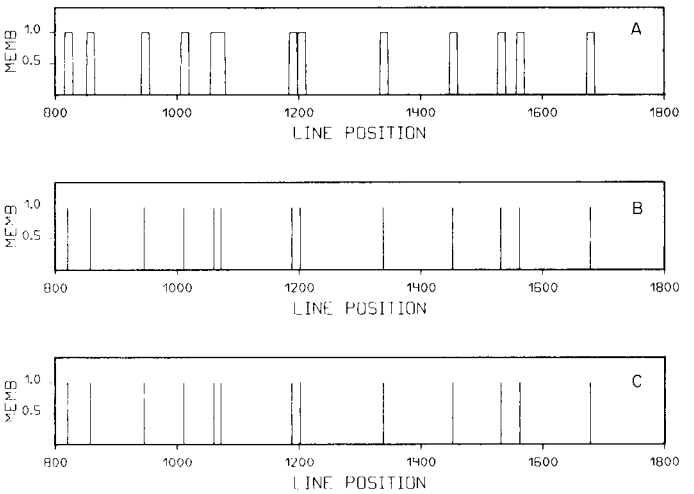

Fig. 6. Fuzzy set connections: comparison of spectra using the hard window approach.

Gaussian distribution could be a good choice when the uncertainty derives from a randomly distributed measurement error.

The procedure of assigning a broad membership function to a sharply defined feature (i.e., a line of a spectrum) is called fuzzing. The fuzzed spectrum is the fuzzy union of the fuzzed lines

$$\tilde{S} = \bigcup_{j=1}^{n} \tilde{S}^j \tag{5}$$

with $f_{\tilde{S}^j}(x) = \exp[-(x^j - x)^2/2\sigma^2]$ if $x \in [x^j - \alpha\delta, x^j + \alpha\delta]$, x^j being the location of the jth peak; otherwise $f_{\tilde{S}^j}(x) = 0$. This is equivalent to

$$f_{\tilde{S}}(x) = \max_j [f_{\tilde{S}^j}(x)] \tag{6}$$

Figure 4A shows a spectrum fuzzed according to Eqn. 5. The Gaussian distributions in the fuzzed spectrum must be distinguished from a line profile; they do not represent an intensity distribution but a position-dependent error distribution.

Fuzzy sets compared with linear operators

Superficially, the fuzziness related to Eqn. 6 seems to be similar to a convolution of an initial δ-signal with a Gaussian convolution kernel. However, there are mathematical and semantic differences between both operations. The convolution

$$\hat{f}(x) = \Sigma f(x - j) * k(j) \tag{7}$$

is a linear operation, whereas the fuzzy min/max operations are nonlinear. A convolution, as shown in Fig. 7, yields functional values larger than 1,

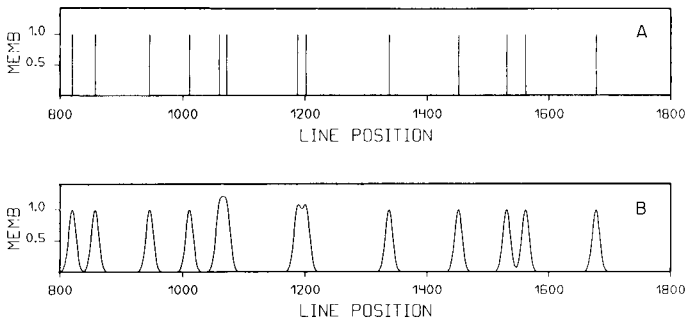

Fig. 7. Fuzzy set connections: (A) spectral lines; (B) convoluted set.

resulting from contributions of more than one initial spectral line. In contrast, the "max" union operator implies a decision on which spectral line contributes to a membership value.

Another method of determining the similarity between sample and reference spectra is to calculate the variance

$$s^2 = \Sigma(x_j - x_{jR})2/(n-1) \tag{8}$$

Pairs of related lines x_j, x_{jR} are needed, which have to be selected by additional rules. The problem is that the jth reference line does not necessarily correspond to the jth line in the spectrum because missing lines in the spectrum, extra lines from additional components, unresolved doublets, etc., distort the order of lines in a list. Sets are compared rather than vectors.

Comparison by fuzzy intersection and fuzzy power

Fuzzy intersection, as defined by Eqn. 1, performs a formulation of the comparison step between fuzzed measurement and reference, where the latter is an unfuzzed set denoted by

$$R_k = \bigcup_{j=1}^{n_k} R_k^j \tag{9}$$

with $f_{R_k^j}(x) = 1$ if x is the location of the jth line of reference K, but is otherwise equal to zero. Here, k is a reference number in the reference library, and n_k is the number of lines in reference k. The application of the intersection operator leads to a result set

$$\tilde{S} \cap R_K = S \cap (\bigcup_{j=1}^{n_k} R_k^j) = \bigcup_{j=1}^{n_k} (\tilde{S} \cap R_k^j) \tag{10}$$

with $f_{\tilde{S} \cap R_k^j}(x) = \min[f_{\tilde{p}}(x), f_{R_k^j}(x)]$, which equals $f_{\tilde{p}}(x)$ if x is the location of the jth line of reference K but is otherwise equal to zero.

The remaining problem is to find a score value which gives the confidence limit between the intersection set and the intrisic reference set. This value is

given by the fuzzy set power (Eqn. 3). It must be assumed that the support (spectrum range) consists only of finite elements, but this is always true in computerized spectral analyses. In the special case of intersection (Eqn. 10), this power is

$$N_{\tilde{S}\cap R_K} = \sum_{j=1}^{n_k} f_{\tilde{S}}(x_k^j) \tag{11}$$

where x_k^j is the location of the jth line of reference K.

This power or, alternatively, the containment measure ($C_{AB} = N_{A\cap B}/N_A$) is the final number representing the goodness of fit between a reference and a measured spectrum. Sorting after all power computations gives a list of best-fitting references.

Spectra obtained from multicomponent samples

Clearly the described method can be used if the spectrum is obtained from a mixture of different compounds (Fig. 8). The method indicates which sample and reference lines are related. Constituent compounds are not lost in this comparison, as can happen with an algorithm in which identified lines are removed from the peak table. Only extra compounds with line combinations derived from the mixing process can be found. They can be eliminated by additional use of intensity information (see below).

Lines which are overlapped by a strong line from a different component or hidden in the background noise, can also be examined with the fuzzy set procedure. Missing lines will decrease the set power by 1 and lower the position of a correct reference pattern in the score list. Of course this gives a worse result, but the correct pattern is still in the list and has not totally disappeared.

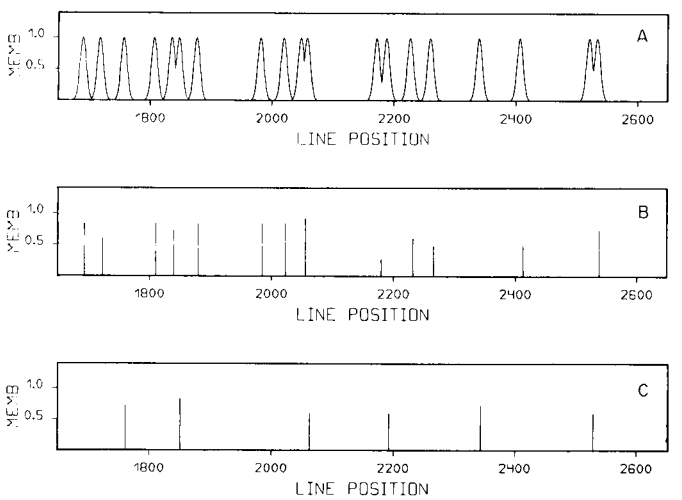

Fig. 8. Comparison of reference spectra with a two-component unknown sample: (A) the measured spectrum; (B) and (C) two reference sets after a fuzzy intersection.

Extension of the fuzzy set concept to line intensities

The discussion of spectral interpretation with fuzzy sets has so far been limited to line positions. A mathematical extension of this concept to line intensities or even other (new) features is easy. The physical and instrumental influences should be considered and included in the construction of the membership function; only carefully selected parameters guarantee a good discrimination between reference candidates, and therefore an accurate result from the identification procedure.

As an example, Fig. 9 shows the match between a spectrum and a reference on positions and line intensities. The one-dimensional axis of peak positions is replaced by a two-dimensional plane, where each point denotes a peak with a certain position and a certain intensity. A well defined line, like a reference line, is marked by a single stroke (Fig. 9B); this means that this line element is contained in the reference set. The measured lines are, analogously to the two-dimensional case, fuzzed in the x- and i-directions (Fig. 9A). Random variations in the intensity determine the broadness of the i-fuzzing. All one-dimensional fuzzy relationships still hold, except that the variable x must be replaced by a vector $\mathbf{x} = (x, i)$.

Including intensities in the compound identification gives rise to the problem of concentration. This means that line intensities, which are given relatively to the most intense line in a reference spectrum, are shifted simultaneously towards lower values in a multicomponent sample as a result of lower concentration. For example, a 100% line of a reference can occur as a 50% line in a measured spectrum. Such systematic errors can be corrected by transforming the relative intensities to a logarithmic scale and shifting all intensity values by the same amount until the maximum fuzzy set power is obtained.

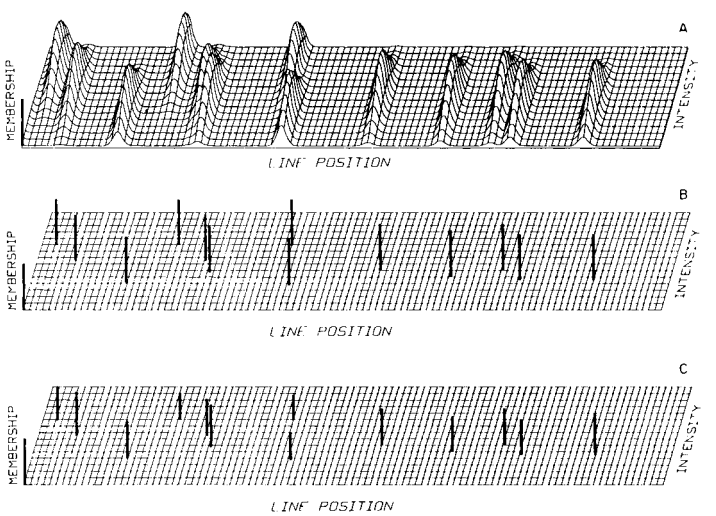

Fig. 9. Line comparison with fuzzy sets including line intensities. A fuzzed set (A) intersected by a reference (B) yields set (C).

The component identification selects those reference spectra from the score list, which are actually in the sample. This is done by combining the reference spectra which score highest in the match according to their predicted concentrations and comparing the result with the original sample spectrum. In this step, intensity variations related to overlapping lines from different compounds are evaluated. All references in the combination with the highest power are considered as identified.

The identification of components can also be modelled with fuzzy set concepts. The reference spectra are combined by unifying them (Eqn. 2); the united set is then fuzzed and intersected with the unfuzzed measured spectrum, and the fuzzy power is computed (Fig. 10).

Table 1 shows the list of compounds found in the library search on the sample used for Fig. 1, and scored in the fuzzy match. The score indicates

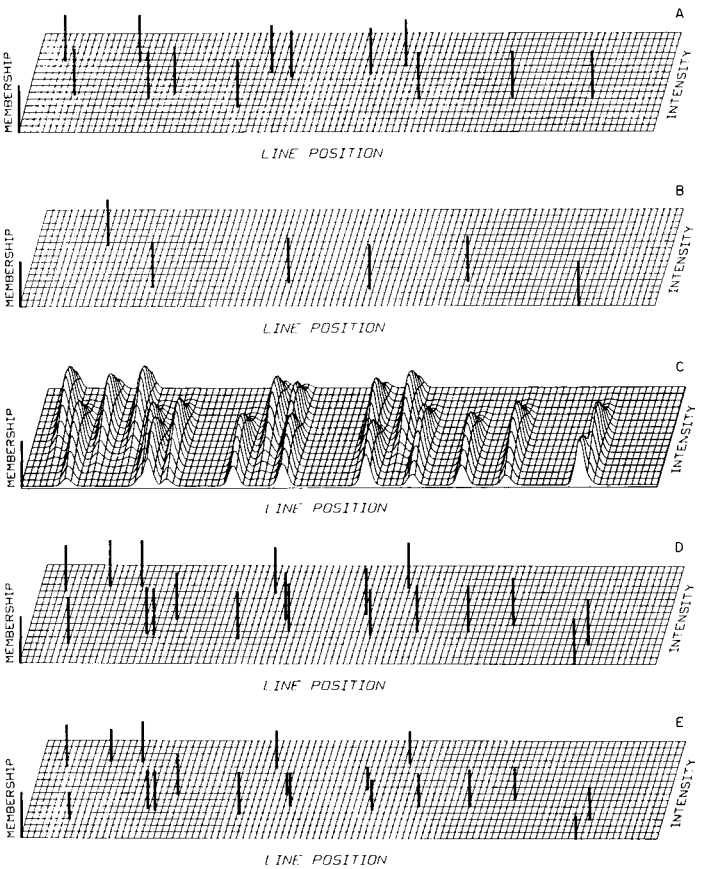

Fig. 10. Comparison of the measured set (D) with the fuzzed combination (C) of reference spectra (A, B) by a fuzzy intersection (E).

TABLE 1

Score table of the fuzzy match and the component identification [CIF Version 2.1 (IR)] for the sample mixture of Fig. 1. All 4 components are correctly identified in the best combination (*a*). In the remaining combinations (*b*, *c*, *d*), the hexane is replaced by another similar compound

No.	Score	Comb.	*I* (%)	Chemical name	Reference no.
1	9.8	*abcd*	36	Benzyl alcohol	0022
2	5.1	*a*	72	Hexane	0067
3	4.8	*abcd*	91	Butan-2-one	1701
4	4.8		44	Toluene	0019
5	4.7		76	Pentane	0208
6	4.7		91	2-Methylbutane	0003
7	4.7		91	2-Methylbutane[a]	0772
8	4.6	*b*	83	Nujol	0781
9	4.5		91	Nonane	0070
10	4.4	*d*	91	Octane	0069
11	4.2	*c*	83	Heptane	0068
12	3.9		55	2-Methyl-2-butene[a]	0215
13	3.7		58	2-Methyl-2-butene	0044
14	3.5		97	*o*-Xylene	1755
15	2.8		50	ABS	0656
16	2.0	*abcd*	95	Carbon tetrachloride	1764
17	1.6		95	Hexadecane	0075
18	1.4		100	2,2-Dimethylbutane	0035
19	1.4		63	2-Methyl-1-butene	0214
20	1.1		44	Benzyl benzoate	1233

[a]Spectrum recorded with higher resolution.

the number of fitting lines, and the *I*% value gives an estimate of the relative concentrations. The compounds belonging to the four best possible combinations are marked with *A*, *B*, *C*, *D*; all compounds with an "*A*" belong to the best combination, all compounds with a "*B*" to the second best, etc. A list with the combinations printed together is presented in Table 2.

CONCLUSION

In x-ray diffractometry, several search programs are available for the JCPDS reference library [5—9]. The present work was based on the SANDMAN search/match/identify program, which uses variable scoring rather than fixed window scoring [5, 10]. The parts of SANDMAN particular to x-ray diffractometry were incorporated into the new CIF program, where expression in terms of fuzzy set formulation makes adjustment of parameters associated with the search/match straightforward. This increased the reliability of CIF.

The CIF program, initially applied to x-ray powder diffraction, was

TABLE 2

List of best combinations [CIF Version 2:1 (IR)] for the sample mixture of Fig. 1; compounds belonging to a combination are printed together

No.	Score	Comb.	*I* (%)	Chemical name	Reference no.
Score of combination a = *25.5*					
1	9.8	*abcd*	36	Benzyl alcohol	0022
2	5.1	*a*	72	Hexane	0067
3	4.8	*abcd*	91	Butan-2-one	1701
16	2.0	*abcd*	95	Carbon tetrachloride	1764
Score of combination b = *25.3*					
1	9.8	*abcd*	36	Benzyl alcohol	0022
3	4.8	*abcd*	91	Butan-2-one	1701
8	4.6	*b*	83	Nujol	0781
16	2.0	*abcd*	95	Carbon tetrachloride	1764
Score of combination c = *24.4*					
1	9.8	*abcd*	36	Benzyl alcohol	0022
3	4.8	*abcd*	91	Butan-2-one	1701
11	4.2	*c*	83	Heptane	0068
16	2.0	*abcd*	95	Carbon tetrachloride	1764
Score of combination d = *24.2*					
1	9.8	*abcd*	36	Benzyl alcohol	0022
3	4.8	*abcd*	91	Butan-2-one	1701
10	4.4	*d*	91	Octane	0069
16	2.0	*abcd*	95	Carbon tetrachloride	1764

adapted to infrared spectroscopy. Changes had to be made for the conversion of the peak position and intensities (wavenumbers and %-transmittance) to an internally consistent format, and to produce the output in the appropriate scales.

The fuzzy set theory offers a new approach to spectrum library search problems. Fuzzy sets with a two-dimensional support can be used to describe membership of spectrum lines including positions and heights in the match and identify steps. The method was implemented in the CIF program, which is capable of resolving multicomponent samples in infrared spectroscopy as well as x-ray powder diffractometry. The usage of fuzzy set theory does not give the answer to problems caused by experimental errors, but supports the integration of chemical and physical knowledge into computerized interpretation of spectra in an illustrative manner.

The author thanks W. J. Dallas for helpful discussions and P. Smit for his advice on crystallographic problems and the preparation of samples for the program tests. The author also appreciates the work and helpful comments of R. Jenkins and W. N. Schreiner, which provided a basis for the CIF

implementation with the SANDMAN search/match/identify program. This work was sponsored by the German Federal Ministry for Research and Technology, grant number 08 IT 15227.

REFERENCES

1 K. S. Fu (Ed.), Digital Pattern Recognition, Springer-Verlag, New York, 1980.
2 L. A. Zadeh, Inf. Control, 8 (1965) 338.
3 L. A. Zadeh, Fuzzy Sets and Their Applications to Cognitive and Decision Processes, Academic Press, New York, 1975.
4 A. Kandel and W. J. Byatt, Proc. IEEE, 66 (1978) 1619.
5 W. N. Schreiner, C. Surdukowski and R. Jenkins, J. Appl. Cryst., 15 (1982) 513.
6 G. G. Johnson and V. Vand, Ind. Eng. Chem., 59 (1967) 19.
7 L. K. Frevel, C. E. Adams and L. R. Ruhberg, J. Appl. Cryst., 9 (1975) 199.
8 M. C. Nichols and R. C. Basinger, American Crystallographic Meeting, Berkeley, CA, 1974.
9 L. Tian-Hui, Z. Sai-Zhu, C. Li-Jun and C. Xin-Xing, J. Appl. Cryst., 16 (1983) 150.
10 W. N. Schreiner, C. Surdukowski and R. Jenkins, J. Appl. Cryst., 15 (1982) 524.

Analytica Chimica Acta, 161 (1984) 149—161
Elsevier Science Publishers B.V., Amsterdam — Printed in The Netherlands

ESTIMATION OF COMPONENT SPECTRA BY THE PRINCIPAL COMPONENTS METHOD

ARMIN MEISTER

Zentralinstitut für Genetik und Kulturpflanzenforschung, Akademie der Wissenschaften der DDR, DDR-4325 Gatersleben (German Democratic Republic)

(Received 6th December 1983)

SUMMARY

The principal components method enables component spectra from pigment mixtures to be estimated by evaluating the eigenvectors of the second moment matrix. The components are linear combinations of these eigenvectors, but cannot be identified unambiguously. With the conditions of non-negativity of spectral values and of concentrations, this ambiguity can be limited; component spectra for 2 and 3 components were calculated earlier. In the present work, maximal dissimilarity of component spectra is assumed as a further condition. An algorithm based on linear programming is described; it enables any number of components to be estimated from eigenvectors of the second moment matrix with better reliability than previously.

The principal components technique has often been used for the deconvolution of spectra or other distributions representing a sum of unknown components [1—4]. The number of independent components can be estimated from the variation of eigenvalues of the second moment matrix [2], from an indicator function which has a minimum for the correct number of eigenvalues [5], or from comparison of the experimental error with the residual error of fit (i.e., the difference between the experimental data and the data reproduced from the eigenvectors) [1, 3, 6]. The last criterion makes it possible to establish as many eigenvectors as are necessary to reproduce the data within the limits of experimental error.

However, the eigenvectors are not identical to the spectra of the components, which are linear combinations of the eigenvectors. Thus, any set of (linearly independent) linear combinations of the eigenvectors may be used as a basis for reproducing the experimental spectra. Consequently, it is impossible to establish the component spectra unambiguously by means of the principal components method. However, it is possible to limit this ambiguity by enforcing the condition that the component spectra (and the concentration coefficients which establish their relative contribution to the total spectrum) be not negative. The possible range of component spectra can then be limited significantly. In this way, reasonable component spectra were obtained for two [7, 8] and three [2] components. With an increasing

0003-2670/84/$03.00

number of components, such searches for reasonable component spectra become very complicated and even impossible in practice.

This paper introduces an algorithm which gives useful solutions for any number of components.

THEORY

General problem

A spectrum measured at h wavelengths can be formally represented by an h-dimensional vector $\vec{a}$, each element of which gives the signal intensity at one wavelength. Information about the number and spectral properties of the single components can be obtained only by measurement of a number of spectra containing the components in different amounts. The totality of measured spectra can be represented by a matrix A, each row containing the different spectra $\vec{a}_i$ and each column containing the data for one wavelength λ_j. Information on the number and shape of spectral components can be obtained from the eigenvalues and eigenvectors of the (non-central) second moment matrix M [2] with $\mathbf{M} = \mathbf{A}^T\mathbf{A}$. However, the eigenvectors $\vec{e}_m$ are not identical with the component spectra $\vec{b}_l$ which are linear combinations of the eigenvectors: $\mathbf{B} = \mathbf{T}\,\mathbf{E}$, where B, T and E are the component spectra matrix, a transformation matrix and the matrix of eigenvectors, respectively. The matrix T can be any nonsingular matrix. Its ambiguity can be restricted by two conditions which are valid for absorption and fluorescence spectra (but not, e.g., for circular dichroism spectra, which contain negative values). First, the component spectra must not contain negative values, i.e., the vectors $\vec{b}_l$ have only non-negative elements. Second, the experimental spectra $\vec{a}_i$ must be combined from the component spectra $\vec{b}_l$ only with non-negative coefficients (which correspond to the relative concentrations in the case of spectra).

The first condition can be expressed by

$$b_{lj} = t_{l1}\,e_{1j} + t_{l2}\,e_{2j} + \ldots + t_{lk}\,e_{kj} \geqslant 0 \quad (l = 1, 2 \ldots k; j = 1, 2 \ldots h) \tag{1}$$

for each element of B. In the k-dimensional space spanned by the k eigenvectors, these inequalities give $(k - 1)$-dimensional hyperfaces containing the origin and restricting the range of possible values for t_{lm}. These hyperfaces form an irregular (hyper)pyramid which opens in the direction of the (non-negative) first eigenvector and has its apex at the origin. Considering the non-negativity of the elements of the first eigenvector [7], the dimensionality can be reduced by one without loss of generality by replacing t_{lm} by $s_{lm} = t_{lm}/t_{l1}$. This means that the component spectra are normalized in such a way that they contain the first eigenvector with amount $s_{l1} = 1$ and the portions of the other eigenvectors are adjusted accordingly. This provides $(k - 2)$-dimensional restricting hyperfaces in a $(k - 1)$-dimensional space. These geometric facts are shown in Fig. 1 for $k = 3$ components. Figure 1(a) represents the pyramid, the volume of which contains the allowed range of

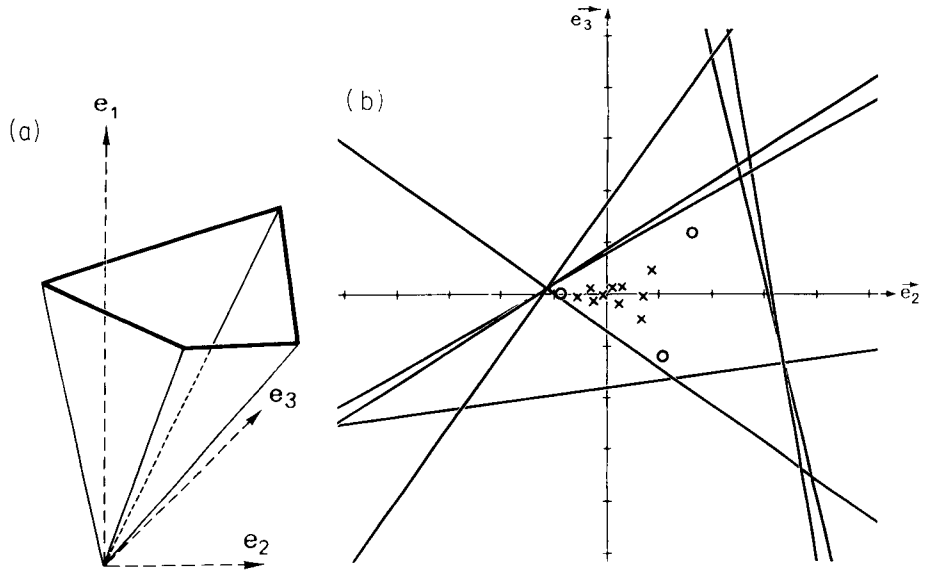

Fig. 1. Geometric description of the restrictions for $k = 3$ components. (a) The possible range is inside a pyramid, and the restrictions are essentially boundary surfaces. (b) A section of the pyramid at unit height, showing the restrictions as straight lines in a plane; the simulated spectra are indicated as crosses whereas the circles give 3 possible components.

parameters. If a plane is located perpendicularly to the first eigenvector at unit distance from the plane formed by the other two eigenvectors, Fig. 1(b) is obtained. Here the restrictions are given by lines (i.e., one-dimensional hypersurfaces) within a two-dimensional space.

In order to understand the geometric significance of the second condition, the location of 10 simulated spectra within the space spanned by the eigenvectors is indicated by crosses in Fig. 1(b). To make the spectra comparable, they have to be adjusted previously to contain the first eigenvector with the amount 1, i.e., they are projected onto the plane shown in Fig. 1(b). Now it becomes clear that the points of the plane representing the component spectra must have the following properties: (a) the points must be located within the restrictions given by the first condition; (b) the points representing the 3 components must form a triangle with all the points corresponding to simulated spectra inside it. In general, the points form a simplex [9], in the sense of linear programming theory. Any point $\vec{a}_i$ inside a simplex can be obtained from the component vectors $\vec{b}_l$:

$$\vec{a}_i = \sum_{l=1}^{k} \mu_l \vec{b}_l \quad \text{with } \mu_l \geqslant 0 \text{ and } \sum_{l=1}^{k} \mu_l = 1 \tag{2}$$

This latter condition is fulfilled in the present case because the amounts of $\vec{e}_1$ in $\vec{a}_i$ as well as in $\vec{b}_l$ (s_{l1}) are set arbitrarily to unity

$$\vec{a}_i = \sum_{l=1}^{k} \mu_l \vec{b}_l = \sum_{l=1}^{k} \sum_{m=1}^{k} \mu_l s_{lm} \vec{e}_m = \vec{e}_1 \sum_{l=1}^{k} \mu_l s_{l1} + \sum_{l=1}^{k} \sum_{m=2}^{k} \mu_l s_{lm} \vec{e}_m \qquad (3)$$

The proportion of $\vec{e}_1$ in $\vec{a}_i$ is set equal to 1 and so (with $s_{l1} = 1$)

$$\sum_{l=1}^{k} \mu_l s_{l1} = \sum_{l=1}^{k} \mu_l = 1 \qquad (4)$$

This consideration is valid for any number of dimensions: one has to find a simplex within the constraints which contains all the experimental points. For example, in Fig. 1(b), the circles mark a possible set of 3 component spectra which fulfil both conditions. For $k = 2$, the simplex is a straight line (the simplest case), for $k = 3$ a triangle (as in Fig. 1b), for $k = 4$, a tetrahedron, etc. In general, with both conditions, a wide range of ambiguity remains and it is necessary to consider how the vertices of the simplex should be established. A simplex of minimal volume may be a reasonable solution, provided that some of the mixtures measured contain each component in the nearly pure state. Otherwise the component spectra estimated depend strongly on the random nature of the measured compositions. Therefore, the method chosen in this paper gives the simplex with the maximal volume within the limitations of the first condition mentioned above; this is equivalent to selection of the most dissimilar component spectra. These spectra will generally not exactly agree with the real components but will exhibit their typical spectral properties (possibly in an exaggerated way). The problem is thus reduced to the determination of a $(k-1)$-dimensional simplex with maximal volume.

The volume of a simplex is given [9] by the determinant

$$\begin{vmatrix} 1 & 1 & 1 & \ldots 1 & \ldots 1 \\ \vec{b}_1 & \vec{b}_2 & \vec{b}_3 & \ldots \vec{b}_l & \ldots \vec{b}_k \end{vmatrix}$$

$\mathbf{b}_l$ being the $(k-1)$-dimensional column vectors of the vertices of the simplex. This would lead to a complicated problem of nonlinear programming. Therefore another way was used which enables the solution to be reduced to linear programming and application of the simplex method in an iterative way.

Determination of a simplex with maximal volume

It is assumed that any simplex is possible within the given restrictions consisting of k vertices and k constraint hypersurfaces. Proceeding from one of the k hyperfaces (which is defined by $k-1$ vertices), it is then possible to determine the point which is most distant from this hypersurface and meets the inequality given in Eqn. 1. If this point is different from the vertex opposite the hyperface, the new point will replace the old vertex, otherwise the old vertex will be preserved. Thus a simplex is found, the volume of which is not less than that of the former one. The immediate problems, of

course, are how this approach should be begun and when the iteration should be ended.

The initial set of component vectors is formed by the $(k-1)$ intersections of the eigenvectors $\vec{e}_m$ $(m \neq 1)$ with the constraint hypersurfaces and by the first eigenvector (i.e., the origin) itself. Because $\vec{e}_1$ is not located on a constraint hypersurface, it will be replaced first. The search for a larger simplex is ended when k successive iterations (i.e., proceeding once from each constraint hypersurface) do not produce an increased volume. The procedure is demonstrated in Fig. 2, which uses the example of Fig. 1(b): the first simplex is given by triangle OXY. In the search for the allowed point

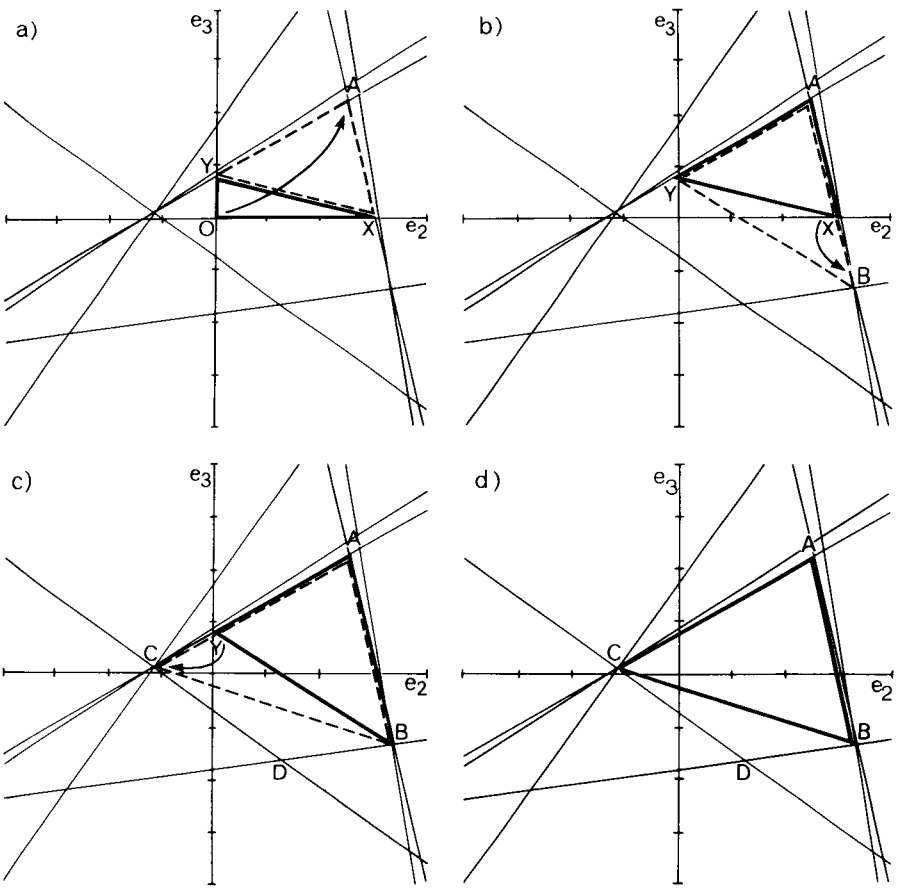

Fig. 2. Algorithm for finding the largest simplex within the given restrictions (Fig. 1 is used as example). (a) The initial simplex is given by the origin O and the intersections X and Y of the axis with the restrictions; the origin is replaced first by vertex A. (b) The intersecting point X is replaced by vertex B. (c) The intersecting point Y is replaced by vertex C; larger simplices are not possible. (d) Final simplex.

most distant from the line XY, O is replaced by A. The base of the next search is AY, and X is replaced by B; finally, C replaces Y. No larger triangle than ABC is possible: thus after three fruitless searches for a more distant point relative to the three sides of ABC, the calculation stops.

Construction and change of the simplex system

In the following geometric considerations, only the $(k-1)$-dimensional hypersurface which results from the condition $s_{l1} = 1$ will be considered. All vectors and simplices (except, of course, $\vec{e}_1$ itself) are thought to be located within this plane. The first eigenvector $\vec{e}_1$ marks the origin.

Initial points. The eigenvectors $\vec{e}_m$ (except the first one) intersect the constraint hypersurfaces at two points. These two points are given by

$$\vec{b}_m(1) = \vec{e}_1 - \mathrm{Min}_j(e_{1j}/e_{mj})\vec{e}_m$$

$$\vec{b}_m(2) = \vec{e}_1 - \mathrm{Max}_j(e_{1j}/e_{mj})\vec{e}_m$$

for all $e_{1j}/e_{mj} > 0$ or <0, respectively; $m = 2,3 \ldots k$. For the initial simplex, the point farthest from the origin is chosen. A matrix of component vectors (i.e., vertices of the simplex) is set up with the rows corresponding to the component vectors and the columns containing the amounts of the respective eigenvectors. These vectors in the rows describe the assumed components in the eigenvector space.

If V_m is the greater of the two extremes, the initial matrix of component vectors is given by

$$\mathbf{C} = \begin{pmatrix} 1 & -V_2 & 0 & 0 & \ldots & \ldots & 0 & 0 \\ 1 & 0 & -V_3 & 0 & \ldots & \ldots & 0 & 0 \\ 1 & 0 & 0 & -V_4 & \ldots & \ldots & 0 & 0 \\ & & & & & & & \\ 1 & 0 & \ldots & \ldots & \ldots & \ldots & 0 & -V_k \\ 1 & 0 & \ldots & \ldots & \ldots & \ldots & 0 & 0 \end{pmatrix}$$

Any set of $(k-1)$ component vectors (i.e., rows of **C**) defines one of the constraint hypersurfaces of the simplex, the kth vector being the vertex opposite this plane. Initially, the upper $(k-1)$ components are considered, and the point farthest from the corresponding hypersurface is calculated. The distance of this new point from the hypersurface is compared with those of the kth vertex (stored in the lowest row of **C**). If the new point is more distant, it will replace the old kth point in matrix **C**. The rows of **C** are then cyclically exchanged in such a way that the first row becomes the last. The process is then repeated with the new kth point.

Objective function. In order to set up the simplex system, an expression for the objective function is needed. It is given [10] by the distance d of the point considered from the corresponding hypersurface: $d = |\vec{r}\,\vec{n} - p|$, where p is the distance of the hypersurface from the origin, $\vec{n}$ is the normal vector of the hypersurface, and $\vec{r}$ gives the coordinates of the respective point.

The constraint hypersurface is defined by the upper $(k-1)$ vectors of matrix C. The normal vector of the face can be calculated as follows. The $(k-1)$ vertices located on the hypersurface considered have $d = 0$. The corresponding position vectors $\vec{v}_l$ are given by the lth row of matrix C except for the first element. These $(k-1)$ vertex vectors are sufficient to evaluate the $(k-1)$ elements of $\vec{n}$, using the system of equations: $\vec{v}_l \vec{n} = p$ (for $l = 1, 2, \ldots k-1$). Because the objective function need only be proportional to the distance, the unknown value of p can be set arbitrarily to 1 (i.e., the distances are normalized in such a way that the hyperface is distant by one unit from the origin). The equations can then be solved and the objective function is given by: $y = |\vec{r}\vec{n} - 1|$, where $\vec{r}$ is the position vector of the corresponding point.

Restrictions. The restrictions follow from the condition of non-negativity of spectral components

$$\mathbf{b}_{lj} = \sum_{m=1}^{k} \mathbf{s}_{lm}\, \mathbf{e}_{mj} \geqslant 0 \tag{5}$$

where l $(= 1, 2, \ldots k)$ denotes the respective component vector, m the respective eigenvector, and j $(= 1, 2, \ldots h)$ the elements of the vectors. Because $\mathbf{s}_{m1} = 1$,

$$\sum_{m=2}^{k} \mathbf{s}_{lm}\, \mathbf{e}_{mj} \geqslant -\mathbf{e}_{1j} \tag{6}$$

The simplex algorithm allows only non-negative variables, whereas in the present case, the $\mathbf{s}_{lm}$ values are not restricted to positive values. This problem can be evaded by splitting the $\mathbf{s}_{lm}$ values into $\mathbf{s}_{lm} = \mathbf{s}^{+}_{lm} - \mathbf{s}^{-}_{lm}$ with $\mathbf{s}^{+}_{lm} \geqslant 0$ and $\mathbf{s}^{-}_{lm} \geqslant 0$. Thus the restrictions have the final form

$$\sum_{m=2}^{k} (\mathbf{s}^{+}_{lm}\, \mathbf{e}_{mj} - \mathbf{s}^{-}_{lm}\, \mathbf{e}_{mj}) \geqslant -\mathbf{e}_{1j} \tag{7}$$

Consideration of the influence of the experimental error

The application of the simplex algorithm to the problem stated above does not supply a reasonable solution in every case. Sometimes the calculated component vectors are rather similar, e.g., in the experimental example of Fig. 3 (see also below). The plot of the restrictions in $(k-1) = 2$ dimensions is shown in Fig. 3(a). Most of the constraints are quite regular, but some seem to cross the pattern in an apparently arbitrary way. This effect can be explained by the high uncertainty of constraints in the case of very small coefficients of inequality (Eqn. 1) comparable with the experimental error.

The effect of error can be judged better by transforming the constraints (relation 6) to Hesse's normal form [10]

$$\vec{r}\,\vec{n} = \vec{r}\,\vec{e}_j^{*}/|\vec{e}_j^{*}| = -\mathbf{e}_{1j}/|\vec{e}_j^{*}| = d \tag{8}$$

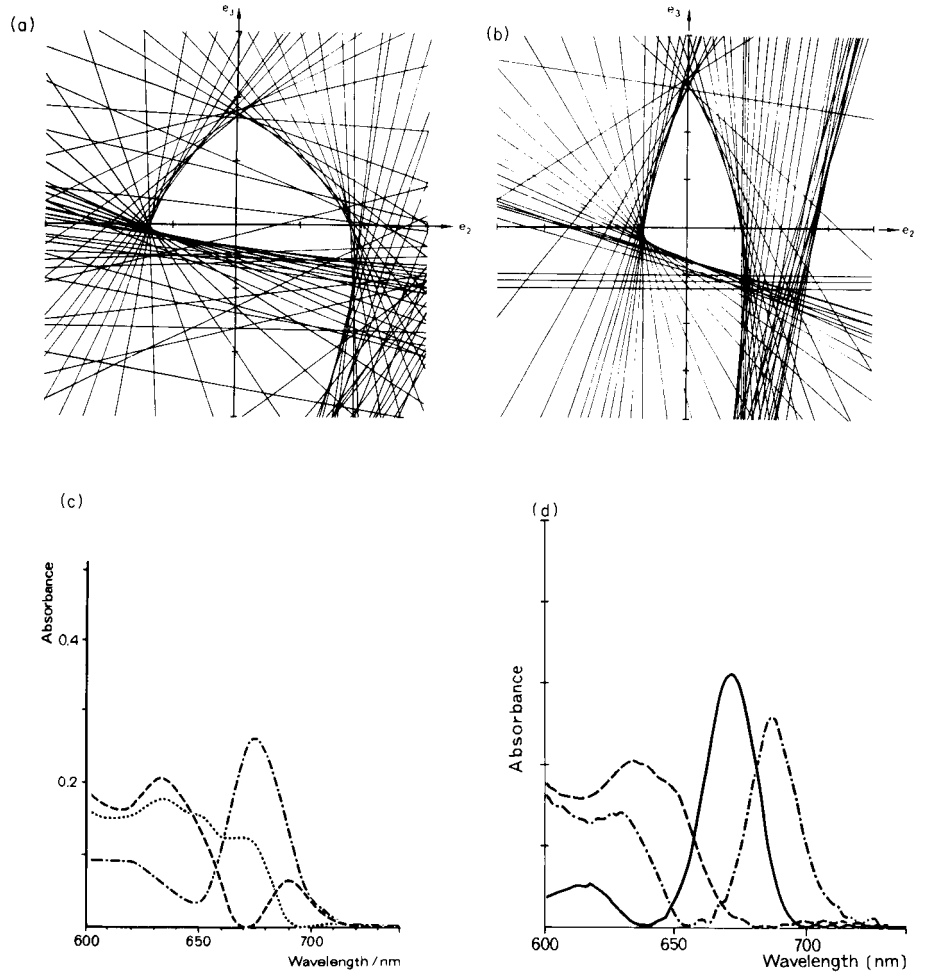

Fig. 3. Restriction lines and component spectra for the estimation of $k = 3$ components of pigment forms during the Shibata shift of chlorophyll biosynthesis. (a, b) Restriction lines without (a) and with (b) consideration of the experimental error. (c, d) Calculated component spectra without (c) and with (d) consideration of the experimental error. See text for further detail.

(for $j = 1, 2, \ldots h$). In Eqn. 8, $\vec{r}$ is the position vector of any point on the constraint hypersurface, and $\vec{e}_j^*$ is the column vector containing the jth elements of all the k eigenvectors except the first.

The normal vector $\vec{n} = \vec{e}_j^*/|\vec{e}_j^*|$ determines the orientation of the faces; $d = -e_{1j}/|\vec{e}_j^*|$ determines the distance from the origin. If all elements of $\vec{e}_j^*$ are very small compared to the experimental error, then $\vec{e}_j^*$ also becomes small and d and $\vec{n}$ become highly uncertain. In order to consider the error, appropriate weights must be given to the eigenvectors to make them com-

parable with each other and with the experimental data. These weights are proportional to the square root of the eigenvalues η [11]. The error of the absolute values of weighted eigenvectors is determined by the sum of the non-significant eigenvalues with the total weight $w = \Sigma_{m=k+1}^{\min} \eta_m$, where min indicates the number of rows or columns of the data matrix, whichever is the smaller.

Because each element of a (normalized) eigenvector with h elements has an average value of $1\ h^{-1/2}$, the error of the elements of weighted eigenvectors is: $\epsilon = [(\Sigma_{m=k+1}^{\min} \eta_m)/h]^{1/2}$. The following changes are then needed in the restrictions: (a) the $\mathbf{e}_{mj}$ values are weighted by $\eta_m^{1/2}$; (b) all elements $\mathbf{e}_{mj}\eta_m^{1/2} \leqslant \epsilon$ are eliminated; (c) the condition $\mathbf{b}_{ij} \geqslant 0$ is changed to $\mathbf{b}_{ij} \geqslant -\epsilon$, in order to allow small negative values within the limits of experimental error. The restrictions (Eqn. 1) thus change to

$$\mathbf{b}_{ij} = \sum_{m=1}^{k} \eta_m^{1/2} \mathbf{s}_{lm}\, \mathbf{e}_{mj} \geqslant -\left[\left(\sum_{m=k+1}^{\min} \eta_m\right)\Big/ h\right]^{1/2} \tag{9}$$

or

$$\mathbf{b}_{ij} = \sum_{m=2}^{k} \eta_m^{1/2}\, \mathbf{s}_{lm}\, \mathbf{e}_{mj} \geqslant -\eta_1^{1/2} \mathbf{e}_{1j} - \left[\left(\sum_{m=k+1}^{\min} \eta_m\right)\Big/ h\right]^{1/2} \tag{10}$$

The plot of the restrictions in the 2-dimensional example after weighting shows an essential improvement (Fig. 3b); the irregular restrictions vanish and the corresponding component spectra are more clearly distinguished.

Additional solutions

In most cases, the simplex volume can be increased by searching in two opposite directions proceeding from one simplex hyperface. For example, in the final configuration of Fig. 2(c) (broken line), the simplex side BC can be completed by either vertex A or vertex D. Generally, the larger increase in volume is used for the further search. It may be, however, that physical or chemical information indicates the other solution to be more relevant. For example, in Fig. 2(c), the vertex D might represent a more useful solution in the physical sense (cf. the position of data points in Fig. 1b). Therefore these additional solutions (simplex vertices) can be output if their simplex volume exceeds a given percentage of the volume of the main solution.

EXPERIMENTAL

The program is written in FORTRAN. A minicomputer KRS-4201 (VEB Kombinat ROBOTRON, Dresden) with 64K memory is used. The subroutine for the simplex algorithm is a simplified version of an ALGOL program described by Paulin and Griepentrog [12]. Because the coefficients of restrictive inequalities of successive wavelengths are often very similar, rather ill-conditioned matrices can result during computation. Therefore the simplex subroutine uses double-precision arithmetic (37 mantissa bits).

Absorption spectra were measured with a Unicam SP-800 spectrophotometer for solutions and with the apparatus described earlier [13] on light scattering on samples such as leaves and homogenates.

RESULTS

Figure 4 illustrates a simple theoretical example: three gaussian components with absorbance maxima at 650, 670 and 680 nm, respectively, are combined in different ratios. The resulting spectra are measured every 10 nm between 640 and 700 nm, giving 7 data points per spectrum. The eigenvectors are given in Fig. 4(a); the restrictions in the $\vec{e}_2$—$\vec{e}_3$ plane are plotted in Fig. 4(b). The greatest simplex is given by the vertices B1, B2 and B3, corresponding to the basic vectors. However, the basic vectors (Fig. 4c) do not agree well with the real components; the second basic vector (B2) behaves like a mixture of the components with peaks at 650 and 680 nm. Therefore, the additional vector **Z** is tested; it is really very similar to the component with a peak at 680 nm. The corresponding points in the plane of restriction lines (Fig. 4b) show that basic vectors B1 and B3 agree well with the real components C670 and C650, whereas Z is indeed very similar to C680.

The influence of weighting the eigenvectors and considering the experimental error is shown in Fig. 3 (see above). The data are absorption spectra from bean leaves (*Phaseolus coccineus*) grown in the dark, before and during the first 30 min of illumination. Seven spectra with 80 equidistant data each are measured between 603 and 739 nm. These spectra reflect the formation of chlorophyll from protochlorophyllide (maxima at 635 and 650 nm) by illumination and the interchange of two spectral chlorophyll forms absorbing at 672 and 684 nm [14]; thus, three components are to be expected. The eigenvalues confirm expectation. The restrictions (without weighting) are shown in Fig. 3(a); most of the restricting lines form a triangular shape,

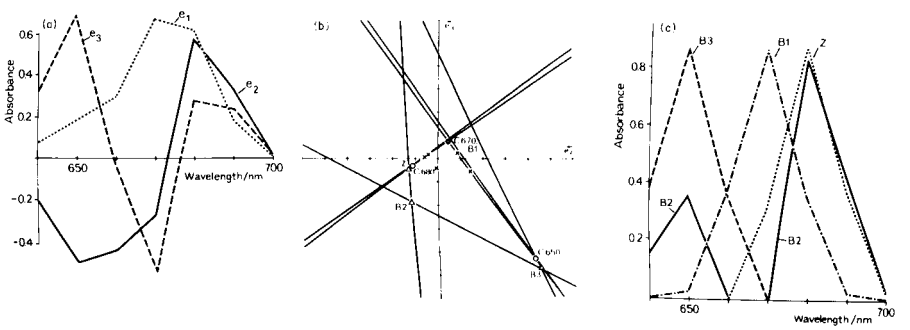

Fig. 4. Five mixtures of three simulated Gaussian components with absorption maxima at 650, 670 and 680 nm, respectively, and 18-nm half-width (measured at 7 wavelengths). (a) Eigenvectors. (b) Restriction lines: (×) data points; (○) points of real components; (△) points of calculated components (B1, B2, B3 = basic components, Z = additional component). (c) Calculated spectra of basic components (B1, B2, B3) and additional solution (Z).

though some disturb the pattern, probably because of the strong influence of experimental errors. The corresponding component spectra (Fig. 3c) are not clearly different, but seem to be mixtures of the supposed components. Therefore the eigenvectors were weighted and the elements less than the experimental error were omitted as explained above. The result is shown in Fig. 3(b), which exhibits a regular pattern with clear vertices which correspond to the assumed components. Figure 3(d) shows the corresponding calculated basic components which are much better separated and agree quite well with the expected pigment spectra.

Mixtures with variable amounts of chlorophyll a and b in acetone were prepared in order to check the applicability of the algorithm (Fig. 5a). If two components are assumed, the simplex degenerates to a line ($k - 1 = 1$ dimension), the final points of which correspond to the components. This case has been treated in principle by Lawton and Sylvestre [7]. Figure 5(b) demonstrates that the calculated basic spectra agree quite well with the real component spectra.

With a 4-component mixture of chlorophyll a and b and their magnesium-free analogues pheophytin a and b, a 3-dimensional simplex has to be considered. Despite the strong overlapping of the component spectra (the differences between peak positions are less than 20 nm, the average half-width of bands), the calculated basic spectra show at least the essential features of the component spectra. The real peak positions of the components are 644 nm (chlorophyll b), 652 nm (pheophytin b), 662 nm (chlorophyll a) and 665 nm (pheophytin a). Because of the search for maximal dissimilarity, the algorithm tends to overstate the differences.

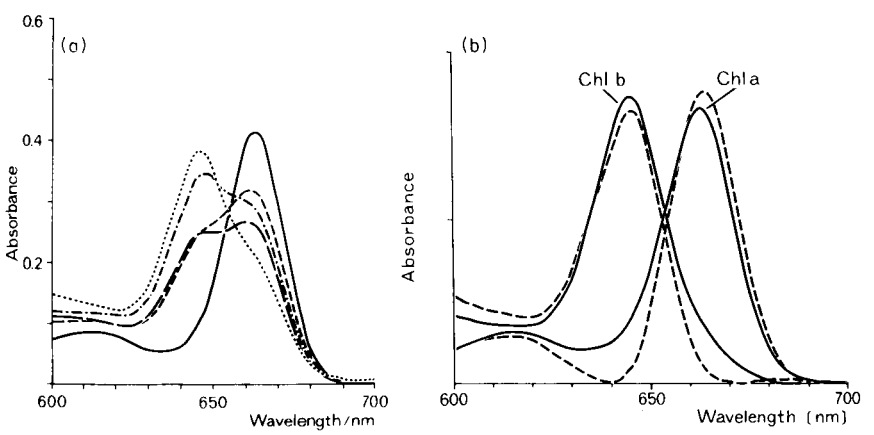

Fig. 5. (a) Experimental spectra of mixtures of chlorophyll a and chlorophyll b in acetone. (b) Spectra of chlorophyll a and b in acetone (solid lines) and the calculated component spectra (broken lines).

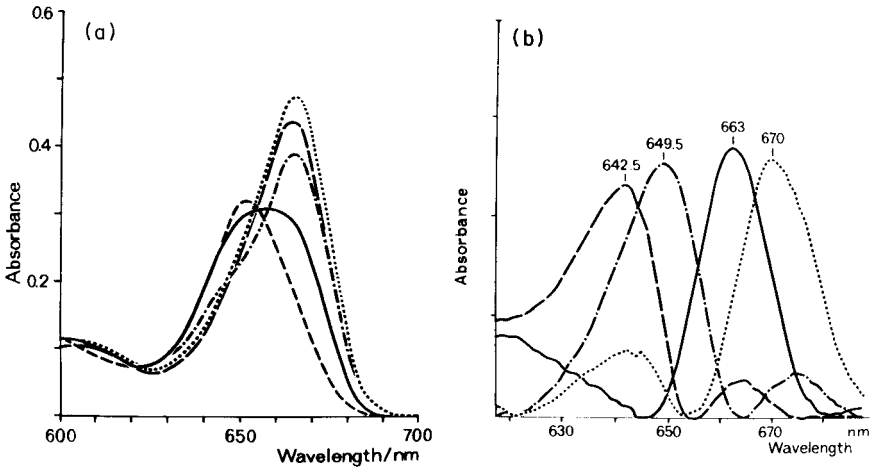

Fig. 6. (a) Experimental spectra of mixtures from chlorophyll a and b and pheophytin a and b in acetone. (b) Calculated component spectra (from the spectra of Figs. 5a and 6a). See text for further detail.

DISCUSSION

The principal components method allows an estimation of the number of independent components in a spectrum but does not provide information on the spectral properties of these components. The eigenvectors corresponding to the components span only the space of the component vectors (spectra), but the relation between eigenvectors and components is not unique. Each non-singular transformation of the eigenvectors can serve as a basis for evaluating the components. Useful component vectors can be obtained by different methods [15]: rotation of factors (orthogonal or oblique) can be used to maximize the variance of quadratic factor loadings (e.g., the varimax algorithm), or target vectors can be determined by attempting to span the eigenvector space by vectors which are assumed to be similar to the real components.

If the components are known to have only positive values and are to be combined with positive concentration coefficients, the multiplicity of solutions is considerably limited. Although in this case the components cannot be determined unambiguously, algorithms have been given [2, 7], which provide useful solutions. The disadvantage of these methods is their restriction to a maximum of three components. Furthermore, the possible combinations of three eigenvectors are evaluated by a trial-and-error process which requires a multitude of single calculations depending on the necessary density of points and the number of dimensions [2]. The algorithm presented in this paper establishes the extremely dissimilar component spectra which are in agreement with the conditions of non-negativity, and is applicable to any number of dimensions.

Considering the example given by Ohta [2], it becomes clear that the

algorithm described above will give essentially the same result for three components, i.e., it positions the component vectors in the corners of the triangular pattern (Figs. 4 and 6 of Ohta's paper). Because the algorithm locates the k components in the vertices of a $(k - 1)$-dimensional simplex, the vertices will touch at least $(k - 1)$ constraint hypersurfaces. However, each constraint hypersurface corresponds to one waveband, which means that the calculated component spectra have at least $(k - 1)$ zero elements. Thus, the more zero (or near zero) elements the real components contain, the more the calculated evaluation will pertain to the real situation.

If the spectra are measured at many wavelengths, there will be many constraint hyperfaces, which usually give a clear $(k - 1)$-dimensional structure and suggest an unambiguous solution (see, e.g., Fig. 3b). The existence of very similar restricting planes, however, will give rise to numerical problems in the simplex algorithms which have to be dealt with by using, for example, double precision arithmetic.

Although the algorithm presented cannot determine the component spectra unambiguously, like many before it, it may help the experimenter to find a useful solution. This can be important if there is no prior knowledge about the components that might be used as target vectors [15]. The application is confined to spectra or distributions which cannot contain negative values for physical reasons and which combine additively with positive coefficients (concentrations). This condition is met by conventional absorption and fluorescence spectra. The algorithm cannot, of course, take the ultimate decision about the real shape of possible components.

REFERENCES

1 J. J. Kankare, Anal. Chem., 42 (1970) 1322.
2 N. Ohta, Anal. Chem., 45 (1973) 553.
3 E. R. Malinowski, Anal. Chem., 49 (1977) 606.
4 J. M. Halket, J. Chromatogr., 175 (1979) 229.
5 E. R. Malinowski, Anal. Chem., 49 (1977) 612.
6 R. H. Morris and J. H. Morrissey, J. Opt. Soc. Am., 44 (1954) 530.
7 W. H. Lawton and E. A. Sylvestre, Technometrics, 13 (1971) 617.
8 I. M. Warner, G. D. Christian, E. R. Davidson and J. B. Callis, Anal. Chem., 49 (1977) 564.
9 W. Dück, Numerische Methoden der Wirtschaftsmathematik, Vol. 2, Akademie-Verlag, Berlin, 1973, p. 46.
10 I. N. Bronstein and K. A. Semendjajew, Taschenbuch der Mathematik für Ingenieure und Studenten der Technischen Hochschulen, Teubner Verlagsgesellschaft, Leipzig, 1958, p. 189.
11 E. Weber, Einführung in die Faktorenanalyse, VEB Gustav Fischer Verlag, Jena, 1974, p. 94.
12 G. Paulin and E. Griepentrog, Numerische Verfahren der Programmiertechnik, VEB Verlag Technik, Berlin, 1975, p. 69.
13 A. Meister, Exp. Tech. Phys., 14 (1966) 168.
14 K. Shibata, J. Biochem., 44 (1957) 147.
15 E. R. Malinowski and D. G. Howery, Factor Analysis in Chemistry, Wiley-Interscience, New York, 1980.

Analytica Chimica Acta, 161 (1984) 163—173
Elsevier Science Publishers B.V., Amsterdam — Printed in The Netherlands

APPLICATION OF THE GENERALIZED INTERNAL REFERENCE METHOD FOR THE CHARACTERIZATION OF PARAMETERS CAUSING DRIFT IN INDUCTIVELY-COUPLED PLASMA EMISSION SPECTROMETRY

AVRAHAM LORBER and ZVI GOLDBART
Nuclear Research Centre-Negev, P.O. Box 9001, Beer-Sheva 84190 (Israel)

(Received 26th September 1983)

SUMMARY

Drift in signals limits the performance of inductively-coupled plasma (i.c.p.) emission spectrometry. The generalized internal reference method was applied to deconvolute the drift of an i.c.p. system. The plasma parameters were correlated to the drift components and the error boundary for the method was found. In the system studied, it was found that fluctuations in the nebulizer uptake rate were responsible for short-term signal changes. Long-term signal drift was caused mainly by flow variations of both cooling gas and aerosol carrier gas. The incident power to the plasma was found to be stable compared to other sources of drift. The method was found to be adequate for evaluating the origins of i.c.p. drift.

The precision of an instrumental analytical system and its limit of detection (LOD) are characteristic figures for its performance and both are noise-dependent. The precision of inductively-coupled plasma emission spectrometry (i.c.p.e.s.) is limited by the non-random fluctuations of analyte signals at the wavelengths chosen for measurements, while the LOD is dependent on the fluctuations of the background signal taken at the wavelength chosen for the analyte. Boumans et al. [1] showed that for i.c.p.e.s. both characteristics are limited by flicker noise, statistical (shot) noise being negligible. An exception is the spectral range below 250 nm where the plasma continuum emission background is low, thus the LOD in this region is limited by statistical noise. Boumans et al. found that in their i.c.p. system the flicker noise was 0.5% for the background and 1% for the analytical signals. Therefore, it is important to examine the parameters affecting the noise in order to improve system performance.

An important method of system noise analysis is characterization of the noise by its power spectrum; this enables noise sources in the frequency range 0.01—100 Hz to be found. The fast Fourier transform (FFT) method has been applied to find the noise power spectrum of the background and analytical signals of i.c.p. systems [2—5]. Walden et al. [2] observed three types of noise: low-frequency noise, white noise and high-frequency (h.f.)

0003-2670/84/$03.00

proportional noise. They found that the h.f. proportional noise increased with analyte supply while low-frequency noise dominated when the observation point was raised. Belchamber and Horlick [3] also analysed the noise power spectrum of the i.c.p. system. They found that h.f. noise peaks corresponded to acoustic emission signals and studied the low-frequency region (0—5 Hz) which was found to be highly dependent on the type of nebulizer; they concluded that analyte flicker was the dominant noise source in this region. In order to confirm their conclusion, they studied the effect of increasing integration time on the noise in the analytical signals and found that although the statistics of the signal increased with increasing integration periods, there was no improvement in signal-to-noise ratio (S/N), and in some cases this ratio even worsened because of increased flicker noise. Duursma et al. [4] assumed that the nebulizing system is the major noise source in the i.c.p. system. They characterized the noise in the 0.01—100 Hz region by autocovariance function and power spectral density, and found a strong correlation between the emission signal noise and the nebulizing system noise as measured by aerosol density.

The above-mentioned methods succeeded in correlating signal fluctuations to fluctuations in one particular parameter which was supposed to be responsible for most of the analyte signal fluctuation. However, the characterized frequency range was limited in the high range down to 0.01 Hz. During the time needed for a single measurement (10 s), frequencies higher than 1 Hz are averaged. For a whole analytical procedure, (>0.5 h), frequency analysis is meaningless, because drift in system parameters causes signal variations.

In this paper, the adequacy of a method that can characterize fluctuations in all system parameters in the time region of analytical interest is verified. In a previous publication [6], a generalization of the well known internal reference method was suggested. This generalization detects variations in plasma parameters and thereafter corrects for their effect. Its adequacy in correcting for non-random noise in analytical signals was demonstrated [7].

THEORY

In the generalized internal reference (GIR) method, p internal standard spectral lines are correlated to r plasma parameters by the following set of equations [6]

$$
\begin{aligned}
I_{\mathrm{ref}}^{\mathrm{R}} &= \prod_{j=1}^{r} I_{\mathrm{ref},j}^{\mathrm{R}} \\
I_{2}^{\mathrm{R}} &= \prod_{j=1}^{r} f_{2,j}(I_{\mathrm{ref},j}^{\mathrm{R}}) \\
&\vdots \\
I_{i}^{\mathrm{R}} &= \prod_{j=1}^{r} f_{i,j}(I_{\mathrm{ref},j}^{\mathrm{R}})
\end{aligned}
\qquad (1)
$$

where I_i^{R} is the intensity of the signal in channel i divided by the intensity

of the same channel in the first measurement; $I^{R}_{ref,j}$ is the relative variation caused by change in plasma parameter j of the intensity in a channel chosen as a reference spectral line; $f_{i,j}$ is a function relating the jth component of the reference signal to ith internal standard.

It is convenient to express $f_{i,j}$ as a power series that passes through the origin (first measurement)

$$I^{R}_{i} - 1 = \prod_{j=1}^{r} [\alpha_{i,j}(I^{R}_{ref,j} - 1) + \beta_{i,j}(I^{R}_{ref,j} - 1)^2 + \ldots] \tag{2}$$

The coefficients $\alpha_{i,j}, \beta_{i,j}$, may be found by regression of a set of preliminary measurements to Eqn. 2. Assuming that the changes of the various parameters are relatively small, the set of Eqns. 1 can be expressed as a set of linear equations [6] which takes the form $\mathbf{Ax} = \mathbf{d}$. Here $\mathbf{A}$ is a $p \times r$ matrix of the linear coefficients $\alpha_{i,j}$; $\mathbf{x}$ is the plasma parameter drift vector of r parameters which are defined by $x_j \equiv I^{R}_{ref,j} - 1$; $\mathbf{d}$ is the signal drift vector for p internal standards defined by $d_i \equiv I^{R}_{i} - 1$.

When the GIR method is applied to compensate for changes in signals [7], $\mathbf{x}$ is calculated as an intermediate in the calculation of corrected signals. While the compensated signal may be very close to the true value of the signal, the error in calculating the various components of $\mathbf{x}$ can be large. When the GIR method is applied to calculate drift in plasma parameters, the deviation between the calculated value and the true value cannot be estimated as the precision of measurement of plasma parameters (such as gas flows and pressure) is insufficient. In that case, an estimate for the computation error must be found theoretically. The linear approximation, $\mathbf{Ax} = \mathbf{d}$, is very convenient for this purpose, as it provides an analytical expression for the error.

Perturbation bounds for the error in the computation of the vector $\mathbf{x}$

It is common to estimate computational errors by using norms. The "Euclidian vector norm" for the vector $\mathbf{v}$ of n elements is defined by

$$\|\mathbf{v}\| \equiv (\mathbf{v}^{T}\mathbf{v})^{1/2} = (\sum_{i=1}^{n} v_i^2)^{1/2} \tag{3}$$

The "spectral matrix norm" for the $m \times n$ matrix is defined by

$$\|\mathbf{G}\| \equiv \max_{\|\mathbf{v}\| = 1} \|\mathbf{G}\,\mathbf{v}\| = \lambda_1^{1/2} \tag{4}$$

where λ_1 is the largest eignevalue of matrix $\mathbf{G}^{T}\mathbf{G}$.

Solving $\mathbf{Ax} = \mathbf{d}$ for x_j results in an inaccuracy δx_j, as the measured values d_i have errors δd_i and the matrix coefficients $\alpha_{i,j}$ are evaluated with errors $e_{i,j}$. The equation $\mathbf{Ax} = \mathbf{d}$ then becomes

$$(\mathbf{A} + \mathbf{E})(\mathbf{x} + \delta\,\mathbf{x}) \simeq \mathbf{d} + \delta\,\mathbf{d} \tag{5}$$

When this equation is inverted to find **x**, the error is propagated by the following mathematical situations. First, the matrix **A** is nearly singular, in which case some rows or columns are linearly dependent. When the matrix is nearly singular, small deviations in **d** and **E** are propagated and δ **x** becomes large. No error propagation results when the columns of **A** are orthogonal. The spectral norm $\|\mathbf{A}^+\|$ of the Moore-Penrose pseudoinverse $\mathbf{A}^+$ is used to measure the singularity of matrix **A** [8]. The spectral norm is $\|\mathbf{A}^+\| = \lambda_k^{-1/2}$ where λ_k is the smallest significant eignevalue of matrix with rank (**A**) = k. The higher the spectral norm, the nearer **A** is to singularity.

Secondly, the differences ρ_i between the measured and calculated values of d_i are $\rho = \mathbf{d} - \mathbf{Ax}$, which measures the degree of matching between the experimental values and the mathematical model.

The above causes lead to the following perturbation boundary for **x** [8]

$$\|\delta\,\mathbf{x}\| \leqslant \|\mathbf{A}^+\|\,[(\|\mathbf{E}\|\cdot\|\mathbf{x}\|)/(1-\|\mathbf{E}\|\cdot\|\mathbf{A}^+\|) + (\|\delta\,\mathbf{d}\|)/(1-\|\mathbf{E}\|\cdot\|\mathbf{A}^+\|) + (\|\mathbf{E}\|\cdot\|\mathbf{A}^+\|\cdot\|\rho\|)/(1-\|\mathbf{E}\|\cdot\|\mathbf{A}^+\|) + \|\mathbf{E}\|\cdot\|\mathbf{x}\|] \quad (6)$$

For $p > r$ and rank (**A**) = $k < r$ and when $\|\mathbf{E}\|\cdot\|\mathbf{A}^+\| < 1$, the following special cases exist for Eqn. 6: when rank (**A**) = $k = r$, the fourth term vanishes; when rank (**A**) = $k = p = r$, the third term also vanishes. When $\|\mathbf{E}\|\cdot\|\mathbf{A}^+\| \geqslant 1$, the rank is lower than assumed, and λ_{k-1} should be taken as the smallest significant eigenvalue. The physical reasons for rank (**A**) = $k < r$ were discussed previously [6].

EXPERIMENTAL

The experimental facilities, including a simultaneous multichannel photodiode system, were as described earlier [7]. Two holographic gratings were used: 3000 grooves mm^{-1}; resulting in a 10-nm spectral window (416–426 nm), and 2400 grooves mm^{-1} with a 13-nm spectral window (395–408 nm). Drift measurements in Fig. 1 were taken every 1 min to point 20 and every 15 min from then on. In Fig. 2 the measurements were taken every 30 s for 30 min. The plasma parameters (incident power, plasma gas flow rate, aerosol carrier gas flow rate and solution uptake rate) were the same as previously [7]. The effect of solution uptake rate was calibrated in this work by contracting the feed solution tube to various degrees.

RESULTS AND DISCUSSION

Selection of spectral lines and plasma parameters

The spectral lines that are used in the GIR method should have a wide range of excitation and ionization potentials, so that the response of the various spectral lines to the variations of plasma parameters will be different. This is necessary in order to avoid singularity of the matrix **A**. Spectral lines with different excitation and ionization potentials will respond dif-

ferently to changes in plasma parameters. Table 1 presents two sets of spectral lines, chosen according to this criterion, with the corresponding excitation and ionization energies. The set of spectral lines within the 416—426-nm spectral window served previously [7] to correct for drift in analytical lines. However, the coefficient matrix resulting from this set was close to singularity. It has been claimed that the Ar 404.44-nm line, is most sensitive to changes in incident power [9]. Therefore a second set was taken in the 395—408-nm spectral window that included this argon line.

Another possible cause for singularity is that the chosen plasma parameters are interdependent. It was suspected that the calibration of sample uptake rate by changing the hydraulic head is not independent of the other parameters; therefore, the uptake rate was changed by squeezing the liquid intake tube.

Calibration of the coefficients in Eqn. 2.

Solution of Eqn. 1 determines the relative changes of intensity of the components of the reference line, $I^{R}_{ref,j}$. In order to solve this equation, the changes in reference line intensity must be calibrated against changes in internal standard lines, i.e., the coefficients $\alpha_{i,j}$, $\beta_{i,j}$, in Eqn. 2 must be evaluated.

Data obtained by changing one plasma parameter with all the rest held constant, was regressed to Eqn. 2. The first and second terms were included, but higher terms were neglected. The calculated linear coefficients, $\alpha_{i,j}$, are presented in Table 2; both reference lines are ionic europium lines.

TABLE 1

Spectral lines and their relevant physical constants for the two data sets

Spectral window (nm)	Element	Wavelength (nm)	Excitation energy (eV)	Ionization energy (eV)	Sum of energies (eV)
395—408	Al I	396.15	3.14	5.98	—
	Ca II	396.85	3.12	6.11	9.23
	Eu II	397.20	3.33	5.64	8.97
	Mn I	403.08	3.08	7.43	—
	Ar I	404.44	14.68	15.76	—
	Sr II	407.77	3.04	5.69	8.73
416—426	Ga I	417.21	3.07	6.00	—
	Ar I	419.83	14.74	15.76	—
	Eu II	420.51	2.95	5.64	8.59
	Sr II	421.55	2.94	5.69	8.63
	Ca I	422.67	2.93	6.11	—
	Sc II	424.68	3.23	6.54	9.77
	Cr I	425.44	2.91	6.76	—

TABLE 2

Linear term regression coefficients of correlating Eqn. 2 for the two data sets

Spectral window (nm)	Spectral line (nm)		Uptake rate	Incident power	Aerosol carrier gas	Cooling gas
395–408	Al I	396.15	1.003	0.820	0.517	−0.076
	Ca II	396.85	1.016	1.341	1.092	0.973
	Eu II	397.20	1.000	1.000	1.000	1.000
	Mn I	403.08	1.183	−1.127	−3.224	−0.189
	Ar I	404.44	−0.445	0.521	6.533	−2.774
	Sr II	407.77	0.995	1.129	1.235	1.013
416–426	Ga I	417.21	−1.503	0.210	−0.124	0.000
	Ar I	419.83	0.412	1.284	0.208	−1.124
	Eu II	420.51	1.000	1.000	1.000	1.000
	Sr II	421.55	1.258	1.187	1.157	1.141
	Ca I	422.67	−2.821	−0.198	−0.737	−0.423
	Sc II	424.68	1.708	1.431	1.418	1.377
	Cr I	425.44	−2.334	−0.369	−0.691	−0.384

Computation of the error boundary

The reliability of the results obtained by the GIR method is critically dependent on accurate estimation of the errors associated with the drift determined for the plasma parameters. The error boundaries are calculated from Eqn. 6. The various numerical quantities were evaluated as follows. First, the eigenvalues were calculated by the singular value decomposition technique [8], which gives the values of singular values which are the square roots of the eigenvalues. The values are presented in Table 3. Secondly, the relative standard deviation in measuring each spectral line intensity, I_i^R, was found to be 0.07% [7]. For a six spectral-line vector, the 95% confidence interval is $7.49 \times 10^{-4} < \|\delta \mathbf{d}\| < 2.33 \times 10^{-3}$. Thirdly, the norm of the vector ρ defined by $\rho = \mathbf{d} - \mathbf{Ax}$ was found to range from 0.001 to 0.0001. The results for the 416–426-nm spectral window have been presented in detail [7].

Finally, the uncertainty in the matrix **A** depends on both the deviation of the linear approximation from the real case and the quality of the regression. The maximum values of $\|\mathbf{d}\|$ observed for consecutive measurements were 2%; considering that the quadratic coefficients were usually lower than the linear ones, the error resulting from neglecting the quadratic coefficient is less than 0.04%. The quality of regression was estimated from the regression coefficients that ranged from 0.95 to 0.999, with mean values of 0.99 [7]. Therefore, $\|\mathbf{E}\|$ may be estimated as 1% of the value $\|\mathbf{A}\|$, i.e., the contribution of the quadratic term is negligible.

The validity of Eqn. 6 depends on satisfying the condition, $\|\mathbf{E}\| \|\mathbf{A}^+\| < 1$. Inserting the calculated values yields 1.1 for the 416–426-nm and 0.15 for the 395–408-nm spectral window. Therefore, Eqn. 6 may be used for the

TABLE 3

Singular values of the coefficient matrices presented in Table 2

Spectral window (nm)	Singular values[a]			
	1	2	3	4
416—426	7.83	3.61	1.74	0.43
395—408	5.57	2.22	1.71	0.04

[a]The singular values are the square roots of the eigenvalues.

data gathered from the latter window. This result was also confirmed by checking for singularity. The following ratio is used for singularity test [10]: $\Sigma_{j=k+1}^{r} \lambda_j^{1/2} / \Sigma_{j=1}^{k} \lambda_j^{1/2}$. This ratio presents the relative contribution of the kth eigenvalue to the total data reproducibility. Inserting the values from Table 3 yields the values 0.4% and 3.3% for the 416—426-nm and 395—408-nm spectral windows, respectively. The low value obtained for the 416—426-nm data indicates that this case is very probably singular. Therefore, no error boundary may be obtained for the 416—426 nm spectral window. The following calculation of error boundary will be related only to the 395—408-nm data.

The fourth term in Eqn. 6 may be omitted because rank (A) = $r = k$. The third term also vanishes, as it contains a multiple of two comparatively small values. The denominator is close to unity, and is assumed to be unity. Equation 6 is then simplified to

$$\|\delta \mathbf{x}\| \leqslant \|\mathbf{A}^{+}\| [\|\mathbf{E}\| \cdot \|\mathbf{x}\| + \|\delta \mathbf{d}\|] \tag{7}$$

The relative significance of the remaining two terms can be compared by using the inequality $\|\mathbf{x}\| \leqslant \|\mathbf{A}\| \cdot \|\mathbf{d}\|$. When this is inserted into expression 7, the resulting expression is

$$\|\delta \mathbf{x}\| / \|\mathbf{x}\| \leqslant \mathrm{Cond}(\mathbf{A}) \cdot [(\|\mathbf{E}\| / \|\mathbf{A}\|) + (\|\delta \mathbf{d}\| / \|\mathbf{d}\|)] \tag{8}$$

where $\mathrm{Cond}(\mathbf{A}) \equiv \|\mathbf{A}\| \cdot \|\mathbf{A}^{+}\| = (\lambda_1 / \lambda_k)^{1/2}$ is the condition number [8]. It is obvious that, as that the first term equals 0.01, the major contributor to the error is the second term, and the first can be neglected. Then, from expression 7, the term for error boundaries simplifies to

$$\|\delta \mathbf{x}\| \leqslant \|\mathbf{A}^{+}\| \cdot \|\delta \mathbf{d}\| \tag{9}$$

which is independent of the actual experimental values for each measurement. When the values of $\|\delta \mathbf{d}\|$ obtained above are inserted in expression 9, the 95% confidence interval obtained for the error boundary is $1.7 \times 10^{-3} < \delta \mathbf{x} < 5.4 \times 10^{-3}$. This error boundary acts as a maximal expected error, and is lower than the expected fluctuations of the plasma parameters.

Determination of the drift in the plasma parameters

Solution of Eqn. 1 determines the relative changes in the intensities of the components of the reference line. In order to relate these to changes in the plasma parameters, one must calibrate the changes in the reference line intensity to changes in plasma parameters. The calibration curve was assumed to match a quadratic equation

$$y_j = a_j x_j + b_j x_j^2 \tag{10}$$

where a_j and b_j are the linear and quadratic coefficients for the jth plasma parameter.

The coefficients found are presented in Table 4. The uptake rate was not calibrated, as it was assumed that the relative measured change in the components of the reference line attributable to it would be the same as the relative change in uptake rate.

Noise analysis

In multi-element atomic emission spectrometry two main modes for data gathering are used: sequential scanning or multichannel detection. The high-frequency noise analysis is important for the sequential scanning monochromator; when a direct-reading spectrometer is used, this region is of diminishing importance as the integration period is increased. Increasing the integration period above 1—5 s did not give any improvement although the signal statistic improved [3]. Those facts indicate that non-random fluctuations that are not averaged during 10 s are of main interest for both types of detection systems but especially for direct-reading spectrometers. There

TABLE 4

Coefficients of the calibration function and regression coefficients r for the quadratic equation

Spectral window (nm)	Plasma parameter	a_j	b_j	r
395—408	Incident power	0.328	−0.173	0.999
	Aerosol gas	−1.850	−0.067	0.995
	Cooling gas	−2.380	2.093	0.995
416—426	Incident power	1.074	0.031	0.998
	Aerosol gas	−2.600	−4.190	0.946
	Cooling gas	−2.137	1.033	0.990

are two time domains which are of analytical interest: (a) 10—60 s, which is the time needed for one sample analysis or the time between samples, fluctuations within this interval affecting measurement repeatability; (b) 0.5—2 h, which is the time needed for a complete analytical procedure. Fluctuations in the latter range will affect the applicability of the calibration curve (taken at zero time) to the sample.

Figure 1 depicts the fluctuations of the Eu II 397.20-nm line which served as reference spectral line in the 395—408-nm region, that were recorded for 2.5 h. The four computed components related to the four plasma parameters are also shown. It is obvious that the calculated fluctuations are larger than the error boundary.

The data from the first 20 measurements served for evaluation of the 0.1-Hz region. The components of the reference line were transformed by Eqn. 10 and by the coefficients presented in Table 4 to calculate the fluctuations of the plasma parameters. The RSD and mean value for these points are presented in Table 5. From Fig. 1 and the data in Table 5, the following conclusions and observations can be drawn.

Uptake rate. The component of the reference line related to the uptake rate in Fig. 1 remains constant over 10 min with RSD of 0.46%, which is larger than the RSD of the reference line (0.28%), while the deviation is 0.11%. The drift for two more hours is negligible; thus, this parameter does not contribute to the drift of the reference signal. It was noticed, however, that deviations in the uptake rate are correlated to those of the Eu reference

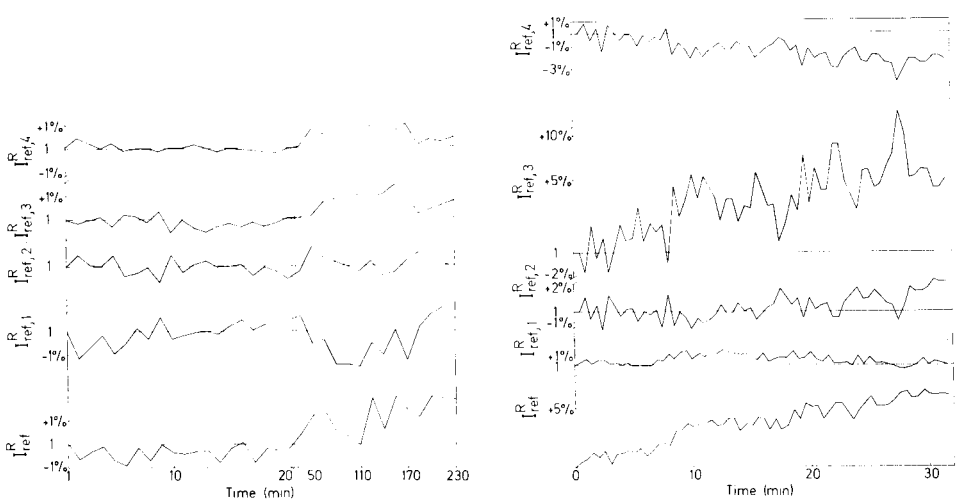

Fig. 1. Fluctuation of Eu II 397.20-nm reference line with its four computed components related to the four plasma parameters: $I^{R}_{ref,1}$, uptake rate; $I^{R}_{ref,2}$, incident power; $I^{R}_{ref,3}$, nebulizing gas flow rate; $I^{R}_{ref,4}$, plasma gas flow rate.

Fig. 2. Fluctuation of the Eu II 420.51-nm reference line with its four computed components related to the four plasma parameters. Symbols as for Fig. 1.

TABLE 5

Mean and RSD of the reference line and its components in the 395—408-nm region for the first 20 intervals

Variable	Mean	RSD (%)
Uptake rate	0.9993	0.46
Incident power	0.9995	0.32
Aerosol gas	0.9987	0.23
Cooling gas	1.0001	0.16
Eu II 397.20	0.9966	0.28

line. This explains the results of previous work [2—5] that considered this plasma parameter as the major source of drift; their noise analysis was limited to frequencies higher than 0.01 Hz.

Incident power. The component representing power variation shows no long-term drift; the 0.32% RSD is in accordance with manufacturers' specification (<0.5%). This finding explains the results of Anderson et al. [11] who controlled the gas flow rates by mass flow meters and used an improved type of nebulizer to eliminate nebulizer contribution to the fluctuations. With these improvements, the remaining noise was about 0.3—0.4%, which can be regarded as the effect of power instability.

Argon flow rates. Both aerosol carrier gas and cooling gas flow rates show small short-term variations (RSD 0.2%), but exhibit step function changes in the long term. It seems that, in the system examined, the argon supply drift is the major source of drift for the entire system.

Figure 2 shows the changes in the component of the reference line (Eu II 420.51 nm) and in the signal itself for the 416—426-nm window. This case is found to be singular, therefore, it is interesting to consider how the GIR method succeeded in resolving the components in this data set. Surprisingly, Fig. 2 shows that the components of the reference line varied in the same manner as the well-conditioned case. It is also obvious that the main source of drift is the argon flow, while other parameters exhibit short-term fluctuation only.

CONCLUSIONS

The study of noise reported above demonstrated the applicability of the GIR method to noise analysis if appropriate spectral lines and plasma parameters are selected. The frequency range studied is of interest to users of multichannel systems, while studies of higher frequencies may benefit users of sequential monochromators and investigators of dynamic processes and excitation mechanism of the i.c.p.

The RSD of the low-frequency (0.01—0.002 Hz) noise, arising from plasma parameters, can be interpreted for the contribution of each plasma

parameter as follows. The noise from incident power to the plasma and gas flows is comparatively low and well below specification. Sample uptake rate noise is the limiting factor in the compounded noise, causing short-term (1 min) variations. The very low-frequency (<0.002 Hz) behavior of the plasma parameters should be examined cautiously, as it may depend on a specific date and configuration of the system. Nevertheless, some conclusions can be drawn for the system examined. Thus, long-term drift cannot be foreseen as it depends on laboratory conditions and human intervention. The argon flow control should be improved, as it is the main cause of noise in this frequency range. To eliminate this noise, the system should be recalibrated at short intervals, or preferably the GIR method should be coupled to data treatment for drift correction.

Different nebulizers and other subsystems are under study. The method described can be applied not only to i.c.p. systems but to any flicker noise-limited multichannel system.

REFERENCES

1 P. W. J. M. Boumans, R. J. McKenna and M. Bosveld, Spectrochim. Acta, Part B, 36 (1981) 1031.
2 G. L. Walden, J. N. Boewer, S. Nikdel, D. L. Bolton and J. D. Winefordner, Spectrochim. Acta, Part B, 35 (1980) 535.
3 R. M. Belchamber and G. Horlick, Spectrochim. Acta, Part B, 37 (1982) 17, 71.
4 R. P. J. Duursma, H. C. Smit and F. J. M. J. Maessen, Anal. Chim. Acta, 133 (1981) 393.
5 P. Benetti, A. Bonelli, M. Cambiaghi and P. Frigieri, Spectrochim. Acta, Part B, 37 (1982) 1047.
6 A. Lorber and Z. Goldbart, Anal. Chem., 56 (1984) 37.
7 A. Lorber, Z. Goldbart and M. Eldan, Anal. Chem., 56 (1984) 43.
8 C. L. Lawson and R. J. Hanson, Solving Least Squares Problems, Prentice-Hall, Englewood, NJ, 1974.
9 S. Greenfield, ICP Inf. Newsl., 4 (1978) 199.
10 E. R. Malinowski and D. G. Howery, Factor Analysis in Chemistry, Interscience-Wiley, New York, 1980.
11 H. Anderson, H. Kaiser and B. Meddings, in R. M. Barnes (Ed.), Developments in Atomic Plasma Spectrochemical Analysis, Heyden, London, 1981, p. 251.

Analytica Chimica Acta, 161 (1984) 175—189
Elsevier Science Publishers B.V., Amsterdam — Printed in The Netherlands

SOFTWARE PACKAGE FOR QUANTITATIVE ANALYSIS OF SOLID MATERIALS BY ENERGY-DISPERSIVE X-RAY FLUORESCENCE SPECTROMETRY WITHOUT ABSOLUTE CALIBRATION

BJARNE BO JENSEN, JØRN NICOLAJ MARCUSSEN and NIELS PIND*

Department of Chemistry, Aarhus University, Langelandsgade 140, DK-8000 Aarhus C (Denmark)

(Received 9th January 1984)

SUMMARY

A software package for quantifying elements in solids from energy-dispersive x-ray fluorescence data is described. The algorithm is based on the fundamental parameter approach and facilitates the simultaneous determination of several elements at widely varying concentrations. The software comprises three programs. One program, for spectrometer control and data acquisition, resides in a dedicated microcomputer. The two other programs, for spectra deconvolution and data evaluation, reside in a larger central computer. On-line communication between the computers is feasible, and the system facilitates the implementation of new improved programs. The performance of the system was tested on standard reference materials, and satisfactory accuracy was obtained for up to 21 elements.

X-ray fluorescence spectrometry is well suited for direct elemental analysis of solid samples. Quantitative analysis, however, is often hampered by inter-element effects [1], and in general there is no simple relationship between measured fluorescence intensities and element concentrations. When element concentrations have to be determined in a series of samples of fairly constant composition, quantitative information can often be obtained by influence coefficient techniques [1]. However, to obtain accurate results, the elemental composition of the standards must be close to the composition of the unknown sample, and the approach is not suitable for the analysis of materials of widely variable composition. The fundamental parameter technique is better suited for the analysis of materials of essentially unknown composition, and the necessary number of standards is much smaller. However, for the technique to be practicable, the x-ray spectrometer must be connected to a computer which is sufficiently large to execute programs containing suitable algorithms. Mostly, commercially available spectrometers are equipped with a microcomputer, which takes care of the data acquisition and spectral deconvolution and algorithms for quantitative evaluation are sometimes provided. However, mostly the source texts of these programs are not available to the user, and the implementation of new programs based on improved mathematical models is not possible.

0003-2670/84/$03.00

Access to large and medium-sized computers is now common in many laboratories, and microcomputers are cheap. Thus, for quantitative x-ray fluorescence spectrometry, advantage can be taken of combining the speed of a dedicated microcomputer for data acquisition and spectrometer control with the size and extensive access to peripherals of a time-shared central computer. The present paper describes a software system developed and used in this laboratory. The system is composed of three modules, one for data acquisition, one for spectral deconvolution, and one for quantitative evaluation. Special attention is given to the quantitative procedure, which is based on the use of fundamental parameters. A standardless procedure based on the work of Mantler and Ebel [2] and on the mathematical development suggested by Sparks [3] for secondary target energy-dispersive spectrometry has been developed and is included as an option in the quantitative program. The program is designed to permit easy change of the calculation algorithms.

Results obtained from the standardless analysis of NBS alloys SRM 1158, 1198, 1199, 1200, 1201, 1208-1 and NBS environmental samples SRM 1633a (Coal Fly Ash) and SRM 1645 (River Sediment) are given to illustrate the performance of the system. The lead contents in SRM 1633a and 1645 were confirmed by an independent technique. These concentrations were used as internal standards to calculate the remaining element concentrations from the x-ray fluorescence data.

EXPERIMENTAL

Apparatus

The energy-dispersive x-ray spectrometer included a laboratory-built excitation chamber, a conventional high-power spectrometer tube and x-ray generator, a conventional solid-state detector and associated electronics, and a microcomputer with laboratory-built interfacing. The excitation chamber was based on the secondary fluorescence principle and was equipped with six easily changeable secondary targets (Ti, Se, Mo, Ag, Te and Gd), which allowed effective excitation over a wide range of elements. Apart from a few minor changes, the excitation chamber was as described in detail by Christensen et al. [4]. The secondary targets were excited by a spectrometer tube with a gold anode. When Mo, Ag, Te or Gd was chosen as target, interferences from the Au *L*-lines were eliminated by a 1-mm thick aluminium (99.99%) filter in front of the tube window. The tube was powered by a Philips PW 1732/10 high-voltage generator (60 kV, 80 mA, max. 4 kW). The solid-state detector was a DTG Si(Li) detector with pulsed optical feedback (crystal dimensions 30 mm^2 × 4 mm, resolution 160 eV at 5.9 keV). The main amplifier was a CANBERRA model 2020 spectroscopy amplifier with pulse pileup rejection, and the analog-to-digital converter (ADC) was a CANBERRA model 2070. The digitized signals were stored in a MOTOROLA 68000 microcomputer, which also provided on-line control of the spectrometer, data acquisition, spectrum display and data transmission to the central computers.

Computer configuration

The MOTOROLA 68000 microcomputer has an internal store of 16K 16-bit words. This computer was connected to the analog-to-digital converter of the spectrometer via a laboratory-built interface, and to the departmental time-shared VAX 11/780 via a common teletype line. The VAX 11/780 is equipped with several devices, in particular a CALCOMP plotter, and is connected to a PDP 11/44 via a DECnet. The microcomputer was loaded from one of the central computers, and once loaded it acted as an independent computer and communicated with the user via an alphanumeric screen.

Chemicals and preparation of samples

For efficiency calibration, single-element samples were used: Al, Ti, Fe, Ni, Cu, Zn, Zr, Mo and Pb (Goodfellow Metals, Cambridge, England), Si (Topsil, Denmark) and S, Cr, Mn, Co, Ge, Se, Y, Nb, Ag, Cd, In, Ta, W, Gd, Au and Bi (prepared from analytical-grade chemicals in the laboratory). In cases where single element samples were not available, pressed pellets of analytical-grade chemicals were used: NaCl, KCl, KBr, $K_2Cr_2O_7$, LaF_3 and $BaCl_2 \cdot 2H_2O$.

The standard reference materials examined were SRM 1158 (High-Nickel Steel), SRM 1198 (Incoloy 901), SRM 1199 (L605), SRM 1200 (S816), SRM 1201 (Hastelloy X), SRM 1208-1 (Inco 718), SRM 1633a (Trace Elements in Coal Fly Ash) and SRM 1645 (River Sediment); all were from the U.S. National Bureau of Standards.

The SRM 1158, 1198, 1199, 1200, 1201 and 1208-1 alloys were carefully cleaned in ethanol and placed in the spectrometer. NBS SRM 1633a and NBS SRM 1645 were prepared as follows: 3—7 g of sample was ground in a hard metal agate mortar for 10 min; then the sample was just moistened with distilled water and pressed to a pellet, which was dried in a desiccator and placed in the spectrometer.

Measurements

For efficiency calibration of the silver target, the single-element samples and pressed pellets were measured at a generator setting of 50 kV and 5 mA; vacuum was not applied to the excitation chamber. The counting time was chosen to give suitable counting statistics. The alloys were analyzed with the same spectrometer settings as above. Each alloy was analyzed four times. The acquisition time was varied between 1000 s and 4000 s, depending on the counting statistics. A 1500-s spectrum was obtained for SRM 1633a and a 40000-s spectrum for SRM 1645. These spectra were accumulated in vacuum, with the molybdenum secondary target in use. The excitation of the specimen by the Mo L lines was minimized by placing a 0.025-mm molybdenum (99.9%) filter between the target and the specimen.

SOFTWARE

The data-handling programs are divided into three separate programs. Each program covers one step in the x-ray fluorescence procedure. The division into three programs has the advantage that each data-handling step can be changed separately. Thus, programs with new algorithms or including new facilities are easily implemented. The three programs are described in detail below.

The MOTOROLA program is written in assembler and translated to machine code on the PDP 11/44. The translated program is transferred to the microcomputer. The MOTOROLA program is used for real-time data acquisition, previewing of the spectra on a graphical display and finally for spectrum transfer to the VAX 11/780.

The PROFIT package consists of programs, subroutines and data files. The software is written in VAX-11 FORTRAN and executed on the VAX 11/780. The program is run interactively. A set of simple commands is used to read in spectra from the microcomputer and store them on data files, to identify elements in the sample, to calculate intensities, to subtract one spectrum from another, etc.

The VAP package consists of programs, subroutines and data files. The software is written in VAX-11 FORTRAN and executed on the VAX 11/780. The program uses the fundamental parameter technique to calculate the concentrations from the measured fluorescence intensities.

The MOTOROLA program

This program allows the user to communicate with the microcomputer, and it enables him to collect intensity data and to manipulate these to a certain extent. The program receives, interprets and executes a number of commands from a keyboard. It is also capable of letting the user communicate with the central computers via the keyboard while accumulating data in the software multichannel analyzer. The MOTOROLA program is divided into three parts. First, the main program contains the list of possible commands, command interpreter, various service routines such as a routine converting hexadecimal numbers into BCD's and vice versa, a routine which displays the contents of registers and variables in case of bus or address errors or if tracing is requested, etc. This part also contains the routines handling the interrupts from the ADC, the real-time clock, the clock which corrects for deadtime, the keyboard, and the PDP 11/44 or VAX 11/780. The second part is a subprogram with subroutines for data acquisition and delivery of accumulated data to one of the central computers, i.e., subroutines corresponding to commands MT, ME, and ST (cf. Table 1 for a complete list of possible commands). The third part is a MONITOR subprogram which contains subroutines for real-time display of accumulated spectra on a dynamic graphical display. It also contains subroutines for display of expanded spectra, the limits of which can be chosen by typing

TABLE 1

List of commands to the MOTOROLA microcomputer

Command	Description
MT — n	The duration of the measurement is set, n being the number of seconds.
ME — xy	A measurement is commenced. The spectrum will be stored in xK channels in data section y. Possible x's are 1 (y = 1, 2, 3, or 4), 2 (y = 1 or 2) and 4 (y = 1).
ST — xy	A spectrum is stored in the PDP 11 or the VAX 11 (x and y as above).
DI — xy	A spectrum is displayed on the monitor (x and y as above).
>	Moving cursor to the right.
<	Moving cursor to the left.
@	The contents of the channel corresponding to the present cursor position are written on the terminal.
/	Present cursor position is fixed.
XP — n, m	The part of the spectrum limited by channels n and m is expanded and displayed on the graphical display.
SUM — n, m	Summation of channels between n and m.
ADC	The dead-time meter is started, thus enabling the user to choose a suitable generator setting.
ctrl S	The current measurement is stopped.
ctrl P	Communication between keyboard and the central computers is enabled.
ctrl A	Communication between keyboard and the MOTOROLA is re-enabled.

the first and last channel numbers on the keyboard or by fixing these via cursors. Peak integration can be done by summation of channel contents between given limits, etc.

Apart from this program, which occupies about 3300 words, there is room for storing four 1K spectra, two 2K spectra or one 4K spectrum (32 bits or 2 words per channel) in the 16K word RAM.

The PROFIT program

The spectra accumulated by the microprocessor are read and stored by the PROFIT program, which does all calculations for which the original spectrum data are used. PROFIT consists of a main program and 33 subroutines. The routines communicate between themselves and the outer world (the user) via data files and common variables. Each file is identified by the system by a number preceded by the prefix FOR (e.g., FOR020, FOR007). Inside the program, the number is equivalent to the unit number used in input/output statements. The unit numbers and files are described in Table 2.

A back-up file, FOR011, provides a memory for the user, i.e., the qualitative evaluation of a spectrum can be interrupted at any time and restarted again; FOR011 contains data points for a single spectrum, energy calibration data and results of the curve-fitting procedure. The file is defined by the operator during the early phase of program execution, and the spectrum data on FOR011 are read into common array *IY*, which always contains the counts of the spectrum to be evaluated.

TABLE 2

Definition of files used by PROFIT

FOR001	Assigned as outputfile for subroutine FUMILI.
FOR002	Back-up file defined by the program.
FOR005	Assigned as current input file.
FOR006	Assigned as current output file.
FOR007	If CALCOMP plot is wanted, this unit must be assigned to the plotter device before the program is run.
FOR008	Back-up file defined by the program.
FOR009	Back-up file defined by the program.
FOR011	Back-up file defined by the user.
FOR019	User-defined spectrum data file, which contains the original measured data points.
FOR020	Assigned as extra output file.

The main purpose of the program is to provide qualitative data and intensity calculations. To facilitate these calculations, the fluorescence lines are assumed to be Gaussian with a linear or parabolic background. For N lines in a selected range (maximum 500 channels) of the spectrum the counts, I, in each channel, x, is defined by the background plus a sum of Gaussians

$$I(x) = B_0 + B_1x + B_2x^2 + \sum_{i=1}^{N} A_i \exp[(1.665(C_i - x)/F_i)^2] \quad (1)$$

where the constants B are background parameters and A is the amplitude, C the line centre and F the full width at half maximum (FWHM). The fluorescence line intensity is then defined by integration of each Gaussian and is proportional to AF.

The qualitative evaluation comprises background subtraction, Gaussian adjustment, energy calibration, plotting of spectra, smoothing, etc. Each of these operations is initiated by a command (cf. Table 3). Three parts of the PROFIT package are adapted from other programs: (1) subroutine FUMILI and routines used by FUMILI, which performs χ^2 minimization [5, 6]; (2) subroutine FORSY and routines used by FORSY, which performs polynomial regression with orthogonal polynomials [7]; (3) subroutine SMOOTH, which performs a seven-point quartic algorithm to smooth a spectrum [7].

The VAP program

This program exploits the fundamental parameter technique, and monoenergetic excitation is assumed. The excitation energy is found as the weighted mean value of the K lines of the secondary target. A detailed description of the equations involved in the fundamental parameter technique has been given by Sparks [3]. The basic equation for the fluorescence intensity, I, of an analyte line, i, excited by a target, t, is

TABLE 3

List of commands to PROFIT

Command	Description
BACKPLOT	Results from a selected fit stored on FOR011 are printed. A plot is also available if the plot option is on.
CALDATA	Calibration constants are printed.
CALIN	Calibration constants are read in.
CLEAR	The spectrum appearing on FOR011 in the start or from the last call of DATAIN is read on FOR002 into common array *IY* and restored on FOR011.
CONTENT	Prints spectrum numbers, measuring time and spectrum size for the spectra stored on a selected spectrum data file, FOR019.
DATAGRAPH	Produces a printer plot of the current spectrum for a selected channel range.
DATAIN	Finds a spectrum on a FOR019 spectrum data file and stores the spectrum on FOR011, FOR002 and in common array *IY*.
DATAPLOT	Makes a CALCOMP plot of the current spectrum.
DIFF	The difference between two spectra stored on spectrum data files, FOR019, is stored on FOR011 and in common array *IY*.
ENDO	Energy corresponding to peak centre found by SHAPEDO is read in. ENDO can only be used after a SHAPEDO command.
ENIN	Energy calibration is done by reading in corresponding values of channel and energy.
FITREPEAT	Full control of the resulting fit variables from the last call of FITS is established. The fit variables may be changed and the fit procedure is repeated.
FITS	Gaussian peak shapes are adjusted to a number of peaks in a selected spectrum range. The fit variables, centre, amplitude and FWHM for each peak, are stored on FOR011.
FOURIER	Spectrum smoothing by a fast Fourier transformation procedure. The smoothed spectrum is stored on FOR011.
GIGI	Makes plot on the terminal of the current spectrum using ReGIS graphic commands.
IDENTIFY	Prints suggestions for qualitative interpretation of the peaks stored on FOR011.
MODEL	A theoretical spectrum is prepared from the intensities calculated by the program VAP; theoretical intensities can be read in from a data file created by VAP.
MOTOROLA	A spectrum accumulated in the MOTOROLA is transmitted to the VAX 11/780 and stored on FOR002, on FOR011, on a selected FOR019 spectrum data file and in common array *IY*.
OPTIONS	Setting of plot and print flags.
RESULT	All results of curve fitting stored on FOR011 are printed.
SHAPEDO	A single Gaussian peak is adjusted to a peak in a selected channel range.
SMOOTH	Seven-point quartic smoothing of the current spectrum. The smoothed spectrum is stored in common array *IY* and on FOR011.
STOP	Terminates the program.
SUBTRACT	Counting values generated from fit variables of a selected fit stored on FOR011 are subtracted from the current spectrum, and the results are stored in common array *IY* and on FOR011.
SUM	Makes count summation in a selected channel range.

$$I_{i,t} = G_t K_{i,t} A_{i,t} (1 + H_{i,t}) W_i \quad (2)$$

Here, G is the absolute calibration constant and depends on generator settings, kv and mA, the secondary target and the collimation of the exciting and fluorescent radiation; K is the relative calibration constant and includes the excitation and detection efficiency for the fluorescence line; A corrects for self-absorption of both exciting and fluorescent radiation, and H corrects for enhancement effects (both A and H depend on the excitation energy and the specimen composition); W is the concentration of the analyte expressed as a weight fraction; K, A and H are calculated from tabulated physical parameters [8—10]. The equations are given elsewhere [3]. The value of K may also be established experimentally [11, 12]. The VAP program contains experimental K values for a few secondary targets, and data for further targets are easily included in the program. At present, the experimental K values from a titanium target (in vacuum), selenium target (no vacuum), molybdenum target (no vacuum), silver target (no vacuum) and gadolinium target (no vacuum) are available. The experimental K values are obviously specific for the spectrometer used. For the enhancement correction, three calculation options are available: (1) both secondary and tertiary effects are included in H; (2) only secondary enhancement is assumed; (3) the enhancement is neglected, i.e., $H = 0$. Equation (2) is used to determine the theoretical intensities (K_α, K_β, L_α and L_β lines) for a given sample composition (maximum 40 elements) and a set of secondary targets (maximum 6 targets).

The value of G_t is obtained by the following procedure. The fluorescence intensities of a specimen of known composition are measured. Equation 2 is rewritten and G_t for a given spectrometer setting is found as the weighted mean value from all measured intensities

$$G_t = \Sigma\{(g_{i,t}/\Sigma g_{i,t})\ I_{i,t}/[K_{i,t} A_{i,t} (1 + H_{i,t}) W_i]\} \quad (3)$$

where $g_{i,t} = I_{i,t}^{1/2}$ is the weighting factor.

To obtain quantitative results for an unknown sample, Eqn. 2 is rewritten, and W_i is found as the weighted mean value for all measured intensities for a given element i

$$W_i = \Sigma\{(g_{i,t}/\Sigma g_{i,t}) I_{i,t}/[K_{i,t} A_{i,t} (1 + H_{i,t}) G_t]\} \quad (4)$$

Because A and H depend on the sample composition, an iterative procedure must be applied to solve the concentration equations. In the first calculation of concentrations, the iterative procedure is initiated by setting $A = 1$ and $H = 0$ in Eqn. 4. The iterative scheme is then: (1) for a set of W values, A and H are calculated; (2) a new set of W values is calculated by Eqn. 4; (3) the new concentration set is normalized to unity; (4) the iteration is stopped if no change in W values is observed.

For an infinitely thick specimen, $A_{i,t}$ is inversely proportional to $\Sigma W_i a_i$, where a_i is an element-dependent factor, which contains the mass absorption coefficients for both the excitation and the fluorescence energies, Thus, G

may be treated as a normalization factor, which is found by the normalization criteria. Therefore, in the case where all elements can be determined with one target, no absolute calibration is necessary, because the calculation of G can be included in the iterative procedure.

Quantitative evaluation of specimens containing considerable amounts of light elements can be done in several ways. The VAP program has facilities for two calculation schemes: (a) a set of light elements with fixed weight-fraction ratios is included in the iterative scheme, thus the normalization criteria produce no change of the weight-fraction ratios for the light elements, and the sum of weight fractions for light elements is found by difference; (2) oxygen is assumed to be the only light element in the specimen, and all analytes in the specimen are assumed to exist as the oxides. Hence, $W_{\text{oxygen}} = \Sigma W_i b_i$, where $b_i = (lM_{\text{oxygen}})/(kM_X)$ for the oxide X_kO_l of the analyte X. The VAP program contains b_i values for the following most probable oxides: Al_2O_3, SiO_2, P_2O_5, K_2O, CaO Sc_2O_3, TiO_2, V_2O_5, Cr_2O_3, MnO_2, Fe_2O_3, CoO, NiO, CuO, ZnO, Ga_2O_3, GeO_2, As_2O_3, SeO_2, Rb_2O, SrO, Y_2O_3, ZrO, Nb_2O_5, MoO_3, Cs_2O, BaO, La_2O_3, CeO_2, HfO_2, Ta_2O_5, WO_3, HgO, PbO, Bi_2O_3, ThO_2 and UO_2. For the fixed ratio scheme, an absolute calibration is always needed, but for the most probable oxide scheme, the calibration constant can again be included in the iterative procedure if the specimen can be measured with only one target.

Finally, G_t may be determined from internal standards in the specimen. Thus, in the iterative scheme, G_t is found by Eqn. 3, summing only over the internal standard intensities.

The calculation to be done by VAP is selected by one of the codes listed in Table 4. The programs described are available from the authors on request.

RESULTS AND DISCUSSION

Calculations

For all the measured spectra, PROFIT was used interactively to produce qualitative results and intensity calculations. An example of the peak assignment done by the PROFIT command FITS is given in Fig. 1, which shows the result of adjusting a linear background and six Gaussian functions, each with three parameters to the CrK_α, CrK_β, FeK_α, CoK_α, Ni$K\alpha$ and CoK_β lines in the spectrum of NBS SRM 1200.

Fluorescence intensities obtained from infinitely thick samples were used to calculate relative excitation and detection efficiencies. Relative efficiencies, $G_tK_{i,t}$, were calculated by rewriting Eqn. 2. To eliminate the absolute calibration constant, G_t, the efficiencies were normalized to an elemental line within a secondary target group. Polynomial regression with orthogonal polynomials [7] was applied to the experimental efficiencies, and missing values were found by interpolation.

With the assumption that all elements were identified by the qualitative x-ray analysis, the standardless quantitative procedure was applied to NBS

TABLE 4

List of codes to VAP

W	For a known sample and a given set of targets, the fluorescence intensities are calculated from Eqn. 2; G_t is set equal to unity.
WG	For a known sample and a given set of targets with known values of G_t, the fluorescence intensities are calculated from Eqn. 2.
WI	For a known sample and a set of known fluorescence intensities, G_t is found from Eqn. 3.
GI	For a set of known fluorescence intensities and known absolute calibration constants, unknown concentrations, W_i, are found from Eqn. 4. Light elements with fixed weight-fraction ratios can be included in the calculation.
I	For a set of known fluorescence intensities measured by one secondary target, unknown concentrations, W_i, are found from Eqn. 4, and the absolute calibration constant is calculated as the scaling factor given by the condition $\Sigma W_i = 1$.
IS	In a set of known fluorescence intensities, one or more of the intensities originate from a known standard in the sample. Thus G_t is calculated from these values, and the unknown concentrations are found.
GIO	As for GI, but here an oxygen content is included as the content of the most possible oxides.
IO	As for I with the addition from GIO.
ISO	As for IS with the addition from GIO.

SRM 1158, 1198, 1199, 1200, 1201 and 1208-1 alloys. The data were quantified by VAP, with use of the control code *I*. Thus, the absolute calibration factor, G, for the silver target was found as the normalization factor given by $\Sigma W_i = 1$. In accordance with earlier results [11], secondary and tertiary enhancement was applied in the calculation.

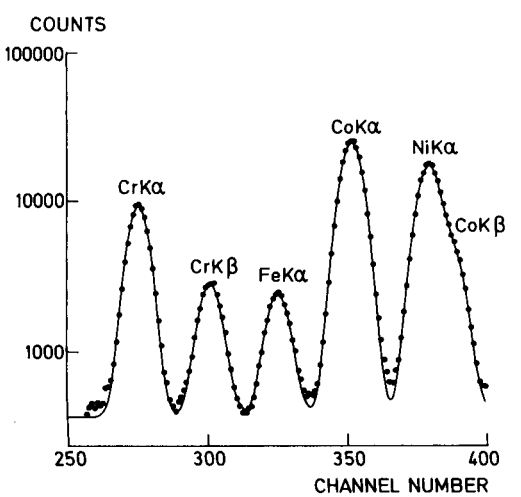

Fig. 1. Curve fit of six Gaussians plus a linear background to the Cr K_α, Cr K_β, Fe K_α, Co K_α, Ni K_α and Co K_β fluorescence lines in the x-ray fluorescence spectrum of NBS SRM 1200. (•) experimental values; (—) fitted curve.

For SRM 1633a and SRM 1645, two independent procedures were used by VAP for the quantitative evaluation. Either of the procedures makes an absolute calibration obsolete. First, the analytes were assumed to be present as oxides, and the procedure using the most probable oxides was employed. Secondly, the lead content as found by potentiometric stripping analysis [13] was used as internal standard for the calculation of the remaining element concentrations by the procedure outlined above. Three preliminary calculations were used: (1) no enhancement included; (2) only secondary enhancement included; (3) secondary and tertiary enhancement included. The third step showed that the secondary enhancement correction was sufficient for the calculations.

For cases in which severe peak overlap could not be solved by PROFIT (e.g., the As K_α and Pb L_α lines, the following numerical procedure was employed: (1) weight fractions were found as in the above procedure; (2) for these weight fractions, theoretical intensities were calculated from Eqn. 2; (3) the theoretical intensities were used for a numerical correction of the experimental intensities. The numerical procedure is done automatically by VAP for correction of the lines listed in Table 5.

Excitation and detection efficiencies

Figure 2 shows the theoretically evaluated and experimentally found excitation and detection efficiencies, K, for a silver secondary target and atmospheric pressure. Polynomials fitted to the experimental efficiencies are also shown. The efficiencies are shown relative to the value for the Mo K_α fluorescence line. The figure is on an arbitrary scale, and it cannot be deduced whether the theoretical values of the K_β lines are too small or the theoretical values of the K_α lines are too large compared to the experimental values. On this scale, however, the experimental and theoretical efficiencies of the K_α and L_α line agree well. The experimental values of the K_β and L_β efficiencies are significantly higher than the theoretical values. Thus, when K_α, K_β, L_α and L_β lines are used in the calculations, experimental efficiencies should be employed.

Analysis of NBS standard reference materials

Alloys. The six NBS alloys were analysed in order to examine the validity of the standardless calibration procedure when a single target was used for

TABLE 5

Lines for which severe peak overlap occurs and numerical correction may be employed

Analyte line	Overlap line	Analyte line	Overlap line	Analyte line	Overlap line
Ca K_α	K K_β	Mn K_α	Cr K_β	Y K_α	Rb K_β
Ti K_α	Ba L_α + Fe K_α escape	Fe K_α	Mn K_β	Zr K_α	Sr K_β
Ba L_β	Ti K_β	Co K_α	Fe K_β	Nb K_α	Y K_β
Cr K_α	Fe K_β escape	As K_α	Pb L_α	Mo K_α	Zr K_β

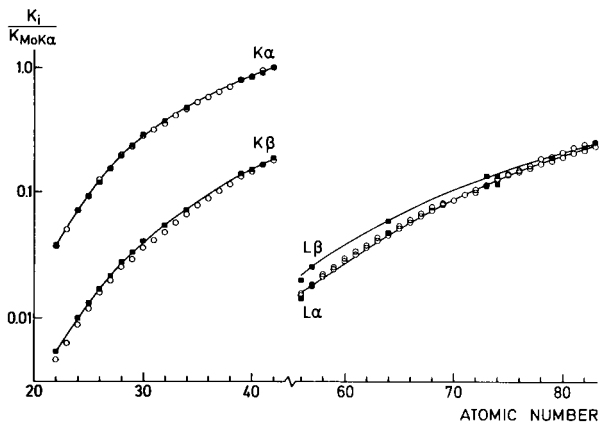

Fig. 2. Excitation and detection efficiencies for the silver secondary target (no vacuum). The values are normalized by the Mo K_α efficiency. (▪) Experimental values; (○) Theoretical values; (—) fitted polynomials. $K_i/K_{Mo\,K_\alpha}$ is given by the fitted polynomials, where Z_i is the atomic number. K_α: $3.9521 - 0.51016Z_i + 0.023307Z_i^2 - 0.00044706Z_i^3 + 0.0000033686Z_i^4$. K_β: $0.051312 - 0.0036808Z_i - 0.00003035Z_i^2 + 0.0000046587Z_i^3$. L_α: $0.67380 - 0.025276Z_i + 0.00024163Z_i^2$. L_β: $0.42850 - 0.017787Z_i + 0.00018788Z_i^2$.

the determination of all elements in the specimen. Table 6 shows the results obtained for the six alloys for two computational modes: (1) experimentally found excitation and detection efficiencies were used; (2) theoretically evaluated excitation and detection efficiencies were used. For most of the major elements, the accuracy is better than 97% and the relative standard deviation is better than 2%. In most cases, the results indicate no significant difference between the use of experimental or theoretical efficiencies in the calculations. The manganese results were found by the use of the numerical procedure and calculated Cr K_β intensities were subtracted from the fitted Mn K_α + Cr K_β curve. The manganese results were slightly better when the experimental efficiencies were used in the calculations. The significant discrepancies between some of the results can be attributed to poorer counting statistics and severe peak overlap.

Coal Fly Ash and River Sediment. These analyses were done to examine the possibility of analyzing materials with a high content of light elements without conducting an absolute calibration of the x-ray spectrometer. Table 7 shows the results of a simultaneous determination of up to 21 elements in NBS Coal Fly Ash and River Sediment by the use of two different computational schemes: (1) the light-element fraction was assumed to consist of oxygen bound to the analytes as oxides; (2) the absolute calibration was found by using lead as internal standard and the light-element fraction was arbitrarily chosen to consist of oxygen. For the fly ash, nearly identical results with reasonable accuracy were obtained by the use of either most probable oxides or lead as internal standard. Thus, the algorithm based on the oxides seems to give reliable concentrations for the analysis of fly ash.

TABLE 6

Quantitative analysis of NBS alloys with the silver secondary target (mean values and standard deviations of four independent measurements are given)

Element[a]	Element concentration (%)					
	SRM 1158	SRM 1198	SRM 1199	SRM 1200	SRM 1201	SRM 1208-1
Ti (1)	—	2.21 ± 0.17	—	—	—	0.43 ± 0.06
(2)	—	2.31 ± 0.17	—	—	—	0.45 ± 0.06
(3)	—	2.59	—	—	—	0.46
Cr (1)	0.12 ± 0.04	13.21 ± 0.16	20.6 ± 0.4	20.88 ± 0.19	21.21 ± 0.13	18.03 ± 0.17
(2)	0.12 ± 0.04	13.13 ± 0.16	20.0 ± 0.4	20.32 ± 0.19	21.10 ± 0.13	17.81 ± 0.17
(3)	0.062	12.9	19.9	19.9	20.7	17.5
Mn (1)	0.49 ± 0.03	—	1.39 ± 0.08	1.34 ± 0.06	—	0.45 ± 0.09
(2)	0.52 ± 0.03	—	1.75 ± 0.08	1.71 ± 0.06	—	0.80 ± 0.09
(3)	0.468	—	1.42	1.34	—	0.385
Fe (1)	64.64 ± 0.07	37.85 ± 0.17	1.0 ± 0.4	3.4 ± 0.6	24.23 ± 0.09	19.84 ± 0.08
(2)	64.73 ± 0.07	37.91 ± 0.17	0.9 ± 0.4	3.3 ± 0.6	24.29 ± 0.09	19.72 ± 0.08
(3)	—	36.2	0.65	3.19	23.2	19.2
Co (1)	—	—	50.3 ± 0.4	41.4 ± 0.6	—	0.89 ± 0.17
(2)	—	—	50.2 ± 0.4	42.0 ± 0.6	—	1.24 ± 0.17
(3)	—	—	51.6	42.0	—	0.82
Ni (1)	34.73 ± 0.04	40.8 ± 0.4	11.21 ± 0.16	20.6 ± 0.5	45.9 ± 0.2	52.03 ± 0.14
(2)	34.62 ± 0.04	40.7 ± 0.4	10.72 ± 0.16	19.9 ± 0.5	45.8 ± 0.2	51.68 ± 0.14
(3)	36.03	40.1	10.2	20.0	45.7	51.9
Nb (1)	—	—	—	3.25 ± 0.06	—	5.22 ± 0.09
(2)	—	—	—	3.17 ± 0.06	—	5.18 ± 0.09
(3)	—	—	—	3.18	—	5.38
Mo (1)	0.015 ± 0.01	5.8 ± 0.2	0.031 ± 0.010	3.87 ± 0.09	8.7 ± 0.3	3.10 ± 0.07
(2)	0.015 ± 0.01	5.9 ± 0.2	0.031 ± 0.010	3.84 ± 0.09	8.8 ± 0.3	3.13 ± 0.07
(3)	0.010	6.08	<0.02	4.00	9.18	3.24
Ta (1)	—	—	—	1.08 ± 0.08	—	—
(2)	—	—	—	1.22 ± 0.08	—	—
(3)	—	—	—	1.08	—	—
W (1)	—	—	15.42 ± 0.12	4.19 ± 0.19	—	—
(2)	—	—	16.38 ± 0.12	4.54 ± 0.19	—	—
(3)	—	—	15.4	3.86	—	—

[a](1) Calculated by the use of experimental efficiencies, $K_{i,t}$. (2) Calculated by the use of theoretical efficiencies, $K_{i,t}$. (3) Certified values.

Obviously, the concentrations found for Cr, Mn and Cu are much larger than the certified values; but spectra recorded on samples which did not contain these elements exhibited significant intensities for the Cr, Mn and Cu lines and the excessive concentrations found can be attributed to impurities in the spectrometer material. Severe peak overlap between the Mn K_α line and the Fe K_α line may also have influenced the manganese result. For the analysis of the river sediment, the computational schemes give different results; the internal standard method is usually in better agreement with the certified values for trace elements for which such values are available.

TABLE 7

Quantitative analysis of SRM 1633a (Coal Fly Ash) and SRM 1645 (River Sediment) using the Mo secondary target and Mo filter between secondary target and specimen (Evaluation was done without absolute calibration by using the most probable oxides, IO, or the internal standard, IS. Tentative values are given in parentheses)

Element	Element concentration (% w/w)					
	SRM 1633a			SRM 1645		
	IO	IS	Certified	IO	IS	Certified
Al	17.5	17.4	(14)	2.11	1.68	2.26
Si	22.5	22.4	22.8	19.7	15.4	—
S	—	—	—	5.02	3.68	(1.1)
K	2.31	2.29	1.88	8.57×10^{-1}	6.08×10^{-1}	1.26
Ca	1.27	1.27	1.11	6.55	4.59	(2.9)
Ti	6.71×10^{-1}	6.66×10^{-1}	(8×10^{-1})	—	—	—
Cr	4.86×10^{-2}	4.82×10^{-2}	1.96×10^{-2}	6.28	4.17	2.96
Mn	1.01×10^{-1}	1.00×10^{-1}	1.90×10^{-2}	—	—	—
Fe	8.60	8.54	9.4	20.1	12.3	11.3
Ni	1.06×10^{-2}	1.05×10^{-2}	1.27×10^{-2}	8.5×10^{-3}	4.8×10^{-3}	4.58×10^{-3}
Cu	1.88×10^{-2}	1.86×10^{-2}	1.18×10^{-2}	3.79×10^{-2}	2.13×10^{-2}	1.09×10^{-2}
Zn	2.37×10^{-2}	2.35×10^{-2}	2.20×10^{-2}	3.24×10^{-1}	1.81×10^{-1}	1.72×10^{-1}
Ga	3.4×10^{-3}	3.3×10^{-3}	(5.8×10^{-3})	7.1×10^{-3}	4.0×10^{-3}	—
Ge	3.4×10^{-3}	3.4×10^{-3}	—	—	—	—
As	1.52×10^{-2}	1.51×10^{-2}	1.45×10^{-2}	1.72×10^{-2}	9.5×10^{-3}	6.6×10^{-3}
Se	7×10^{-4}	7×10^{-4}	1.03×10^{-3}	—	—	(1.5×10^{-4})
Rb	1.36×10^{-2}	1.35×10^{-2}	1.31×10^{-2}	7×10^{-3}	3.9×10^{-3}	—
Sr	8.90×10^{-2}	8.82×10^{-2}	8.3×10^{-2}	1.75×10^{-1}	9.6×10^{-2}	—
Y	8.2×10^{-3}	8.1×10^{-3}	—	—	—	—
Ba	2.37×10^{-1}	2.35×10^{-1}	(1.5×10^{-1})	—	—	—
Pb	7.3×10^{-3}	$7.2^{a} \times 10^{-3}$	7.24×10^{-3}	1.27×10^{-1}	$7.05^{a} \times 10^{-2}$	7.14×10^{-2}
Th	1.1×10^{-3}	1.1×10^{-3}	2.47×10^{-3}	3.4×10^{-3}	1.9×10^{-3}	1.62×10^{-4}

[a] Lead concentration found by potentiometric stripping analysis [13].

Conclusion

The software package presented is applicable for the analysis of various samples with a standardless procedure based on fundamental parameters. For samples in which the content of light elements can be neglected (e.g., alloys), accuracies better than 97% and a precision better than 2% were obtained for most elements. For samples in which the content of light elements is not negligible, two standardless procedures can give results of reasonable accuracy. The scheme which uses most probable oxides gives accurate results for most elements in coal fly ash. The results for river sediment are much less accurate.

The authors are grateful to the Danish National Technical Research Council for financial support (grant nos. 16-0193, 16-1792 and 16-1866), to J. K. Christensen and L. Kryger for doing the potentiometric stripping analysis, and to L. Kryger for his advice on the preparation of the paper.

REFERENCES

1 R. Tertian and F. Claisse, Principles of Quantitative X-ray Fluorescence Analysis, Heyden, London, 1982.
2 M. Mantler and H. Ebel, X-Ray Spectrom., 9 (1980) 146.
3 C. J. Sparks Jr., Adv. X-ray Anal., 19 (1976) 19.
4 L. H. Christensen, S. E. Rasmussen, N. Pind and K. Henriksen, Anal. Chim. Acta, 116 (1980) 7.
5 S. N. Sokolov and I. N. Silin, CERN Report P810, 1961.
6 I. Silin and A. Kobine, CERN computer 6000 series Program Library, D510 long write-up, 1971.
7 K. J. Johnson, Numerical Methods in Chemistry, M. Dekker, New York, 1980.
8 W. H. McMaster, N. Kerr Del Grande, J. H. Mallett and J. H. Hubbell, Compilation of X-ray Cross-Sections, Sect. 2, Rev. 1, 1979, UCRL-50174.
9 M. O. Krause, J. Phys. Ref. Data, 8 (1979) 307.
10 J. H. Scofield, At. Data and Nucl. Data Tables, 14 (1974) 121.
11 L. H. Christensen and N. Pind, X-Ray Spectrom., 10 (1981) 156.
12 L. H. Christensen and N. Pind, Nucl. Instrum. Methods, 193 (1982) 95.
13 J. K. Christensen, L. Kryger and N. Pind, Anal. Chim. Acta, 136 (1982) 39; 141 (1982) 131.

Analytica Chimica Acta, 161 (1984) 191—199
Elsevier Science Publishers B.V., Amsterdam — Printed in The Netherlands

QUANTITATION AND IDENTIFICATION OF POLYNUCLEAR AROMATIC HYDROCARBONS BY LIQUID CHROMATOGRAPHY AND MULTIWAVELENGTH ABSORPTION SPECTROMETRY

DAVID T. ROSSI, DAVID J. DESILETS and HARRY L. PARDUE*
Department of Chemistry, Purdue University, West Lafayette, IN 47906 (U.S.A.)
(Received 23rd February 1984)

SUMMARY

This paper describes the combined use of liquid chromatographic separation with multiwavelength absorption detection for the quantitation and identification of polynuclear aromatic hydrocarbons. Quantitative results are presented for three- and four-component mixtures with complete and partial separation. Qualitative data are presented for a twelve-component synthetic mixture and for extracts from a filter used to collect particulate emissions from a biomass-gasifier system. It is shown that multiwavelength data-processing methods commonly applied to absorption spectra can be applied with significant advantage to second-derivative spectra. Results indicate that significant improvements can be achieved by the use of different wavelength ranges for different components in mixtures. Detection limits for single-component samples varied between 3 and 11 $\mu g\ l^{-1}$ for eleven hydrocarbons and the scatter about calibration plots for mixtures was in the range of 0.05 to 0.4 $\mu g\ ml^{-1}$. The identities of all twelve components in the synthetic mixture were confirmed and nineteen components were identified in the sample from the biomass gasifier filter.

With the advent of low-cost computers capable of acquiring and processing complex data sets, it has become possible to make more effective use of information obtainable from each of several steps in a chemical determination than was possible in the recent past. By making more complete use of the combined capabilities of chemical reaction, separation, measurement, and data-processing steps, it is frequently possible to achieve performance characteristics that are superior to more conventional approaches that focus primary attention on just one step in the process. One of these multidimensional approaches that has received significant attention recently has involved the combination of liquid chromatographic separations with multiwavelength absorption measurements and a variety of data-processing options [1, 2]. Although the principal focus has been on quantitative applications, these combined processes also have significant promise for qualitative applications. This paper explores the capabilities of this general approach for the quantitation and identification of polynuclear aromatic hydrocarbons (PAH) in mixtures. Quantitative results are presented for synthetic mixtures that are and are not completely separated and qualitative data are presented for synthetic mixtures and for samples from a biomass gasifier system.

0003-2670/84/$03.00

EXPERIMENTAL

Instrumentation and reagents

A pump (Milton/Roy; minipump) and six-port valve (Rheodyne; 7010) were configured in the conventional way for liquid chromatography. A nonpolar stationary phase (reverse phase) column (RP18; Bioanalytical Systems) was used. The effluent stream was monitored in a quartz flow cell (Hellma, 10-mm light path, 8-μl volume) with a diode-array based spectrophotometer (Hewlett-Packard 8450A).

Spectroscopic-grade acetonitrile (Baker Resianalyzed) was distilled and filtered (Gelman 60044) before use. The chromatographic mobile phase and solvent for PAH samples and standards consisted of acetonitrile and water (distilled, deionized, and filtered) in a volume ratio of 75:25. All solid reagents were analytical grade. Standard solutions and samples were filtered before being injected into the chromatographic column.

Procedure

The volumes of sample used were 20 μl throughout. Absorption spectra of the column effluent were recorded between 220 and 400 nm at 1-, 2-, or 5-s intervals, depending on the nature of the experiment conducted. Data were processed with programs in the HP-8450A spectrophotometer. These programs include multiwavelength fitting methods similar to those described earlier [1, 3].

RESULTS AND DISCUSSION

Quantitative results

Results are reported for single-component solutions and for mixtures for which components were and were not completely separated. All detection limits correspond to a signal-to-noise ratio of three (S/N = 3).

Detection limits. Single-component solutions were used to evaluate detection limits for selected hydrocarbons. Results are summarized in Table 1 for eleven compounds and three sets of measurement conditions. The first two columns show the substantial improvements in detection limits that can be achieved by being able to select the wavelength of maximum absorptivity (λ_{max}) relative to a fixed-wavelength approach. The third data column shows the additional improvements that can be gained by integration of the chromatographic peak at the wavelength of maximum absorptivity for each component. These latter limits of detection are in the range of a few parts per billion (ng ml^{-1}).

Mixtures with complete separation. Five three-component samples containing naphthalene, phenanthrene, and pyrene (between 2 and 15 μg ml^{-1} each) were examined. Fig. 1 shows a typical plot of absorbance vs. time and wavelength, proving that these components are well separated for the conditions used here. For all such samples, the data at each wavelength were

TABLE 1

Extrapolated detection limits[a] for selected polynuclear aromatic hydrocarbons with different conditions

Compound	Detection limits (μg ml^{-1})			λ_{max} (nm)
	Without integration		With integration λ_{max}	
	254 nm	λ_{max}		
Acenaphthylene	1.1	0.02	0.006	227
Fluorene	0.07	0.06	0.011	262
Phenanthrene	0.06	0.06	0.004	254
Fluoranthene	0.27	0.10	0.005	287
Pyrene	0.49	0.07	0.003	241
Benzo(b)fluorene	0.13	0.08	0.006	264
Benz(a)anthracene	0.19	0.10	0.003	288
Benzo(b)fluoranthene	0.20	0.17	0.007	258
Benzo(k)fluoranthene	0.16	0.11	0.005	308
Benzo(ghi)perylene	1.4	0.40	0.005	304
Benzo(a)pyrene	0.14	0.10	0.003	296

[a]S/N = 3 corresponds to an absorbance uncertainty of 0.003.

summed across the chromatographic peak for each sample, and the resulting sums were processed in several different ways. Some results are summarized in Table 2.

The first three rows of data in Table 2 correspond to single-wavelength computations with standards that were treated in exactly the same way as the samples. The data indicate excellent performance. Other results based on the same standards, but with data summed over different wavelength ranges on either side of λ_{max}, exhibited comparable performance for wavelength ranges up to 10 nm, but slightly poorer performance (intercepts and

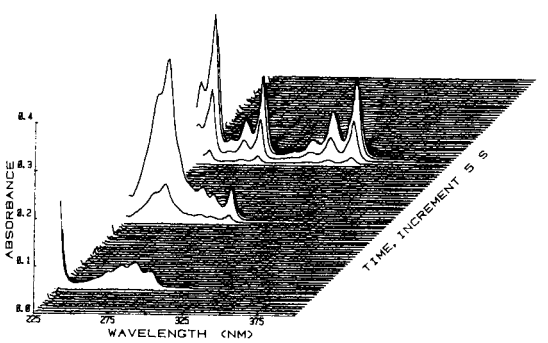

Fig. 1. Absorbance vs. wavelength and time for complete separation of three components. Front to back: naphthalene, 204 ng; phenanthrene, 199 ng; pyrene, 218 ng.

TABLE 2

Least-squares statistics for computed vs. prepared concentrations for mixtures with complete separation

Compound[a]	Wavelength (nm)	Slope ± s	Intercept ± s (μg ml^{-1})	SEE[b] (μg ml^{-1})	Correlation coefficient
Standards passed through chromatographic column					
Naphthalene	275	1.00 ± 0.02	−0.2 ± 0.2	0.20	0.9998
Phenanthrene	250	0.98 ± 0.004	0.02 ± 0.4	0.43	0.9993
Pyrene	240	1.01 ± 0.04	−0.05 ± 0.4	0.73	0.9994
Standards not passed through column					
Naphthalene	250—300	0.91 ± 0.02	0.3 ± 0.2	0.23	0.9992
Phenanthrene	230—300	1.01 ± 0.02	−0.06 ± 0.02	0.26	0.9994
Pyrene	245—300	1.08 ± 0.03	0.4 ± 0.3	0.41	0.999

[a]Concentrations of all components varied between 2 and 15 μg ml^{-1}. [b]Standard error of the estimate.

standard errors of estimate) for a wavelength range of 30—40 nm. The second three rows of data in Table 2 exhibit poorer performance when calculations are based on a relatively wide wavelength range with standards that are not passed through the chromatographic column. All results beyond this point are based on standards that were passed through the chromatographic column. Standard deviations of results for three samples at each of five concentrations for three components varied between 0.004 and 0.02 μg ml^{-1} with most values being near 0.01 μg ml^{-1}.

Mixtures with incomplete separation. To evaluate the capabilities of the approach in more complex situations, a four-component mixture was selected for which there was severe overlap of chromatographic peaks for each of two sets of components. The capabilities of several different data-processing approaches that might be used to resolve the individual components were evaluated.

Figure 2A shows a typical plot of absorbance vs. time and wavelength for the four-component sample. Although conventional single-wavelength monitoring shows only one unresolved peak for each chromatographic band, careful examination of spectral data can help to establish whether or not such peaks represent single components. Figure 2B shows plots of log A vs. wavelength at the leading edge, near the peak, and at the trailing edge of the second chromatographic peak. Because the shape of the log A vs. wavelength plot is independent of concentration, it is apparent from these plots that the peak contains two or more components. Using procedures to be discussed later, it can be shown that the second peak corresponds to a mixture of benzo(e)pyrene, B(e)P, and benzo(b)fluoranthene, B(b)F, and that the first peak represents a mixture of the structural isomers, chrysene and benz(a)anthracene, B(a)A. Once the compounds had been "identified" in each peak, several procedures were evaluated for their utility in resolving the

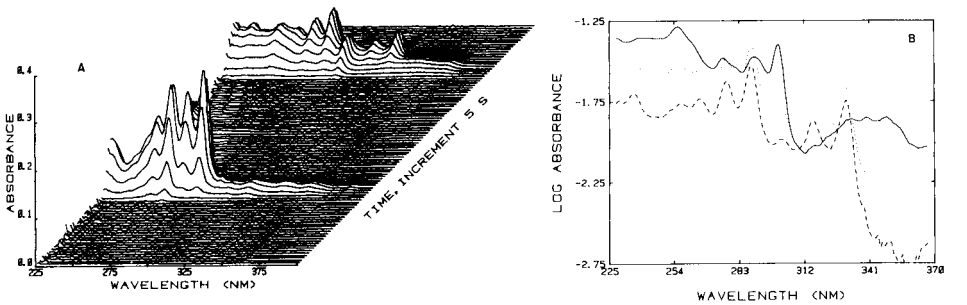

Fig. 2. Spectral and chromatographic data for partial separation of four components. A. First band, chrysene (202 ng) and benz(a)anthracene (154 ng); second band, benzo(e)-pyrene (206 ng) and benzo(b)fluoranthene (180 ng). B. Log absorbance vs. wavelength for leading edge (—), peak (···), and trailing edge (- - -) of the second chromatographic band.

components quantitatively. To provide a basis for comparison, spectral data for two-component mixtures that had not been passed through the chromatographic column were also processed.

The most common approach for resolving such mixtures is to use multiwavelength absorbance data. The first two sets of data in Table 3 represent results obtained with this approach for samples that had and had not been subjected to chromatographic separation. The chromatographic data are based on standards that had been passed through the column. Except for benzo(b)fluoranthene, results for two-component fractions in the chromatographic data are only slightly degraded relative to results for two-component mixtures prepared separately. For the twelve concentrations in the chromatographic data set for chrysene, benz(a)anthracene, and benzo(e)-pyrene, differences between computed and prepared values ranged from 0.01 to 0.69 $\mu g\ ml^{-1}$, with an average (absolute values) of 0.20 $\mu g\ ml^{-1}$. Results for benzo(b)fluoranthene deviated more than expected from ideal behavior and so alternative data-processing options were considered.

Although second-derivative data have been used extensively for quantitative spectrophotometry, most applications have depended on the selection of interference-free regions of the spectrum or on complete separation of interfering components. Figure 3 shows second-derivative spectra for each of the components in the two mixtures discussed above. Although benzo(e)-pyrene could be quantified in the presence of benzo(b)fluoranthene with the peak near 337 nm, it is improbable that a single wavelength for each component could be found at which all the components could be quantified reliably in the presence of variable concentrations of the others. However, the derivative spectra are sufficiently different that multiwavelength fitting methods [3] could be useful.

The third data set in Table 3 shows results obtained when the multiwavelength approach normally used with absorbance data is used with second-derivative data over carefully selected wavelength ranges. As a group, the

TABLE 3

Least-squares statistics for computed vs. prepared concentrations of PAH

Compound[a]	Slope ± *s*	Intercept ± *s* (μg ml^{-1})	SEE (μg ml^{-1})	Correlation coefficient
Two-component mixtures without separation (A *vs.* λ)				
Chrysene	1.01 ± 0.03	−0.18 ± 0.07	0.053	0.999
B(a)A	1.01 ± 0.04	−0.11 ± 0.07	0.076	0.998
B(e)P	1.06 ± 0.02	0.04 ± 0.06	0.077	0.999
B(b)F	0.82 ± 0.07	0.02 ± 0.16	0.19	0.991
Four-component mixtures with separation (A *vs.* λ)[b]				
Chrysene	0.95 ± 0.03	0.15 ± 0.22	0.19	0.999
B(a)A	1.08 ± 0.07	−0.06 ± 0.28	0.26	0.995
B(e)P	0.93 ± 0.07	0.45 ± 0.40	0.45	0.995
B(b)F	1.16 ± 0.08	−0.31 ± 0.43	0.52	0.994
Four-component mixtures with separation ($d^2A/d\lambda^2$ *vs.* λ)				
Chrysene[c]	0.95 ± 0.03	0.17 ± 0.20	0.17	0.999
B(a)A[c]	1.03 ± 0.05	0.09 ± 0.19	0.19	0.998
B(e)P[d]	0.98 ± 0.01	−0.34 ± 0.08	0.08	0.9998
B(b)F[d]	0.96 ± 0.03	0.11 ± 0.15	0.15	0.9991

[a] 0—10 μg ml^{-1}. [b] 225—370 nm. [c] 250—300 nm. [d] 297—340 nm.

least-squares statistics are substantially better than those for the absorbance data for the same experiments. Several other wavelength ranges were examined, and in all cases, results based on second derivative data for benzo(e)pyrene and benzo(b) fluoranthene were better than those for the absorbance data.

It should be noted that the second-derivative results in Table 3 represent the best compromise when the same wavelength range is used for both components in each mixture. However, there is no reason to limit the options in

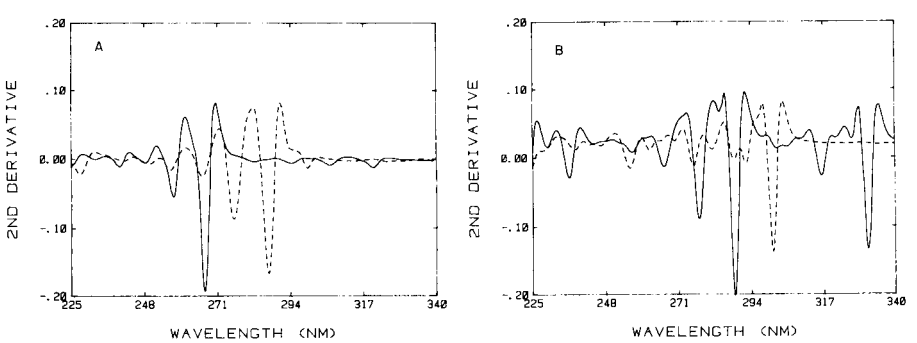

Fig. 3. Second-derivative spectra of the pure components of mixtures in Fig. 2. A. (—) Chrysene, 3.10 μg ml^{-1}; (- - -) benz(a)anthracene, 3.37 μg ml^{-1}. B. (—) Benzo(e)pyrene, 3.40 μg ml^{-1}; (- - -) benzo(b)fluoranthene, 3.54 μg ml^{-1}.

this way, and it seems reasonable that a wavelength range that emphasizes one component over the other could prove useful. For example, the best correlation for benzo(e)pyrene (slope = 0.994, intercept = —0.15, SEE = 0.10) was obtained with a wavelength range of 240—260 nm and the best correlation for benzo(b) fluoranthene (slope = 0.98, intercept = 0.05, SEE = 0.26) was obtained with a wavelength range of 297—331 nm. Results for the other component were degraded substantially in each case. No significant improvements were obtained for chrysene or benz(a)anthracene when other wavelength ranges were used (e.g., 250—271 nm for chrysene and 271—300 nm for benz(a)anthracene).

Qualitative results

Multiwavelength procedures [3] used above to quantify components of known identity also have the potential to aid in the identification of components that have been separated into groups that contain just a few components. To apply the method, one must have reference spectra of the target compounds. To evaluate the potential of this approach, data were processed for a sample prepared from twelve known components, for two-component fractions of four-component samples discussed above (Fig. 2), and for a sample from a biomass gasifier filter [4] that contained a complex mixture of PAH's.

Twelve-component mixture. Figure 4 shows a portion of the chromatogram for a synthetic mixture of twelve known components. The procedure evaluated is to assume that a peak may contain any of the target compounds, to fit the unknown spectrum with the standard spectra, and to evaluate the results.

Table 4 shows the results obtained when spectral data for one of the peaks were fitted to standard spectra for twelve components. When factors such as signs and magnitudes of predicted concentrations and relative standard

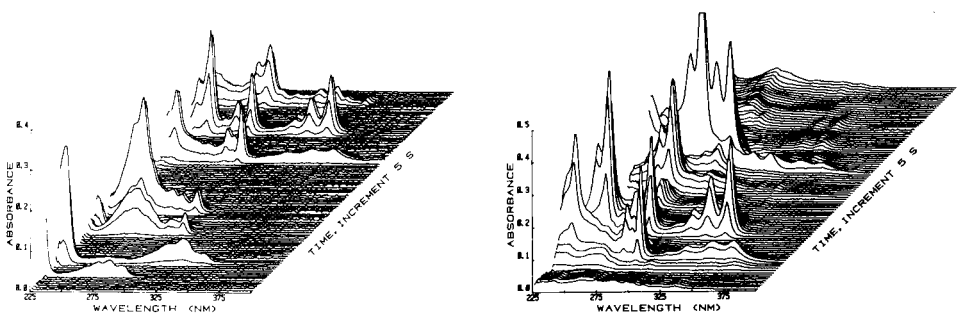

Fig. 4. Segment of chromatogram (225—770 s) from separation of twelve-component mixture.

Fig. 5. Segment of chromatogram (520—1025 s) from separation of extract from filter of a biomass-gasifier process.

TABLE 4

Identification with multiwavelength absorption data

Twelve-component sample (complete separation)			Two-component fraction of four-component sample		
Compound	Computed conc. (μg ml^{-1})	R.s.d. (%)	Compound	Computed conc. (μg ml^{-1})	R.s.d. (%)
Acenaphthene	−2.61	10	Fluoranthene	−1.23	12
Fluorene	0.39	104	Benzo(b)fluorene	−0.42	39
Fluoranthene	−0.03	292	Chrysene	0.88	15
Benzo(b)fluorene	0.08	119	Benzo(b)phenanthrene	−6.96	1
1-Methylphenanthrene	−0.02	1223	Benz(a)anthracene	3.75	12
Anthracene	−0.84	12	Tetracene	0.47	22
Naphthalene	−0.22	256	Benzo(b)fluoranthene[a]	12.8	1.9[a]
Pyrene	0.10	37	Benzo(a)pyrene	−0.08	192
Phenanthrene	0.80	21	Benzo(e)pyrene[a]	15.2	1.1[a]
2-Methylfluorene	−0.73	49	Perylene	1.50	10
9-Methylanthracene	−0.005	1607	Benzo(ghi)perylene	0.77	28
Acenaphthylene[a]	13.2	1.9[a]	Pyrene	−0.03	257

[a]Probable identities of components.

deviations for the predicted concentrations are considered, it is highly probable that the peak corresponds primarily to acenaphthylene. However, to test this conclusion, subsequent fits were examined in which all components with positive concentrations (five in Table 4) were included in the fit, regardless of the relative error. After two additional iterations, only acenaphthylene remained with a computed concentration of 10.8 μg ml^{-1} and a relative standard deviation of 2.3% for the fit.

Identities of all twelve components in the mixture were confirmed unambiguously with this procedure.

Two-component fractions. Results for one of the two-component fractions (Fig. 2) are included in Table 4. Results of the first pass included in the table strongly suggest that the two components are benzo(b)fluoranthene and benzo(e)pyrene; subsequent passes confirmed these identifications.

Biomass gasifier sample. Figure 5 shows a segment of the chromatogram of an extract from a biomass gasifier filter [4]. Applying the procedures illustrated above made it possible to identify nineteen components in the extract. Of the compounds identified, thirteen are in agreement with results obtained by using more conventional methods [4] based primarily on retention times, and six were not previously identified. It is clear that the multiwavelength approach can serve as an effective complement to retention times and other parameters that are used for qualitative purposes.

The general approach of using different forms of multiwavelength data offers several options for quantitation and identification of components in complex mixtures that have not yet been explored fully.

This work was supported by Contract DE-ACOZ-79EV10240 from the U.S. Department of Energy.

REFERENCES

1 A. E. McDowell and H. L. Pardue, Anal. Chem., 49 (1977) 1171.
2 M. J. Milano and E. Grushka, J. Chrom., 133 (1977) 325.
3 J. C. Sternberg, H. S. Stello and R. H. Schwendeman, Anal. Chem., 32 (1960) 84.
4 D. J. Desilets, P. T. Kissinger, F. E. Lytle, M. A. Horne, M. S. Ludwiczak and R. B. Jacko, Environ. Sci. Technol., 18 (1984) 386.

Analytica Chimica Acta, 161 (1984) 201—209
Elsevier Science Publishers B.V., Amsterdam — Printed in The Netherlands

AMPEROMETRIC DETECTION FOR LIQUID CHROMATOGRAPHIC SEPARATION OF POLYNUCLEAR HYDROCARBONS

MORTEZA G. KHALEDI and JOHN G. DORSEY*
Department of Chemistry, University of Florida, Gainesville, FL 32611 (U.S.A.)
(Received 14th December 1983)

SUMMARY

Oxidative electrochemical detection is used for liquid chromatographic separation of polynuclear aromatic hydrocarbons (PAH's). The amperometric response is shown to be dependent on the working potential, ionic strength, flow rate, pH, temperature and pretreatment of the glassy carbon electrode surface. These experimental factors were optimized by choosing the maximum signal-to-noise ratio for anthracene and benz(a)-anthracene. The figures of merit (sensitivity, limit of detection and linear dynamic range) of six PAH's are reported and compared with ultraviolet absorption detection. Varying the applied potential gives the capability for selective detection.

Polynuclear aromatic compounds, including both polycyclic aromatic hydrocarbons (PAH) and heterocyclic compounds, are one of the most heavily studied classes of environmental pollutants. This widespread interest stems from the demonstrated carcinogenic activity of many of these compounds. In fact, the polynuclear aromatic compounds are the largest class of chemical carcinogens known today. These materials are produced in virtually all combustion processes and their determination is therefore of interest in air, water, sludges and almost every conceivable type of sample matrix. The polynuclear aromatic compounds are present in real samples as extremely complex mixtures, the compositions of which are mainly dependent on their sources, and can typically contain hundreds of components of widely ranging concentrations. The determination of these compounds then necessarily includes a separation step before measurement. The high resolving power of open tubular gas chromatography when dealing with complex polynuclear aromatic mixtures was demonstrated as early as 1964 [1] and has been reviewed [2]. Gas chromatography/mass spectrometry (g.c./m.s.) has also been used extensively to quantify complex mixtures of PAH's [3, 4]. However, the difficulties associated with distinguishing the mass spectra of isomeric PAH's from each other and the inherent problems of g.c. such as the inability to handle high-molecular-weight or thermally unstable compounds are the major limitations of this technique.

Liquid chromatography has been receiving increasing emphasis in the separation of these complex samples. The ability to handle high-molecular-

0003-2670/84/$03.00

weight, thermally unstable compounds and the possibility of using selective detection to measure overlapping or unresolved compounds, makes h.p.l.c. ideal for separation of these compounds. Detectors have been based predominantly on fluorescence emission and u.v. absorption, or both, with series detectors. Christensen and May [5] concluded that the most powerful system then available was a 254-nm u.v. detector in series with a spectrofluorimeter. This combination offers excellent limits of detection as well as some selectivity through the choice of excitation and emission wavelengths of the spectrofluorimeter. Recently an electrochemical detector was used for the determination of polynuclear aromatic amines [6, 7]. Here, the application of a new detection scheme is discussed, viz., oxidative electrochemical detection, which has heretofore not been applied to PAH's. The merits of this selective detector, such as sensitivity, limits of detection, and linear range are compared with those of 254-nm u.v. absorption detection. Varying the applied potential gives the capability for selective detection of one of a pair of overlapping compounds.

EXPERIMENTAL

Liquid chromatography system

The system incorporated a Spectra-Physics, Model 8700 solvent delivery system (Spectra-Physics, Santa Clara, CA), either an Altex 210 (Altex Scientific, Berkeley, CA) or a Rheodyne 7125 (Rheodyne, Cotati, CA) injection valve with 20-μl loop and either an Altex Ultrasphere octyl column, 4.6 mm × 25 cm, or a Rainin Microsorb octyl column, 4.6 mm × 15 cm, both having 5-μm particle diameter. A saturator precolumn was prepared by using irregularly shaped silica gel (25—40 μm diameter; Macherey-Nagel) and was located before the injector. The mobile phase temperature was controlled by using water jackets for both the precolumn and the separator column. Either a Neslab model 850 (NESLAB, Porthsmouth, NH) or a Haake model D1 bath circulator was used to thermostat the columns.

Detection systems

An Altex model 153 fixed wavelength 254-nm u.v. absorbance detector with a time constant of 1.1 s was placed in series before an LC-4 amperometric controller which was connected to a 3-electrode thin-layer detection cell (Bioanalytical Systems, West Lafayette, IN). The working electrode was glassy carbon and was polished to a mirror finish with 0.1-μm alumina (Fisher Scientific) and polishing paper (Buehler Co., Evanston, IL) and was preanodized at +1.50 V and precathodized at −1.50 V each for 5 min immediately before each experiment. The reference electrode was Ag/AgCl. A dual-pen recorder (Scientific Products, Austin, TX) was used in conjunction with the detectors.

Cyclic voltammetry system

A CV-1A cyclic voltammeter and electrochemical cell (Bioanalytical Sys-

tems) were used. Glassy carbon and Ag/AgCl served as working and reference electrodes, respectively. An x-y recorder (PAR model RE0074) and a digital voltmeter were used for recording.

Reagents

Standard solutions of PAH's were prepared in the mobile phase solutions. The mobile phase consisted of various ratios of acetonitrile (h.p.l.c. grade) and deionized, distilled water, using sodium perchlorate as supporting electrolyte, and was continuously purged with helium.

RESULTS AND DISCUSSION

The amperometric response is affected by numerous variables such as applied potential, temperature, flow rate and ionic strength of the mobile phase, size and composition of the working electrode, and detector cell design [8—10]. With the exception of the last three factors which were fixed by using a commercial electrochemical (e.c.) detector, the others were optimized to achieve maximum signal-to-noise ratio. With a glassy carbon working electrode, other factors such as pretreatment of the electrode surface and pH also affect the detector response.

Hydrodynamic voltammogram

The optimum potential was determined from hydrodynamic voltammograms of each individual PAH, some of which are shown in Fig. 1. The current was measured over a range of applied potentials (0.80 V—1.40 V), and the potential at which the corresponding current reached the limiting current plateau was chosen as the working potential [11]. Because these plots were measured on different days under varying conditions, the currents are not directly comparable, but the shapes of the curves are still valid. To maximize the quantitative signal, a potential of 1.30 V (vs. Ag/AgCl), which is on the limiting plateau for many of the compounds, was used throughout the study. However, to demonstrate the selectivity of e.c. detectors for these compounds, other potentials from the rising part of the curves were chosen for synthetic PAH mixtures.

Flow rate

The current/flow rate relationship in thin-layer electrochemical detectors has been studied previously [12]. Whether i_l (limiting current) is proportional to $u^{1/2}$ or to $u^{1/3}$ (flow velocity) for channel electrodes, has been a matter of discussion for almost 30 years [13]. However, to apply this concept in practice for chromatography, both have the same meaning, i.e., current increases as flow rate increases. Here the electrochemical responses of seven PAH's were studied as a function of flow rate and are shown in Fig. 2. The flow rate of 2 ml min^{-1} was chosen as optimum for all the compounds for further studies.

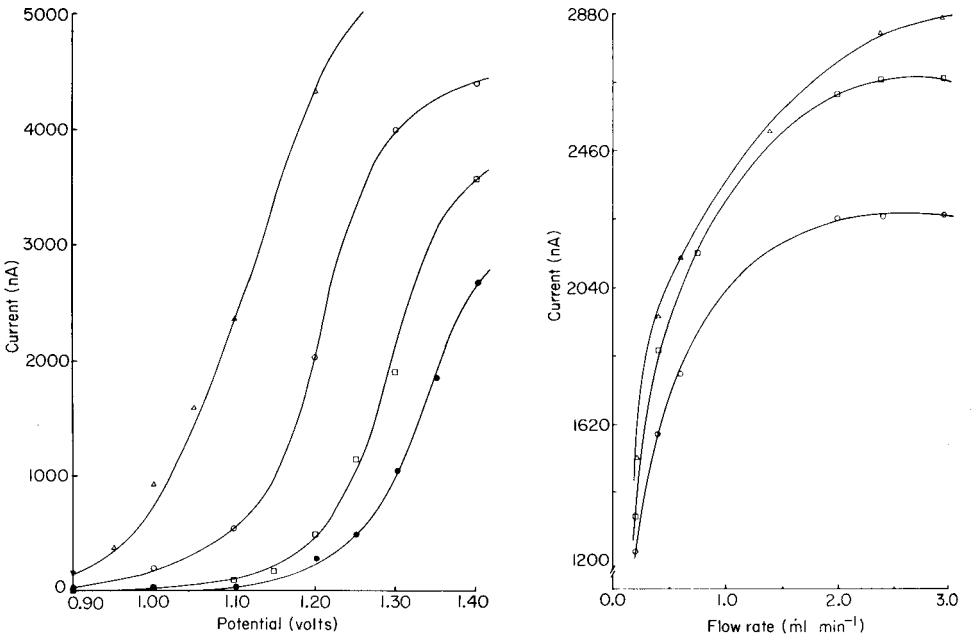

Fig. 1. Hydrodynamic voltammograms: (△) benzo(a)pyrene (1.8 μg); (○) 1-methylpyrene (2.9 μg); (□) pyrene (2.2 μg); (●) benzo(e)pyrene (2.0 μg). Mobile phase, (90:10) CH_3CN: H_2O, 0.1 M $NaClO_4$. Flow rate 1 ml min^{-1}.

Fig. 2. Flow rate dependence of current: (△) anthracene (0.5 μg); (□) 9,10-dimethylanthracene (1.9 μg); (○) 1-methylpyrene (0.12 μg). E = 1.30 V vs. Ag/AgCl; other conditions as in Fig. 1.

Effect of pH

The response of glassy carbon electrodes can be affected by pH variation [14], manifesting itself in at least an apparent potential shift of hydrodynamic voltammograms. The signal-to-noise ratio at different pH values was measured for anthracene and benz(a)anthracene at a potential of 1.3 V and was found to be essentially constant. However, the pH of the mobile phase was adjusted to 7.5 for the rest of the study to prevent any possible changes in the e.c. response when the detector was operated at potentials lower than the limiting plateau.

Pretreatment of glassy carbon

The effect of electrochemical pretreatment on the response of glassy carbon, in terms of halfwave potentials, has been reported [15, 16]. Here, the influence of both polishing and electrochemical preconditioning of the electrode surface on signal-to-noise ratio and reproducibility for anthracene and benz(a)anthracene were studied. The results from no pretreatment at all were similar to those when the electrode was either only electrochemically

pretreated or only polished. However, poor reproducibility was observed for the first two cases for which the electrode was not polished. Better signal-to-noise ratio and reproducibility were achieved when the electrode surface was polished mechanically and preconditioned electrochemically. In order to achieve consistent results, it is crucial to reproduce the surface conditions of the electrode. An operating potential of 1.30 V is large enough to oxidize the impurities present from the supporting electrolyte and water of the mobile phase. For this reason, high operating potentials for l.c.e.c. have never been popular. The formation of an oxide layer on the carbon surface has been reported, once the anodization is accomplished at potentials where oxygen evolution is possible [15, 17]. Engstrom [15] reported that the oxide layer strongly inhibits the oxidation of hexacyanoferrate(II) and hydrazine, but has no effect on hydroquinone oxidation. The application of an operating potential of 1.30 V after electrode pretreatment may result in the formation of this oxide layer. If the layer inhibits the oxidation of PAH's, the whole process of pretreatment is simply invalidated. However, such behavior was not observed; the pretreatment procedure always yielded better results. This was also verified by cyclic voltammetry. The voltammograms of both blanks and anthracene solute in mobile phase solution were exactly the same for freshly pretreated electrodes and those for which the electrode was held at 1.30 V for 30 min after the pretreatment procedure.

The polishing and duration of preanodization and precathodization were carefully reproduced. A reciprocating motion was used for polishing, in contrast to a rotary motion which could produce large background currents by turbulent flow on a microscale at the electrode surface [18]. A reproducible background current of 450 nA for a surface area of 0.07 cm^2 was observed. This high background current is undoubtedly due to the high operating potential. The peak-to-peak noise measurements were made for 20 min prior to the first injection when the electrode surface was freshly polished and pretreated. The entire pretreatment method was chosen from the literature [15]. A detailed study of the pretreatment procedure could give better results for PAH's, because its effectiveness is reported to be dependent on the electrochemical species [15].

Temperature

The rate of diffusion of molecules to the electrode surface and the rate of oxidation of molecules reaching the surface are both dependent on temperature. A temperature fluctuation of one degree (C) can cause a change of 1.5—9% in the amperometric response [19]. In this experiment, only the column temperature was controlled and the e.c. detector cell was held at ambient temperature. Heat transfer between mobile phase, cell body, and the environment could cause some error. However, increasing the flow rate through the system and operating the electrode potential on the limiting current plateau are reported to minimize the temperature effect [19]. The amperometric response increases with temperature because the limiting

current for a thin-layer electrode is proportional to the two-thirds power of the diffusion coefficient and the rate of oxidation of molecules is also a function of temperature [19, 20]. However, both peak-to-peak noise and background current also increased dramatically with increasing temperature. As a result, a maximum signal-to-noise ratio (S/N) was observed at 23°C, and this was chosen as the optimum temperature. This occurrence of maxima was also reported by Miner [19] who studied the effect of temperature on electrochemical response of other compounds. While small changes in temperature have only limited effects on chromatographic resolution, changes of only a few degrees have been shown to cause reversal of elution order for certain PAH pairs [21]. Temperature control is then mandatory for reproducible separation of these compounds.

Concentration of supporting electrolyte

A sodium perchlorate concentration of 0.025 M was used to study the figures of merit. Using a higher concentration of supporting electrolyte will likely yield a greater linear dynamic range because it reduces the uncompensated resistance of the solution [8]. However, lower salt concentration may be advantageous in terms of extended column lifetimes. No S/N dependence on background electrolyte concentration was found.

The figures of merit of six PAH's for both u.v. and e.c. detectors are reported in Table 1. The limit of detection (LOD) defined as 3 times the standard deviation of blank divided by sensitivity, is in the subnanogram range for both e.c. and u.v. detectors. The LOD in chromatography is an ambiguous number, being dependent on both the detector and chromatographic variables such as capacity factor, void volume, column efficiency and

TABLE 1

Analytical figures of merit for PAH's[a]

Compound (m.w.)	LOD				Sensitivity		Upper limit[b]		Slope log/log		λ_{max}
	E.c.		U.v.		(nA ng^{-1})	(10^{-4} abs. ng^{-1})					
	(ng)	(pmol)	(ng)	(pmol)			E.c. (ng)	U.v. (ng)	E.c.	U.v.	
Anthracene (178)	0.45	2.5	0.03	0.2	2.0	30.7	240	240	1.02	0.95	255
Pyrene (202)	0.82	4.1	0.41	2.0	1.1	2.2	400	2800	1.03	0.96	334
Benzo(a)pyrene (252)	0.34	1.3	0.23	0.9	2.7	4.0	210	2100	1.00	0.99	331
9,10-Dimethyl-anthracene (206)	0.31	1.5	0.070	0.3	2.9	12.8	250	750	1.06	0.97	260
1-Methylpyrene (216)	0.42	1.9	0.56	2.6	2.2	1.6	260	2600	1.04	0.97	342
Benz(g, h, i)perylene	0.39	1.4	0.53	1.9	2.3	1.7	200	2000	0.92	1.00	331

[a]Conditions: mobile phase (80:20) CH_3CN, 0.025 M $NaClO_4$; flow rate 2 ml min^{-1}, 23°C, pH 7.50, 1.30 V vs. Ag/AgCl, glassy carbon (pretreated). [b]Upper limit of linear range.

injection volume [22]. By operating the two detectors in series, these variables were held constant and a comparison of the detectors is valid. Care must be exercised however in comparing these values with others obtained under different chromatographic conditions. As can be seen, the LOD for the u.v. detector is better than for the e.c. detector by almost an order of magnitude for both anthracene and 9,10-dimethylanthracene. This is because the detector wavelength, 254 nm, happened to be similar to λ_{max} for anthracene (λ_{max} = 253 nm) and 9,10-dimethylanthracene (260 nm). The wavelengths of maximum absorption for PAH's under study are also listed in Table 1.

Selective detection

Electrochemical detection can complement the selectivity inherent in the chromatographic separation.

Two mixtures of standard solutions, each containing six PAH's, were prepared. The chromatograms of mix A (Fig. 3) and mix B (Fig. 4) are shown. As can be seen from the u.v. response at 81% acetonitrile, phenanthrene overlaps with anthracene (peak 1, 2) while 9,10-dimethylanthracene, benz-(a)anthracene and chrysene (peaks 3—5) are virtually unresolved (Fig. 3a). The e.c. detector at 1.05 V detected only three of the PAH's in the mixtures

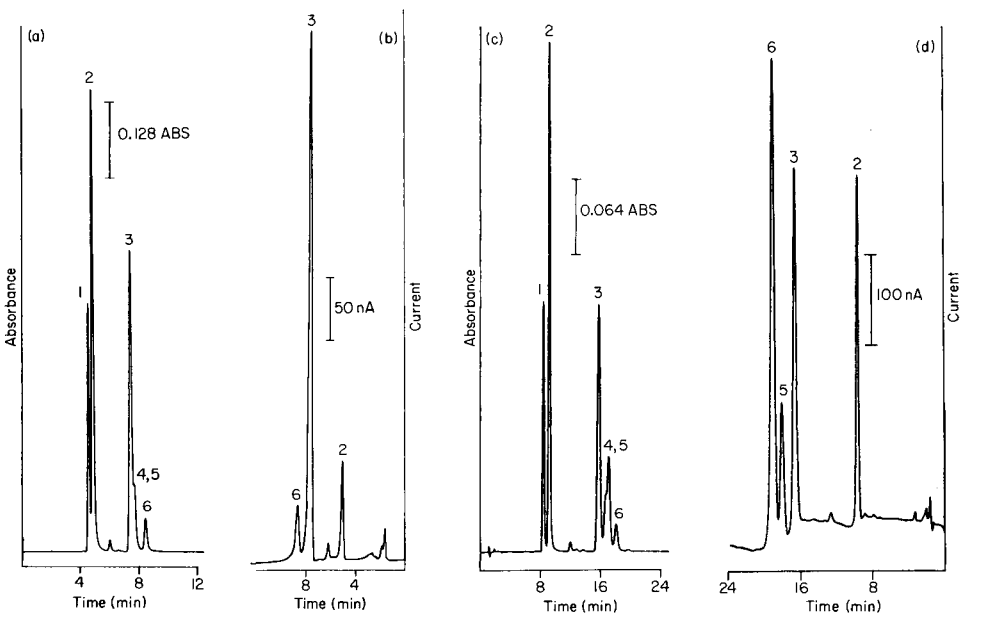

Fig. 3. Chromatograms of Mix A. Peaks: (1) phenanthrene (1.3 nmol); (2) anthracene (1.1 nmol); (3) 9,10-dimethylanthracene (0.97 nmol); (4) chrysene (0.98 nmol); (5) benz-(a)anthracene (1.1 nmol); (6) 1-methylpyrene (0.96 nmol). Flow rate 1 ml min^{-1}; column, Rainin 150 × 4.6 mm, Microsorb C-18, 5 μm; 27°C. Chromatograms: (a) u.v. detector (254 nm), mobile phase (81:19) CH_3CN:H_2O; (b) e.c. detector, E = 1.05 V vs. Ag/AgCl, mobile phase as in (a); (c) u.v. detector (254 nm) mobile phase (67.5:32.5) CH_3CN:H_2O; (d) e.c. detector, E = 1.25 V vs. Ag/AgCl, mobile phase as in (c).

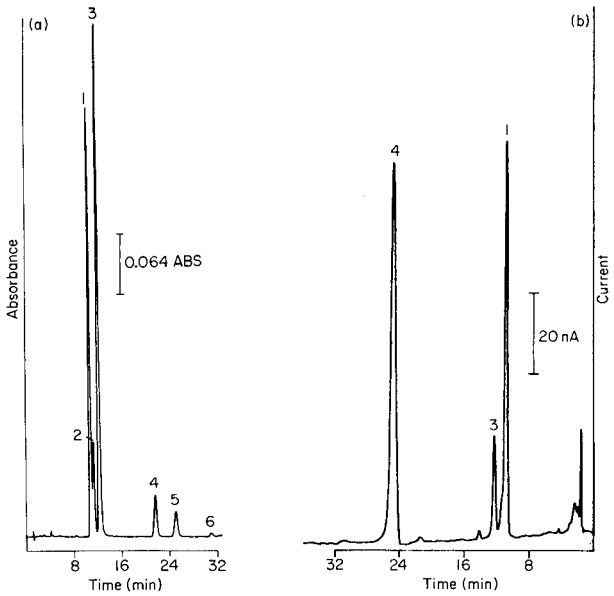

Fig. 4. Chromatograms of Mix B. Peaks: (1) 9-methylanthracene (1.3 nmol); (2) pyrene (2.2 nmol); (3) 2-methylanthracene (1.1 nmol); (4) benzo(e)pyrene (0.95 nmol); (5) benzo(a)pyrene (0.7 nmol); (6) dibenz(a, h)anthracene (1.2 nmol). Mobile phase (70:30) CH_3CN H_2O; other conditions as in Fig. 3(a). Chromatograms: (a) u.v. detector; (b) e.c. detector, E = 0.95 V vs. Ag/AgCl.

(Fig. 3b). Changing to a weaker mobile phase composition of 67.5% acetonitrile resulted in the separation of phenanthrene from anthracene, and 9,10-dimethylanthracene from the still unresolved peaks of benz(a)anthracene and chrysene (Fig. 3c). Using the same mobile phase composition and applying a potential of 1.25 V resulted in selective detection of benz(a)anthracene in the presence of chrysene (Fig. 3d). The u.v. response for mix B, at 70% acetonitrile is shown in Fig. 4(a), with the pyrene and 9-methylanthracene peaks overlapped. Benzo(a)pyrene, 9-methylanthracene and 2-methylanthracene were selectively detected electrochemically at 0.95 V (Fig. 4b).

In real samples, one can find a variety of PAH's with a wide range of concentrations. As a result, the familiar problem of simultaneous detection of major, minor and trace concentrations should be addressed. Examples of such problems are illustrated in the chromatograms with u.v. detection (Figs. 3a and 4a). For instance, comparison of the u.v. response of benz(a)-anthracene (16 ppm) and pyrene (22.4 ppm) with that of the 2-methyl-anthracene (10.4 ppm) (Fig. 4a) shows that although the concentrations of the former compounds are larger (1.5—2 fold) than the latter one, their peak heights are almost 100 and 5 times smaller than that of 2-methylanthracene. As another example, in mix A, the response for anthracene (9.6 ppm) is 15 times greater than that of the 1-methylpyrene (10.4 ppm), despite the similar

concentrations. This problem is more pronounced if trace or minor concentrations of large PAH compounds with low absorptivities at 254 nm are to be quantified simultaneously with major concentrations of smaller PAH's with high absorptivities. However, as shown in Figs. 3(d) and 4(b), this is not the case for e.c. detection where responses for benzo(a)pyrene and 1-methylpyrene are similar to those of the 9-methylanthracene and anthracene at 0.95 V and 1.25 V, respectively. Table 1 gives a more complete comparison of the sensitivities of u.v. and e.c. detection for PAHs.

The authors are grateful to Anna Brajter-Toth for many valuable discussions and suggestions, and to Michael McCown, Altex Scientific, for a gift of the Ultrasphere column. J.G.D. gratefully acknowledges Eli Lilly and Company, the Alcoa Foundation and the Donors of the Petroleum Research Fund, administered by the American Chemical Society, for support of this research.

REFERENCES

1 A. Liberti, G. P. Cartoni and V. Cantuli, J. Chromatogr., 15 (1964) 141.
2 M. L. Lee and B. W. Wright, J. Chromatogr. Sci., 18 (1980) 345.
3 M. L. Lee, M. V. Novotny and K. D. Bartle, Analytical Chemistry of Polycyclic Aromatic Compounds, Academic Press, 1981.
4 K. D. Bartle, M. L. Lee and S. A. Wise, Chem. Soc. Rev., 10 (1981) 113.
5 R. G. Christensen and W. E. May, J. Liq. Chromatogr., 1 (1978) 385.
6 V. Concialini, G. Chiavari and P. Vitah, J. Chromatogr., 258 (1983) 244.
7 W. L. Caudill, M. V. Novotny and R. M. Wightman, J. Chromatogr., 261 (1983) 415.
8 P. T. Kissinger, Anal. Chem., 49 (1977) 447A.
9 R. J. Rucki, Talanta, 27 (1980) 147.
10 R. Stulik and V. Pacakova, J. Electroanal. Chem., 129 (1981) 1.
11 J. L. Anderson, D. E. Weisshaar and D. E. Tallman, Anal. Chem., 53 (1981) 908.
12 S. G. Weber and W. C. Purdy, Anal. Chim. Acta, 100 (1978) 531.
13 S. G. Weber, J. Electroanal. Chem., 145 (1983) 1.
14 H. Gunasingham and B. Fleet, Analyst (London), 108 (1983) 316.
15 R. C. Engstrom, Anal. Chem., 54 (1982) 2310.
16 W. J. Blaedel and R. A. Jenkins, Anal. Chem., 47 (1975) 1337.
17 D. Laser and M. J. Ariel, J. Electroanal. Chem., 52 (1974) 291.
18 J. D. McLean, Anal. Chem., 54 (1982) 1169.
19 D. J. Miner, Anal. Chim. Acta, 134 (1982) 101.
20 H. B. Hanekamp and H. J. van Nieuwkerk, Anal. Chim. Acta, 121 (1980) 13.
21 J. Chmielowiec and H. Sawatzky, J. Chromatogr. Sci., 17 (1979) 245.
22 J. P. Foley and J. G. Dorsey, Chromatographia, in press.

Analytica Chimica Acta, 161 (1984) 211—219
Elsevier Science Publishers B.V., Amsterdam — Printed in The Netherlands

REVERSED-PHASE ION-PAIR CHROMATOGRAPHIC METHOD FOR THE DETERMINATION OF NITROPRUSSIDE IN PHOTOLYZED SOLUTIONS

O. R. LEEUWENKAMP*, E. J. VAN DER MARK, P. M. VAN DER KLAUW, W. P. VAN BENNEKOM and A. BULT

Department of Pharmaceutical Analysis and Analytical Chemistry, Subfaculty of Pharmacy, State University of Leiden, Gorlaeus Laboratories, P.O. Box 9502, 2300 RA Leiden (The Netherlands)

(Received 25th November 1983)

SUMMARY

A rapid reversed-phase ion-pair chromatographic method for disodium pentacyanonitrosylferrate(II) (nitroprusside) and its photodegradation products nitrite, nitrate, hexacyanoferrate(II) and hexacyanoferrate(III) is described. For chromatography, phenyl-bonded pellicular silica gel (10 μm) was used with a mobile phase consisting of water (0.005 M tetrabutylammonium phosphate, 0.0011 M n-octylamine, 0.01 M potassium dihydrogenphosphate, pH 7.0) and methanol (0.005 M tetrabutylammonium phosphate, 0.0011 M n-octylamine) (65:35); the detector was set at 220 nm. In 5% (w/v) dextrose solutions, the calibration graph for nitroprusside was linear over the concentration range 10—120 μg ml^{-1}. A qualitative explanation for the order of retention: hexacyanoferrate(II) < hexacyanoferrate(III) < nitroprusside is given. The method is suitable for the selective determination of nitroprusside in photolyzed infusion solutions (100 μg ml^{-1} in aqueous 5% dextrose) and gives an impression of the decomposition products formed.

Sodium nitroprusside ($Na_2[Fe(CN)_5NO] \cdot 2H_2O$) is a potent hypotensive drug with a rapid onset of action when administered intravenously by injection or infusion [1]. It has long been recognized that nitroprusside is photosensitive, especially in solution [2—5]. Its photodegradation, a disadvantage for clinical usage, has often been studied to elucidate the pathway of degradation [6—10] and to develop more stable pharmaceutical formulations [10—12]. In the first stage of the photochemical process, nitric oxide and/or NO^+ are released from the nitroprusside ion [6—10], followed by rapid aquation of the resulting pentacyanoferrate(III) and pentacyanoferrate(II) [6—10]. Nitrite is formed in secondary reactions involving the released nitrosyl moiety and nitrate is also produced when oxygen is present in the solution [6—8, 10]. Besides, decomposition of pentacyanoaquoferrate(III) and pentacyanoaquoferrate(II) yields iron(III), iron(II) and cyanide ions [10, 12]. As a result of displacement of water in both pentacyanoaquoferrate ions by cyanide, hexacyanoferrate(II) and hexacyanoferrate(III) are

0003-2670/84/$03.00

subsequently formed [10, 12]. Ultimately, combination of iron(II) and iron(III) with hexacyanoferrate(II) and hexacyanoferrate(III) leads to formation of classical Prussian blue and analogues [8, 10].

Particularly on the point of the above-mentioned iron-containing decomposition products, Prussian blue excluded, the results and conclusions of the various studies are not consistent. Much of the experimental evidence rested on direct spectrophotometric characterization and identification of these products. These substances possess very similar spectral properties [10], thus the lack of consensus is not surprising.

In stability studies, the increase in absorbance at 394 nm, occurring on photo-irradiation, is usually employed as the measure for the degree of degradation. The method is not reliable, because it is based on the unproven assumptions that pentacyanoaquoferrate(III), which absorbs considerably at that wavelength in contrast to nitroprusside, is primarily formed and that its concentration is indicative of the degree of decomposition. Direct spectrophotometry is clearly not the method of choice for the analysis of photo-irradiated nitroprusside solutions.

In view of the inadequacy of direct spectrophotometry, a chromatographic separation prior to detection is very attractive. Recently, Baaske et al. [13] described a reversed-phase ion-pair chromatographic system for the separation of nitroprusside from photodegradation products. Hexacyanoferrate(III) and hexacyanoferrate(II) were employed to test the discriminatory properties of the system used. However, the applicability is considered doubtful because nitroprusside and hexacyanoferrate(III), one of the possible photodegradation products, are not resolved. Moreover, attempts to reproduce the results of Baaske et al. [13] failed.

A chromatographic procedure is described here for the separation of nitrite/nitrate, hexacyanoferrate(II), hexacyanoferrate(III) and nitroprusside. Additionally, a qualitative explanation is given for the observed order of retention. The procedure appeared to be suitable for selective determination of nitroprusside in photodegraded solutions.

EXPERIMENTAL

Chromatographic equipment

The liquid chromatograph consisted of a Constametric I solvent delivery system (Laboratory Data Control, Riviera Beach, FL, U.S.A.), a Rheodyne 7125 injection valve (20-μl loop) and a PU-4020 LC multi-wavelength detector (Pye-Unicam).

A 25-cm stainless steel column (3.0 mm i.d.; Valco) was packed with 2.2 g of μ-Bondapak phenyl-bonded pellicular material (10 μm; Waters) suspended in isopropanol utilizing the up-flow pressurized slurry technique [14]. The packed column was flushed with 100 ml of methanol at a pressure of approximately 350 bar (Haskel MCP-71 pump, HPLC Technology, Macclesfield, U.K.).

Throughout the experiments, a flow rate of 1.0 ml min^{-1} was maintained (pressure <140 bar). The response of the u.v. detector, which was set at 220 nm, was recorded with a Kipp BD-40 y-t recorder (10 mV f.s.d.) (Kipp & Zonen, Delft).

Reagents and mobile phases

Sodium nitroprusside, potassium hexacyanoferrate(II), potassium hexacyanoferrate(III), sodium nitrate and sodium nitrite were all of analytical grade (Merck). These chemicals were used for the preparation of aqueous solutions of mixtures, each substance being present at 50 $\mu g\ ml^{-1}$ concentration; these mixtures were employed for testing and characterization purposes. In order to prevent photochemical degradation, the solution containers were wrapped in aluminium foil and the mixtures were prepared daily. Water obtained from a Millipore Milli-Q Water Purification System was used throughout. Acetonitrile and methanol (Merck, analytical grade) were used as organic modifiers.

The aqueous phase of the eluent was prepared by stirring potassium dihydrogenphosphate (Merck) and the ion-pairing agent tetrabutylammonium phosphate (Eastman Kodak) into water, to give a solution of 0.01 M potassium dihydrogenphosphate containing the desired concentration of the counter-ion. Subsequently, the pH was adjusted to 7.0 by dropwise addition of 1 M potassium hydroxide (Merck, analytical grade). Tetrabutylammonium phosphate (TBA) was also dissolved in the organic solvent to the same concentration. Finally, aqueous and organic phase were mixed and the resulting eluent was degassed in an ultrasonic bath prior to use. n-Octylamine-containing mobile phases were made by adding n-octylamine to both phases in addition to tetrabutylammonium phosphate.

Columns were conditioned by recycling the eluent overnight at a flow rate of 0.5 ml min^{-1}. All chromatographic experiments were done at ambient temperature. After prolonged use (two months), the retention times of all components decreased by about 15%. The initial properties of the column could be restored by flushing overnight with methanol/water (50:50).

Irradiation experiments

Sodium nitroprusside solutions, 100 $\mu g\ ml^{-1}$ in aqueous 5% (w/v) dextrose, were photo-irradiated in a Rayonet photochemical reactor (Southern New England Ultraviolet Co., Middletown, CT, U.S.A.) utilizing two tubes (350 nm) diametrically positioned. The nitroprusside solutions, in pyrex conical flasks, were placed between the two tubes.

RESULTS AND DISCUSSION

Initially the liquid chromatographic conditions of Baaske et al. [13] were adopted. In contrast to the results of these authors, separation of hexacyanoferrate(III) and nitroprusside was observed but hexacyanoferrate(II) and

hexacyanoferrate(III) were not resolved, even when the acetonitrile content in the eluent was decreased from 25 to 15% (Fig. 1). The reason for this discrepancy is unclear.

Gritzner et al. [15] have observed that hexacyanoferrate(II) is unstable in low acceptor solvents such as acetonitrile, but is stabilized in high acceptor solvents (water, methanol). Therefore acetonitrile was replaced by methanol. This resulted in a selective retention of nitrite/nitrate, hexacyanoferrate(II), hexacyanoferrate(III) and nitroprusside (Fig. 2). Increase of the methanol content in the mobile phase results in shorter retention times (Fig. 3). Thus it can be concluded that hexacyanoferrate(II) elutes more quickly than hexacyanoferrate(III) regardless of the percentage of methanol in the eluent.

This is in accordance with n.m.r. experiments which have shown, contrary to expectation, that ion-pair formation in water with hexacyanoferrate(II) is very modest in comparison with hexacyanoferrate(III) [16]. These results were confirmed by Basu and Das [17], who used e.m.f. and solubility measurements. Gritzner et al. [15] explained the weaker ion-pair formation with hexacyanoferrate(II) by the stronger coordinative interaction with strong acceptor solvents such as water and methanol. The interference of the interaction with strong acceptor solvents accounts for the weaker tendency to form ion-pairs with, for instance, the tetrabutylammonium cation. Because of this weaker tendency, hexacyanoferrate(II) will be eluted more quickly than hexacyanoferrate(III) in a reversed-phase ion-pair chromatographic system. The stronger coordinative interaction between hexacyanoferrate(II) and high acceptor solvents is understandable in terms of a higher electron density

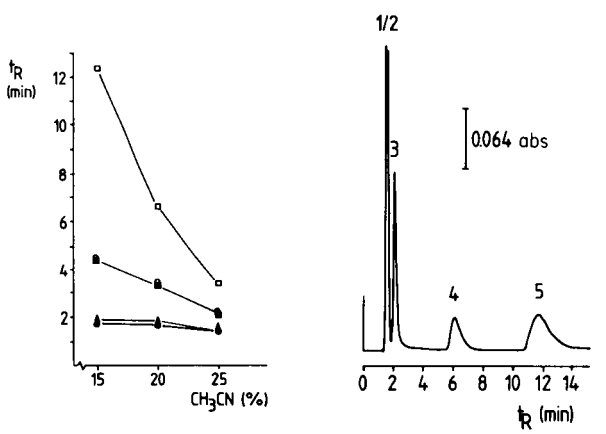

Fig. 1. Dependence of the retention time (t_R) on the percentage of acetonitrile in the mobile phase. Mobile phase: acetonitrile (0.005 M TBA)/water (0.005 M TBA, 0.01 M KH_2PO_4, pH 7.0) at 1.0 ml min^{-1}. (•) Nitrite; (▲) nitrate; (○) hexacyanoferrate(II); (■) hexacyanoferrate(III); (□) nitroprusside.

Fig. 2. Chromatogram showing the separation of nitrite/nitrate (1, 2), hexacyanoferrate-(II) (3), hexacyanoferrate(III) (4) and nitroprusside (5), with methanol (0.005 M TBA)/water (0.005 M TBA, 0.01 M KH_2PO_4, pH 7.0) (30:70) as eluent at 1.0 ml min^{-1}.

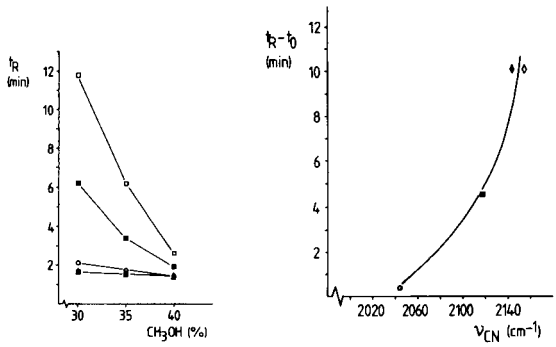

Fig. 3. Dependence of retention time (t_R) on the percentage of methanol in the mobile phase. Mobile phase: methanol (0.005 M TBA)/water (0.005 M TBA, 0.01 M KH_2PO_4, pH 7.0) at 1.0 ml min^{-1}. For the symbols, see Fig. 1.

Fig. 4. $t_R - t_O$ (min) versus ν(C≡N) (cm^{-1}) [18]. Mobile phase as for Fig. 2. (○) hexacyanoferrate(II); (■) hexacyanoferrate(III); (♦) ν(C≡N) (eq.), (◇) ν(C≡N) (ax.) nitroprusside.

located on the nitrogen atoms of the cyanide ligands in hexacyanoferrate(II). Experimental evidence for the higher electronic density has been provided by infrared measurements, which have revealed a significantly lower C≡N stretching frequency, ν(C≡N), for hexacyanoferrate(II) [18].

The concept outlined above explains why nitroprusside is retained more strongly than hexacyanoferrate(III). The greater C≡N stretching frequency for nitroprusside than for hexacyanoferrate(III) means that nitroprusside will have a greater tendency to form outer-sphere complexes with tetrabutylammonium, inferring stronger retention of nitroprusside than hexacyanoferrate(III). To demonstrate the relation between ν(C≡N) and the retention times, the ν(C≡N) values [18] were plotted versus the individual retention times (Fig. 4).

In addition to variation of the percentage of methanol in the mobile phase, the concentration of tetrabutylammonium was increased. This resulted in a stronger increase of retention in the order nitrite/nitrate, hexacyanoferrate(II), hexacyanoferrate(III), nitroprusside (Fig. 5). The observed chromatographic behaviour is in accordance with the above concept. At higher tetrabutylammonium concentrations in the eluent, the nitrite/nitrate and hexacyanoferrate(II) peaks are resolved. However, there is a concomitant strong increase in retention time of hexacyanoferrate(III) and particularly nitroprusside.

In order to resolve the hexacyanoferrate(II) peak from the nitrite/nitrate peak, n-octylamine was added to the mobile phase to give a concentration of 0.0011 M. Such an approach was also adopted by Wittmer et al. [19], who separated tartrazine, sulfanilic acid and pyrazolone by using tridecylamine (6×10^{-4} M) in addition to tetrabutylammonium (3×10^{-3} M) in the mobile phase. As can be seen in Fig. 6, the addition of the n-octylamine to the

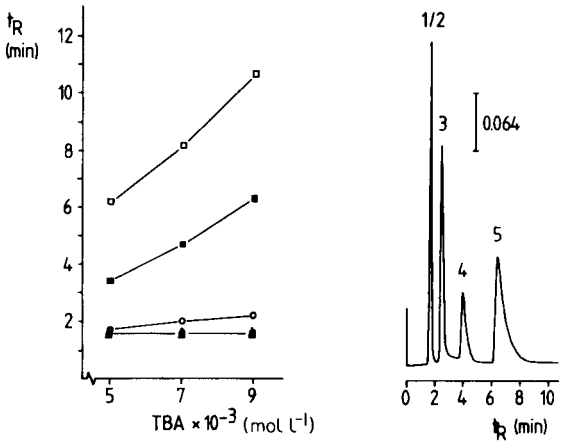

Fig. 5. Dependence of the retention times t_R on the TBA concentration in the mobile phase consisting of methanol (TBA)/water (TBA, 0.01 M KH_2PO_4, pH 7.0) (35:65) at 1.0 ml min^{-1}. For the symbols, see Fig. 1.

Fig. 6. Chromatogram showing the separation of nitrite, nitrate (1, 2), hexacyanoferrate-(II) (3), hexacyanoferrate(III) (4) and nitroprusside (5) utilizing methanol (0.005 M TBA, 0.0011 M n-octylamine)/water (0.005 M TBA, 0.0011 M n-octylamine, 0.01 M KH_2PO_4, pH 7.0) (35:65) as eluent at 1.0 ml min^{-1}.

eluent resulted in a good separation of the nitrite/nitrate peak from the hexacyanoferrate(II) peak. The relatively strong increase of the retention time for hexacyanoferrate(II) was accompanied by a smaller increase in the retention of hexacyanoferrate(III), while the retention time of nitroprusside remains unchanged. This behaviour is in accord with the conceptual framework outlined above. Most probably, the interaction between n-octylamine and the sample ions is not solely based on ion-pair formation. The stronger but still weak influence on the retention of hexacyanoferrate(II) can be explained by assuming that association with protonated n-octylamine is involved. Proton association with hexacyanoferrate(II) is stronger than that with hexacyanoferrate(III) [20]; thus hexacyanoferrate(II) will be more strongly influenced than hexacyanoferrate(III). The greater tendency for hexacyanoferrate(II) to be protonated also reflects the greater electron density on the nitrogen atoms. At a n-octylamine concentration of 0.0023 M, the retention has further increased resulting in less sharp resolution of hexacyanoferrate(II) and hexacyanoferrate(III) (Fig. 7). Consequently, a n-octylamine concentration of 0.0011 M was employed for the analysis of photo-irradiated solutions of nitroprusside.

Prior to photo-irradiation experiments concerning 0.01% (w/v) nitroprusside infusion solutions in aqueous 5% (w/v) dextrose, the applicability of the chromatographic system to nitroprusside was tested. A linear calibration graph was obtained for nitroprusside in aqueous 5% (w/v) dextrose in the

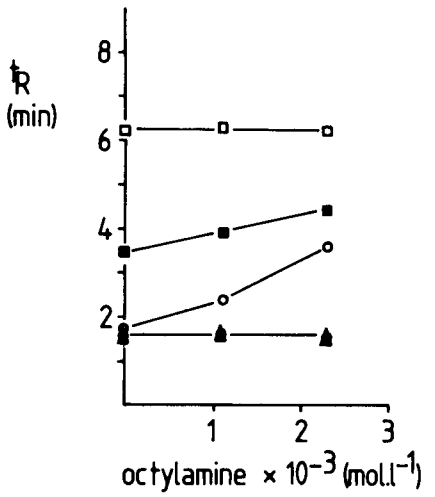

Fig. 7. Dependence of the retention time t_R on the n-octylamine concentration in the mobile phase. Mobile phase: methanol (0.005 M TBA, n-octylamine)/water (0.005 M TBA, n-octylamine, 0.01 M KH_2PO_4, pH 7.0) (35:65) at 1.0 ml min^{-1}. For the symbols, see Fig. 1.

concentration range 10—120 μg ml^{-1}; the slope was 3.104 × 10^{-3} A ml μg^{-1} with a standard deviation of 7.9 × 10^{-6} and an intercept of 7.6 × 10^{-4} A, where A indicates absorbance. The percentage of methanol in the mobile phase was increased to 36% in order to reduce measurement time. Very symmetric nitroprusside peaks were observed, thus evaluation of peak heights rather than peak areas was acceptable.

In the photolysis study, samples were taken at appropriate time intervals from the photolyzed solution and injected immediately. Chromatograms of an unirradiated (t = 0 min) and a photolyzed solution (t = 80 min) are shown in Fig. 8. The decay of the nitroprusside concentration during the course of photolysis is nearly linear, as shown in Fig. 9. A zero-order decay of the nitroprusside concentration is expected in the case of an uncomplicated photochemical degradation process. Nitroprusside is clearly resolved from the degradation products and consequently the method is appropriate for stability studies. The peaks at the retention times of nitrite/nitrate, hexacyanoferrate(II) and hexacyanoferrate(III) can be presumably ascribed to these species. Before hexacyanoferrate(III), there is a peak (arrowed in Fig. 8B) which can probably be attributed to the photodegradation intermediates, pentacyanoaquoferrate(II) and pentacyanoaquoferrate(III). Because pentacyanoferrate(II), as generated in solution [21, 22], has an identical retention time, this species is more likely.

The chromatographic procedure described seems very suitable for the selective determination of nitroprusside in photodegraded solutions, nitroprusside being resolved from its degradation products including hexacyano-

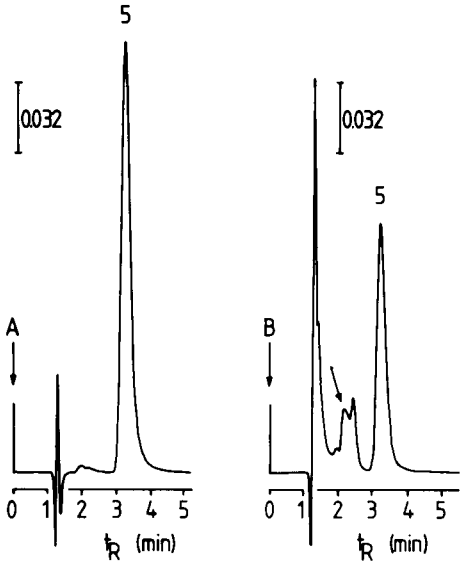

Fig. 8. Chromatograms for (A) an unirradiated nitroprusside solution in aqueous 5% dextrose (100 μg ml^{-1}) and (B) a photolyzed solution, t = 80 min. Mobile phase: methanol (0.005 M TBA, 0.0011 M n-octylamine)/water (0.005 M TBA, 0.0011 M n-octylamine, 0.01 M KH_2PO_4, pH 7.0) (36:64) at 1.0 ml min^{-1}. Photolysis conditions as outlined in Experimental.

ferrate(III). The method also provides an impression of the decomposition products formed.

We are grateful to Mr. J. W. van Duijn (RIGO, Leiden, The Netherlands) for providing the facility to pack the columns.

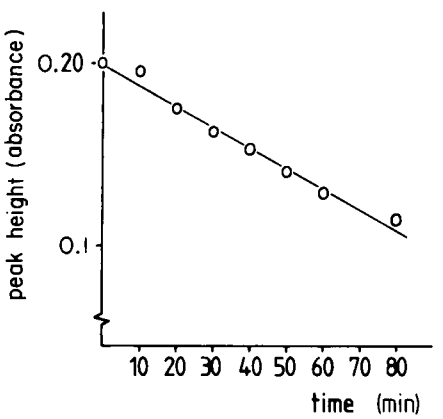

Fig. 9. Decrease of the nitroprusside peak height versus duration of photolysis (min). Irradiation conditions as mentioned under Experimental; chromatographic conditions: see legend Fig. 8.

REFERENCES

1 A. Goodman Gilman, L. S. Goodman and A. Gilman, The Pharmacological Basis of Therapeutics, 6th edn., MacMillan, New York, 1980, pp. 805, 806.
2 A. Overbeck, Arch. Pharm. (Weinheim), 124 (1853) 189.
3 I. M. Kolthoff, Z. Anal. Chem., 62 (1923) 216.
4 E. Justin-Mueller, Bull. Soc. Chim. Fr., 2 (1935) 1932.
5 O. Baudisch, Science, 108 (1948) 443.
6 R. P. Mitra, D. V. S. Jain, A. K. Banerjee and K. V. R. Chari, J. Inorg. Nucl. Chem., 25 (1963) 1263.
7 G. V. Buxton, F. S. Dainton and J. Kalecinski, Int. J. Radiat. Phys. Chem., 1 (1969) 87.
8 S. K. Wolfe and J. H. Swinehart, Inorg. Chem., 14 (1975) 1049.
9 T. Jarzynowski, T. Senkowski and Z. Stasicka, Pol. J. Chem., 55 (1981) 3.
10 A. C. van Loenen and W. Hofs-Kemper, Pharm. Weekbl., 114 (1979) 52.
11 G. E. Schumacher, Am. J. Hosp. Pharm., 23 (1966) 532.
12 S. E. Ronco and P. J. Aymonino, Inorg. Chim. Acta, 77 (1983) 631.
13 D. M. Baaske, M. D. Smith, N. Karnatz and J. E. Carter, J. Chromatogr., 212 (1981) 339.
14 L. R. Snyder and J. J. Kirkland, Introduction to Modern Liquid Chromatography, 2nd edn., Wiley-Interscience, New York, 1979, p. 216.
15 G. Gritzner, K. Danksagmuller and V. Gutman, J. Electroanal. Chem., 72 (1976) 177.
16 D. W. Larsen and A. C. Wahl, Inorg. Chem., 4 (1965) 1281.
17 M. K. Basu and M. N. Das, Inorg. Chem., 9 (1970) 2781.
18 L. Tosi and J. Danon, Inorg. Chem., 3 (1964) 150.
19 D. P. Wittmer, N. O. Nuessle and W. G. Haney Jr., Anal. Chem., 47 (1975) 1422.
20 J. Jordan and G. J. Ewing, Inorg. Chem., 9 (1970) 2781.
21 H. E. Toma, Inorg. Chim. Acta, 15 (1975) 205.
22 D. J. Kenney, T. P. Flynn and J. B. Gallini, J. Inorg. Nucl. Chem., 20 (1961) 75.

Analytica Chimica Acta, 161 (1984) 221—229
Elsevier Science Publishers B.V., Amsterdam — Printed in The Netherlands

EXTRACTION OF ORGANIC ACIDS BY ION-PAIR FORMATION WITH TRI-N-OCTYLAMINE
Part 1. Extraction Rate and Influence of pH and Ionic Strength

M. PUTTEMANS, L. DRYON and D. L. MASSART*

Pharmaceutical Institute, Vrije Universiteit Brussel, Laarbeeklaan 103, B-1090 Brussels (Belgium)

(Received 10th February 1984)

SUMMARY

The extraction scheme for dyes, developed previously, is applied to benzoic acid and its hydroxylated derivatives. Extractions are done with tri-n-octylamine at pH 5.5 and an ionic strength of 0.1 into chloroform. Equilibrium is attained in 20 min or less. The influences of pH and ionic strength of the extraction medium on the recoveries are described. The scheme developed for dyes is applicable for benzoic acid and salicylic acid; for more polar acids the pH and ionic strength must be changed in order to maximize the recovery.

Ion-pair extraction of acids consists in the formation of a complex between an ionized substance and an ion of opposite charge [1—7]. The so-formed complex is less hydrophilic and extracts better into an organic phase. This technique has been applied to the extraction of food dyes [8—10], yielding quantitative results in the monitoring of commercial food products. Two counter-ions have been used, tetrabutylammonium and tri-n-octylamine (TnOA). The latter was shown to be more powerful, because of its higher hydrophobicity, and was selected for further work [8].

This paper, which is the first of a series, will investigate if the extraction with TnOA can also be applied to other acids than dyes. The extraction rate and the influence of the pH and the ionic strength on the extraction are described. Other papers will discuss the extraction mechanism and the applicability of the extraction scheme for quantifying acids in biological or food samples.

EXPERIMENTAL

Apparatus, chemicals and reagents

All ultraviolet (u.v.) and visible photometric measurements were done with a Hitachi 200 Perkin-Elmer spectrophotometer with 10- or 50-mm quartz cells. For pH measurements, an Orion 601 Ionalyzer was used with a combined glass and calomel electrode.

The organic acids and salts used were: 3-hydroxybenzoic acid, 2,5-di-

0003-2670/84/$03.00

hydroxybenzoic acid (both analytical grade) and benzoic acid (pure), all from Fluka; 4-hydroxybenzoic acid (99% pure) and 3,4-dihydroxybenzoic acid (97% pure) (Aldrich Europe, Beerse, Belgium); sodium benzoate (analytical grade, Merck); and sodium salicylate (analytical grade, Baker Chemical Company); salicylic acid is 2-hydroxybenzoic acid.

Tri-n-octylamine (Aldrich Europe) was used as received. All other reagents and solvents were of analytical grade from Merck. Chloroform was freed from ethanol and saturated with water by repeated shaking with water. Buffers of constant ionic strength were prepared by using phosphoric acid and sodium phosphate. All buffer solutions were saturated with chloroform. The TnOA solutions were prepared in water-saturated chloroform.

Extraction procedure

The extractions were done in stoppered centrifuge tubes using equal volumes (10 ml) of aqueous and organic phase. The aqueous phase, consisting of a solution of the acid, with concentration C_0 (5×10^{-5} M unless otherwise stated) in a buffer of given ionic strength, was shaken with the organic phase in a mechanical reciprocating shaker for 30 min (unless otherwise stated) at room temperature. The shaker was set to a shaking speed of 60 strokes/min. The phases were separated after centrifugation. The concentration of the acid in the aqueous phase was determined by spectrophotometry. Each partition experiment was done in triplicate.

Definitions

In the distribution of an acid HX between an aqueous (subscript w) and an organic phase (subscript o) containing a long-chain amine A, the following equilibria compete, if no side-reactions occur [10]

(1) liquid—liquid distribution of the acid HX, with distribution constant K_d

$$HX_w \rightleftharpoons HX_o; \quad K_d = [HX]_o/[HX]_w \tag{1}$$

(2) dissociation of HX in the aqueous phase, with acidity constant K_a

$$HX_w \rightleftharpoons H_w^+ + X_w^-; \quad K_a = [H^+]_w [X^-]_w/[HX]_w \tag{2}$$

(3) extraction of the anion X^- by ion-pair formation, with the ion-pair extraction constant K_{ex}

$$A_o + H_w^+ + X_w^- \rightleftharpoons AHX_o; \quad K_{ex} = [AXH]_o/[A]_o[H^+]_w [X^-]_w \tag{3}$$

The result of the partition experiment may be expressed by the percent extraction or by the distribution ratio D, defined as the total concentration of X in the organic phase divided by the total concentration of X in the aqueous phase, or $[X]_o/[X]_w$.

RESULTS AND DISCUSSION

It has already been demonstrated [10] that chloroform is a good solvent for ion-pair extractions with tri-n-octylamine (TnOA), and this solvent was used throughout the whole work. Furthermore, the conditions used for the extraction of dyes [8—10], e.g., a phosphate buffer of pH 5.5 and an ionic strength of 0.1 were also employed here.

Influence of the extraction time

In order to determine the minimum time necessary to attain equilibrium, four acids were extracted at room temperature under standardized conditions. The % extracted is given in Table 1 as a function of the extraction time. At zero time a certain % extraction was obtained which increases along with the % extraction at equilibrium. This point at zero time was obtained by filling the centrifuge tubes with the chloroform and aqueous phases, putting them in the shaking apparatus and removing them immediately. The time given in Table 1 is in fact the shaking time and not the contact time.

TABLE 1

Kinetics of the extractions
(k = rate constants, r = correlation coefficient. Ionic strength 0.1, 0.1 M TnOA in chloroform, pH 5.5)

Time (min)	% Extracted						
	3,4-Dihydroxybenzoic acid		4-Hydroxybenzoic acid		Benzoic acid		Tartrazine 10 mg l^{-1}
	10 mg l^{-1}	100 mg l^{-1}	10 mg l^{-1}	100 mg l^{-1}	10 mg l^{-1}	100 mg l^{-1}	
0	0.0 ± 0.0	5.1 ± 0.3	4.7 ± 0.5	8.7 ± 0.8	2.4 ± 4.2	21.7 ± 1.6	37.2 ± 1.4
0.25	0.1 ± 0.1	5.8 ± 0.2	8.3 ± 1.0	12.6 ± 0.3	13.4 ± 5.5	41.8 ± 2.0	57.2 ± 1.8
0.5	0.4 ± 0.6	6.5 ± 0.6	10.7 ± 0.5	16.2 ± 0.4	35.6 ± 5.4	55.4 ± 3.0	67.2 ± 1.6
1	0.2 ± 0.4	6.8 ± 0.8	17.6 ± 2.4	19.2 ± 1.7	40.9 ± 2.1	51.6 ± 2.8	82.6 ± 1.2
2	3.7 ± 0.9	8.2 ± 0.7	27.0 ± 4.1	25.7 ± 0.8	65.8 ± 3.8	61.0 ± 4.5	97.3 ± 1.0
5	5.2 ± 0.7	10.3 ± 1.0	41.7 ± 0.8	38.6 ± 1.6	81.4 ± 3.3	89.5 ± 1.3	99.9 ± 0.2
10	11.1 ± 1.7	14.5 ± 0.1	44.8 ± 1.2	60.4 ± 0.8	85.1 ± 5.8	94.0 ± 0.7	100.0 ± 0.2
15	11.2 ± 0.3	14.6 ± 0.1	46.0 ± 1.2	62.4 ± 0.8	91.4 ± 1.0	96.8 ± 0.2	
20	12.1 ± 1.2	14.8 ± 0.3	46.2 ± 0.3	61.1 ± 1.6	93.9 ± 2.1	98.2 ± 0.3	
25	12.4 ± 0.6	14.9 ± 0.2	47.0 ± 0.4	59.4 ± 0.4	95.2 ± 0.6	98.0 ± 0.3	
30	11.2 ± 0.4	14.5 ± 0.8	46.0 ± 0.3	59.6 ± 0.2	93.6 ± 2.3	98.2 ± 0.7	
45	11.8 ± 0.3	14.5 ± 0.2	45.7 ± 0.8	59.3 ± 0.2	94.3 ± 0.5	98.3 ± 0.2	
First order							
r	0.989	0.992	0.988	0.997	0.968	0.963	0.996
k_1	0.012	0.010	0.097	0.080	0.323	0.252	1.303
Second order							
r	0.990	0.990	0.996	0.991	0.997	0.999	0.937
k_2	0.001	0.0001	0.013	0.001	0.088	0.015	20.250

From the data listed in Table 1, it is obvious that the rate of extraction is higher for tartrazine [3-carboxy-5-hydroxy-1-(*p*-sulphophenyl)-4-(*p*-sulphophenylazo)-pyrazole, trisodium salt] than for the other acids. It appears that after 2 min, the extraction yield of tartrazine already attains 97% of its final value, 69% for benzoic acid, 60% for 4-hydroxybenzoic acid and 28% for 3,4-dihydroxybenzoic acid if one considers the 10 mg l^{-1} level. At the 100 mg l^{-1} level the corresponding amounts are 62% for benzoic acid, 40% for its 4-hydroxyderivative and 55% for 3,4-dihydroxybenzoic acid.

The extraction rate may also be expressed by kinetic parameters. The experimental data were fitted to both a first-order and a second-order model. In the case of a first-order mechanism, plots of log (C/C_0) versus the extraction time, t, are linear with a slope of k_1; C_0 is the initial concentration and C is the concentration at time t. For second-order reactions, the relation between C and the elapsed time may be expressed as follows: $1/C = k_2 t - 1/C_0$ [11]. The results expressed as the correlation coefficient r and the rate constants k_1 and k_2 are also given in Table 1.

For the hydroxylated derivatives of benzoic acid, both models fit the experimental results equally well. For benzoic acid, the second-order mechanism correlates better with the data, whereas the first-order mechanism fits better for tartrazine.

For benzoic acid, equilibrium is attained after 20 min but for all the other substances equilibration is faster. Therefore, in the determination of experimental equilibrium constants, extraction times of 30 min should be sufficient because a 50% safety margin is provided.

Influence of the pH

As discussed before [10], the pH has a double effect on the extraction yield. Indeed, ion-pair formation takes place only when TnOA is protonated and when the acid is dissociated. Extractions done under different pH conditions and with or without TnOA in the chloroform phase permit the calculation of conditional equilibrium constants. The liquid—liquid distribution of acids between buffer solutions and chloroform enables the K_a and K_d values to be determined from a graphical representation of the following equation [4]

$$1/D = 1/K_d + (K_a/K_d)\,(1/[H^+]) \qquad (4)$$

which is obtained from Eqns. 1—3. The y-intercept of the graph $1/D$ versus $1/[H^+]$ yields K_d, and K_a can be calculated from the slope of the same graph.

The values of K_a and K_d, determined for benzoic acid and its hydroxy derivatives, are given in Table 2. It can be observed that the K_a values calculated from batch extraction data do not match exactly with the theoretical values. It is also obvious that there is an influence of the structure of the extracted species on the difference between the batch and theoretical values (Δ). This difference between experimental and theoretical values indicates side-reactions, e.g., the formation of acid—acid dimers.

TABLE 2

Acidity constants (pK_a) and partition constants (K_d)
The pK_a values were obtained from the literature (theoretical), or were determined by batch experiments (batch) ($\Delta = pK_a$ (batch) $- pK_a$ (theoretical))

	pK_a			K_d
	Theoretical [12]	Batch	Δ	
Benzoic acid	4.19	4.87	0.68	0.481
Salicylic acid	2.97	3.26	0.29	0.189
3-Hydroxybenzoic acid	4.06	1.83	−2.23	0.021
4-Hydroxybenzoic acid	4.48	2.22	−2.26	0.007
3,4-Dihydroxybenzoic acid	4.48	1.94	−2.54	0.047
2,5-Dihydroxybenzoic acid	2.97	2.30	−0.67	0.033

From the data listed in Table 2, the Δ values are as follows: +0.68 for benzoic acid, +0.29 for salicylic acid, while all the other hydroxy derivatives have negative Δ values. Clearly, the presence of a hydroxy function causes side-reactions, probably because of hydrogen bonding. It is well known [2] that in salicylic acid, the hydroxyl function on position 2 undergoes intramolecular hydrogen bonding with the carboxyl function. It is highly probable that this phenomenon also occurs in 2,5-dihydroxybenzoic acid. For these compounds, this results (as shown in Table 2) in less negative Δ values than for the derivatives substituted in position 3 or 4. This indicates that hydroxyl functions in the *m*- or *p*- position relative to the carboxyl function have a higher capability to interact with surrounding molecules than when the hydroxyl function is in the *o*-position.

In Fig. 1 the extraction efficiency is shown graphically as a function of the pH for benzoic acid and its hydroxy derivatives. Figure 1(a) is a plot of the percentage extraction of acids with 0.01 M TnOA in chloroform. Figure 1(b) shows the extraction yield with pure chloroform and Fig. 1(c) visualises the effect of the pH on the ion-pair formation itself. Figure 1(c) is obtained by subtracting the % extraction by chloroform alone from the total extraction yield. It is clear that only two acids, i.e., benzoic acid and salicylic acid, provide a distinct difference between Fig. 1(a) and (c). Indeed, the other acids are extracted only to a small extent by chloroform, as shown in Fig. 1(b), even at very low pH. These observations are confirmed by the K_d values (the distribution constants of the undissociated acids) listed in Table 2. In fact, the K_d values computed with Eqn. 1 for benzoic acid and salicylic acid are much higher than the partition constants calculated for the other acids. Furthermore, it is valuable to note that the optimum pH for ion-pair formation with TnOA is not the same for benzoic acid and salicylic acid as for the other hydroxy derivatives. For benzoic and salicylic acid, this optimal pH (pH_{opt}) is 5.5. The other acids have a pH_{opt} of about 2.5.

Consequently, for benzoic acid and salicylic acid, optimal extraction by

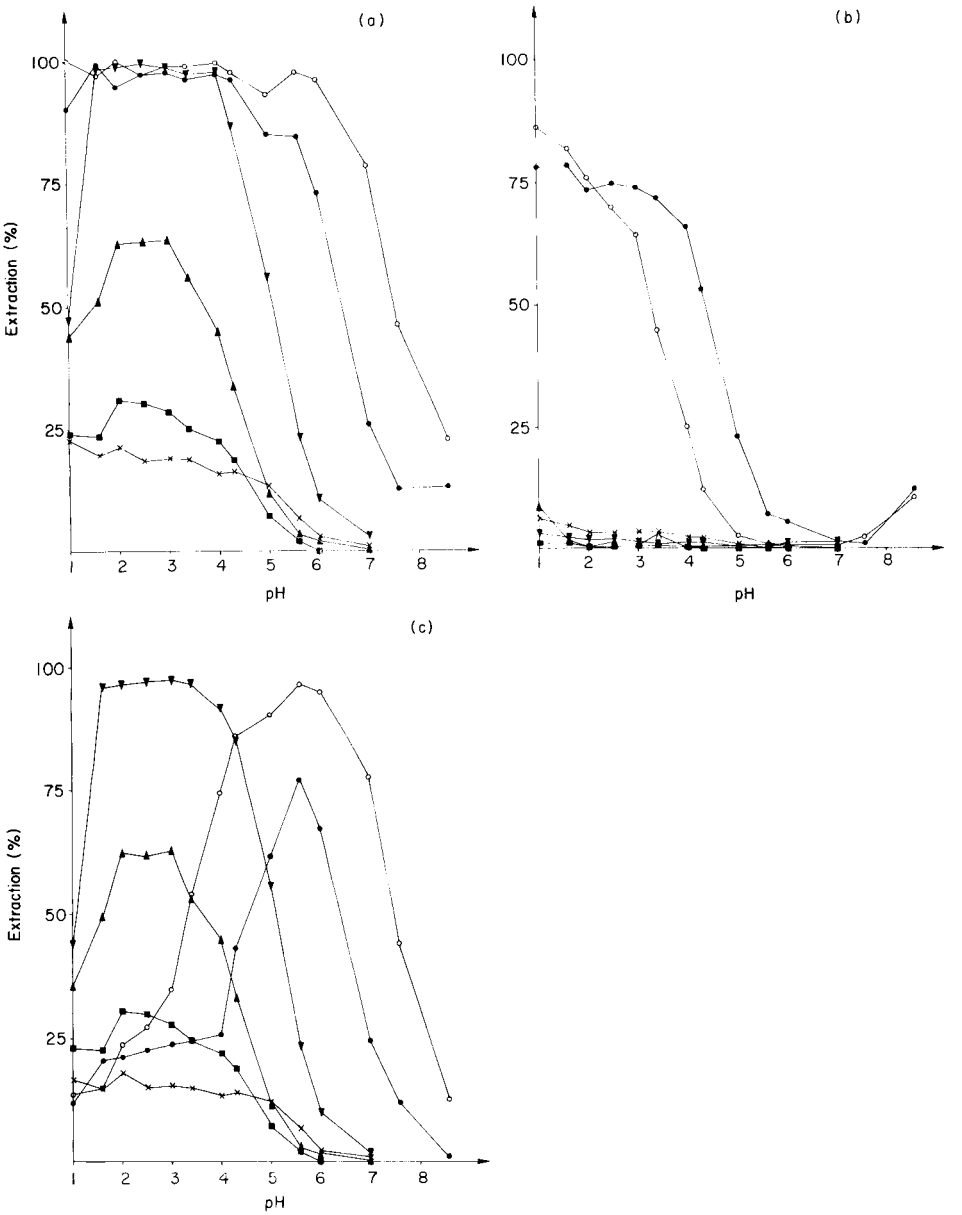

Fig. 1. Extraction (%) as a function of pH at 0.1 ionic strength: (a) extraction with 0.01 M TnOA in chloroform; (b) extraction with chloroform; (c) difference (a—b). Compounds: (•) benzoic acid; (○) salicylic acid; (▲) 3-hydroxybenzoic acid; (■) 4-hydroxybenzoic acid; (×) 3,4-dihydroxybenzoic acid; (▼) 2,5-dihydroxybenzoic acid.

ion-pair formation with TnOA takes place when the analytes are more than 95% ionized. The other derivatives of benzoic acid, with hydroxyl functions on position 3 or 4 are extracted best, with TnOA, at ionization degrees lower than 2.5%. The 2,5-dihydroxy derivative is an intermediate between these two extremes: optimal extraction is obtained when the analyte is ca. 25% ionized. It follows that a sufficient amount of undissociated acid HX is necessary to achieve a good extraction with TnOA of these hydrophilic, hydroxylated derivatives of benzoic acid. When no undissociated acid is present, i.e., at high pH values, the hydrophilic analytes are poorly extracted by TnOA. This is probably caused by the hydroxyl functions on position 3 or 4 which are able to undergo hydrogen bonding and consequently to hydrate the analyte, so that the analyte is stabilized in aqueous medium.

Influence of the ionic strength

The influence of the ionic strength (I) of the aqueous phase on the extraction yield was investigated for benzoic acid and its hydroxylated derivatives. The different solutions had only sodium phosphate added and all were at pH 5.5 ± 0.1. As shown in Fig. 2 for the 3- and/or 4-hydroxy derivatives of benzoic acid, the ionic strength seems to have a dual effect. Indeed, increasing ionic strength first causes a decrease of the extraction efficiency, which then goes through a minimum to increase again.

As pointed out by Motomizu and Toei [13] in the case of the ion-pair extraction of cationic azo dyes with inorganic counter-ions, the distribution ratio (D) of the extracted ion-pair is proportional to the activity coefficient. This signifies that D is influenced by the ionic strength of the aqueous phase. The relation between the ionic strength (I) and the activity coefficient (f) is given by the Debye—Hückel law [11] (at low values of I). At ionic strengths above 0.1—0.2 the initial decrease of f with increasing I is followed

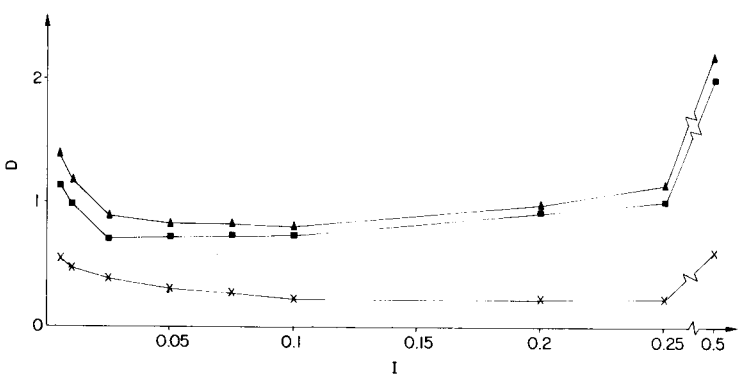

Fig. 2. Effect of the ionic strength (I) on the distribution ratio D with 0.1 M TnOA in chloroform: (▲) 3-hydroxybenzoic acid; (■) 4-hydroxybenzoic acid; (×) 3,4-dihydroxybenzoic acid.

by an increase of the activity coefficient. As shown by the data given in Table 3 and Fig. 2, the theoretical relationship between I and f is reflected on the distribution ratio of the acids.

The observed phenomenon cannot be explained by an effect of the buffer ions themselves (e.g., co-extraction), because it is a well established fact that phosphate ions are very badly extracted by ion-pair formation with amines [14]. It is also known [15] that the ionic strength influences the acid dissociation equilibrium: increasing the ionic strength lowers the pK_a of the acid. This means that at constant pH, a higher degree of ionisation will be obtained. However, it was observed earlier for the hydroxylated derivatives of benzoic acid that the extraction recovery is much higher when a large amount of undissociated acid is present in the system. Consequently, the effect of I on the pK_a value of the acid explains only the first part (the decrease) of the curves shown in Fig. 2.

The observed phenomenon can also be explained in the following manner: a solution is saturated with a slightly soluble complex AHX. On addition of an electrolyte, the solubility of the complex is enhanced because the solubility product, $K_{so} = a[AH^+]\,a[X^-]$, is constant ($a[X^-]$ is the concentration of X^- expressed as activity). The activity coefficients decrease so that the molar concentrations of AH^+ and X^- also increase. In precipitation reactions, this is known as salting in. As the solubility is increased, the distribution ratio decreases at first. When the ionic strength rises further, the solutes are hydrated to a greater extent, the free volume of water is

TABLE 3

Effect of the ionic strength of the aqueous phase on the distribution ratio (pH 5.5; 0.1 M TnOA in chloroform)

	Ionic strength				
	0.005	0.01	0.025	0.05	0.075
Benzoic acid	7.673	7.359	7.298	7.026	6.932
Salicylic acid	83.674	76.809	70.214	65.983	60.030
p-Hydroxybenzoic acid	1.138	0.956	0.708	0.712	0.720
3-Hydroxybenzoic acid	1.395	1.190	0.908	0.836	0.830
3,4-Dihydroxybenzoic acid	0.563	0.473	0.387	0.302	0.279
2,5-Dihydroxybenzoic acid	7.418	7.224	7.158	6.934	6.820
	0.1	0.2	0.25	0.5	
Benzoic acid	6.508	6.684	6.809	8.792	
Salicylic acid	61.506	69.307	150.684	999.9	
p-Hydroxybenzoic acid	0.725	0.923	0.999	2.021	
3-Hydroxybenzoic acid	0.807	0.979	1.142	2.197	
3,4-Dihydroxybenzoic acid	0.209	0.210	0.216	0.608	
2,5-Dihydroxybenzoic acid	6.403	6.573	6.721	8.586	

diminished, the solution is again saturated, solubility decreases, and D rises; this is known as salting out.

An effect of ionic strength on the distribution ratio was observed for all the compounds investigated. The percentage extraction was more strongly influenced for the more hydrophilic substances. Obviously, this indicates that if one wants to extract hydrophilic analytes such as the hydroxy derivatives of benzoic acid, the ionic strength needs to be adjusted in order to increase the extraction yield. An ionic strength of 0.5 seems most appropriate because it yields higher recoveries than 0.005. Furthermore, the buffer capacity of the more diluted buffer solution is much lower than the capacity of the concentrated buffer. At an ionic strength of 0.5, a pH change of 0.1 is observed after the addition of 5.4 ml of a 1 N solution of a strong acid to 1 l of the buffer solution. With the more diluted buffer (I = 0.005) only 4.5 ml of a 0.01 N solution of a strong acid is required to produce a pH shift of 0.1. Consequently, the use of the more concentrated buffer solution seems most appropriate for the analysis of samples such as lemonade because most of them contain a high amount of citric acid.

The authors acknowledge financial help of the Fund for Scientific Medical Research and thank Y. Michotte for statistical evaluation of the results and A. Langlet-De Schrijver and K. Broothaers-Decq for technical assistance.

REFERENCES

1 G. Schill, Separation Methods for Drugs and Related Organic Compounds, Apotekarsocieteten, Uppsala, Sweden, 1978.
2 R. Modin and A. Tilly, Acta Pharm. Suec., 5 (1968) 311.
3 K. O. Borg and G. Schill, Acta Pharm. Suec., 5 (1968) 324.
4 R. Modin and M. Schroder-Nielsen, Acta Pharm. Suec., 8 (1971) 573.
5 R. Modin, Acta Pharm. Suec., 8 (1971) 509.
6 T. Tilly, Acta Pharm. Suec., 10 (1973) 111.
7 T. Nordgren and R. Modin, Acta Pharm. Suec., 12 (1975) 407.
8 M. Puttemans, L. Dryon and D. L. Massart, J. Assoc. Off. Anal. Chem., 65 (1982) 730, 737.
9 M. Puttemans, L. Dryon and D. L. Massart, J. Assoc. Off. Anal. Chem., 66 (1983) 670, 1039.
10 M. Puttemans, L. Dryon and D. L. Massart, Anal. Chim. Acta, 113 (1980) 307.
11 G. Barrow, Physical Chemistry, 2nd edn., McGraw Hill, 1966.
12 R. C. Weast (Ed.), Handbook of Chemistry and Physics, CRC Press, Cleveland, OH, 1975.
13 S. Motomizu and K. Toei, Anal. Chim. Acta, 120 (1980) 267.
14 B. A. Persson, Acta Pharm. Suec., 7 (1970) 343.
15 B. L. Karger, J. N. LePage and N. Tanaka, in C. Horvath (Ed.), High Performance Liquid Chromatography—Advances and Perspectives, Academic Press, New York, 1980.

Analytica Chimica Acta, 161 (1984) 231—244
Elsevier Science Publishers B.V., Amsterdam — Printed in The Netherlands

INVESTIGATION OF SOME ASYMMETRIC TRIAZINES AS REAGENTS FOR THE SPECTROPHOTOMETRIC MICRODETERMINATION OF THE IRON OXIDATION STATE IN SILICATES

E. KISS

Research School of Earth Sciences, The Australian National University, P.O. Box 4, Canberra, A.C.T., 2600 (Australia)

(Received 20th February 1984)

SUMMARY

The preparation and analytical evaluation of two asym-triazines, 3-(1-isoquinolyl)-5,6-diphenyl-1,2,4-triazine (IQDT) and 3,3′-bis(5,6-diphenyl-1,2,4-triazine (BDT), and their sulphonated derivatives (IQDT-TAS and TSBT-TAS) are described. The sulphonated ferroin chromogens formed intensely coloured tris-chelates with iron(II) in molar acid solutions and chelates were also formed with copper(I) ions. The TSBT-TAS reagent showed an exceptionally high acid tolerance in its ability to chelate iron(II) in concentrated acids. Once formed, the chelates of all four compounds possessed a high degree of stability. The IQDT and IGDT-TAS reagents formed maximal colour at pH 3—8 whereas TSBT-TAS was indifferent to pH changes in the acidic range; the molar absorptivities were 38 340 l mol^{-1} cm^{-1} at 375 nm and 27 360 at 596 nm for IQDT-TAS, and 23 500 l mol^{-1} cm^{-1} at 450 nm and 28 240 at 550 nm for TSBT-TAS. Only EDTA, cyanide and comparable amounts of copper(I) and cobalt(II) interfered. The TSBT-TAS reagent and to a lesser extent IQDT-TAS were useful for the spectrophotometric microdetermination of FeO in silicates. Aerial oxidation was prevented by the immediate chelation of iron(II) released from the silicate matrix with a decomposition acid mixture containing TSBT-TAS. More resistant minerals were decomposed in teflon bombs by prolonged heating. Good precision and accuracy were obtained for the analysis of 1—5-mg samples where the average relative standard deviation was 1.73%.

Heterocyclic compounds containing the α,α-diimine structure (i.e., R—C=N—C—C—N=C—R′) have found widespread application in the spectrophotometric determination of several transition metals, most notably iron(II) and copper(I) [1—12]. The plethora of ferroin-type reagents described in these references shows that most compounds require low acidity (pH 1—7) for quantitative chelation. A few are capable of forming stable chelates in highly alkaline medium. These include 4-hydroxy- and 4,7-dihydroxy-1,10-phenanthroline [13, 14] and phenyl-2-pyridyl ketoxime [15]. Even fewer reagents can form stable chelates with iron(II) ions in strong acid: 3-(2-pyridyl)-5,6-diphenyl-1,2,4-triazine (PDT) [16] in the presence of thiocyanate ions and 3-(4-phenyl-2-pyridyl)-5,6-diphenyl-4,4′-(disulphonic acid)-1,2,4-triazine diammonium salt (PPDT-DAS) [17] are effective for chelating iron in strong mineral acid.

0003-2670/84/$03.00

Of the 36 compounds prepared and characterized by Kiss [17], some showed additional and unexpected properties which required more detailed examination. Some are reported here: the spectrophotometric properties of the iron(II) tris-chelates (type L_3Fe^{2+}) of 3-(1-isoquinolyl)-5,6-diphenyl-1,2,4-triazine (IQDT) and its water-soluble sulphonated derivative (IQDT-TAS) are described, together with those of the asymmetric bitriazine, 3,3′-bis(5,6-diphenyl-1,2,4-triazine) (BDT), and its water-soluble sulphonated derivative, tetra-ammonium 5,6,5′,6′-tetra(4-sulphophenyl)-3,3′-bis(1,2,4-triazine) (TSBT-TAS). The IQDT-TAS yielded a highly sensitive colour reaction (ϵ = 38 340 at 375 nm and ϵ = 27.360 l mol^{-1} cm^{-1} at 596 nm) with iron(II) ions whereas TSBT-TAS showed a combination of high sensitivity (ϵ = 28 240 at 550 nm) and extreme acid tolerance in its ability to form chelate with iron(II) ions in the presence of virtually any concentrated acid. Although there is one reference in the literature [18] to another asym-bitriazine as a reagent for iron, TSBT-TAS has not been reported previously. The reagent 3,3′-bis(5,6-dimethyl-1,2,4-triazine) [18], decomposed slowly in the hydrofluoric acid-containing mixed acids commonly used for the dissolution of silicates and thus its usefulness is limited to chelation in conditions of low acidity.

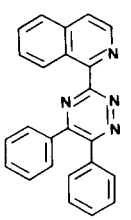

IQDT

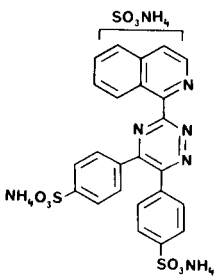

IQDT–TAS

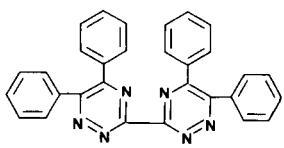

BDT

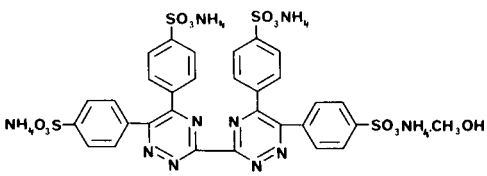

TSBT–TAS

Unlike the isomeric analogue, 3-(2-quinolyl)-5,6-diphenyl-1,2,4-triazine (QDT), which possesses the quinoline ring with steric hindrance and hence specificity to copper(I) chelation (type L_2Cu^+), the new isoquinolyl derivative IQDT reacts with both copper(I) and iron(II) ions because the position 2 of the ring nitrogen permits free co-ordination.

EXPERIMENTAL

Synthesis of reagents

3-(1-Isoquinolyl)-5,6-diphenyl-1,2,4-triazine (IQDT). This compound was prepared by an integrated scheme analogous to that used for PPDT-DAS already described [17], starting with isoquinoline. The hydrazine, obtained via the N-oxide to 1-nitrile intermediates by treatment with hydrazidine hydrate, yielded the desired product when condensed with benzil as yellow-green needles from acetic acid/water (m.p. 224—6°C).

The water-soluble derivative, IQDT-TAS, was prepared by sulphonation of the free base IQDT (2.00 g) with fuming sulphuric acid (30% SO_3; 10 ml) at a gradually increasing temperature (maximum 150°C). The diluted reaction mixture was neutralised with an excess of ammonia solution and the desiccated salts were separated by Soxhlet extraction with anhydrous methanol, leaving a residue of insoluble ammonium sulphate. Column chromatographic separation on alumina (activity I) removed residual impurities such as the iron(II) tris-chelate from the methanolic solution. The pure product was eluted with warm anhydrous methanol and after evaporation of the excess of solvent, the solid residue was dried at 110°C for 8 h. The product was obtained as a bright yellow amorphous powder (yield 3.03 g; 83.8%). Analysis for sulphur showed it to be an unsolvated trisulphonate: $C_{24}H_{25}N_7S_3O_9$ required 14.76% S; found 14.9 ± 0.1% S. Because of the multiplicity of possible substitutions available, the exact position of the sulphonic acid groups is uncertain.

3,3'-Bis(5,6-diphenyl-1,2,4-triazine) (BDT). The starting intermediate, oxamide dihydrazone, was obtained by the action of hydrazine hydrate in ethanol on dithio-oxamide [11]. This was considerably simpler and safer than the Dedichen method [19] involving the action of hydrazine on cyanogen. Cyclocondensation of oxamide dihydrazone with benzil [2, 19] yielded the tetraphenyl asym-bitriazine BDT as a rather insoluble crystalline mass. The product was obtained as yellow needles from hot dimethylformamide or diacetone alcohol, collected by filtration, washed with water and dried at 110°C for 24 h. Analysis: $C_{30}H_{20}N_6$ requires 77.6% C, 4.3% H and 18.1% N; found 77.9% C, 4.4% H and 18.1% N. The substance melted at 298°C.

The parent heteroaromatic compound 3,3'-bis(1,2,4-triazine) was readily prepared by cyclocondensation of oxamide dihydrazone with glyoxal. Similarly, various other α-diketones reacted with the dihydrazone to form substituted asym-bitriazines; 2,3-butanedione formed the tetramethyl derivative [18] whereas α-pyridyl condensed to the corresponding tetra-(2-pyridyl) derivative [2].

Tetra-ammonium 5,6,5',6'-tetra(4-sulphophenyl)-3,3'-bis(1,2,4-triazine) (TSBT-TAS). The free base BDT (10 g) was dissolved in fuming sulphuric acid (30% SO_3; 50 ml) with much darkening and appreciable evolution of heat. The temperature of the solution was maintained at 80°C for 1 h with stirring until the bulk of the material reacted smoothly by forming a

light yellow solution. Final heating to a maximum of 170°C ensured completion of sulphonation. The cooled mixture was poured on ice, neutralised with an excess of ammonia solution and then concentrated to a small volume by boiling. After complete desiccation in an oven, the ammonium sulphonate was separated from the inorganic sulphate by Soxhlet extraction with anhydrous methanol and purified by column chromatography on alumina (activity I). The pure product was eluted with warm methanol and after evaporation of excess of solvent, the residue was dried at 110°C for 8 h (yield 17.2 g, 92%). The light yellow amorphous powder was dried further at 75°C (15 mm Hg) for 12 h. Elemental analysis gave a composition which approximated a mono-methanol solvated formula: $C_{30}H_{32}N_{10}S_4O_{12} \cdot CH_3OH$ requires 42.1% C, 4.1% H, 15.8% N, 14.5% S and 23.5% O; found 42.0% C, 4.0% H, 15.5% N and 15.5% S. The analysis gives a composition of $C_{31.0}H_{35.5}N_{9.8}S_{4.3}O_{12.7}$.

The action of other sulphonating agents on BDT

Chlorosulphonic acid dissolved BDT rapidly with heat evolution forming an intensely red solution which was heated for 1 h at 80°C and allowed to stand for 3 weeks at room temperature. Only one sulphonic acid group could be substituted and the product was sparingly soluble in hot water; the ammonium salt formed a precipitate when the aqueous solution of the acid was neutralized.

When a solution of the free base in concentrated sulphuric acid was gradually heated to 205—210°C with intermittent stirring, a slight effervescence indicated the commencement of sulphonation after ca. 10 min. The reaction was terminated after ca. 1 h and the diluted reaction product was treated in the usual way with ammonia solution. A certain amount of carbonisation (i.e., thermal degradation) was evident and unavoidable. The product was finally purified by column chromatography as previously. The analysis of the product showed that it consisted of a mixture of di- and tri-substituted sulphonic acids. Tetra substitution which is the sole product with fuming sulphuric acid, could not be obtained. The mixed ammonium sulphonates can be salted out with concentrated ammonium sulphate solution, whereas the tetrasulphonate remained in solution.

Reagent solutions

A 0.01 M solution of IQDT was prepared by dissolving 360 mg of pure reagent in 100 ml of absolute ethanol containing a few drops of hydrochloric acid. A 0.01 M solution of IQDT-TAS was prepared by dissolving 652 mg of the ammonium sulphonate in 100 ml of water.

For the 0.3 M TSBT-TAS solution, 8.0 g of the monomethanol solvated salt was dissolved in 30 ml of mixed acid solution containing 25% (v/v) hydrofluoric acid and 35% (v/v) sulphuric acid. This solution is almost saturated at 20°C. The 0.1 M solution of TSBT-TAS was prepared by dissolving 8.85 g of the salt in 100 ml of water.

The acid mixture for total iron was obtained by adding 25 ml of concentrated (72%) perchloric acid to 25 ml of concentrated (40%) hydrofluoric acid in a FEP-teflon bottle and stirring well.

A 40% (w/v) aluminium chloride hexahydrate (iron-free) solution in water was used to complex fluoride in the decomposed sample solutions.

Buffer solutions were as follows: (a) aqueous 2 M ammonium acetate; (b) 2 M ammonium acetate in (1 + 1) acetic acid/water.

Standard metal solutions were prepared by dissolving iron(III) oxide (Specpure), cobalt sponge (99.998%) in dilute (1 + 1) hydrochloric acid and copper powder (99.997%) in dilute (1 + 1) nitric acid.

All other reagents, chemicals and metal salts were of analytical grade.

Apparatus

Absorption spectra and measurements at fixed wavelengths were obtained with a Unicam SP-500 S-2 spectrophotometer equipped with an automatic sample changer, recorder and a digital readout facility. The pH measurements were made with a Metrohm-Herisau potentiograph Type E-436. All sample weighings were obtained by a Cahn G-2 electrobalance with a digital readout facility. The weighing compartment was also equipped with a polonium-210 α-emitter as static eliminator (activity 1.7 mCi). Likewise, the teflon bombs were pre-conditioned with another polonium-210 α-particle source to eliminate sample scatter caused by static charge. Gravimetric dilutions were done with a Mettler PL-200 top-loading electronic balance. Sample digestion apparatus suitable for eight samples was constructed from FEP-teflon and provisions were made for the entry and exit of nitrogen (details are available on request). Teflon micro-digestion bombs [17] were used for the decomposition of more resistant silicates. Sample dissolutions were aided by agitation in an ultrasonic bath. A heating block made from anodised aluminium with 48 wells was also constructed for the micro-teflon bombs. The block was heated by a hot plate (temperature was registered by a bimetallic surface thermometer).

Calibration

A standard stock solution of iron was prepared from high-purity iron(III) oxide dissolved in hydrochloric acid. Aliquots were taken for the preparation of calibration graphs using IQDT-TAS and TSBT-TAS as chromogens.

IQDT-TAS. The procedure for the calibration was identical to the colour development described for total iron (below). Beer's law was obeyed closely within the concentration range tested. For the range 0.22—1.99 $\mu g\ ml^{-1}$ iron, the relative standard deviations for a 10-mm flow-through cell were 0.76% (6 points) at 375 nm, and 0.75% (6 points) at 596 nm. All the measurements were made against a reagent blank as reference.

TSBT-TAS. The procedure used for the calibration was identical to the colour development described for total iron (below). Beer's law was obeyed within the concentration range tested, provided that an adequately large

excess of the reagent was used routinely. For the range 0.1—2.6 $\mu g\ ml^{-1}$ iron, the relative standard deviations for the calibrations in 10-mm flow-through cells were 0.87% (7 points) at 450 nm and 0.56% (7 points) at 550 nm. All measurements were made against appropriate reagent blanks as reference.

In addition, a separate calibration graph for the TSBT-TAS reagent system was prepared for subsequent use in silicate analysis based on the best FeO values available for several international rock standards, such as USGS BCR-1 basalt. It was necessary to reproduce conditions as closely as possible to actual analytical use.

Sample preparation

Prepare the samples as described [17] by thoroughly grinding in a small agate mortar under acetone to avoid oxidation; ensure further that all precautions are taken for (a) the provision of a homogeneous and representative sample, as well as (b) maximal recovery in the grinding process because often only a few crystals of a separated mineral are available.

Method A. Simultaneous decomposition and chelation

Depending on the magnitude of iron(II) oxide in the sample or the amount of material available, weigh 1—5 mg of sample into a 5-ml or 7-ml FEP-teflon vial. Add 200 μl of aqueous 20% (v/v) acetone (as wetting agent) and carefully rock the contents to yield an even suspension. Add 1000 μl of the specified 0.3 M TSBT-TAS solution in mixed acids and further homogenize by swirling or with the aid of an electric vibrating spatula. The digestion is best done in batches of 10 samples because a numbered vial tray is handled more conveniently. Immerse the tray in an ultrasonic bath to aid particle agitation for ca. 30 min. (The bath temperature may increase from 20°C to ca. 52°C during this time; successive sample tray immersions should be made after refilling the bath with cold water.)

After standing for 1 h, wash the intensely coloured sample solutions into a tared 100-ml FEP-teflon bottle containing 5 ml of the specified aluminium chloride solution and add 10 ml of the ammonium acetate/acetic acid buffer. Prepare a reagent blank containing all the chemicals in a similar manner. Dilute to capacity, mix thoroughly and weigh to 1-mg accuracy. After standing for 1 h (or longer) in darkness or diffuse light, measure the absorbance at either 450 nm or 550 nm in a 10-mm quartz flow-through cell against the reagent blank. Calculate the FeO concentration by a suitable program for gravimetric dilution/variable-volume spectrophotometry using the calibration data based on international standard rocks.

When TSBT-TAS is incorporated in the decomposition acid mixture instead of PPDT-DAS [17], a much broader range of acid concentration is tolerated. This procedure may be used for more resistant silicates such as basalts, garnets and eclogites because the faster reaction conditions in a strong acid mixture prevent aerial oxidation more effectively.

Because the intense colour formation takes place immediately, any

undissolved particles often cannot be detected in the opaque solution. To remedy this, use another vial containing a similar quantity of sample (if enough sample is available) and digest with the same acid mixture but without the chromogen added. The clear, transparent solution reveals any undissolved particles and thus serves as a convenient indicator. In general, ultrasonic agitation for 30 min is adequate. Garnets and spinels tend to dissolve with difficulty. If undissolved particles are present after this treatment, the digestion may further be aided by heating at 80°C for ca. 10 min. More prolonged heating, however, may adversely affect the Fe(II) chelate already formed. In this case, Method B (below) should be employed; this involves dissolution under nitrogen flow with an acid mixture and without added reagent.

Method B. Acid decomposition by heating without added chromogen

Some particularly resistant minerals (e.g., garnet, spinel and zircon) may remain only partly dissolved even after ultrasonic agitation (Method A) and it is essential to ensure complete dissolution by more prolonged heating under an atmosphere of nitrogen for as long as necessary.

Dissolution should be done in the micro-digestion apparatus (see above, cf. [17]) as follows. Detach the sample holders (screw mounted 1.5-ml teflon beakers) from the digestion apparatus and proceed by weighing 1—3-mg samples into the sample holder. Add 200 μl of aqueous 20% (v/v) acetone solution and 600 μl of mixed acid [25% (v/v) hydrofluoric acid plus 35% (w/w) sulphuric acid, saturated with nitrogen], mix briefly, replace the perforated lid and re-assemble it into the digestion apparatus (flushed with a continuous flow of nitrogen). A maximum of 8 samples can be digested simultaneously. With a steady nitrogen flow maintained, insert the assembled sample holders into the aluminium heating block kept at sub-boiling temperature (ca. 85°C is sufficient) and digest the samples for as long as is necessary but preferably less than 1 h. Longer heating may be permitted if the acid evaporation is controlled by (a) minimal nitrogen flow and (b) larger volumes (up to 1000 μl) of acid digestion mixture.

Transfer the digestion apparatus to the assembly frame and after cooling to room temperature, turn off the needle valves individually. Remove the sample holder and transfer the digested sample by quantitatively washing with hot water into a tared 100-ml FEP-teflon bottle containing 5 ml of the specified aluminium chloride and 10 ml of aqueous 0.1 M TSBT-TAS solution. Add 10 ml of the ammonium acetate/acetic acid buffer and cool to room temperature. Prepare a reagent blank containing all the chemicals in a similar manner. Dilute to capacity, mix thoroughly and weigh to 1-mg accuracy. Allow ca. 1 h of standing and measure the absorbance at either 450 nm or 550 nm against the reagent blank in a 10-mm quartz flow-through cell. Calculate the FeO concentration by a suitable program for variable-volume spectrophotometry using the calibration data based on international standard rocks.

Method C. Determination of total iron with either IQDT-TAS or TSBT-TAS

Weigh 1—5 mg (±0.1 μg) of finely ground silicate into a teflon micro-digestion bomb. Moisten the sample carefully with 50 μl of water and add 500 μl of the hydrofluoric/perchloric acid mixture specified for total iron. After mixing thoroughly with a vibrating spatula, tighten the screw caps as firmly as possible. Prepare a reagent blank digestion similarly. Transfer the bombs into the well in the aluminium block, pre-heated to 130—140°C, and heat for 20 min.

After an adequate digestion time, remove the heating block to cool the samples to room temperature. Wash the contents of the micro-bomb quantitatively into a tared 100-ml FEP-teflon bottle containing 5 ml of the specified aluminium chloride solution to ca. 40 ml. Mix and heat on a hot plate (surface temperature set at 150°C) and after 10 min, add 10 ml of 10% hydroxylammonium hydrochloride solution, mix again and heat for another 5 min. After cooling, add either (a) 10 ml of aqueous 0.01 M IQDT-TAS solution and 10 ml of 2 M ammonium acetate buffer, or (b) 10 ml of aqueous 0.1 M TSBT-TAS solution and 10 ml of ammonium acetate/acetic acid buffer. Dilute to capacity and weigh the bottle to 1-mg accuracy. After 1 h of standing, measure the absorbance against the reagent blank reference in a 10-mm quartz flow-through cell at either 375 nm or 596 nm (for IQDT-TAS); or at 450 nm or 550 nm (for TSBT-TAS). Calculate the total iron (as Fe_2O_3) concentration by a suitable program for variable-volume spectrophotometry, using the calibration data based on international standard rocks. The results obtained by Methods A, B and C on some standard rocks and other materials are presented in Table 1.

TABLE 1

Microdetermination of the iron oxidation state

Sample	FeO (%)[a]	No. of detns.	Reagent	λ_{max}	Other values
Granite G-2[b]	1.53 (2.60)	5	TSBT-TAS	450	1.44 [20], 1.49
	1.57 (2.33)	5	TSBT-TAS	550	[17], 1.43 [21]
Basalt BHVO-1[b]	8.43 (0.65)	5	TSBT-TAS	450	8.55? [20]
	8.53 (1.34)	5	TSBT-TAS	550	8.67 [21]
Basalt[c]	7.62 (0.86)	15	TSBT-TAS	450	7.66 [21]
Garnet 2507	8.70, 8.89	2	TSBT-TAS	550	8.89, 8.83 [21]
	Total Fe_2O_3 (%)[a]				
Granite G-2[b]	2.69 (2.24)	5	IQDT-TAS	375	2.69 [20]
	2.75 (1.09)	5	IQDT-TAS	596	2.66 [21]
Granodiorite GSP-1[b]	4.17 —	3	IQDT-TAS	596	4.26 [21]
Garnet 2507	10.25 —	2	TSBT-TAS	550	10.55 ± 0.02 [21]

[a]Mean with relative standard deviation in parentheses. [b]USGS samples. [c]From Cabramurra, N.S.W.

Experiments showed that most common rock-forming minerals decomposed completely under these conditions. Among the resistant silicate rocks and minerals, ilmenite, garnet, tourmaline, pyroxene, eclogite and pyroxene-ilmenite xenolith decomposed completely. Pyrites were attacked only partially, but complete decomposition was obtained when the sample size of the pure mineral was kept below 2 mg. Alternatively, heating may be continued for 1 h. Chromite and zircon appeared to be the most resistant to acid attack; even after heating for 1 h at 160°C, the bulk of the sample remained almost intact. Chromite-bearing rocks may be brought into solution if the micro-bomb is jacketed in a copper (or aluminium) protective case and heated with the acid mixture at 250°C for 1 h.

RESULTS AND DISCUSSION

Precision and accuracy

The attainable precision and accuracy of micro-scale iron determination range within 1—3% relative standard deviation, a level which has also been well documented over the years for other reagent systems [17].

The primary factors influencing the precision and accuracy of spectrophotometric microdeterminations of iron in both valency states are the efficiency of acid decomposition and the sample homogeneity. Other factors such as weighing accuracy (±0.05 μg at the 1-mg level and ±0.1 μg at the 1—5 mg level are easily attainable) and manipulative error as well as error from accidental oxidation in Method B during or after dissolution, are more easily controlled; therefore their contribution to overall precision and accuracy levels is minimal.

The ease with which a suitably homogeneous sample is dissolved has a direct bearing on precision and, in general, materials such as glasses, basalts, andesites and granites reflect a higher order of precision than those exhibiting more resistance to acid attack such as pyroxenes, garnets or spinels. Another consideration is that the efficient penetration of hydrofluoric acid may be hindered by the formation of a siliceous coating on the unreacted portion of the sample unless it is agitated during digestion. The dispersion of sample particles by ultrasonic agitation effectively prevents this problem.

Colour reactions

The IQDT, IQDT-TAS and TSBT-TAS reagents formed intensely coloured cationic chelates of the type L_3Fe^{2+} with iron(II) in acidic to slightly alkaline media. Of all the cations tested, only copper(I) and cobalt(II) formed coloured chelates but with significantly lower molar absorptivities; the cobalt(II) chelates of all the reagents exhibited too low a stability to permit useful spectral recordings to be made. The presence of large amounts of strong masking agents such as fluoride and oxalate retarded the formation rate of the iron(II) tris-chelate for the two isoquinoline derivatives; EDTA and cyanide inhibited the colour reaction. The TSBT-TAS reagent was

found to form intensely red chelates with iron(II) ions within much broader pH limits than IQDT-TAS; indeed variations in acidity had insignificant effect on colour intensity. The violet iron(II) chelate of IQDT can be extracted with higher alcohols whereas the water-soluble sulphonate reaction products are inextractable. The low solubility of the free base BDT in most common solvents precludes its practical usefulness although stable iron(II) chelate can be formed in dimethylformamide or diacetone alcohol.

Colour stability of iron(II) tris-chelates

The coloured complexes of both sulphonated reagents and the free base IQDT showed excellent stability over long periods of storage in the dark when buffered appropriately. Although IQDT-TAS had a much lower acid tolerance than PPDT-DAS [17] in its reactions with iron(II) ions, TSBT-TAS proved to be remarkably more tolerant of a much broader range of acidity and consequently a closer examination of both colour stability and acid tolerance was made. When the colour was developed at pH 2 and at acidities of 0.3 M and 0.65 M sulphuric acid and the solutions were stored for up to 7 days in diffuse daylight, the solution absorbances showed close agreement for both the 450-nm and 550-nm absorption maxima.

Absorption spectral characteristics of metal chelates

The absorption spectra of the iron(II) and copper(I) chelates of the ligands IQDT, IQDT-TAS and TSBT-TAS are shown in Fig. 1. It can be seen that all the chelates formed exhibit two absorption maxima: the 1-isoquinolyl derivatives show intense absorption in the long ultraviolet region whereas the blue chelates absorb to a lesser extent in the red end of the spectrum. Likewise, the TSBT-TAS—Fe(II) chelate exhibits very broad double absorption peaks, an apparent characteristic of asym-bitriazines [18]. Furthermore, the 1-isoquinolyl derivatives appear to undergo a slight chromatic shift in absorption maxima (for IQDT, λ_{max} = 380 and 592 nm; for IQDT-TAS, λ_{max} = 375 nm and 596 nm) accompanied by a change in sensitivity.

The copper(I) chelate of IQDT-TAS absorbs intensely in the ultraviolet region, but an extremely weak absorption occurs in the visible spectrum. Despite this, however, when comparable amounts of iron(II) and copper(I) ions are present, spectral resolution and hence the determination of iron cannot be achieved unless mathematical manipulation were to be used. Masking agents such as cyanide might remove the influence of copper but this was not tested.

Molar absorptivities and reagent sensitivities

The molar absorptivities (ϵ) and sensitivities of iron and copper complexes calculated from the spectrophotometric data are shown in Table 2.

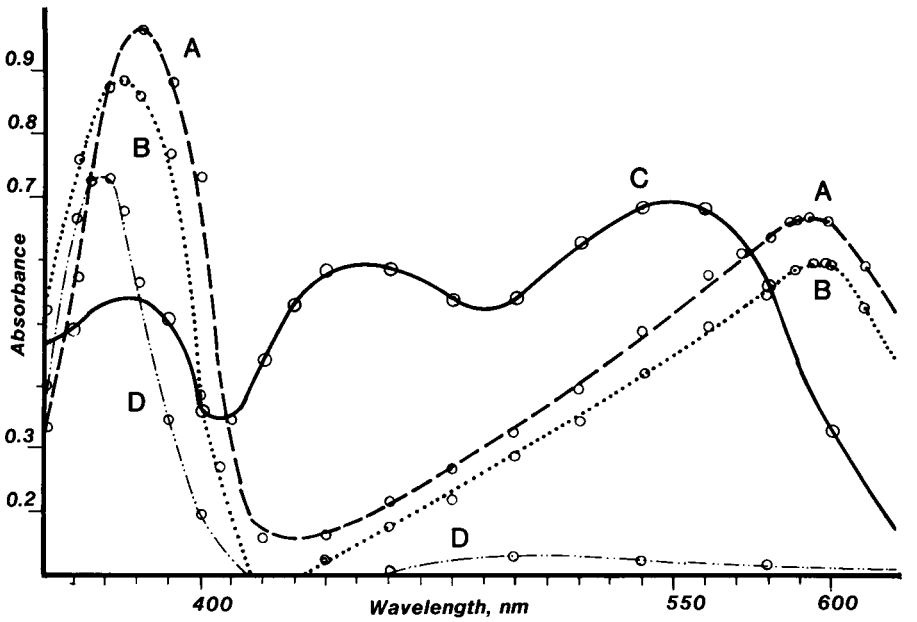

Fig. 1. Absorption spectra of some asym-triazine metal chelates at pH 3.5 measured against appropriate reagent blanks in 10-mm cells. Metal concentration: 2.55×10^{-5} M Fe or Cu. Spectra: (A) IQDT/Fe(II) chelate in 50% ethanol; (B) IQDT-TAS/Fe(II) chelate; (C) TSBT-TAS/Fe(II) chelate; (D) IQDT-TAS/Cu(I) chelate.

Dependence of chelate formation on excess of ligand

Spectrophotometric studies of the iron(II) complexes of IQDT, IQDT-TAS and TSBT-TAS showed that the reaction kinetics depended strongly on the presence of excess of reagent: for both isoquinoline derivatives, a

TABLE 2

Molar absorptivities and Sandell sensitivities for the various chelates

Reagent	Metal	λ_{max} (nm)	ϵ (1 mol^{-1} cm^{-1})	Sensitivity (μg cm^{-2})
IQDT	Fe	380	37 860	0.00148
	Fe	592	26 760	0.00209
IQDT-TAS	Fe	375	34 730[a]; 38 340[b]	0.00161[a]; 0.00146[b]
	Fe	596	23 730[a]; 27 360[b]	0.00235[a]; 0.00204[b]
	Cu	370	29 350	0.00216
	Cu	520	≈5 000	≈0.0127
TSBT-TAS	Fe	450	23 525	0.00237
		550	28 240 ± 200	0.00198

[a]Measured after 1 h. [b]Measured after 48 h.

3.2—4.0-fold molar excess was adequate although higher reagent concentrations would probably be more desirable for shorter colour development times. However, for reproducible complex formation, significantly larger excess concentrations of TSBT-TAS are required than for simpler asym-triazines. Likewise a large reagent concentration was found necessary for another asym-bitriazine, 3,3′-bis(5,6-dimethyl-1,2,4-triazine) [18]. A series of measurements was therefore made to determine the necessary reagent concentration, by measuring the molar absorptivity (ϵ) of test solutions containing fixed concentrations of iron (2.14 μg ml^{-1} Fe) and an excess of reagent (expressed as the molar ratio of ligand to iron) for levels ranging from 4.4 to 78.3 for reaction times of 10 min to 168 h. A reagent concentration similar to that of IQDT-TAS was clearly inadequate: at a ratio of 4.4 the colour reaction was incomplete (91.4%) even after 7 days of standing, whereas at a ratio of 8.7 the value stabilised at a plateau ($\approx$100%) after 24-h standing. At still higher ratios, the colour reaction was completed much more quickly. At a ratio of 17.4, for example, the reaction was 96% complete after 10 min and 100% complete after 1 h of standing. For all other measurements involving higher ratios of reagent to iron, the reaction was essentially complete (99—100%) at the 10-min measurement interval. At very high levels, there was no evidence of error from the strong background colour of the reagent. For practical analytical optimisation, a 20—25-fold excess of reagent was considered adequate.

Acid tolerance of TSBT-TAS

The highly polar character of the tetrasulphonate is further demonstrated by its ability to coordinate with iron(II) ions in virtually any concentrated acid, media which promote powerful protonation of the heterocyclic nitrogen atoms. Qualitative experiments relating to the acid tolerance tests were carried out as follows.

First, comparisons were made with PPDT-DAS [17]. A test solution of this sulphonated asym-triazine was prepared by dissolution of the reagent in the relevant concentrated acid. To this solution was added one drop of the iron(II) sulphate solution, which was immediately stirred in. Any colour change was recorded as a positive reaction. Then, when further information was sought to support observation, the diluting effect of the iron(II) sulphate solution on the concentrated acid was avoided by dissolving the $FeSO_4 \cdot 7H_2O$ crystals directly in the selected acid and mixing the solid reagent with it. In every case, the colour reaction was the same as for the first set of experiments.

The following concentrated acids and mixtures were tested: hydrofluoric (1), hydrochloric (2), hydrobromic (3), perchloric (4), nitric (5), phosphoric (6), hypophosphorous (7), trifluoroacetic (8), sulphuric (9) and trifluoromethanesulphonic (10) acids, and diluted (80%) sulphuric (11), diluted (80%) trifluoromethanesulphonic (12) acids as well as a (1 + 1) mixture of fuming sulphuric (30% SO_3) and hydrofluoric acids (13). The TSBT-TAS

reagent produced an immediate reaction with iron(II) ions in acids 1—8, and a slower positive reaction in acids 11, 12 and 13. Not surprisingly, a colour reaction failed to occur in the anhydrous media provided by the extremely strong acids 9 and 10. However, minimal dilutions represented by acids 11 and 12 permitted chelate formation. In contrast, PPDT-DAS [17] produced a slight reaction in acid media 1, 6, 7 and 8 and no visible colouration occurred in the remaining acids.

This unusual property of TSBT-TAS has important implications in permitting an almost unrestricted selection of acid mixtures which are essential for the effective dissolution of resistant minerals. The in-situ chelation of iron(II) [17] released from a silicate matrix with TSBT-TAS dissolved in a suitable acid mixture containing hydrofluoric acid can be realised for a broad range of silicates without the danger of aerial oxidation.

Cationic interferences

Among the cations tested, only copper(I) and cobalt(II) formed coloured chelates but the sensitivities were considerably lower than for the corresponding iron(II) chelate. With IQDT-TAS as the chromogen, the recovery of added iron (0.9 μg ml^{-1}) in the presence of copper (2.1 μg ml^{-1}) showed a significant positive error: 37.1% at 365 nm and 6.8% at 596 nm.

CONCLUSIONS

The following conclusions may be drawn from the examination of the two asym-triazine reagent systems. First, the water-soluble sulphonated derivatives IQDT-TAS and TSBT-TAS can be dissolved in mixed acids (hydrofluoric/sulphuric acids). In this way, immediate chelation during the dissolution process can prevent aerial oxidation of the iron(II) in silicates. Also the iron(II) tris-chelates of both ligands have two absorption maxima which may be utilised to provide a broader dynamic range for the microanalytical procedures.

The reagent IQDT-TAS has a lower acid tolerance for chelating iron(II) than PPDT-DAS [17]. This property limits its usefulness in analytical geochemistry because most minerals exhibit some resistance towards acid attack. Thus the range of silicate minerals which can be dissolved in the presence of IQDT-TAS is fairly narrow. However, IQDT-TAS is one of the most sensitive ferroins available, especially in the u.v. absorption band; further, its high sensitivity should make it a most useful reagent for trace-level iron determinations.

The TSBT-TAS reagent surpasses all the other ferroin-type compounds hitherto examined in its ability to co-ordinate with iron(II) ions at very high acid concentrations. This unique property was utilised to maximal advantage in efforts to dissolve more resistant silicates in its presence. With a sufficiently large excess of the ligand in the acid mixture, a fast reaction rate ensured protection against aerial oxidation and prevented fluoride

interference in the chelation process. Compared with PPDT-DAS [17], the sulphonated derivative TSBT-TAS offers a broad range of acid tolerance, permitting simultaneous sample dissolution and chelation of released iron(II) for almost any common silicate rock and mineral. Further, the synthesis involved is relatively simple and hence it should cost less.

Among the disadvantages are (i) that the large excess of reagent required in the decomposition acid mixture may negate its lower cost of synthesis and (ii) that the optimised procedure leaves some very resistant minerals (e.g., corundum, zircon, staurolite, tourmaline and pyrite) largely undecomposed. Some of these minerals decompose more or less completely if heated in a bomb with concentrated hydrofluoric and sulphuric acids for prolonged periods under an inert atmosphere. Protection from air oxidation in this case is essential and may be difficult; the reagent should be added after the digestion is terminated in order to avoid its thermal degradation.

Finally, the salient features of TSBT-TAS have been demonstrated by the routine microdetermination (1—5-mg samples) of iron in more resistant silicates than was hitherto possible with an earlier acid-tolerant reagent [17].

The author thanks Dr. J. E. Fildes and her staff of the Analytical Services Unit, A.N.U. for elemental analyses and Dr. W. L. F. Armarego of the Medical Chemistry Group, John Curtin School of Medical Research for helpful discussions relating to heterocyclic chemical nomenclature. He is also indebted to Dr. J. R. Richards of the Research School of Earth Sciences for useful criticism.

REFERENCES

1 A. A. Schilt and G. F. Smith, Anal. Chim. Acta, 16 (1957) 401.
2 F. H. Case, J. Org. Chem., (1965) 931.
3 F. H. Case, J. Heterocyclic Chem., 7 (1970) 1001; 8 (1971) 1043; 10 (1973) 353.
4 F. H. Case and T. J. Kasper, J. Am. Chem. Soc., 78 (1956) 5842.
5 F. H. Case and E. Koft, J. Am. Chem. Soc., 81 (1959) 905.
6 A. A. Schilt and F. H. Case, Talanta, 27 (1980) 55.
7 A. A. Schilt, Talanta, 13 (1966) 895.
8 A. A. Schilt, N. Mohamed and F. H. Case, Talanta, 26 (1979) 85.
9 A. A. Schilt, C. D. Chriswell and T. A. Fang, Talanta, 21 (1974) 831.
10 A. A. Schilt, T. A. Yang, J. F. Wu and D. M. Nitzki, Talanta, 24 (1977) 685.
11 B. M. Culbertson and G. R. Parr, J. Heterocycl. Chem., 4 (1967) 422.
12 W. I. Stephen, Talanta, 16 (1969) 939.
13 D. E. Zacharias and F. H. Case, J. Am. Chem. Soc., 27 (1962) 3878.
14 D. P. Poe, A. D. Eppen and S. P. Whoolery, Talanta, 27 (1980) 368.
15 F. Trusell and H. Diehl, Anal. Chem., 31 (1959) 1978.
16 C. D. Chriswell and A. A. Schilt, Anal. Chem., 46 (1974) 992.
17 E. Kiss, Anal. Chim. Acta, 72 (1974) 127.
18 R. E. Jensen and R. T. Pflaum, Anal. Chim. Acta, 32 (1965) 235.
19 G. Dedichen, Avh. Nor. Vidensk. Akad. Oslo, Mat. Naturvidensk. Kl., 5 (1936) 42; Chem. Abstr., 31 (1937) 4985.
20 S. Abbey, Geol. Surv. Can., Paper 83-15 (1983).
21 E. Kiss, Anal. Chim. Acta, 89 (1977) 303.

Analytica Chimica Acta, 161 (1984) 245—255
Elsevier Science Publishers B.V., Amsterdam — Printed in The Netherlands

DETERMINATION OF MOLYBDENUM IN STEELS BY FLOW-INJECTION SPECTROPHOTOMETRY

F. J. KRUG*, O. BAHIA Fº and E. A. G. ZAGATTO

Centro de Energia Nuclear na Agricultura (CENA) da Universidade de S. Paulo, C. Postal 96, 13400 Piracicaba, SP (Brazil)

(Received 27th February 1984)

SUMMARY

A flow-injection procedure is proposed for the determination of molybdenum in steels based on the thiocyanate method. Effects of iron(III), acidity, reagent concentration and interfering species were investigated by using flow-injection systems with the merging zones approach which reduced drastically the number of standard solutions to be prepared. Full details of system design are given. The procedure can be applied to several types of steel samples of industrial relevance. After dissolution of the steels in aqua regia, molybdenum can be determined in the range 0.10—4.00% (w/w) at a rate of up to 270 samples per hour with relative standard deviations less than 2%. The results agree with those obtained by atomic absorption spectrometry with the standard addition method and by plasma atomic emission spectrometry, and with certified values of standard reference samples.

The availability of fast analytical procedures for determining chemical composition is an important factor in steel manufacture. Instrumental techniques such as atomic absorption spectrometry, x-ray fluorescence spectrometry, emission spectrography, etc. are usually employed but often require standard specimens of exactly defined composition. Also, from time to time, instrumental methods should be compared to chemical procedures to evaluate accuracy. Flow injection analysis (f.i.a.) [1] which has become increasingly accepted as an automated or semi-automated chemical procedure in agricultural, geochemical, clinical and environmental research [2], has already been applied to alloys [3—5], as an alternative to the above physical methods.

The classical spectrophotometric thiocyanate method [6, 7], often recommended for molybdenum determinations in steels [6—9], is improved when modified for f.i.a. The resulting flow-injection system, which is simple and versatile, can be located near the production plant, allowing in situ analyses with very good characteristics of accuracy, precision, sampling rate and cost.

EXPERIMENTAL

Apparatus

An Ismatec MP13 GJ4 peristaltic pump provided with tygon pumping tubes was employed. The Varian model 634S spectrophotometer, furnished with a Hellma 178-OS flow cell (inner volume 80 μl, optical path 10 mm), was connected to a Radiometer REC-61 recorder with a high-sensitivity REA-112 unit. The wavelength was set at 480 nm.

Polyethylene tubing of the non-collapsible wall type (i.d. 0.86 mm) was used to construct the reaction coils and transmission lines. The injector and the connectors were made from perspex. The proportional injector, manually operated, was similar to those already described [10, 11], with an extra insertion hole in one of the fixed external plates (Fig. 1c) which replaces a Y-shaped connector and permits the addition of the confluent reagent stream immediately after the sample injection. This hole was closed in systems with merging zones.

Reagents, standards and samples

All reagents were of analytical grade and distilled-deionized water was used throughout.

The R_1 reagent (Fig. 1c), 5% (w/v) tin(II) chloride in 5 M hydrochloric acid, was prepared by dissolving 12.5 g of $SnCl_2 \cdot 2H_2O$ in about 100 ml of 5 M hydrochloric acid and diluting to 250 ml with the same acid. This reagent should be prepared freshly, requiring filtration if turbid. The R_2 reagent (Fig. 1c) was an aqueous 6% (w/v) potassium thiocyanate solution. The C_S solution (Fig. 1c), about 0.015% (w/v) in iron(III) and with similar acidity as the samples and standards, was prepared by adding 37.5 ml of concentrated hydrochloric acid, 12.5 ml of concentrated nitric acid and 0.542 g of iron(III) nitrate nonahydrate to about 350 ml of water and, after dissolution, diluting to 500 ml with water. With these amounts of reagents, the flow-injection system could be operated for at least four hours.

The stock molybdenum standard solution (1000 mg l^{-1}) was prepared by dissolving 0.4600 g of ammonium heptamolybdate tetrahydrate in about 200 ml of water previously acidified with 2 ml of concentrated nitric acid, and diluting with water to 250 ml. Working standards in the range 5.00–100.0 mg Mo l^{-1} were prepared after suitable dilutions of the above stock with an acidic solution containing 75 ml of concentrated hydrochloric acid plus 25 ml of concentrated nitric acid per litre. This acidity, similar to that of the samples, corresponds to that of a (1 + 9) diluted aqua regia solution.

The steel samples were drilled, the resulting filings being sieved through a 1.19 sieve. The steel filings (250 mg) and 10.0 ml of aqua regia were added to digestion tubes, which were placed in a Technicon BD-40 digestor block and the temperature was set at 100°C. After about 10 min, when dissolution was achieved, the tubes were removed and cooled to room temperature. After filtration, the volume was made up to 100 ml with water.

Flow diagrams

Three flow-injection systems (Fig. 1) were used in this work; the final one (Fig. 1c) proposed for routine analyses was designed after simplifications of systems 1a and 1b, in which the merging zones approach allowed a detailed study of the chemistry involved, without the need for an excessively large set of standard and reagent solutions.

In system 1a, when the injector (I) rests in the sampling position, as shown in the figure, the sample (S) and the iron(III) solution to be added (A) are aspirated to feed their loops (L_S and L_A), the excesses going to waste (W). When the central sliding portion of the injector is moved to the alternative position, the selected volumes of sample and iron(III) solutions are introduced into their carrier streams (C_S and C_A), forming two well defined and reproducible zones which are pushed forward to merge at confluence point x, where iron(III) is added to the sample. Although the mechanism of the reactions is not fully understood [12], it has often been reported [6, 7, 9, 13] that iron(III) ions are required to improve sensitivity in the molybdenum thiocyanate method. At the next confluence point (z), the tin(II) chloride, hydrochloric acid and potassium thiocyanate solutions, previously mixed in the L_1 coil meet the sample zone and in the following L_2 coil, Mo(VI) is reduced to Mo(V) and probably Mo(III) [6, 14] and the Mo(V)-thiocyanate complex is formed. The resulting coloured zone is measured in the flow-through detector (D). The transient absorbance, proportional to the molybdenum content to be determined, is recorded, and

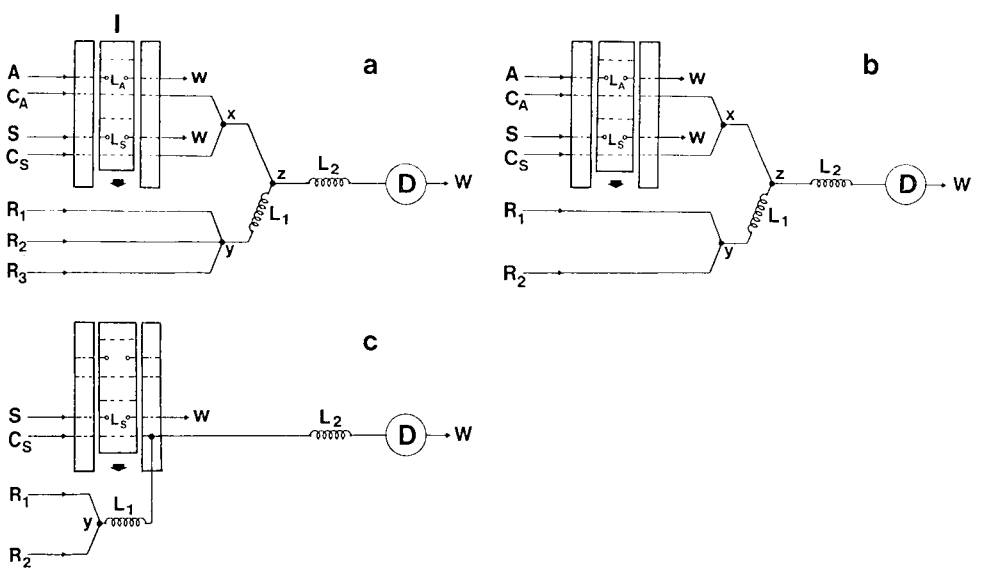

Fig. 1. Flow diagrams of the systems used. System 1c is proposed for routine work with the following parameters: C_S, R_1 and R_2; flow rates 4, 2 and 2 ml min^{-1}, respectively; L_1 and L_S, 150 cm; L_s, 8 cm; wavelength, 480 nm. For details, see text.

peak heights are measured. Systems 1b and 1c are similarly operated. In system 1b, the merging zones approach is exploited to investigate chemical interferences, and system 1c, proposed for routine work, includes iron(III) in the sample carrier stream.

The flow-injection systems were dimensioned to provide large sample dispersion [2], as preliminary tests confirmed the information [9] that sensitivity was not a limiting factor in this method. Thus, small injected volumes, either 20 or 40 μl, were used. Similar flow rates for the confluent streams and a suitable length for the L_2 coil were selected in order to improve the mixing conditions. The pumping rates were set to permit not less than 270 measurements per hour at the 1% carry-over level in all situations. With the symmetrical merging zones configuration [15], cumbersome synchronization procedures were avoided. Finally, the need for a 150-cm L_1 mixing coil was verified in preliminary tests which indicated that if this coil was too short (ca. 30 cm) or even omitted, excessive baseline noise caused by insufficient homogenization between concentrated reagents affected the reproducibility of measurements. Any length above 150 cm could be used, because the L_1 coil is placed outside the analytical path.

Procedures

The effects of iron(III) addition and concentrations of hydrochloric acid and tin(II) chloride solutions were studied with the system in Fig. 1a with the following parameters: C_A and C_S were diluted (1 + 9) aqua regia solution pumped at 2 ml min^{-1}; A was an iron(III) nitrate solution (0, 5, 50, 500 or 5000 mg Fe l^{-1}) in (1 + 9) aqua regia, with a 2 ml min^{-1} aspiration rate; S was a 0.0, 20.0 or 200 mg Mo l^{-1} standard solution aspirated at 2 ml min^{-1}; L_A and L_S were 4-cm long loops with inner volumes of about 20 μl; L_1 and L_2 were 150-cm coils; R_1 was 4, 7 or 10% (w/v) $SnCl_2 \cdot 2H_2O$ in 1 M hydrochloric acid, pumped at 1 ml min^{-1}; R_2 was 12% (w/v) potassium thiocyanate solution pumped at 1 ml min^{-1}; R_3 was 3, 6 or 9 M hydrochloric acid, pumped at 2 ml min^{-1}.

The entire factorial experiment was done with triplicate measurements. In each step of this factorial experiment, standard solutions of potentially interfering species were injected after the molybdenum standards into the sample carrier stream, in order to investigate the possible formation of other coloured thiocyanate complexes. The concentration of the potassium thiocyanate reagent was defined in exploratory experiments as 12% (w/v). Increased concentrations caused only minor changes in the measured signals but the use of concentrations as low as 5% (w/v) produced a serious loss in the linearity of the response plot. The highest added iron concentration was chosen to simulate a sample 100% (w/w) in iron, prepared as described above and undergoing 50% dilution at confluence point x (Fig. 1a and 1b).

After the optimum concentrations of iron(III) nitrate, hydrochloric acid and tin(II) chloride had been defined, system 1a was simplified to system 1b, all reagent concentrations being changed in such a way that

both systems can be considered similar if the quantities of reagents are expressed in terms of amounts added per unit time. Accordingly, the R_1 reagent was 5% (w/v) tin(II) chloride dihydrate solution, 5 M in hydrochloric acid, and the R_2 reagent was 6% (w/v) potassium thiocyanate solution, both reagents being pumped at 2 ml min^{-1}. Effects of potential interfering elements were investigated with this system, the A solution, 500 mg l^{-1} iron(III) in diluted (1 + 9) aqua regia, being prepared with or without the interfering species to be investigated.

Although system 1b could be used in routine analysis, it was decided to simplify it in order to achieve a simpler manifold, with iron(III) nitrate being placed in the sample carrier stream (0.015% w/v Fe). In this system, the L_S loop was 8 cm long, C_S flow rate was 4 ml min^{-1}, and the other parameters were the same as in system 1b.

Sampling rate, precision, system stability and reagent consumption were evaluated for this system 1c. The accuracy was checked by analyzing several samples also by atomic absorption spectrometry and by plasma atomic emission spectrometry. In addition, two standard reference samples from the Max Planck Institute (West Germany) were employed.

RESULTS AND DISCUSSION

Although the precision of the manual thiocyanate method depends critically on the reaction conditions and reagent concentrations [16], in all experiments done with the flow-injection systems, the relative standard deviations of measurements were always lower than 1%. Further, variations in reagent concentrations within broad ranges caused only minor variations in peak heights (Fig. 2). In the manual procedure, liquid—liquid extraction can be used to avoid decomposition of the coloured complex [7, 12], which is somewhat unstable in aqueous solutions [7, 17]. When the infinite volume configuration [18] was used in the flow-injection systems, colour fading was always observed after the peristaltic pump was stopped. However, as timing is perfectly reproducible in flow-injection procedures and chemical interferences investigated further were negligible, liquid—liquid extraction was not used here. The above features are valuable in procedures proposed for routine work.

Choice of reagent concentrations

The addition of iron(III) ions promotes a slight increase in peak heights (Fig. 2), regardless of the acidity and tin(II) chloride concentration. As the effect is minimized above 500 mg Fe l^{-1}, this concentration was selected for system 1b to prevent any interference from the iron present in the samples. The amount of iron(III) added cannot be increased at will, to avoid the need for larger amounts of tin(II) and hydrochloric acid. It should be emphasized that under worst reduction conditions for higher iron(III) levels, quantitative reduction of iron(III) was not attained, significant values being recorded

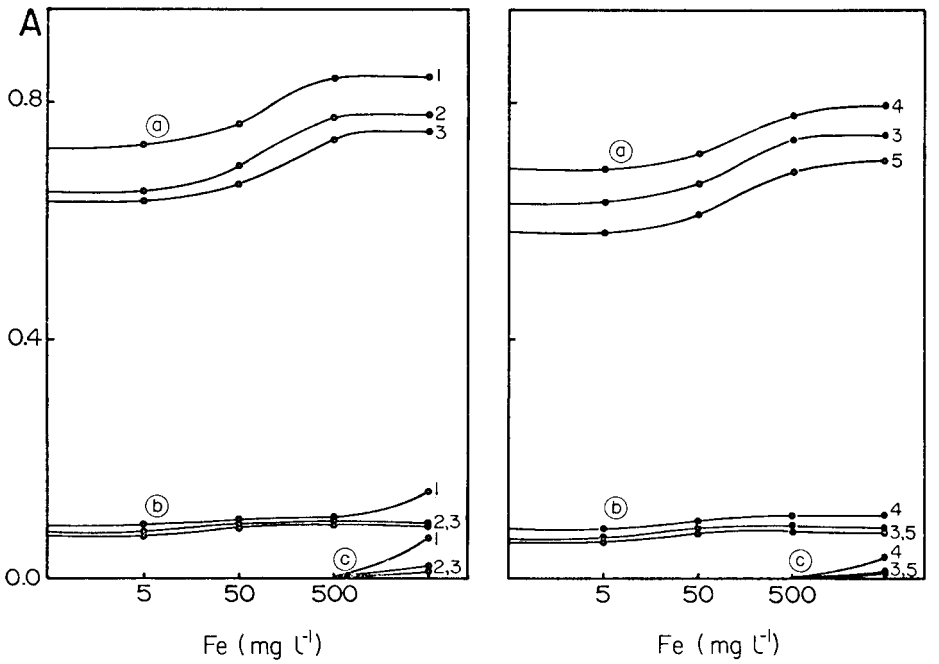

Fig. 2. Effects of iron(III) additions, acidity and tin(II) chloride concentrations. Data referred to system 1a. Tin(II) chloride dihydrate concentration (R_1): (1) 4%; (2) 7%; (3—5) 10% (w/v). Hydrochloric acid present (R_3): (1—3) 6 M; (4) 3 M; (5) 9 M. Molybdenum concentration in the A solution; (a) 200.0; (b) 20.0; (c) 0.00 mg l^{-1}. For details, see text.

when molybdenum was absent (Fig. 2). This interference, caused by the formation of iron(III) thiocyanate, is not additive but diminishes with increased molybdenum concentrations, thus demonstrating the catalytic effect of molybdenum in the iron(III) reduction [7]. Studies of this point were beyond the scope of this work, as quantitative reduction of iron(III) was always attained with the flow-injection system finally proposed.

Increased tin(II) chloride concentrations and/or acidities decreased the peak heights (Fig. 2), possibly because under stronger reduction conditions, molybdenum(VI) is reduced to oxidation states lower than Mo(V) which do not participate in the colour reaction [16] or because different complexes are formed [6]. However, this drop in peak height is not relevant here, as sensitivity is not critical, and it is necessary to have concentrations of tin(II) and hydrochloric acid high enough to prevent interference from the iron in the steel. Given these considerations, a 10% (w/v) tin(II) chloride concentration and a 6 M acidity are recommended for the R_1 reagent in systems 1b and 1c.

Interference study

With these reagent concentrations, addition of 2000 mg l^{-1} vanadium (as ammonium vanadate) via the L_S loop of system 1a did not produce any

coloured vanadium—thiocyanate complexes. Under weaker reduction conditions, however, with 4% (w/v) tin(II) chloride dihydrate and either 6 M or 3 M hydrochloric acid, the same amount of vanadium caused positive absorbances of 0.01 and 0.4, respectively.

Investigations done with system 1b showed that copper (as copper nitrate) interfered when the copper concentration in the A solution exceeded 100 mg l^{-1} (Table 1) which corresponds to a steel sample 2% (w/w) in copper. This effect is caused by the precipitation reaction between copper(I) and thiocyanate [7]. The addition of 5% (w/v) oxalic acid to the sample carrier stream reduced this interference only by about 30%; addition of 5% (w/v) tartaric acid was ineffective. In analyzing steels with higher copper contents, sample dilution could be used to bring the copper content of the injected sample down to about 40 mg l^{-1}. As the copper content in most of the steel samples seldom reaches 0.2% (w/w) which corresponds to 5 mg Cu l^{-1} in the steel digest or 10 mg Cu l^{-1} in the A solution, it can be concluded that the proposed procedure is practically free from this interference.

The tungsten interference would be limiting in applying this procedure to samples with tungsten concentrations higher than about 1% w/w (Table 1). However, preliminary experiments confirmed that such steel samples are not quantitatively solubilized in aqua regia. This interference is, therefore, important in the range 2.5—25 mg W l^{-1} in the injected sample, when a slight decrease in the measured signal is observed, independent of the tungsten concentration (Table 1). For steel digests with tungsten contents in this range, addition of tungsten (1 mg l^{-1} sodium tungstate) to the sample carrier stream is recommended; total suppression of the interference in synthetic samples was then observed up to 25 mg W l^{-1}. This procedure is not required in analyses of steels with negligible (<50 mg kg^{-1}) tungsten contents, which represent several types of steel samples of industrial importance, including the CF3M and CF8M steels.

The cobalt(II) and nickel(II) interferences were negligible but at higher

TABLE 1

Effect of copper and tungsten on the molybdenum determination (the concentration data refer to system 1b, the molybdenum standard solutions being injected via the L_S loop and the copper or tungsten standard solutions, also 500 mg l^{-1} in iron(III), being injected via the L_A loop. After division by two, the concentration values may be extrapolated to system 1c. Other values correspond to peak-height measurements (absorbance). For details, see text)

Mo (mg l^{-1})	Cu (mg l^{-1})					W (mg l^{-1})					
	0	5	50	100	250	0	5	10	20	50	100
0	0.000	0.000	0.000	0.000	0.100	0.000	0.000	0.000	0.000	0.000	0.008
20	0.081	0.081	0.082	0.084	0.192	0.081	0.078	0.078	0.078	0.078	0.084
200	0.809	0.810	0.815	0.872	1.018	0.810	0.713	0.715	0.717	0.713	0.721

levels (2000 mg l^{-1}, as cobalt or nickel chloride), small peaks (about 0.014 absorbance) were noticed when molybdenum was absent. These peaks reflect the colour of the metal aquo or chloro complexes, and can be compensated for by running blanks, i.e., by measuring the samples again after replacement of the R_2 reagent (Figs. 1b and 1c) by water. Parallel experiments indicated that the signal-to-blank ratio is improved when the wavelength is shifted from 470 nm, usually employed, to 480 nm.

A final experiment with system 1b showed that the addition of titanium (50 mg l^{-1}, as $TiCl_4$) to the A solution caused no measurable enhancement in sensitivity, in contrast to a similar procedure involving the Technicon AutoAnalyzer [9].

Assessment of the flow-injection system

In system 1c, the iron(III) concentration of the C_S carrier stream (0.015% w/v) corresponds to the added concentration of 500 mg l^{-1} via the merging zones approach (system 1b) and was calculated from the measured dispersion factors. The iron(III) concentration gradient produced by injection of the sample into an iron(III)-containing carrier solution has no significant effect for three reasons: (a) the gradient diminishes as sample dispersion proceeds, being very small in flow-injection systems with large dispersion [2]; (b) the gradient diminishes when iron(III) is naturally present in the samples; (c) variations in peak heights in the range 500—5000 mg l^{-1} iron added are very small (Fig. 2).

The sample dispersion factor for both systems 1b and 1c was found [5] to be 0.15 when a 10.00 mg l^{-1} molybdenum standard was used. Obviously, the sensitivity can easily be improved simply by minimizing sample dispersion. With the 5.00 mg l^{-1} molybdenum standard in the infinite volume situation, stoppage of the peristaltic pump showed that the reactions were about 97% complete within the mean sample residence time. The exact degree of reaction completion was not, however, evaluated because the coloured complex was unstable, a —10% change of the recorded absorbance being observed after 3 min.

The proposed system is remarkably stable. After four hours of continuous operation, no baseline drift nor any measurable change of the calibration parameters was detected. Table 2 indicates that the results obtained with the proposed procedure compare well with those obtained by other methods and with certified values. The linearity of the calibration plot, measurement reproducibility, system stability and sampling rate can be confirmed from Fig. 3, which is part of a routine run for determinations of molybdenum in steel samples. With a measurement frequency of 270 h^{-1}, only 22 mg of tin(II) chloride dihydrate and 27 mg of potassium thiocyanate are needed per determination.

TABLE 2

Percentage of molybdenum (w/w) in steels, as determined by the proposed procedure (f.i.a.), by atomic emission spectrometry (i.c.p.-a.e.s.) and by atomic absorption spectrometry involving standard additions (s.a.m.-a.a.s.)

Sample	Other components (% w/w)	Molybdenum found (% w/w)[a]		
		F.i.a.	I.c.p.-a.e.s.[b]	S.a.m.-a.a.s.[c]
SAE 4130	0.30C, 0.54Mn, 0.25Si, 0.90Cr	0.28(1.4)	0.25(0.4)	0.30
ASTM A351 Gr CF8	0.07C, 1.20Mn, 0.60Si, 18.4Cr, 8.7Ni	0.59(0.4)	0.62(4.4)	0.58
AISI 329	0.09C, 0.98Mn, 0.48Si, 24.2Cr, 5.5Ni	1.84(0.6)	1.81(2.6)	1.91
SAE 317L	0.02C, 1.40Mn, 0.54Si, 18.9Cr, 12.4Ni	3.15(0.7)	3.15(2.7)	3.18
ASTM A 351 Gr CF3	0.02C, 1.32Mn, 0.64Si, 17.9Cr, 10.4Ni	0.34(2.5)	0.37(2.2)	0.29
ASTM A 217 Gr WC9	0.10C, 0.55Mn, 0.40Si, 2.5Cr	1.08(0.7)	1.10(1.8)	1.14
ASTM A 351 Gr CF3M	0.03C, 1.49Mn, 0.54Si, 18.1Cr, 10.6Ni	2.76(0.4)	2.75(4.1)	2.77
ASTM A 351 Gr CG8M	0.07C, 1.40Mn, 0.80Si, 18.4Cr, 10.4Ni	3.02(0.6)	3.00(0.9)	3.10
ASTM A 351 Gr CF8M	0.08C, 1.24Mn, 0.50Si, 18.5Cr, 10.0Ni	2.13(0.8)	2.09(1.3)	1.96
AISI 329	0.09C, 0.90Mn, 0.40Si, 24.4Cr, 5.9Ni	1.83(0.8)	1.80(2.0)	1.80
MP-01[d]	0.068C, 1.443Mn, 0.482Si, 17.24Cr, 10.32Ni	0.30(2.4)	0.32(1.8)	0.30
MP-05[e]	0.042C, 1.717Mn, 0.238Si, 17.08Cr, 11.95Ni	2.80(1.2)	2.78(3.5)	2.80

[a]Numbers in parentheses indicate the relative standard deviations (%) of three repeated determinations on the same digest; f.i.a. and i.c.p.-a.e.s. results were obtained by using the same digests. [b]Integration period 10 s; wavelength 202.0 nm; calibration by linear regression employing the same Mo standard solutions as for f.i.a.; other parameters as specified previously [10]. [c]Procedure similar to that described by Mostyn and Cunningham [19]: addition of 0.0, 2.5, 5.0 and 7.5 ml of a 150 mg Mo l^{-1} standard solution plus 5 ml of a 5% (w/v) ammonium chloride solution to 10.0 ml of the steel digest; after dilution to 25 ml with water, the four solutions were measured in a Varian AA-175 atomic absorption spectrometer provided with a nitrous oxide/acetylene flame. [d]237-1/552 standard reference steel from Max-Planck Institute, West Germany. Molybdenum content 0.306 ± 0.006%. [e]229-1/1454 standard reference steel from Max-Planck Institute, West Germany. Molybdenum content: 2.769 ± 0.036%.

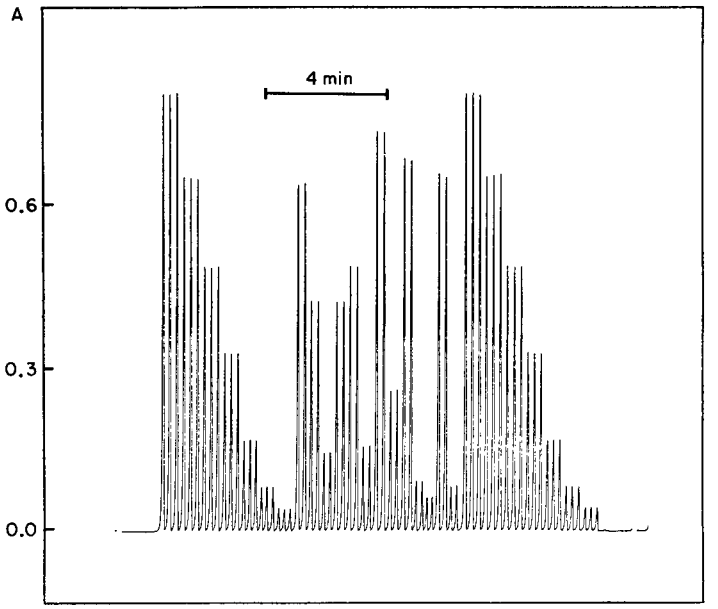

Fig. 3. Recorder output of a routine run for the determination of molybdenum in steels. From the left, the peaks correspond to seven standards (100.0, 80.0, 60.0, 40.0, 20.0, 10.0 and 5.00 mg Mo l^{-1}), two standard reference samples, eleven samples and the standards again. Standard solutions were injected in triplicate and samples, in duplicate.

Partial support of this research by CNPq (Conselho Nacional de Desenvolvimento Científico e Tecnológico and FINEP (Financiadora de Estudos e Projetos) is greatly appreciated. O. B. F° was supported by a Research Studentship from CNEN (Comissão Nacional de Energia Nuclear). The authors express their gratitude to Raul Cancigliero, Director of FUNAPI (Fundição de Aços Piracicaba), for providing the standard reference samples and to Peter B. Vose, for his help with the manuscript.

REFERENCES

1 J. Růžička and E. H. Hansen, Anal. Chim. Acta, 78 (1975) 145.
2 J. Růžička and E. H. Hansen, Flow Injection Analysis, Wiley, New York, 1981.
3 R. Kuroda and T. Mochizuki, Talanta, 28 (1981) 389.
4 T. Mochizuki and R. Kuroda, Fresenius Z. Anal. Chem., 311 (1982) 11.
5 E. A. G. Zagatto, A. O. Jacintho, F. J. Krug, B. F. Reis, R. E. Bruns and M. C. U. Araújo, Anal. Chim. Acta, 145 (1983) 169.
6 F. D. Snell, C. T. Snell and C. A. Snell, Colorimetric Methods of Analysis, D. Van Nostrand, Toronto, Canada, 1959, p. 793.
7 W. T. Elwell and D. F. Wood, Analytical Chemistry of Molybdenum and Tungsten, Pergamon Press, Oxford, 1971.
8 N. Lounamaa, Anal. Chim. Acta, 33 (1965) 21.
9 K. Braithwaite and J. D. Hobson, Analyst (London), 93 (1968) 633.
10 A. O. Jacintho, E. A. G. Zagatto, H. Bergamin F°, F. J. Krug, B. F. Reis, R. E. Bruns and B. R. Kowalski, Anal. Chim. Acta, 130 (1981) 243.

11 F. J. Krug, J. Mortatti, L. C. R. Pessenda, E. A. G. Zagatto and H. Bergamin F°, Anal. Chim. Acta, 125 (1981) 129.
12 E. B. Sandell and H. Onishi, Photometric Determination of Traces of Metals. General Aspects, Wiley, New York, 1978.
13 C. M. Johnson and T. H. Arkley, Anal. Chem., 26 (1954) 572.
14 C. L. Luke, Anal. Chim. Acta, 34 (1966) 302.
15 H. Bergamin F°, E. A. G. Zagatto, F. J. Krug and B. F. Reis, Anal. Chim. Acta, 101 (1978) 17.
16 Z. Marczenko, Spectrophotometric Determination of Elements, Ellis Horwood, Chichester, 1976.
17 R. P. Hope, Anal. Chem., 29 (1957) 1053.
18 F. J. Krug, B. F. Reis, M. F. Giné, E. A. G. Zagatto, J. R. Ferreira and A. O. Jacintho, Anal. Chim. Acta, 151 (1983) 39.
19 R. A. Mostyn and A. I. Cunningham, Anal. Chem., 38 (1966) 121.

Analytica Chimica Acta, 161 (1984) 257—263
Elsevier Science Publishers B.V., Amsterdam — Printed in The Netherlands

SPECTROFLUORIMETRIC FLOW-INJECTION DETERMINATION OF CYANIDE

P. LINARES, M. D. LUQUE DE CASTRO and M. VALCARCEL*

Department of Analytical Chemistry, Faculty of Sciences, University of Córdoba, Córdoba (Spain)

(Received 23rd November 1983)

SUMMARY

The spectrofluorimetric determination of cyanide (0.1—20 $\mu g\ ml^{-1}$) with pyridoxal and pyridoxal-5-phosphate by a normal flow-injection method and a stopped-flow procedure is reported. The large number of interfering species in the normal method is significantly decreased by the use of the stopped-flow method. The relative standard deviation is < 2%.

A few methods have been developed for the determination of cyanide by flow injection analysis (f.i.a.) all of which involve electroanalytical detection. Pihlar et al. [1] reported a voltammetric determination with a wide linear calibration range ($0.5—10^6\ \mu g\ l^{-1}$), a good sampling rate ($100\ h^{-1}$) and a relative standard deviation (r.s.d.) of 2%. Its only shortcoming is the larger number of interferences, which can be drastically diminished by distillation of the sample and u.v. decomposition of cyanide complexes [2], but this detracts from the speed of the method. The only potentiometric determination was devised by Müller [3] who used a silver sulphide electrode and a silver nitrate solution as carrier; the method had an r.s.d. of 5% and a range of $10^{-3}—10^{-6}$ M but interferences were not studied.

This paper presents a spectrofluorimetric determination of cyanide by f.i.a. based on the reaction of cyanide with pyridoxal and pyridoxal-5-phosphate. The reaction of pyridoxal or its phosphate with cyanide has been incorrectly referred to as the "cyanohydrin" method [4] and has been applied to the determination of pyridoxine derivatives in biological samples [5]. The products of the oxidation of pyridoxal and its phosphate in the presence of oxygen and the catalytic action of cyanide are, respectively, 4-pyridoxolactone and 4-pyridoxic acid 5-phosphate [6]. Substances like nicotinamide adenine dinucleotide (NAD^+) interfere, as the excitation and emission maxima of cyanide-treated NAD^+ are close to those of 4-pyridoxolactone [7].

The oxidation reactions are slow, although they are speeded up by an increase in temperature. However, the latter decreases the fluorescence intensity. Thus, in order to obtain an acceptable reaction yield without

0003-2670/84/$03.00

excessive dispersion, a stopped-flow method [8, 9] was used. The stopped-flow mode also helps to remove interfering effects [10].

EXPERIMENTAL

A Tecator 5020 flow injection analyzer was used; its two pumps can be stopped and started individually and are synchronized with the injection system. The injection valve, Tecator L-100-1, has a variable volume. All the reactor coils were made in teflon tubing as were the sample loops which were calibrated spectrophotometrically using a dye. The 25-μl flow cell was a Hellma 176-52-QS. A Perkin-Elmer 650-10S spectrofluorimeter was used as detector, connected to a Radiometer REC-80 recorder. The printer was an Alphacom 40. The accessory instruments were a Beckman 3500 pH meter, a thermostat bath and a Selecta S-382 thermostat.

The stock solutions used included aqueous solutions of pyridoxal (2×10^{-2} M), pyridoxal-5-phosphate (1×10^{-2} M), a pH 7.6 phosphate buffer (0.6 M), a pH 3.2 acetate buffer (0.2 M), 2 M sodium hydroxide and an aqueous 1.000 g l^{-1} solution of potassium cyanide.

Figure 1 shows the manifolds used for the determination of cyanide by conventional f.i.a. as well as by stopped flow. The optimal values of the variables in each determination are also shown.

RESULTS AND DISCUSSION

The fluorescence spectra of both reagents were recorded in the presence and in the absence of cyanide. In both cases, there was a remarkable increase in the fluorescence intensity and a shift towards longer wavelengths (excitation and emission) for the oxidation product compared to the reactant, the maximal values found being as follows: pyridoxal (λ_{ex} = 320 nm, λ_{em} = 380 nm), pyridoxal/cyanide product (λ_{ex} = 355 nm, λ_{em} = 435 nm), pyridoxal-5-phosphate (λ_{ex} = 300 nm, λ_{em} = 384 nm), and pyridoxal-5-phosphate/cyanide product (λ_{ex} = 318 nm, λ_{em} = 455 nm).

For both reactants, the rate of formation of the oxidation product was maximal in slightly alkaline solution. The highest fluorescence intensity for the pyridoxal/cyanide product was obtained at the same pH. In contrast, pyridoxal-5-phosphate required an acidic solution to achieve a suitable analytical signal. Therefore the manifolds reported for the determination of cyanide by use of the two organic compounds are different. For the pyridoxal-5-phosphate system, a second channel was needed to make the sample plug acidic before it reached the detector. A comparison of the two systems with the conventional technique and stopped-flow mode is therefore presented. The variables for both systems were optimized by conventional f.i.a. Under the optimal chemical and f.i.a. conditions, an increase in the fluorescence intensity was observed when the sample plug was stopped in the reaction coil. Thus, the systems were further optimized for stopped-flow operation.

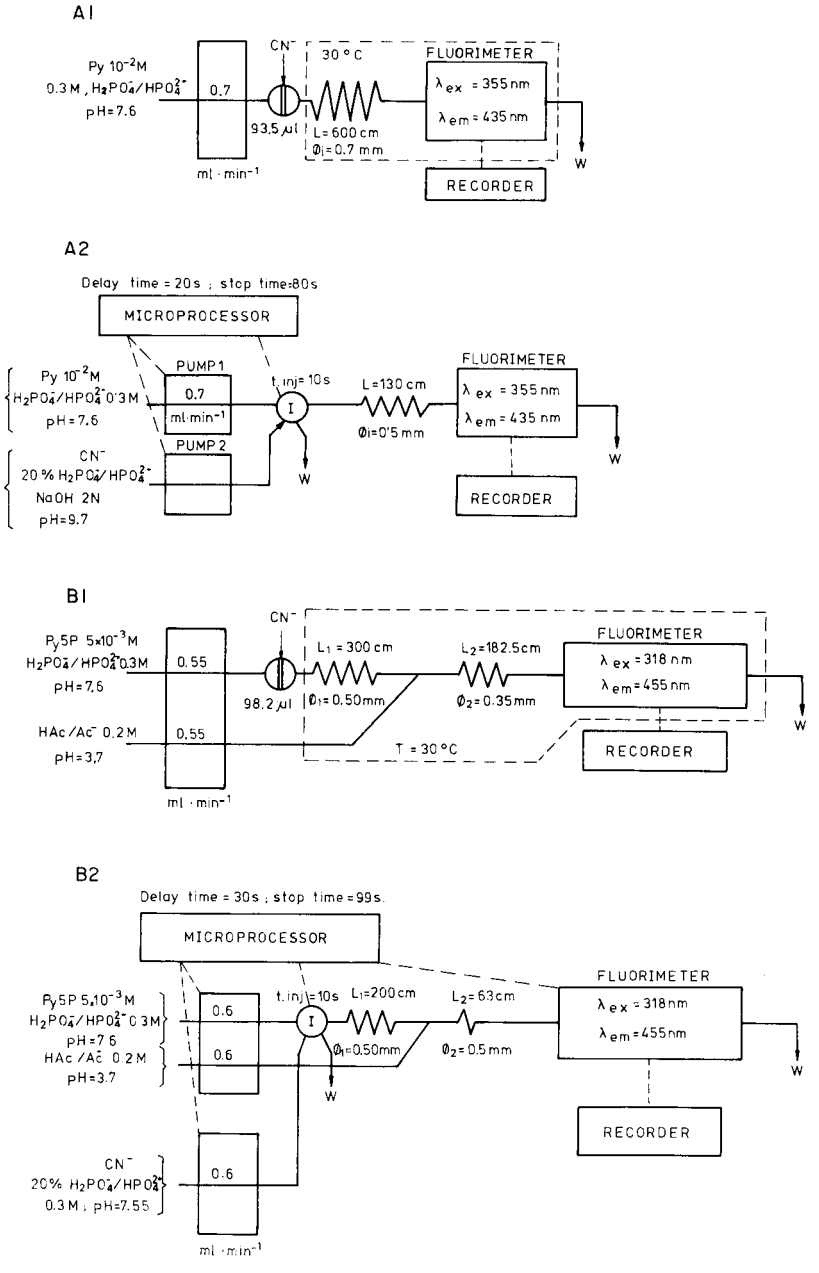

Fig. 1. Manifolds, with optimal values of the variable parameters, for the determination of cyanide with: (A) pyridoxal; (B) pyridoxal-5-phosphate. Manifolds A1 and B1 are for conventional f.i.a., and manifolds A2 and B2 are for stopped flow (ϕ = internal diameter).

Conventional technique

Pyridoxal/cyanide system. There was a narrow pH range (7.0—7.8) for the carrier stream in which the fluorescence intensity was maximal. Within this range, the analytical signal was slightly higher at pH 7.6. At pH <5 or >9, the fluorescence was practically nil. The pH chosen for further experiments was 7.6, adjusted by a phosphate buffer. The intensity of the signal also increased with buffer concentration, reaching a maximum at 0.3 M. Above this concentration the fluorescence intensity was constant, or slightly decreased at values over 0.5 M. The pH of the injected sample had a decisive influence on the signal obtained; the greatest intensity was obtained at pH 9.7, at which cyanide is present as the anion. An increase in temperature increased the reaction rate in such a manner that a decrease in the fluorescence by deactivation resulted in a net linear increase of the signal between 10 and 55°C (3.05% of the fluorescence intensity per °C); for subsequent studies, 30°C was chosen. Changes in pyridoxal concentration were studied between 5×10^{-2} and 1×10^{-4} M. Highest peaks were obtained for 1×10^{-2} M pyridoxal, which was used in all further studies.

The volume of injected sample was critical, because the signal increased with this variable up to 93.5 μl. Above this value a double peak was obtained, which indicated that the reaction in the center of the sample zone had progressed to a lesser extent than at the two carrier-sample interfaces. The fluorescence intensity increased linearly with the length and diameter of the reactor. As a compromise between the optimal signal and the sampling frequency and economy of reagents, a reactor length of 600 cm and an inner diameter of 0.70 mm were chosen for subsequent experiments. The response of the signal to the variation of the flow rate was represented by a decreasing exponential plot, $\Delta I_f = 1460 \exp 0.7688$, with a correlation coefficient (r) of 0.986 (10 results). A value of 0.7 ml min^{-1} was chosen for the flow rate as a compromise between the residence time and the sampling frequency.

Pyridoxal-5-phosphate system. The B1 manifold shown in Fig. 1 was used in order to develop the reaction at its optimum pH (alkaline) and to achieve a suitable fluorescence intensity when the detector was reached (acidic solution). The optimal pH values for the carrier solutions 1 and 2 as well as for the sample were studied; the results are plotted in Fig. 2. Trials with different buffers of different concentrations established the following optimal conditions: carrier 1 and sample, 0.3 M phosphate buffer, pH 7.5; carrier 2, 0.3 M acetate buffer, pH 3.5. An increase in temperature gave rise to an increase in the signal. Because the f.i.a. response above 35°C had two peaks, 30°C was chosen as the working temperature. Greatest intensity was obtained with 5×10^{-3} M pyridoxal-5-phosphate.

An increase in the volume of injected sample again increased the signal up to 98.2 μl, above which two peaks appeared. The effect of the length of the two tubes was studied. Figure 3 shows the results obtained, from which the optimal values were considered to be $L_1 = 300$ cm, $\phi_1 = 0.50$ mm, $L_2 =$

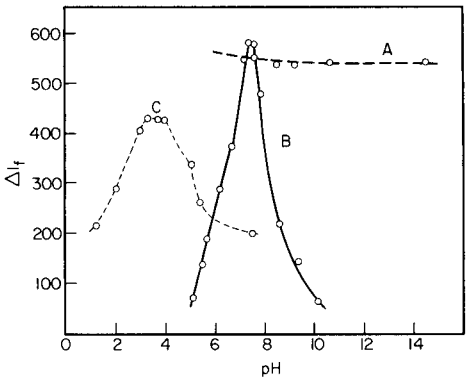

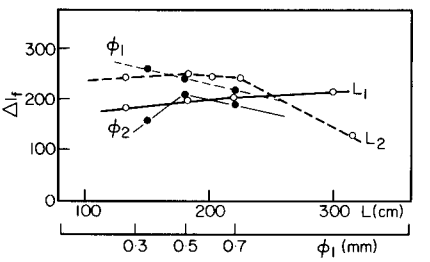

Fig. 2. Influence of pH on the determination of cyanide with pyridoxal-5-phosphate: A) sample; B) carrier 1; C) carrier 2.

Fig. 3. Influence of the lengths and diameters of the reactors on the determination of cyanide with pyridoxal-5-phosphate (see Fig. 1, manifold B1).

183 cm, ϕ_2 = 0.35 mm. The fluorescence intensity increased with increase in L_1 (Fig. 3) because of the longer time of reaction, 300 cm was chosen as a compromise between the determination range and sampling rate and dispersion. The flow rate was simultaneously changed in the two channels. The signal decreased with increasing flow rate because of the shorter reaction time and the greater dispersion. A flow rate of 0.55 ml min^{-1} was used for both channels in subsequent experiments.

Stopped-flow mode

Pyridoxal system. In this mode the sample is retained in the reactor by stopping the pump for a time, thus allowing the maximum reaction, before restarting the pump to allow the sample zone to reach the detector. The optimization of variables yielded the following values: carrier pH 7.6; sample pH 9.2; 1×10^{-2} M pyridoxal; L = 130.0 cm, ϕ = 0.50 mm; delay time 20 s; stop time 80 s; injection time 10 s.

Pyridoxal-5-phosphate system. The sample was stopped in the first reactor. The optimal values of the variables obtained were: carrier 1 and sample, 0.3 M phosphate buffer, pH 7.6; carrier 2, 0.2 M acetate buffer, pH 5.0; L_1 = 200 cm, L_2 = 63 cm, $\phi_1 = \phi_2$ = 0.50 mm, flow rates 0.50 ml min^{-1}, delay time 30 s, stop time 99 s; injection time 10 s.

The working temperature for both stopped-flow methods was 30°C.

Determination of cyanide

Table 1 summarizes the most important analytical characteristics of the four methods. The range is wider when pyridoxal is used, although the r.s.d. is slightly higher. The pseudo stopped-flow mode provides a small increase in sensitivity, but not so large as to justify its use.

TABLE 1

Analytical characteristics of the f.i.a. procedures for cyanide

F.i.a. mode[a]	Calibration equations	r^b	Linear range (mg l^{-1})	R.s.d.[c] (%)
Pyridoxal				
C	$\Delta I_f = 51.44[CN^-] - 6.58$	0.9981	0.1—20.0	1.4
SF	$\Delta I_f = 98.05[CN^-] - 1.72$	0.9997	0.1—20.0	2.0
Pyridoxal-5-phosphate				
C	$\Delta I_f = 125.52[CN^-] - 23.72$	0.9981	0.1—10.0	0.8
SF	$\Delta I_f = 180.77[CN^-] - 26.49$	0.9988	0.07—10.0	1.6

[a]C, conventional. SF, stopped flow. [b]Correlation coefficient. [c]For 5.0 mg l^{-1} cyanide (11 measurements).

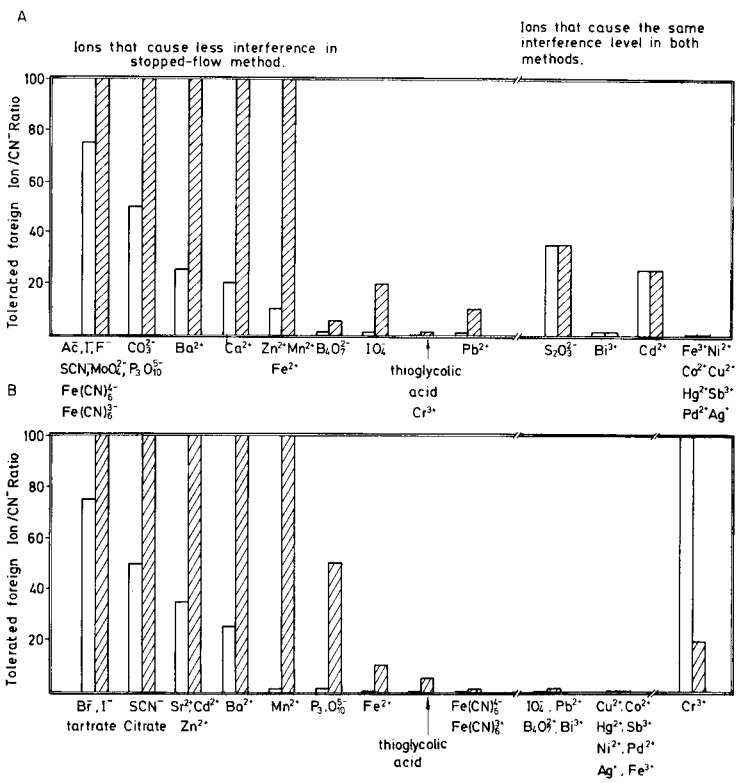

Fig. 4. Tolerable concentrations of foreign ions in the determination of 5 mg ml^{-1} cyanide by the pyridoxal methods (A) and the pyridoxal-5-phosphate methods (B). The open blocks are for the conventional method and the hatched blocks for the stopped-flow method.

Interferences. A systematic study of potential interferents was made for the four procedures. Numerous foreign ions up to a maximal weight ratio of 100 (foreign ion/CN^-) were tested. It was found that the interferences for each reagent were different. When pyridoxal was used, the following did not interfere in either mode: K^+, Na^+, Sr^{2+}, SO_4^{2-}, NO_3^-, Br^-, Cl^-, ClO_4^-, $S_2O_8^{2-}$, $C_2O_4^{2-}$, EDTA, citrate and tartrate. When pyridoxal-5-phosphate was used, the following were found not to interfere in either mode: K^+, Na^+, Ca^{2+}, SO_4^{2-}, NO_3^-, Cl^-, F^-, ClO_4^-, $S_2O_8^{2-}$, $C_2O_4^{2-}$, EDTA, CO_3^{2-}, acetate, $S_2O_3^{2-}$, MoO_4^{2-}. Figure 4 shows the tolerated foreign ion/cyanide ratio for the various procedures. The interference of transition metal ions can be removed by adding EDTA to either the carrier or the sample.

The methods that use pyridoxal are generally slightly more sensitive than those with pyridoxal-5-phosphate, although the latter may be suitable for certain matrices.

REFERENCES

1 B. Pihlar, L. Kosta and B. Hristovski, Talanta, 26 (1979) 805.
2 B. Pihlar, L. Kosta and B. Hristovki, Anal. Chim. Acta, 114 (1980) 275.
3 H. Müller, in E. Pungor (Ed.), Ion-Selective Electrodes, Vol. 3, Elsevier, Amsterdam, 1981, p. 279.
4 V. Bonavita, Arch. Biochem., 88 (1960) 366.
5 S. F. Contractor and B. Shane, Clin. Chim. Acta, 21 (1968) 71.
6 N. Oishi and S. Fukui, Arch. Biochem. Biophys., 128 (1968) 606.
7 S. Takanashi and Z. Tamura, J. Vitaminol, 16 (1970) 129.
8 T. Yamane, Anal. Chim. Acta, 130 (1980) 183.
9 C. S. Lim and J. N. Miller, Anal. Chim. Acta, 114 (1980) 183.

Analytica Chimica Acta, 161 (1984) 265—273
Elsevier Science Publishers B.V., Amsterdam — Printed in The Netherlands

DETERMINATION OF CALCIUM AND BARIUM IN STEEL BY ELECTROTHERMAL ATOMIC EMISSION SPECTROMETRY

B. FU[a], J. M. OTTAWAY*, J. MARSHALL and D. LITTLEJOHN

Department of Pure and Applied Chemistry, University of Strathclyde, Glasgow G1 1XL (Great Britain)

(Received 16th December 1983)

SUMMARY

A simple and rapid method is described for the determination of 1—40 $\mu g\ g^{-1}$ calcium in steels by electrothermal atomic emission spectrometry. The sample is dissolved in nitric acid and does not need preconcentration. The use of a recessed platform is shown to improve reproducibility and sensitivity in the determination of calcium. A similar procedure for the determination of barium ($< 1\ \mu g\ g^{-1}$) in steel is described.

The presence of certain trace elements in steels can have detrimental effects on their properties, and analytical methods of suitable sensitivity, precision and speed are needed for quality control on steel specifications. A number of atomic spectrometric methods has been devised for the determination of a range of minor and trace elements in steel [1—5]. Whilst satisfactory methods have been developed for most transition metals, the determination of calcium and barium, which are present at somewhat lower concentrations, has proved more difficult. Traces of calcium in inclusions have a significant effect of the properties of steel [1]. Atomic absorption methods with a nitrous oxide/acetylene flame are usually proposed for this determination. However, the sensitivity of these methods appears to be insufficient for the determination of low levels of calcium in steel. Scholes [2] reported a working range of 20—200 $\mu g\ g^{-1}$ calcium whilst Headridge and Richardson [3] found it necessary preconcentrate by liquid—liquid extraction. Taylor and Belcher [1] described a flame atomic absorption procedure which allowed the determination of calcium in steel in the range 1—200 $\mu g\ g^{-1}$, but relative standard deviations as large as 100% were obtained at the lower end of this range.

Atomic absorption spectrometry (a.a.s.) with electrothermal atomisation provides a more sensitive method for the determination of calcium; applications to the analysis of phosphatidylethanolamine solutions [6], snow [7] and high-purity water [8] have been reported, but there are none concerning

[a]On leave from the Department of Analytical Science, Beijing Mining and Metallurgical Research Institute, Xizhimen, Beijing (China).

0003-2670/84/$03.00

the determination of calcium in steels, except for recent work in this laboratory [9]. The use of electrothermal atomisers in atomic emission spectrometry (a.e.s.) is well documented [10]. Relatively simple spectra are produced, and background correction can be achieved by wavelength modulation [11, 12]. The technique offers high sensitivity for many elements, such as barium, where the detection limit obtained is significantly better than that obtained by electrothermal a.a.s. [11, 13]. It has previously been applied to the determination of minor elements in steel [5] and of barium in calcium carbonate rocks [14] and potable waters [15].

Platform atomisation is an effective means of overcoming chemical interference effects in electrothermal a.a.s. [16]. It also increases the sensitivity because of the higher vapour temperature experienced by analyte atoms at the time of atomisation in comparison to atomisation from the tube wall [17, 18]. In the present work, a study was made of the effect of cutting a recess into the platform, to contain the sample, on sensitivity and precision in the determination of calcium in steel. A method for the determination of barium in steel is also described.

EXPERIMENTAL

Apparatus

The instrument system used comprised a Spectrametrics echelle monochromator fitted with a wavelength modulation device for automatic background correction and a Hamamatsu R712 visible photomultiplier, an Ortec Brookdeal preamplifier and 9305 lock-in amplifier, and a Bryans Southern Instruments 28000 chart recorder. A laboratory-constructed power supply was used to drive the wavelength modulation chopper and supply the photomultiplier e.h.t. unit. A Perkin-Elmer HGA-72 furnace was used as the atomiser and was mounted on an optical bench attached to the echelle monochromator. A single lens was used to give a 1:1 image of the furnace tube wall at the monochromator entrance slit. The system was used to measure atomic emission signals in the manner described previously [17—19].

Rectangular platforms (8 × 11 mm) were cut from standard HGA-72 tubes, the thickness therefore being that of the HGA-72 tube wall. A circular recess (6 mm diameter, 0.8 mm depth) was cut in the centre of the platform (Fig. 1), which could accommodate ca. 20 μl of sample. The modified platform was placed inside the furnace and coated with pyrolytic graphite as previously described [19]. Instrumental conditions are given in Table 1 for the determination of calcium and barium in steel.

Reagents and solutions

Reagents of the highest available purity were used. Stock solutions containing 100 μg ml^{-1} calcium and 100 μg ml^{-1} barium were prepared in 1% (v/v) nitric acid and stored in polyethylene bottles. Working solutions were freshly prepared from these stock solutions as required.

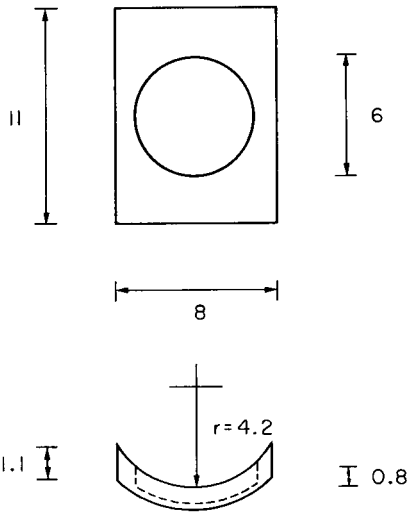

Fig. 1. The recessed platform used for the determination of calcium. (Dimensions in mm.)

Preparation of calibration standard solutions. For calcium ca. 0.25 g of BCS 149/3 high-purity iron was dissolved in 5 ml of 40% (v/v) nitric acid in a 100-ml PTFE beaker; after addition of 0.1 ml of concentrated hydrofluoric acid, the solution was transferred to a 100-ml volumetric flask. The appropriate amount of calcium standard solution was added and the solution was diluted to the mark with distilled water.

For barium, ca. 0.5 g of the high-purity iron was dissolved in 10 ml of

TABLE 1

Instrumental conditions

	Calcium	Barium
Wavelength (nm)	422.7	553.5
Slit width (μm)	200	200
Slit height (μm)	500	500
(Matched entrance and exit slit dimensions)		
Tube type	standard tube[a]	standard tube
Dry	40 s at 150°C	45 s at 100°C
Ash	10 s at 1200°C	10 s at 1250°C
Atomise	8 s at 2450°C	8 s at 2400°C
Gas mode	gas flow	gas stop
Purge gas	nitrogen	nitrogen
Cleaning stage	7 s at 2660°C	5 s at 2400°C
Sample volume (μl)	20	50

[a]Standard tube, with recessed platform with pyrolytic graphite coating.

40% (v/v) nitric acid in a 100-ml PTFE beaker. The solution was transferred to a 50-ml volumetric flask, the appropriate amount of barium standard solution was added and the solution was diluted to the mark with distilled water.

Preparation of sample solutions

For calcium, weighed steel samples (0.25 g) were dissolved in 5 ml of 40% (v/v) nitric acid in a 100-ml PTFE beaker. Hydrofluoric acid (0.1 ml) was added and the solution was gently heated for 10 min. The solution was transferred to a 100-ml polythene volumetric flask and diluted to the mark with distilled water.

For barium, weighed steel samples (0.5 g) were dissolved in 10 ml of 40% (v/v) nitric acid. The solution was transferred to a 50-ml volumetric flask and diluted to the mark with distilled water.

RESULTS AND DISCUSSION

Platform atomisation

When tube-wall atomisation was employed, poor precision was obtained for calcium emission measurements. Replicate measurements of an aqueous solution containing 0.05 μg ml^{-1} calcium (20 μl samples) gave a relative standard deviation (r.s.d.) of $\approx$5%. For acidic solutions, precision was poorer and appeared to deteriorate as the acidity was increased; the r.s.d. was 22% for an 8% (v/v) acid solution. The addition of iron resulted in a further deterioration in precision; 0.05 μg ml^{-1} calcium in 2% acid and in the presence of 2500 μg ml^{-1} iron gave an r.s.d. of 30%. Precision was found to be better for smaller sample volumes and it is likely that the poor performance was related to spreading effects in the tube. Calcium is known to be present in the graphite tube material and variations in solution spreading may have resulted in contamination, causing errors larger than would be expected. Certainly, precision for calcium appeared to be worse than for many other elements under similar conditions [5]. Memory effects appeared to be worse for calcium in the presence of acid, suggesting the possibility of carbide formation as an explanation, but there is insufficient evidence to draw definite conclusions.

It was clear that precision could be improved if the degree of sample spreading could be decreased. Even at the minimum acid concentration required (2%), spreading effects were still significant. The use of platform atomisation improved precision, but during the drying stage of the furnace heating programme, the sample exhibited a tendency to creep off the platform. The recessed platform (Fig. 1) was introduced in an attempt to combat solution spreading. It was found possible to contain a 20-μl sample almost entirely in the recess until drying had occurred, with only a small amount of spreading onto the surface of the platform. A comparison of the precision obtained for various media, using tube wall, platform and recessed

platform atomisation is shown in Table 2. It is evident from these results that the use of the recess prevents sample spreading and thus substantially improves the precision of the measurements. The effect of platform atomisation on the responses and detection limit for calcium is shown in Tables 3 and 4. Calcium atomic emission sensitivity is improved when platform (as opposed to tube wall) atomisation is employed; this observation is in agreement with the trend for other elements [19]. Detection limits appear to be improved primarily because of the better precision achieved with the recessed platform. However, the results presented only serve to illustrate this trend and are not directly comparable in the various media.

TABLE 2

Comparison of electrothermal a.e.s. precision in the measurement of calcium

Medium	Relative standard deviation (%)[a]		
	Standard tube	Standard tube and platform	Standard tube and recessed platform
Aqueous	5.6	4.4	3.7
5% (v/v) HNO_3	15.1	7.7	5.6
2% (v/v) HNO_3 + 2500 μg Fe ml^{-1}	30.3	19.6	6.3

[a]For 10 replicate determinations of a solution containing 0.05 μg Ca ml^{-1}; 20-μl manual injections.

TABLE 3

Comparison of emission responses for calcium (20-μl sample)

Medium	Intensity of calcium signal		
	Standard tube	Standard tube and platform	Standard tube and recessed platform
Aqueous	100	143	171
5% (v/v) HNO_3	100	105	113

TABLE 4

Comparison of electrothermal a.e.s. detection limits for calcium (20-μl sample)

Medium	Detection limits (2σ) (ng ml^{-1})		
	Standard tube	Standard tube and platform	Standard tube and recessed platform
Aqueous	0.87	0.37	0.10
5% (v/v) HNO_3	2.3	1.3	0.68
2% (v/v) HNO_3 + 2500 μg Fe ml^{-1}	6.0	3.9	1.1

Interferences

The effects of various acids on the calcium atomic emission signal was investigated. It was found that in a 2% nitric acid medium there was no interference from 2500 μg ml^{-1} iron on the calcium emission signal (Fig. 2A). This confirmed previous observations that nitric acid provided an interference-free medium for the determination of trace elements in steels with electrothermal atomisation [4, 5]. Hydrochloric acid did not affect the calcium signal, except in the presence of iron (see Fig. 2B), when severe interferences were found. The calcium signal depressed by 68% in 2% (v/v) hydrochloric acid in the presence of 2500 μg ml^{-1} iron, and by 85% in 8% hydrochloric acid with the same iron content. Frech and Cedergren [20, 21] have reported similar interferences in the determination of lead in steel and have suggested that chlorine is retained as $FeCl_2$ which is not removed at 1000 K unless there is a sufficient partial pressure of hydrogen in the atomiser. The interferences observed in the present study are undoubtedly due to the volatilisation of calcium as $CaCl_2$, or to its formation in the gas phase, thus decreasing the atomic emission signal.

When hydrochloric and nitric acids were used in a 1:1 ratio, serious interference effects resulted and the calcium signals from some steel samples were lower than the reagent blanks. Perchloric acid also depressed the calcium signal and caused poor reproducibility (30% r.s.d.). Addition of 2% perchloric acid resulted in a 48% depression of the calcium signal compared to that obtained for an aqueous solution of calcium nitrate. In 1×10^{-2} M nitric acid, iron (2500 μg ml^{-1}) caused a 20% suppression of the calcium signal in comparison to that obtained in 10^{-2} M nitric acid alone, for 0.02—0.1 μg Ca ml^{-1}. Calibration graphs of standard additions of calcium to the steel samples had a different slope to that obtained for calcium in 2% nitric acid. Thus, for the analysis of steel samples, calibration solutions were adjusted to contain the same amount of iron as that in the sample solutions to counteract the interference of the acid alone.

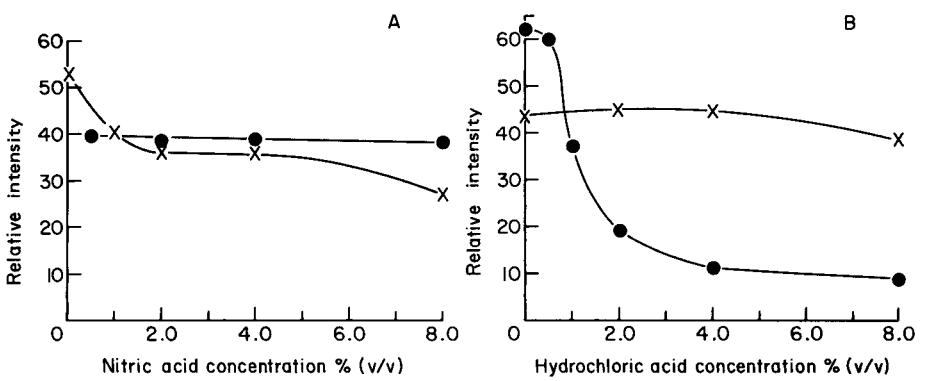

Fig. 2. Effect of nitric acid (A) and hydrochloric acid (B) on the atomic emission signals from 20 μl of 0.05 μg ml^{-1} calcium: (×) alone; (•) in the presence of 2500 μg ml^{-1} iron.

Determination of calcium in steel

The instrumental conditions were as shown in Table 1. Although the sensitivity of the calcium atomic emission measurement increased with temperature, reproducibility became poorer, thus the optimum atomisation temperature was 2450°C. It was also beneficial to employ gas flow conditions during the atomisation stage. Under such conditions, memory effects were decreased although there was also an adverse effect on the sensitivity.

The procedure was applied to the determination of calcium in a range of standard steels. Two drops (0.1 ml) of hydrofluoric acid were added in order to dissolve any silicates present which might retain traces of calcium. Undissolved carbon was allowed to settle at the bottom of the volumetric flask before an appropriate aliquot of solution was withdrawn for injection. The results obtained are presented in Table 5. The comparative results shown were obtained by electrothermal a.a.s. [9] because certificate values were not given for calcium. The reproducibility of the method was tested by injecting the same steel solution (BCS 330) 10 times to give an estimate of instrumental precision, and by repeating the complete procedure 10 times to give a measure of the overall precision. The former gave a mean value of 3.0 $\mu g\ g^{-1}$ calcium with an r.s.d. of 7.3%, whereas the latter gave mean values of 2.9 and 16 $\mu g\ g^{-1}$, with 13.4 and 10.4% r.s.d., for BCS 330 and 401, respectively.

Determination of barium in steel

The atomisation temperature used for the determination of barium was 2400°C. Precision appeared to be better than for calcium, and a standard tube was used to atomise the sample. Nitric acid depressed the atomic emission signal for barium. In 8% (v/v) nitric acid, the signal was depressed by about 30% compared to the equivalent signal for an aqueous barium nitrate solution. Standard addition graphs were parallel to calibration graphs obtained for barium in 8% (v/v) nitric acid solution, indicating that there was no interference from iron in this medium. The calibration graph for

TABLE 5

Electrothermal determination of calcium and barium in steels

Sample	Calcium content ($\mu g\ g^{-1}$)		Barium content ($\mu g\ g^{-1}$)
	A.e.s.[a]	A.a.s. [21]	A.e.s.[a]
BCS 325	3.9 ± 0.4 (5)	4.2	0.4
BCS 330	2.9 ± 0.3 (10)	2.5	—
BCS 401	16 ± 1.7 (10)	—	0.9
BCS 403	5.0 ± 0.5 (5)	6.0	0.5
BCS 405	20 ± 0.9 (5)	17.0	0.8
BCS 409	—	—	0.7

[a]Mean and standard deviation with number of determinations in parentheses.

barium was found to be linear up to a concentration of 0.2 μg ml^{-1} barium. The detection limit (2σ) for barium in distilled water was 0.8 ng ml^{-1}; it was 0.12 μg g^{-1} for barium in steel. Although no interference was observed, iron was incorporated into the standard solutions in order to ensure reproducible atomisation conditions. The results for the determination of barium in steel are shown in Table 5. It was not possible to compare these results with certificate values, since the level of barium in the samples is so low that it cannot be measured by other techniques.

Conclusions

Electrothermal atomic emission spectrometry allows simple rapid methods to be adopted for the determination of calcium and barium in steel samples. Although some chemical interferences are observed, they can be overcome by normal matrix-matching techniques. In the platform method described for calcium, significant advantages in terms of precision were achieved by cutting a recess into the surface of the platform. Platforms used in this and other emission studies [17, 18] in this laboratory have always been made from graphite tubes, and are consequently curved. In studies with a wide range of elements [18], the extreme spreading effects described above for calcium are unique. Thus there appears to be a particular property of calcium solutions which enhances the spreading effect and could explain the poor precisions often observed with this element in electrothermal atomisation. Some commercially available platforms, such as those from Perkin-Elmer, have an elongated recess cut into the surface of the platform and could be expected to be particularly suitable for calcium determinations by electrothermal a.a.s., although this has not been reported. Although this platform has not been used for emission studies (in order to avoid the possibility of atomisation from cooler segments of the tube), it might be a convenient atomisation surface for calcium determinations.

This work was made possible by the award of grants (to J. M. O.) by the Royal Society for purchase of the HGA-72 carbon furnace atomiser and by the SERC for the purchase of the echelle spectrometer. Provision of financial support from the Pye Foundation (for D. L.) and SERC (for J. M.) is also gratefully acknowledged.

REFERENCES

1 M. L. Taylor and C. B. Belcher, Anal. Chim. Acta, 45 (1969) 219.
2 P. H. Scholes, Analyst (London), 93 (1968) 197.
3 J. B. Headridge and J. Richardson Analyst (London), 94 (1969) 968.
4 F. Shaw and J. M. Ottaway, Analyst (London), 99 (1974) 184.
5 J. M. Ottaway and F. Shaw, Anal. Chim. Acta, 99 (1978) 217.
6 S. Christensen, At. Abs. Newsl., 11 (1972) 51.
7 J. H. Cragin and M. M. Herron, At. Abs. Newsl., 12 (1973) 37.
8 A. R. Knott, At. Absorpt. Newsl., 14 (1975) 126.

9 J. Alvarado, Ph.D. Thesis, University of Strathclyde, 1982.
10 J. M. Ottaway, R. C. Hutton, D. Littlejohn and F. Shaw, Wiss Z. Karl-Marx-Univ. Leipzig, 28 (1979) 357.
11 M. S. Epstein, T. C. Rains and T. C. O'Haver, Appl. Spectrosc., 30 (1976) 324.
12 L. Bezur, J. Marshall and J. M. Ottaway, Spectrochim. Acta, Part B, (1984) in press.
13 J. M. Ottaway and F. Shaw, Analyst (London), 100 (1975) 438.
14 R. C. Hutton, J. M. Ottaway, T. C. Rains and M. S. Epstein, Analyst (London), 102 (1977) 429.
15 L. Ebdon, R. C. Hutton and J. M. Ottaway, Anal. Chim. Acta, 96 (1978) 63.
16 W. Slavin, G. R. Carnick, D. Manning and E. Pruszkowska, At. Spectrosc., 4 (1983) 69.
17 J. M. Ottaway, L. Bezur and J. Marshall, Analyst (London), 105 (1980) 1130.
18 L. Bezur, J. Marshall, J. M. Ottaway and R. Fakhrul-Aldeen, Analyst (London), 108 (1983) 553.
19 J. Marshall, L. Bezur, F. Fakhrul-Aldeen and J. M. Ottaway, Anal. Proc., 17 (1980) 10.
20 W. Frech and A. Cedergren, Anal. Chim. Acta, 82 (1976) 83.
21 W. Frech and A. Cedergren, Anal. Chim. Acta, 82 (1976) 93.

Analytica Chimica Acta, 161 (1984) 275—283
Elsevier Science Publishers B.V., Amsterdam — Printed in The Netherlands

A FLOW INJECTION/HYDRIDE GENERATION SYSTEM FOR THE DETERMINATION OF ARSENIC BY INDUCTIVELY-COUPLED PLASMA ATOMIC EMISSION SPECTROMETRY

R. R. LIVERSAGE and J. C. VAN LOON*

Departments of Geology and Chemistry and the Institute for Environmental Studies, University of Toronto, Toronto, M5S 1A1 (Canada)

J. C. DE ANDRADE

Universidade Estadual de Campinas, Instituto de Quimica, C.P. 6154, 13100-Campinas, S.P. (Brazil)

(Received 28th October, 1983)

SUMMARY

A flow-injection system is described for the semi-automatic determination of arsenic (10—1000 $\mu g\ l^{-1}$) by hydride generation and inductively-coupled plasma atomic emission spectrometry. The elements which were found to interfere were Co, Ni, Ag, Au, Bi, Te and Sn. Standard reference materials were analyzed with good accuracy. Approximately 200 injections h^{-1} are possible. The detection limit is 1.4 ng arsenic.

Hydride generation is widely used to obtain good sensitivity in the determination of arsenic by atomic absorption spectrometry (a.a.s.). Direct determination of arsenic by inductively-coupled plasma atomic emission spectrometry (i.c.p.a.e.s.) also suffers from poor sensitivity. There have been several studies of the use of hydride generation with the inductively-coupled plasma for the determination of arsenic [1—9], of which most [1—7] employ a continuous flow system for the generation of arsine. Autosampler equipment has been employed widely in hydride generation procedures for automating these systems.

The recently introduced technique of flow injection analysis (f.i.a.) can be employed to advantage in automatic instrumentation. Only Astrom [10] seems to have employed this approach for hydride generation and he investigated its application to a.a.s. In the following report an arsine generation method is proposed which employs f.i.a. coupled with i.c.p.a.e.s.

EXPERIMENTAL

Apparatus

A schematic diagram of the experimental set-up is shown in Fig. 1. The apparatus consists of an Applied Research Laboratories 34000 Quantometer,

0003-2670/84/$03.00

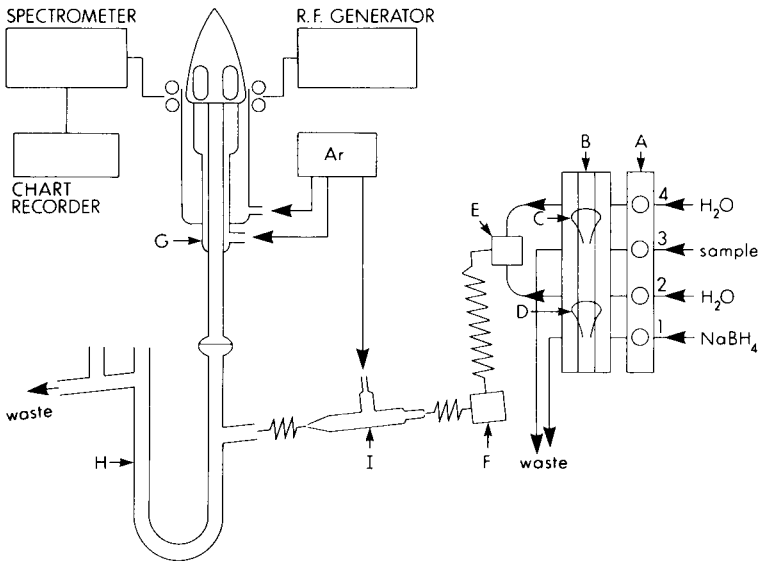

Fig. 1. Block diagram of experimental set-up. Tube lengths: peristaltic pump (A) to injection block (B), 16 cm; (B) to confluence point (E), 5 cm; (E) to mixing point (F), 4 cm; (F) to nebulizer (I), 12 cm; (I) to U-tube (H), 8 cm. (C, D) are the sample and reagent loops, respectively. (G) is the torch.

an Omniscribe 13-5000 chart recorder (Houston Instruments), a PDP-11/03 computer and a Buckler Instruments 4-channel peristaltic pump. The spectrometer has a Pashen-Runge mounting, 1-m focal length, with a 1080 lines mm^{-1} grating blazed at 600 nm (1st order), reciprocal linear dispersion of 0.926 nm mm^{-1} (1st order), a primary slit-width of 20 μm, and a secondary slit-width of 50 μm. The resolving power was 43,200, and the bandpass was 0.023 nm (both 1st order). The r.f. generator was a crystal-controlled type, 27.12 MHz, with a power output of 2.5 kW continuous rating. The plasma torch was an all-quartz Fassel type. Argon was used as coolant, plasma and carrier gas. A pneumatic nebulizer was used.

The flow injection block, made from perspex, is shown in Fig. 2. It consisted of a moveable inner block (A; 75 × 38 × 13 mm) sandwiched between two blocks (B; 75 × 38 × 10 mm), both of which were bolted to the perspex base (C), in adjustable positions. Rubber gaskets between the blocks prevented leakage, and were cemented to the outer blocks. The separation between bores in the blocks was 3 mm; the bores were 1 mm i.d. The separation between the blocks could be altered by adjusting the tension of the spring and bolt assemblies, or by adjusting bolts at the base of the outer blocks. The confluence T-joint (E, Fig. 1) and mixing point (F, Fig. 1) was also made of perspex. The pump tubing was Tygon (3/32 in. i.d.). The polythene tubing used for sample and reagent loops and for all connections from injection to the nebulizer was 0.8 mm i.d. and 1.4 mm o.d. The tubing was

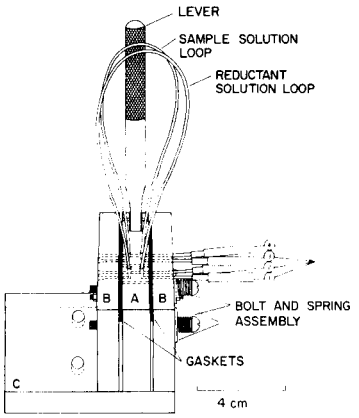

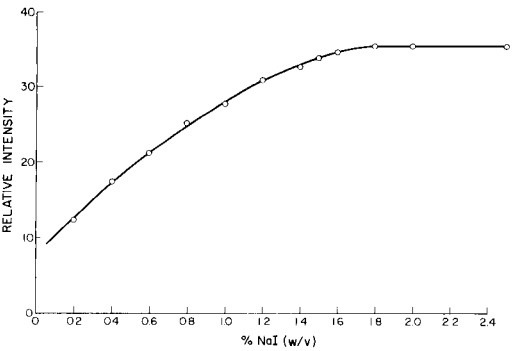

Fig. 2. Injection block. For explanation, see text.

Fig. 3. Effect of NaI concentration on emission intensity (100 μg l^{-1} As).

fitted via h.p.l.c. fittings with teflon reducing ferrules to the confluence and mixing points. The pump tubing was connected to the flow injection block by fitting pieces of concentrically smaller o.d. tubing into the ends of the pump tubing as shown in Fig. 2. The ends of the smallest o.d. tubing (0.8 mm i.d. × 1.4 mm o.d. polyethylene tubing) were fitted to the bores in the block. The large holes in the base (C) were provided so that the block could be bolted to the bench top. The reaction manifold was 20 cm from confluence point to nebulizer. The sample and reagent loops were 0.17 ml in volume.

Reagents

A stock solution (1000 μg ml^{-1}) of arsenic(V) was prepared by weighing 1.3203 g of dried primary standard arsenic(III) oxide into a 100-ml beaker, dissolving in 25 ml of 20% (w/v) sodium hydroxide and neutralizing with 20% (v/v) sulfuric acid to a phenolphthalein end-point. Then 10 ml of concentrated nitric acid, 2 ml of concentrated sulfuric acid and 2 g of potassium peroxodisulfate were added and the solution was heated to white fumes of sulfur trioxide. The cooled solution was transferred to a 1-l volumetric flask and diluted to the mark with distilled water. Working solutions were prepared by appropriate dilution of the stock solution a few hours before use. The reductant solution was prepared by dissolving 0.60 g of reagent-grade sodium tetrahydroborate and a few pellets of reagent-grade sodium hydroxide in 100 ml of distilled water. The sodium hydroxide was added to stabilize the solution.

Procedure

The powdered samples were first oven-dried at 80°C for 2 h and cooled in a desiccator. A 0.5-g sample was accurately weighed into a 100-ml teflon

beaker and 2 ml of concentrated perchloric acid and 10 ml of concentrated nitric acid were added. The covered beakers were heated at 120°C for 2–3 h. The digestion was continued until white fumes of perchloric acid appeared. After cooling, the contents of the beakers were transferred to teflon dishes with several distilled water washes so that the final volume was ca. 25 ml. After addition of 5 ml of concentrated hydrofluoric acid, the dishes were warmed at ca. 80°C for 15 min to remove any siliceous residue. The cooled solutions were transferred to 50-ml plastic volumetric flasks, 7 ml of concentrated hydrochloric acid and 1 g of sodium iodide were added and the solutions were diluted to the mark.

The pump was turned on for a few minutes to fill the U-tube with water before the plasma was ignited. This prevented air from extinguishing the plasma. Sample solutions were then pumped through channel 3 (Fig. 1) and reductant solution was pumped through channel 1, the excess going to waste, while distilled water carrier streams were pumped through channels 2 and 4. The lever on the block was then moved to the injection position, so that sample and reagent were injected into the carrier streams. The transient emission signal was measured at the 189.0-nm emission line, and recorded. Peak heights were measured.

The optimal operating conditions are summarized in Table 1.

RESULTS AND DISCUSSION

Optimization of operating parameters

Various chemical and instrumental operating parameters were studied individually and optimized with respect to the emission intensity of 100 μg l^{-1} arsenic while all the other parameters were at their optimum values.

Hydrochloric acid concentration. Hydrochloric acid was used exclusively in this study. Thompson et al. [1] studied the effect of various acids, including hydrochloric, sulfuric, perchloric, orthophosphoric and hydrobromic acids, on arsenic emission intensity and found that the greatest intensities were obtained from hydrochloric acid solutions. In this study, the emission intensity was found to be independent of hydrochloric acid concentration above ca. 12% (v/v), and to decrease at lower concentrations. Thompson et al. [1] and Nakahara [2] observed similar trends using continuous genera-

TABLE 1

Optimal operating conditions

Incident power	1500 W	$NaBH_4$ conc.	0.6% (w/v) with NaOH added
Reflected power	< 10 W		
Coolant gas pressure	50 psi	HCl conc. in sample	15% (v/v)
Plasma gas pressure	30.5 psi	NaI conc. in sample	2% (w/v)
Carrier gas flow rate	0.76 l min^{-1}	Sample and reagent loop volume	0.17 ml
Pump flow rate	7.3 ml min^{-1} $channel^{-1}$		

tion flow systems with the i.c.p. Both found the intensity to be independent of the acid concentration above 2 M, which is equivalent to 17% v/v.

Sodium iodide concentration. The effect of sodium iodide concentration on the emission intensity is shown in Fig. 3. Sodium iodide was added to the sample solutions to reduce arsenic(V) to arsenic(III). The emission intensity increased with increasing sodium iodide concentration up to 1.8% (w/v), above which the intensity was independent of sodium iodide concentration. Nakahara [2] also studied the effect of sodium iodide concentration, and concluded that arsenic(V) must be reduced prior to hydride generation when sodium tetrahydroborate is used as reductant. In the present study, the preparation of the 1000 μg ml^{-1} stock solution included oxidation of arsenic(III) with peroxodisulfate because arsenic(V) is the more stable state in solution over long periods of time [11]. Nakahara [2] found the intensity to be independent of sodium iodide concentration above 1.5% (w/v), whereas Thompson et al. [3] found the intensity to reach a plateau at ca. 0.05% (w/v) sodium iodide in concentrated hydrochloric acid, which suggests that the concentration of iodide needed to effect complete reduction of arsenic(V) is pH-dependent.

Sodium tetrahydroborate concentration. Figure 4 illustrates the effect of sodium tetrahydroborate concentration on the emission intensity; the intensity was constant at 0.5—0.6% (w/v). When a 0.8% solution was used, the excess of hydrogen evolved extinguished the plasma. Ebdon and Wilkinson [12] and Thompson et al. [1] both observed an optimum sodium tetrahydroborate concentration of 1% (w/v), using continuous generation pump systems with a.a.s. and i.c.p.a.e.s., respectively. However, whereas equivalent volumes of sample and reductant were always used here, Thompson et al. used a sample flow rate of 9.2 ml min^{-1} and a reductant flow rate of 4.5 ml min^{-1}; Ebdon and Wilkinson used a sample flow rate of 7.0 ml min^{-1} and a reductant flow rate of 2.5 ml min^{-1}. Thompson et al. attributed the decrease in intensity at tetrahydroborate concentrations greater than the optimum to dilution of the arsine by the excess of hydrogen produced by the reductant.

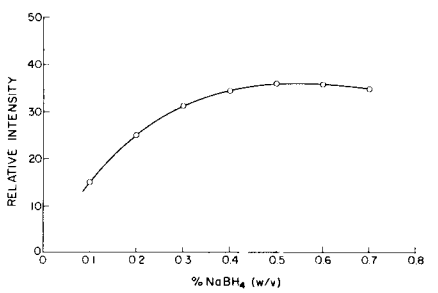

Fig. 4. Effect of sodium tetrahydroborate concentration on emission intensity (100 μg l^{-1} As).

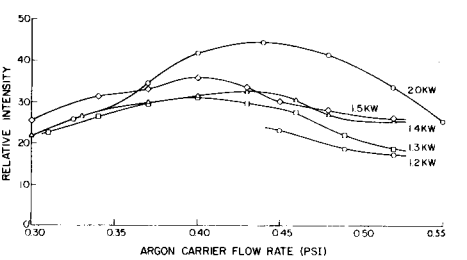

Fig. 5. Effect of argon carrier gas flow rate and r.f. power on emission intensity (100 μg l^{-1} As).

Sample and reductant volumes and solution flow rate. Equivalent sample and reductant volumes were always employed. The emission intensity increased with increasing volume throughout the 0.03 ml of 0.22 ml range studied. As no optimum value or plateau was reached, a compromise had to be made between intensity and consumption of sample and reagent. Sample and reagent loops of 0.17 ml are recommended. The emission intensity increased in a roughly linear fashion with increasing flow rate throughout the 2—11.5 ml min^{-1} per channel range studied. Again, a compromise had to be made between intensity and consumption of sample. A flow rate of 7.3 ml min^{-1} in each channel is recommended.

Argon carrier gas flow rate and r.f. power. The effects of argon carrier gas flow rate and r.f. power on intensity are illustrated in Fig. 5. Argon flow rates were not directly measured; the flow was metered by the nebulizer pressure gauge. Nebulizer pressures between 0.30 and 0.52 psi and r.f. powers between 1.2 and 2.0 kW were investigated. Both the argon carrier flow rate and the r.f. power had a pronounced effect on the emission intensity (Fig. 5). Generally, the intensity increased with increasing r.f. power throughout the range studied. As expected, the plasma was more stable at the higher powers; at 1.2 kW the plasma could not be maintained at or below a nebulizer pressure of 0.45 psi. Thompson et al. [1] attributed poor plasma stability at low r.f. powers to the introduction of the hydrogen produced as a by-product into the torch; with a Fassel torch and an r.f. power of 2.7 kW, the plasma could not be maintained at hydrogen flow rates exceeding 150 ml min^{-1}. However, Ikeda et al. [4], who also used a Fassel torch, found that the plasma became unstable and extinguished at hydrogen flows exceeding 750 min ml^{-1}, regardless of the r.f. power between 1.2 and 2.0 kW. Both groups used continuous generation flow systems.

As the r.f. power is increased, the temperature of the plasma increases, so that the plasma and coolant argon flow rates must be increased to prevent the torch melting. Although the greatest intensity was observed at 2.0 kW, in order to conserve argon, a power of 1.5 kW and an optimum nebulizer pressure of 0.40 psi were preferred. For the nebulizer used, a pressure of 0.40 psi corresponded to a carrier flow rate of 0.76 l min^{-1}. Other workers have reported an optimum argon flow rate of 0.8 l min^{-1} at an r.f. power of 2.7 kW [1] and an optimum flow rate of 1.0 l min^{-1} at an r.f. power of 1.2 kW [4]. However, as Berman and McLaren [13] pointed out, the performance varies from one nebulizer to another, so that the carrier flow rate should be optimized for each given nebulizer system. Also, because the argon carrier gas flow rate has such a pronounced effect on emission intensity, a constant flow must be maintained to ensure reproducibility and accuracy of results.

Interferences

Very comprehensive interference studies were reported by Thompson et al. [3], Nakahara [2] and Peacock and Singh [14]. The elements that were found not to interfere were Al, B, Ba, Be, Ca, Ce, Cd, Cr(III), Cs, Ce, Hg, In, K, La, Li, Mg, Mn, Mo, Na, Nb, P, Pb, Rb, Sb, Si, Sn, Sr, Ta, Th, Ti, Tl and

Zr. Platinum and gold were found to interfere [2, 14], with regard to other elements investigated (Co, Ni, Cu, Ag, Fe, Ga, W, V, Pd, Zn, Cr(VI), Bi, Se and Te), there was no complete agreement between these investigators. Only Nakahara [2] reported interference by some of the other hydride-forming elements (Se, Bi and Te).

Nakahara [2] suggested that most interferences result from reduction of the interfering element by tetrahydroborate; these elements included the hydride-forming elements and the elements of periodic Groups IB, IIB and VIII. The addition of 2% sodium iodide eliminated the interference of Bi, Cr(VI), Cu, Fe, Ga, Se, W and V. In the procedure of Peacock and Singh, [14] sodium tetrahydroborate solution was injected into a reaction vessel containing the sample solution, and the signal was integrated for 16 s from the start of injection. Thus, whereas chromium(VI) was found to interfere by Thompson et al. [3] and Nakahara [2], who measured steady-state signals, Peacock and Singh [14] found that while the evolution of arsine was retarded somewhat, the integrated signal indicated complete recovery of arsenic, which suggests that interference is probably due to competition for the reductant. However, Peacock and Singh [14] also observed interferences from Co, Ni, Pt, Cu, Ag and Au, which probably resulted from formation of stable complexes with arsenic species.

Ions found earlier [2, 3, 14] to interfere and other hydride-forming elements (Sb, Bi, Te, Sn and Se) were studied again under the recommended conditions. Interference was considered to have occurred when the emission intensity differed by >5% from that obtained for 100 μg l^{-1} arsenic alone. The results are shown in Table 2. The elements that were found to interfere were Ni, Ag, Au, Bi, Te and Sn.

TABLE 2

Effect of foreign ions on emission intensity of 100 μg l^{-1} arsenic (15% HCl, 2% KI)

Ion	Conc. (μg l^{-1})	Relative intensity	Ion[a]	Relative intensity
Sb(V)	100	1.0	Cu(II)	1.0
	500	1.0	Ni(II)	0.61
Bi(III)	100	0.71	Ag(I)[b]	0.74
	500	0.74	W(VI)[b]	1.0
Te(VI)	100	1.0	Fe(III)	1.0
	500	0.82	Au(III)	0.47
Sn(II)	100	1.0	Cr(III)	1.0
	500	0.72	V(V)	1.0
Se(IV)	100	1.0	Co(II)	0.60
	500	1.0		

[a] All at 50 mg l^{-1}. [b] Precipitated out.

Determination of arsenic in standard samples

National Research Council of Canada (NRCC) and NBS standard reference materials, listed in Table 3, were digested and analysed in triplicate by the proposed procedure. The results are shown in Table 3. All the values obtained fall within the certified limits.

When the digestion procedure was repeated with the hydrofluoric acid treatment omitted, the values obtained were noticeably lower than those given in Table 3, although still within the certified limits. Previous workers [15, 16] have concluded that a simple nitric-perchloric acid digestion does not completely decompose clay, feldspar, quartz and basalt, as evidenced by the low recoveries of arsenic. The hydrofluoric acid step is necessary to liberate arsenic trapped in the silicate lattice [15]. The sample should not be heated strongly or evaporated after the hydrofluoric acid has been added.

Strong oxidizing agents such as nitric acid, permanganate and peroxodisulfate, which are often used in the digestion of biological and geological samples [15—18], must be removed prior to addition of iodide. In this study, digested standards from which the nitric acid had not been evaporated reacted violently with sodium iodide or tetrahydroborate, and produced much lower intensities.

Calibration, detection limit and precision

The standard solutions used were prepared by appropriate dilution of the 1000 μg ml^{-1} stock solution. All solutions, including the blank, contained 15% hydrochloric acid and 2% sodium iodide. The calibration graph was linear over the range 0.01—1 mg l^{-1} arsenic under the recommended conditions. The detection limit was evaluated by calculating the mean standard deviation of 5 sets of replicate blank determinations, measured on different occasions. The detection limit (2 × std. dev.) was 1.4 ng for 0.17-ml sample volumes. The relative standard deviation obtained from 10 replication determinations of 100 μg l^{-1} arsenic was 7.2%.

TABLE 3

Analysis of standard reference materials

Sample	Arsenic content (μg g^{-1})	
	Certified	Measured
NBS Orchard leaves	10 ± 2	9.8, 10.1, 10.0
NBS Coal fly ash	145 ± 15	141, 142, 139,
NBS River sediment	66[a]	64, 64, 66,
NRCC Mess-1	10.6 ± 1.2	10.4, 10.7, 10.7,
NRCC Bess-1	11.1 ± 1.4	11.6, 12.0, 12.1

[a]Not certified.

This work was supported by a grant from the National Sciences and Engineering Council of Canada. The paper was presented at the 23rd Colloquium Spectroscopicum, Amsterdam, May, 1983.

REFERENCES

1 M. Thompson, B. Pahlavanpour, S. J. Walton and G. F. Kirkbright, Analyst (London), 103 (1978) 568.
2 T. Nakahara, Anal. Chim. Acta, 131 (1981) 73.
3 M. Thompson, B. Pahlavanpour, S. J. Walton and G. F. Kirkbright, Analyst (London), 103 (1978) 705.
4 M. Ikeda, J. Nishibe, S. Hamada and R. Tujino, Anal. Chim. Acta, 125 (1981) 109.
5 P. D. Goulden, D. H. Anthony and K. A. Austen, Anal. Chem., 53 (1981) 2027.
6 S. Steig and A. Denis, Anal. Chem., 54 (1982) 606.
7 B. Pahlovanpour, M. Thompson and L. Thorne, Analyst (London), 106 (1981) 467.
8 C. J. Pickford, Analyst (London), 106 (1981) 464.
9 M. H. Hahn, K. A. Wolnik, F. L. Fricke and J. A. Caruso, Anal. Chem., 54 (1982) 1048.
10 O. Astrom, Anal. Chem., 54 (1982) 190.
11 J. C. Van Loon, Analytical Atomic Absorption Spectroscopy: Selected Methods, Academic Press, Toronto, 1980, p. 132.
12 L. Ebdon and J. R. Wilkinson, Anal. Chim. Acta, 136 (1982) 191.
13 S. S. Berman and J. W. McLaren, Appl. Spectrosc., 32(4) (1978) 372.
14 C. J. Peacock and S. C. Singh, Analyst (London), 106 (1981) 931.
15 H. Agemian and E. Bedek, Anal. Chim. Acta, 119 (1980) 323.
16 S. Terashima, Anal. Chim. Acta, 86 (1976) 43.
17 W. B. Robbins and J. A. Caruso, Analyst (London), 104 (1979) 35.
18 H. Agemian and R. Thomson, Analyst (London), 105 (1980) 902.

Analytica Chimica Acta, 161 (1984) 285—291
Elsevier Science Publishers B.V., Amsterdam — Printed in The Netherlands

DETERMINATION OF TRACE IMPURITIES IN HIGH-PURITY ALUMINUM OXIDE BY INDUCTIVELY-COUPLED PLASMA ATOMIC EMISSION SPECTROMETRY

T. ISHIZUKA*, Y. UWAMINO and A. TSUGE

Government Industrial Research Institute, Nagoya Hirate-cho, Kita-ku, Nagoya 462 (Japan)

T. KAMIYANAGI

Taimei Chemical Industry Co., Ltd., Minami-Minowamura, Kami-Inagun, Nagano Prefecture 399-45 (Japan)

(Received 3rd January 1984)

SUMMARY

Trace impurities (Ca, Cu, Fe, Mg, Mn, Na and Si) in 99.99% aluminum oxide were determined by inductively-coupled plasma atomic emission spectrometry (i.c.p./a.e.s.). The sample was fused with lithium carbonate/boric acid to determine Ca, Cu, Mg, Mn, Na and Si or dissolved in phosphoric/sulphuric acids to determine iron. Matrix effects on the calibration graphs for each element were studied: for accurate determinations, calibration solutions must contain lithium and boric acid (or aluminum and phosphoric and sulfuric acids for iron).

Recently, high-purity aluminum oxide has been increasingly used as a translucent ceramic material, and as an electronic substrate. Impurities associated with the alumina raw material significantly affect the resultant microstructure, and thus the quality of the products. Therefore, the determination of impurities in aluminum oxide is very important. This has been achieved by atomic absorption spectrometry (a.a.s.) [1—4], flame emission spectrometry [5], emission spectrography [6—9], inductively-coupled plasma-atomic emission spectrometry (i.c.p./a.e.s.) [10], x-ray fluorescence spectrometry (x.r.f.) [11], neutron activation [12], etc. Neutron activation analysis is a highly sensitive method for most of elements, but cannot easily be used; a.a.s., f.e.s., e.s. and x.r.f. and the emission methods without the i.c.p. are not always best for some of most important trace impurities (e.g., Si, Mg and Ca) in high-purity aluminum oxide. Inductively-coupled plasma atomic emission spectrometry is excellent for the determination of trace elements in various samples, and more sensitive for the above elements than most other methods.

In this paper, an i.c.p./a.e.s. method is described for the determination of trace impurities in high purity (99.99%) aluminum oxide. Prior to the measurement, fusion with lithium carbonate/boric acid or dissolution in

0003-2670/84/$03.00

phosphoric acid and sulfuric acid were used for the determination of Ca, Cu, Mg, Mn, Na and Si, or of iron, respectively.

EXPERIMENTAL

Apparatus and reagents

A Nippon Jarrell-Ash Model ICAP-1000S spectrometer with an i.c.p. source was used, as described elsewhere [13]. Sample solution was introduced into a crossflow nebulizer with a peristaltic pump (Atto SJ-1211). Table 1 summarizes the operating conditions and the analytical lines used for the determination of each element studied. An electric furnace (Thermolyne 10500) was used to fuse aluminum oxide samples. An atomic absorption spectrometer (Varian Techtron AA-275) was also used to determine sodium.

Standard solutions for each element (1 mg ml^{-1}) were prepared from reagent-grade chemicals (Wako Pure Chemicals). Lithium carbonate and boric acid (Suprapur, Merck) were used to fuse aluminum oxide samples. Nitric acid (super special grade, Wako Pure Chemicals) was used to dissolve the fused samples. Phosphoric acid (Suprapur, Merck) and sulfuric acid (super special grade, Wako Pure Chemicals) were used to dissolve the alumina samples. Aluminum chloride (Johnson Matthey JMC-346, 99.9995%) was used as the aluminum matrix.

Procedure

An accurately weighed aluminum oxide sample (1 g) was thoroughly mixed with 2 g of lithium carbonate and 1 g of boric acid in a platinum crucible. The crucible was maintained at 500°C in the electric furnace for 30 min; the furnace temperature was raised to 1000°C to fuse the sample for 30 min. The crucible was removed from the furnace, cooled in air, and heated gently with 100 ml of 7.5% nitric acid in a teflon beaker until the fused sample was dissolved. The sample solution was completely transferred to a 250-ml polypropylene volumetric flask and diluted to volume with distilled water. This solution was nebulized for Ca, Cu, Mg, Mn, Na and Si.

A platinum crucible contains a very small amount of iron as impurity [14], which will be liable to transfer into the sample during fusion. There-

TABLE 1

Operating conditions and analytical lines

R.f. power	1.2 kW	Sample uptake rate	1.8 ml min^{-1}
Carrier gas flow rate	0.5 l Ar min^{-1}	Signal measurement	10 s integration
Coolant gas flow rate	14 l Ar min^{-1}	Analytical line	Ca II 393.37 nm;
Plasma gas flow rate	1 l Ar min^{-1}		Cu I 324.75 nm;
Observation height	15 mm above load coil		Fe II 238.20 nm;
Slit widths	Entrance, 30 μm; exit, 50 μm		Mg II 279.55 nm;
Slit height	3 mm		Mn II 257.61 nm;
			Na I 589.59 nm;
			Si I 251.61 nm

fore, fusion in a platinum crucible is unsuitable for the determination of iron in 99.99% aluminum oxide. When 99.999% aluminum oxide samples (Spex) were fused in platinum crucibles, 20—50 μg of iron was extracted from each crucible. Thus, iron was determined in solutions obtained by dissolving aluminum oxide in a phosphoric/sulfuric acid mixture.

An accurately weighed aluminum oxide sample (0.4 g) was placed in a quartz beaker and 5 ml of concentrated phosphoric acid and 6 ml of concentrated sulfuric acid were added. The covered beaker was heated on a hot plate (Corning PC-100) at about 300°C for 15—30 min until the sample had dissolved. After cooling, the sample solution was transferred to a 100-ml volumetric flask, diluted to volume with distilled water, and nebulized for iron measurement.

RESULTS AND DISCUSSION

Matrix effects

In the lithium carbonate/boric acid fusion system, the sample solution introduced into the i.c.p. contained 0.15% lithium, 0.40% boric acid and 0.21% aluminum in 3% nitric acid. In the phosphoric acid/sulfuric acid system, the matrix components in the sample solution were 0.21% aluminum, 4% phosphoric acid and 6% sulfuric acid. The presence of these matrices affects the emission signals of the elements to be determined [15, 16]. Matrix effects in both systems were studied by constructing calibration graphs for the 7 elements in each of several matrix solutions.

Figure 1 shows the matrix effects on the calibration graphs for calcium and silicon in the lithium carbonate/boric acid system. The blank solution

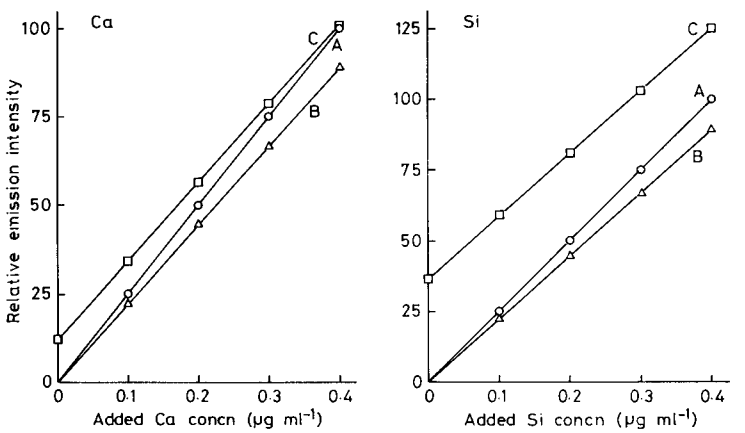

Fig. 1. Matrix effects on calibration graphs for calcium and silicon. (A) 3% nitric acid; (B) 0.15% lithium/0.40% boric acid in 3% nitric acid; (C) solution prepared according to the fusion procedure for aluminum oxide samples (contains 0.21% Al).

(matrix only) contained ca. 30 ng Ca ml^{-1}. Thus the graphs for calcium in the fusion matrix (Fig. 1B, C) are corrected for this calcium contamination. The graphs for both elements in the fusion matrix had a smaller slope than those in nitric acid alone; the addition of aluminum to the fusion mixture had almost no effect. The matrix effects on Cu, Mg, Mn and Na were similar to those on Ca and Si. The intensities for Ca, Cu, Mg, Mn, and Si (0.4 $\mu g\ ml^{-1}$) and sodium (1 $\mu g\ ml^{-1}$) were decreased by 11%, 14%, 10%, 10%, 11% and 15%, respectively. The decrease must be caused by a lowering of nebulization efficiency, and may be minimized by applying an internal standard. However, an internal standard was not used here.

Figure 2 shows the matrix effects on the calibration graph for iron in phosphoric/sulfuric acid. The mixed acids decreased the slope, as did the presence of aluminum. The emission intensity of iron (0.4 $\mu g\ ml^{-1}$) in the mixed acids was 15% less than in nitric acid, and that in the presence of aluminum and mixed acids was 20% less. This change is also probably caused by a change in nebulization efficiency.

In determinations of trace elements by i.c.p./a.e.s., the problem of changes in background induced by matrix components must be considered [17]. In the fusion system, the presence of lithium and boric acid affected background intensities in the vicinities of each analyte line, raising the background levels by 15%, compared to a nitric acid solution for all elements studied. Aluminum had no effect. In the mixed acids system, the presence of 4% phosphoric acid and 6% sulfuric acid raised the background signal by ca. 50% in the vicinity of Fe II 238.20 nm; solutions containing aluminum as well as these acids raised the background signal by ca. 60%. The back-

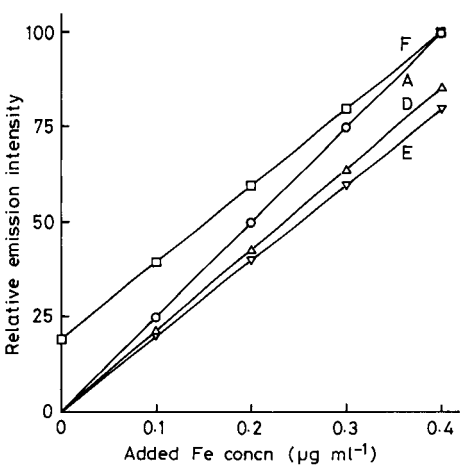

Fig. 2. Matrix effects on calibration graph for iron: (A) 3% nitric acid; (D) 4% phosphoric acid/6% sulfuric acid; (E) solution prepared by dissolving aluminum chloride corresponding to 0.21% Al in solution D; (F) solution prepared according to the dissolution procedure for aluminum oxide in phosphoric and sulfuric acids.

ground shifts are thought to be due to continuum emission from ion-electron recombinations.

From these results, the calibration graphs constructed from results obtained from solutions containing 0.15% lithium and 0.40% boric acid as matrices in 3% nitric acid can be used to determine Ca, Cu, Mg, Mn, Na and Si in aluminum oxide. To determine iron accurately, calibration must be done with solutions containing 0.21% aluminum in 4% phosphoric acid/6% sulfuric acid.

Detection limits

Detection limits of the elements studied were determined from solutions containing the matrix components mentioned above. A signal integration method (10 s) was used to obtain detection limits as low as possible. Table 2 shows the values obtained. The detection limit was defined as the concentration which gave a net signal equal to three times the standard deviation of the background level. Detection limits for each element in solutions containing the matrix components were somewhat higher than those in 3% nitric acid.

Although lithium carbonate, and boric, nitric, phosphoric and sulfuric acids of especially high purity were used, these reagents contained traces of various impurities. Calcium and magnesium were clearly detected in the blank solution from the lithium carbonate/boric acid fusion; the concentrations were 30 ng Ca ml^{-1} and 3 ng Mg ml^{-1}. The presence of these impurities raised the detection limits in aluminum oxide, as shown in Table 2.

Calibration and precision

Prior to the analyses of aluminum oxide samples, calibration graphs for the 7 elements were constructed in the concentration ranges shown in Table 3. Two series of solutions containing 0.15% lithium and 0.40% boric

TABLE 2

Detection limits

Element	In solution (ng ml^{-1})		In Al_2O_3 ($\mu g\ g^{-1}$)[a]
	3% HNO_3	0.15% Li/0.40% H_3BO_3	
Ca	0.3	0.4(2[b])	0.1(0.5[b])
Cu	5	6	2
Fe	4	6[c]	2
Mg	0.2	0.3(0.4[b])	0.08(0.1[b])
Mn	0.7	0.9	0.2
Na	50	60	15
Si	9	10	3

[a] 250 × solution value. [b] Determined by considering the variation reagent blanks. [c] In a solution containing 0.21% aluminum in 4% phosphoric acid/6% sulfuric acid.

TABLE 3

Concentration ranges and precision for calibration

Element	Range (μg ml^{-1})	R.s.d. (%)[a]	Element	Range (μg ml^{-1})	R.s.d. (%)[a]
Ca	0—0.3	0.5—2.3	Mn	0—0.3	0.6—2.5
Cu	0—0.3	0.9—2.0	Na	0—1.0	2.7—4.7
Fe	0—0.3	0.8—2.8	Si	0—0.3	1.3—2.3
Mg	0—0.3	1.0—2.6			

[a]5 measurements at each concentration.

TABLE 4

Results (μg ml^{-1}) for aluminum oxide samples

Element	Sample A[a]	Sample B[a]	Sample C[a]
Ca	1.6 ± 0.6(1.9)	1.3 ± 0.5(1.1)	2.8 ± 0.8(2.6)
Cu	7.2 ± 0.7(6.8)	6.5 ± 0.5(5.9)	5.7 ± 0.8(6.1)
Fe	19 ± 2(17)	18 ± 1(20)	17 ± 1(16)
Mg	5.9 ± 0.8(6.3)	4.1 ± 0.3(3.8)	5.1 ± 0.1(5.6)
Mn	0.8 ± 0.2(0.7)	0.9 ± 0.2(0.9)	0.4 ± 0.1(0.6)
Na	<15(11)	<15(13)	19 ± 5(23)
Si	33 ± 1(32)	46 ± 2(49)	35 ± 3(33)

[a]Mean ± standard deviation (5 determinations); values in parentheses were obtained by standard addition and i.c.p./a.e.s. for Ca, Cu, Fe, Mg, Mn and Si, or a.a.s. for Na.

acid in 3% nitric acid were used to calibrate for Ca, Cu, Mg, Mn and Na, and for silicon. A series of solutions containing 0.21% aluminum in 4% phosphoric acid/6% sulfuric acid was used to calibrate for iron. Each calibration graph was linear over the concentration range given. For calibration, solutions of each concentration were measured five times; the precision of the measurements is shown in Table 3.

Analysis of aluminum oxide samples

The 7 trace impurities in 99.99% aluminum oxide samples were determined by using the recommended procedures. Table 4 shows the results. It also shows the values obtained by a standard addition method, with i.c.p./a.e.s. for Ca, Cu, Fe, Mg, Mn and Si, and with a.a.s. for sodium. As the sensitivity for sodium by i.c.p./a.e.s. was not good, it was not possible to determine sodium in samples A and B, and a.a.s. was necessary. The values obtained in this way agreed well with those obtained directly by i.c.p./a.e.s. It was impossible to obtain standard high-purity alumina samples with known impurity composition, so that the accuracy of this method was not judged further.

REFERENCES

1 P. N. W. Young, Analyst (London), 99 (1974) 588.
2 I. Havezov and B. Tamnev, Fresenius Z. Anal. Chem., 290 (1978) 299.
3 T. Kántor, L. Bezúr and E. Pungor, Mikrochim. Acta, (I) (1981) 289.
4 Z. Slovák and B. Dočekal, Anal. Chim. Acta, 129 (1981) 263.
5 F. Yamauchi and Y. Otaka, Bunseki Kagaku, 17 (1969) 1384.
6 E. B. Owens, Appl. Spectrosc., 16 (1962) 86.
7 P. E. Lemieux, Appl. Spectrosc., 17 (1963) 153.
8 G. A. Pevtsov, V. Z. Krasil'shchik and A. F. Yakovleva, Zavod. Lab., 35 (1969) 1340.
9 W. A. Bettison, J. Br. Ceram. Soc., 5 (1968) 173.
10 W. Zamechek, R. T. Lewsadowski, R. G. Parkhurst and A. J. Elgren, in R. M. Barnes (Ed.), Applications of Inductively Coupled Plasmas to Emission Spectroscopy, Franklin Institute Press, Philadelphia, PA, 1978, p. 169.
11 H. Bennett, G. J. Oliver and M. Holmes, Trans. J. Br. Ceram. Soc., 76 (1977) 11.
12 J. Vučina, V. Šćepanović and R. Drašković, J. Radioanal. Chem., 44 (1978) 371.
13 T. Ishizuka, K. Nakajima and H. Sunahara, Anal. Chim. Acta, 121 (1980) 197.
14 I. M. Kolthoff, E. B. Sandell, E. J. Meehan and S. Bruckenstein, Quantitative Chemical Analysis, 4th edn. (Japanese), Hirokawa Publishing Co., Tokyo, 1975.
15 J. H. Kalivas and B. R. Kowalski, Anal. Chem., 53 (1981) 2207.
16 G. J. Schmidt and W. Slavin, Anal. Chem., 54 (1982) 2491.
17 G. F. Larson and V. A. Fassel, Appl. Spectrosc., 33 (1979) 592.

Analytica Chimica Acta, 161 (1984) 293—302
Elsevier Science Publishers B.V., Amsterdam — Printed in The Netherlands

POTENTIOMETRIC STRIPPING ANALYSIS FOR MANGANESE(II) IN NATURAL WATERS

HELÉN ESKILSSON* and DAVID R. TURNER[a]

Department of Analytical and Marine Chemistry, Chalmers University of Technology and University of Göteborg, S-41296 Göteborg (Sweden)

(Received 10th January 1984)

SUMMARY

Potentiometric stripping analysis (p.s.a.) methods for the measurement of manganese(II) in natural waters are described; batch and flow approaches are discussed. The more versatile flow p.s.a. technique is suitable for concentrations in the range 2 nM—30 μM. Application of these techniques is illustrated by measurements in a variety of natural waters. Interferences arising from manganese—copper interactions in the mercury electrode can be suppressed by the addition of zinc or gallium depending on the concentration of the interfering copper. The relative merits of the batch and flow p.s.a. techniques are discussed.

The redox chemistry of manganese in natural waters is of particular importance because it is one of the more abundant redox-active trace elements and because of the slow oxidation kinetics of the thermodynamically unstable manganese(II) oxidation state in oxic waters [1]. Electrochemical techniques provide the best means of measuring manganese(II) in the presence of other oxidation states, and polarographic methods have been used to measure Mn(II) in both lacustrine [2, 3] and estuarine [4, 5] waters. The latter work showed that in some circumstances Mn(II) constituted only a small fraction of the total "dissolved" manganese, i.e., that passing a filter. These investigations were however hampered by the lack of sensitivity of direct polarography, which resulted in a practical detection limit of 0.2 μM. More recently O'Halloran [6] has shown that anodic stripping voltammetry can be used to measure low levels of Mn(II) in ocean waters (>0.2 nM), and reported linear response to added spikes up to a concentration of 0.2 μM.

This paper is concerned with the application of flow potentiometric stripping analysis (p.s.a.) to the determination of Mn(II) in natural waters in the concentration range 2 nM—30 μM, and the determination of total dissolved manganese following pretreatment with hydroxylamine.

---

[a]Permanent address: Marine Biological Association, Citadel Hill, Plymouth PL1 2PB, England.

0003-2670/84/$03.00

EXPERIMENTAL

Instrumentation, cells and reagents

The p.s.a. measurement system, consisting of a Radiometer ISS-820 ion scanning system and a purpose-built laboratory microcomputer system, has been described previously [7—9]. A block diagram of the system used for flow measurements is shown in Fig. 1, and the flow cell is shown in detail in Fig. 2. An Altex 6-way valve was used for switching between different solutions, and suction was provided by a Gilson Minipuls-2 peristaltic pump using 1.14-mm diameter tubing, giving a maximum flow rate of 3 ml min^{-1}. All connections were made with 1-mm diameter teflon tubing. Batch measurements were done in a conventional beaker cell with an off-centre rotating glassy carbon electrode (2-mm diameter) with rotation speeds variable in the range 0—2000 rpm. The counter electrode was separated from the sample solution by a salt bridge in order to prevent oxidizing species produced at the counter electrode from diffusing into the sample. Saturated

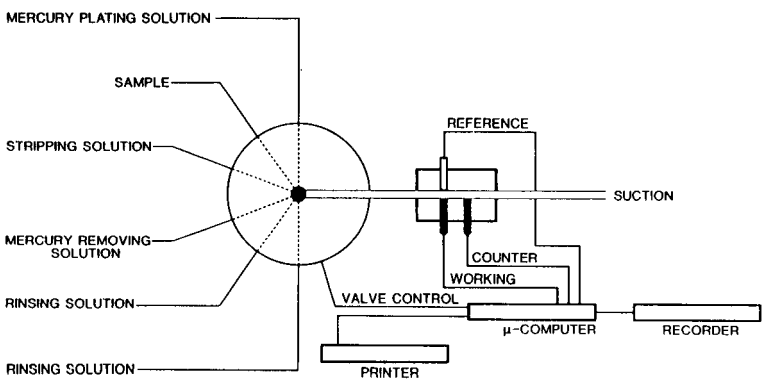

Fig. 1. Block diagram of the p.s.a. flow system.

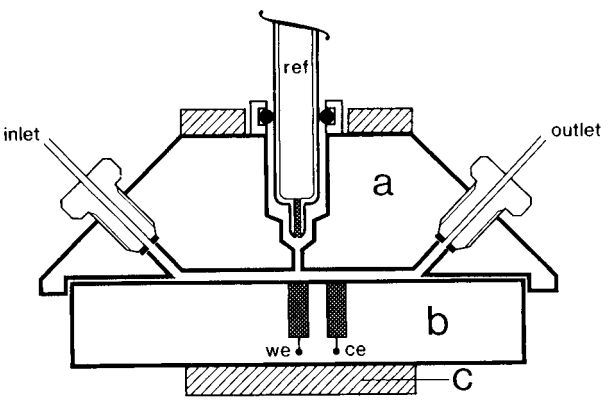

Fig. 2. P.s.a. flow cell: (a) perspex block with reference electrode compartment and 1-mm flow channel; (b) teflon block containing glassy carbon working (we) and counter (ce) electrodes; (c) clamp to hold cell together.

calomel reference electrodes were used throughout, and all potentials are referred to this electrode. The glassy carbon electrodes were polished with 1-μm diamond paste and rinsed with ethanol before use.

All solutions were prepared from analytical-grade reagents. Saturated calcium bromide solution was electrolysed at a mercury pool electrode (—1.5 V, minimum 6 h) in order to remove trace metal impurities.

Procedures

General method. Flow measurements were done according to the sequence shown in Table 1. The entire procedure was controlled by the microcomputer system except for changes in the flow rate and the change in potential from —1.0 to —1.7 V, both of which were controlled manually. Sample deposition times varied from 5 s to 440 s depending on the concentration of manganese being measured. The use of saturated calcium bromide as the stripping solution allows a very slow stripping rate because the solubility of oxygen, the usual stripping oxidant, is very low in this medium (Fig. 3). The iodine/iodide solution removed the mercury film cleanly after each measurement by mild chemical oxidation.

Batch measurements followed a similar sequence, although a greater degree of manual manipulation was required. The mercury film electrode was preplated in a mercury solution of the composition shown in Table 1 (plating time 60 s, electrode rotation speed 2000 rpm). The mercury solution was then replaced with the sample (2—25 ml), spiked with 75 μM Hg(II) to act as the oxidant during the stripping process. In some of the measurements, oxygen was removed by bubbling with argon for 10 min. Manganese was accumulated at —1.8 V for 2, 4 or 8 min, depending on the manganese concentration, at a rotation speed of 2000 rpm; 30 s before the end of this

TABLE 1

Sequence of solutions passing through the flow cell

Solution	Duration (s)	E (v)	Flow rate (ml min^{-1})	Remarks
1 mM Hg(II) pH 2	30—45	—1.0	3	Plating Hg film
Sample	5—440	—1.7	3	Mn accumulation
Saturated	10	—1.7	0.3—3[a]	
$CaBr_2$	Variable[b]	None	0.3—3[a]	Stripping curve recorded
	2.5	—1.7	0.3—3[a]	Background accumulation
	Variable[b]	None	0.3—3[a]	Background stripping
0.5 mM I_2/1 M KI	>30 s	None	10	Mercury film removal
40 mM $Na_2S_2O_3$ in 50% ethanol	Until next measurement	None		Rinsing solution

[a]Flow rates faster than 10% were used when high Mn concentrations were measured.
[b]Dependent on length of stripping curve.

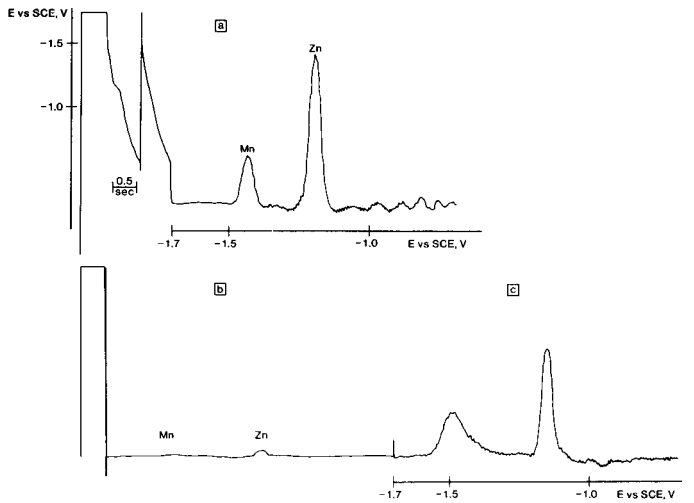

Fig. 3. P.s.a. curves (E vs. time and dt/dE vs. E) obtained from a sample of 0.5 M calcium chloride containing 0.9 μM Mn(II) and 0.8 μM Zn(II). The sample is buffered to pH 9 with ammonia/ammonium chloride. (a) Deposition time 5 s, stripping in saturated calcium bromide, maximum flow rate (3 ml min^{-1}); (b) deposition time 15 s, stripping in sample, maximum flow rate; (c) same as in (b) but the output signal is enlarged 20 times.

accumulation time, the rotation speed was reduced to 100 rpm in order to achieve a slow stripping rate. Recording of the stripping curve and background followed the automated sequence shown in Table 1. The mercury film was removed by wiping with a tissue after each measurement.

Interferences. The major interference in the manganese measurement arises from the formation of an intermetallic compound with copper in the amalgam [6]. This type of interference can be suppressed by the addition of a third element which preferentially forms an intermetallic compound with copper [10]. Although in many natural waters the copper concentration is relatively low so that the natural level of zinc may be sufficient to act as the third element, it has been shown that interferences in a.s.v. from up to 0.3 μM copper(II) can be effectively suppressed by the addition of 0.15–0.3 μM zinc(II) [6]. This approach was adopted in this work where appropriate.

Measurement of metal concentrations. Stripping curves were stored and manipulated in the microcomputer as counts vs. potential curves, i.e., dt/dE vs. E [7], thus giving a peak for each metal stripped (Fig. 4). In all cases, the background curve was first subtracted from the stripping curve, giving an approximately level baseline. The limits of each peak were then either entered manually into the microcomputer or determined by a search program based on a derivative [9]. Peak areas were determined by the microcomputer with reference to a linear baseline drawn between the filtered values of dt/dE at the two peak limits. The resulting peak area was converted

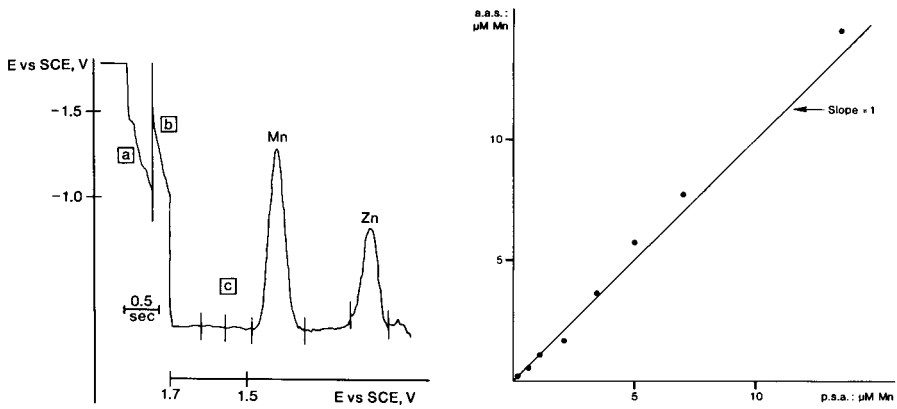

Fig. 4. P.s.a. stripping curves for 2.7 μM Mn in 0.5 M calcium chloride: (a) primary potential-time stripping curve; (b) background stripping curve; (c) counts vs. potential curve. Peak limits are marked by vertical lines.

Fig. 5. Comparison between results obtained for total manganese in sea-water samples by potentiometric stripping analysis (p.s.a.) and atomic absorption spectrometry (a.a.s.).

to a concentration either by using a calibration graph or by standard addition.

Atomic absorption spectrometry (a.a.s.). Certain samples were also analysed for manganese by a.a.s. for comparison with p.s.a. For these measurements, a Perkin-Elmer 4000 spectrometer was used with a HGA-400 heated graphite atomiser. The two techniques showed good agreement for total manganese levels (Fig. 5).

RESULTS

Batch measurements

The method was tested on manganese-free sea water under the following conditions: deposition for 8 min and additions of 0.15 μM zinc(II) (to suppress copper interference) and 75 μM mercury(II) (to act as stripping oxidant) to the sample; the samples were deoxygenated before measurement. Linear response was obtained for additions of 3.6—14.6 nM Mn, with relative standard deviations on 4 measurements ranging from 11% to 3%, respectively. The detection limit under these conditions is estimated as 1.3 nM on the basis of 3× standard deviation. Proportionately higher detection limits are obtained at shorter deposition times. Linear response was obtained only up to a concentration of 55 nM at a deposition time of 4 min; a similar limitation was noted in a.s.v. measurements by O'Halloran and Blutstein [11] where linear response could not be obtained at concentrations higher than 0.18 μM.

This method was used to measure manganese levels in nine North Atlantic

water samples taken in 1981 [12]. Manganese was first preconcentrated 15-fold by coprecipitation with magnesium hydroxide and dissolution of the precipitate in concentrated nitric acid [13]. The resulting solutions were buffered to pH 9 with ammonia/ammonium chloride buffer before measurement. Concentrations of manganese were determined by standard addition and corrected to the volume of the original samples; the results are shown in Table 2. It can be seen that the measurements in deaerated samples agree well with a.a.s. measurements, whereas lower values were generally obtained in non-deaerated samples. This effect may be due to the lower precision involved in the use of oxygen as the stripping oxidant, or to some interference of dissolved oxygen in the deposition process. However, no such effect was evident in flow measurements where non-deaerated samples were used.

Flow measurements

In contrast to the batch measurements, linear response could be obtained up to at least 30 μM manganese by the use of short deposition times as described below. The detection limit of the flow technique was estimated from a series of eight consecutive measurements in 0.7 M sodium chloride, pH 9.5, containing 9.1 nM manganese(II) and 0.38 μM zinc(II). Other conditions were a deposition time of 200 s and a stripping flow rate of 0.3 ml min^{-1} (Table 1). The relative standard deviation of these measurements was 7%, giving a detection limit of 1.8 nM on the basis of 3× standard deviation. The reproducibility of the measurements depended to some extent on the pH of the samples; below pH 7 the reproducibility became poorer and formation of hydrogen bubbles was visible on the electrode surface.

Manganese was measured in a series of samples taken from the Norwegian fjord Framvaren in September 1983. While the surface waters of this fjord

TABLE 2

Measurements of manganese in Atlantic water after preconcentration[a]

Station	Depth (m)	Mn concentration (nM)		
		P.s.a.		A.a.s.
N 64°00'00	0	1.37[b]		1.88
W 01°00'00	20	1.13[b]		1.55
	100	1.07[b]		1.13
	200	0.98[b]		1.28
N 63°28'28	20	0.97[b]	1.37[c]	1.22
W 06°57'86	100	0.35[b]	0.72[c]	0.75
	200	1.22[b]	1.33[c]	1.88
	500		1.88[c]	1.79
	1200		1.77[c]	1.88

[a]Batch method; the concentrations quoted are those in the original samples. [b]Measurements on non-deaerated samples. [c]Measurements on deaerated samples.

are oxic to a depth of about 18 m, the deeper waters down to the maximum depth of 170 m are permanently anoxic with high levels of sulphide [14]. Manganese was measured in a series of unfiltered, untreated samples representing a depth profile (Fig. 6). An addition of 0.05 M hydroxylamine was made to reduce the higher oxidation states of manganese to Mn(II) (pH 5 in the samples after addition) and the total manganese in these samples was measured after buffering to pH 9 with ammonia/ammonium chloride. Separate experiments confirmed that the p.s.a. response remained linear in the presence of hydroxylamine. Manganese concentrations in the treated samples were estimated by comparison with a calibration curve prepared in 0.5 M calcium chloride, pH 9, using a deposition time of 5 s and a stripping flow rate of 3 ml min^{-1} (Table 1). Linear response was obtained for eight additions in the range 0.18—18 μM. The results are shown in Fig. 6. It can be seen that the measurements on untreated samples resulted in concentrations lower than the total manganese, as would be expected where higher oxidation states of manganese are present. However, it can be expected that the delay of a week between sampling and p.s.a. may have introduced some changes in the levels of manganese(II), particularly in those samples from the redox-cline between 20 and 30 m depth (Fig. 6); field measurements are to be preferred for detailed investigations of such systems. Total manganese concentrations were measured by both p.s.a. and a.a.s. after hydroxylamine treatment and the agreement was generally good, although between 20 and 30 m depth, potentiometric stripping gave significantly higher values than a.a.s. This may reflect slow reduction of refractory manganese oxides during

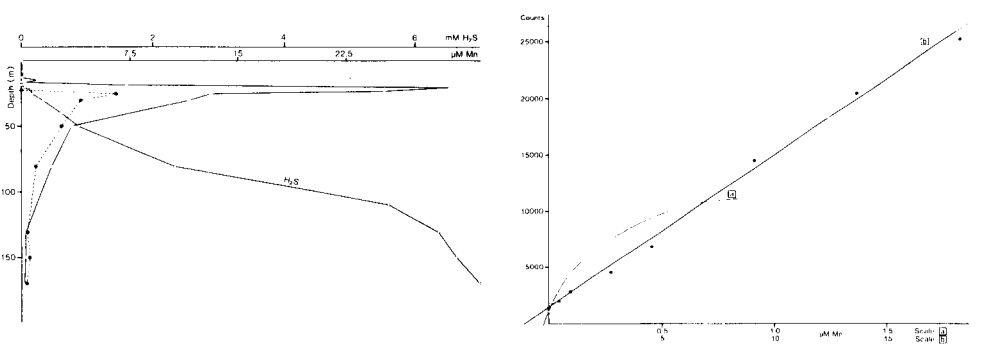

Fig. 6. Manganese concentrations measured by p.s.a. in samples taken at different depths from Framvaren fjord, Norway: (•) untreated samples, 1 week after sampling; (□) 2 weeks after addition of hydroxylamine; (○) H_2S concentration.

Fig. 7. Standard addition graphs for manganese in tapwater. (a) Water buffered to pH 7 with phosphate buffer, deposition time 90 s; the line shown was drawn by hand to emphasise the trend of the data. (b) Water buffered to pH 9 with ammonia/ammonium chloride and 30 μM Ga added before the measurements (deposition time 5 s). The regression line shown is linear up to 30 μm, has a correlation coefficient of 0.998 and an intercept of 1.05 μM on the concentration axis. A.a.s. measurements on other samples of tap water gave an average concentration of 0.9 μM.

the time (one week) between the two sets of measurements. The choice of a calibration graph for the evaluation of the determinations from the anoxic regions might also have contributed to this deviation. The calibration graph was used because even large standard additions of manganese resulted in little change in peak height, an effect which is undoubtedly related to the unusual chemistry of these samples, e.g., high concentration of hydrogen sulphide and high alkalinity. These aspects of the hydroxylamine technique merit further investigation.

Tap water which contained significant levels of both copper and manganese (of the order of 0.8 and 0.9 μM, respectively) were examined. Measurements on tap water buffered to pH 7 showed that even in the presence of a large excess of zinc it was not possible to measure manganese reliably. Standard additions resulted in a curved calibration graph (Fig. 7a) and an unrealistically low estimate of manganese concentration; the results were similar for phosphate and ammoniacal buffers. However, the addition of 30 μM gallium nitrate, which has been recommended for suppression of the copper/zinc interference owing to the strong interaction between copper and gallium in the mercury electrode [10], resulted in a straight calibration line and a realistic estimate of manganese concentration (Fig. 7b).

DISCUSSION

Measurement of manganese by stripping analysis is difficult for a number of reasons; the negative potential required for deposition can cause concurrent reduction of H^+ and other dissolved species, and implies strong possibilities for interference from intermetallic compound formation. Furthermore, the reoxidation of amalgamated Mn to Mn(II) is not fully reversible [11] so that very rapid stripping rates result in broad and indistinct stripping peaks. The results obtained here show that these problems can be overcome in p.s.a. by careful design of the experimental procedure, resulting in a largely automated measurement.

Oxidation rate

The rate of chemical oxidation during the p.s.a. stripping process is a key parameter which is controlled by the concentration of oxidant in the stripping solution and by its rate of transport to the electrode (flow rate or rotation speed). In both the batch and flow measurements, both these parameters are manipulated in order to achieve a slow stripping rate. The oxidant concentration is lowered in the batch measurements by deoxygenation, thus leaving mercury(II) as the sole oxidant, and in the flow measurements by the use of saturated calcium bromide as the stripping solution. This approach is necessitated by the difficulty of transporting a deoxygenated solution through flexible tubing which is highly permeable to oxygen, a problem which disappears if oxygen is not soluble in the solution as in this case. The identity of the stripping oxidant in this solution is assumed to be

the low residual oxygen content. That this low oxidant level is adequately reproducible is evident from the results presented above. Use of a saturated calcium chloride stripping solution also results in a significant improvement in the detection limit for other metals such as Cd, Cu, Pb by flow p.s.a. [15]; calcium bromide was preferred in the present work because of the higher sensitivity for manganese obtained with this medium. The major disadvantage of this approach is the high viscosity of the solution which requires all joints in the flow system, and particularly that between the two parts of the cell, to be well sealed because of the increased pressure drop across the cell. The scope for reducing the stripping rate by reducing the transport rate is limited in both the flow and batch techniques. The flux of oxidant must be constant in order to achieve a constant stripping rate, so that the rate of transport must be fast enough to render transport by chance convection negligible. The stripping flow rate and electrode rotation speed used in this work correspond to these limits. The effect of these changes is greater in the batch method, where flux is proportional to the square root of rotation speed, than in the flow method where the flux is proportional to the cubic root of the flow rate [8].

Batch vs. flow methods

These results provide an interesting comparison between the two different approaches. The detection limits are similar in both techniques, but in practical terms the flow technique possesses many advantages over the batch technique. The flow measurement is faster and is readily automated; the remaining manual operations shown in Table 1 will also be controlled by the microcomputer in the near future, resulting in a completely automated measurement cycle. The flow technique can therefore handle a greater throughput of samples, while greater automation should result in improved precision as the conditions for each measurement become more reproducible. Furthermore, sample handling can be reduced to an absolute minimum of flow through a teflon tube. These features are particularly important for field analysis of natural water samples, to which this particular technique is well suited. The greater flexibility of the flow approach is illustrated by the use of saturated calcium bromide as a stripping solution in place of the time-consuming deoxygenation required in the batch technique, and the measurement of very high manganese concentrations by the use of very short deposition times.

The major disadvantage of the flow technique is the large sample volumes required at low concentrations where long deposition times are necessary. This might be improved by the use of a narrower flow channel which would give the same deposition rate at a lower volume flow rate, provided that the viscous calcium bromide solution can be transported through the cell without leakage.

We thank Stig Westerlund and Conny Haraldsson for the provision of field samples and for the a.a.s. measurements, and Mats Josefson and Daniel Jagner for many valuable discussions. D. R. T. thanks the Royal Society for the award of a European Fellowship enabling him to work in Göteborg.

REFERENCES

1 W. Stumm and J. J. Morgan, Aquatic Chemistry, Wiley, New York, 1981, p. 778.
2 W. Davison, J. Electroanal. Chem., 72 (1976) 229.
3 W. Davison, Limnol. Oceanogr., 22 (1977) 746.
4 S. Knox and D. R. Turner, Est. Cstl. Mar. Sci., 10 (1980) 317.
5 S. Knox, D. R. Turner, A. G. Dickson, M. I. Liddicoat, M. Whitfield and E. I. Butler, Est. Cstl. Mar. Sci., 13 (1981) 357.
6 R. J. O'Halloran, Anal. Chim. Acta, 140 (1982) 51.
7 A. Graneli, D. Jagner and M. Josefson, Anal. Chem., 52 (1980) 2220.
8 L. Andersson, D. Jagner and M. Josefson, Anal. Chem., 54 (1982) 1371.
9 M. Josefson, Doctoral Thesis, University of Göteborg, Sweden, 1983.
10 E. Ya. Neiman, L. G. Petrova, V. I. Ignatov and G. M. Dolgopolova, Anal. Chim. Acta, 113 (1980) 277.
11 R. J. O'Halloran and H. Blutstein, J. Electroanal. Chem., 125 (1981) 261.
12 L. Brügman, L-G. Danielsson, B. Magnusson and S. Westerlund, Rep. Chem. Seawater, XXIX, Dept. Anal. Mar. Chem., Göteborg, Sweden, 1982.
13 H. Eskilsson, C. Haraldsson, B. Magnusson and S. Westerlund, unpublished work.
14 J. M. Skei, in R. O. Hallberg (Ed.), Environmental Biogeochemistry Ecological Bulletins (Stockholm), 35 (1983).
15 D. Jagner and K. Årén, unpublished work.

Analytica Chimica Acta, 161 (1984) 303—314
Elsevier Science Publishers B.V., Amsterdam — Printed in The Netherlands

EVALUATION OF SOME DRY ASHING METHODS FOR ANODIC STRIPPING VOLTAMMETRIC DETERMINATION OF CADMIUM AND LEAD IN BIOLOGICAL MATERIALS

S. B. ADELOJU and A. M. BOND*

Division of Chemical and Physical Sciences, Deakin University, Waurn Ponds, Victoria 3217 (Australia)

M. L. NOBLE

Australian Government Analytical Laboratories, Department of Science and Technology, Melbourne, Victoria 3000 (Australia)

(Received 7th February 1984)

SUMMARY

Several dry-ashing methods were evaluated for the accurate determination of cadmium and lead in biological materials by anodic stripping voltammetry. The method utilizing sulphuric acid as the ashing aid at 500°C was found to be most suitable for the determination of both elements. However, a carbonaceous residue still required that substantial sample dilution be made after dissolution of the sample ash to avoid interferences to the stripping electrode process(es). The dissolution of the sample ash with hydrochloric acid is preferred to the use of nitric acid in obtaining more reproducible results.

The accurate determination of trace elements in biological materials requires complete and thorough decomposition of the organic matter while also demanding quantitative retention of the analyte(s) in a state or form amenable for quantifying by the chosen analytical technique. The two types of decomposition method commonly employed for the determination of trace elements in various sample materials are wet digestion and dry ashing. Although dry ashing is well accepted for the determination of trace elements with most analytical techniques, in the case of stripping voltammetry its use has been restricted [1—3]. In fact, with anodic and cathodic stripping voltammetric techniques there appears to be an increasing tendency to use wet digestion methods for the determination of trace elements in biological materials possibly because of the simplicity of the apparatus required and the reduced danger of losses associated with this type of decomposition method [4]. However, the lower blank levels resulting from dry ashing methods and their capability in handling large sample size, up to 10 g, sometimes make them desirable for trace determinations, particularly when the work has to be done in normal laboratory conditions without specialized clean air facilities. The problem of losses associated with dry ashing noted in early work can be overcome (or reduced) by use of ashing

0003-2670/84/$03.00

aids such as nitric acid [5—7], magnesium nitrate [5, 6, 8—10], sulphuric acid [5—8, 11] and potassium hydrogensulphate [12—14] or by careful manipulation of the ashing temperature [5, 6, 8].

Lead and cadmium are two of the elements for which differing approaches to dry ashing methods for biological materials have been described. Seiser et al. [11], Dalton and Malanoski [9], Usher [15] and Friend et al. [16] showed that the use of ashing aids provided quantitative recoveries of lead and cadmium from foods and other biological materials. Abson and Lipscomb [8] and Gorsuch [5, 6] demonstrated that complete recovery of both elements could be achieved by careful manipulation of the ashing temperature. The effect of ashing temperature is now well known and there is widespread acceptance of 500°C and 450°C for dry ashing with and without ashing aid, respectively. Although it is possible to use higher ashing temperatures in the presence of an ashing aid, the recovery of lead can be significantly affected at temperatures >550°C [5, 6].

Despite the successful establishment of the conditions best suited for dry ashing, it is still necessary to evaluate these methods for any new materials or when the method is used in conjunction with a new technique for quantifying trace elements. Some dry ashing methods have been evaluated for techniques such as atomic absorption spectrometry [15—17], spectrophotometry and colorimetry [8, 18] and radiochemical and neutron activation techniques [5, 6] to ensure that the adopted method is the most satisfactory for the determination of trace elements in the material considered. However, with stripping voltammetric techniques, dry ashing procedures have been adopted, in a few cases [1—3], without any endeavour to evaluate and select the procedure most adequate for the analyte(s) and/or sample material considered. Unlike techniques such as atomic absorption spectrometry which relies on atomisation of the element from solution and which is not so prone to organic interferences, the evaluation of dry ashing methods for anodic stripping voltammetry (a.s.v.) and cathodic stripping voltammetry (c.s.v.) needs to be more comprehensive because organic residues from incomplete decomposition can foul up the electrode by blockage or interference mechanisms of the adsorption type. Adsorption of organic residue may inhibit the electrode process and distort the response by catalysis of hydrogen evolution [19—21]. Hence the precision and accuracy of the results obtained by stripping voltammetry for biological materials will be more dependent on how well the sample is decomposed than with many other analytical techniques.

In the present study, several dry ashing methods have been evaluated for the simultaneous determination of cadmium and lead in biological materials by anodic stripping voltammetry. The methods considered are (1) direct dry ashing, (2) dry ashing with nitric acid as ashing aid, and (3) dry ashing with sulphuric acid as ashing aid. Magnesium nitrate was not tested as an ashing aid because purification of this reagent is often necessary for accurate determination of trace elements [1]. Bovine liver was chosen as the test

material because previous investigations have indicated that it is a complex sample material for stripping voltammetric determinations [1, 4]. The influence of the type of acid used for dissolution of the sample ash on the reproducibility and accuracy of the results obtained for cadmium and lead in liver and veal samples by a.s.v. were also examined.

EXPERIMENTAL

All this work was done under clean air conditions at a temperature of 22.5 ± 0.5°C. All sample preparations were done in a class-100 clean room while the analytical measurements were made in a class-1000 clean room.

Reagents and standard solutions

All acids used were Aristar grade (B.D.H. Chemicals) while other reagents were of analytical-grade purity. A stock solution of cadmium and lead (each 1 g l^{-1}) was prepared by dissolving their nitrate salts in 0.1 M hydrochloric acid and stored in pre-washed polyethylene bottle. The required standards were prepared daily or weekly (depending on concentration) by appropriate dilution of the stock solution with 0.1 M hydrochloric acid. Distilled-deionized water obtained through a Barnstead Sybron "Nanopure" water purification system (Barnstead Sybron Corporation, Boston, MA) was used in all sample and solution preparations and for rinsing.

Instrumentation and glassware

An EG & G Princeton Applied Research microprocessor-based polarographic analyzer (PAR Model 384) equipped with a PAR Model 303 static mercury drop electrode and a PAR Model 305 stirrer was used to record all stripping voltammograms. The electrode compartment contains a hanging mercury drop electrode (HMDE), silver/silver chloride (saturated KCl) and a platinum wire as the working, reference and auxiliary electrodes, respectively. Deposition of cadmium(II) and lead(II) ions into the mercury drop was achieved by using a fast stirring rate and a medium drop size with a surface area of 0.015 cm^2. All solutions were deoxygenated with highly purified nitrogen at the start of each experiment for 10 min and a flow of nitrogen was maintained over the solution to prevent oxygen interference during the measurements.

Standard solutions of cadmium and lead were added to the polarographic cell with fixed-volume Socorex micropipettes with disposable tips.

All glassware and polyethylene bottles were soaked in 2 M nitric acid for at least seven days, washed three times with water, soaked in water, and finally soaked in 0.1 M hydrochloric acid until ready for use.

Biological standard reference material and samples

Bovine liver was obtained from the U.S. Bureau of Standards, Washington, DC, and was treated as recommended by the supplier.

The beef liver and veal samples were prepared by slicing a portion into small sections and then homogenizing in a Waring Blendor. Sufficient water was added to form a liquid paste and the samples were blended for another 5 min at high speed. The homogenized sample was then freeze-dried, ground to a fine powder and finally sieved to ensure uniform particle size.

Sample decomposition

The three dry-ashing procedures considered were as follows.

(1) Direct dry ashing without ashing aid. Accurately weigh 0.5 g of sample into a pre-cleaned silica dish and heat gently on a hot plate at medium rate to volatilize as much moisture and organic matter as possible. Spread out the sample from time to time with a silica rod to speed drying. When the sample is reasonably dry (about 1 h), transfer the dish to a temperature-controlled muffle furnace set to 450°C or 500°C and leave overnight to complete decomposition. Remove the dish from the furnace and allow to cool before adding 5 ml of 5% (v/v) nitric acid (0.80 M) or 5 ml of 2.5% (w/v) hydrochloric acid (0.81 M). Warm on a water bath to effect dissolution and extraction of elements from the residue. Transfer quantitatively to a 10-ml standard volumetric flask and dilute to volume with the appropriate acid. If the sample contained residue, it was left to settle before taking an aliquot for the determination. Further dilution to 50 ml with water may be necessary, depending on suitability for the a.s.v. of cadmium and lead.

(2) Dry ashing with sulphuric acid as ashing aid. The procedure described by Allenby et al. [22], which is currently used at the Australian Government Analytical Laboratories in Victoria, was adopted. The procedure was slightly modified for this study. Accurately weigh 0.5 g of sample into a pre-cleaned silica dish and add 5 ml of 20% (v/v) sulphuric acid (3.6 M). Heat on a water bath for 3 h and transfer to a hot plate, heating until white fumes cease to be evolved and the residue is completely dry. Transfer the dish to the muffle furnace set to 500°C and leave overnight to complete decomposition. Dissolve the residue and make up the solution as described above. If the sample contains carbonaceous residue, leave to settle before taking an aliquot for determination.

(3) Dry ashing with nitric acid as ashing aid. The procedure was similar to (2) except that 5 ml of 5% (v/v) nitric acid was added in place of sulphuric acid and the ashing was done at 450°C.

Stripping voltammetry

Transfer an aliquot (5 ml) of the sample digest to the polarographic cell, deoxygenate and determine cadmium and lead under the following conditions: differential pulse mode, deposition potential −0.9 V vs. Ag/AgCl, scan increment +4 mV, duration between pulses 1 s, scan rate +4 mV s^{-1}, pulse height +50 mV, deposition time 165 s (stirred), equilibration period 15 s (unstirred). The two elements were quantified by the standard addition technique.

RESULTS AND DISCUSSION

The use of the direct ashing method for the decomposition of the bovine liver sample at 500°C gave low recoveries for both cadmium and lead by anodic stripping voltammetry (Table 1). These results conform with those previously obtained by other workers [5, 6, 8] and also support the view that the direct ashing of biological materials at temperatures >470°C is unsatisfactory for complete recovery of some trace elements, as losses by volatilization may occur under such conditions. The use of a lower ashing temperature of 450°C improved the recoveries for both elements considerably, as is clearly evident from Table 1. The stripping voltammograms obtained in both cases were similar and showed no distinct dependence on the ashing temperature other than peak heights (Fig. 1a, b). The similarity of the stripping curves obtained for the bovine liver samples decomposed by ashing with nitric acid (Fig. 1c) or sulphuric acid (Fig. 2) indicates that the direct ashing method at 450°C is quite adequate for the determination of cadmium and lead in biological materials by a.s.v. This view is confirmed by the data in Table 1 which show satisfactory agreement for these three procedures. The use of sulphuric acid as an ashing aid gave mean results closest to the certified values. The conversion of the two elements to their sulphate forms by this ashing aid may reduce the risk of losses by volatilization but the significance of the data is dubious.

The retention of carbonaceous residue in the final sample ash by these procedures is, in principle, undesirable because the presence of such material in solution can create problems with the determination of the elements by a.s.v. For this reason, dilution of the sample to 50 ml, after dissolution, was necessary to allow adequate separation of the carbon from solution by settling. The carbon can be removed by moistening the ash with water or nitric acid and then re-ashing [8]. The use of nitric acid to remove the carbon

TABLE 1

Determination of cadmium and lead in Bovine Liver by a.s.v. after various dry-ashing procedures

Procedure	Cadmium found ($\mu g\ g^{-1}$)[a]	Lead found ($\mu g\ g^{-1}$)[a]
Direct ashing at 450°C	0.25 ± 0.02	0.30 ± 0.02
Direct ashing at 500°C	0.21 ± 0.02	0.27 ± 0.02
Dry ashing with HNO_3 at 450°C	0.25 ± 0.01	0.29 ± 0.02
Dry ashing with H_2SO_4 at 500°C (carbon present)	0.27 ± 0.02	0.34 ± 0.02
Dry ashing with H_2SO_4 at 500°C (carbon removed)	0.26 ± 0.02	0.32 ± 0.03
Certified value[b]	0.27 ± 0.04	0.34 ± 0.08

[a]With mean deviation (n = 4). [b]With standard deviation.

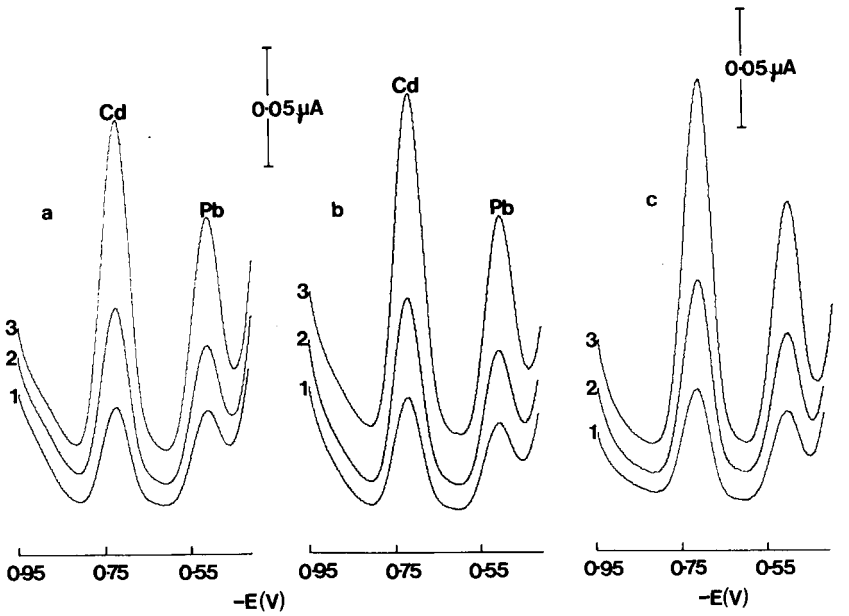

Fig. 1. Determination of cadmium and lead in Bovine Liver by ashing without and with nitric acid: (a) 500°C; (b) 450°C; (c) 450°C with nitric acid. Dilution volume 50 ml. Standard added: (1) 0; (2) 2 ng ml^{-1} (Cd and Pb); (3) 6 ng ml^{-1} (Cd and Pb).

from the sulphated ash led to removal of the small shoulder sometimes observed at about −0.85 V vs. Ag/AgCl close to the cadmium peak (Fig. 2a). The removal of the carbon also reduces the high cathodic background current (Fig. 1) which may be a result of catalysis of hydrogen evolution by carbon in the solution. However, as shown in Table 1, the removal or presence of the carbon residue does not significantly affect the results obtained for cadmium and lead in the bovine liver sample within the limit of experimental error, provided that the dissolved ash is sufficiently diluted to permit separation of carbon from the bulk of the solution. Ashing of the bovine liver sample with nitric acid added produced an almost white ash but also left a small carbon residue at 450°C. The results obtained by this ashing method (Table 1) also confirm that the carbon residue has no significant bearing on the determination of cadmium and lead in bovine liver by a.s.v. Generally, the reproducibility of the three dry ashing methods considered was excellent. Comparison with the certified values suggests that the method with sulphuric acid as ashing aid is superior. To confirm this view and the general adequacy of the sulphuric acid/dry ashing method, other biological samples were also examined by anodic stripping voltammetry.

The decomposition of an ordinary bovine liver sample by the sulphuric acid/dry ashing method produced carbon residues similar to those obtained for the NBS standard and again caused no problem for the a.s.v. measurements when the ash was diluted to 50 ml and left to settle. The results in

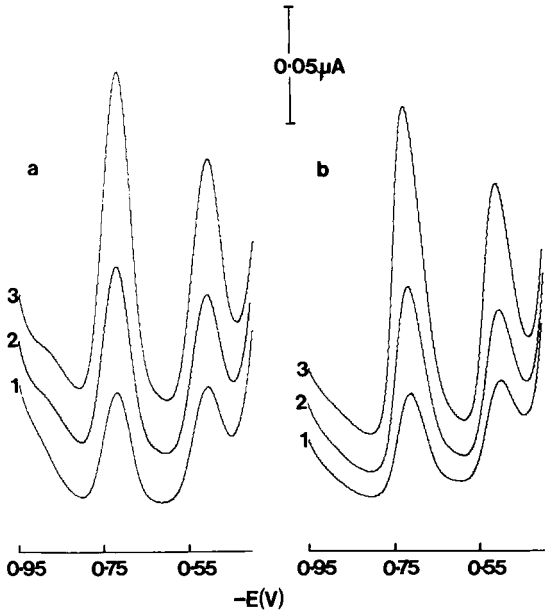

Fig. 2. Influence of carbonaceous residue on the determination of cadmium and lead in Bovine Liver by dry ashing with sulphuric acid at 500°C: (a) carbon present; (b) carbon removed with nitric acid treatment. Other conditions as for Fig. 1.

Table 2 show, however, that the reproducibility under these conditions can be significantly influenced by the acid used for the dissolution of the sample ash. Dilute hydrochloric or nitric acid is commonly used for dissolution of sample ash but no preference for either of these acids has been previously indicated. The use of hydrochloric acid for the dissolution of the ashed sample gave more reproducible results for the determination of cadmium by a.s.v. than the nitric acid dissolution. Figure 3 shows that the stripping voltammograms obtained after dissolution of the ash in hydrochloric acid gave better defined and more sensitive peaks for both cadmium and lead than those obtained after dissolution of the ash in nitric acid.

The decomposition of the veal sample by the sulphuric acid/dry ashing method, on the contrary, proved to be comparatively simple, giving very little, or no carbon residue and thus permitting dissolution and dilution of the dissolved ash to a smaller volume (10 ml). Figure 4(a, b) shows that the use of hydrochloric acid for dissolution of the ash gave much better response and lower cathodic background current than the use of nitric acid. However, the 10-ml dilution volume was disadvantageous to the reproducibility of the results, possibly because of the higher acidity ($\approx$0.8 M) present and perhaps because of interferences from fine ash particles in solution. Dilution of the dissolved ash to 50 ml gave more reproducible results (Table 2).

TABLE 2

Influence of dissolution acid on the a.s.v. determination of cadmium and lead in ordinary bovine liver and veal

Acid	Bovine liver		Veal	
	Cd found[a] ($\mu g\ g^{-1}$)	Pb found[a] ($\mu g\ g^{-1}$)	Cd found[a] ($\mu g\ g^{-1}$)	Pb found[a] ($\mu g\ g^{-1}$)
Nitric	0.25 ± 0.04	0.32 ± 0.03	0.41 ± 0.03	0.24 ± 0.03
Hydrochloric	0.27 ± 0.02	0.41 ± 0.03	0.35 ± 0.01	0.19 ± 0.02

[a]Average and mean deviation (n = 4).

Nevertheless, because the dissolution with hydrochloric acid gave more reproducible results for cadmium and lead in the liver samples, it is recommended generally for biological materials. Figure 4(c) shows that dilution to 50 ml of the ash dissolved with nitric acid improved the cathodic background current (cf. Fig. 4b), which is advantageous for measurements of the cadmium peak particularly. However, when the ash was dissolved in hydrochloric acid, dilution to 10 or 50 ml had little effect on the shapes of the voltammograms and dissolution with hydrochloric acid is certainly the more

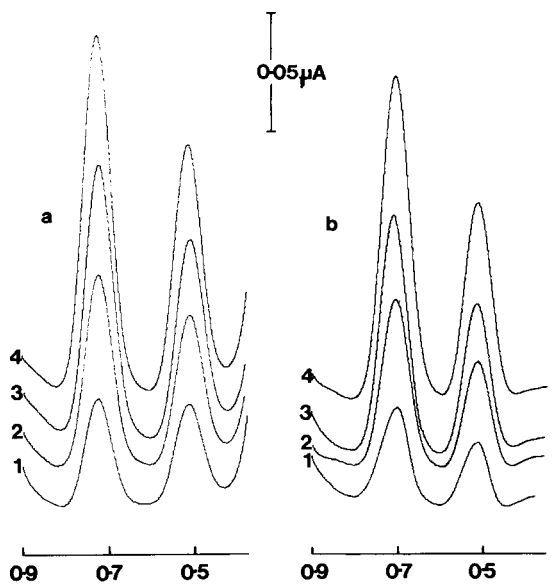

Fig. 3. Influence of dissolution acids on the determination of cadmium and lead in ordinary bovine liver by dry ashing with sulphuric acid at 500°C: (a) dissolution with HCl; (b) dissolution with HNO_3. Standards added: (1) 0; (2) 2 ng ml^{-1} (Cd and Pb); (3) 4 ng ml^{-1} (Cd and Pb); (4) 6 ng ml^{-1} (Cd and Pb). Other conditions as for Fig. 1.

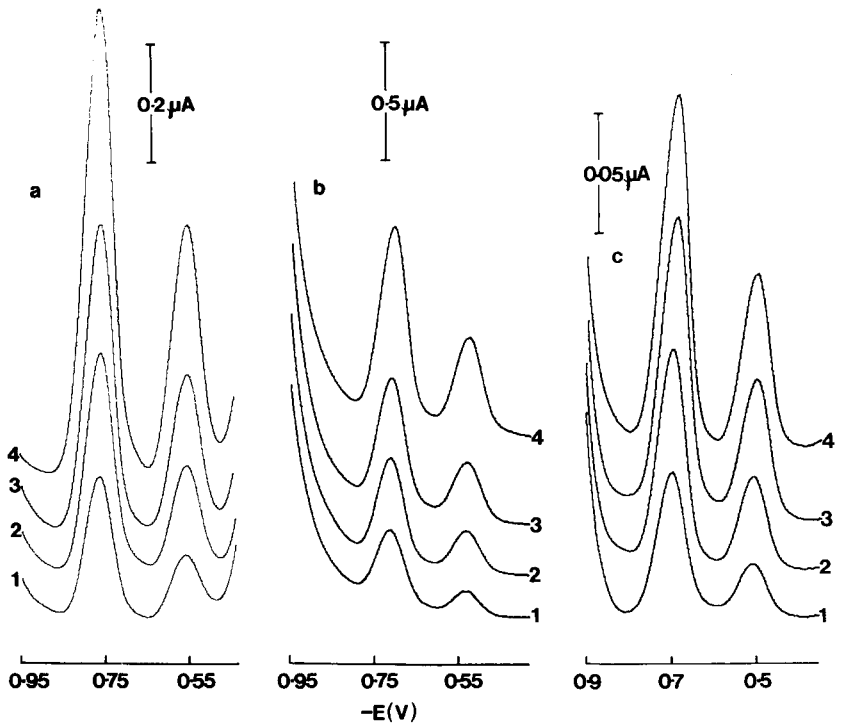

Fig. 4. Influence of dissolution acids on the determination of cadmium and lead in veal by dry ashing with sulphuric acid at 500°C; (a) and (b) as for Fig. 3 but with dilution to 10 ml; standards added for (c) as for Fig. 3. Standards added: (1) 0; (2) 10 ng ml^{-1} (Cd and Pb); (3) 19.8 ng ml^{-1} (Cd and Pb); (4) 39.2 ng ml^{-1} (Cd and Pb).

attractive alternative in terms of background current. The suitability of this acid for ash dissolution with the liver and veal samples suggests that it may also be appropriate for other biological materials but similar comparisons would be necessary in applying the same approach for the determination of other trace elements by a.s.v. or c.s.v.

To provide further data on the differences in behaviour with the two dissolution acids, the anodic stripping voltammetry of cadmium and lead in nitric and hydrochloric acids, at comparable acid concentration ($\approx$0.8 M), was investigated. Figure 5(a) shows that nitric acid introduces an additional process compared with hydrochloric acid (Fig. 5b) which gave only the expected two peaks. The additional peak in nitric acid solution even with a 3-min deposition time, indicates that the process involved may indeed contribute to the reproducibility differences observed for cadmium and lead in the ashed samples.

Nitric acid can react with the mercury drop via a redox process. The main reactant, and the possible interfering ion in the a.s.v. determination of cadmium and lead, is nitrite which may be produced as a reduction product and

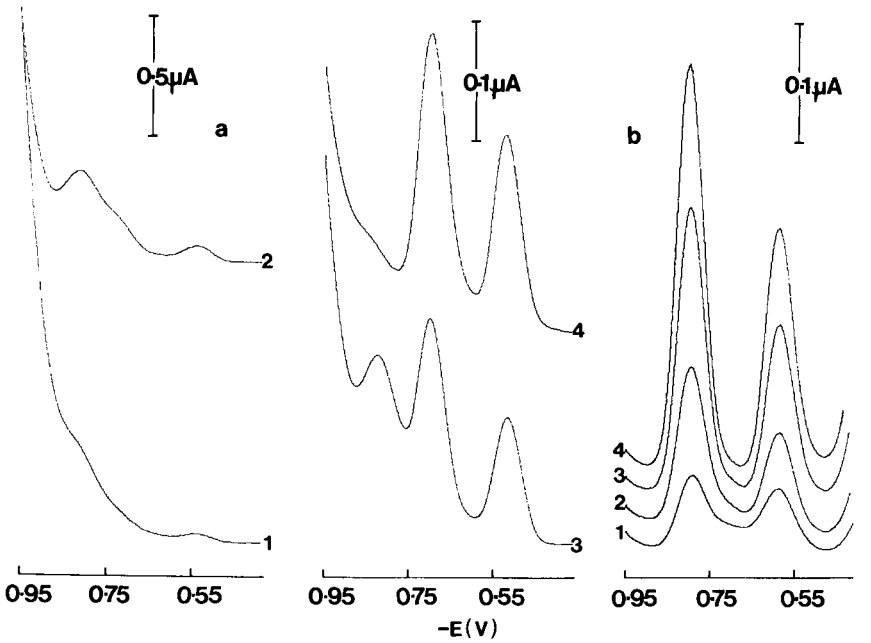

Fig. 5. The influence of nitric and hydrochloric acids on the anodic stripping voltammetry of cadmium and lead: (a) 5% (v/v) HNO_3 and (b) 2.5% (v/v) HCl. Concentration of elements, 20 ng ml^{-1}. Total electrolysis time: (1) 30 s; (2) 60 s; (3) 120 s; (4) 180 s.

can readily be oxidized. Hamilton et al. [23] indicated that nitrite can adversely affect the electrode process during stripping voltammetry and thus needs to be removed to obtain reliable results. This effect can be eliminated or reduced by treatment with urea, hydrogen peroxide or by boiling gently, but such additional treatments are undesirable because they are a likely source of contamination. Because the use of hydrochloric acid is less problematic, it is certainly preferable for the determinations discussed here.

Despite the possible interference associated with nitric acid, cadmium and lead can be quantified by standard addition (Fig. 6). Similar linear responses were obtained for the bovine liver and veal samples. However, the results in Table 2 clearly indicate that such linear responses can still be misleading concerning the precision and accuracy of results when a possible interferent is present. Obviously, it is preferable, particularly in trace analysis, to use an electrolyte which has no contributory effect on the electrode process(es) of the analyte(s). The preference for hydrochloric acid is further supported by the higher sensitivity shown for cadmium and lead after dissolution by this acid compared with nitric acid.

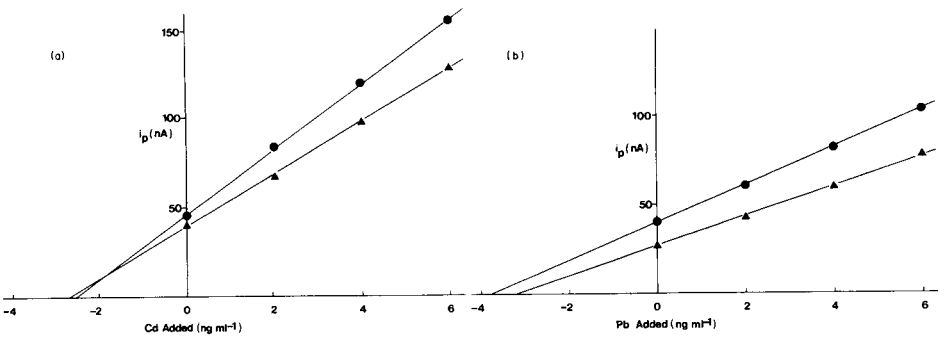

Fig. 6. Influence of dissolution acids on the quantitation of (a) cadmium and (b) lead in beef liver by the standard addition technqiue: (•) HCl; (▲) HNO_3. Other conditions as in Fig. 3.

Conclusion

The use of dry ashing methods for accurate determinations of trace elements in biological materials by stripping voltammetry requires careful consideration of the acid employed for the dissolution of the ash and the possible effect of the carbonaceous residue commonly remaining after most ashing methods. Investigation of these problems showed that, for the a.s.v. determination of cadmium and lead, hydrochloric acid is preferable to nitric acid for the dissolution of the ashed sample, and that substantial dilution of the sample is needed to allow settling of the carbon particles from the bulk of the solution. Dry ashing with sulphuric acid as an ashing aid proved to be most satisfactory here. However, it is recommended that similar comparisons be made to establish the most appropriate acid for the dissolution of the ashed sample when other trace elements are to be measured by anodic or cathodic stripping voltammetry.

This work was supported financially by the Australian Government Analytical Laboratories, Victoria and the Deakin University Research Committee. We are grateful to both bodies.

REFERENCES

1 S. B. Adeloju, A. M. Bond and H. C. Hughes, Anal. Chim. Acta, 148 (1983) 59.
2 W. Holak, J. Assoc. Offic. Anal. Chem., 59 (1976) 650.
3 T. M. Florence, J. Electroanal. Chem., 35 (1972) 237.
4 S. B. Adeloju, A. M. Bond and M. H. Briggs, Anal. Chem., in press.
5 T. T. Gorsuch, Analyst (London), 84 (1959) 135.
6 T. T. Gorsuch, The Destruction of Organic Matter, Pergamon Press, Oxford, 1970.
7 G. Middleton and R. E. Stuckey, Analyst (London), 78 (1953) 152.
8 D. Abson and G. Lipscomb, Analyst (London), 82 (1957) 152.
9 E. F. Dalton and A. J. Malanoski, J. Assoc. Offic. Anal. Chem., 52 (1969) 1035.
10 P. J. Leblane and A. L. Jackson, J. Assoc. Offic. Anal. Chem., 56 (1973) 383.
11 A. Seiser, A. Necke and H. Muller, Z. Angew. Chem., 42 (1929) 96.

12 R. B. Bradstreet, The Kjeldahl Method for Organic Nitrogen, Academic Press, London, 1965.
13 E. Boyland, Analyst (London), 71 (1946) 230.
14 R. E. Stanton and A. J. Hardwick, Analyst (London), 92 (1967) 387.
15 C. D. Usher, J. Sci. Food Agric., 26 (1975) 554.
16 M. T. Friend, C. A. Smith and D. Wishart, At. Abs. Newsl., 16 (1977) 46.
17 D. L. Heanes, Analyst (London), 106 (1981) 182.
18 D. L. Heanes, Analyst (London), 106 (1981) 172.
19 P. Valenta, H. Rutzel, N. W. Nürnberg and M. Stoepler, Z. Anal. Chem., 285 (1977) 25.
20 H. W. Nürnberg, Electrochim. Acta, 22 (1977) 935.
21 Princeton Applied Research Workshop Manual, Princeton, NJ, 1973.
22 P. Allenby, J. W. Roberts and F. C. Shenton, J. Assoc. Public Anal., 15 (1977) 61.
23 T. W. Hamilton, J. Ellis and T. M. Florence, Anal. Chim. Acta, 110 (1979) 87.

Analytica Chimica Acta, 161 (1984) 315—324
Elsevier Science Publishers B.V., Amsterdam — Printed in The Netherlands

DETERMINATION OF TRICHLOROBIPHENYL BY ADSORPTIVE STRIPPING VOLTAMMETRY

N. K. LAM and M. KOPANICA*

Institute of Physical Chemistry and Electrochemistry CAS, Jilská 16, 110 00 Prague 1 (Czechoslovakia)

(Received 9th January 1984)

SUMMARY

Trichlorobiphenyl is determined in the concentration range 0.004—1 mg l^{-1} by adsorptive stripping voltammetry at a hanging mercury drop electrode. Preconcentration is achieved by adsorption at a potential of −0.40 V (vs. Ag/AgCl), and desorption at −1.10 V. Biphenyl interferes with the determination only when present in 5-fold molar amounts compared to trichlorobiphenyl. The interference of DDT is eliminated by prior treatment of the sample solution with sulphuric acid. The method was applied for the analysis of waste and natural waters, the relative standard deviation being <5%.

Polychlorinated biphenyls (PCBs) have been produced in many countries under different trade-names, e.g., Araclor (U.S.A.), Delor (Czechoslovakia), Sovtol (U.S.S.R.) and Kanerol (Japan). The release of PCBs from industrial processes, combined with their insolubility in water and their resistance to biological degradation has resulted in widespread contamination of water and soil. The PCBs are toxic, the lethal oral dose (LD_{50}) being 2—10 g kg^{-1} in mammals; in man, ingestion of 10 mg kg^{-1} for 50 days causes chloracne. An increased incidence of cancer was reported in men exposed occupationally to PCBs, which therefore appeared on the list of carcinogens of the U.S. Department of Health in 1981. Because of their toxicity, the use of PCBs is subject to various governmental regulations in many countries. The content of PCBs must be controlled in some classes of food (milk, poultry, baby food, fish, shellfish) and in food packaging.

The conventional method for quantifying PCBs is gas chromatography/mass spectrometry or gas chromatography with electron capture detection [1]. Electrochemical methods have rarely been applied for quantifying PCBs. Biphenyl and its chloro derivatives are reduced on the dropping mercury electrode only at very negative potentials in a medium containing tetralkylammonium salts [2]. This reduction process was used to quantify chlorinated biphenyls and naphthalenes by Farwell et al. [3] who applied the method of interrupted sweep voltammetry [4] at a mercury-coated platinum electrode and simultaneously determined various isomers of the studied compounds.

0003-2670/84/$03.00

The present paper is devoted to the problems connected with the voltammetric determination of trichlorobiphenyl (TCB) after its preconcentration by adsorption on a hanging mercury drop electrode.

EXPERIMENTAL

Equipment

The polarographic analyzer PA-4 (Laboratorní přístroje, Prague) was used in the three-electrode configuration for the recording of d.c., differential pulse polarographic (d.p.p.), fast-scan d.p.p. and normal pulse polarographic (n.p.p.) curves. A static mercury drop electrode (SMDE-1; Laboratorní přístroje, Prague) served as the working electrode, either as a dropping mercury electrode (DME) or as a hanging mercury drop electrode (HMDE); a Ag/AgCl electrode served as the reference electrode and a platinum wire as the auxiliary electrode. Dissolved oxygen was removed from the test solutions by pre-purified nitrogen.

The electrocapillary curves were measured by the modified method of Novotný et al. [5]; the capillary used had an internal diameter of 55 μm and a drop time of 93 s.

Samples and reagents

A solution of trichlorobiphenyl (TCB) was prepared from a chemical synthesized in the Technological University, Pardubice. The chemical was shown to contain 41.3% chlorine, which corresponds to three chlorine atoms per biphenyl molecule. The isomers 3,4,4′-TCB, 4,4′,5-TCB and probably 4,5,6′- or 4,3′,4′-TCB were identified in this chemical by mass spectrometry (Technological University, Pardubice). The biphenyl used was a commercial product (Lachema, Brünn). The 1,1,1-trichloro-2,2-bis(4-chlorophenyl)ethane (DDT) was a standard chemical prepared in the Institute of Hygiene and Epidemiology, Prague.

The nitrating mixture consisted of concentrated nitric and sulphuric acids in the ratio 1:2. Unless otherwise specified, conventional Britton-Robinson buffers were used as supporting electrolytes.

All solutions were prepared from reagent-grade chemicals. Twice-distilled water (quartz apparatus) was used throughout.

Recommended procedure for waste and natural waters

The water sample (1 ml) is added to 25 ml of the supporting electrolyte (Britton-Robinson buffer solution, pH 6.5, containing 20% (v/v) methanol), which has previously been deaerated with purified nitrogen in the electrolytic cell. After brief mixing with nitrogen, the stirrer is switched on, the applied potential is adjusted to −0.40 V (vs. Ag/AgCl) and a new drop is dialled on the static mercury drop electrode operated in the HMDE mode. From the instant of the new drop formation, the accumulation time is measured. After the stirrer has been switched off, the solution is left for 15 s to

become quiescent and then the cathodic potential scan is started from −0.40 V to −1.30 V using the fast-scan d.p.p. mode with a scan rate of 20 mV s^{-1}. This procedure is repeated with the addition of known amounts of standard TCB solution.

In a preliminary run, an accumulation time of 60 s is usually applied; from these results, the appropriate amount of sample (or suitable accumulation time) is chosen. Some samples of waste water require prior filtration and dissolution of the insoluble material in methanol.

If the sample contains DDT, a peak is recorded at −0.30 V in the polarization scan from 0 to −1.0 V. In that case, the sample is treated with sulphuric acid (1 + 8) for 15 min at 80°C, the solution is neutralized with 10% (w/v) sodium hydroxide and TCB is measured by the procedure given above.

RESULTS

Polarographic and voltammetric behaviour of TCB

Trichlorobiphenyl yielded a badly developed d.c. polarographic wave in media composed of methanol and buffer solution (1 + 2) in the pH range 4—9. The use of d.c. polarography was inadequate for the determination of low amounts of TCB and even d.p.p. did not give the necessary sensitivity. Higher limiting currents were obtained when the HMDE was used under otherwise identical conditions.

The cyclic voltammogram of TCB (Fig. 1) yielded a sharp cathodic peak, about four times higher than the anodic peak. During these measurements, it was observed that the cathodic peak current increased when the HMDE was kept at the initial potential value (−0.40 V) for some time before polarization was started, while the anodic peak current remained constant. This indicated that TCB accumulated on the surface of the HMDE in the more positive potential range and then stripped off at more negative potentials. To verify this, electrocapillary curves of mercury in solutions of TCB were measured under the same solution conditions as the cyclic voltammograms, i.e., Britton-Robinson buffer pH 6.8 containing 20% methanol. The maximum of the electrocapillary curves (Fig. 2) decreased with increasing TCB concentration. At the electrocapillary maximum (−0.40 V), TCB is adsorbed on the HMDE and is desorbed at −1.05 V, the potential at which the surface tension becomes identical whether or not TCB is present. This interpretation of the observed phenomena agrees well with the results of the polarographic and voltammetric measurements. When n.p.p. was applied for the determination of TCB, a wave with sharp maximum was obtained; the height of this maximum depended on the value of the initial potential (Fig. 3). This verified that the current recorded under the given conditions in voltammetric and polarographic measurements is adsorption-controlled.

This adsorption effect can be used analytically. Very sensitive determinations can be achieved, analogously to cathodic stripping voltammetry (c.s.v.): the analyte is preconcentrated by adsorption and is then stripped by desorption from the surface of the mercury electrode [6].

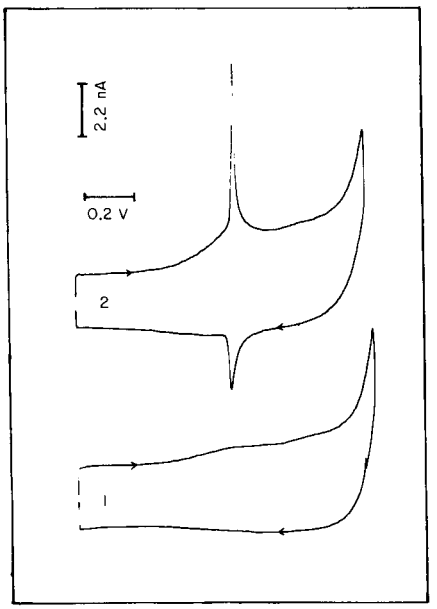

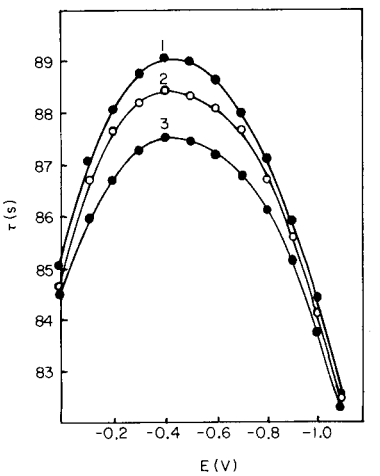

Fig. 1. Cyclic voltammogram of TCB: (1) Buffer pH 6.4 with 20% methanol; (2) Supporting electrolyte with 1×10^{-5} mol l^{-1} TCB. Curves from —0.40 to —1.50 V, d.c., HMDE, sweep rate 50 mV s^{-1}.

Fig. 2. Electrocapillary curves of TCB in buffer pH 6.4 with 20% methanol. TCB concentration: (1) none; (2) 2×10^{-6} mol l^{-1}; (3) 6×10^{-6} mol l^{-1}.

Optimization of the analytical procedure

As mentioned above, the current measured in the voltammetric determination of TCB depended on the pH of the supporting electrolyte. Figure 4 shows the dependence of the peak current (fast-scan d.p.p.) and the peak potential on pH, together with the potential of the hydrogen evolution of the supporting electrolyte. The optimum pH for the TCB determination seems to lie in the range 6—7, where the peak of TCB is well separated from the hydrogen evolution.

Because of the insolubility of TCB in water, voltammetric determinations must be done in the buffer solution containing methanol. The optimum content of methanol was 20% (v/v); the dependence of the peak current on the amount of methanol present in the electrolyte showed a maximum at this concentration.

Preconcentration of TCB

Preconcentration of the TCB on the surface of the HMDE is the essential condition for highly sensitive determinations. The amount of adsorbed TCB depends on the accumulation potential used, on the duration of the accumu-

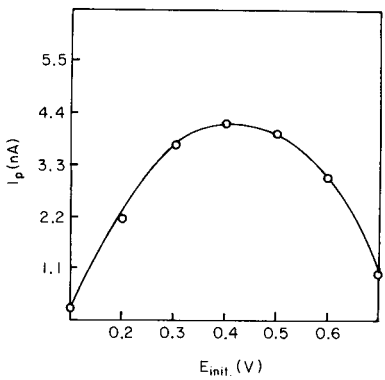

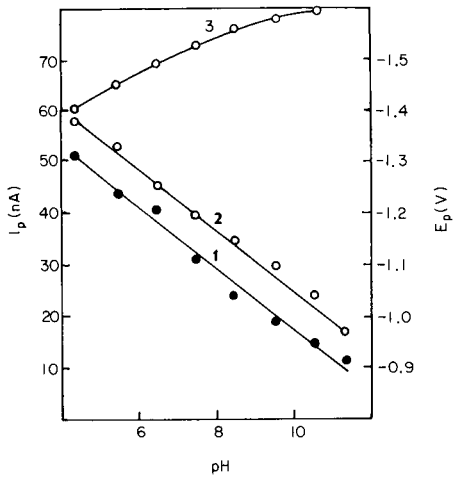

Fig. 3. Influence of initial potential value on n.p.p. maximum current of TCB (2×10^{-6} mol l^{-1}). Supporting electrolyte pH 6.5 with 20% methanol.

Fig. 4. Influence of pH on: (1) peak current, I_p, of TCB; (2) peak potential, E_p, of TCB; (3) potential of hydrogen evolution. Supporting electrolyte with 20% methanol, 5×10^{-7} mol l^{-1} TCB, accumulation potential —0.40 V, accumulation time 30 s.

lation time, and on the intensity of stirring. The optimum value of the accumulation potential follows from the interpretation of the electrocapillary curves, from the n.p.p. data and from the measurement of the dependence of the fast-scan d.p.p. peak current on the accumulation potential chosen. In all these measurements, the optimum value was found to be —0.40 V.

The duration of the accumulation period is limited by complete coverage of the electrode surface. The time necessary for complete coverage depends on the surface area of the electrode, the concentration of TCB, the value of the accumulation potential and the rate of stirring. In an experiment where the weight of one drop of mercury was about 5 mg, complete coverage was accomplished after 180 s with 1×10^{-7} mol l^{-1} TCB and after 90 s with 4×10^{-6} mol l^{-1} TCB at the optimum accumulation potential value (—0.40 V). Given these results, it is clear that the method of standard addition must be used cautiously for evaluation of results; the TCB concentrations must correspond to the concentration range in which the I_p values increase with prolonged accumulation time.

Sensitivity

The dependence of the peak current on the TCB concentration was measured in the concentration range from 1×10^{-8} to 1×10^{-5} mol l^{-1} TCB. The dependence was linear in the range 1×10^{-8} mol l^{-1} to 1×10^{-6} mol l^{-1} TCB (0.004—1 mg l^{-1}). Linear regression of the data obtained yielded the following

results: slope of the linear dependence $x = 4.18 \times 10^7$ nA mol^{-1}, intercept $y = 0.4822$, calibration line $I_p = 4.18 \times 10^7$ nA mol^{-1} + 0.48; regression coefficient $r = 0.9996$. The detection limit was found to be 1.5 μg l^{-1}.

Adsorptive stripping voltammetry of nitrated TCB

Because aromatic compounds are readily nitrated and thus converted to electroactive forms, further experiments were directed towards finding the best conditions for determination of the nitrated TCB. The optimum conditions for the nitration were as follows: a volume of the nitrating mixture 10 times greater than the sample volume was added and the mixture was heated at 60°C for 20—30 min; 20% (w/v) sodium hydroxide solution was then added to neutralize the mixture. The nitrated TCB derivative yielded two d.p.p. peaks with peak potentials at —0.45 V (reduction of the nitro group) and at —1.05 V in a supporting electrolyte of pH 5. The sensitivity of the direct d.p.p. determination was, however, less than that obtained by the adsorptive accumulation procedure. The peak current corresponding to the desorption of TCB (—1.05 V) obtained after nitration was about 20 times less than that recorded without nitration and was thus without analytical value.

Attempts to increase the sensitivity led to an examination of the adsorptive properties of the nitrated TCB. Measurement of the electrocapillary curves, and the dependence of n.p.p. and d.p.p. results on the chosen accumulation potential (as outlined above) showed that the nitrated TCB was adsorbed on the HMDE similarly to TCB. The optimum conditions for the adsorptive voltammetric determination were as follows: supporting electrolyte pH 5.0, accumulation potential 0 V, accumulation time 30 s. Under these conditions, TCB could be determined in the concentration range 4×10^{-8}—1×10^{-6} mol l^{-1}. The reproducibility of the results was, however, worse than that in the case described above. This poor reproducibility was clearly caused by the nitration process, but variation of the nitration conditions did not improve the results, and the relatively optimum conditions for the nitration were as described above.

Adsorptive stripping voltammetry of biphenyl

The polarographic behaviour of biphenyl would be expected to be similar to that of its chlorinated derivative. Biphenyl was found to yield a cathodic wave ($E_{1/2}$ = —1.02 V) or a d.p.p. peak (E_p = 1.01 V) in supporting electrolytes of pH 5—6. The cyclic voltammogram of biphenyl had almost the same shape as that of TCB and the course of the electrocapillary curves measured in the presence of biphenyl also corresponded to that of TCB. The potential of maximum adsorption of biphenyl was —0.60 V, and the potential of desorption —1.01 V. These data were verified by n.p.p. measurement of biphenyl at varied initial potential values.

The data obtained confirmed that biphenyl could be determined by stripping voltammetry with adsorptive accumulation, similarly to TCB. When the

fast-scan d.p.p. mode was applied, and accumulation was done in the supporting electrolyte at pH 5—7 (Britton-Robinson buffer) at —0.60 V, the dependence of the peak current on the concentration of biphenyl was linear in the range 0.008—3.0 mg l^{-1} and the detection limit was 6.5 μg l^{-1}.

Measurements with nitrated biphenyl showed that nitration of biphenyl proceeded under the same conditions as described above for TCB. The results of adsorptive stripping voltammetry obtained after nitration showed better reproducibility for biphenyl than for TCB. The nitrated biphenyl yielded a d.p.p. peak at —0.48 V, a value identical with that of nitrated TCB.

Adsorptive stripping voltammetry of DDT

1,1,1-Trichloro-2,2-bis(4-chlorophenyl)ethane (DDT) is structurally similar to PCBs and traces of this compound may be present in samples analyzed for environmental monitoring. The adsorption properties and voltammetric behaviour of DDT were therefore examined briefly. The compound can be reduced polarographically; well developed d.c. waves were obtained in supporting electrolyte containing tetralkylammonium salts [7]. The electrocapillary curves, measured exactly as described above, differed from those obtained in solutions containing TCB or BP (Fig. 5). The characteristic phenomenon observed on these curves was the sudden decrease in surface tension at a potential of —0.30 V, which indicates some change in the nature of the surface activity, probably caused by the presence of methanol in the solution. On the d.p.p. curves, recorded under exactly the same conditions as those used for the electrocapillary curves, a peak was recorded at —0.30 V; this peak must be tensammetric in nature because no reduction of DDT can be expected in this potential range.

Besides this peak, DDT also yielded a second and higher peak with E_p = —1.10 V. This more negative peak was caused by desorption of the DDT adsorbed on the HMDE at more positive potentials; this was verified by measurement of the peak current dependences on the accumulation potential, accumulation time and concentration of DDT. Maximum peak current was obtained when the accumulation potential was kept in the range —0.20 to —0.40 V. These results show that DDT can be determined under practically the same conditions as TCB and thus interferes with the TCB determination.

Analytical applications

The results presented above show that the application of adsorption accumulation permits very sensitive voltammetric determinations of TCB. The accumulation process, however, leads to interferences caused by surface-active substances or compounds of similar adsorptive properties.

The influence of surface-active compounds on the determination of TCB was examined first. Surfactants such as dodecylsulphate had practically no influence when present at concentrations comparable with that of TCB. At higher dodecylsulphate concentration (more than 1 mg l^{-1}), a peak corre-

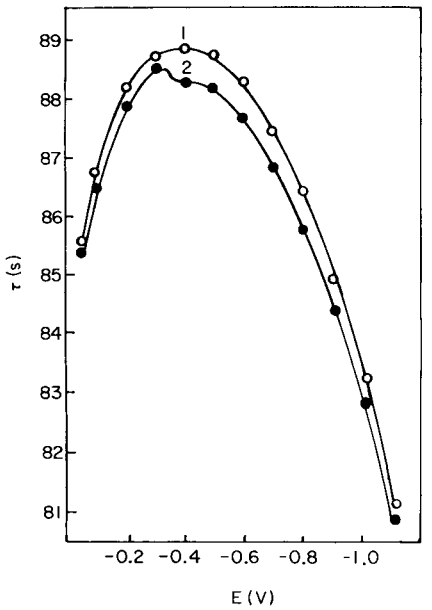

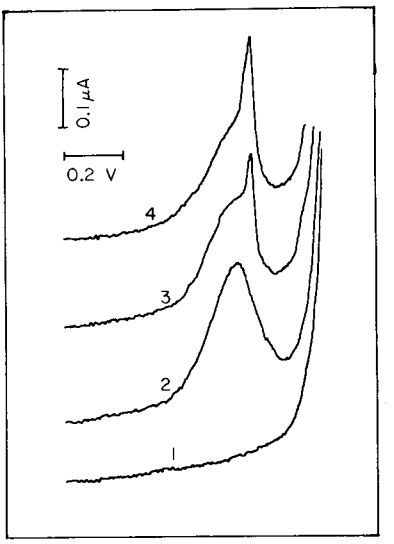

Fig. 5. Electrocapillary curve of DDT in buffer pH 6.5 with 20% methanol: (1) no DDT; (2) 2×10^{-6} mol l^{-1} DDT.

Fig. 6. Fast-scan d.p.p. curves of mixtures of TCB and biphenyl in supporting electrolyte at pH 6.5 with 20% methanol. Curves: (1) no addition; (2) 5×10^{-7} mol l^{-1} biphenyl added; (3) as (2) plus 1×10^{-7} mol l^{-1} TCB; (4) as (2) plus 2×10^{-7} mol l^{-1} TCB. Curves start at —0.40 V, accumulation time 30 s, accumulation potential —0.40 V, HMDE, polarization rate 20 mV s^{-1}.

sponding to the desorption of dodecylsulphate appeared, the detection limit for TCB increased to 20 μg l^{-1} and the range of linearity of calibration plot became narrower. Substances such as gelatine or Triton X-100 caused a decrease of the peak current when they were present in large amounts compared to TCB. The peak currents decreased to 10% of their original value when the concentration of Triton X-100 was 10 mg l^{-1}.

Polarographically active metal ions such as Cu^{2+}, Pb^{2+}, Cd^{2+} or Zn^{2+} had no effect on the TCB determination, provided that their concentration in the sample solution was not ten times greater than that of TCB; otherwise, masking with EDTA was necessary.

The interferences caused by the presence of organic compounds exhibiting adsorption properties similar to those of TCB are clearly serious. It was found that TCB could be determined in the presence of biphenyl only if the concentration ratio of TCB to biphenyl was $\geqslant 0.25$. Under these conditions, the peak of TCB was separated from that of biphenyl and its height increased linearly with increasing TCB concentration (Fig. 6). Biphenyl could not be determined in this way because its peak height decreased with increasing

TABLE 1

Determination of TCB in waste and natural waters

Sample no.	TCB found (mg l^{-1})		
	Spectr. method	Proposed method[a]	RSD (%)
1	0.07	0.065 ± 0.001[b]	1.6
2	1.04	1.025 ± 0.04[c]	4.2
3	11.20	10.75 ± 0.19[d]	1.8
4	68.30	67.8 ± 3.05[d]	4.5
5	167.80	160.2 ± 5.3[d]	3.3

[a]Mean and standard deviation for four measurements. [b]Potable water. [c]Creek water. [d]Waste water.

TCB concentration. The sum of TCB and biphenyl could be determined only after nitration of their mixture by the procedure described above. In this determination the peak corresponding to reduction of the nitro group was measured.

Severe interference was caused by DDT, because its desorption peak occurs at almost the same potential as that of TCB. Basically, there are two ways of eliminating the interferences caused by DDT; either the stability of TCB to acids can be applied or the compounds can be separated by high-performance liquid chromatography (h.p.l.c.). The possibilities of electrochemical detection of DDT and TCB in h.p.l.c. will be reported separately.

The influence of acids on the stability of TCB and DDT was studied. When a solution of DDT was treated with a 5-fold volume of diluted sulphuric acid (1 + 8) at elevated temperature (80°C for 15 min, no d.p.p. peak appeared in the subsequent voltammetric determination even after a 60-s accumulation period at −0.40 V. In contrast, identical treatment of TCB produced no change in the adsorptive voltammetric behaviour of this compound. Thus the interface of DDT can be eliminated chemically.

Analysis of waste and natural water

All the above experimental data led to the recommended procedure given under Experimental for the determination of TCB in water. The measurement cycle can be automated. In the present work, measurements were done automatically with the PA-4 analyzer, which enables all steps in the measurement cycle to be programmed.

Table 1 summarizes the results of the analysis of various types of water. These results agree very well with those obtained by spectrophotometric measurements [8].

REFERENCES

1 T. Cairns and E. G. Siegmund, Anal. Chem., 53 (1981) 1183A, 1599.
2 M. von Stackelberg and W. Stracke, Z. Elektrochem., 53 (1949) 118.
3 S. O. Farwell, F. A. Beland and R. D. Geer, Anal. Chem., 47 (1975) 895.
4 S. P. Perone, D. O. Jones and W. F. Gutknecht, Anal. Chem., 42 (1970) 1151.
5 L. Novotný, I. Smoler and J. Kuta, Collect. Czech. Chem. Commun., 48 (1983) 964.
6 R. Kalvoda, Anal. Chim. Acta, 138 (1982) 11.
7 M. Březina and P. Zuman, Polarography in Medicine, Biochemistry and Pharmacy, Interscience, New York, 1958, p. 208.
8 J. Jenik, to be published.

Analytica Chimica Acta, 161 (1984) 325—331
Elsevier Science Publishers B.V., Amsterdam — Printed in The Netherlands

STOPPED-FLOW LINEAR SWEEP VOLTAMMETRY AT THE RETICULATED VITREOUS CARBON ELECTRODE IN A FLOW INJECTION SYSTEM
Determination of Dopamine in the Presence of Ascorbic Acid

T. P. TOUGAS[a] and D. J. CURRAN*
Department of Chemistry, University of Massachusetts, Amherst, MA 01003 (U.S.A.)
(Received 27th June 1983)

SUMMARY

A flow injection system was used to introduce a sample into a flow-through electrochemical cell based on a reticulated vitreous carbon (r.v.c.) electrode. Products of the initial electrolysis are trapped in the porous electrode by stopping the flow. Linear sweep voltammetry under stopped-flow conditions forms the basis of a determination of a reversibly electrolyzed species in the presence of an irreversibly electrolyzed species. The determination of dopamine in the presence of ascorbic acid was used as an illustrative example. Response varied linearly with dopamine concentration between 8×10^{-7} and 3×10^{-5} M and the detection limit (S/N = 3) was 5×10^{-7} M dopamine.

Controlled-potential electrochemical detectors are well suited for use with flow injection systems. However, in some cases the selectivity of the method is inadequate when operating in a direct current (d.c.) amperometric mode. The use of either differential pulse [1] or alternating current (a.c.) [2, 3] approaches increases detector selectivity by allowing the detection of an analyte in the presence of a more easily electrolyzed species. One of the most difficult situations occurs when the analyte and interference are electrolyzed at the same potential. Sometimes, this problem can be solved by discriminating between the species on the basis of reaction mechanisms. Detectors with two working electrodes in series [4, 5] are capable of selectively determining a reversible (or quasireversible) species in the presence of an irreversible species even if the voltammetric waves overlap. The drawback of this approach is that it requires independent control of the potential of two working electrodes in contact with the same carrier stream. Combining a flow injection system with stopped-flow linear sweep voltammetry achieves the same degree of selectivity as the two-electrode approach, but has the advantage of using only one working electrode.

The dopamine/ascorbic acid system was selected to demonstrate the

---

[a]Department of Chemistry, University of Lowell, One University Avenue, Lowell, MA 01854 (U.S.A.)

0003-2670/84/$03.00

stopped-flow approach because the presence of large amounts of ascorbic acid has been previously recognized as a major interference in the direct electrochemical determination of catecholamines in brain tissue [6]. The described procedure relies on the irreversible behavior of the ascorbic acid oxidation [7, 8] and the quasi-reversible behavior of dopamine [9, 10] in acidic media.

A coulometric detector employing a porous glassy carbon working electrode was used to achieve this selectivity. The porous structure of this reticulated vitreous carbon (RVC) electrode had a void volume of approximately 150 μl. This volume is large enough to contain a substantial portion of the sample peak volume. Flow-injection/stopped-flow linear sweep voltammetry involves the following: (1) setting the working electrode potential at a value at which the analyte can be completely electrolyzed, (2) injecting a sample volume with a loop injection valve, (3) monitoring the detector response to the injected sample, (4) trapping part or all of the sample peak volume in the porous electrode, (5) applying a linear potential ramp to the working electrode, and (6) monitoring the current from the reduction or oxidation of the species trapped in the working electrode (product of the first electrolysis). Quantitative information is obtained from the height of the current-voltage curve (step 5). This technique requires that the electron-transfer process for the analyte be electrochemically reversible or quasireversible because the quantitative signal is derived from a sequence of oxidation (or reduction) of analyte followed by reduction (or oxidation) of this product back to the original species. It therefore discriminates against any species which are irreversibly electrolyzed because either the electron transfer reaction is irreversible or the product is lost because of a coupled homogeneous reaction.

EXPERIMENTAL

Reagents and solutions

Catecholamines as free bases or hydrochloride salts were from Sigma Chemical Co. Ascorbic acid was certified ACS grade. Distilled-deionized water was used throughout. All other reagents were reagent grade. Stock solutions of dopamine and ascorbic acid were prepared in 0.28 M sulfuric acid at concentrations of approximately 2 mM. The stock solution of ascorbic acid was prepared each day immediately before use to prevent loss by oxidation. In addition, the 0.28 M sulfuric acid was deoxygenated with nitrogen for 20 min prior to use in preparing solutions. The dopamine stock solution was stored sealed at 2°C. A series of dilutions of the dopamine stock solution was prepared with or without ascorbic acid present. The 0.28 M sulfuric acid was also used as the carrier stream.

Equipment

An EG&G Princeton Applied Research Model 173 potentiostat equipped with a PARC Model 179 digital coulometer, and PARC Model 179 universal

programmer were used for applying the electrochemical signals and measuring the current response. A Heath Model EU80A voltage reference source with voltage-to-current converter was used to supply current for offset purposes. The electrochemical cell and flow system have been described [11]. Briefly, the cell is based on a RVC working electrode and features a 2.8-mm diameter RVC cylinder which is 24.2 mm long, surrounded on the sides of the cylinder by a Millipore HVLP-147-00 porous membrane. A cylinder of stainless steel placed on the other side of the membrane serves as the counter electrode. The reference electrode contacts the flow stream before the stream left the nylon cell block. Fittings used to make connections to the cell were a combination of grippers and 1/4-28 threaded nylon LC connectors (Rainin). Teflon tubing used in the flow line was 1.6-mm o.d., 0.5-mm i.d. The inlet fitting was seated against the top of the RVC piece and therefore the diameter of the entrance stream was considerably smaller than the electrode diameter. A gravity feed system was used. A glass reservoir was placed 1.5 m above the cell. The flow was controlled by a stopcock and measured with a Gilmont flowmeter. Non-teflon parts of the flow line were glass. Samples were introduced with a Rheodyne injection valve (Model 50-20). A loop volume of 62.8 ± 0.06 μl was found by a gravimetric procedure involving twenty injections of 1.217 M sodium chloride solution. Flow rates up to 5 ml min^{-1} could be achieved. The entire apparatus (flow system, injection valve, cell and instrumentation) was placed in a Faraday cage grounded to a water pipe.

RESULTS AND DISCUSSION

Hydrodynamic voltammograms of ascorbic acid, dopamine, epinephrine, and L-dopa were obtained by pumping solutions of these compounds continuously through the cell and applying a linear potential ramp. These individual voltammograms, superimposed on the same potential axis, are displayed in Fig. 1. This figure shows clearly that it is impossible to detect catecholamines selectively in the presence of ascorbic acid by d.c. amperometry because ascorbic acid is more easily oxidized than the catecholamines in this acidic medium. Thus, at a potential at which catecholamine oxidation occurs, ascorbic acid also undergoes oxidation. The potential for the flow injection step in the procedure was selected from these experiments to be well out on the limiting current plateau of the hydrodynamic wave of dopamine at 900 mV vs. SCE.

Cyclic voltammetry of ascorbic acid at a glassy carbon electrode in quiet solution confirmed the well known irreversible nature of this oxidation. An anodic peak corresponding to the oxidation was observed, but a cathodic peak was not present. This is consistent with previous studies [7] which characterize this reaction as an EC mechanism. Dopamine, in contrast, exhibits both an anodic and cathodic peak characteristic of a quasireversible system. It is on the basis of this difference in reaction mechanism that

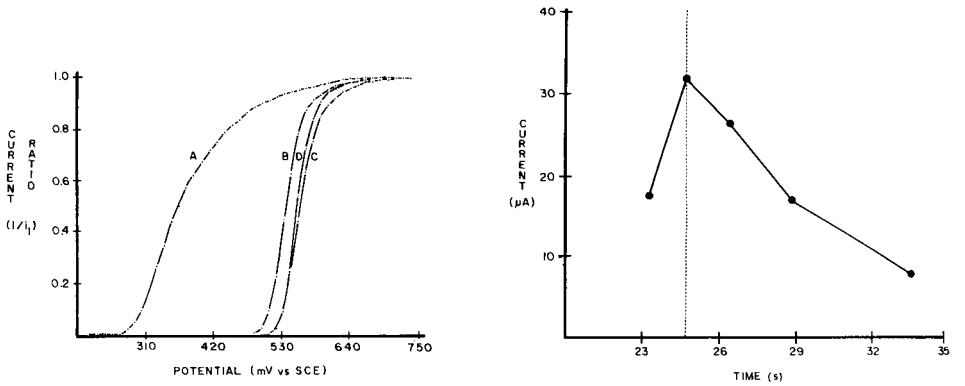

Fig. 1. Hydrodynamic voltammograms: (A) ascorbic acid; (B) dopamine; (C) epinephrine; (D) L-DOPA. Ratio of current to limiting current vs. potential at a scan rate of -2 mV s^{-1} and a flow rate of 1.0 ml min^{-1}.

Fig. 2. Peak current of the linear sweep voltammogram as a function of time of valve closing after injection. Dashed line represents the time at which the flow-injection peak maximum was detected.

flow-injection/stopped-flow linear-sweep voltammetry can achieve the direct measurement of dopamine in the presence of ascorbic acid.

An experimental condition to be considered is the timing of closing the valve to stop the flow and trap the peak volume. The peak current of the linear sweep experiment was measured as a function of time of valve closing after injection (Fig. 2). The maximum response was obtained when the valve was closed at the time when the flow injection peak reach a maximum. This is represented by the dashed line in Fig. 2. Flow was interrupted by manually turning the injection valve halfway between the inject and load position. This was possible because gravity feed was used for solvent delivery. The data for Fig. 2 were obtained by stopping the flow at various points on the detected flow-injection peak. A high chart speed (20 cm min^{-1}) was used so that the time from injection to stopping the flow could be measured. This latter point was detected as a sudden distinct drop in current. It was advantageous that the maximum response occurred when the valve was closed at the flow injection peak maximum because this provides an unambiguous signal for closing the valve.

The typical current-voltage curve for the linear sweep portion of the experiment when either dopamine or a mixture of dopamine and ascorbic acid is injected is illustrated in Fig. 3. This wave is due to the reduction of the corresponding quinone back to the original dopamine (ascorbic acid has no effect on the position of the wave) and when ascorbic acid alone is injected, no wave is observed. In the absence of ascorbic acid, the average peak potential was 485 ± 3 mV (SCE). Peak potentials were measured over a concentration range of 8.62×10^{-7} to 3.45×10^{-5} M dopamine. The average

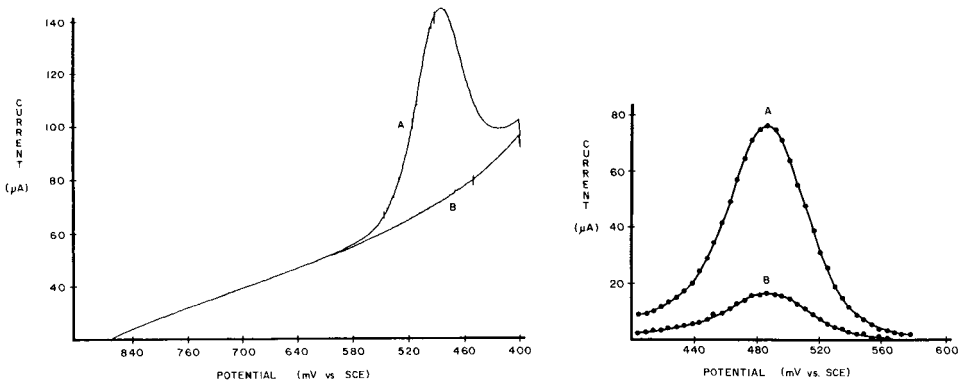

Fig. 3. Stopped-flow linear sweep voltammogram of dopamine: (A) 3.45×10^{-4} M dopamine; (B) background current. Experimental conditions are listed in Table 1.

Fig. 4. Stopped-flow linear sweep voltammograms for dopamine corrected for the background current: (A) 3.45×10^{-4} M; (B) 6.89×10^{-5} M.

peak potential over the same concentration range in the presence of 1.36×10^{-4} M ascorbic acid was 485 ± 2 mV (SCE).

When the current-voltage curves were corrected for background (Fig. 4), the resulting curves more closely resembled the gaussian shape of the wave for a reduction in a thin-layer cell [12] than the response typically associated with a linear sweep experiment at a stationary electrode under diffusion-controlled conditions [13]. This suggests that one way to view the porous electrode is as a series of interconnected thin-layer cells. The pore radius (125 μm) would be analogous to the spacer thickness.

The response shown in Fig. 4 also provides a way to estimate the fraction of oxidized dopamine that is reduced back to dopamine. The area under these current—voltage curves is proportional to the coulombs of charge passed and is easily related to the number of equivalents electrolyzed. The area found corresponded to electrolysis of 63% of the original dopamine injected. A value less than 100% was expected and is consistent with the relationship between the flow-injection peak volume and the void volume of the RVC electrode. The latter was estimated to be 150 μl based on the electrode dimensions and the manufacturer's specifications. The average flow-injection peak volume, 249 μl, was determined from the strip chart recording of the flow injection response.

The linearity of response with concentration was established with a calibration curve. Dopamine calibration curves were obtained both in the presence and absence of ascorbic acid. Table 1 summarizes the experimental conditions used to obtain calibration curves and presents the results of one such set of curves. The curves covered a range of dopamine concentration from 8.62×10^{-7} to 3.45×10^{-5} M and indicated that ascorbic acid had little

TABLE 1

Results for dopamine calibration graphs[a]

Conc. of ascorbic acid (μM)	0	136
Slope (A M^{-1})	0.2123	0.2020
Intercept (A)	-6.6×10^{-8}	-5.3×10^{-8}
Data points	11	8
r (correlation coeff.)	0.9993	0.9995
Std. error of estimate (A)	1.06×10^{-14}	7.97×10^{-15}
Std. dev. of slope (A M^{-1})	0.0028	0.0027
Std. dev. of intercept (A)	4.7×10^{-8}	5.3×10^{-8}

[a]Conditions: volume injected, 62.8 μl; carrier stream, 0.28 M H_2SO_4; flow rate, 1.42 ml min^{-1}; initial potential, +900 mV (SCE); sweep rate, -2 mV s^{-1}.

effect on the dopamine response. The detection limit (S/N = 3) was 5×10^{-7} M based on the background noise and the lowest point on the calibration curve.

While this work focused on the determination of dopamine in the presence of ascorbic acid, it should be a relatively simple matter to determine both compounds. By using the area of the flow injection peak, the combined number of equivalents of ascorbic acid and dopamine can be determined. This is possible because of the coulometric nature of the RVC detector [11]. Because total electrolysis occurs, the peak area is directly proportional to the equivalents of ascorbic acid and dopamine injected. If the stopped-flow technique is used to obtain the amount of dopamine, the amount of ascorbic acid can be obtained by difference. Determination of the dopamine by the stopped-flow technique, unlike the flow injection portion, requires a calibration curve; the conversion back to dopamine is less than complete because of the relative sizes of the flow injection peak and the electrode void volume.

One improvement would be to achieve total conversion in the stopped-flow step as well as in the flow injection experiment. The area under the current-voltage curve resulting from the linear potential sweep could then be directly related to the amount of dopamine present. To achieve total conversion, the entire flow injection peak must be trapped in the electrode. A combination of smaller injection volume, larger electrode, and smaller dead volume between injection valve and detector would improve the percentage of peak volume trapped.

This research was aided by a Grant-in-Aid of Research from Sigma Xi, The Scientific Research Society. This paper was taken in part from the Ph.D. thesis of T. P. Tougas and was presented in part at the 12th Northeast Regional ACS Meeting, University of Vermont, June 1982.

REFERENCES

1 D. G. Swartzfager, Anal. Chem., 48 (1976) 2189.
2 W. Kemula and W. Kutner, J. Chromatogr., 204 (1981) 131.
3 M. Alkayer, J. Vallon, Y. Pegon and C. Bichon, Anal. Chim. Acta, 124 (1981) 113.
4 C. L. Blank, J. Chromatogr., 117 (1976) 35.
5 D. A. Roston and P. T. Kissinger, Anal. Chem., 54 (1982) 429.
6 R. N. Adams, Anal. Chem., 48 (1976) 1126A.
7 S. Perone and W. J. Kretlow, Anal. Chem., 38 (1966) 1760.
8 J. J. Ruiz, A. Aldaz and M. Dominguez, Can. J. Chem., 55 (1977) 2799.
9 A. W. Sternson, R. McCreedy, B. Feinberg and R. N. Adams, J. Electroanal. Chem., 46 (1973) 313.
10 M. D. Hawley, S. V. Tatawawada, S. Piekarski and R. N. Adams, J. Am. Chem. Soc., 89 (1967) 447.
11 D. J. Curran and T. P. Tougas, Anal. Chem., 56 (1984) 672.
12 A. T. Hubbard and F. C. Anson, J. Electroanal. Chem., 4 (1970) 129.
13 R. S. Nicholson and I. Shain, Anal. Chem., 36 (1964) 706.

Analytica Chimica Acta, 161 (1984) 333—341
Elsevier Science Publishers B.V., Amsterdam — Printed in The Netherlands

THE BEHAVIOUR OF THE SILVER SULPHIDE PRECIPITATE-BASED ION-SELECTIVE ELECTRODE IN THE LOW CONCENTRATION RANGE

E. G. HARSÁNYI, K. TÓTH and E. PUNGOR*

Institute for General and Analytical Chemistry, Technical University, 1502-Budapest (Hungary)

(Received 28th February 1984)

SUMMARY

The anomalous behaviour of the precipitate-based silver sulphide ion-selective electrode in the low concentration range of silver and sulphide ions is described. The excess of silver ion at the electrode surface, caused by adsorption or oxidation, is responsible for the deviations from the ideal Nernstian response. The adsorption/desorption processes were studied in a microcell by using combined potentiometric and atomic absorption measurements. The oxidation—reduction processes were studied by using polarized electrodes.

The silver sulphide electrode responds both to silver and sulphide ions. The solubility product of the silver sulphide is very low (1.6×10^{-49} at 18°C [1]). The dissolution of silver sulphide in water at different pH values was measured by radiochemical methods by Schwarzenbach and co-workers, who showed that the dissolution, in the form of silver ion or different silver complexes, could provide as much as 10^{-8}—10^{-7} mol l^{-1} total silver in solution [2]. This means that the solubility of the membrane itself does not play a significant role in establishing the practical lower limit of detection of the electrode. However, the ideal Nernstian response is usually valid only down to 10^{-4}—10^{-5} mol l^{-1} silver or sulphide ion concentration [3]. Below this level, a positive deviation in the response to silver ion can be observed, i.e., the electrode potentials measured are higher than the theoretical values and correspond to higher concentrations of silver ion. In the case of sulphide, the response shows the opposite effect, i.e., the positive deviation generally observed in the electrode potential corresponds to lower concentrations of sulphide. Different authors have tried to explain this anomaly and have attempted to eliminate it so as to reach lower detection limits [4—8].

The deviations mentioned have been attributed to heavy metal contaminants in the system, adsorption of the test ions or counter ions at the surface, or oxidation of sulphide decreasing the concentration of free sulphide ions in the solution phase. In analytical practice, ascorbic acid is used to prevent oxidation of the sulphide in solution. Different authors have applied different concentrations of ascorbic acid and obtained similar detection limits for

0003-2670/84/$03.00

sulphide. Samples are generally made up in sodium hydroxide solutions to avoid loss of sulphide as hydrogen sulphide. However, the alkaline medium with reducing agents was not recommended by Gulens et al. [9, 10] because in these conditions the surface of the silver sulphide pellet is reduced and some metallic silver is formed on the surface. In their opinion, the super-Nernstian behaviour could be due to a mixed potential caused by the partly reduced surface. The role of oxidizing agents in producing anomalies in low concentration ranges was stressed by Wilson and Pool [11].

The aim of this work was to identify the reasons for the anomalies observed with the silver sulphide electrode in low concentration ranges and to develop satisfactory procedures for determining sulphide in the concentration range 10^{-4}—10^{-6} mol l^{-1}. Adsorption and oxidation processes, which are supposed to be reasons for the anomalies mentioned, were studied by using preconditioned electrodes and also polarized electrodes.

EXPERIMENTAL

Electrode potential measurements and the silver sulphide electrode

Home-made precipitate-based pellets were used as sensing membranes. The electrode membranes were made in the usual manner with precipitates prepared from 2.0 mol l^{-1} solutions of silver nitrate and sodium sulphide in a 2:1 mole ratio. The pellets were glued to glass tubes of 12-mm external diameter. The internal electrolyte was 10^{-3} mol l^{-1} $AgNO_3$ and the internal electrode was a silver wire. Separate electrodes were used for the studies of the responses to silver and sulphide ions. A Radelkis OP-082OP Ag/AgCl reference electrode was used. Electrode potentials were measured with a Radelkis OP-211/1 type digital pH meter. The volumes of the test solutions were 25 ml or 300 μl; in the latter case, the processes occurring at the electrode/solution interface could also be followed by measuring the concentration changes in the solution by atomic absorption spectrometry, as has already been shown [12, 13].

The potentials were read after a measuring time of 3 min for the large volumes and after 10 min for the 300-μl volumes, when the calibration curves were prepared. Potentials as a function of the time were recorded on a Radelkis OH-814/1 recorder. All measurements were made at 25 ± 0.5°C.

Polarization procedure. Several authors [5, 11] have attributed a large role to oxidation of the silver sulphide membrane material in the low sulphide concentration range. Oxidation and reduction processes were studied by using anodically and cathodically polarized electrodes. The simple arrangement used is shown in Fig. 1. Again, test volumes of 25 ml and 300 μl were used. The anodic or cathodic current applied was 5.9, 11.8 or 17.7 μA.

Solutions

Silver nitrate solutions were prepared from a 1.0 mol l^{-1} stock solution made from the reagent-grade chemical. Standard solutions were prepared by

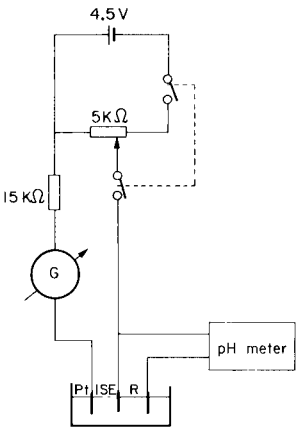

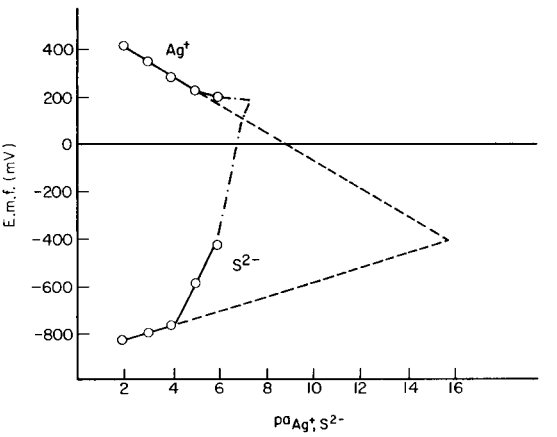

Fig. 1. Arrangement used for the polarization experiments.

Fig. 2. Calibration curves for silver and sulphide ions measured in 25 ml of solution.

dilution in the concentration range 10^{-6}—10^{-2} mol l^{-1}, 0.1 mol l^{-1} potassium nitrate being used to maintain the ionic strength.

Sulphide solutions were made from reagent-grade sodium sulphide. The 0.1 mol l^{-1} stock solution was prepared in 0.5 mol l^{-1} sodium hydroxide in order to avoid H_2S or HS^- formation. The sulphide concentration was determined by iodimetric titration [14]. Ascorbic acid (5 g l^{-1}) was added to avoid formation of sulphur in the solution. The ionic strength in the standard solutions was kept constant with sodium hydroxide.

Before calibration measurements, the electrodes were conditioned in distilled water or in the chosen conditioning solutions for 30 min, while stirring.

RESULTS

The electrode behaviour was first checked by preparing calibration curves for silver and sulphide ions. The electrodes were first polished and then washed with distilled water. The calibration curves are shown in Fig. 2. The deviations from Nernstian response in the low concentration ranges are in accordance with the results found in the literature. The practical lower limits of detection found here for the electrodes studied were 3.6×10^{-6} mol l^{-1} and 4×10^{-5} mol l^{-1} for silver and sulphide, respectively. Figure 2 also indicates the theoretical limit of detection, i.e., the point of intersection of the extrapolated linear portions of the silver and sulphide calibration plots.

There are three possible reasons for the deviations obtained: (a) adsorption of ions at, and dissolution of ions from, the membrane surface; (b) redox

reactions at the electrode/solution interface; (c) some influence of the activity of defects in the solid phase on the behaviour of the sensors at low concentrations, as suggested by Morf et al. [8] for semiconductor-type electrodes. It has already been shown for silver iodide-based electrodes that deviations from Nernstian response at low concentrations cannot be attributed to the third factor only [12].

The dissolution of silver ions from the membrane surface and their adsorption at the surface was proved by measurements in the small solution volumes, and polarized electrodes were used to assess any oxidation processes.

Measurements in silver nitrate solutions in the small cell

Pretreatment in distilled water. A calibration curve for silver ion was evaluated in the concentration range 10^{-6}—10^{-2} mol l^{-1}. Figure 3A shows the potential readings taken immediately after immersion of the electrodes and after 10 min, plotted against the negative logarithm of silver ion activity. The difference between the two curves shows that the silver concentration in the solution decreased with time. Supporting evidence was given by atomic absorption spectrometry (a.a.s.) of silver in the solutions: the silver concentrations measured after 10 min were lower than the nominal values. When the potentials measured 10 min after immersion of the electrodes were plotted as a function of the actual silver ion concentration found by a.a.s., a straight line with Nernstian slope was obtained down to 10^{-6} mol l^{-1} silver

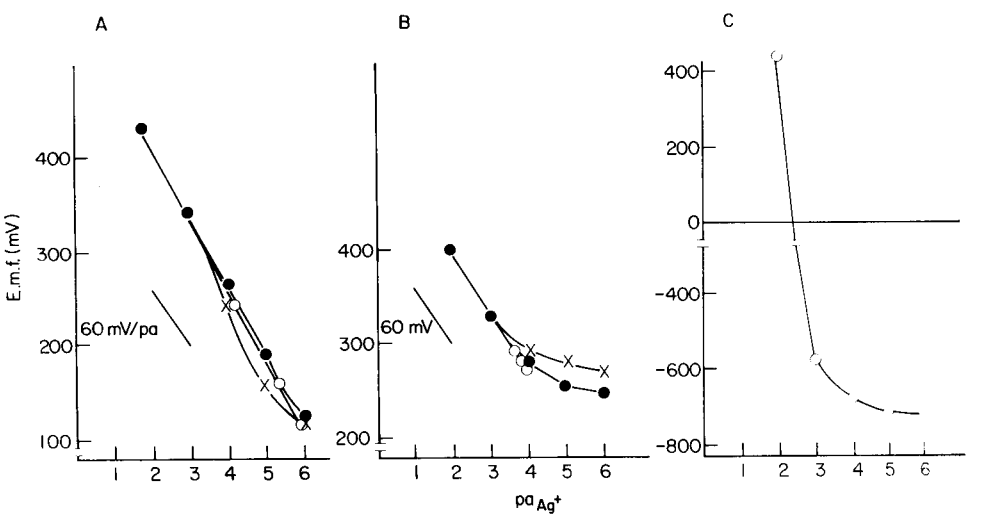

Fig. 3. Silver ion calibration curves with measurements in 300 µl of solution: (A) with a polished and cleaned electrode; (B) with an electrode pretreated in 10^{-2} mol l^{-1} silver nitrate; (C) with an electrode pretreated in 10^{-2} mol l^{-1} sodium sulphide. Curves: (•) measurements done immediately after insertion of electrodes; (×) measurements after 10 min; (○) measurements after 10 min and correction of silver concentration based on a.a.s. measurements.

concentration. The difference in the two concentrations (i.e., nominal and actual) corresponds to the silver adsorbed from the solution. The amount of silver adsorbed at different nominal silver ion concentrations was calculated and the Freundlich adsorption isotherm was evaluated from the data, analogously to earlier work [12, 13]. The amount of silver adsorbed on the cell wall was corrected for. The adsorption isotherm fitted well in three parallel cases up to 10^{-4} mol l^{-1} silver ion.

Pretreatment in 10^{-2} mol l^{-1} silver nitrate. As in the previous experiment, calibration curves were evaluated in the concentration range 10^{-2}—10^{-6} mol l^{-1} silver ion (Fig. 3B). In this case, the difference between the curves obtained immediately and after 10 min (i.e., a potential increase with time) corresponds to an increase in the silver ion concentration in the solution because of desorption from the electrode surface. Again, the data were supported by a.a.s. results for silver ion in the solution (Fig. 3B); the calibration plot based on the actual (measured by a.a.s.) silver concentrations has a Nernstian slope down to 10^{-4} mol l^{-1}.

Pretreatment in 10^{-2} mol l^{-1} sodium sulphide. Pretreatment in a solution of the counter ion resulted in the calibration curve given in Fig. 3C. Silver ion response was obtained only at concentrations exceeding 10^{-2} mol l^{-1} silver ion. Below this silver ion concentration, sulphide present at the surface gradually reacts with the silver ions from the test solution. Figure 3C illustrates the effect of the ion excess at the membrane surface on the formation of the actual electrode potential.

Measurements in sodium sulphide solutions

Pretreatment in distilled water. The calibration curves obtained in the concentration range 10^{-6}—10^{-2} mol l^{-1} sulphide were the same in 25-ml volumes as in 300-μl volumes (Fig. 4A); a super-Nernstian response below 10^{-4} mol l^{-1} was recorded in both cases.

Pretreatment in 10^{-2} mol l^{-1} sodium sulphide. After pretreatment in the sulphide solution, negative deviation from the Nernstian curve was observed (Fig. 4B), which means that the sulphide ion concentration in the solution increased because of desorption of sulphide from the membrane.

Pretreatment in 10^{-2} mol l^{-1} silver nitrate. After treatment of the electrode in a solution of the counter ion, a response to sulphide was obtained only at concentrations exceeding 10^{-2} mol l^{-1} (Fig. 4C). Below this concentration, the excess of silver ion at the membrane surface has a predominant effect on the potential.

Measurements with polarized electrodes

These measurements were used only to study the response to sulphide, in order to elucidate the role of oxidation—reduction processes in the formation of the super-Nernstian response.

Anodic polarization. When different anodic currents were applied, the potential increase of the calibration curve increased with increasing current,

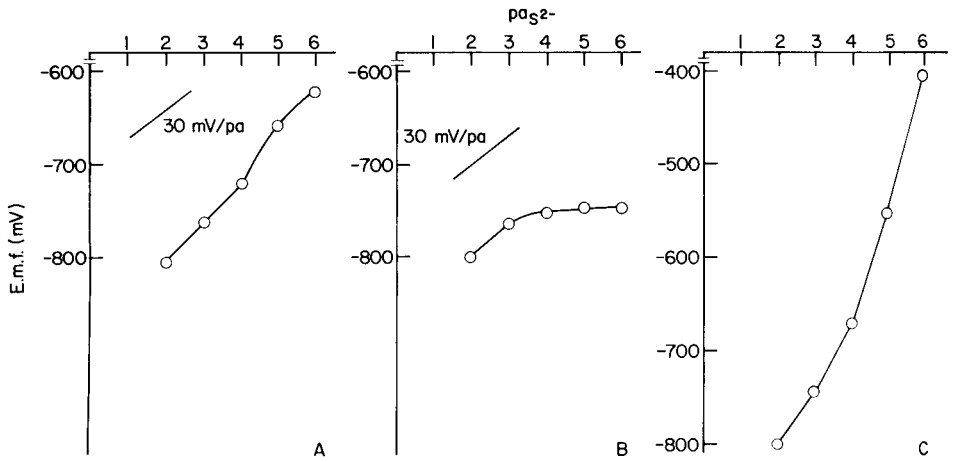

Fig. 4. Sulphide ion calibration curve in 300 μl of solution: (A) with a polished and cleaned electrode; (B) with an electrode pretreated in 10^{-2} mol l^{-1} sodium sulphide; (C) with an electrode pretreated in 10^{-2} mol l^{-1} silver nitrate.

and the E^0 value shifted to higher potentials as shown in Fig. 5A. The E^0 shift in the direction of more positive potentials means an increased sulphur/metal ratio at the surface of the electrode, as indicated by Koch [15]. For these measurements, the solution volume was 25 ml.

Cathodic polarization. When cathodic polarization was used at different applied currents (Fig. 5B), the super-Nernstian portion of the calibration curve gradually disappeared.

Dissolution of silver ion. The dissolution of silver ion from the electrode under anodic polarization conditions was measured for 300-μl volumes of 10^{-1} mol l^{-1} KNO_3. The dissolved silver ion concentration is shown as a function of applied current in Fig. 6. The silver ion concentration increases

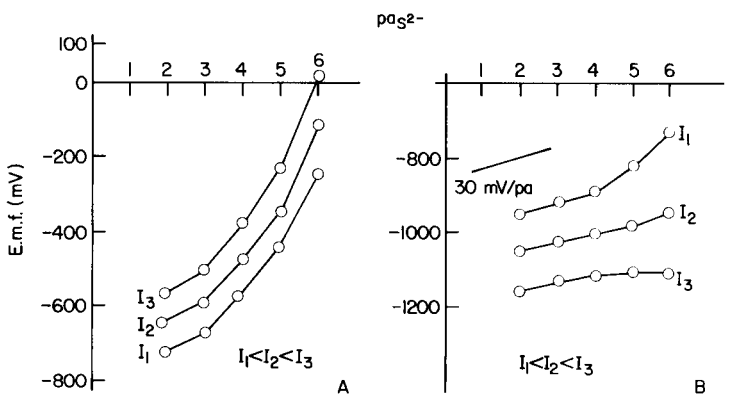

Fig. 5. Calibration curves for sulphide: (A) with anodic current; (B) with cathodic current. Applied current: I_1 = 5.9 μA; I_2 = 11.8 μA; I_3 = 17.7 μA.

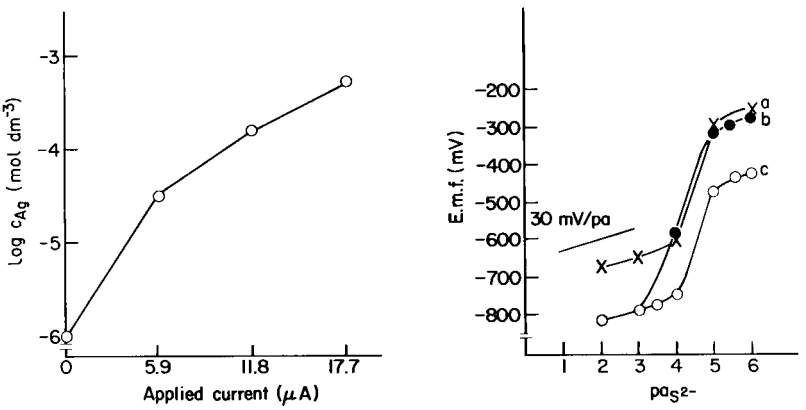

Fig. 6. Silver ion concentration measured in 300 μl 0.1 mol l^{-1} KNO_3 as function of the anodic current applied.

Fig. 7. Standard addition curves with the silver sulphide electrode: (a) conditioned in 10^{-2} mol l^{-1} silver nitrate solution; (b) polarized with an anodic current of 2.9 μA; (c) untreated, polished and cleaned. For details, see text.

rapidly as the anodic current is increased. Without current, the silver ion concentration measured in 300 μl of 0.1 M KNO_3 was 10^{-6} mol l^{-1}. The silver concentrations decreased when a cathodic current was applied. These results show that anodic polarization causes oxidative dissolution of the membrane material, resulting in an excess of silver ion at the surface of the electrode.

DISCUSSION

The deviations from ideal Nernstian response of the silver sulphide precipitate-based electrode can be explained in the following way. The positive deviation in the case of the silver ion function is due to an excess of silver ion at the membrane surface. This excess probably originates from previously adsorbed silver ions which cannot be removed completely. The super-Nernstian positive deviation in the case of the sulphide ion response is also due to the excess of silver ions at the membrane surface. In the above model experiments, similar super-Nernstian behaviour was observed when the electrode was pretreated in silver nitrate solution or when an anodic current was applied (Figs. 4C and 5A).

This similarity is illustrated better in Fig. 7, which shows standard addition curves for the silver sulphide electrode. These measurements were done by adding portions of standard sulphide solution gradually to 25 ml of solution which contained 0.5 mol l^{-1} sodium hydroxide and 5 g l^{-1} ascorbic acid. Curve (a) gives the results obtained with an electrode conditioned in 10^{-2} mol l^{-1} silver nitrate solution; curve (b) was obtained with the electrode polarized (2.9-μA anodic current). Curve (c) relates to an untreated polished

and cleaned electrode. From this "titration" curve, the potential corresponding to the "equivalence point" was found to be about 600 mV, corresponding to 10^{-8} mol l^{-1} sulphide ion, by using a sulphide calibration graph, which should be the practical detection limit of the electrode. The excess of silver ion on anodic polarization is a consequence of the reaction: $Ag_2S \rightarrow 2Ag^+ + S^0 + 2e^-$, which has been identified by several authors [16—19]. The surface deterioration after anodic polarization can be seen clearly on the electron micrographs shown in Fig. 8.

The effect of cathodic polarization is similar to that observed with electrodes pretreated in sodium sulphide solution. In this case, excess of sulphide is present at the membrane surface. On cathodic reduction, the reaction is probably $Ag_2S + 2e^- \rightarrow 2Ag + S^{2-}$, which was also mentioned in the work of Sato [19].

The anomalies in the low concentration range with the silver sulphide-based electrode are due to excess of silver ion at the membrane surface. This excess is due to physical adsorption of ions or to redox reactions; the two processes cannot be separated in practical measurements.

The super-Nernstian response can be stabilized by using an anodically polarized electrode, and measurements of sulphide ion are then possible down to the 10^{-6} mol l^{-1} level by using calibration under similar conditions. Calibrations and measurements can also be done by using anodic polarization for pretreatment only; this proved to be more reproducible than measurements under applied current.

The detection limit attainable with the silver sulphide-based electrode is highly dependent on the history of the electrode. Both the method of

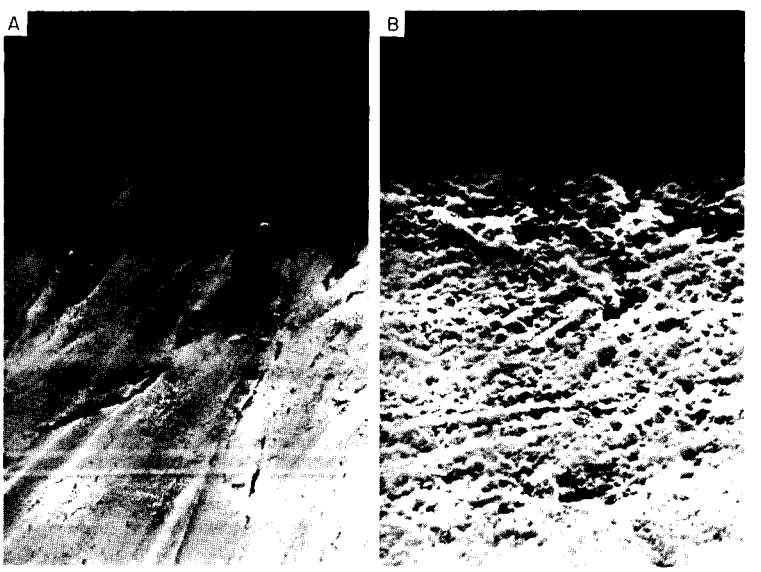

Fig. 8. Electron micrographs: (A) an untreated Ag_2S electrode; (B) an Ag_2S electrode pellet after anodic polarization.

pretreatment (chemical or electrochemical) and the direction of the calibration measurements are important, because these features influence the electrode surface actually used.

REFERENCES

1 CRC Handbook of Chemistry and Physics, 62nd edn., CRC Press, Boca Raton, FL, 1981—82.
2 J. Eggers, Physikalische und Chemische Eigenschaften der Silberhalogenide und des Silbers, Akademische Verlaggesellschaft, Frankfurt am Main, 1968.
3 D. Midgley, Ion Select. Elect. Rev., 3 (1981) 43.
4 I. Sekerka and J. F. Lechner, Anal. Chim. Acta, 93 (1977) 139.
5 D. J. Crombie, G. J. Moody and J. D. R. Thomas, Anal. Chim. Acta, 80 (1975) 1.
6 E. W. Bauman, Anal. Chem., 46 (1974) 1345.
7 R. Bock and H. J. Puff, Z. Anal. Chem., 240 (1968) 381.
8 W. E. Morf, G. Kahr and W. Simon, Anal. Chem., 46 (1974) 1538.
9 J. Gulens, K. Jessome and C. K. MacNeill, Anal. Chim. Acta, 96 (1978) 23.
10 J. Gulens and B. Ikeda, Anal. Chem., 50 (1978) 782.
11 A. C. Wilson and K. H. Pool, Anal. Chim. Acta, 109 (1979) 149.
12 E. G. Harsányi, K. Tóth, L. Pólos and E. Pungor, Anal. Chem., 54 (1982) 1094.
13 E. G. Harsányi, K. Tóth and E. Pungor, Anal. Chim. Acta, 152 (1983) 163.
14 E. Schulek and Z. L. Szabó, A. Kvantitativ Analitikai Kémia Elvi Alapjai és Módszerei, Tankönyvkiadó, Budapest, 1966.
15 D. F. A. Koch, in J. O. M. Bockris and B. E. Conway (Eds.), Modern aspects of Electrochemistry, Vol. 10, Plenum, New York, 1975.
16 F. G. K. Baucke, Z. Anal. Chem., 282 (1976) 105.
17 W. Jaenicke, E. M. Khairy and W. Schäfer, Ber. Bunsenges. Phys. Chem., 70 (1966) 421.
18 W. Naddack, K. Wrabetz and W. Herbst, Z. Elektrochem., 59 (1955) 96.
19 M. Sato, Econ. Geol., 55 (1960) 1202.

Analytica Chimica Acta, 161 (1984) 343—348
Elsevier Science Publishers B.V., Amsterdam — Printed in The Netherlands

Short Communication

CONSTRUCTION OF AN IMMOBILIZED ASPARAGINASE SENSOR AND DETERMINATION OF ASPARAGINE AND ASPARAGINASE IN HUMAN BLOOD SERUM

D. P. NIKOLELIS

Laboratory of Analytical Chemistry, 104 Solonos Street, University of Athens, Athens 106 80 (Greece)

(Received 2nd December 1983)

Summary. The sensor is based on asparaginase held on an ammonia gas sensor. Asparagine in the range 2.0×10^{-5}—2.3×10^{-3} M gives a linear calibration graph with response times of 5—2 min. Asparagine can be determined in human serum. Asparaginase (0.01—0.2 U in 0.1 ml of sample) is determined in aqueous solution or serum by adding asparagine to the sample, and measuring the ammonia evolved. Results for both methods agree well with those obtained by the combined Conway—Russell method.

L-Asparaginase of *Escherichia coli* is an effective therapeutic agent for certain types of malignant disease whereas asparagine is an essential amino acid in the sensitive tumors, which depend on the host for the supply of asparagine [1]. A relatively simple and sensitive method is needed for the direct determination of asparagine concentration, as well as of asparaginase activity, in serum and other body fluids in order to assess the effectiveness of therapy. Various methods for the determination of asparagine or asparaginase based on potentiometric sensors have been developed [2—4], but they have not been applied to biological fluids (e.g., human serum), probably because many interferences are likely.

This communication describes the development and evaluation of an immobilized asparaginase probe for asparagine monitoring. Asparagine can be determined with this electrode in the range 2.0×10^{-5}—2.3×10^{-3} M with an average error of about 1.3%. A potentiometric method was developed for the determination of asparaginase activity using the ammonia gas-sensing electrode. Both methods are applicable to the determination of asparagine or asparaginase in human serum. The results obtained are compared with values obtained by the combined Conway and Russell method.

Experimental

Apparatus and reagents. The equipment was as reported previously [5].

Asparaginase (E.C.3.5.1.1. from *Escherichia coli*) was obtained (Serva Feinbiochemica, Heidelberg, Federal Republic of Germany) as solution in 50% glycerol, with an activity of about 80 U mg^{-1}. (One unit of asparaginase

0003-2670/84/$03.00

is the amount of enzyme which liberates 1.0 μmol of ammonium nitrogen from L-asparagine per minute at pH 8.6 at 37°C.) The enzyme activity was measured as recommended by the supplier. All other chemicals were of analytical grade. Distilled-deionized water was used throughout.

A stock solution of 0.0100 M asparagine was prepared by dissolving 0.1501 g of L-asparagine monohydrate in 25 ml of 0.025 M sodium hydroxide and diluting to 100.0 ml with water; this solution was stored in a refrigerator. Working solutions were prepared daily by appropriate dilutions of the stock with 0.1 M Tris—HCl buffer, pH 8.0. Calibration graphs for the determination of asparagine and asparaginase in human blood serum were constructed from results obtained by use of Wellcome reference solutions (Wellcome Reagents, Beckenham, England) to which known amounts of substrate or enzyme had been added.

Aqueous standard asparaginase solutions were prepared by appropriate dilutions of the commercial enzyme preparation just before the measurements.

Sensor preparation. The electrode for asparagine was constructed by placing 10 μl of enzyme suspension (approximately 4 U) between an outer circular cellophane dialysis membrane and the gas-permeable membrane of the ammonia sensor and dispersing them uniformly on the surface of the membrane. The enzyme layer was about 0.2 mm thick. The electrode was preconditioned by soaking for 2 h in 0.1 M Tris—HCl buffer, pH 8.0, and was stored in this buffer at 4°C [6].

Determination of asparagine in aqueous solutions. Pipet 5.00 ml of standard asparagine or unknown sample solution buffered with 0.1 M Tris—HCl, pH 8.0 (1 + 4), into the thermostatted cell at 32 ± 0.2°C, immerse the asparagine electrode in the solution, start the stirrer, and read the e.m.f. when it is constant to within ±0.1 mV (2—5 min). Calculate the asparagine concentration from a calibration graph of e.m.f. vs. log (asparagine concentration).

Determination of asparagine in human serum. Pipet 4.00 ml of 0.1 M Tris—HCl buffer, pH 8.0, and 1.00 ml of serum into the thermostatted cell (32°C). Complete the determination as above.

Determination of asparaginase. Pipet 5.00 ml of 2×10^{-3} M standard asparagine solution (in 0.1 M Tris—HCl buffer, pH 8.0) into the thermostatted cell (32°C), immerse the ammonia gas sensor in the solution, inject 100 μl of standard asparaginase or sample solution, start the stirrer and read the e.m.f. when it is constant to within ±0.1 mV (6—7 min). Calculate the asparaginase activity from an appropriate calibration graph.

Results and discussion

The asparagine electrode is based on the specific deamination of asparagine in the presence of L-asparaginase to form L-aspartate and ammonia. Asparagine diffuses into the immobilized enzyme layer, producing a stoichiometric quantity of ammonia which gives a potential linearly related to the

logarithm of asparagine concentration in the solution. A typical calibration graph for stirred asparagine solutions, buffered at pH 8.0 with 0.1 M Tris—HCl, is shown in Fig. 1 (line B). The electrode has a linear response over the range 2.0×10^{-5}—2.3×10^{-3} M asparagine; the slope is 40.3 mV per decade at 32°C, with a correlation coefficient of —0.9998.

This reaction is also used in the determination of asparaginase activity. The enzyme sample is mixed with a standard asparagine solution and the ammonia produced is measured.

Effect of the amount of enzyme. The effect of variation in the amount of asparaginase used for the enzyme layer on the sensitivity of measurement is shown in Fig. 2. The slope of the calibration graph increases with the amount of the enzyme used up to 4 U of asparaginase, which was therefore chosen for making the enzyme layer. The enzyme is efficient, which reduces the cost of the method. Other procedures for the immobilization of the enzyme, e.g., cross-linking with glutaraldehyde or entrapment within polyacrylamide gel, are available [3, 4]. In all cases, the enzyme activities of the immobilized preparations were much greater than that needed here.

Dynamic response of the probe. The response times for 2.0×10^{-5} and 2.3×10^{-3} M substrate solutions were about 5 and 2 min, respectively, whether the sequence of measurements was from low to high concentrations or vice versa. For the enzyme determination, the response times were 6—7 min.

Effects of pH and temperature. The selection of optimum solution conditions requires some compromise between the optimum conditions for the enzyme reaction [7] and those for the NH_3—NH_4^+ equilibrium [8] involved

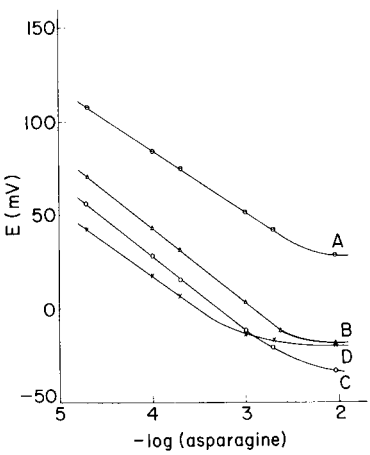

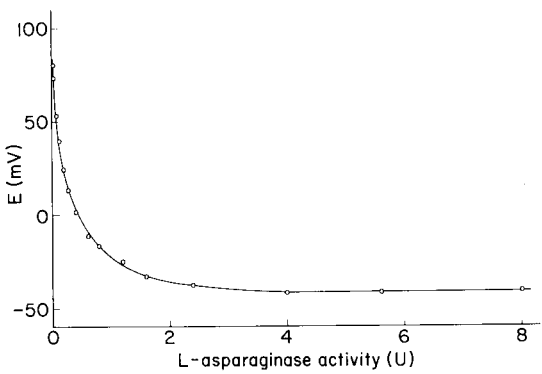

Fig. 1. Calibration graphs for asparagine in 0.1 M Tris—HCl buffer: (A) pH 7.5; (B) pH 8.0; (C) pH 8.5; (D) pH 9.0. Other conditions as in text.

Fig. 2. Effect of asparaginase on the potential for 2×10^{-3} M asparagine. Other conditions as in text.

in the ammonia sensor. The widest linear range was obtained at pH 8.0 (Fig. 1, line B), which agrees with earlier reports [7]. The small shift towards the higher pH values is due to the ammonia gas electrode.

An increase in temperature from 27 to 32°C increased the precision of measurements. Further increase to 37°C decreased the linear calibration range to 1×10^{-4}—1×10^{-3} M. Therefore a temperature of 32°C was preferred.

Interferences. High selectivity of the proposed sensor to asparagine is assured by the fact that purified preparations of asparaginase are not reactive with amino acids, amides and other compounds [9].

Long-term stability and operative life. The stability of performance and the working lifetime of the sensor depend on the operational conditions and storage. The lifetime was about three weeks if the sensor was stored at 4°C when not in use. During the first week, the slope of the calibration graph remained constant at 41.3 ± 1.5 mV/decade at 32°C. During the next two weeks, this slope decreased to 32.1 ± 1.8 mV, which was constant and large enough for quantitative work. However, although the lower limit of the electrode was unaffected as the electrode began to age, the upper limit decreased from 2.31×10^{-3} to 9.1×10^{-4} M and the response times increased. When the sensor was stored at room temperature, its lifetime was shortened drastically; the slope of the calibration graph remained constant for only four days, thereafter decreasing continuously, and the response time increased.

Applications. Results for the determination of asparagine in aqueous solutions (Table 1) show that 2.00×10^{-5}—2.31×10^{-3} M asparagine can be measured with an average error of 1.26%. The relative standard deviation was 1.52% for a 1.96×10^{-4} M asparagine sample (6 results).

Results for the determination of asparaginase in aqueous solutions (Table 2) indicate that 0.01—0.2 U asparaginase per 0.1 ml of sample can be measured with an average error of 1.42%. The relative standard deviation for 0.06 U asparaginase was 1.48% (6 results).

The electrode behaved in almost the same manner in both aqueous and serum solutions. For the determination of asparagine or asparaginase in human serum, the accuracy of the method was tested by adding asparagine or asparaginase to a serum reference (Wellcomtrol), formulated so as to approximate normal levels for frequently tested serum constituents. Accuracy and precision were very similar to those obtained for aqueous solutions. Results are shown in Tables 1 and 2.

In the course of evaluating the efficacy of L-asparagine as an anticonvulsant [9], body fluid levels of asparagine in a small group of patients were assayed with the enzyme probe. Table 3 shows the levels of asparagine in serum after a single intravenous dose of 1 mmol of L-asparagine per kg of body weight to an 80-kg man. Serum asparaginase activity was also measured in 3 patients receiving L-asparaginase for the treatment of malignant tumours. Samples obtained prior to the treatment with L-asparaginase

TABLE 1

Determination of asparagine in aqueous solution or Wellcomtrol standard (WS)

Asparagine ($\times 10^{-5}$ M)				
Taken[a]	Found[b]		Relative error (%)	
	In aq. soln.[c]	In WS[d]	In aq. soln.	In WS
2.00	2.03	—	+1.5	—
4.98	5.02	—	+0.8	—
9.90	9.79	10.2	−1.1	+3.0
19.6	19.2	20.0	−2.0	+2.0
29.1	29.7	28.7	+2.1	−1.4
47.6	47.4	47.9	−0.4	+0.6
90.9	92.5	89.6	+1.8	−1.4
231	230	234	−0.4	+1.3
			Av. 1.26%	1.62%

[a]In aqueous solution or added to a Wellcomtrol standard, after dilution with the Tris—HCl buffer, pH 8.0 (1 + 4). [b]From interpolation of calibration graph, average of two determinations. [c]Regression equation: $E = -40.3 \log [\text{asparagine}] - 118.8$; correlation coefficient, −0.9998. [d]Regression equation: $E = -38.6 \log [\text{asparagine}] - 112.8$; correlation coefficient, −0.998.

TABLE 2

Determination of asparaginase activity in aqueous solution or added to a Wellcomtrol standard (WS)

Asparaginase (U)				
Taken	Found[a]		Relative error (%)	
	In aq. soln.[b]	In WS[c]	In aq. soln.	In WS
0.0100	0.0101	0.0101	+1.0	+1.0
0.0200	0.0198	0.0199	−1.0	−0.5
0.0300	0.0294	0.0303	−2.0	+1.0
0.0400	0.0394	0.0391	−1.5	−2.2
0.0600	0.0610	0.0593	+1.7	−1.2
0.0800	0.0816	0.0809	+2.0	+1.1
0.120	0.118	0.123	−1.7	+2.5
0.200	0.199	0.204	−0.5	+2.0
			Av. 1.43%	1.44%

[a]From interpolation of calibration graph, average of two determinations. [b]Regression equation: $E = -65.0 \log [\text{units of asparaginase activity}] - 18.7$; correlation coefficient, −0.9997. [c]Regression equation: $E = -63.8 \log [\text{units of asparaginase activity}] - 16.9$; correlation coefficient, −0.9996.

TABLE 3

Asparagine levels (μmol ml^{-1}) in serum with time after intravenous administration of L-asparagine to a human subject

Time (min)	Asparagine found (μmol ml^{-1})	
	Present method	Combined Conway and Russell method
0	3.25	3.30
5	2.50	2.45
10	0.980	1.00
30	0.520	0.500

had no activity; 4 h after dosages of 500, 2500 and 5000 units, the activities in serum were 0.198, 1.05 and 1.91 U ml^{-1}, respectively. These samples were also analyzed by the combined Conway—Russell method [10—12]; the results were 0.201, 1.03 and 1.85 U ml^{-1}, respectively, which shows satisfactory agreement between the methods. The reported normal values for ammonia nitrogen in sera are in the range 75—195 μg N/100 ml, thus the free ammonia in serum at pH 8.0 should be in the range 3×10^{-6}—7×10^{-6} M, which is negligible in terms of interference with the ammonia sensor.

REFERENCES

1 Y. Kojima and W. E. C. Wacker, J. Lab. Clin. Med., 74 (1969) 521.
2 G. G. Guilbault, R. K. Smith and J. G. Montalvo, Jr., Anal. Chem., 41 (1969) 600.
3 G. G. Guilbault and E. Hrabankova, Anal. Chim. Acta, 56 (1971) 285.
4 T. T. Ngo, Can. J. Biochem., 54 (1976) 62.
5 D. P. Nikolelis, D. S. Papastathopoulos and T. P. Hadjiioannou, Anal. Chim. Acta, 126 (1981) 43.
6 D. S. Papastathopoulos and G. A. Rechnitz, Anal. Chim. Acta, 79 (1975) 17.
7 A. Meister, L. Levintow, R. E. Greenfield and P. A. Abendschein, J. Biol. Chem., 215 (1955) 441.
8 J. N. Butler, Ionic Equilibrium, a Mathematical Approach, Addison-Wesley, Reading, MA, 1964, p. 132.
9 D. B. Tower, E. L. Peters and W. C. Curtis, J. Biol. Chem., 238 (1963) 983.
10 E. J. Conway, Microdiffusion Analysis and Volumetric Error, 4th edn., Crosby-Lockwood, London, 1957, p. 90.
11 J. A. Russell, J. Biol. Chem., 156 (1944) 457.
12 D. B. Tower, J. Neurochem., 3 (1958) 185.

Analytica Chimica Acta, 161 (1984) 349—353
Elsevier Science Publishers B.V., Amsterdam — Printed in The Netherlands

Short Communication

INDIRECT POTENTIOMETRIC DETERMINATION OF α-AMINO ACIDS WITH A COPPER-SELECTIVE ELECTRODE AND DETERMINATION OF DOPA AND METHYLDOPA IN PHARMACEUTICAL PREPARATIONS

E. M. ATHANASIOU-MALAKI and M. A. KOUPPARIS*

Laboratory of Analytical Chemistry, University of Athens, 104 Solonos Str., Athens 10 680 (Greece)

(Received 4th January 1984)

Summary. α-Amino acids which form soluble copper complexes can be determined by stoichiometric reaction with an excess of copper(II) phosphate suspension and measurement of the copper ions produced with a copper(II) ion-selective electrode. Amino acids in the range 5×10^{-4}—1×10^{-2} M, separately or as a total value, can be determined with an accuracy better than 3%. L-Dihydroxyphenylalanine (dopa) and methyl derivative were determined in pharmaceutical preparations without interference from excipients; agreement with the results of USP methods was good.

The formation of complexes with copper(II) ions has often been used in the detection or determination of amino acids and other complexing agents [1—3]. Copper-selective membrane electrodes have been used as the indicator electrode in titrations of amino acids [4, 5] and as the detector in high-performance liquid chromatography [6]. It has been shown that a copper-selective electrode responds to complexing agents even in the absence of copper(II) ions in the solution [1]. The main disadvantage of these potentiometric measurements is the inherent non-linearity of the calibration curve. A large excess of copper(II) ions is needed to obtain stoichiometric reaction with the amino acid, so that the change in electrode potential is small. The response is slow and the electrode is susceptible to poisoning by the complexing agents [7, 8].

The reaction of amino acids at controlled pH with excess of an insoluble copper(II) precipitate can solve these problems. Kober and Sugiura [9] proposed a method in which the amino acid is reacted with freshly precipitated copper hydroxide. Pope and Stevens [10] recommended reaction with copper phosphate suspended in an alkaline borate buffer. The reaction mixture is filtered and the soluble copper complex is quantified in the filtrate. Numerous modifications of this procedure have involved iodimetric titration, titration with EDTA after oxidative destruction of the complex, spectrophotometry of the copper/amino acid complex or of copper ions with conventional reagents, as well as polarographic, flame photometric and radiometric techniques.

0003-2670/84/$03.00

In this communication, the reaction of α-amino acids with copper phosphate is re-investigated in order to establish a simple means of determining those amino acids that form soluble copper complexes. A copper-selective membrane electrode is used to measure the copper brought into the solution, after acidification with nitric acid. Glycine, alanine, valine, tyrosine, serine, glutamic acid, lysine, aspartic acid, threonine and proline were determined separately or in mixtures as total amino acids; L-dihydroxyphenylalanine (dopa) and its methyl derivative were determined in pharmaceutical preparations. The results were in good agreement with those obtained by official procedures.

Experimental

Reagents. All solutions were prepared with deionized-distilled water from reagent-grade materials.

Copper(II) phosphate suspension was prepared as described by Schroeder et al. [11] with slight modifications. To 20 ml of 0.18 M potassium phosphate, add 10 ml of 0.16 M copper(II) chloride with swirling. Centrifuge for 5 min, remove the supernatant solution, and resuspend the precipitate in 30 ml of 5×10^{-2} M borax buffer pH 9.1. Repeat the centrifugation and washing and finally suspend the precipitate in 50 ml of borax buffer containing 3 g of sodium chloride. The reagent must be left for 24 h before use and is then stable for about 15 days.

Amino acid standard solutions. Standards in the range 5×10^{-4}—1×10^{-2} M were prepared daily from 0.1000 M stock solutions made from analytical-grade amino acids (Fluka) with 1 M sodium hydroxide added if needed to dissolve the amino acids. Stock solutions (1×10^{-2} M) of L-dihydroxyphenylalanine (dopa) and its methyl derivative (methyldopa) were prepared by dissolving the appropriate amount of drug in 5 ml of 0.1 M hydrochloric acid and diluting with water to 100 ml; these solutions darkened on standing because of rapid oxidation by atmospheric oxygen but this did not affect the determination.

Instrumentation. An Orion Model 94-29A solid-state copper(II)-selective electrode was used with an Orion Model 90-02 double-junction reference electrode. Potentials were measured with an Orion Model 801 digital pH/mV meter. All of the measurements were made in a thermostated cell at 25 ± 0.2°C with continuous magnetic stirring.

The copper(II)-selective electrode was polished with a fine-grain diamond paste and treated with silicone oil every week. Between measurements and overnight, the electrode was stored dry in air.

Procedure. Into centrifuge tubes, pipet 2.00 ml of the recently swirled copper(II) phosphate suspension and 2.00 ml of the amino acid standard or unknown solution. (Neutralize samples when necessary by adding one drop of phenolphthalein plus sodium hydroxide to a faint pink.) Mix thoroughly on a Vortex mixer and let stand for 5 min. Centrifuge for 5 min at 2000 rpm and transfer 2.00 ml of the clear supernatant solution to the measurement

cell. Add 20.00 ml of 0.1 M nitric acid, start the stirrer and read the potential after it has stabilized (1 min). Empty the cell by suction, rinse the electrodes and the cell with water and dry by suction. For each series of unknowns, include four standards.

Calibration graphs of potential (mV) vs. log[amino acid] are prepared by the least-squares method.

Determination of dopa and methyldopa in pharmaceutical preparations. For capsules or tablets, weigh $\lessdot 20$ tablets or the contents of $\lessdot 20$ capsules, powder finely or mix, and transfer an accurately weighed portion of the powder containing 0.05—1 mmol of drug to a 100-ml volumetric flask. Add 5 ml of 0.1 M hydrochloric acid, mix on a Vortex mixer for 5 min and dilute with water. Filter or centrifuge a portion of the sample solution and proceed as above.

Results and discussion

The use of the reaction of amino acids with copper(II) phosphate suspension, resulted from the failure of attempts to use the copper-selective electrode to monitor the reaction of amino acids with copper(II) ions in solution. The optimum pH of the reaction (9—10) was out of the working pH range of the electrode (3—7). Thus the stoichiometric reaction of amino acids with excess of copper(II) phosphate and direct measurement of copper ions after acidification of the solution of the soluble copper/amino acid complexes was preferred.

In the re-investigation of the Pope and Stevens procedure based on a copper phosphate suspension, the blank values obtained as directed in the procedure for a freshly prepared suspension were imprecise and high. After aging for 1 day, blank values were generally consistent and ranged from 0.001—0.002 mM, copper concentration. A fresh suspension was prepared every two weeks.

The stoichiometry of the reaction was studied by measuring the copper ions brought into solution by the amino acid complex, using a calibration curve from copper standard solutions. The results obtained for alanine are shown in Table 1; the slope of the plot of alanine taken vs. copper found was 1.994 with intercept —0.051 and correlation coefficient (r) 1.000. Similar results with slopes (μmol amino acid/μmol copper) of 1.95—2.05 were found for glycine, valine, tyrosine, serine, glutamic acid, lysine, aspartic acid, threonine and proline. The same behavior was shown by the drugs dopa and methyldopa (Aldomet). This group of amino acids gives soluble copper complexes. The other amino acid tested (arginine, glutamine, histidine, tryptophan, cysteine, leucine, phenylalanine, methionine) give partially or totally insoluble complexes and the method cannot be applied except sometimes in the 5×10^{-4}—5×10^{-3} M range.

To improve the accuracy and to avoid errors from any gradual loss of the suspension activity, calibration graphs from the individual amino acid were used. The calibration equations used are shown in Table 2. The standard deviation for four measurements in the whole concentration range and in all

TABLE 1

Results for the alanine reaction with copper phosphate suspension

Alanine (μmol)[a]	0.200	1.200	2.000	12.00	20.00
Cu found (μmol)	0.107	0.584	1.052	6.145	9.995

[a]In a 2-ml aliquot of sample.

TABLE 2

Equations for calibration graphs used for the determination of amino acids in aqueous solutions

Amino acid (5×10^{-4}—1×10^{-2} M)	Equation[a] E (mV) vs. log[conc.]	r
1 Glycine	$E = 220.6 + 27.50$ log[gly]	0.9990
2 Alanine	$E = 221.6 + 27.62$ log[ala]	0.9992
3 Serine	$E = 221.6 + 27.40$ log[ser]	0.99993
4 Threonine	$E = 221.6 + 27.83$ log[thr]	0.9991
5 Tyrosine	$E = 221.4 + 27.18$ log[tyr]	0.9995
6 Aspartic acid	$E = 221.5 + 26.86$ log[asp]	0.9998
7 Lysine	$E = 219.7 + 27.03$ log[lys]	0.9990
8 Dopa	$E = 228.5 + 29.65$ log[dopa]	0.9997
9 Methyldopa	$E = 237.0 + 30.61$ log[m dopa]	0.9990
10 Phenylalanine[b]	$E = 219.5 + 26.81$ log[phe]	1.000
11 Histidine[b]	$E = 217.0 + 24.34$ log[his]	0.9996
12 Methionine[b]	$E = 205.8 + 22.09$ log[met]	0.9996

[a]Obtained on different working days. [b]Concentration range 5×10^{-4}—5×10^{-3} M; at higher concentrations insoluble complexes are formed.

cases is 0.2—0.4 mV which causes a measurement error of about 3%. The results in Table 2 indicate that the total amino acid concentration in a mixture of compounds 1—7 can be measured by using standard solutions of only one amino acid. Mixtures of glycine, alanine, serine and threonine were determined using glycine standards and the relative errors found were 2—5%.

The proposed method was tested for the determination of dopa and methyldopa in pharmaceutical preparations; the values obtained showed good agreement with those obtained by the USP standard spectrophotometric methods [12] (Table 3).

To study the interference of some common excipients used in tablet preparation, synthetic tablets containing 200 mg of the diluent and 100 mg of methyldopa were analyzed. The results given in Table 4 (97.1—101.1% recovery, mean 98.7%) show that the excipients did not interfere. Attempts to determine lysine in stimulant solutions failed, because of the presence of interferences such as vitamins C and B6, and niacinamide.

In order to check the reliability of the copper(II)-selective electrode

TABLE 3

Comparison of results obtained by the potentiometric and USP spectrophotometric methods for the determination of dopa and methyldopa in commercial capsules and tablets

Nominal content (mg)	Methyldopa found (mg)		Nominal content (mg)	Dopa found (mg)	
	Present method	USP method		Present method	USP method
Aldomet tablets (M.S.D.)			*Madopar capsules (Roche)*		
250	258	260	50	52.1	51.6
500	504	503	100	108	112
			200	205	207

TABLE 4

Recovery of methyldopa (100 mg) added to 200 mg of various excipients

Excipient	Recovery (%)	Excipient	Recovery (%)	Excipient	Recovery (%)
Starch	97.1	Sodium lauryl sulfate	98.4	Magnesium stearate	97.1
Lactose	99.6	Glucose	101.1	Sugar	98.9
Sorbitol	98.3	Carbowax 4000	99.6	NaCl	98.2

in 0.1 M nitric acid solutions, the calibration graph for copper standard solutions was measured every day for one month. The equation obtained was $E = 252.1(\pm 0.6) + 26.76(\pm 0.31) \log C$, which shows excellent stability and reproducibility.

In conclusion, the proposed method is a simple and rapid way of determining amino acids separately or in mixtures. Dopa and methyldopa can be determined in tablets and capsules without interference from the excipients even in turbid solutions.

REFERENCES

1 M. F. El-Taras, E. Pungor and G. Nagy, Anal. Chim. Acta, 82 (1976) 285.
2 P. W. Alexander and C. Maitra, Anal. Chem., 53 (1981) 1950.
3 W. Th. Kok, H. B. Hanekamp, P. Bos and R. W. Frei, Anal. Chim. Acta, 142 (1982) 31.
4 A. Libicky and L. Wünsch, Collect. Czech. Chem. Commun., 26 (1961) 2663.
5 Y. A. Gawargious, A. Besada and M. E. M. Hassouna, Microchim. Acta, (1974) 1003.
6 C. R. Loscombe, G. B. Cox and J. A. W. Dalziel, J. Chromatogr., 166 (1978) 403.
7 J. C. Westall, F. M. Morel and D. N. Hume, Anal. Chem., 51 (1979) 1792.
8 T. Sekerka and J. F. Lechner, Anal. Lett., AII (1978) 415.
9 P. A. Kober and K. Sugiura, J. Biol. Chem., 13 (1912) 1.
10 C. G. Pope and M. F. Stevens, Biochem. J., 33 (1939) 1070.
11 W. A. Schroeder, L. M. Kay and R. S. Mills, Anal. Chem. 22 (1950) 760.
12 U. S. Pharmacopeia XX, pp. 442, 518.

Analytica Chimica Acta, 161 (1984) 355—358
Elsevier Science Publishers B.V., Amsterdam — Printed in The Netherlands

Short Communication

BIOLUMINESCENT DETERMINATION OF REDUCED NICOTINAMIDE ADENINE DINUCLEOTIDE WITH IMMOBILIZED BACTERIAL LUCIFERASE AND FLAVIN MONONUCLEOTIDE OXIDOREDUCTASE ON COLLAGEN FILM

LOÏC J. BLUM and PIERRE R. COULET*

Laboratoire de Biologie et Technologie des Membranes du C.N.R.S., Université Claude Bernard, Lyon I 43, Boulevard du 11 Novembre 1918, 69622 Villeurbanne Cedex (France)

(Received 17th January 1984)

Summary. Bacterial luciferase and flavin mononucleotide oxidoreductase were co-immobilized on collagen strips. Reduced nicotinamide adenine dinucleotide was determined in the range 1×10^{-9}—2×10^{-5} M, with a precision of 5%. The immobilized system retained 70% of its initial activity after two weeks.

The determination of metabolites and measurements of enzymatic activities are usually achieved by using one or several auxiliary enzymes, and in a final step reduced nicotinamide adenine dinucleotide (NADH) is monitored spectrophotometrically at 340 nm. The detection limit for the coenzyme is about 1×10^{-6} M. Improvements have been obtained by using enzymatic cycling [1] but this requires the use of three auxiliary enzymes and an incubation time of at least 30 min.

Luminescent bacteria contain enzymes which catalyze the following reactions [2]

$$NAD(P)H + H^+ + FMN \rightarrow NAD(P)^+ + FMNH_2 \quad (1)$$

$$FMNH_2 + O_2 + RCHO \rightarrow FMN + RCOOH + H_2O + \text{light} \quad (2)$$

Reaction (1) is catalyzed by NAD(P)H: flavin mononucleotide (FMN) oxidoreductase and reaction (2), which produces light in the presence of oxygen and a long-chain aldehyde (R—CHO), is catalyzed by bacterial luciferase. If NAD(P)H is the limiting substrate, the light intensity is proportional to the NAD(P)H concentration. With soluble enzymes, NADH concentrations as low as 1×10^{-12} M can be measured [3].

Considering the sensitivity of the bioluminescent bacterial system with respect to NADH, it appeared attractive to co-immobilize luciferase and the oxidoreductase on a suitable support. For this purpose, collagen membranes were chosen for their high mechanical strength and ease of use compared to the particulate and gel supports used by other groups [4—6]. The conditions

0003-2670/84/$03.00

allowing sensitive measurements with such a reusable material are described in this communication.

Experimental

Reagents. The bacterial luciferase/oxidoreductase system from *Photobacterium fischeri*, lyophilized powder, and *N*-decylaldehyde (decanal) were from Sigma Chemical Co. Dithiothreitol (DTT) and NADH were obtained from Calbiochem and FMN from Boehringer Mannheim. All other reagents were of the highest grade commercially available.

Immobilization procedure. Flat sheets (15 × 18 cm) of highly polymerized insoluble collagen were a gift of the Centre Technique du Cuir, Lyon, France. Strips of 1 × 4.5 cm cut from the collagen films were used for the immobilization of the enzymes. The collagen activation, which involves the conversion of surface-available carboxyl groups to acyl-azide groups, and the coupling of enzymes were done according to the general method described previously [7]. The activated collagen strip was dipped into a standard cuvette (1 × 1 × 4.5 cm) containing 1.3 mg of lyophilized enzyme preparation dissolved in 1 ml of 0.1 M phosphate buffer, pH 7.8, containing 2×10^{-3} M DTT, to prevent luciferase inactivation. After coupling, the strips were washed in 0.1 M phosphate buffer, pH 6.4, containing 2×10^{-3} M DTT and 1 M potassium chloride and stored at 4°C in the same solution but without potassium chloride.

Apparatus. Light emission was measured with a Berthold Biolumat LB 9500 luminometer. There is no accepted light standard, thus all luminescence measurements are relative. The contents of the reaction vessel (a round flat-bottomed cuvette of 12 × 47 mm) were stirred with a small stirring bar (5 × 2 mm) by placing a magnetic stirrer close to the luminometer. The sample chamber was thermostated at 23°C.

Bioluminescent assay procedure. The enzymatic strip was introduced into the reaction vessel and set close to the inner wall of the cuvette. Maximum light intensity was measured upon injection of 10 µl of aqueous NADH solution into 990 µl of 0.1 M phosphate buffer, pH 6.4, containing FMN and decanal at the appropriate concentrations and 2×10^{-3} M DTT. Only part of the strip, which is 4.5 cm long, was immersed in the reaction mixture. The natural adherence of collagen onto smooth surfaces helped to maintain the strip motionless in the vessel. Under these conditions, only part of the inner wall was covered by the strip enabling the emitted light to reach the photomultiplier. An emulsion of decanal (0.2% v/v) in water and ethanol (0.8% v/v) was made fresh every 4 h and stored at 4°C. Aqueous FMN solutions were prepared each day and stored light-protected at 4°C. After each assay, the collagen strips were washed in 0.1 M phosphate buffer, pH 6.4, containing 2×10^{-3} M DTT and 1 M potassium chloride.

Results and discussion

Luminescent signal. Figure 1 shows the typical time-course of light production from the collagen-bound luciferase/oxidoreductase system on injection of NADH. After a transient phase, the light intensity reaches a steady state which signifies a constant reaction rate. The steady-state response is reached in 8 min when there is no DTT in the reaction medium, but in only 2 min in the presence of 2×10^{-3} M DTT.

Optimum conditions for NADH determination. The concentrations of substrates (NADH, FMN, decanal) required to give maximum intensity were determined by measuring the intensity at different concentrations of one of the substrates at fixed concentrations of the other two. Maximum intensity was obtained with 1.3×10^{-5} M FMN, 0.004% decanal and 2×10^{-4} M NADH.

Figure 2 shows the pH/activity profile of the immobilized and soluble bacterial systems. For the soluble bienzymatic system the optimum pH value of 6.8 is a compromise between the optimum pH values for the oxidoreductase and luciferase which are respectively 6.5 and 7.0 [8]. After immobilization, the pH activity profile is modified. The optimum value becomes 6.4 (close to the value for the oxidoreductase) and the shoulder at pH 7.0 corresponds to the optimum pH for the luciferase. Thus after immobilization the activity of the luciferase/oxidoreductase system seems to be limited by the oxidoreductase.

Calibration graph and precision. The calibration graph (log—log plot) for NADH obtained by measurements of the maximum light intensity is linear from 1×10^{-9} M to 2×10^{-5} M NADH. At higher concentrations, the response levels off. The relative standard deviation for 10 replicate assays of 1×10^{-8} M NADH was 5.6%.

Stability of the immobilized system. The stability of the system was

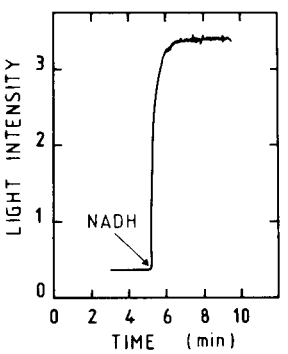

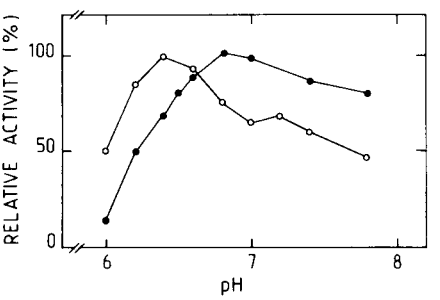

Fig. 1. Time-course of light emission from the immobilized luciferase/oxidoreductase system. The final NADH concentration was 1×10^{-7} M; reaction conditions as in the experimental section. Intensity in arbitrary units.

Fig. 2. pH/activity profiles for: (○) immobilized; (●) soluble luciferase/oxidoreductase. (Phosphate buffer (0.1 M) was used throughout.)

greatly improved by immobilization. After two weeks of storage under the conditions described, 70% of the initial activity remained whereas the soluble preparation was not usable after this period.

In conclusion, the collagen-bound two-enzyme system appears to be superior to the soluble system by being more stable and reusable. Moreover, the film form of the collagen support is very easy to handle, particularly for repeated use.

REFERENCES

1 J. V. Passonneau and O. H. Lowry, in H. U. Bergmeyer (Ed.), Methods of Enzymatic Analysis, Vol. 4, Academic Press, 1974, p. 2059.
2 J. W. Hastings, in M. A. Deluca (Ed.), Methods in Enzymology, Bioluminescence and Chemiluminescence, Vol. 57, Academic Press, New York, 1978, p. 125.
3 P. E. Stanley, Anal. Biochem., 39 (1971) 441.
4 E. Jablonski and M. Deluca, Proc. Natl. Acad. Sci. USA, 73 (1976) 3848.
5 O. Rodriguez and G. G. Guilbault, Enzyme Microb. Technol., 3 (1981) 69.
6 G. K. Wienhausen, L. J. Kricka, J. E. Hinkley and M. Deluca, Appl. Biochem. Biotechnol., 7 (1982) 463.
7 P. R. Coulet, J. H. Julliard and D. C. Gautheron, Biotechnol. Bioeng., 16 (1974) 1055.
8 K. Puget and A. M. Michelson, Biochimie, 54 (1972) 1197.

Analytica Chimica Acta, 161 (1984) 359—364
Elsevier Science Publishers B.V., Amsterdam — Printed in The Netherlands

Short Communication

INDIRECT SPECTROFLUORIMETRIC KINETIC DETERMINATION OF PALLADIUM AND NICKEL BASED ON THE OXIDATION OF 2,2'-DIPYRIDYLKETONE HYDRAZONE AND DIPYRIDYLGLYOXAL HYDRAZONE

F. GRASES* and C. GENESTAR

Department of Analytical Chemistry, Faculty of Sciences, University of Palma de Mallorca (Spain)

(Received 3rd January 1984)

Summary. Kinetic methods for palladium (0.1—0.8 mg l^{-1}) and nickel (0.1—0.7 mg l^{-1}) are based, respectively, on the uncatalyzed bromate oxidation of 2,2'-dipyridylketone hydrazone (DPKH) in acidic media and of dipyridylglyoxal hydrazone (DPDKH) in basic media, to yield fluorescent products. Complexation of DPKH and DPDKH by Pd(II) and Ni(II), respectively, causes a decrease in ligand concentration and thus in reaction rate, which can be related to the concentration of metal. The method for palladium is relatively free from interferences.

The spectrofluorimetric determination of inorganic species has largely been restricted to equilibrium methods based on the formation of chelates. The number of known ligands with fluorescent properties is small, and most transition metals cannot form fluorescent chelates because of their paramagnetism. The development of kinetic-fluorimetric methods allows the appearance of fluorescence to be used to determine any inorganic species, because any reaction or system in which a fluorescent product participates can be used. There are three groups of non-enzymatic spectrofluorimetric reaction-rate methods of inorganic analysis. One includes those procedures in which a fluorescent organic compound is oxidized by an inorganic species with an appropriate rate [1—3]. Those procedures in which the determination of inorganic species is based on catalytic reactions are included in another group; most of these correspond to redox processes [1] although systems based on hydrolysis [4] and condensation [5] reactions have been described. This group also includes procedures based on activation or inhibition [6]. The third group includes those methods based on a combination of two or more chemical systems so that the fluorescence intensity depends on the concentration of the inorganic species to be determined. Methods based on bromate oxidation of chelating agents such as benzyl-2-pyridylketone, 2-pyridylhydrazone and pyridine-2-aldehyde-2-pyridylhydrazone, and their complexation with various metal ions (Fe(III), Co(II), Ni(II), Pd(II)) in acidic media fall into this group [7, 8]. Another example is a determination

0003-2670/84/$03.00

of iron(III) and thallium(III) based on their oxidation of the hydrolysis product of 1,4-diamino-2,3-dihydroanthraquinone [9].

In this communication, a method for palladium based on bromate oxidation of 2,2′-dipyridylketone hydrazone in acidic media and complexation with palladium, and another for nickel based on hydrogen peroxide oxidation of dipyridylglyoxal hydrazone in alkaline media and complexation with nickel, are described. These methods involve a relatively slow redox conversion of the chelating agent to a fluorescent product in the same medium as complex formation takes place. The decrease in the concentration of the ligand which is to be oxidized, caused by complexation with the metal ions, causes a decrease in reaction rate which can be related to the concentration of the metal.

Experimental

Apparatus. A Perkin-Elmer model LS-5 fluorescence spectrophotometer was used. The fluorescence intensity/time curves were obtained by fixing the excitation and emission wavelengths and using a constant chart speed (see below). A UV Atom-70 ultraviolet lamp (λ_{ex} 360 nm) was also used.

Reagents and solutions. 2,2′-Dipyridylketone hydrazone (DPKH) was synthesized as described previously [10]. Aqueous solutions (1 g l^{-1}) were prepared weekly. Dipyridylglyoxal hydrazone (DPDKH) was synthesized as described previously [11]; solutions (0.1 g l^{-1}) were prepared weekly in ethanol. A stock standard potassium bromate solution (5.99×10^{-3} M, 1 g l^{-1}) was used. A 0.1000 M palladium solution was prepared by dissolving 1.418 g of palladium dichloride in 1 l of 0.05 M hydrochloric acid. For the 0.1000 M nickel solution, 29.081 g of nickel nitrate hexahydrate was dissolved in 1 l of deionized water.

Procedure for palladium determination. Into a 50-ml beaker, place exactly 0.1 ml of 5.05×10^{-5} M DPKH solution, an aliquot of sample containing 0.1—0.8 mg l^{-1} palladium and 0.9 ml of 2 M hydrochloric acid. Add enough deionized water to give a final volume of 10 ml and start the reaction, 5 min after cation addition, by adding 0.8 ml of 5.99×10^{-3} M potassium bromate. After a further 60 s, start recording the intensity/time curve (λ_{ex} = 359 nm, λ_{em} = 430 nm, chart speed 10 cm min^{-1}). From the curve obtained, calculate the initial rate (tan α) of the response curve extrapolated to zero time; tan α is the slope of the response curve.

Procedure for nickel determination. Into a 50-ml beaker, place exactly 4.6 ml of 9.04×10^{-6} M DPDKH solution, an aliquot of sample containing 0.1—0.7 mg l^{-1} nickel and 0.5 ml of 2 M sodium hydroxide. Add enough deionized water to give a final volume of 10 ml and start the reaction by addition of 2 ml of 10% hydrogen peroxide. After a further 60 s, start recording the intensity/time curve (λ_{ex} = 340 nm, λ_{em} = 454 nm, chart speed 2.5 cm min^{-1}). Proceed further as for palladium.

Results and discussion

Addition of a metal ion to a solution containing an appropriate complexing agent causes a change in the rate of oxidation of the ligand, by decreasing the effective ligand concentration in solution. This effect can be used analytically if the solution conditions are chosen to give an optimum oxidation rate in the absence of metal ion (reference reaction). In the systems studied here, three major experimental variables can be modified to adjust this oxidation rate: pH, and the concentrations of oxidant and ligand. In order to achieve accurate and reproducible results, rapid oxidation of the ligand is necessary, to avoid measuring only small fluorescence intensities. At the same time, the ligand concentration should be as small as possible, so as to be most susceptible to changes in metal ion concentration, provided, of course, that the stability constant is high enough to allow sufficient formation of chelate at such concentrations.

The bromate/DPKH/palladium(II) system. Decreased acidity should favour chelate formation in this system. The rate of the bromate oxidation of DPKH, however, decreases with decreasing acidity (Fig. 1). Moreover, the oxidation product has maximum fluorescence intensity in acidic medium [10]. Thus an acidity has to be chosen to satisfy those conflicting requirements. The bromate concentration should be chosen so as to give rapid oxidation of the ligand at this acidity, and a large concentration is desirable to prevent interference by reductants, but very high concentrations are unsuitable because the oxidation of the reagent is then too vigorous, leading to non-fluorescent products. As a result, the following experimental conditions were selected for the monitoring reaction: 4.8×10^{-4} M bromate and 0.18 M hydrochloric acid. The effect of the DPKH concentration on the rate under these conditions was examined. Maximum sensitivity was achieved with $5—10 \times 10^{-7}$ M DPKH; with $1—4 \times 10^{-7}$ M DPKH, the sensitivity increased gradually.

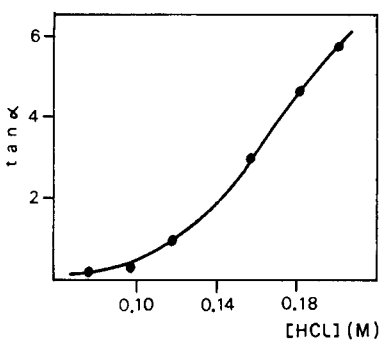

Fig. 1. Effect of acidity on the rate of oxidation of DPKH. 5.05×10^{-7} M DPKH, 4.8×10^{-4} M bromate, sensitivity × 1.

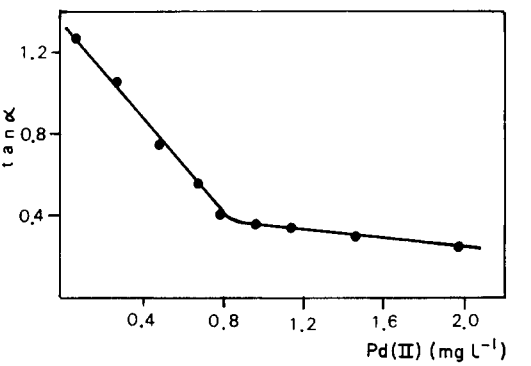

Fig. 2. Dependence of rate on the concentration of palladium, under the recommended conditions (sensitivity × 1).

Figure 2 shows the calibration graph for palladium obtained under the selected conditions. The extent of complexation increases with time (Fig. 3), thus when several minutes are allowed to elapse between adding palladium and bromate, greater sensitivity is achieved. The calibration graph is linear for 0.1—0.8 $\mu g\ ml^{-1}$ palladium. The relative standard deviation in this range was 2.7% (n = 11). For equimolar ratios of palladium and DPKH, there is hardly any change in the rate of oxidation of the reagent, demonstrating that under such conditions the chelate is highly dissociated.

Interferences can arise from substances reducing bromate, complexing palladium or decreasing the concentration of DPKH by oxidation or complexation. Because of the inverse relationship between rate and palladium concentration, substances which decrease the rate will cause positive interferences. Spectral interferences should be minimal, because of the selectivity of fluorimetry and the comparative nature of kinetic measurements. The results of the interference study are summarized in Table 1. The principal effects are caused by Au(III), Fe(III) and Tl(III) and can be attributed to their oxidizing properties in acidic solutions. Metal ions such as Ni(II), Co(II), Hg(II) and Cu(II), that form chelates with the ligands or catalyze its aerial oxidation, only slightly affect the palladium determinations, because in such an acidic medium the chelating capacity of DPKH is notably decreased and autoxidation processes are less favoured.

The hydrogen peroxide/DPDKH/nickel system. The product of the oxidation of DPDKH has its maximum fluorescence intensity in basic media [11]. Hydrogen peroxide was therefore used as oxidant; a concentration of 2% was chosen in order to obtain rapid oxidation of the ligand, which was greatest at a sodium hydroxide concentration of 0.1 M (Fig. 4). A greater concentration of the oxidant is again undesirable because of the formation of non-fluores-

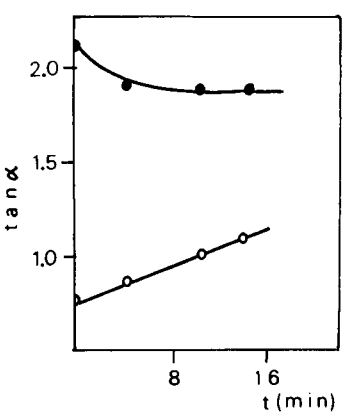

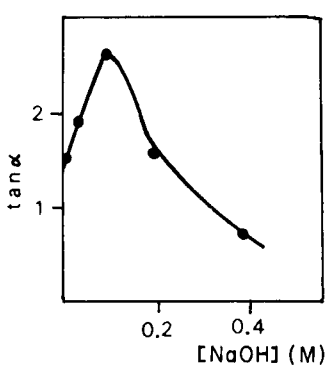

Fig. 3. Effect of time before oxidant addition: (•) 0.1 mg l^{-1} Pd(II) (sensitivity × 1); (○) 0.5 mg l^{-1} Ni(II) (sensitivity × 10). Other conditions as recommended.

Fig. 4. Effect of NaOH concentration on the rate of oxidation of DPDKH. (4.16×10^{-5} M DPDKH, 2% H_2O_2, 6% ethanol, sensitivity × 10).

TABLE 1

Concentrations of foreign ions tolerated for 0.3 mg l^{-1} palladium (error ≤2.7%) or 0.5 mg l^{-1} nickel (error ≤3.5%)

Ion	Amount tolerated[a] (mg l^{-1})
Palladium method	
Ca, Ba, Sr, Mg, Zn, Cl^-, NO_3^-	30
Cr(III), Mn(II), SO_4^{2-}, AsO_4^{3-}, F^-[b]	10
Al, Ni, Th(IV), U(VI), Mo(VI), $C_2O_4^{2-}$, EDTA, Cd[b], Ag[b]	5
Co(II)[b], Cu(II)[b], Hg(II)[b], V(V)[b]	1
Tl(III), Fe(III)[b]	0.1
Au(III)	0.005
Nickel method	
Ca, Ba, Mg, Sr, Th(IV), U(VI), NO_3^-, Cl^-	20
Mo(VI), F^-, SO_4^{2-}, AsO_4^{3-}	10
$C_2O_4^{2-}$	5
Cd, Mn(II), Cr(III), Al[b]	2
Zn, Ag	0.5
Pd(II), Tl(III), Au(III), V(V), EDTA, Fe(III)[b]	0.1
Hg(II)[b]	0.01
Co(II)[b], Cu(II)[b]	0.005

[a]These are the maximum concentrations tested, except where noted otherwise. [b]Maximum tolerable concentration.

cent products. The rate of DPDKH oxidation increased rapidly when the ethanol concentration was increased up to 25% but levelled off up to 46% (v/v), which concentration was therefore selected. The effect of DPDKH concentration on the rate is shown in Fig. 5. The maximum initial rate was approached with ca. 4×10^{-6} M DPDKH.

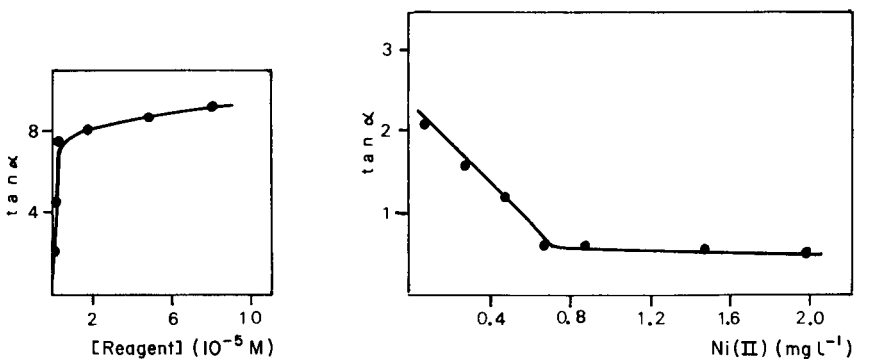

Fig. 5. Effect of DPDKH concentration on the rate. (0.1 M NaOH, 2% H_2O_2, 46% ethanol, sensitivity × 10).

Fig. 6. Dependence of rate on the concentration of nickel, under the recommended conditions (sensitivity × 10).

Figure 6 shows the calibration graph for nickel obtained under the specified conditions. The effect of nickel is slightly less (Fig. 3) if, before addition of hydrogen peroxide, there is a delay of several minutes; this can be attributed to slow decomposition of the chelate in the very alkaline solution used. The calibration graph was linear for 0.1—0.7 mg l^{-1} nickel(II) and the relative standard deviation in this range was 3.5% (n = 11). Again, for an equimolar ratio of nickel and ligand, the rate of oxidation of the reagent was scarcely affected. This again demonstrates that under such conditions the chelate is highly dissociated.

The results of the interference study are shown in Table 1. As can be seen, the number of important interferents is much larger than for the palladium system. This can be attributed to the strong chelating behaviour of DPDKH in alkaline media or to the pronounced catalytic action in this medium of ions such as Cu(II), Co(II), Hg(II) and Ag(I) on the aerial oxidation of the reagent.

REFERENCES

1 M. Valcárcel and F. Grases, Talanta, 30 (1983) 139.
2 F. Grases, C. Genestar and F. Salinas, Anal. Chim. Acta, 148 (1983) 245.
3 F. Grases, C. Genestar and J. G. March, Microchem. J., in press.
4 R. Alarcón, M. Silva and M. Valcárcel, Anal. Lett., 15 (1982) 891.
5 F. Grases, C. Genestar and G. Far, Microchem. J., in press.
6 A. Navas, M. Santiago, F. Grases, J. J. Laserna and F. Garcia Sánchez, Talanta, 29 (1982) 615.
7 F. Garcia Sánchez, A. Navas Diaz and J. J. Laserna, Anal. Chem., 55 (1983) 253.
8 F. Garcia Sánchez, A. Navas, J. J. Laserna and M. R. Martinez de la Barrera, Fresenius Z. Anal. Chem., 315 (1983) 491.
9 F. Salinas, C. Genestar and F. Grases, Anal. Chim. Acta, 130 (1981) 337.
10 F. Grases, F. Garcia Sánchez and M. Valcárcel, Anal. Chim. Acta, 119 (1980) 359.
11 F. Grases, F. Garcia Sánchez and M. Valcárcel, An. Quim., 76B (1980) 402.

Analytica Chimica Acta, 161 (1984) 365—368
Elsevier Science Publishers B.V., Amsterdam — Printed in The Netherlands

Short Communication

DETERMINATION OF BISMUTH IN ATMOSPHERIC PARTICULATE MATTER BY HYDRIDE GENERATION AND ATOMIC ABSORPTION SPECTROMETRY

K. DE DONCKER, R. DUMAREY, R. DAMS and J. HOSTE*

Institute of Nuclear Sciences, Rijksuniversiteit Gent, Proeftuinstraat 86, B-9000 Ghent (Belgium)

(Received 4th January 1984)

Summary. The particulates are collected on Whatman 41 cellulose filters and decomposed with sulfuric acid and hydrogen peroxide; bismuth is then measured by hydride generation/atomic absorption spectrometry. The detection limit is 0.08 ng m^{-3} if 500 m^3 of air is filtered through an 11-cm filter. Generally, the precision is better than 10%. The concentrations found in Ghent, Belgium varied between 0.1 and 0.8 ng m^{-3}. Bismuth was also determined in NBS Orchard Leaves (SRM 1571); a value of 98.5 ± 15 ng g^{-1} was found.

Very low concentrations of bismuth are present in airborne particulates. In a compilation with concentration data on 104 locations in the world, Rahn [1] gave a few values varying from 0.5 to 3 ng m^{-3}, for some large cities in the U.S.A.; these approximate data were obtained by spark-source mass spectrometry [2]. For Sutton in England a value of 0.2 ng m^{-3} has been reported [3]. One of the obvious reasons for this scarcity of data is the difficulty associated with the determination of such low concentrations.

Hydride generation combined with atomic absorption spectrometry provides a sensitive and selective method for the determination of bismuth and other hydride-forming elements such as As, Se, Sb. This technique becomes highly sensitive and largely free from interferences because the element can be volatilized as its covalent hydride and larger amounts of bismuth can be introduced into the atomization tube. Preconcentration of the hydride and subsequent rapid introduction into an atomizer can further improve the sensitivity compared to that of the continuous method [4, 5]. However, this procedure is only useful for those elements which have hydrides stable enough to be handled at ambient temperature. For this reason, the collection of BiH_3 has not so far been successful [6, 7].

This communication describes the use of a continuous hydride method for the determination of bismuth in atmospheric particulates, collected on a Whatman 41 filter paper.

0003-2670/84/$03.00

Experimental

Sampling. The sampling was based on the LIB method [8]. The particulate matter was collected by using a carbon vane rotary pump (Becker VT 25), with a free-air capacity of 25 m^3 h^{-1}. The actual flow rate through the 11-cm diameter Whatman 41 cellulose filters was approximately 20 m^3 h^{-1}. Air volumes were measured with a Contigea SG integrating gasmeter. The sampling typically lasted 48 h during which nearly 1000 m^3 of air was sampled. The air intake was at 7 m above ground level slightly south of the city of Ghent but at a distance of only 50 m from a busy highway.

Apparatus. The Perkin-Elmer 503 atomic absorption spectrometer used was equipped with a bismuth Perkin-Elmer hollow-cathode lamp and a Perkin-Elmer model 56 strip-chart recorder. For the generation of the bismuth hydride, an automatic mercury/hydride system (Perkin-Elmer model MHS-1) was used. The optimized operating parameters are summarized in Table 1.

Reagents. All reagents were of at least analytical grade: hydrofluoric acid (50%, Carlo Erba), hydrogen peroxide (30%, UCB), sulfuric acid (95—98%, J. T. Baker). The solutions prepared were 2% (w/v) hydrazine sulfate (Merck) and 5% (w/v) sodium tetrahydroborate (Aldrich) stabilized with 2% (w/v) sodium hydroxide.

Standards were prepared by diluting a 1000 mg l^{-1} standard solution of bismuth (Fluka).

Sample decomposition. The procedure recommended for the digestion of particulate matter collected on filters in the determination of antimony [9] was evaluated and also applied in the present work. It consists of digestion in 11 ml of sulfuric acid and 5 ml of hydrogen peroxide. For the dissolution of residual silicates, a few ml of hydrofluoric acid are added and later evaporated. After digestion, the solution is filtered if necessary and diluted to 50 ml.

Absorbance measurements. A 4-ml aliquot of this solution is injected into the reaction flask of the hydride generator which contains 10 ml of 1.0 M sulfuric acid solution. The parameters for the measurements are summarized in Table 1. The absorbance was evaluated from peak heights.

Calibration. Two procedures were applied. A calibration graph was made with standard solutions in the range 20—180 ng of bismuth. The linear range extended to at least 180 ng of bismuth per 10 ml of sample; the equation was $y = x\,(0.00462 \pm 0.00002)\,A\ ng^{-1} \pm (0.0024 \pm 0.0021)\,A$ with a

TABLE 1

Operating parameters for the determination of bismuth

Liquid volume	10 ml of 1.0 M H_2SO_4 + 4 ml of sample	Atomization temperature	750°C
Reductant	2.5 ml of 5% (w/v) $NaBH_4$	Hollow-cathode lamp	10 mA
Argon flow	250 ml min^{-1}	Wavelength	223.0 nm
Hydride program	I	Spectral bandwidth	0.2 nm (slit
		Background correction	off
		Damping	2

correlation coefficient of 0.9993. The method of standard additions was also applied by injecting, together with the solution of a digested filter, known amounts (20 and 50 ng) of bismuth into the reaction flask of the generation system. The equation of the straight line then obtained was $y = x\,(0.0058 \pm 0.0001)A$ ng^{-1} + $(0.0638 \pm 0.0030)A$. The results obtained by the two methods agreed within 10%.

Results and discussion

Ten samples of atmospheric aerosols collected during the period February to May 1983, were each divided in two equal parts and each half was treated as described above. For all samples, both types of calibration were applied. The results given as means of two half-filter fractions, are summarized in Table 2. It can be seen that the concentrations vary between 0.12 and 0.78 ng m^{-3}. For concentrations above 0.3 ng m^{-3}, the standard deviation does not exceed 10%. These values are similar to the literature value for Sutton, England [3].

The precision of the technique was evaluated by measuring the amount of bismuth in the four quarters of one filter. The relative standard deviation of the entire procedure, including the quartering, was 2.0% for a mean value of 0.26 ng m^{-3} in one sample and 9.6% for a mean value of 0.15 ng m^{-3} in another sample.

No certified standard reference materials were available, which made direct evaluation of the accuracy impossible. Therefore the method was tested by analyzing particulate-loaded filters to which a known amount of bismuth was added before the digestion. The average recovery was 104.0% ± 5.0% (n = 10).

Secondly, bismuth was quantified in Orchard Leaves (NBS, SRM 1571). Only one tentative value of 0.1 μg g^{-1}, obtained by polarography, is available. For the digestion of this sample, a slightly modified procedure was used; 6.0 ml of 30% hydrogen peroxide was added cautiously to a 500-mg sample and 10 ml of concentrated sulfuric acid. The mixture was heated for about 20 min and after cooling, 5 ml of 2% (w/v) hydrazine sulfate was added to remove all the peroxide. Finally the digest was diluted to 50 ml

TABLE 2

Bismuth concentrations in atmospheric aerosols

Sampling		Bi found (ng m^{-3})	Sampling		Bi found (ng m^{-3})
Period	Number		Period	Number	
24/02—28/02	1	0.78 ± 0.01	29/04—02/05	6	0.17 ± 0.03
18/04—21/04	2	0.24 ± 0.01	02/05—04/05	7	0.12 ± 0.01
21/04—25/04	3	0.31 ± 0.02	04/05—06/05	8	0.36 ± 0.02
25/04—27/04	4	0.27 ± 0.05	06/05—09/05	9	0.21 ± 0.01
27/04—29/04	5	0.29 ± 0.03	20/05—24/05	10	0.47 ± 0.04

with distilled water. By hydride generation, with the parameters in Table 1, four analyses gave a mean value of 98.5 ± 15 ng g^{-1} was obtained, which is in agreement with the tentative value.

The detection limit, defined as the bismuth concentration corresponding to three times the standard deviation of the blank, was about 3 ng or 30 ng in 50 ml of the digest if 5-ml portions are measured. This corresponds to 0.08 ng m^{-3} for a sample of 500 m^3 of air.

This work was supported by the "Interuniversitair Instituut voor Kernwetenschappen" to whom we are sincerely grateful.

REFERENCES

1 K. A. Rahn, The chemical composition of the atmospheric aerosol, Tech. Rep., Univ. Rhode Island, USA, 1976.
2 W. M. Henry and E. R. Blosser, Identification and estimation of ions, molecules and compounds in particulate matter collected from ambient air, Tech. Rep. CPA-70-159, Battelle Columbus, OH, 1971.
3 E. I. Hamilton, Sci. Total Environ., 3 (1974) 3.
4 F. J. Fernandez, At. Absorpt. Newsl., 12 (1973) 93.
5 F. Chapman and L. S. Dale, Anal. Chim. Acta, 111 (1979) 137.
6 F. L. Fricke, W. D. Robbins and J. A. Caruso, J. Assoc. Off. Anal. Chem., 61 (1978) 1118.
7 D. S. Lee, Anal. Chem., 54 (1982) 1682.
8 Verein Deutscher Ingenieure, VDI 2463 - Blatt 4, VDI Verlag GmbH, Düsseldorf, 1976.
9 K. De Doncker, R. Dumarey, R. Dams and J. Hoste, Anal. Chim. Acta, 153 (1983) 33.

Analytica Chimica Acta, 161 (1984) 369—373
Elsevier Science Publishers B.V., Amsterdam — Printed in The Netherlands

Short Communication

DETERMINATION OF INDIUM IN GEOLOGICAL MATERIALS BY ELECTROTHERMAL-ATOMIZATION ATOMIC ABSORPTION SPECTROMETRY WITH A TUNGSTEN-IMPREGNATED GRAPHITE FURNACE

LIYI ZHOU[a], T. T. CHAO* and A. L. MEIER
U.S. Geological Survey, Box 25046, Federal Center, Denver, CO 80225 (U.S.A.)
(Received 8th February 1984)

Summary. The sample is fused with lithium metaborate and the melt is dissolved in 15% (v/v) hydrobromic acid. Iron(III) is reduced with ascorbic acid to avoid its coextraction with indium as the bromide into methyl isobutyl ketone. Impregnation of the graphite furnace with sodium tungstate, and the presence of lithium metaborate and ascorbic acid in the reaction medium improve the sensitivity and precision. The limits of determination are 0.025—16 mg kg^{-1} indium in the sample. For 22 geological reference samples containing more than 0.1 mg kg^{-1} indium, relative standard deviations ranged from 3.0 to 8.5% (average 5.7%). Recoveries of indium added to various samples ranged from 96.7 to 105.6% (average 100.2%).

Indium is widely dispersed in geological materials at very low concentrations [1]. It exhibits a distinctly chalcophile behavior in the minerals of the earth's crust and occurs in solid solutions in sulfide minerals with tetrahedral metal—sulfur bonds [2]. The crustal abundance of indium has been estimated to be 0.11—0.14 mg kg^{-1} [1, 3]. Indium in rocks and minerals can be quantified by atomic-emission spectrometry [3—6], neutron activation [7—10], or flame atomic-absorption spectrometry [11]. Some of the methods are either not sufficiently sensitive to determine the low concentrations of indium commonly found in geological materials, or require expensive instrumentation.

The electrothermal atomic-absorption method proposed here provides very low detection limits capable of determining indium to a lower limit of 0.025 mg kg^{-1}, well below the crustal abundance. Both lithium metaborate used for sample decomposition and ascorbic acid used to reduce interference from iron(III) enhance the absorbance values of indium significantly.

Experimental

Apparatus and calibration. An IL (Instrumentation Laboratory) 951 Model atomic absorption spectrometer was used with the following accessories:

[a]Permanent address: Institute of Geophysical and Geochemical Prospecting, Beijing, China.

0003-2670/84/$03.00

controlled-temperature furnace atomizer (IL 555 CTF), auto-sampling device (IL 254 FASTAC), deuterium arc background corrector, and indium hollow-cathode lamp. Settings for the spectrometer were as follows: lamp current 8 mA, wavelength 303.9 nm, bandwidth 0.5 nm, integration time 8 s, and readout as peak height; photomultiplier voltage was set by adjusting the HV control until the log intensity meter read between 0.2 and 0.8 V. Settings for the controlled-temperature furnace atomizer involved nitrogen at 15 SCFH as the purge gas, automatic operation mode, with temperature feedback on and autoclean off; atomization programs are summarized in Table 1.

Settings for the auto-sampling device involved a door calibration of 150°C, a sample deposition time of 5 s, and a delay time of 5 s. The FASTAC sample-delivery system aspirates the sample solution through a pneumatic nebulizer and deposits it as an aerosol in the graphite furnace.

Pyrolytic-graphite tubes were impregnated by immersing them overnight in a 7.8% solution of sodium tungstate dihydrate and drying them at 120°C in an electric oven for 4 h [12]. Before use, each impregnated tube was conditioned by going through the atomization program five times.

Reagents and standards. Reagents included lithium metaborate (anhydrous; G. Frederick Smith Chemical Company), ascorbic acid (30—80 mesh), and methyl isobutyl ketone (MIBK). A 1000 μg ml^{-1} stock solution of indium was prepared by dissolving 0.6045 g of specpure In_2O_3 in 250 ml of concentrated hydrobromic acid (48%) and diluting to 500 ml with water. A 1 μg ml^{-1} standard solution was prepared in 15% (v/v) hydrobromic acid by serial dilution of the stock solution. The dilute indium solution is stable for at least three months in a pyrex glass bottle.

Standard solutions in MIBK were prepared as follows: Eppendorf micropipets were used to transfer 0—4.00 ml (9 steps) of the 1 μg ml^{-1} standard to individual 25 × 200 mm screw-cap tubes; these were diluted to 50 ml with 15% hydrobromic acid and 0.75 g of ascorbic acid was added to each tube. Tubes were mixed on a vortex mixer to dissolve the solid. Exactly 10 ml of MIBK was added to each tube, tubes were shaken for 5 min, and the capped tubes were centrifuged to separate the organic phase. The organic extracts were transferred to 16 × 150 mm test tubes which were capped to prevent evaporation. The indium in the extract is stable for at least 48 h in a refrigerator.

TABLE 1

Summary of atomization programs

	Drying		Charring		Atomizing	
Step	1	2	3	4	5	6
Temp. (°C)	0	150	275	600	2200	2200
Time (s)	0	5	20	20	0	10

Procedure. Weigh 0.75 g of lithium metaborate and 0.250 g of soil, rock, or stream sediment (<100 mesh) into a 10-ml platinum crucible. Mix the flux and sample with a thin glass rod and fuse the sample in a muffle furnace at 1000°C for 1 h. After cooling, place the crucible in a 50-ml beaker and put a small magnetic stirring bar in the crucible. Add 30 ml of 15% hydrobromic acid to immerse the crucible. Heat the beaker at 50–60°C for about 30 min on a hotplate with stirring. Transfer the solution to a 25 × 200 mm screw-cap tube and wash the beaker with 10 ml of 15% hydrobromic acid. Add 0.75 g of ascorbic acid and extract the indium as described above. Measure the absorbance values for the organic extracts using the parameters listed above.

Results and discussion

Conditions. Lithium metaborate is a very effective flux for the decomposition and dissolution of silicate rocks and minerals [13], although certain minerals are only partially decomposed [14]. In this study, the combination of fusion with lithium metaborate with dissolution of the melt in 15% hydrobromic acid always yielded completely clear solutions for all the samples examined. The enhancement of the absorbance readings of indium by lithium metaborate is discussed below.

Liquid–liquid extraction of indium into MIBK serves to separate and concentrate indium prior to the measurement step. The extraction of indium from 15% hydrobromic acid (1.35 M) was confirmed to be greater than 95% [11]. Iron tends to be co-extracted with hydrobromic acid [15] and causes

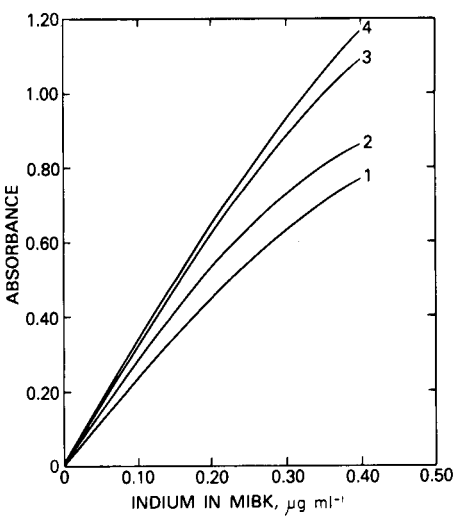

Fig. 1. Relationship between absorbance and concentration of indium in MIBK as affected by chemical reagents in the aqueous solution: (1) 15% (v/v) HBr; (2) 15% HBr + 0.75 g $LiBO_2$; (3) 15% HBr + 0.75 g ascorbic acid; (4) 15% HBr + 0.75 g $LiBO_2$ + 0.75 g ascorbic acid.

significant suppression of indium absorbance. Addition of ascorbic acid to reduce iron(III) decreases the extraction of iron into MIBK.

Lithium metaborate, ascorbic acid, and tungsten in the graphite tubes can significantly enhance the absorbance of indium. Therefore, standards and samples should be treated identically. As shown in Fig. 1, the enhancement by ascorbic acid is greater than that by lithium metaborate. Although the combination of lithium metaborate and ascorbic acid shows greater enhancement than either one alone, the effects are not additive. The tungsten-impregnated graphite tubes can be used for at least 500 firings, with little if any carryover.

The amount of indium required to give a 0.0044 absorbance change is

TABLE 2

Replicate determination (n = 5) of indium in various reference samples

Sample	Mean concentration (mg kg^{-1})	R.s.d. (%)	Recovery[a] (%)
Geochemical exploration reference samples			
GXR-1, jasperoid	0.39 ± 0.02	5.1	101.1[b], 97.3[c]
GXR-2, soil	0.084 ± 0.005	6.0	
GXR-3, Fe-Mn deposit	0.058 ± 0.004	6.9	96.7[b], 97.8[c]
GXR-4, Cu mill head	0.20 ± 0.008	4.0	
GXR-5, soil	0.11 ± 0.006	5.5	
GXR-6, soil	0.063 ± 0.008	12.7	
Sediment reference samples			
GSD-1, stream sediment	0.13 ± 0.007	5.4	100.0[b], 102.2[c]
GSD-2, stream sediment	0.10 ± 0.007	7.0	
GSD-3, stream sediment	0.11 ± 0.008	7.2	
GSD-4, pond sediment	0.13 ± 0.008	6.2	
GSD-5, pond sediment	0.13 ± 0.008	6.2	
GSD-6, stream sediment	0.17 ± 0.009	5.3	
GSD-7, stream sediment	0.092 ± 0.008	8.5	100.0[b], 104.8[c], 97.6[d]
GSD-8, stream sediment	0.074 ± 0.005	6.8	
Glass reference samples			
GSB	0.47 ± 0.01	2.1	104.2[b], 97.3[c]
GSC	3.74 ± 0.04	1.1	
Rock reference samples			
BHVO-1, basalt	0.18 ± 0.009	5.0	
MAG-1, marine mud	0.18 ± 0.009	5.0	
QLO-1, quartz latite	0.18 ± 0.008	4.0	
RGM-1, rhyolite	0.15 ± 0.005	3.3	100[b], 95.8[c]
SCo-1, Cody shale	0.11 ± 0.008	7.3	
SDC-1, mica shist	0.12 ± 0.007	5.8	103.3[b], 105.6[c]
SGR-1, oil shale	0.096 ± 0.010	10.0	
STM-1, nepheline syenite	0.15 ± 0.005	3.0	

[a] Recovery of approximately equal[b], two-fold[c], and three-fold[d] amounts of In.

1.2×10^{-13} g. For a 0.250-g sample, the practical range of indium concentrations that can be accurately determined is 0.05—16 mg kg^{-1} (curve 4, Fig. 1). If the volume of MIBK used for extraction is reduced to 5 ml, indium can be quantified down to 0.025 mg kg^{-1} which is considered to be well below the crustal abundance.

Results for geological samples. The proposed method was applied to four sets of geological samples. Samples included six USGS geochemical exploration reference samples [16], eight Chinese sediment reference samples [17], two USGS glass samples [18], and eight USGS rock standards [19]. Most of the natural geological materials contain indium in concentrations close to crustal abundance. Except for two samples which contain less than 0.1 mg kg^{-1} indium, the average relative standard deviation of the method is 5.7% with a range of 3.0—8.5%.

Recoveries of indium added to various samples ranged from 96.7 to 105.6% with an average of 100.2% (Table 2).

The proposed method has promise for the determination of indium in a wide variety of geological materials of diverse chemical composition.

REFERENCES

1 R. A. Weeks, U S Geol. Surv. Prof. Pap., 820 (1973) 237.
2 K. H. Wedepohl (Ed.), Handbook of Geochemistry, Springer-Verlag, New York, 1974, p. 49-A-1.
3 D. M. Shaw, Geochim. Cosmochim. Acta, 2 (1952) 185.
4 L. H. Ahrens, Am. Mineral., 35 (1950) 571.
5 G. M. Eskenazy and E. I. Mincheva, Analyst (London), 103 (1978) 1179.
6 Ruiping Shen, Geol. Rev. (China), 29 (1983) 87.
7 A. A. Smales, J. van R. Smit and H. Irving, Analyst (London), 82 (1957) 539.
8 O. Johansen and E. Steinnes, Talanta, 13 (1966) 1177.
9 P. A. Baedecker and J. T. Wasson, Science, 1967 (1970) 503.
10 J. W. Morgan, G. A. Wandless, R. K. Petrie and A. J. Irving, Proc. Lunar Planet. Sci. Conf., 11 (1980) 213.
11 A. E. Hubert and H. W. Lakin, in M. J. Jones (Ed.), Geochemical Exploration 1972, Institution of Mining and Metallurgy, London, 1973, p. 383.
12 H. Fritzche, W. Wegscheider, G. Knapp and H. M. Ortner, Talanta, 26 (1979) 219.
13 C. O. Ingamells, Anal. Chim. Acta, 52 (1970) 323.
14 M. Cremer and J. Schlocker, Am. Mineral., 61 (1976) 318.
15 A. R. Denaro and V. J. Occleshaw, Anal. Chim. Acta, 13 (1955) 339.
16 G. H. Allcott and H. W. Lakin, in I. L. Elliot and W. K. Fletcher (Ed.), Geochemical Exploration 1974, Elsevier, Amsterdam, 1975, p. 659.
17 Eight Geochemical Reference Sediment Samples: 1st Rep. Usable Values. Geophys. Geochem. Prospecting Rep. No. 7, 1981, Ministry of Geology, Beijing, China (in Chinese).
18 T. Myers, R. G. Havens, J. J. Connor, N. M. Conklin and H. J. Rose, Jr., U S Geol. Surv. Prof. Pap., 1013 (1976) 29.
19 F. J. Flanagan (Ed.), U S Geol. Surv. Prof. Pap., 840 (1976) 192.

Analytica Chimica Acta, 161 (1984) 375—379
Elsevier Science Publishers B.V., Amsterdam — Printed in The Netherlands

Short Communication

FLOW INJECTION SPECTROPHOTOMETRY FOLLOWED BY ATOMIC ABSORPTION SPECTROMETRY FOR THE DETERMINATION OF IRON(II) AND TOTAL IRON

J. L. BURGUERA and M. BURGUERA

Departamento de Química, Facultad de Ciencias, Universidad de Los Andes, Apartado 542, Mérida 5101-A (Venezuela)

(Received 30th January 1984)

Summary. In the flow system described, iron(II) is measured spectrophotometrically with 1,10-phenanthroline, and total iron is determined in the same flow line by atomic absorption spectrometry. Linear calibration ranges are 0.1—35 and 0.1—10 $\mu g\ ml^{-1}$ for iron(II) and total iron, respectively.

Flow injection analysis (f.i.a.) has been used in conjunction with amperometry for the determination of ca. 10^{-6} M of both iron(II) and iron(III) [1]. For iron(II), linear calibration was obtained over the range 1×10^{-5}—5×10^{-4} M, and for iron(III), over the range 10^{-5}—10^{-3} M. Although the standard deviations were good (ca. 2.0 and 2.9% for iron(II) and iron(III), respectively), it was necessary to use large sample volumes (490 μl). More recently, Mortatti et al. [2] described a flow-injection system for the spectrophotometric determination of total iron in waters and plant material by the 1,10-phenanthroline method. Their proposed procedure allowed the determination of total iron concentrations in the range 0.1—30 mg l^{-1}, with a relative standard deviation of less than 1%.

A combination of f.i.a. with two different detection techniques used in series has not been reported before. The purpose of this communication is to describe some of the analytical potentialities of spectrophotometry used in series with atomic absorption spectrometry in a flow-injection system. A procedure for the simultaneous determination of iron(II) and total iron is described. Iron(II) is determined by measuring the absorbance of its 1,10-phenanthroline complex at 510 nm [3], and total iron is determined by measuring the atomic absorbance at 248.3 nm.

Experimental

Equipment. A schematic diagram of the flow-injection system is shown in Fig. 1. The sample (150 μl) was injected into a 0.15% (w/v) 1,10-phenanthroline carrier solution pumped at 0.80 ml min^{-1}. The polyethylene tubing used in the manifold was 0.5 mm i.d., l_1 (Fig. 1) constituted the reaction tube, in which the iron(II) chelate was formed. As the chelate

0003-2670/84/$03.00

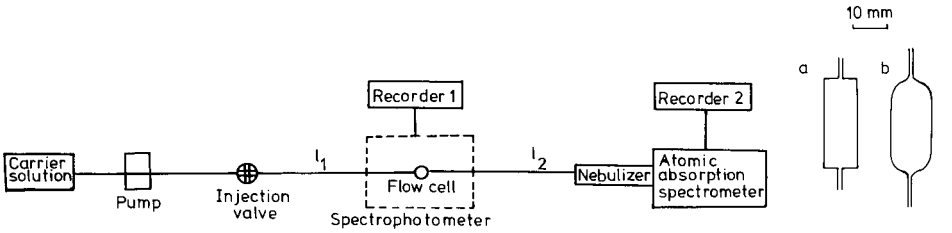

Fig. 1. Flow diagram of the system. The flow-through cells tested (a and b) are shown to the right. For details, see text.

passed through the flow-through cell in the Shimadzu UV-110-02 spectrophotometer, the absorbance at 510 nm was recorded on recorder 1. After the sample plug left the flow cell, it passed through l_2 to a Varian 1475-BD atomic absorption spectrometer, where it was nebulized and the absorbance signal response of total iron was measured at 248.3 nm, and recorded on recorder 2. The conditions for the measurement of iron atomic absorption signals were adjusted for maximum instrumental stability and sensitivity, and were as follows: acetylene flow, 1.6 l min^{-1}; air flow, 9.0 l min^{-1}; hollow-cathode lamp operating current, 5 mA; slit width, 0.2 mm; burner height, 11 mm. The concentrations of iron(II) and total iron were obtained from the absorbance peak heights on recorders 1 and 2, respectively.

Two quartz flow-through cell designs were considered (Fig. 1), both with a path-length of 10 mm, internal dimensions of 5 × 10 mm and 0.5-ml capacity. Each cell was connected so that the carrier stream entered it from below. For the spectrophotometric determination of iron(II), the flow cell design did not have a significant influence on the absorbance signal ($<2\sigma$), but it did affect significantly the absorbance signal obtained for total iron ($>4\sigma$). Thus, when flow cell (a) was used, irreproducible, lower and broader peak responses were obtained (Fig. 2), whereas when flow cell (b) was used, results were reproducible. Clearly, each flow cell behaves like a small mixing chamber, but the dispersion in flow cell (a) is excessive. Therefore, cell (b) was used throughout.

Chemicals. All chemicals used were of analytical grade. Iron(II) ammonium sulphate and iron(III) nitrate (Merck) were used for preparation of the standard solutions of iron(II) and iron(III), respectively, in acetate buffer (0.2 M acetic acid/0.2 M sodium acetate, pH 4.0). Double-distilled water was used. A 0.15% (w/v) 1,10-phenanthroline (Merck) solution was prepared in the acetate buffer, stored in a black bottle and kept in the dark. If a color developed, the solution was discarded.

Results and discussion

The flow-injection system described (Fig. 1) was constructed in a single line without the use of special components. The introduction of the sample into the carrier stream gives one peak response on each recorder, as illustrated

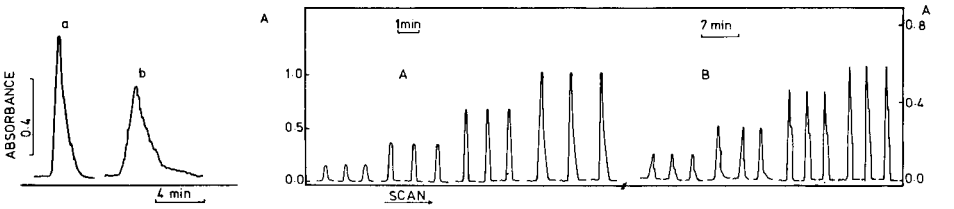

Fig. 2. Typical f.i.a. responses from total iron: (a) with flow cell b; (b) with flow cell a. Conditions: 6 mg l^{-1} each of Fe(II) and Fe(III); 150-μl sample; 0.80 ml min^{-1} flow rate; l_1 = 300, l_2 = 35 cm (0.5 mm i.d.).

Fig. 3. (A) Recorder 1 output for iron(II); signals from left to right correspond to 1, 10, 20 and 35 mg l^{-1} Fe(II). (B) recorder 2 output for total iron with Fe(II); Fe(III) = 1:1; signals from left to right correspond to 2, 4, 8 and 10 mg l^{-1} total Fe (l_2 = 40 cm, other conditions as in Fig. 2).

in Fig. 3. The peak height obtained from recorder 1 (Fig. 3A) corresponds to the absorbance of iron(II) complex, while the peak height obtained from recorder 2 (Fig. 3B) corresponds to the atomic absorbance of total iron.

Determination of iron(II). The optimal conditions for iron(II) determination were first established. The effects of changing the length of l_1, sample volume and flow rate were examined. When the length of l_1 was changed within the range 100—500 cm, almost the same signal was obtained with a 100-cm tube as with a 300-cm tube when a 150-μl sample was injected. This indicates that the colored complex was formed within a few seconds. A 300-cm length gave the best precision and sensitivity. An increase in the length above 450 cm broadened the peak and almost halved its height, as well as giving poor reproducibility, because of increased dispersion. The peak heights increased with increasing sample volume in the range 50—300 μl. With sample volumes smaller than 100 μl, irreproducible results were obtained; above 150 μl, the signal increases were small. Therefore, a sample volume of 150 μl was used in all subsequent work. The flow rate was varied between 0.5 and 1.40 ml min^{-1}. The higher the flow rate, the higher the peak, but the reproducibility was poor when the flow rate exceeded 1.0 ml min^{-1}. Thus 0.80 ml min^{-1} was used for subsequent work. Thus, the behavior of the iron(II) absorbance peak was basically the same as in previously reported flow-injection studies where other chemical species were determined spectrophotometrically [4, 5].

Under optimal conditions, the dispersion [6, 7] was always about 1.4 and the calibration graph was linear for 0.015—5.25 μg (0.1—35 mg l^{-1}) of iron(II) with a correlation coefficient (r) of 0.9982 (6 points). The relationship between the maximum absorbance ($A_{Fe(II)}$) and the iron(II) concentration was $A_{Fe(II)} = 0.031 + 0.194\ m_{Fe(II)}$ where $m_{Fe(II)}$ is the mass of iron(II) in μg.

Determination of total iron. For the determination of total iron, the parameters previously described and the flow cell design, the degree of

dispersion of the sample pumped into the atomic absorption spectrometer nebulizer depended not only on the above-mentioned parameters of the system but also on the length and diameter of tubing l_2 (Fig. 1), which was therefore optimized. With a constant length of tubing l_1, the peak height remained almost constant for l_2 between 25 and 50 cm (Fig. 4A), but became slightly lower and broader for longer tubes ($\geqslant$60 cm), because of increased dispersion; the instrumentation did not allow the use of l_2 <25 cm. Broadening and tailing of peaks were found when the internal diameter of l_2 was increased from 0.5 to 0.75 or 1.0 mm, again because of increased dispersion (Fig. 4B). Therefore, l_2 of length 35 cm and diameter 0.5 mm was used subsequently. Under these conditions, the dispersion was always ca. 1.9, and the calibration graph was linear for 0.015—1.5 μg (0.1—10 mg l^{-1}) of total iron, with r = 0.9996 (6 results). The relationship between the maximum absorbance and total mass of iron was expressed by the equation: $A_{Fe} = 0.004 + 0.381 m_{Fe}$ where A_{Fe} represents peak absorbance and m_{Fe} represents the total mass of iron in μg. When equal amounts of iron(II) or iron(III) were injected, the same atomic absorption responses were obtained, probably because a fuel-lean air-acetylene flame was used [8].

In the system described, good reproducibility was obtained, with relative standard deviations of 1.2 and 1.5% for 5 mg l^{-1} iron(II) and total iron (8 determinations), respectively. A dispersion of ca. 1.4 and 1.9 for the spectrophotometric and atomic absorption detectors, respectively, was always found at the optimal conditions, thus indicating low dispersion in both cases. The signals for iron(II) and total iron were available within 30 and 100 s after sample injection, respectively. The rate of injection is about 60 h^{-1}.

The results obtained by the proposed flow-injection system were checked against results found by conventional spectrophotometric [3] and atomic absorption methods [8]. The results (Table 1) are in good agreement. This flow-injection system is faster and uses smaller sample volumes than the earlier flow-injection procedure [2] and has the advantage that the iron species can be determined with a single injection, without using confluence streams and avoiding distinct chemical reactions, thus decreasing dispersion.

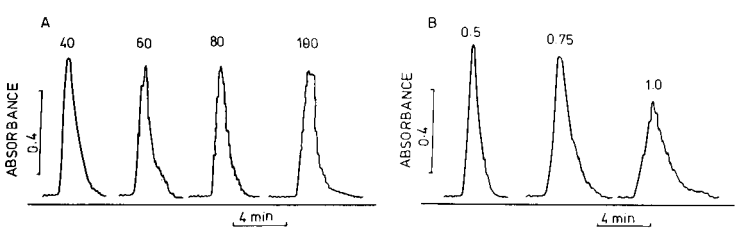

Fig. 4. Effects of (A) length and (B) internal diameter of l_2 on the peak height and shape for total iron. (A) Numbers indicate length in cm, for 0.5 mm i.d. tubing; (B) numbers indicate i.d. in mm for 40 cm of tubing. Other conditions as for Fig. 2.

TABLE 1

Determination of iron(II) and total iron

Conc. of iron added ($mg\ l^{-1}$)		Conc. of iron found ($mg\ l^{-1}$)			
		F.i.a.[a]		Spectrophotometry[b]	A.a.s.[c]
Fe(II)	Fe(III)	Fe(II)	Total iron	Fe(II)	Total iron
30.0	0.0	29.8	—[d]	29.5	—[d]
5.0	7.5	4.8	12.3	4.9	12.5
1.0	1.0	0.8	2.0	0.9	2.0
0.0	10.0	0.0	9.8	0.0	9.8

[a]150-μl sample. [b]Conventional method, 1.2-ml sample volume, r.s.d. 2.1%. [c]Direct aspiration atomic absorption procedure, 5-ml sample volume, r.s.d. 1.5%. [d]Out of linear range.

REFERENCES

1 J. W. Dieker and W. E. van der Linden, Anal. Chim. Acta, 114 (1980) 267.
2 J. Mortatti, F. J. Krug, L. C. R. Pessenda, E. A. G. Zagatto and S. S. Jørgensen, Analyst (London), 107 (1982) 659.
3 W. Horwitz (Ed.), Association of Official Analytical Chemists, Official Methods of Analysis, 13th edn., A.O.A.C., Washington, DC, 1980, p. 600.
4 T. Yamane and T. Fukasawa, Anal. Chim. Acta, 119 (1980) 389.
5 G. Nakagawa, H. Wada and C. Wei, Anal. Chim. Acta, 145 (1983) 135.
6 J. Růžička and E. H. Hansen, Anal. Chim. Acta, 99 (1978) 37.
7 E. A. G. Zagatto, A. O. Jacintho, L. C. R. Pessenda, F. J. Krug, B. F. Reis and H. Bergamin F°., Anal. Chim. Acta, 125 (1981) 37.
8 K. C. Thompson and K. Wagstaff, Analyst (London), 105 (1980) 641.

Analytica Chimica Acta, 161 (1984) 381—386
Elsevier Science Publishers B.V., Amsterdam — Printed in The Netherlands

Short Communication

EXTRACTION OF ORGANIC ACIDS BY ION-PAIR FORMATION WITH TRI-N-OCTYLAMINE
Part 2. Back-extraction

M. PUTTEMANS, L. DRYON and D. L. MASSART*

Pharmaceutical Institute, Vrije Universiteit Brussel, Laarbeeklaan 103, B-1090 Brussels (Belgium)

(Received 10th February 1984)

Summary. Acids, extracted with tri-n-octylamine, are extracted back to an aqueous phase. The back-extraction is based on a displacement reaction. Several displacing ions were used: chloride, bromide, iodide, nitrate and perchlorate. The efficiency increases in the order chloride < bromide < iodide < perchlorate. The back-extraction yield is directly proportional to the concentration of the displacing ion and inversely proportional to the tri-n-octylamine concentration.

The extraction of some organic acids by ion-pair formation with tri-n-octylamine (TnOA) was discussed in the first part of this series [1]. Quantitative recoveries can be obtained even with hydrophilic substances. The extracted species have to be identified and quantified by techniques such as thin-layer (t.l.c.) or high-performance liquid chromatography (h.p.l.c.). It was demonstrated earlier [2] that TnOA-dye ion-pairs can be chromatographed directly both in t.l.c. and h.p.l.c. However, in t.l.c. the mobile phase must be relatively polar and in h.p.l.c. the column must be rinsed regularly in order to elute the adsorbed TnOA which disturbs the elution of the solutes. Similar problems were also observed in liquid—liquid ion-pair chromatography on injection of solutes as ion-pairs with a hydrophobic counter-ion [3]. Therefore, for h.p.l.c., it is preferable to extract the analytes back to an aqueous phase by means of a displacement reaction for which several anions have been tested [4]. Such a back-extraction can also yield purer extracts, which may be of high importance in some cases.

This communication discusses the influence of the nature and concentration of the displacing ion on the back-extraction yield.

Experimental

Apparatus. Ultraviolet and visible photometric determinations were done with a Hitachi 200 Perkin-Elmer spectrophotometer. Ion concentrations were measured with an Orion 601 Ionalyzer, with a combined glass electrode, a combined bromide electrode and a combined iodide electrode (Orion).

Chemicals and reagents. Tri-n-octylamine was from Aldrich Europe (Beerse, Belgium). Sodium sorbate (Fluka) and sodium benzoate (Merck)

0003-2670/84/$03.00

were both analytical grade. Quinoline yellow (E 104) and amaranth (E 123) were from P. Entrop (Machelen, Belgium). All other reagents used were analytical grade from Merck. All aqueous solutions were prepared in twice-distilled water.

Extraction. Batch extractions were done with equal volumes of aqueous and organic phase. After 30 min of extraction, the concentration of the acid was determined in the aqueous phase. Full details about the procedure were given in Part 1 [1].

Back-extraction. A portion (5 ml) of the TnOA extract in chloroform was extracted for 30 min with 5 ml of a sodium salt solution of given concentration. After phase separation, the concentration of the acid in the aqueous layer was determined by spectrophotometry. Each partition experiment was done in triplicate.

Extraction of bromide and iodide ions. Solutions of sodium iodide and sodium bromide (0.001 and 0.005 M) were prepared in twice-distilled water which had been saturated with chloroform. Each solution (10 ml) was shaken for 30 min with 10 ml of a TnOA solution in chloroform (0.1 or 0.01 M). After phase separation, the bromide or iodide concentration in the aqueous phase was measured by means of ion-selective electrodes. Standards, in a 10^{-5}—10^{-3} M range, were prepared in chloroform-saturated water. In most cases, the aqueous phase was diluted 10 times in order to adjust the bromide or iodide concentration to fall within the calibration range.

Theory

The extraction, from an aqueous (subscript w) to an organic (subscript o) phase, of the anion X^- by ion-pair formation with TnOA is described by the following equilibrium, with extraction constant K_{ex}

$$TnOA_o + H^+_w + X^-_w \rightleftharpoons TnOAHX_o ; K_{ex} = [TnOAHX]_o/[TnOA]_o [H^+]_w [X^-]_w \quad (1)$$

The back-extraction of X^- by a displacement reaction, with the equilibrium constant K_{back}, is

$$TnOAHX_o + Y^-_w \rightleftharpoons TnOAHY_o + X^-_w ;$$

$$K_{back} = [TnOAHY]_o [X^-]_w/[TnOAHX]_o [Y^-]_w \quad (2)$$

The extraction of Y^- can also be described by its extraction constant K_Y:

$$K_Y = [TnOAHY]_o/[TnOA]_o [H^+]_w [Y^-]_w \quad (3)$$

The back-extraction yield can be expressed as a percentage or as the distribution ratio for back-extraction, D_{back}: $D_{back} = [X^-]_w/[TnOAHX]_o$. From Eqn. 2, it can be derived that

$$D_{back} = K_{back}[Y^-]_w/[TnOAHY]_o \quad (4)$$

Substitution of Eqn. 3 into this equation gives

$$D_{back} = K_{back}/K_Y [H^+]_w [TnOA]_o \quad (5)$$

Results and discussion

Effect of the concentration of the displacing ion. In previous work [4], the eleven food dyes permitted in the EEC, were extracted with 0.1 M TnOA and extracted back to an aqueous phase with 0.1 M solutions of sodium chloride, bromide, iodide or perchlorate; perchlorate gave the highest yields. The effect of the concentration of the displacing ion on the recovery obtained for this back-extraction is described here.

The theoretical influence of the concentration of the displacing ion on the back-extraction yield is given by Eqn. 4. Back-extractions were done with 0.005—0.5 M solutions of sodium chloride, bromide, iodide, nitrate or perchlorate. The analytes investigated were amaranth and quinoline yellow, two food dyes, and benzoic acid and sorbic acid, two preservatives. The dyes showed 100% recovery with 0.1 M sodium perchlorate, whereas only 50% of benzoic acid and 84% of sorbic acid were recovered when an initial TnOA concentration of 0.1 M was used.

As can be seen in Table 1, where the slopes of the graphs of D_{back} versus the displacing ion concentration are given, the slopes increase in the order chloride < bromide < iodide < perchlorate for most of the substances investigated. This confirms some former conclusions [4] and also the data found on the interference of inorganic anions with the extraction of long-chain amines by an anionic dye (disulfine blue) [5]. In the latter study, it was observed that the interference followed the order chloride < nitrate < bromide < iodide < perchlorate. However, Gindil et al. [6] concluded that these ions should rather be arranged according to their tendency to be extracted by ion-pair formation: chloride < bromide < nitrate < iodide < perchlorate. The present data (Table 1) also suggest that the nitrate ion

TABLE 1

Slopes of the graph D_{back} (distribution ratio for the back extraction) versus C_Y (concentration of the displacing ion)

	TnOA conc. (M)	Slope of graph				
		Cl^-	Br^-	I^-	NO_3^-	ClO_4^-
E 104	0.1	39	103	403	82	368
E 104	0.01	116	156	459	574	5902
E 123	0.1	67	92	805	3153	1469
E 123	0.01	8445	10418	11619	916	15423
Sorbic acid	0.1	2	381			1099
Sorbic acid	0.01	2	23			107
Benzoic acid	0.1	2	12			9
Benzoic acid	0.01	5	10			7

cannot be classified so easily. Indeed, different sequences are observed not only for amaranth and quinoline yellow, but also with different TnOA concentrations for a given analyte.

The slopes of the graphs listed in Table 1 for the preservatives, especially benzoic acid, are much lower than the slopes obtained for the dyes, i.e., there is a large difference between the low back-extraction yield for benzoic acid and the quantitative recovery of the dyes. As the preservatives were measured by u.v. spectrophotometry, back-extraction yields with nitrate and iodide could not be measured for benzoic and sorbic acids, because of the high u.v. absorbance of the displacing ion itself.

In Table 2, back-extraction data are given at different TnOA concentration levels. According to Eqn. 5, the distribution ratio for back-extraction is inversely proportional to the amine concentration. This is also reflected by the slopes of the graphs listed in Table 1; in most cases the slopes obtained are higher with 0.01 M TnOA than with 0.1 M TnOA. This indicates that at a lower counter-ion (TnOA) concentration, the back-extraction is more successful. This is shown in Table 2 for benzoic acid and sorbic acid. The extraction yields with 0.1 and 0.01 M TnOA are quite similar for the initial extraction: the difference is ca. 2% for sorbic acid and ca. 5% for benzoic acid. It is obvious that these small losses are largely compensated by the much more successful back-extraction when the lower TnOA concentration is used, providing a higher overall extraction yield with 0.01 M TnOA.

Extraction of bromide and iodide with TnOA. Amines can extract acids by neutralization, addition and anion-exchange reactions [7]. The extraction of mineral acids with tri-n-octylamine has been described by several authors. Allen [8] and Wilson [9] described the extraction of sulfuric acid into benzene. Sato [10] used benzene to extract sulfuric, hydrochloric, nitric and perchloric acids, whereas Keder and Wilson [11] used benzene, tetrachloromethane and trichloromethane to extract the same acids as well as hydrobromic acid and hydroiodic acid. Typically, acids in concentrations between 0.1 and 10 N, were extracted with an organic solvent containing 0.1 M TnOA [8, 10, 11]. Gérin and Fresco [12] first prepared TnOA salts such as TnOAHCl, TnOAHBr, and then partitioned these salts between

TABLE 2

Back-extraction with 0.1 M sodium salt solutions as a function of the TnOA concentration

	TnOA conc. (M)	Extr. with TnOA (%)	Back-extraction (%)		
			Cl^-	Br^-	ClO_4^-
Sorbic acid	0.1	99	22.7 ± 0.1	65.4 ± 0.7	83.8 ± 0.3
Sorbic acid	0.01	96.8	43.7 ± 0.4	99.7 ± 0.9	99.9 ± 0.2
Benzoic acid	0.1	99	21.0 ± 0.1	63.6 ± 0.1	59.2 ± 0.3
Benzoic acid	0.01	93.8	57.5 ± 0.2	79.3 ± 0.1	78.4 ± 0.3

TABLE 3

Extraction of bromide and iodide ions to TnOA in chloroform

Ion	Initial conc. (M)	Extraction (%)	
		0.1 M TnOA	0.01 M TnOA
Iodide	0.001	54.0 ± 0.8	14.2 ± 2.3
Iodide	0.005	12.7 ± 2.8	8.1 ± 1.8
Bromide	0.001	38.7 ± 3.5	16.7 ± 1.5
Bromide	0.005	30.0 ± 1.3	6.0 ± 0.03

water and nitrobenzene. All these authors extracted the acid and explained the extraction as neutralization of the amine.

In the present study, a neutral medium was chosen; the sodium salts of the above-mentioned acids were used. Indeed, as the analytes to be extracted were acids, they would, under acidic conditions, tend to partition as undissociated acids between the organic and aqueous phases. Such a partition would hinder considerably the back-extraction of the analytes. Furthermore, as the back-extracted analytes had to be identified and quantified by t.l.c., h.p.l.c. or spectrophotometry, it was preferable to avoid very acidic extracts.

In order to confirm the displacement reaction (based on an exchange of ions), the transfer of bromide and iodide ions from the aqueous to the organic phase was investigated. Solutions (0.001 M) of sodium bromide and sodium iodide were extracted with 0.1 M and 0.01 M TnOA in chloroform. The data listed in Table 3 show that the concentration of bromide and iodide ions in the aqueous phase decreased after equilibration with the TnOA solution in chloroform. This decrease must be due to interaction with the counter-ion because the TnOA concentration exerts a distinct effect. It is also obvious that iodide is more readily extracted than bromide, which supports the observation that iodide gives higher back-extraction yields than bromide. By determining the distribution ratio for 0.005 M sodium bromide and sodium iodide solutions at different TnOA concentrations, it is possible to calculate the value of K_Y from the intercept of the graph D_Y versus $[TnOA]_o[H^+]_w$. The values found for log K_Y were 0.48 for bromide and 2.72 for iodide.

In conclusion, it can be stated that acids extracted as ion-pairs with TnOA, can be extracted back to an aqueous phase with sodium chloride, bromide, iodide, nitrate and perchlorate. Highest recoveries were obtained with perchlorate. If the yield is less than 100%, it is preferable to use the following scheme: extraction with 0.01 M TnOA and back-extraction with 0.1 M sodium perchlorate.

The authors acknowledge financial help from the Fund for Scientific Medical Research and thank A. Langlet-De Schrijver and K. Broothaers-Decq for technical assistance.

REFERENCES

1 M. Puttemans, L. Dryon and D. L. Massart, Anal. Chim. Acta, 161 (1984) 221.
2 M. Puttemans, L. Dryon and D. L. Massart, J. Assoc. Off. Anal. Chem., 65 (1982) 730.
3 S. Eksborg and G. Schill, Acta Pharm. Suec., 12 (1975) 1.
4 M. Puttemans, L. Dryon and D. L. Massart, J. Assoc. Off. Anal. Chem., 65 (1982) 737.
5 H. K. Biswas and B. M. Mandal, Anal. Chem., 44 (1972) 1636.
6 Gindil, cited by V. S. Shmidt, Amine Extraction, Israel Program for Scientific Translations, Jerusalem, 1971, p. 53.
7 V. S. Shmidt, Amine Extraction, Israel Program for Scientific Translations, Jerusalem, 1971.
8 K. Allen, J. Phys. Chem., 60 (1956) 230.
9 A. Wilson, Solv. Extr. Chem., (1967) 369.
10 T. Sato, J. Appl. Chem., 15 (1965) 10.
11 W. E. Keder and A. S. Wilson, Nucl. Sci. Eng., 17 (1967) 287.
12 M. Gérin and J. Fresco, Anal. Chim. Acta, 97 (1978) 165.

Analytica Chimica Acta, 161 (1984) 387—391
Elsevier Science Publishers B.V., Amsterdam — Printed in The Netherlands

Short Communication

MATRIX-DEPENDENT INSTABILITY OF SELENIUM(IV) STORED IN TEFLON CONTAINERS

THOMAS W. MAY* and DONALD A. KANE

U.S. Fish and Wildlife Service, Columbia National Fisheries Research Laboratory, Route 1, Columbia, MO 65201 (U.S.A.)

(Received 26th September 1983)

Summary. Solutions of selenium(IV) standards with different acid matrices were stored in containers constructed of borosilicate glass, conventional polyethylene, and fluorinated ethylenepropylene (teflon FEP). After 50 days of storage in FEP, there were highly significant losses of Se(IV) from standards in either 5% HCl/5% H_2SO_4 or 5% H_2SO_4. Increasing the hydrochloric acid concentration, e.g., 15% HCl/5% H_2SO_4, greatly reduced this loss. Addition of selenium-75 (selenate-free) indicated that the losses did not result from physical adsorption onto container surfaces. It is shown that the losses were caused by oxidation of Se(IV) to Se(VI).

Methods of storing solutions of selenium involving various pH conditions and container materials are primarily intended to preserve Se(IV) and Se(VI) in natural water samples until acid digestion or instrumental quantitation [1—5]. There is little information about the storage of Se(IV) in standard solutions or acid digestates. Although Shendrikar and West [6] studied the rate of loss of selenium from standards at varying pH in different containers, they used only nitric acid for sample acidification, which is incompatible with the fluorimetric and hydride generation procedures [1, 7, 8]. The shelf life of Se(IV) in standard solutions or acid digestates involving both different acids and different container materials has not been investigated. The need for such information became apparent when a substantial loss of Se(IV) was discovered from 2-mg l^{-1} working stock solutions in dilute sulfuric acid with or without hydrochloric acid stored in fluorinated ethylenepropylene (FEP) containers. The influence of container material and acid on the stability of Se(IV) in aqueous solutions was therefore investigated.

Experimental

Materials. All storage containers used had a capacity of 125 ml and were made of borosilicate glass (Wheaton "400" brand), conventional polyethylene (Bel Art), or teflon FEP (Nalge).

Reagents. Concentrated hydrochloric acid (Baker; ACS grade) was purified by subboiling distillation. A 3% solution of sodium tetrahydroborate (Alfa Products, 98%) was prepared as needed and stabilized by adding 1%

sodium hydroxide (MCB, ACS grade). Concentrated nitric and sulfuric acids were from Baker (ACS grade). Selenium-75 radionuclide (selenate-free) as selenous acid in 0.5 M HCl was from New England Nuclear. Selenium(IV) standards were prepared by dilution of a Fisher 1000-ppm atomic absorption reference standard.

Cleaning procedure for containers. The cleaning procedure was designed to accommodate the shorter leaching period recommended by Karin et al. [9], but included an additional leaching acid (HCl), as recommended by Moody and Lindstrom [10]. Containers were filled to overflowing with a solution containing 2 parts of nitric acid, 1 part of hydrochloric acid and 2 parts of water, capped, and stored for at least three days. After this leaching period, each container was thoroughly rinsed, filled with ultrapure water (15—18 Mohm cm), and sealed until use.

Design of storage study. A total of 15 storage containers, 5 of each type of material, were filled with the same volume of a Se(IV) standard solution (2 mg l^{-1}) in a specific acid solution. After 50 days, the containers were cleaned as described above and filled with another Se(IV) standard (2 mg l^{-1}) in a different acid matrix. Four acid matrices were studied in the following order: 15% HCl, 5% HCl/5% H_2SO_4, 15% HCl/5% H_2SO_4, and 5% H_2SO_4. In addition, each standard contained enough selenium-75 to provide >10 000 cpm ml^{-1}. From a 2 l volumetric flask, an equivalent weight of standard solution (100 g) was poured into each of the 15 containers on the first day (Day 1) of the storage study. All solutions were stored at room temperature and selenium was quantified on days 1, 4, 12, 20, 28, 36 and 50.

Hydride generation and γ-counting. Selenium was determined with a Perkin-Elmer (P-E) MHS-10 hydride system interfaced to a P-E Model 5000 atomic absorption spectrometer. A portion (30 μl) of an acidified 2-mg l^{-1} working stock solution and 10 ml of diluent with the same acid(s) was mixed in an MHS-10 polypropylene reaction flask to yield an effective selenium concentration of 6 μg l^{-1}. This solution was treated with the tetrahydroborate solution, and hydrogen selenide was flushed with argon into an open-ended quartz cell heated in an air-acetylene flame. Each storage solution was processed in triplicate and the average peak height was displayed.

Concurrent with selenium quantitation, a 1-ml aliquot of each 2 mg l^{-1} stock solution was measured for selenium-75 activity. A Beckman Gamma 8000 counting system (2-channel) equipped with a 3 × 3-in. sodium iodide (Tl) crystal was used to count the entire γ-spectrum; the relative standard deviation was <1% [11].

Statistical treatment. Analysis of variance (ANOVA) was done by the General Linear Models procedure [12]. The General Linear Models class level information was as follows: 6 days, 4 acid solutions, 3 container types, and 5 samples (5 bottles of standard solution for each container type). For confirmation of Se(IV) loss (95% probability level), all Se(IV) concentration data were analyzed as a split plot in time, in which the main plot was arranged as a 3 × 4 (3 container types × 4 acid solutions) factorial design. In

this factorial arrangement, the "within" container type × matrix interaction was used as the main plot error. The subplot contained the main effects of time (days) and all possible interactions of time, container type, and matrix. If significant interactions were indicated, specific means were compared with Fisher's protected least significant difference test (LSD) [13]. Equal cell size (equal n) was necessary so that potential inequality of variances would have little effect on inferences about means [14].

Results and discussion

The storage behavior of the Se(IV) plus selenium-75 solutions over a 50-day period is shown in Fig. 1. For all acid solutions and container materials, selenium-75 concentrations on day 50 varied by $\leqslant 2\%$ from the ^{75}Se concentrations determined on day 1 (Fig. 1). This small change confirmed that all of the acid solutions prevented adsorption of selenium onto glass, polyethylene, and FEP surfaces. Therefore, any loss of Se(IV) from solution, as indicated by the hydride generation method, must involve a chemical change in the form of selenium rather than physical adsorption. The first phase of the storage study concerned Se(IV) solutions in 15% hydrochloric acid. There was no significant change in Se(IV) concentrations over time in any of the containers studied (Fig. 1). Because all possible interactions of time, container type, and acid solution were highly significant ($p > F = 0.001$),

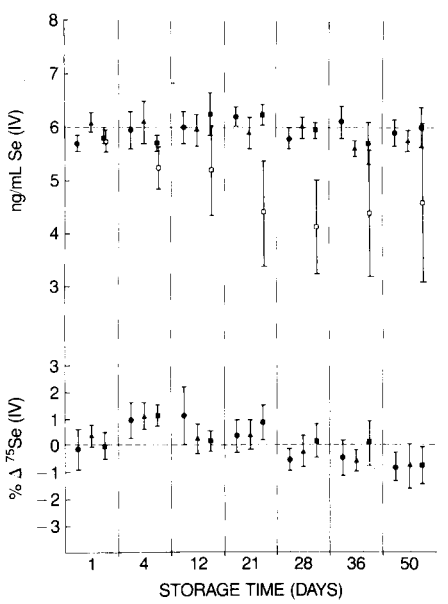

Fig. 1. Effects on the concentration of Se(IV) and ^{75}Se of storage in different acid solutions (solid symbols, 15% HCl; open symbols, 5% HCl/5% H_2SO_4) and in different container materials: (●) borosilicate glass; (▲) conventional polyethylene; (■) FEP. Symbol and bars represent mean and standard deviation of selenium concentrations from 5 containers of each material.

specific means (LSD) were compared. No significant differences between days 1 and 50 were indicated for any material associated with the 15% hydrochloric acid solution.

In the next set of tests, Se(IV) solutions 5% HCl/5% H_2SO_4 were stored. This acid mixture in FEP produced a major, progressive loss of Se(IV) from solution (Fig. 1). No significant change in Se(IV) concentrations occurred from solutions stored in glass and polyethylene. The average of Se(IV) concentrations from all five FEP containers on day 1 was significantly different from that on day 50 ($p < 0.01$). The large standard deviation about the mean for FEP solutions, as apparent in Fig. 1, indicated a difference in effect among FEP containers. For example, on day 50 the Se(IV) concentrations stored in FEP containers ranged from 2.79—6.40 ng ml^{-1}. A significant difference ($p < 0.001$) between solutions in bottles of the same material was apparent only for FEP.

When Se(IV) solutions in 15% HCl/5% H_2SO_4 were stored for 50 days, the mean Se(IV) concentrations for glass and FEP between days 1 and 50 were significantly different ($p < 0.05$). However, this difference was probably a result of variability in quantitation rather than a true loss. For example, mean Se(IV) concentrations in both glass and FEP were about 6 ng ml^{-1} on day 36 (no loss), and there was no indication of an overall steady and progressive Se(IV) loss across the seven time segments, such as was apparent with the 5% HCl/5% H_2SO_4 solution (Fig. 1).

With 5% sulfuric acid, the results were nearly identical to those with the 5% HCl/5% H_2SO_4 solution. Whereas solutions stored in glass and conventional polyethylene displayed no apparent change in Se(IV) concentrations over a 50-day period, there was a major loss of Se(IV) in FEP containers beginning on day 15 and then continuing. Mean Se(IV) concentrations during days 1—50 differed significantly only for those solutions stored in FEP ($p < 0.001$). Again, there was a large standard deviation about the mean for solutions stored in FEP caused by substantial differences in Se(IV) loss among FEP containers, with Se(IV) concentrations ranging from 3.69 to 5.65 ng ml^{-1}. The only container material for which a significant difference among bottles ($p < 0.001$) was indicated was FEP.

Inasmuch as quantitation by hydride generation is specific for Se(IV), not Se(VI), a hydrochloric acid reduction experiment was conducted to establish if the loss of Se(IV) was actually due to its oxidation to Se(VI). Storage of Se(IV) solutions in 5% HCl/5% H_2SO_4 for 50 days was repeated with the original FEP containers in which the loss was first demonstrated. In two of these Se(IV) solutions, losses after 50 days were found to be 16% and 29%, respectively. Duplicate 10-ml aliquots from these solutions were placed in a 100-ml pyrex beaker with watchglass; 15 ml of concentrated hydrochloric acid was added to each beaker; and all solutions were heated to boiling on a hotplate at 200°C. After cooling and dilution to 100 ml, selenium was quantified immediately by hydride generation/atomic absorption spectrometry. All the expected Se(IV) was found in all solutions. These results indicate

that the effect of an FEP combination with sulfuric acid was partial oxidation of Se(IV) to Se(VI), which is not reduced by tetrahydroborate. Moreover, the FEP container effect may be different from one container to another, as experienced in this work. Until this phenomenon is better understood and can be controlled, the use of combinations of Se(IV), FEP, and sulfuric acid should be avoided in sample preparation methods when selenium(IV) is required for the final measurement step.

REFERENCES

1 V. Cheam and H. Agemian, Anal. Chim. Acta, 113 (1980) 237.
2 G. A. Cutter, Anal. Chim. Acta, 98 (1978) 59.
3 C. I. Measures and J. D. Burton, Anal. Chim. Acta, 120 (1980) 177.
4 H. J. Robberecht and R. E. Grieken, Anal. Chem., 52 (1980) 449.
5 H. Uchida, Y. Shimoishi and K. Toei, Environ. Sci. Technol., 14 (1980) 541.
6 A. D. Shendrikar and P. W. West, Anal. Chim. Acta, 74 (1975) 189.
7 F. D. Pierce and H. R. Brown, Anal. Chem., 48 (1976) 693.
8 F. D. Pierce and H. R. Brown, Anal. Chem., 49 (1977) 1417.
9 R. W. Karin, J. A. Buono and J. L. Fasching, Anal. Chem., 47 (1975) 2296.
10 J. R. Moody and R. M. Lindstrom, Anal. Chem., 49 (1977) 2264.
11 C. H. Wang and D. L. Willis, Radiotracer Methodology in Biological Science, Prentice-Hall, Englewood Cliffs, NJ, 1965.
12 A. A. Ray (Ed.), SAS User's Guide: Statistics, SAS Institute, Cary, NC, 1982.
13 G. W. Snedecor and W. G. Cochran, Statistical Methods, 6th edn., Iowa State University Press, Ames, IA, 1967.
14 H. Scheffe, The Analysis of Variance, Wiley, New York, Ch. 10, 1959.

Analytica Chimica Acta, 161 (1984) 393—396
Elsevier Science Publishers B.V., Amsterdam — Printed in The Netherlands

Short Communication

BIOCHEMICAL DATA-PROCESSING WITH MICROCOMPUTERS
Part 3. On-line Data Acquisition from a Continuous Flow Analyzer

MICHAEL G. GORE and IAN G. GILES*

Department of Biochemistry, University of Southampton, Southampton SO9 3TU (Great Britain)

(Received 12th March 1984)

Summary. A program, written in BASIC, is described which allows data acquisition from a continuous flow analyzer. The program was developed for a readily available microcomputer, but should be easily modified for use on similar machines. Once the peak height has been measured, the concentration of the analyte is calculated by reference to a previously defined calibration. The program is designed to handle data from more than one channel, although there is a practical limit of 3—4 simultaneously active channels. The results of the separate assays are collated and printed as a group for each specimen, even when the analytical methods require different times for completion.

Continuous flow analyzers are indispensable for routine assays of one particular substance in large numbers of samples. The substance of interest is usually detected spectrophotometrically after suitable reactions. The results are normally presented as a recorder trace showing a series of peaks, the heights of which are proportional to the amount of product formed in the chemical reaction(s). In ideal conditions, the trace would show a series of perfect square waves, each corresponding to a different specimen; in practice, curves are produced because of lateral diffusion, but each sample zone gives a plateau region from which data can be gathered for quantitative purposes. The spacing of adjacent plateau regions is dictated by the rate of sampling.

If more than one compound is of interest in a single specimen, the sample aliquot is split into two (or more) streams, each of which is fed into parallel analytical systems, separate traces on one (or more) chart recorders being obtained. The separate traces, therefore, have to be collected to extract the information relating to a single specimen. This can cause difficulty if the times required to produce the coloured product differ between the various analytical channels.

The computer program described here samples data from several (3—4) analytical channels, calculates the amount of substance present by reference to a predefined calibration graph, and collates the data such that all the results relating to one specimen are printed together. The program also includes routines to store the collated data on disc (or cassette tape) for archive purposes.

0003-2670/84/$03.00

Experimental

Equipment. The Technicon AAII AutoAnalyzer used was equipped with an automatic sampler IV, peristaltic pump III, various assay cartridges, and colorimeters giving 0—60-mV output. The output voltage is linearly proportional to the absorbance of the solution in the flow cell. A linear amplifier was used to provide a voltage compatible with the input requirements (0—10 V) of the 16-channel, 8-bit ADC (analog-to-digital converter) interfaced between the colorimeter and the Commodore 3000 series PET microcomputer used. The ADC employed (3D Digital Design & Development, London) has a conversion time of 10 μs, although the maximum effective sampling rate is reduced to 60 samples per second when driven from BASIC. A single channel of the ADC is used for each detector. The PET "jiffy" clock (incremented every 1/60th second) was used for timing. Results were printed out on a Commodore 4022 dot-matrix printer.

Reagents and methods. All reagents were purchased from BDH Chemicals. Standard analytical methods were employed [1—4].

Program and implementation

In normal usage, continuous flow analyzers have a sample throughput of 60—150 h^{-1}, the rate depending on the chemistry of the assays used. In a single-channel system, successive plateaux are separated by 25—60 s and there is ample time for a microcomputer using a relatively slow BASIC interpreter to sample, store, process, and print out results between peaks. When the program is applied with a multichannel system, the maximum number of channels (3—4) is actually set by the ability of the operator to synchronize the system.

The algorithm used is shown in Table 1. There is an initial dialogue during which operational parameters (including time between peaks, number of analytical channels, and composition of the calibration graph) are specified. The program then waits for the operator to synchronize the autosampler timing cycle with the computer timing cycle. This is achieved by pressing a given key once the plateau region of the first peak to emerge has appeared on the chart recorder. Subsequently, the computer samples (and stores) the output voltage of the detector at the predefined rate, e.g., every 60 s.

Synchronization of two (or more) channels is achieved by pressing a specified key (1, 2, ...) when the relevant recorder indicates emergence of the first peak from that analytical channel. Once a channel has been synchronized, samples are taken at the predefined rate, even if other channels have still to emerge. The peak height data are stored in a two-dimensional array of dimensions (number of analytical channels by maximum number of specimens). An array of pointers is used to indicate where the next data point for each channel is to be stored. It is then a relatively minor problem to print out the data for each specimen, once the last result for that specimen has been collected.

The program continues either until a predetermined number of specimens

TABLE 1

Algorithm of the program used for peak height determination and collation of data

```
Procedure SAMPLE
BEGIN
number of peaks [channel]: = number of peaks [channel] + 1
next time [channel]: = next time [channel] + time between peaks
peak height [number of peaks [channel], channel]: = average of 30 ADC (channel)
IF (number of peaks [channel] < = number of initial standards) THEN update regression accumulators for this channel
IF (number of peaks [channel] = number of initial standards) THEN calculate regression coefficients for this channel
IF (channel = last channel started) AND
(number of channels started = number of channels requested) THEN PRINT RESULTS
END

BEGIN                                   (Main Program)
perform initialisation dialogue
number of channels started: = 0
FOR channel: = 1 TO number of channels requested DO
BEGIN
number of peaks [channel]: = 0
next time [channel]: = 0
channel start order [channel]: = 0
quadratic regression accumulators [channel]: = 0
END

REPEAT
i: = 0
REPEAT
IF (number of channels started < number of channels requested) AND (keypressed) THEN
BEGIN
channel: = key
IF (channel not already started) THEN
BEGIN
next time [channel]: = current time
number of channels started: = number of channels started + 1
last channel started: = channel
channel start order [number of channels started]: = channel
SAMPLE
END
END
i: = i + 1
channel: = channel start order [i]
IF (current time > = next time [channel]) AND
(number of peaks [channle] < number of peaks requested) THEN SAMPLE
UNTIL (i = number of channels started)
UNTIL (keyboard abort) OR
(number of peaks [last channel started] = number of peaks requested)
END.
```

has been processed, or until the program is aborted by the operator. At this stage, the accumulated data, together with the relevant operating parameters can be stored to, or recalled from, either floppy disc or tape.

ADC conversion. When the output voltage of the detector is sampled, 30 consecutive conversions are performed and summed, the arithmetic mean being stored and used in subsequent calculations. The speed of this averaging is limited by the BASIC interpreter; about 0.5 s is needed. This step results in an improvement in the electronic signal-to-noise ratio of about 5.5, and the points have a temporal separation sufficient to filter out the higher frequency noise (e.g., 50 Hz).

Calibration. In order to convert the raw peak-height data into analytically meaningful units, reference is made to a calibration plot. In the version of the program used in this laboratory, calibration is obtained by the operator placing a predeclared number of standard solutions into the first few sample cups of the autosampler. The program uses the peak heights from these solutions to calculate the least-squares coefficients of an interpolating second-order (quadratic) polynomial. These coefficients are then used to convert subsequent peak heights to amount of material. This is then printed out only if it is between the limits of zero and the highest amount specified in the calibration curve, ensuring that all amounts output are the result of interpolation.

Discussion

The software can be modified easily to alter the presentation of the data. For example, the data may be printed only if certain threshold criteria are fulfilled, allowing the system to act as a filter for high or low concentrations of the substance(s) under test. Additionally, the program can be used to drive a signal-conditioning device to avoid losing information as peaks approach full scale deflection. The need to divide the amplification factor of the signal-conditioning amplifier can be ascertained from the magnitude of the ADC value itself; when this exceeds a given maximum value, an internal flag is set and one bit of the peripheral user port (connected to the 6522 VIA) is set high. A TTL sensor monitoring this line actuates a relay when this bit is set, resulting in a reduction in the gain of the conditioning amplifier. Thus it is possible to have an easily implemented software control of the voltage input to the ADC.

REFERENCES

1 J. H. Hagen and P. B. Hagen, Can. J. Biochem. Physiol., 40 (1962) 1129.
2 K. Stewart, Anal. Biochem., 51 (1973) 11.
3 Q. W. Osborn, D. E. Lemmel and R. L. Downey, Environ. Sci. Technol., 8 (1974) 363.
4 M. G. Gore, Anal. Biochem., 75 (1976) 604.

ANALYTICA CHIMICA ACTA, VOL. 161 (1984)

AUTHOR INDEX

ELSEVIER is going ELSWARE

'**Elsware**' with its software.
Elsevier, publisher of many journals in all of the major scientific fields, is now going elsewhere with the launch of its first series of programs for both mini and micro-computers.

Unlike other software publishers, we have some unique features .....

programs are extensively refereed and operationally tested; program manuals usually include source code listings; free updates are provided for a year and comprehensive information is available before ordering.

PROGRAMS AVAILABLE

REFVALUE: calculates reference intervals from total hospital-patients laboratory data. (Baadenhuysen and Smit) **for PDP and HP 85 (and in prep. for IBM-PC).**
Price: Mini computer US$ 1080,00
Micro computer US$ 500,00

BALANCE: a program to statistically compare two series of measurements (Massart) **for IBM-PC and APPLE.**
Price: US$ 150,00

CLEOPATRA: Chemometrics Library: an Extendable set Of Programs as an Aid in Teaching, Research and Application. (Kateman) **for HP 9845 B (and in prep. for IBM-PC).**
Price: US$ 600,00

INSTRUMENTUNE-UP: helps the user to improve the performance of common scientific laboratory instruments (Deming and Morgan) **for IBM-PC and APPLE.**
Price: US$ 150,00

and in preparation:

CHEOPS: CHEmometrical OPtimization by Simplex. The program offers an intelligent, sequential experimental plan, based on the modified or super-modified simplex method. It optimizes the response of a system by varying up to ten instrumental parameters.

CLUE: a program for heirarchical divisive clustering.

E
ESS
ESSESSESSESSESSESS

Please send me further information on:

☐ REFVALUE ☐ BALANCE ☐ CHEOPS
☐ CLEOPATRA ☐ INSTRUMENTUNE-UP ☐ CLUE

ESS
ELSEVIER SCIENTIFIC SOFTWARE

Name _____
Address _____
City _____ Country _____

send this coupon to:

Keith Foley, Elsevier Scientific Software,
P.O. Box 330, 1000 AH Amsterdam,
The Netherlands. (Tel.: 020 - 5803 447)

or:
John Tagler, Elsevier Scientific Software (NASD),
52 Vanderbilt Ave, New York, NY 10017.
(Tel.: 212 867 9040)

(Continued from inside back cover)

0003-2670/84/$03.00

Printed in The Netherlands

(Continued from outside back cover)

(Continued on facing page)

CONTENTS

(Abstracted, Indexed in: Anal. Abstr.; Biol. Abstr.; Chem. Abstr.; Curr. Contents Phys. Chem. Earth Sci.; Life Sci.; Index Med.; Mass Spectrom. Bull.; Sci. Citation Index; Excerpta Med.)

(Continued on inside back cover)